

DISSERTATION

AEROSOL SINGLE-SCATTERING ALBEDO RETRIEVAL OVER NORTH AFRICA  
USING CRITICAL REFLECTANCE

Submitted by

Kelley C. Wells

Department of Atmospheric Science

In partial fulfillment of the requirements for the degree of

Doctor of Philosophy

Colorado State University

Fort Collins, Colorado

Fall 2010

Doctoral Committee:

Department Head: Richard Johnson

Advisor: Sonia Kreidenweis

Graeme Stephens

Jeffrey Collett

Lorraine Remer

Jennifer Peel

## ABSTRACT

### AEROSOL SINGLE-SCATTERING ALBEDO RETRIEVAL OVER NORTH AFRICA USING CRITICAL REFLECTANCE

The sign and magnitude of the aerosol radiative forcing over bright surfaces is highly dependent on the absorbing properties of the aerosol. Thus, the determination of aerosol forcing over desert regions requires accurate information about the aerosol single-scattering albedo (SSA). However, the brightness of desert surfaces complicates the retrieval of aerosol optical properties using passive space-based measurements. The aerosol critical reflectance is one parameter that can be used to relate top-of-atmosphere (TOA) reflectance changes over land to the aerosol absorption properties, without knowledge of the underlying surface properties or aerosol loading. Physically, the parameter represents the TOA reflectance at which increased aerosol scattering due to increased aerosol loading is balanced by increased absorption of the surface contribution to the TOA reflectance. It can be derived by comparing two satellite images with different aerosol loading, assuming that the surface reflectance and background aerosol are similar between the two days.

In this work, we explore the utility of the critical reflectance method for routine monitoring of spectral aerosol absorption from space over North Africa, a region that is predominantly impacted by absorbing dust and biomass burning aerosol. We derive the critical reflectance from Moderate Resolution Spectroradiometer (MODIS) Level 1B

reflectances in the vicinity of two Aerosol Robotic Network (AERONET) stations: Tamanrasset, a site in the Algerian Sahara, and Banizoumbou, a Sahelian site in Niger. We examine the sensitivity of the critical reflectance parameter to aerosol physical and optical properties, as well as solar and viewing geometry, using the Santa Barbara DISORT Radiative Transfer (SBDART) model, and apply our findings to retrieve SSA from the MODIS critical reflectance values. We compare our results to AERONET-retrieved estimates, as well as to measurements of the TOA albedo and surface fluxes from the Geostationary Earth Radiation Budget (GERB) experiment, Atmospheric Radiation Measurement (ARM) program, and Clouds and the Earth's Radiant Energy System (CERES) data. Spectral SSA values retrieved at Banizoumbou result in TOA forcing estimates that agree with CERES measurements within  $\pm 5 \text{ W m}^{-2}$  for dusty conditions; however, the retrieved SSA translates to a much larger positive TOA forcing than CERES in the presence of dust-biomass burning mixtures. At Tamanrasset, the retrieval captures changes in aerosol absorption from day to day, but the SSA appears to be biased high when compared to AERONET and CERES. This may be due to the higher surface reflectance in this region, an overestimation of the dust aerosol size, or changing background aerosol between the clean and polluted day. Our retrieval results indicate that we can be most confident in the retrieved SSA for scattering angles between  $120^\circ$  and  $160^\circ$ , satellite view angles less than  $\sim 45^\circ$ , and in cases when the background aerosol on the cleaner day is non-absorbing.

## ACKNOWLEDGEMENTS

I have been so lucky to have such wonderful mentors and collaborators throughout my time at CSU. First, I would like to thank my advisor, Sonia Kreidenweis, for her guidance and enthusiastic support of me and this project, for helping me to always find new ways to look at an existing problem, and for her warm sense of humor. Many thanks also to committee member Lorraine Remer for her endless encouragement and helpful input, and for keeping me motivated with the occasional ice cream. I am very grateful to Vanderlei Martins for the many helpful conversations and analysis tools—without his critical reflectance expertise this work would not have been possible. Thanks to committee member Graeme Stephens for his support and ideas, and for his help with numerous radiative transfer problems throughout this project. I also sincerely thank my other committee members, Jeffrey Collett and Jennifer Peel, for their expertise and help in refining this work.

Thanks to Rob Levy and Shana Mattoo for their help with the details of the MODIS operational aerosol retrieval, and to Tom Eck for his help in interpreting the AERONET data. Thanks also to Li Zhu for her suggestions on making my analysis more efficient, and for her efforts in our method comparison. Additionally, I would like to thank Didier Tanré, Emilio Cuevas-Agullo, and Mohamed Mimouni for their efforts in establishing and maintaining the Banizoumbou and Tamanrasset AERONET sites. Thanks to Ben Johnson for providing data from the DABEX campaign, and for his help

with its interpretation. I also wish to extend thanks to Mark Ringerud for help with computing and data management, and to Chris Kummerow for providing additional computing resources for this work. Furthermore, my utmost appreciation goes to everyone in the CSU Atmospheric Chemistry groups—particularly those in the Kreidenweis group—for their support, advice, and friendship during my time at CSU and beyond. Finally, I would like to thank my family for their unyielding support, love, and encouragement throughout this work and all the years leading up to it. My sincerest thanks go especially to John for being so willing to go on this adventure with me. I would not have made it to this point without him at my side.

This work was generously supported by the Center for Earth Atmosphere Studies through NASA grant NNG06GB41G.

## TABLE OF CONTENTS

<b>1</b>	<b>INTRODUCTION.....</b>	<b>1</b>
1.1	OVERVIEW OF AEROSOL INTERACTIONS WITH RADIATION .....	2
1.1.1	<i>Definition of Optical Parameters.....</i>	2
1.1.2	<i>Impact of Aerosols on Earth's Energy Budget over Land .....</i>	5
1.2	MEASURING AEROSOL ABSORPTION REMOTELY.....	8
1.2.1	<i>Geometry Considerations .....</i>	8
1.2.2	<i>Satellite-Based Retrievals.....</i>	10
1.2.2.1	TOMS AI.....	10
1.2.2.2	DeepBlue.....	11
1.2.3	<i>Ground-Based Retrievals.....</i>	12
1.3	OVERVIEW OF AEROSOL IMPACTS IN NORTH AFRICA .....	13
1.3.1	<i>Aerosol Types and Seasonality .....</i>	13
1.3.2	<i>Physical and Optical Properties.....</i>	18
1.4	CRITICAL REFLECTANCE PRINCIPLE.....	21
1.4.1	<i>Definition and Assumptions .....</i>	21
1.4.2	<i>Foundational Work and Applications.....</i>	23
1.4.2.1	Demonstration of Principle.....	23
1.4.2.2	Saharan Dust Absorption.....	24
1.4.3	<i>Other Applications of the Principle .....</i>	25
1.4.3.1	Average Saharan Dust Absorption .....	26
1.4.3.2	Aerosol Properties over Saudi Arabia.....	27
1.5	OBJECTIVES.....	27
<b>2</b>	<b>RETRIEVAL METHOD AND SENSITIVITY.....</b>	<b>29</b>
2.1	OBSERVATIONS .....	29
2.1.1	<i>The MODIS Instrument.....</i>	29
2.1.2	<i>Processing MODIS Level 1B Data .....</i>	30
2.1.2.1	Correction for Gaseous Absorption and Clouds .....	31
2.1.2.2	Remapping.....	33
2.1.2.3	Data Fitting and Assumptions .....	34
2.1.2.4	Post Processing and Error Estimation.....	36
2.2	FORWARD MODEL.....	37
2.2.1	<i>Radiative Transfer Model Set-Up .....</i>	38
2.2.2	<i>Aerosol Models and Phase Function Calculations .....</i>	40
2.2.3	<i>Critical Reflectance LUT Building .....</i>	42
2.3	INVERSION.....	47
2.4	LUT RESULTS: IMPLICATIONS FOR SENSITIVITY TO AEROSOL CHARACTERISTICS .....	49
2.4.1	<i>Sensitivity to Solar and Viewing Geometry.....</i>	49
2.4.2	<i>Sensitivity to Size and Shape.....</i>	59
2.4.3	<i>Sensitivity to Fitting Method.....</i>	63
2.5	SENSITIVITY STUDIES IN SBDART: IMPLICATIONS FOR FORWARD MODEL UNCERTAINTIES ....	63
2.5.1	<i>Sensitivity to Assumed Refractive Index.....</i>	63
2.5.2	<i>Sensitivity to Varying AOD.....</i>	66
2.5.3	<i>Sensitivity to Vertical Stratification .....</i>	69
2.5.4	<i>Sensitivity to Number of Streams Used in SBDART.....</i>	71
2.5.5	<i>Summary of Findings .....</i>	73

<b>3</b>	<b>CASE STUDY RESULTS .....</b>	<b>74</b>
3.1	TAMANRASSET AERONET SITE.....	75
3.1.1	<i>MODIS Reflectances</i> .....	75
3.1.2	<i>Critical Reflectance and SSA Results</i> .....	82
3.1.2.1	SSA Image Retrievals.....	82
3.1.2.2	Spectral SSA Retrievals near AERONET Site .....	86
3.2	BANIZOUMBOU AERONET SITE .....	98
3.2.1	<i>MODIS Reflectances</i> .....	98
3.2.2	<i>Critical Reflectance and SSA Results</i> .....	102
3.2.2.1	SSA Image Retrievals.....	102
3.2.2.2	Spectral SSA Retrievals near AERONET Site .....	104
3.3	DISCUSSION OF CASE STUDY RESULTS.....	120
3.3.1	<i>Terra-Aqua and Three-Day Comparisons</i> .....	120
3.3.2	<i>SSA Relationships with Geometry</i> .....	124
<b>4</b>	<b>UNCERTAINTY ANALYSIS AND FORCING ESTIMATION.....</b>	<b>137</b>
4.1	OBSERVATION UNCERTAINTIES.....	137
4.1.1	<i>The AOD is Constant over the Retrieval Pixel</i> .....	137
4.1.2	<i>Surface Reflectance is Invariant between the Polluted and Clean day</i> .....	141
4.1.3	<i>The Surface Reflectance is Lambertian</i> .....	144
4.1.4	<i>Background Aerosol and Gases are Similar between the Polluted and Clean Day</i> .....	150
4.2	FORWARD MODEL UNCERTAINTIES .....	156
4.2.1	<i>Assumed Particle Properties</i> .....	156
4.2.1.1	Size.....	156
4.2.1.2	Refractive Index and Sphericity .....	163
4.2.1.3	Aerosol Properties are Independent of AOD .....	166
4.2.2	<i>Aerosol Mixtures and Vertical Stratification: 19 January 2006 Case Study</i> .....	170
4.3	AEROSOL FORCING ESTIMATION .....	175
4.3.1	<i>Tamanrasset</i> .....	175
4.3.2	<i>Banizoumbou</i> .....	185
<b>5</b>	<b>SUMMARY AND FUTURE WORK .....</b>	<b>198</b>
5.1	KEY FINDINGS .....	199
5.2	SUGGESTIONS FOR CRITICAL REFLECTANCE APPLICATION .....	204
5.3	FUTURE WORK .....	205
	<b>APPENDIX A LUT RESULTS AT 0.553 <math>\mu\text{M}</math>.....</b>	<b>216</b>
	<b>APPENDIX B SENSITIVITY TEST RESULTS AT 0.553 <math>\mu\text{M}</math>.....</b>	<b>253</b>
	<b>APPENDIX C IMAGE RETRIEVALS AT 0.553 <math>\mu\text{M}</math>.....</b>	<b>272</b>
	<b>APPENDIX D SPECTRAL RESULTS NEAR AERONET SITES .....</b>	<b>315</b>

# 1 Introduction

Estimating the climate effects of atmospheric aerosol with models and remote sensing techniques has been of much interest to climate scientists in recent decades. The wealth of global datasets currently available from ground and space-borne sensors provides the possibility of quantifying the perturbation of both solar and terrestrial radiation due to particulate matter of both anthropogenic and natural origin. There have been significant advances in retrieving the physical and optical properties of aerosols from remote sensing measurements (e.g. Remer et al., 2005), and in using this information to estimate the climate effects of aerosols in clear sky conditions over ocean. The Intergovernmental Panel on Climate Change (IPCC) 4<sup>th</sup> Assessment report indicates that there is general agreement on the effect of aerosol over ocean, and that it is of similar magnitude but opposite sign as the greenhouse gas forcing (IPCC, 2007). However, the effects of aerosols over land are not as well known (Yu et al., 2006), especially over bright land surfaces where it is difficult to separate the effects of surface and aerosol reflectance in passive spectral measurements (e.g. Kaufman et al., 1997).

Over bright land surfaces, the climate effects of aerosol can vary on a regional scale, and depend strongly on the absorption properties of the aerosol. Over dark surfaces, aerosols will cool the earth-atmosphere system, and the effect is driven solely by aerosol loading; over brighter surfaces, however, aerosols could exert a warming effect if they absorb enough radiation as to appear darker than the underlying surface

(Kaufman, 1987). Additionally, bright surfaces such as deserts can be sources of mechanically-generated dust aerosols, which are present at sizes large enough to exert a significant longwave direct effect (e.g. Haywood et al., 2005; Zhang and Christopher, 2003). Thus, the improvement of aerosol retrievals over land, and deserts specifically, remains an important area of research for the remote sensing community.

## **1.1 Overview of Aerosol Interactions with Radiation**

Aerosols interact with solar and (for larger particles) terrestrial radiation by both scattering and absorption. These effects are a function of the particle size and optical properties, which are dependent upon their formation mechanism and chemical make-up. The following section defines some of the parameters that are commonly used to describe the interaction of aerosol with radiation, particularly when this interaction is being sensed remotely using satellite and ground-based measurement platforms.

### **1.1.1 Definition of Optical Parameters**

The complex refractive index contains the most fundamental information about the interaction of aerosol with radiation, as it is an intrinsic property of the aerosol composition. It varies as a function of the wavelength of incident light, and is defined as:

$$m = n - ik \tag{1.1}$$

where  $n$  is the real part of the refractive index, and  $k$  is the imaginary part of the refractive index. Both quantities are unitless. The real part of the refractive index is the ratio of the speed of light in a vacuum to the speed of light through the medium of interest; the higher the value, the greater the medium affects the initial speed of the wave.

The imaginary part of the refractive index indicates the amount of absorption that occurs when light interacts with the medium.

The aerosol extinction coefficient,  $b_{ext}$ , is a function of the complex refractive index, as well as the particle size and wavelength of incident light. It has units of inverse length ( $m^{-1}$ ), and is defined for a population of particles of varied sizes as:

$$b_{ext}(\lambda) = \int_{D_p^{\min}}^{D_p^{\max}} \frac{\pi D_p^2}{4} Q_{ext}(m, x) n(D_p) dD_p \quad (1.2)$$

where  $D_p$  is the particle diameter,  $n(D_p)$  is the number concentration of particles of a size  $D_p$  ( $cm^{-3}$ ), and  $Q_{ext}$  is the dimensionless extinction efficiency, which is a function of the complex refractive index and the aerosol size parameter ( $x = \pi D_p / \lambda$ ).  $D_p^{\min}$  and  $D_p^{\max}$  represent the upper and lower limits of the aerosol size distribution, respectively. The extinction coefficient represents the sum of the scattering and absorption coefficients ( $b_{scat} + b_{abs}$ ).

The single-scattering albedo (SSA) describes the relative effects of scattering and absorption by an aerosol population. It has no units, as it is simply the ratio of the scattering to extinction coefficients:

$$SSA = \frac{b_{scat}}{b_{ext}} \quad (1.3)$$

Thus, a SSA value of 1.0 corresponds to a purely-scattering aerosol, and lower values correspond to aerosol that absorbs some fraction of incoming radiation. SSA values in this document will typically represent column-integrated values. Typical column-integrated visible SSA values in the atmosphere range from  $\sim 0.7$  for urban aerosol with a high black carbon content to close to 1.0 for sulfate-dominated aerosol.

The aerosol optical depth (AOD) is the most common parameter derived from satellite measurements of aerosol radiative effects, as it is a simple, unitless measure of the total column aerosol extinction. It is often represented by a lowercase tau and is defined as the vertically-integrated aerosol extinction coefficient from the surface to the top-of-atmosphere (TOA):

$$\tau_a = \int_0^{TOA} b_{ext}(z) \cdot dz \quad (1.4)$$

The scattering phase function,  $P(\Theta)$ , describes the angular intensity of light scattered by a population of particles. It is unitless, as it is normalized by the integrated scattered intensity over all angles:

$$P(\Theta) = \frac{I(\Theta)}{\int_0^\pi I(\Theta) \sin \Theta d\Theta} \quad (1.5)$$

where  $I(\Theta)$  is the intensity at scattering angle  $\Theta$ . The scattering angle is defined with respect to the incoming radiation, so that  $\Theta = 0^\circ$  represents the forward scattering direction, and  $\Theta = 180^\circ$  represents the backscattering direction. Because it is dependent on the aerosol refractive index, the scattering phase function varies with wavelength, as well as particle size.

Another parameter commonly derived from remotely-sensed observations is the Angstrom exponent,  $\alpha$ . The Angstrom exponent describes the wavelength dependence of the aerosol extinction, such that

$$b_{ext} \approx \lambda^{-\alpha} \quad (1.6)$$

The angstrom exponent can be calculated from two measures of the extinction coefficient, or AOD, at two different wavelengths using Equation 1.7:

$$\alpha = -\frac{\log\left(\frac{b_{ext_1}}{b_{ext_2}}\right)}{\log\left(\frac{\lambda_1}{\lambda_2}\right)} \quad (1.7)$$

Values of  $\alpha$  generally range from 3 to 4 for very small particles, and from 0 to 1 for coarse particles (Eck et al., 1999). The presence of very large particles can result in  $\alpha$  values that are less than 0.

The role of aerosols in the earth's energy budget will be discussed in more detail in the following section, so we will simply define the most common terms used to describe aerosol climate effects here. The direct climate forcing of aerosols at TOA is simply defined as the change in the radiative flux ( $\text{W m}^{-2}$ ) at TOA:

$$\Delta F_{TOA} = F_{clear\uparrow} - F_{aer\uparrow} \quad (1.8)$$

where  $F_{clear}$  is the upwelling flux in the absence of aerosol, and  $F_{aer}$  is the upwelling flux over the aerosol plume. The climate forcing of aerosols at the surface is simply defined as the difference between the fluxes incident on the surface in polluted and clean conditions:

$$\Delta F_{SFC} = F_{aer\downarrow} - F_{clear\downarrow} \quad (1.9)$$

The forcing efficiency of aerosols is sometimes used in lieu of the forcing to describe the effect of aerosols that is independent of their atmospheric loading:

$$E = \frac{\Delta F}{\tau_a} \quad (1.10)$$

### 1.1.2 Impact of Aerosols on Earth's Energy Budget over Land

The total upward radiance,  $I$  ( $\text{W m}^{-2} \text{sr}^{-1}$ ), at the top of the Earth's atmosphere contains contributions from both the atmosphere and the underlying surface. Figure 1.1 shows the components of the upward radiance above an atmosphere containing aerosol

(and gases) with a reflecting surface below. Beam 1 represents the contribution from aerosol and gaseous scattering to the upward radiance. Beam 2 represents radiation that was redirected due to atmospheric scattering, reflected off the surface, and transmitted back through the atmosphere. This redirected beam also represents the diffuse component of solar radiation that reaches the Earth's surface. Beam 3 represents radiation that is transmitted through the atmosphere, reflected off the surface, and transmitted back through the atmosphere. This beam represents the direct component of solar radiation reaching the Earth's surface. Beam 4 represents radiation that undergoes multiple scattering between the surface and the aerosol layer before it is transmitted back through the atmosphere.

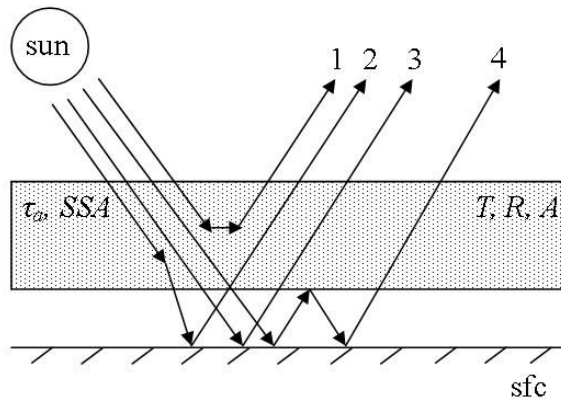


Figure 1.1: Components of the upward radiance at TOA above an atmosphere containing aerosol and gases.

The propagation and attenuation of radiation due to interactions with aerosols in the layer is governed by the transmissivity ( $T$ ), reflectivity ( $R$ ), and absorptivity ( $A$ ) of that layer. The transmissivity (and the corresponding downwelling flux at the surface) is simply proportional to  $\tau_a$ , the absorptivity is proportional to the product of  $\tau_a$  and the co-albedo ( $1-SSA$ ), and the reflectivity is proportional to the aerosol backscatter. The backscatter is a function of both  $\tau_a$  and  $SSA$  (as well as the aerosol phase function). A purely scattering aerosol can result in the same backscatter at low AOD as an absorbing

aerosol at high AOD. At low surface reflectivity, the aerosol layer reflectivity dominates the total upward radiance at TOA; at higher surface reflectivity the contribution of the surface becomes increasingly important.

The TOA upward flux,  $F_{\uparrow}$ , is simply the upward radiance, integrated over all solid angles (and wavelengths in the case of a broadband flux) projected onto a horizontal surface. As defined in Section 1.1.1, TOA aerosol forcing,  $\Delta F_{\text{TOA}}$ , is simply the difference between the TOA upward flux in a clean condition and the TOA upward flux in a polluted condition. Over land, the sign of  $\Delta F_{\text{TOA}}$  will depend on SSA. The SSA value at which the transition point from TOA cooling to TOA warming occurs has been referred to as the critical SSA (e.g. Liao and Seinfeld, 1998). On a global average, Hansen et al. (1997) determined that the transition point between a cooling and a warming effect at TOA will occur for a visible SSA of  $\sim 0.91$  when one considers the effect of absorbing aerosols on cloud cover in climate models. Over bright desert surfaces the critical SSA can be higher, however, and on the order of values commonly accepted for dust aerosol. As a result, the TOA forcing over bright desert surfaces is very sensitive to small changes in absorption.

An example of this sensitivity was demonstrated in a modeling study of aerosol effects on the West African monsoon by Solmon et al. (2008). As shown in Figure 1.2, a SSA of 0.95 at  $0.55 \mu\text{m}$  (for dust aerosol with  $D_p < 1 \mu\text{m}$ ) results in a negative TOA forcing south of  $15^\circ \text{N}$ , a positive TOA forcing between  $15^\circ \text{N}$  and  $20^\circ \text{N}$ , and a near zero forcing north of this region. A 5% decrease in the SSA results in a positive forcing everywhere north of  $15^\circ \text{N}$ , altering atmospheric heating rates and modifying

precipitation patterns associated with the WAM. A 5% increase in the SSA results in a negative TOA forcing across the entire North African region.

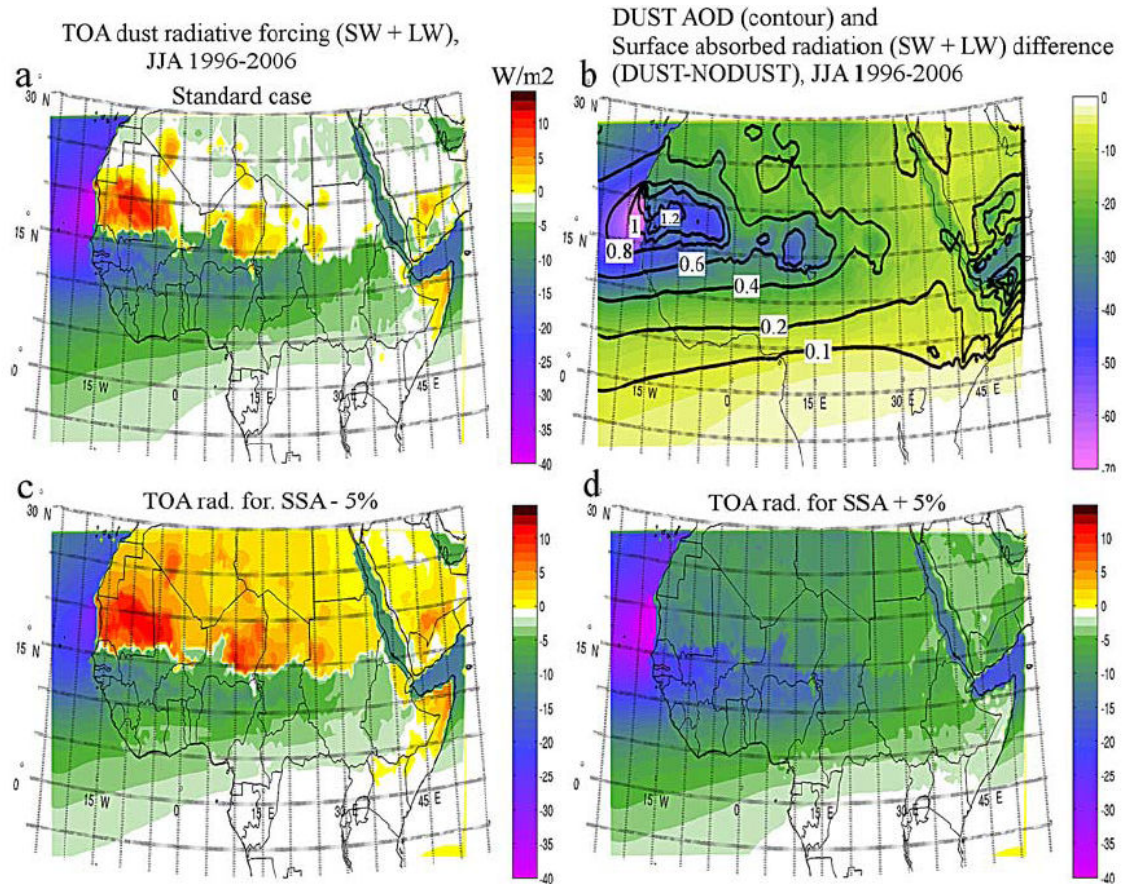


Figure 1.2: TOA SW + LW clear sky radiative forcing (a), AOD and surface absorbed SW + LW radiation difference (b), TOA radiative forcing for SSA - 5% (c), TOA radiative forcing for SSA + 5% (d). From Solmon et al. (2008)

## 1.2 Measuring Aerosol Absorption Remotely

### 1.2.1 Geometry Considerations

Before discussing remote-sensing retrieval methods in the following sections, and in subsequent chapters, it is helpful to define the frame of reference for passive remote sensing observations (in which the sun is the source of radiation). This document will use a terrestrial frame of reference, in which the sun and sensor positions are defined relative to an axis which is normal to the earth's surface. A depiction of this frame of reference is

displayed in Figure 1.3, where  $\theta$  and  $\theta_o$  are the sensor and solar zenith angle, respectively, and  $\varphi$  and  $\varphi_o$  are the sensor and solar azimuth angle.

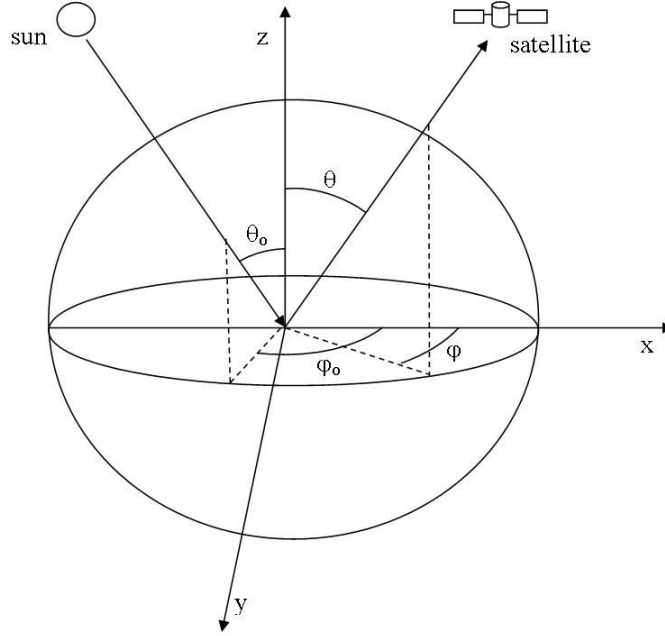


Figure 1.3: Depiction of the terrestrial frame of reference for satellite and solar positions.

A zenith angle of zero corresponds to the position which is directly overhead (also referred to as the nadir direction), a zenith angle of  $90^\circ$  corresponds to the direction along the horizon. The azimuth angle refers to the compass position of the sun or the sensor. The relative azimuth angle is defined relative to the forward scattering direction of the radiation, and is defined as:

$$\varphi_{rel} = |(\varphi_o - \varphi - 180)| \quad (1.11)$$

Thus, when the sun and sensor have the same azimuth angle, the relative azimuth is  $180^\circ$ ; when they are at opposite azimuth angles, their relative azimuth is  $0^\circ$ . The scattering angle that corresponds to a given sun-sensor geometry is calculated from the sun and sensor zenith angles and the relative azimuth angle as follows:

$$\cos \Theta = -\cos \theta_o \cos \theta + \sin \theta_o \sin \theta \cos \varphi_{rel} \quad (1.12)$$

Orbiting satellite-based instruments with a fixed viewing geometry can only sample one scattering angle at a time; many are designed to scan along or perpendicular to their orbit track in order to make measurements at a larger range of scattering angles. Because satellite-based instruments are measuring light scattered from the sun, their observations generally occur at backscattering angles ( $\Theta > 90^\circ$ ).

## 1.2.2 Satellite-Based Retrievals

While there have been several studies that propose a combination of measurements from multiple satellite sensors (e.g. Hu et al., 2007; Satheesh et al., 2009; Vermote et al., 2007) for real-time aerosol absorption monitoring from space, there are currently only a few existing single-sensor satellite retrieval algorithms that provide regular monitoring of aerosol absorption over land. Two examples will be discussed here.

### 1.2.2.1 TOMS AI

The Total Ozone Mapping Spectrometer (TOMS), an ultra-violet (UV) monitoring instrument that was mounted on three different polar-orbiting satellites, provided the first global information about the location and relative abundance of UV-absorbing aerosols in the atmosphere (Herman et al., 1997; Hsu et al., 1996). The TOMS Aerosol Index (AI) is a unitless measure of aerosol absorption, calculated as

$$AI = -100 \log_{10} \left[ \left( \frac{I_{340}}{I_{380}} \right)_{meas} - \left( \frac{I_{340}}{I_{380}} \right)_{calc} \right] \quad (1.13)$$

where  $I_{340}$  and  $I_{380}$  refer to the backscattered radiances at wavelengths of 340 and 380 nm, respectively. The ratio of the radiances measured at these two wavelengths is compared to a calculated ratio assuming a purely gaseous atmosphere. Negative values of AI

correspond to non-absorbing aerosols; positive values correspond to aerosols that absorb in the UV, a large component of which is dust and biomass burning emissions. While the AI is not in itself a measure of the absorbing efficiency of particles, attempts have been made to use the information to retrieve the aerosol complex index of refraction in the UV (e.g. Colarco et al., 2002). It should be noted, however, that the AI is sensitive to the height of the aerosol plume (Torres et al., 1998), which will affect the retrieval uncertainty.

### ***1.2.2.2 DeepBlue***

One method currently being applied to passive satellite measurements for absorption retrievals over land is the DeepBlue algorithm (Hsu et al., 2004; , 2006). The algorithm was designed specifically to tackle the problem of retrieving aerosol properties over bright desert surfaces by making use of the fact that desert surfaces are much darker in the blue channels (412 and 490 nm) than they are in the red. The operational retrieval algorithm for the Moderate Resolution Imaging Spectroradiometer (MODIS, see Chapter 2 for a full description) employs a dark-target approach (Kaufman et al., 1997) that relies on the reflectance at 2.1  $\mu\text{m}$  to be less than 0.25 (Remer et al., 2005). Over desert, the surface reflectance exceeds this value, and thus the contribution of the surface cannot be isolated from the reflectance of the earth-atmosphere system.

The DeepBlue algorithm uses a database of land surface reflectivity to construct look-up tables of the TOA reflectance ratio between the blue and red channels as a function of AOD and SSA. An example of the look-up table at 490 nm for dust aerosol is shown in Figure 1.4. The optical properties of the aerosol are assumed in the red channel,

and retrieved in the blue channels. Results from the retrieval have produced AODs that are generally within 20% of ground-based measurements.

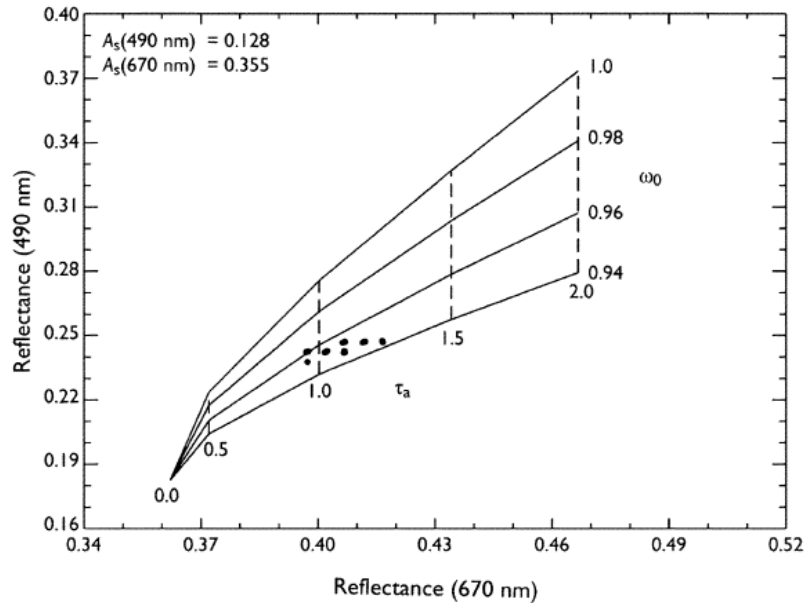


Figure 1.4: Simulated TOA reflectance for various AODs and SSAs at 490 nm versus 670 nm for dust aerosol. Reflectance data from SeaWiFS is shown by the filled circles. From Hsu et al. (2004).

### 1.2.3 Ground-Based Retrievals

The Aerosol Robotic Network (AERONET, Holben et al., 1998) is a global network of automated sunphotometers dedicated to aerosol monitoring and characterization at high temporal resolution and multiple spectral bands. Locations of the AERONET stations are shown in the map in Figure 1.5. The AERONET sunphotometers can sample a fuller range of scattering angles than satellite-based instruments (when the sun is at a lower elevation), given that they scan the sky throughout the day. Almicantar measurements scan the sky at the elevation of the sun, whereas principle plane measurements scan the sky in the plane of the sun. Direct sun measurements of spectral AOD are also made. An inversion combines these measurements to retrieve the columnar aerosol size distribution, refractive index, and SSA (Dubovik and King, 2000; Dubovik et al., 2002). Accuracy of the retrievals of these properties is found to improve with a larger

coverage of scattering angles of  $100^\circ$  or larger (Dubovik et al., 2000), and when the aerosol loading is higher ( $\text{AOD} > \sim 0.4$  at  $0.44 \mu\text{m}$ ).

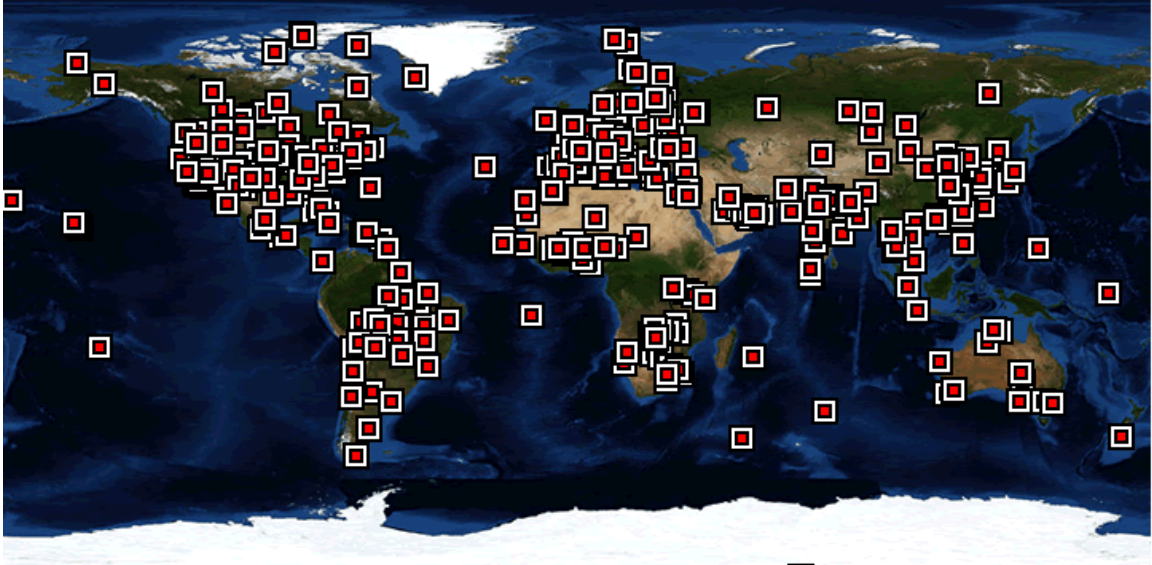


Figure 1.5: Locations of past and existing AERONET stations. From <http://aeronet.gsfc.nasa.gov>.

### 1.3 Overview of Aerosol Impacts in North Africa

#### 1.3.1 Aerosol Types and Seasonality

Much of our understanding about aerosol sources and transport in North Africa has come from remote sensing observations. The largest component of the aerosol mass in North Africa is dust aerosol, which originates from the region's numerous dust sources. TOMS AI data suggest that the majority of airborne dust in North Africa (and the world) originates in topographical lows, where alluvial flows are collected from wadi beds and salt playas (Prospero et al., 2002). Nearly all of the active dust sources in North Africa are located north of  $15^\circ \text{N}$ , where annual rainfall is less than  $200 \text{ mm yr}^{-1}$  (Figure 1.6). The single largest source in the region is the Bodele depression in Chad, as indicated by the near-persistent frequency of TOMS AI values exceeding 1.0 (Figure 1.6, region near  $15^\circ \text{N}$ ,  $15^\circ \text{E}$ ), and by visibility data from a nearby meteorological station which

show significant visibility reduction throughout the year, with some decreased frequency in the fall months (Mbourou et al., 1997).

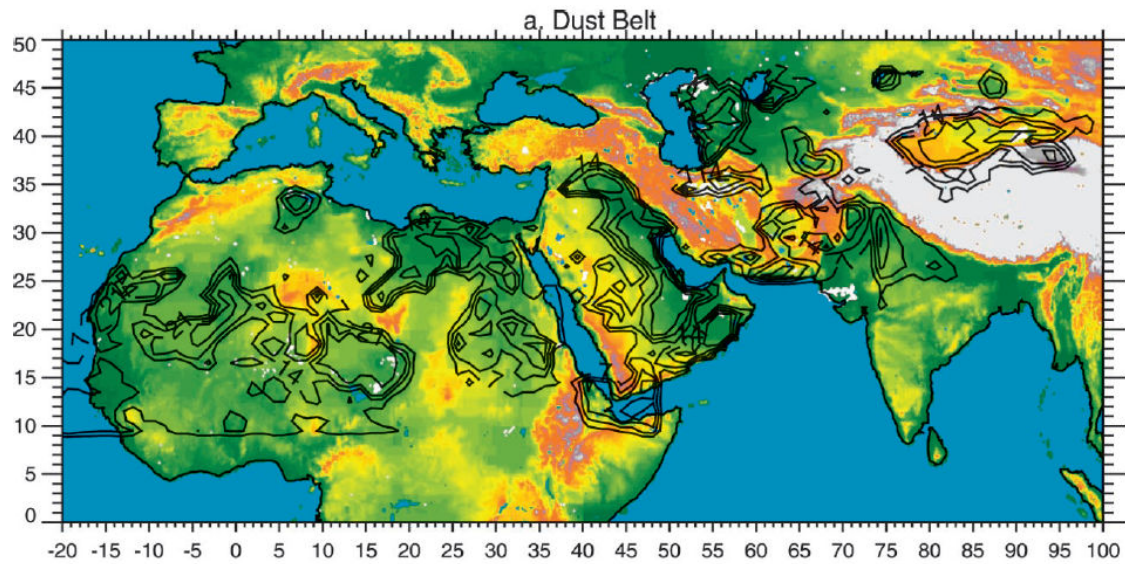


Figure 1.6: Map of dust sources and elevation (shaded colors) in the global dust belt. Contours are the mean values of frequency of days per month with TOMS AI > 1.0. From Prospero et al. (2002).

The seasonality and interannual variability of dust emissions from North African sources is demonstrated in Figure 1.7. Dust activity begins at low latitudes in the winter months, when strong surface winds activate production in the Bodele depression (Washington and Todd, 2005; Washington et al., 2006). This dust is transported across the Atlantic to South America (Prospero et al., 1981), serving as an important source of nutrients for the Amazon basin (Koren et al., 2006). Dust activity shifts northward, and also exhibits the largest spatial extent, in the spring and summer months. Strong surface heating results in rapid convective mixing that activates additional sources in western North Africa. As summer daytime boundary layers in this region extend to 600 millibars on average (Parker et al., 2005), dust is easily lofted to heights of 3-5 km, where it is transported across the Atlantic to North America (e.g. Perry et al., 1997).

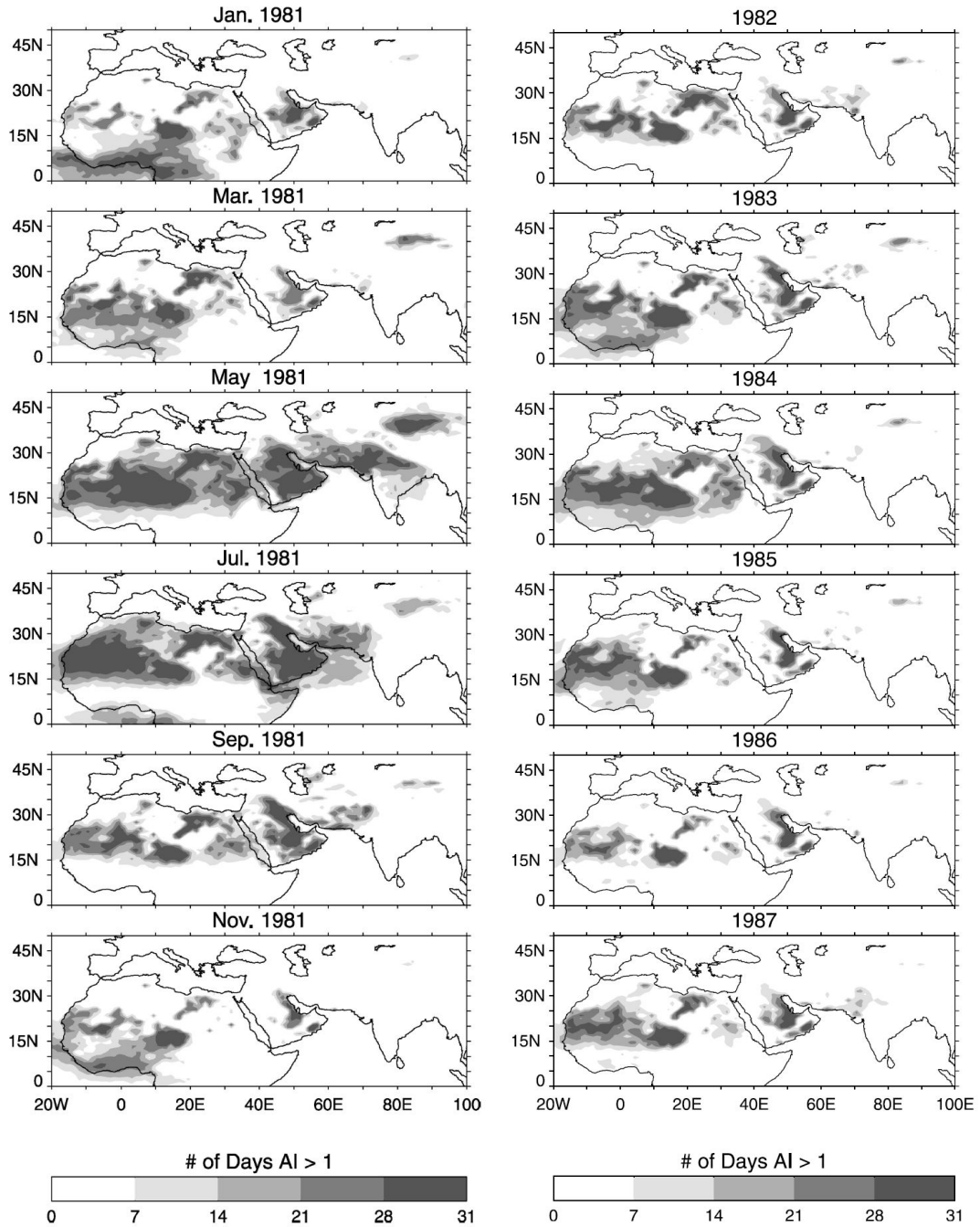


Figure 1.7: Seasonal variability in 1981 (left) and interannual variability from 1982-1987 (right) of dust sources as indicated by frequency of days per month with TAMS AI > 1.0. From Prospero et al. (2002).

The onset of peak activity in dust aerosol emissions from the Bodele depression in winter coincides with the peak season of the other dominant aerosol source in North Africa: biomass burning in the Sahel. During this dry season, human-induced agricultural burning activities are widespread south of 11° N. Using satellite measurements of active

fire counts, Giglio et al. (2006) find that the peak months of fire activity in the Sahelian region are November to February (Figure 1.8). They also find that the maximum density of fires occurs in equatorial Africa with very little inter-annual variability.

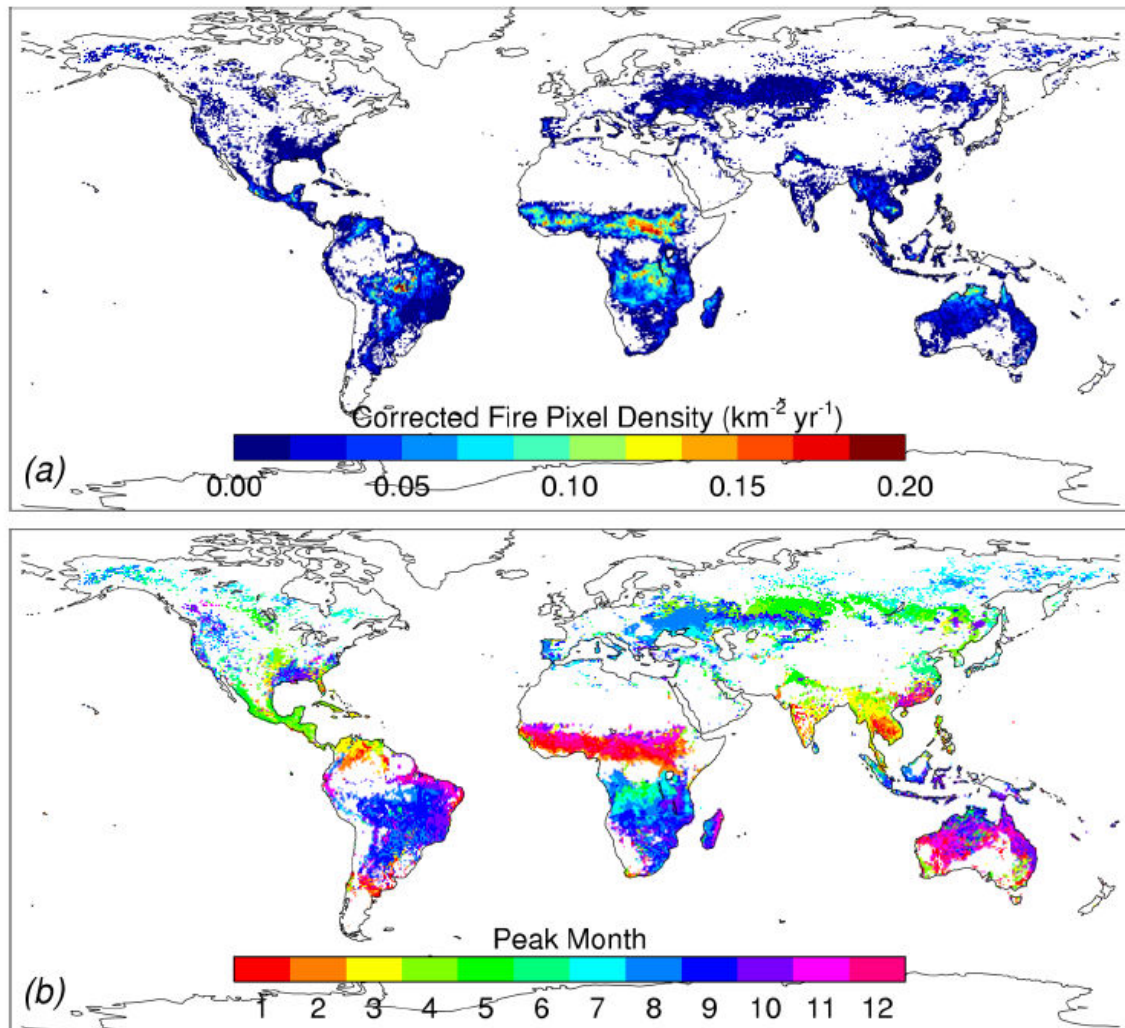


Figure 1.8: Corrected fire pixel density (a) and peak month of fire activity (b) derived from Terra MODIS observations from 2000-2005. From Giglio et al. (2006).

As the dust emissions from Bodele and other regional sources are carried southward by cool, dry northwesterly winds, they intersect the biomass burning emissions, which are moving slowly northward in a region of convective instability (Haywood et al., 2008). The biomass burning emissions are pushed upward by the dust “front”, rising to higher and higher altitudes as they move further north (Figure 1.9,

Haywood et al., 2008). Some of this dust is also transported westward over the Atlantic; the plume of absorbing aerosol in January in Figure 1.7 is likely biomass-burning dominated.

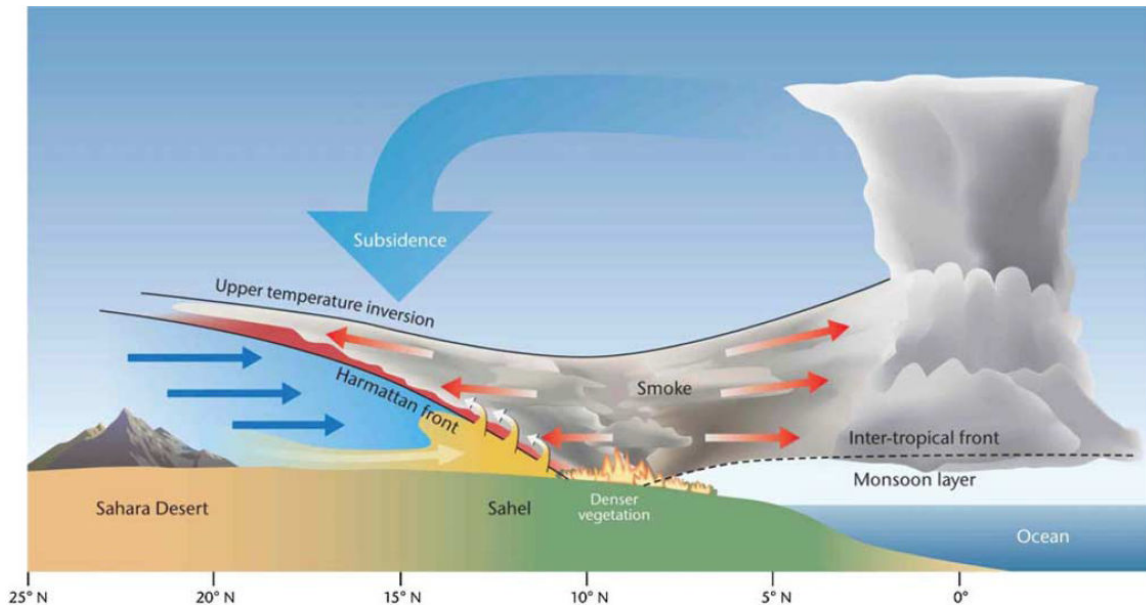


Figure 1.9: Schematic cross section of the intersection between southward transported dust and northward transported biomass burning during the winter dry season in the Sahel. From Haywood et al. (2008).

During the Dust and Biomass-burning Aerosol Experiment (DABEX) campaign, which was a component of the African Monsoon Multidisciplinary Analysis (AMMA) study, research flights were performed through aerosol plumes during January and February 2006 near Niamey, Niger. Although there was significant variability in individual profiles of aerosol measured during the campaign, they typically included an elevated layer of biomass burning aerosol, with dust dominating the boundary layer (Johnson et al., 2008a). An example from 19 January 2006 is shown in Figure 1.10. The dominance of dust aerosol below 1 km is indicated by the near-zero spectral dependence of aerosol scattering, and the fact that the aerosol volume concentration is primarily made up of coarse mode particles. Above this layer, the spectrally-dependent aerosol scattering and increased fine mode particle concentration indicate the presence of biomass burning

aerosol; however, since coarse mode concentrations are similar to those in the boundary layer, the biomass burning aerosol has mixed with dust. Indications of aging of biomass burning aerosol are also present, which does result in a larger mean size of the aerosol. A mid-level inversion, which is a common feature of the seasonal circulation pattern in this region (Figure 1.9) keeps the aerosol confined below 4 km.

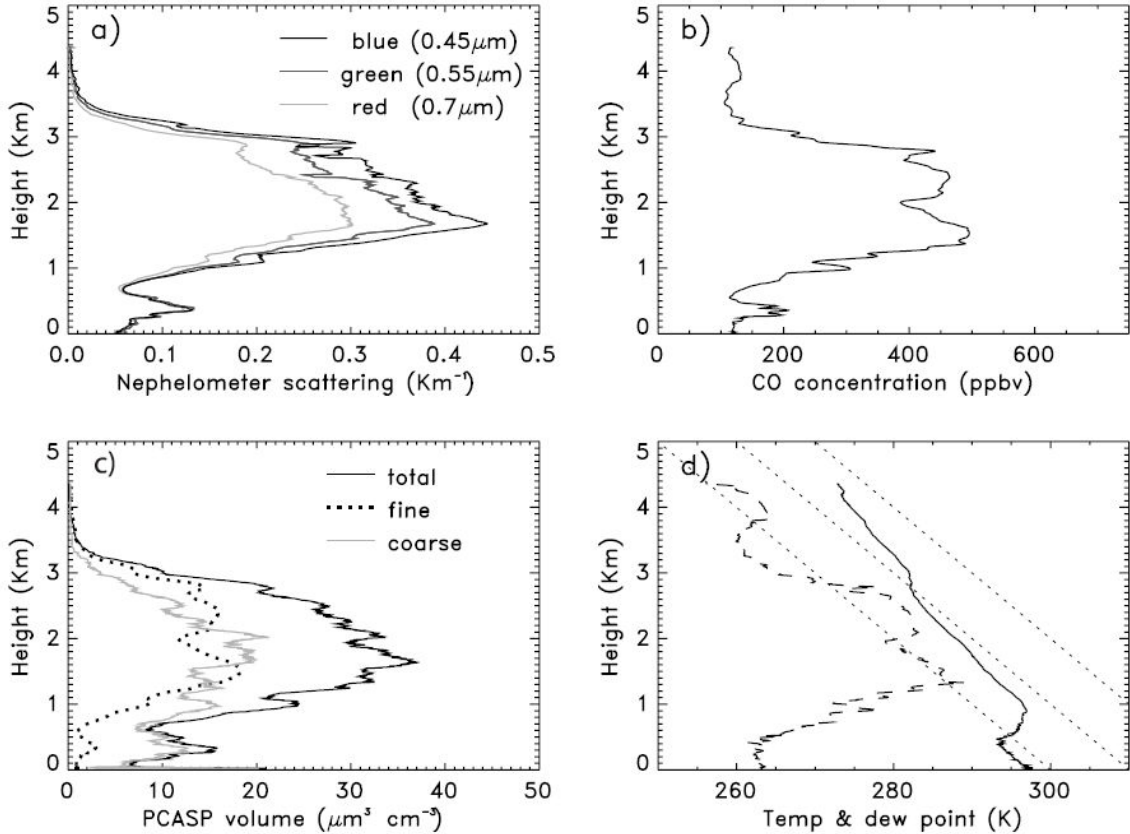


Figure 1.10: Vertical profiles of nephelometer scattering (a), CO concentration (b), aerosol volume concentration (c), and temperature and dew point (d) determined from in situ aircraft measurements near Niamey, Niger on 19 January 2006. From Johnson et al. (2008a).

### 1.3.2 Physical and Optical Properties

Several field campaigns and lab studies have been performed in an effort to characterize the optical properties of dust and biomass burning aerosol originating from North Africa (e.g. Haywood et al., 2008; Tanré et al., 2003; Volz, 1973). A few key results will be described here.

As mentioned above with respect to vertical profiles of aerosol, the majority of biomass burning aerosol mass is located in the fine mode ( $D_p < 1 \mu\text{m}$ ), whereas the majority of dust aerosol mass is located in the supermicron coarse mode. Johnson et al (2008a) find that the particle volume measured in biomass burning aerosol plumes during DABEX was dominated by particles smaller than  $0.35 \mu\text{m}$  in diameter. The size distribution of both aerosol types can change as their atmospheric residence time increases. As biomass burning particles age, they increase in size due to coagulation and condensation, and may also grow by water uptake (Carrico et al., 2010). As dust plumes are transported away from sources, larger particles are lost due to gravitational settling, although Maring et al. (2003) find that dust size distributions exhibit little change in the contribution of particles with diameters smaller than  $\sim 7 \mu\text{m}$ , even in cases of trans-Atlantic transport.

Both dust and biomass burning aerosol optical properties are dependent on their source, age, and size. Although many studies confirm that fine mode dust aerosol is almost non-absorbing in the visible ( $\text{SSA} \sim 0.99$  at  $0.55 \mu\text{m}$ ), McConnell et al. (2008) find that including the coarse mode from their dust measurements resulted in a SSA that was closer to 0.9. Furthermore, dust absorption is dependent on the mineral composition (e.g. Sokolik and Toon, 1999) and there is some evidence that dust from certain source regions is more absorbing than others. Formenti et al. (2008) find that dust from sources near the Sahel and in Mauritania has a higher content of iron oxides such as hematite, which is absorbing in shorter wavelengths, than dust from the Bodele depression. Alfaro et al. (2004) find similar evidence that dust collected in Niger is more absorbing than dust from the northern Sahara. Results using the DeepBlue algorithm (Hsu et al., 2004) also

suggest that Bodele dust may be less absorbing in the blue channels than dust from other sources (Figure 1.11). Over the Saharan desert, these variations in absorption could lead to changes in the sign and/or magnitude of the TOA forcing.

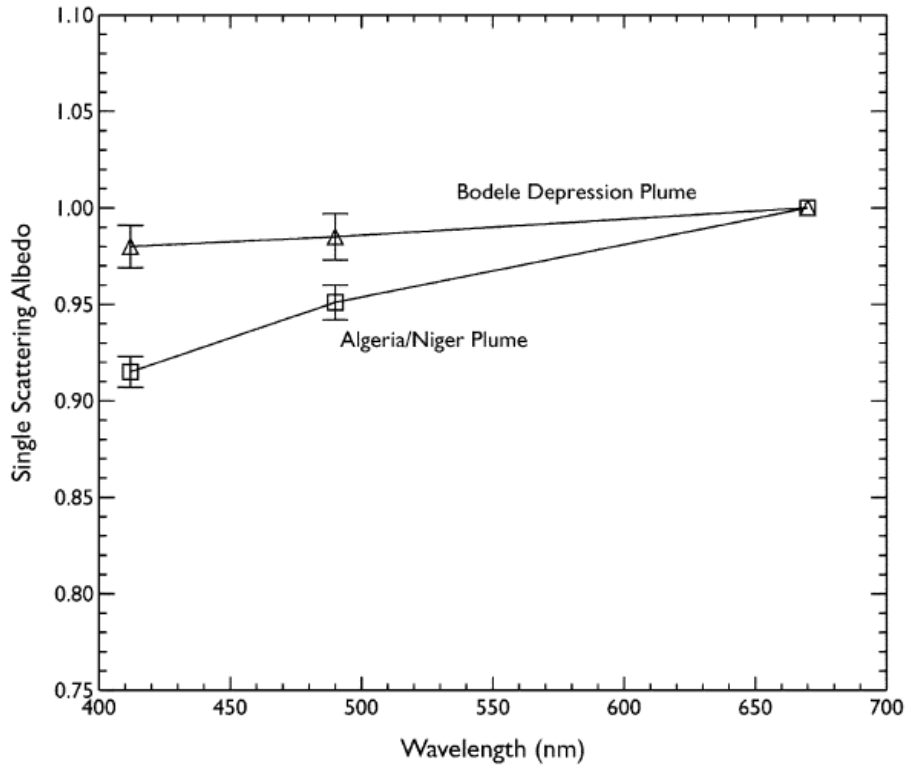


Figure 1.11: DeepBlue retrievals of SSA at 412 and 490 nm (value at 670 is assumed to be 1.0) downwind of Bodele and an Algeria/Niger dust source. From Hsu et al. (2004).

The absorptivity of biomass burning aerosol depends on the fraction of elemental carbon and organic species that are present in the aerosol, which varies with fuel type and fire conditions (McMeeking et al., 2009; Reid and Hobbs, 1998). The results of Johnson et al. (Johnson et al., 2008a) indicate that fresh biomass burning emissions in North Africa are more absorbing than those measured in southern African during the SAFARI-2000 campaign (Haywood et al., 2008), which could be due to differences in fuel type between the two regions.

## 1.4 Critical Reflectance Principle

The previous sections have shown that aerosol absorption over North Africa can be highly variable in space and time, and accurate knowledge of aerosol absorption properties is critical for understanding the impact of aerosols on climate in desert regions, and for tracking their emission and transport patterns. Because of the highly-reflective surface, the sign of the TOA aerosol forcing is quite sensitive to SSA. But, without reliable information about the underlying properties of the desert surface, one cannot determine the critical SSA at which the transition from TOA cooling to TOA warming occurs. The aerosol critical reflectance (Fraser and Kaufman, 1985; Kaufman, 1987), however, is a parameter that can be determined without knowledge of the surface reflectance and is uniquely related to the SSA for aerosol of a fixed size and scattering phase function. It can also be used to determine the relationship between the observed SSA and the critical SSA, and can thus provide some information about the sign of the TOA aerosol forcing, as well as its spectral dependence.

### 1.4.1 Definition and Assumptions

The critical reflectance principle was introduced by Fraser and Kaufman (1985) and further developed by Kaufman (1987) as an intrinsic property of aerosol that could provide information about the absorption properties of aerosol. It states that, for a given aerosol of fixed SSA and phase function, there is a certain surface reflectance,  $\rho_c$ , at which a change in aerosol loading does not affect the reflectance of the earth-atmosphere system. If a more-absorbing aerosol is added over the critical surface reflectance, or if the aerosol is moved over a surface with a reflectance that is greater than  $\rho_c$ , the aerosol will have a positive effect at TOA (warming). The opposite is true if a less-absorbing aerosol

is added, or if the aerosol is moved over a surface with a reflectance less than  $\rho_c$ . Because the critical surface reflectance is relatively independent of AOD, its determination does not require information about the aerosol loading.

The demonstration of the critical reflectance concept is shown in Figure 1.12, using radiative transfer calculations with an assumed aerosol size distribution and refractive index at a wavelength of 0.61  $\mu\text{m}$ . The difference between the TOA reflectance and the surface reflectance (y-axis) is plotted as a function of the surface reflectance for AODs of 0, 0.2, 0.4, and 0.6 for an SSA of 0.96 and 0.81 (assuming a fixed scattering phase function for both). For each SSA there is a surface reflectance at which the TOA reflectance is not sensitive to changes in AOD. Physically, this point represents a balance between increased aerosol backscatter at TOA and increased absorption of the surface contribution as the aerosol loading increases. This balance occurs at a lower critical reflectance for the more absorbing SSA, and will also change as a function of the solar zenith angle, satellite view angle, and relative azimuth, all of which were held constant in the calculations shown in Figure 1.12.

Provided the underlying surface has some variability over which to see changes in the TOA reflectance across an image, the critical reflectance can be used to derive SSA from satellite images of the same scene with different aerosol loadings but the same solar and viewing geometries. The assumptions required to apply the critical reflectance principle to derive SSA from satellite images are (Kaufman, 1987):

1. The aerosol optical depth is constant over the area contained by the pixel
2. The surface reflectance is invariant between the two comparison days

3. The surface is Lambertian, or, its angular variability in reflectance does not affect the TOA reflectance between the two comparison days
4. The phase function of the “background” aerosol and gaseous composition is similar between the two days

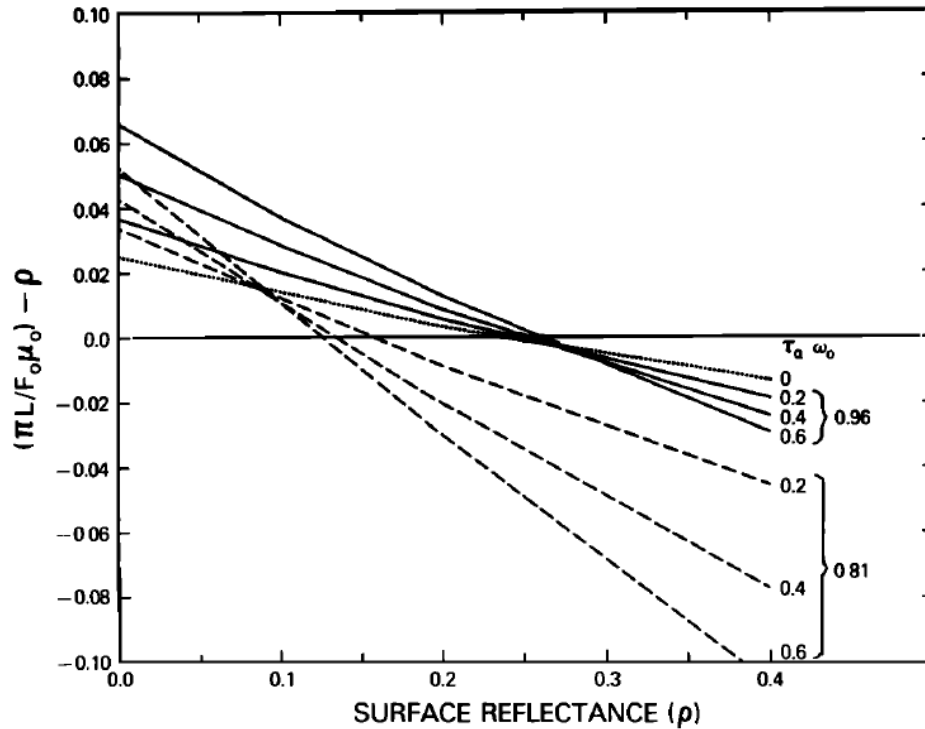


Figure 1.12: The difference between the TOA upward reflectance and the surface reflectance,  $\rho$ , as a function of  $\rho$  for AOD = 0, 0.2, 0.4 and 0.6 and two different SSAs, 0.81 and 0.96. From Kaufman (1987).

## 1.4.2 Foundational Work and Applications

### 1.4.2.1 Demonstration of Principle

Fraser and Kaufman (1985) demonstrated the use of the critical reflectance principle on satellite imagery by plotting the reflectance measured by the Landsat instrument on a polluted day over Washington, D.C. against reflectances measured on a cleaner day over the same area (Figure 1.13). From this figure, the critical reflectance was determined to be 0.18. Kaufman (1987) ascribes the scatter in the data to various effects:

1. Variation in the surface reflectance between the two days
2. Different background aerosol composition between the two days
3. Changing atmospheric characteristics between the two days
4. Differences in the registration between the two images
5. Adjacency effects due to atmospheric scattering
6. Difference in surface reflectivity between the two days that is due to small variations in the solar zenith angle and satellite view angle and a non-Lambertian surface

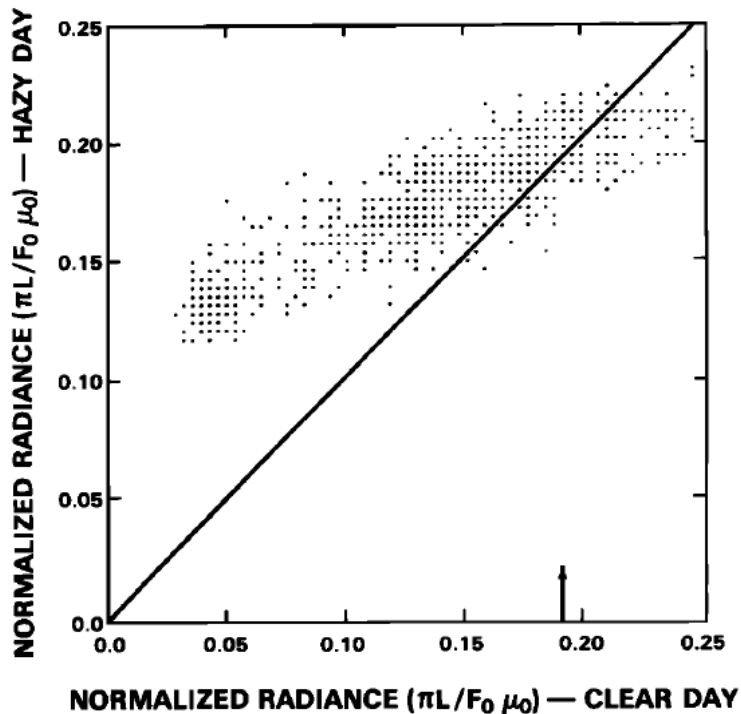


Figure 1.13: Scatter diagram of Landsat reflectances measured on a polluted day compared to reflectances measured on a clean day over Washington, D.C. From Kaufman (1987).

#### 1.4.2.2 Saharan Dust Absorption

Kaufman et al. (2001) used the critical reflectance principle to demonstrate that the absorption of Saharan dust aerosol was much smaller than currently accepted values, or those being used in global models to estimate aerosol effects (e.g. Sokolik and Toon,

1999; Sokolik et al., 1998). The World Meteorological Organization suggested that the imaginary index of refraction,  $k$ , for Saharan dust was 0.008 at a wavelength of 0.5  $\mu\text{m}$  (WMO, 1983) corresponding to a SSA of 0.63. Kaufman et al. (2001) compared a Landsat image of a major dust event to a cleaner image to show that the dust systematically increased the spectral reflectance at nadir view across the Western Sahara. Using the critical reflectance technique, they derived a SSA of  $0.97 \pm 0.02$  at 0.64  $\mu\text{m}$ , with a more absorbing SSA at 0.47  $\mu\text{m}$  ( $<0.9$ ) and near-zero absorption in the near-IR channels. Results of the case study are shown in Figure 1.14.

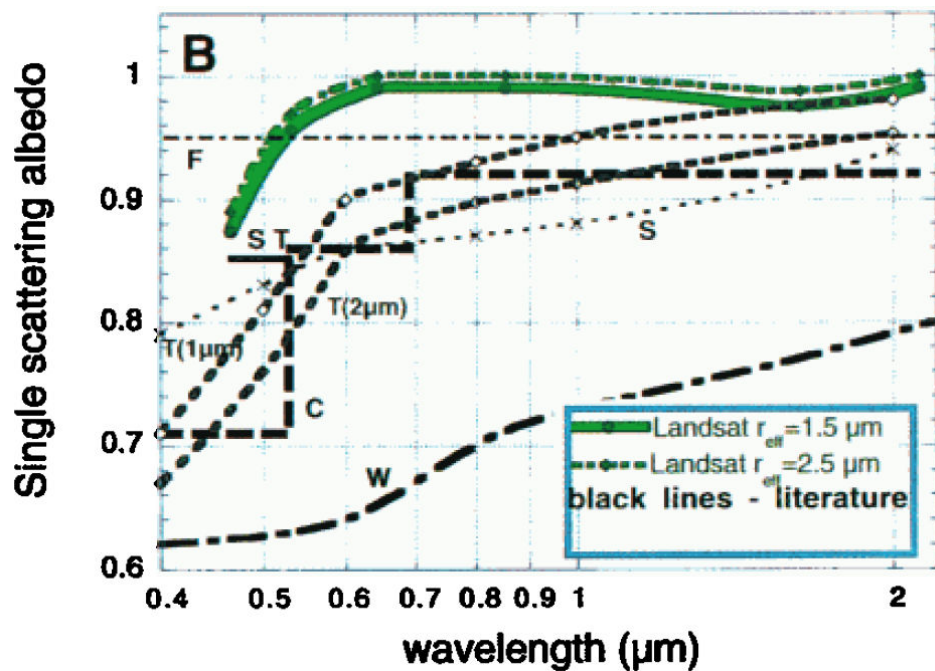


Figure 1.14: Spectral SSA for a Saharan dust event retrieved from Landsat measurements (green lines) compared to other estimates from the literature (black lines). From Kaufman et al. (2001).

### 1.4.3 Other Applications of the Principle

Since the application of the principle for the Saharan dust case in 2001, critical reflectance has been used to derive aerosol optical properties, but mainly in instances where temporally- and spatially-averaged SSA is sought. Two such studies that have been reported in the peer-reviewed literature are described here.

### 1.4.3.1 Average Saharan Dust Absorption

Yoshida and Murakami (2008) used the critical reflectance in order to determine average dust aerosol properties in the entire Sahara region. They used four years of data from the MODIS instrument to derive average reflectances during clean conditions and dusty conditions respectively. They compared the difference between these reflectances to find the TOA reflectance on the clean day that corresponded to a zero change in the TOA reflectance between the two days. They defined this as the critical reflectance at TOA, and used average AOD values from AERONET to derive a corresponding SSA. They retrieved an average SSA of 0.936 at 0.466  $\mu\text{m}$ , and 0.976 at 0.553  $\mu\text{m}$ . Their resulting SSAs (Figure 1.15) agree quite well with the estimates from Kaufman et al. (2001), although Yoshida and Murakami (2008) found the dust to be less absorbing at 0.466  $\mu\text{m}$ .

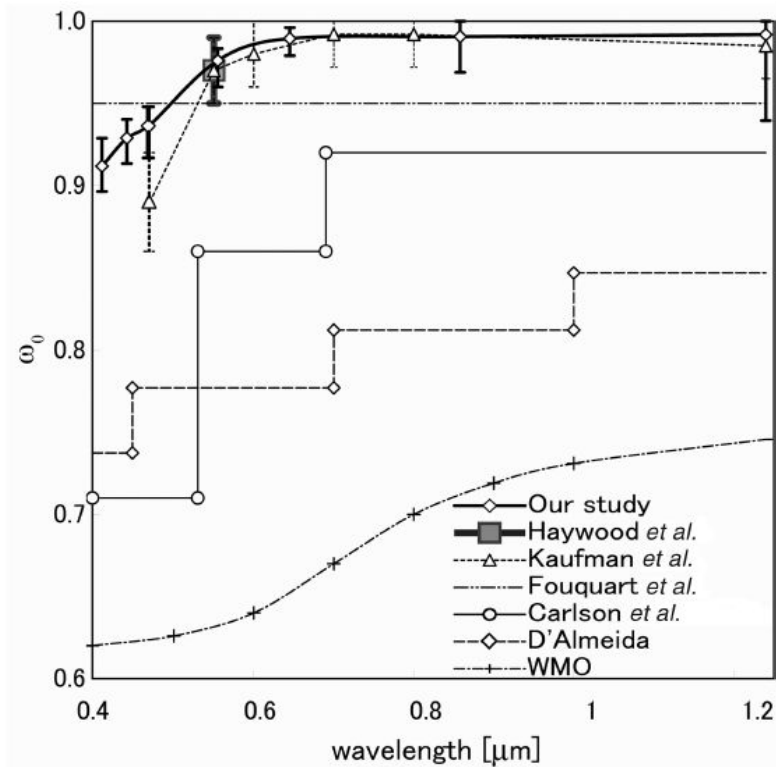


Figure 1.15: Average spectral SSA for Saharan dust retrieved from MODIS measurements, compared to other estimates from the literature. From Yoshida and Murakami (2008).

### 1.4.3.2 Aerosol Properties over Saudi Arabia

Satheesh and Srinivasan (2005) extended the critical reflectance principle to an application that does not require assumptions about aerosol properties. They compared satellite measurements of TOA albedo change and ground-based measurements of AOD at the Solar Village AERONET station in Saudi Arabia to derive a critical aerosol optical depth that results to a zero change in the TOA albedo during November and July 2000 (Figure 1.16, shown for November), the two months corresponding to periods of high and low absorption at the site, respectively. Assuming that the bulk aerosol properties were unchanged over the course of the month, they derived an SSA of 0.89 and 0.97 for the two months at a wavelength of 0.5  $\mu\text{m}$ . These estimates agreed well with SSA-critical AOD relationships simulated with a radiative transfer model.

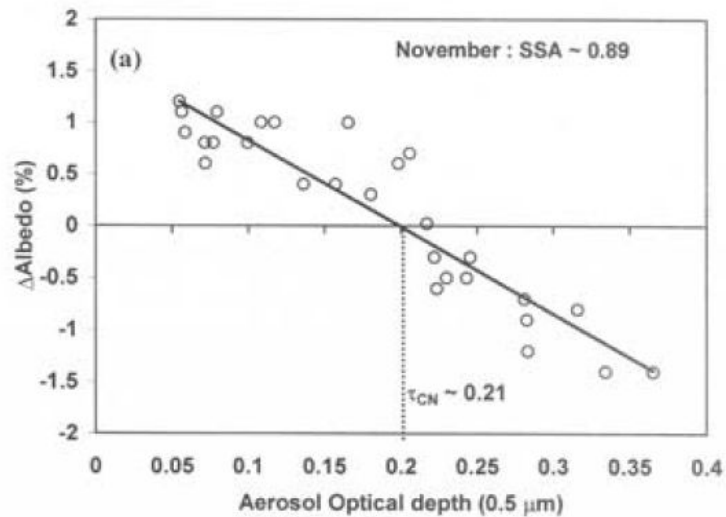


Figure 1.16: Change in TOA albedo measured by satellite as a function of AOD measured by AERONET at Solar Village, Saudi Arabia. From Satheesh and Srinivasan (2005).

## 1.5 Objectives

Although previous applications of the critical reflectance method have produced SSA estimates that are in agreement with estimates from other retrieval techniques, they do not demonstrate the feasibility of using the principle for real-time aerosol absorption

monitoring at finer spatial resolution over desert surfaces. Kaufman (1987) outlined some of the limitations and sources of uncertainty in applying the critical reflectance to estimate SSA, but a full assessment of the utility of critical reflectance retrievals over desert, and over North Africa in particular, has not been reported to date. This work investigates the sensitivity of the critical reflectance parameter to assumed aerosol physical and optical properties, as well as solar and viewing geometries that are representative of satellite-based observations, using the SBDART radiative transfer model and a T-matrix code. We use our findings to build look-up-tables which we apply to retrieve spectral SSA from critical reflectance, derived from MODerate resolution Imaging Spectroradiometer (MODIS) Level 1B data, in the vicinity of two North African AERONET sites: Tamanrasset, a site in the Algerian Sahara, and Banizoumbou, a site in Niger. We evaluate our results with comparisons to the AERONET-retrieved SSA and size distributions, DeepBlue SSA, as well as measurements of TOA and surface fluxes from the RADAGAST experiment (Slingo et al., 2009) and TOA albedo from CERES. Our results reveal the main sources of uncertainty in the spectral SSA derived over North Africa from the critical reflectance, and help us to define the conditions in which the retrieval will be best applied in this region. Implications of the SSA uncertainties for the ability to estimate TOA aerosol forcing over the AERONET sites are also explored.

## **2 Retrieval Method and Sensitivity**

### **2.1 Observations**

#### **2.1.1 The MODIS Instrument**

The Moderate Resolution Imaging Spectroradiometer (MODIS) is a passive radiometer aboard NASA's Terra and Aqua satellites, with 36 spectral channels ranging from 0.41  $\mu\text{m}$  to 15  $\mu\text{m}$ . Both satellites follow a sun-synchronous near-polar orbit, with the Terra-MODIS instrument crossing the equator at roughly 10:30 a.m. local time, and the Aqua-MODIS instrument crossing the equator at roughly 1:30 p.m. local time. MODIS achieves global coverage approximately every two days, with repeat orbits occurring every 16 days. The Aqua-MODIS instrument is part of the A-train, a constellation of satellites in which both active and passive sensors observe the same spot on earth within a few minutes of each other during local afternoon time. One of the reasons for these near-simultaneous measurements is to better quantify the anthropogenic aerosol effect at the top of the atmosphere (Anderson et al., 2005).

The seven channels that are used in the MODIS operational aerosol retrieval algorithm over ocean (Remer et al., 2005) are Bands 1 – 7, which span the spectral range from 0.459 – 2.155  $\mu\text{m}$ . The bandwidths, weighted central wavelengths, and spatial resolutions of these channels are listed in Table 2.1. The weighted central wavelengths were determined by integration of the channel-averaged response function of the MODIS instrument (Remer et al., 2006).

Table 2.1: Bandwidth, central wavelength and spatial resolution of MODIS Bands 1 – 7.

Band	Bandwidth ( $\mu\text{m}$ )	Weighted central wavelength ( $\mu\text{m}$ )	Spatial resolution at nadir (m)
1	0.620 – 0.670	0.646	250
2	0.841 – 0.876	0.855	250
3	0.459 – 0.479	0.466	500
4	0.545 – 0.565	0.553	500
5	1.230 – 1.250	1.243	500
6	1.628 – 1.652	1.632	500
7	2.105 – 2.155	2.119	500

### 2.1.2 Processing MODIS Level 1B Data

The analysis used in this study begins with MODIS Level 1B data, obtained from LAADS (Level 1 and Atmosphere Archive and Distribution System) Web (<http://ladsweb.nascom.nasa.gov/>). Because the critical reflectance must be derived by comparing images with the same solar and viewing geometry, we obtain data for pairs of images with different aerosol loading that are 16 days apart. The Level 1B files contain geolocated reflectance factors at the 36 MODIS bands; we use only the seven bands used in the operational MODIS algorithm, along with one additional band (1.38  $\mu\text{m}$ ) for cloud screening purposes. The reflectance is a unitless quantity that is simply the outgoing radiance at TOA normalized by the incoming solar irradiance, which has also been corrected for solar zenith angle variation. The reflectance,  $\rho_\lambda$ , is defined as

$$\rho_\lambda = \frac{\pi L_\lambda}{F_{o,\lambda} \cos(\theta_o)} \quad (2.1)$$

where  $L_\lambda$  is the measured radiance (in  $\text{W m}^{-2} \text{ster}^{-1}$ ),  $F_{o,\lambda}$  is the solar irradiance (in  $\text{W m}^{-2}$ ), and  $\theta_o$  is the solar zenith angle. The reflectance factor given in the MODIS Level 1B data is simply the product of  $\rho_\lambda$  and  $\cos(\theta_o)$ , therefore we normalize the data by  $\cos(\theta_o)$  to obtain the TOA reflectance.

### 2.1.2.1 Correction for Gaseous Absorption and Clouds

To isolate the component of the reflectance that is due to aerosol scattering, we correct the reflectance data for absorption due to water vapor, ozone, and carbon dioxide, and for the presence of clouds within the image. The gaseous absorption correction is the same as that used in the operational MODIS aerosol retrieval algorithm (Remer et al., 2006), and requires ancillary data on trace gas concentrations. Column precipitable water data from  $1^\circ \times 1^\circ$  NCEP reanalysis (obtained from <http://www.esrl.noaa.gov/psd/data/reanalysis/reanalysis.shtml>) are used for the water vapor correction; the ozone correction is done using the  $1^\circ \times 1^\circ$  TOAST (Total Ozone Analysis using SBUV/2 and TOVS) column ozone product (obtained from <http://www.osdpd.noaa.gov/ml/air/toast.html>). We assume climatological values of optical depth for the carbon dioxide correction.

We calculate transmission factors,  $T_\lambda$ , for each gas from the ancillary gas concentration data. For water vapor:

$$T_\lambda^{H_2O} = \exp(\exp(K_{1,\lambda}^{H_2O} + K_{2,\lambda}^{H_2O} \ln(Gw) + K_{3,\lambda}^{H_2O} (\ln(Gw))^2)) \quad (2.2)$$

For ozone:

$$T_\lambda^{O_3} = \exp(GK_\lambda^{O_3} D) \quad (2.3)$$

For carbon dioxide:

$$T_\lambda^{CO_2} = \exp(G\tau_\lambda^{CO_2}) \quad (2.4)$$

where  $w$  is the column precipitable water vapor (in centimeters),  $D$  is the column ozone (in Dobson units),  $K_\lambda$  is the absorption coefficient for water vapor or ozone, and  $\tau_\lambda^{CO_2}$  is the climatological optical depth of carbon dioxide. The absorption coefficients and climatological optical depth values used in the correction can be found in Table 2.2.  $G$  is

the air mass factor, which is calculated from the solar ( $\theta_o$ ) and sensor ( $\theta$ ) zenith angles as follows:

$$G = \frac{1}{\cos(\theta_o)} + \frac{1}{\cos(\theta)} \quad (2.5)$$

The corrected reflectance,  $\rho_{aer,\lambda}$ , is calculated from the MODIS Level 1B reflectance by

$$\rho_{aer,\lambda} = T_{\lambda}^{gas} \rho_{\lambda} \quad (2.6)$$

where  $T_{\lambda}^{gas}$  is the total gas transmission factor, which is simply the product of the individual gas transmission factors for water vapor, ozone, and carbon dioxide:

$$T_{\lambda}^{gas} = T_{\lambda}^{H_2O} T_{\lambda}^{O_3} T_{\lambda}^{CO_2} \quad (2.7)$$

Table 2.2: Gas absorption coefficients for water vapor and ozone, and climatological optical depth values of carbon dioxide.

Wavelength ( $\mu\text{m}$ )	$K_{1,\lambda}^{H_2O}$	$K_{2,\lambda}^{H_2O}$	$K_{3,\lambda}^{H_2O}$	$K_{\lambda}^{O_3}$	$\tau_{\lambda}^{CO_2}$
0.466				$4.26 \times 10^{-6}$	
0.553				$1.05 \times 10^{-4}$	
0.646	-5.73888	0.925534	$1.543 \times 10^{-2}$	$5.09 \times 10^{-5}$	
0.855	-5.32960	0.824260	$1.947 \times 10^{-2}$		
1.243	-6.39296	0.942186	$1.184 \times 10^{-2}$		$4.196 \times 10^{-4}$
1.632	-7.76288	0.979707	$9.367 \times 10^{-3}$		$8.260 \times 10^{-3}$
2.119	-4.05388	0.872951	$5.705 \times 10^{-2}$		$2.164 \times 10^{-2}$

We perform cloud screening on the reflectance data using the same technique as described by Martins et al. (2002) for the MODIS over-ocean cloud screening algorithm, which we have modified to be applicable over land. It consists of a combined test using the spatial homogeneity of the reflectance along with absolute reflectance thresholds. We use 0.466  $\mu\text{m}$  to identify low clouds, and Band 26 (1.38  $\mu\text{m}$ ) to identify high clouds. Figure 2.1 demonstrates that the reflectance associated with aerosol plumes (shown at 0.553  $\mu\text{m}$ , a channel we do not use for our cloud screening) tends to be much more spatially-homogeneous than that associated with clouds, although there is a relatively broad transition region between the two. Martins et al (2002) estimate that their chosen

threshold allows for 1 – 5% cloud contamination of the pixels. Our algorithm constructs a 3 x 3 pixel mask that is flagged as cloud if the standard deviation of the reflectance of the 3 x 3 pixels is greater than 0.01 at 0.466  $\mu\text{m}$  or 0.007 at 1.38  $\mu\text{m}$ . It is also flagged as cloud if the gas-corrected reflectance in either of these bands exceeds a maximum threshold value (0.4 at 0.466  $\mu\text{m}$  and 0.1 at 1.38  $\mu\text{m}$ ). The effectiveness of these thresholds over land has not been rigorously tested, however, so it is possible that our algorithm allows for a higher fraction of cloud contamination than the over-ocean algorithm.

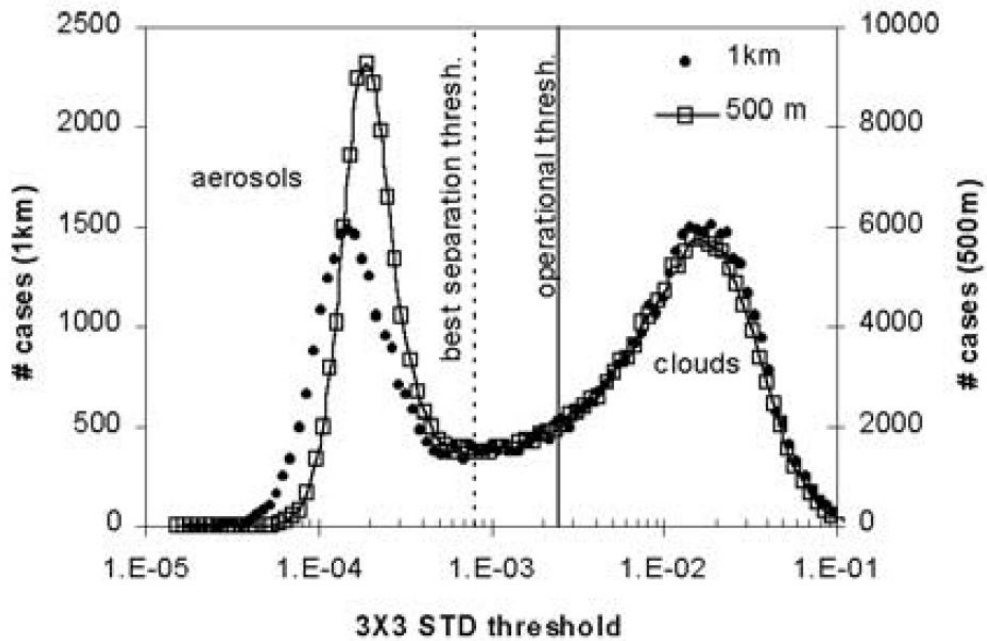


Figure 2.1: Histogram of 3 x 3 pixel reflectance standard deviation for 0.553  $\mu\text{m}$ , demonstrating the separation between aerosol and cloud. The “operational thresh” line refers to the threshold used in the operational over-ocean MODIS aerosol retrieval algorithm. From Martins et al. (2002).

### 2.1.2.2 Remapping

Next, in order to facilitate pixel-to-pixel comparison of two images, we remap the reflectance data onto an equal latitude-longitude grid. Even though this analysis makes use of the MODIS 16-day repeat viewing cycle to compare images with the same geometry, the two images will not be identical. Small orbital shifts cause slight changes

in viewing and solar zenith angle for a given pixel relative to 16 days prior. Also, because MODIS has a relatively large footprint, the images it produces are not on a regular grid. The instrument samples by scanning from left to right over the curved surface of the earth, resulting in an increased pixel size as the sensor moves away from nadir. This is known as the “bowtie effect”, where consecutive scans partially overlap at non-nadir angles (Figure 2.2) resulting in over-sampling of these pixels. We do not assess the effects of the overlapping sampling in our analysis, but we do consider the change in pixel size when choosing our remapping grid. The pixels at the edge of a MODIS image are about three times the length and width of those at nadir, so, in order to not perform subpixel interpolation in our remapping process, we aggregate the reflectances up to a grid of about 1.5 km. This is done at all seven channels, despite the fact that Channels 1 and 2 have a resolution of 250 meters.

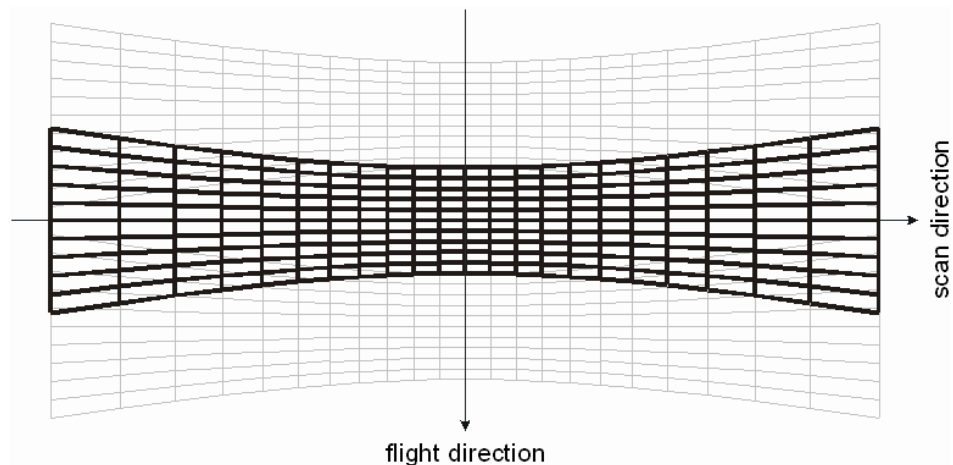


Figure 2.2: Representation of three consecutive MODIS scans consisting of 10 pixels along the flight direction, and 22 along the scan direction. From [eoweb.dlr.de](http://eoweb.dlr.de).

### 2.1.2.3 Data Fitting and Assumptions

Once the data are remapped to the same grid, the area of a larger pixel upon which to retrieve a constant SSA is defined. The area must be large enough to contain some variability in surface reflectance, so that there is some dynamic range of clean day

reflectances over which to perform a data regression. But, the pixel must not be too large as to contain significant spatial variations in aerosol loading. We choose an area of 10 by 10 pixels (approximately 15 by 15 km). Within each box, which we will call the retrieval pixel, the remapped reflectance data are matched in space, and the reflectances on the polluted day are regressed against the reflectances of the cleaner day. The slope and intercept are determined using a robust linear fitting procedure, in order to give less weight to data outliers. An example scatter plot containing a few outlying reflectance points is shown in Figure 2.3. The point at which the fit line crosses the one-to-one line is the critical reflectance at TOA. The y-intercept will be referred to as the path radiance, which is proportional to the optical depth difference between the clean and the polluted day. If there are any missing data within the retrieval pixel due to cloud screening, no retrieval is performed within the box.

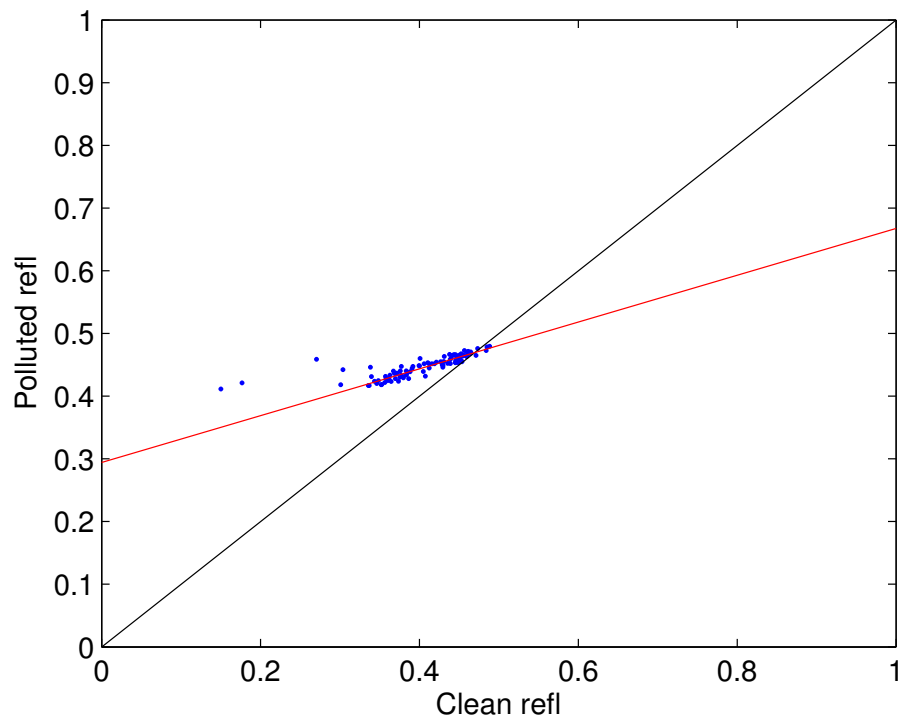


Figure 2.3: Example of a scatter plot of polluted versus clean reflectances for one 10 x 10 pixel box. The black line is the one-to-one line; the red line is the linear fit determined using the robust regression routine.

#### 2.1.2.4 Post Processing and Error Estimation

There are a few diagnostic tests that we use to determine if a retrieval pixel should be eliminated *a posteriori*. First, in order to ensure that the slope of the fit line is not so similar to the one-to-one line that it inhibits the precise determination of the critical reflectance, and to prevent the inclusion of pixels in which the cleaner day is actually more polluted than the polluted day (resulting in negative path radiance), we arbitrarily ascribe a minimum path radiance threshold of 0.02. Secondly, if the robust fit results in a negative critical reflectance, or a critical reflectance that exceeds 1.0, that pixel is also discarded.

Because the uncertainty in the measured reflectances from MODIS is only on the order of  $\pm 2\%$  (Remer et al., 2005), we assume that the uncertainty in the critical reflectance is a combination of the uncertainties associated with the data fitting routine and the assumptions listed in Section 1.4.1. We will address the former uncertainty source here, and the latter sources using sensitivity tests in subsequent chapters. We consider one measurement of the uncertainty due to data fitting to be the standard deviation of the residuals of the fit line:

$$\sigma_{resid} = \sqrt{\frac{\sum_{i=1}^N (y_i - y_{fit,i})^2}{N-1}} \quad (2.8)$$

where  $y_i$  the TOA reflectance value of a single pixel on the polluted day, and  $y_{fit,i}$  is the  $y$ -value of the linear fit to the TOA reflectance data. In order to consider the number of outliers in the determination of which pixels to keep from the retrieval, we also throw out those in which more than 10 pixels have a residual reflectance greater than  $2\sigma_{resid}$ .

A second measure of the fitting uncertainty is determined through error propagation. Given that we perform a linear fit to the reflectance data, the critical reflectance,  $R_{crit}$ , is simply

$$R_{crit} = \frac{b}{1-m} \quad (2.9)$$

where  $m$  is the slope of the linear fit and  $b$  is the y-intercept. Given the general error propagation equation

$$S_x = \sqrt{\left(\frac{\partial x}{\partial y}\right)_x^2 S_y^2 + \left(\frac{\partial x}{\partial z}\right)_z^2 S_z^2} \quad (2.10)$$

the error in the critical reflectance is

$$\sigma_{R_{crit}} = \sqrt{\left(\frac{1}{1-m}\right)^2 \sigma_b^2 + \left(\frac{b}{1-m}\right)^2 \sigma_m^2} \quad (2.11)$$

where  $\sigma_b$  is the uncertainty in the y-intercept as determined from the robust fitting routine and  $\sigma_m$  is the uncertainty in the slope of the linear fit.

## 2.2 Forward Model

We use a standard, publicly-available radiative transfer model, SBDART, to build a look-up table (LUT) of critical reflectance as a function of SSA for different assumed aerosol size distributions and refractive indices, as well as a range of solar and viewing geometries that are applicable to the MODIS instrument orbit and scanning characteristics. This section details the radiative transfer model set-up, aerosol model assumptions and phase function calculations, and the LUT-building procedure. LUT results and their implications for the critical reflectance sensitivity to aerosol physical and optical properties, as well as the model set-up, will be included in Section 2.3.

### 2.2.1 Radiative Transfer Model Set-Up

The Santa Barbara DISORT Atmospheric Radiative Transfer (SBDART) model (Ricchiazzi et al., 1998) is a multi-stream radiative transfer model that uses DISORT (Discrete Ordinate Radiative Transfer, Stamnes et al., 1988) to integrate the radiative transfer equation for a plane-parallel vertically-inhomogeneous atmosphere. We use the most recent version of the code, version 2.4 (obtained from <ftp://ftp.ices.ucsb.edu/pub/esrg/sbdart/>). The model can handle a maximum of 40 streams, but we use the default 20 streams because the simulations can be performed 10 times faster in this mode. A discussion of the impact of the number of streams used in SBDART can be found in Section 2.5.4.

The model set-up we use ascribes 32 layers to the atmosphere: 25 equidistant layers between 0 and 25 km, 5 equidistant layers between 25 and 50 km, and 2 equidistant layers between 50 and 100 km. Gaseous concentrations are assumed based on the standard subarctic summer atmosphere contained in the SBDART database. Because we correct the MODIS data for gaseous absorption, we set column ozone, water vapor, and carbon dioxide concentrations to zero in the model. We also ascribe the average surface elevation of each region of interest (given in Chapter 3 for the case study sites), so as to scale the Rayleigh scattering accordingly. We apportion the total aerosol optical depth into the lowest 5 km of the atmosphere. This height was chosen based on average vertical profiles of aerosol extinction measured in the Sahel region during the Dust and Biomass Burning Experiment (DABEX) campaign (Figure 2.4, Johnson et al., 2008b). The assumed vertical distribution of the fractional optical depth ( $d\tau(z)/\tau$ ) of each layer is

shown in Figure 2.5, for both aerosol extinction and Rayleigh scattering (at 0.466  $\mu\text{m}$ ). Below the atmosphere, isotropic scattering from the surface is assumed.

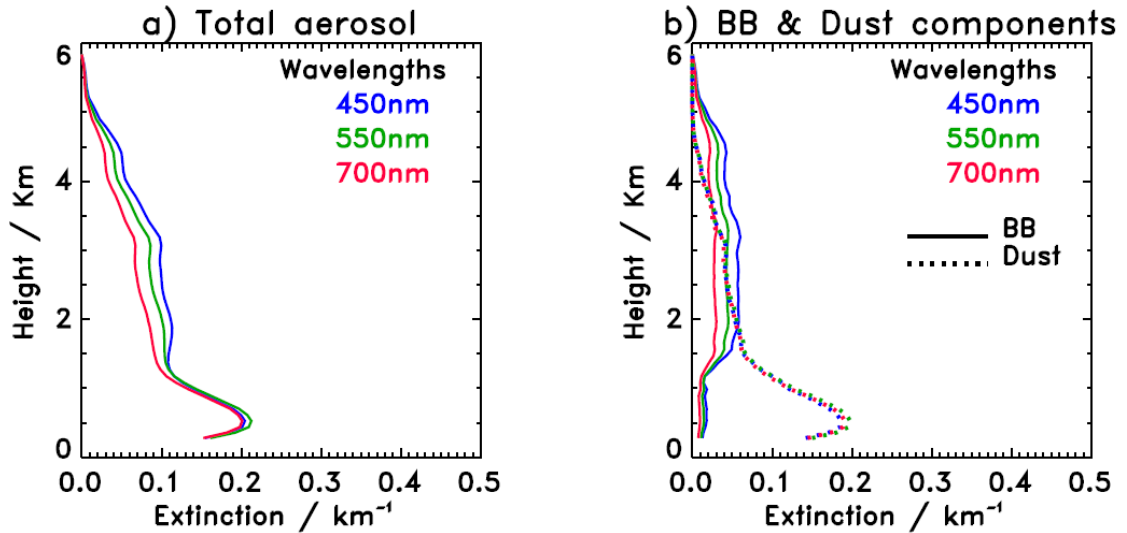


Figure 2.4: Average vertical profiles of aerosol extinction from the DABEX campaign for (a) total aerosol and (b) biomass burning and dust components, separately. From Johnson et al. (2008b).

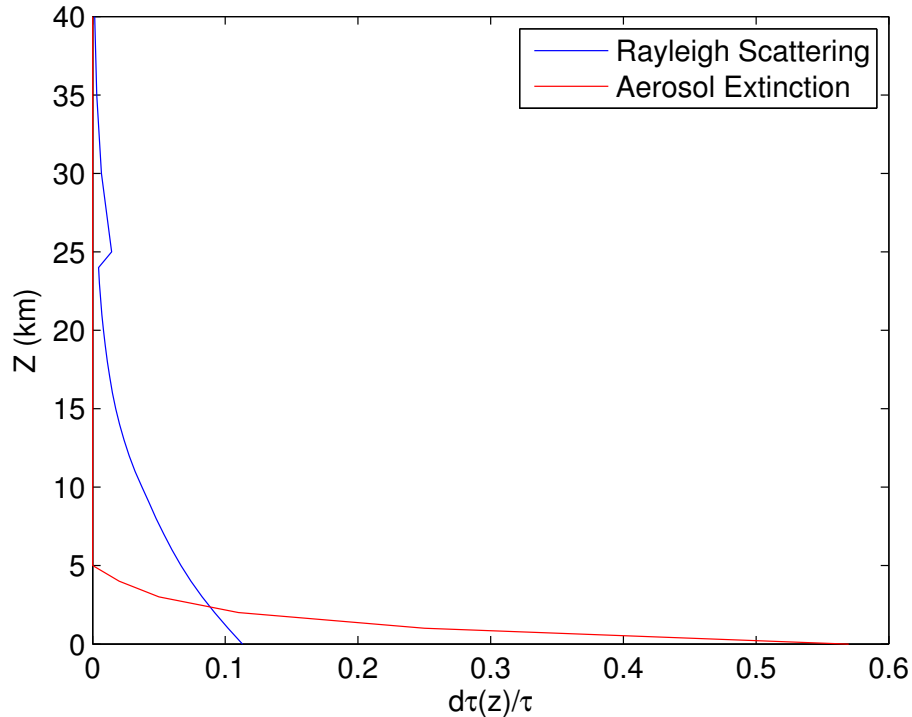


Figure 2.5: Vertical profile of the fractional optical depth assumed for Rayleigh scattering (blue) at 0.466  $\mu\text{m}$  and aerosol extinction (red) at all wavelengths in SBDART.

Aerosol single-scattering albedo, optical depth, and scattering phase function are input into SBDART for each layer below 5 km. Expansions of the scattering phase

function are performed in the model using Legendre polynomials of the order  $N$ . The expansion takes the form

$$P(\mu) = \sum_{l=0}^N \chi_l P_l(\mu) \quad (2.12)$$

where  $\mu$  is the cosine of the scattering angle,  $P_l$  is the  $l^{\text{th}}$  order Legendre polynomial and  $\chi_l$  are the  $l^{\text{th}}$  order expansion coefficients

$$\chi_l = \frac{(2l+1)}{2} \int_{-1}^1 P(\mu) P_l(\mu) d\mu \quad (2.13)$$

The phase function inputs required by SBDART are the Legendre moments of the phase function,  $M_l$ , given as

$$M_l = \frac{\int_{-1}^1 P(\mu) P_l(\mu) d\mu}{\int_{-1}^1 P(\mu) d\mu} \quad (2.14)$$

We use polynomials with 128 terms in our simulations, in order to sufficiently represent more complicated Mie phase functions when spherical particles are assumed.

## 2.2.2 Aerosol Models and Phase Function Calculations

Because we are performing retrievals over a region that is often impacted by non-spherical dust particles, we do not use a Mie code to determine the scattering characteristics of our aerosol models. Aerosol phase functions and single-scattering albedos are instead modeled using a modified T-matrix code (Dubovik et al., 2002) for the seven MODIS channels we use in the retrieval. The code simulates a population of particles as spheres, spheroids, or a mixture of both. The user specifies the particle size distribution and the percent sphericity (as the fraction of the total particle volume made up of spherical particles) of a particle population. We use 22 size bins evenly spaced on a

log scale, ranging from 0.05 to 15  $\mu\text{m}$  in radius, which is consistent with the length and range of the size distribution vector output by the standard AERONET retrieval. We assume four different aerosol models: fine mode spheres, a coarse mode made of primarily spheroids (percent sphericity = 0.5%), bimodal spheres, and bimodal spheroids (percent sphericity = 4%). The bimodal size distribution (Figure 2.6) was taken from an AERONET retrieval over the Banizoumbou station on 19 January 2006. For the coarse model, we simply assume the coarse mode of this distribution, and the fine mode for the fine model. The value chosen for percent sphericity of the bimodal spheroid distribution is assumed based on the reported value from AERONET on 19 January 2006.

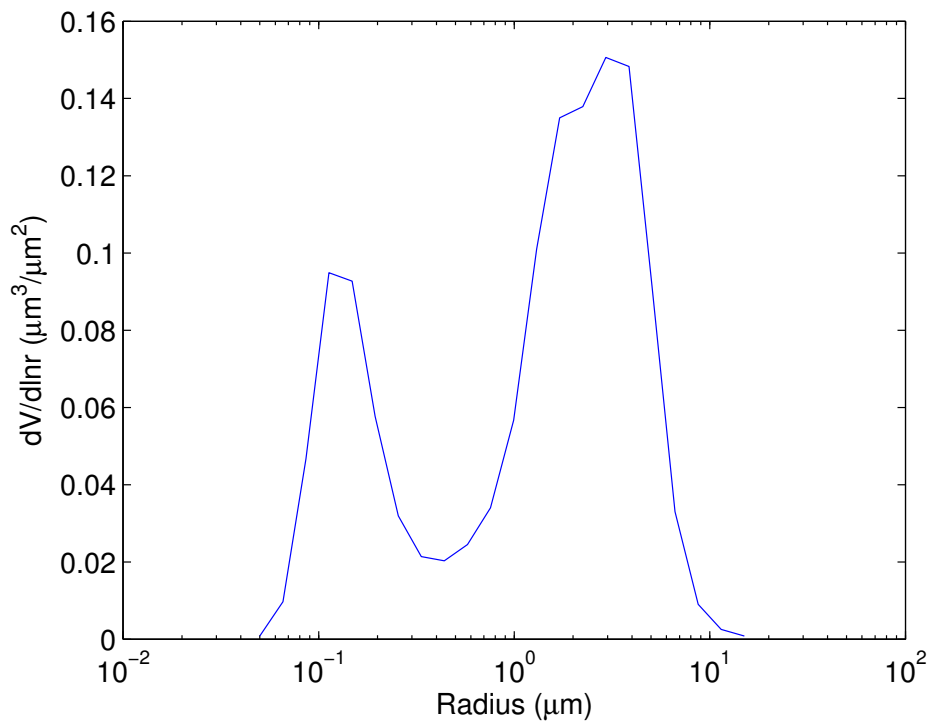


Figure 2.6: Bimodal size distribution model (from Banizoumbou AERONET site on 19 January 2006).

For each wavelength and size model we assume the real refractive index to be 1.53, which is the same value assumed in the MODIS operational algorithm from 0.466 to 0.855  $\mu\text{m}$  for the dust-like aerosol model (Remer et al., 2005). We vary the imaginary part of the refractive index in order to simulate a wide range of aerosol absorption values.

For each refractive index and wavelength, the code estimates the scattering phase function at 83 scattering angles, as well as the SSA of the particle population. The minimum imaginary refractive index that can be input into the T-matrix code is 0.0005, so the largest SSA we can simulate is slightly less than 1.0 (Table 2.3). For the fine and bimodal models we vary the imaginary part from 0.0005 to 0.030. For the coarse model, we vary the imaginary part from 0.0005 to 0.015. The corresponding SSAs for the maximum imaginary values assumed are listed in Table 2.4.

Table 2.3: SSAs estimated using the T-matrix code with  $k = 0.0005$  for the four aerosol models.

Wavelength ( $\mu\text{m}$ )	Fine Model	Coarse Model	Bimodal Sphere Model	Bimodal Spheroid Model
0.466	0.9973	0.9819	0.9922	0.9922
0.553	0.9970	0.9848	0.9917	0.9917
0.646	0.9966	0.9868	0.9912	0.9914
0.855	0.9955	0.9896	0.9906	0.9911
1.243	0.9920	0.9923	0.9912	0.9920
1.632	0.9860	0.9938	0.9925	0.9932
2.119	0.9741	0.9950	0.9939	0.9943

Table 2.4: SSAs estimated using the T-matrix code with  $k = 0.015$  for the coarse aerosol model and 0.030 for the other three models.

Wavelength ( $\mu\text{m}$ )	Fine Model	Coarse Model	Bimodal Sphere Model	Bimodal Spheroid Model
0.466	0.8584	0.7582	0.7978	0.8009
0.553	0.8465	0.7787	0.7796	0.7844
0.646	0.8298	0.7947	0.7609	0.7678
0.855	0.7841	0.8185	0.7324	0.7441
1.243	0.6726	0.8462	0.7208	0.7382
1.632	0.5431	0.8661	0.7372	0.7541
2.119	0.3915	0.8835	0.7633	0.7761

### 2.2.3 Critical Reflectance LUT Building

The computed phase functions and SSAs for each size model and refractive index are input into SBDART to simulate top-of-atmosphere radiances from which a critical reflectance can be determined. We perform our simulations at the same geometries as the MODIS operational algorithm: nine solar zenith angles (6, 12, 24, 36, 48, 54, 60, 66, and

72°), 13 satellite view angles (0 to 72°, in increments of 6°), and 16 relative azimuths (0 to 180°, in increments of 12°). The AOD is varied from 0 to 1 in increments of 0.2, and the surface albedo is varied from 0 to 0.9 in increments of 0.02.

We calculate the reflectance from the simulated radiances by normalizing by the solar zenith angle-corrected downward TOA flux that is output with each radiance record in SBDART, and multiplying by a factor of pi. For each solar/viewing geometry, aerosol size model, and SSA simulated, we then compare the TOA reflectance for each simulated AOD to the TOA radiance for AOD = 0. A linear fit between the TOA reflectances at AOD = 0 and the reflectances for AODs of 0.2, 0.4, 0.6, 0.8 and 1.0 is then determined, using two methods that will be described in the following discussion. We then take the resulting linear fit lines and determine the TOA reflectance of the polluted day that represents the intersection of these curves with the one-to-one line. Due to the fact that the critical reflectance is not completely insensitive to AOD, these intersections do not converge at a precise point, so we define the simulated critical reflectance as the average of the intersections of the fit lines for AOD = 0.2, 0.4, 0.6, and 1.0 with the one-to-one line.

The first fitting method we apply to the simulated reflectances, which we call the all albedo fitting method, is to simply perform a linear regression between the TOA reflectances on the polluted day (AOD > 0) and the TOA reflectances on the clean day (AOD = 0) that correspond to the entire range of simulated surface albedos. An example of this method is displayed in Figure 2.7. The data points represent the simulated reflectances for surface albedos ranging from 0 to 0.9, and the solid lines represent the linear fit to the data.

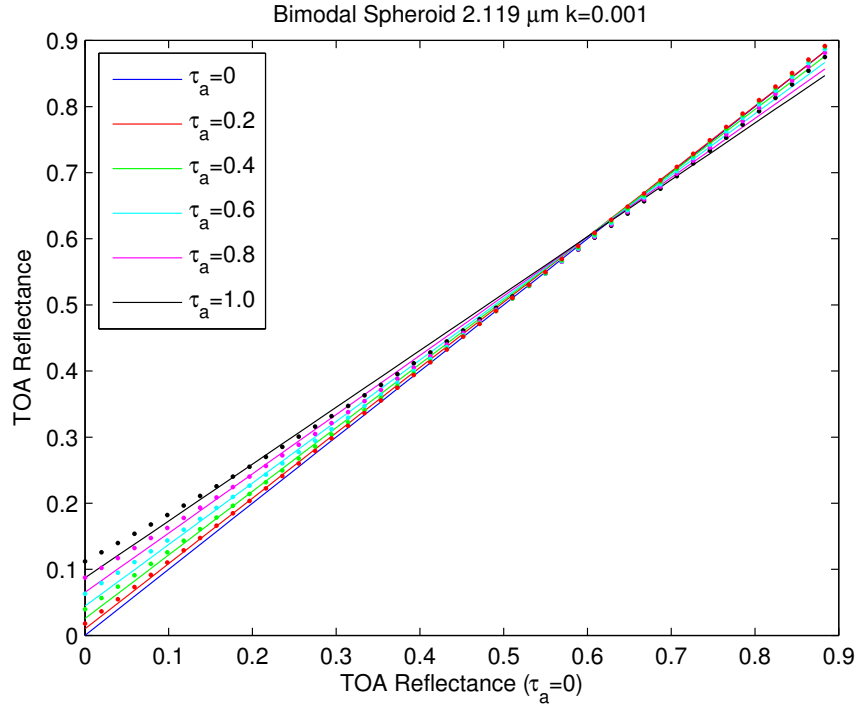


Figure 2.7: TOA reflectance for AOD = 0 (blue), 0.2 (red), 0.4 (green), 0.6 (cyan), 0.8 (magenta) and 1.0 (black) plotted against TOA reflectance for AOD = 0 for the bimodal spheroid model at 2.119  $\mu\text{m}$  and  $k = 0.001$ . The points represent the simulated reflectance, and the solid lines represent a linear fit to the data.

Because the slope of the simulated TOA reflectance increases somewhat with increasing surface albedo, particularly when the aerosol is weakly absorbing, we institute a fitting method that will attempt to account for this. The second fitting method, which we call the albedo range method, involves fitting only the data that coincide with a wavelength-appropriate range of surface albedos for the land surface type of interest. Because we are focusing on North Africa, we use observations of spectral surface reflectance in a desert area (Pinker and Karnieli, 1995) to estimate an appropriate surface albedo range over which to fit the data. The values we choose for our surface albedo ranges are taken from Figure 2.8, and listed in Table 2.5. Because there is no information available past a wavelength of 1.0  $\mu\text{m}$ , we assume a constant albedo range past this point. An example of this fitting method is shown Figure 2.9, where only the data points for the

appropriate albedo range (0.26-0.56 at 2.119  $\mu\text{m}$ ) are shown, and the solid lines represent the linear fit to those data.

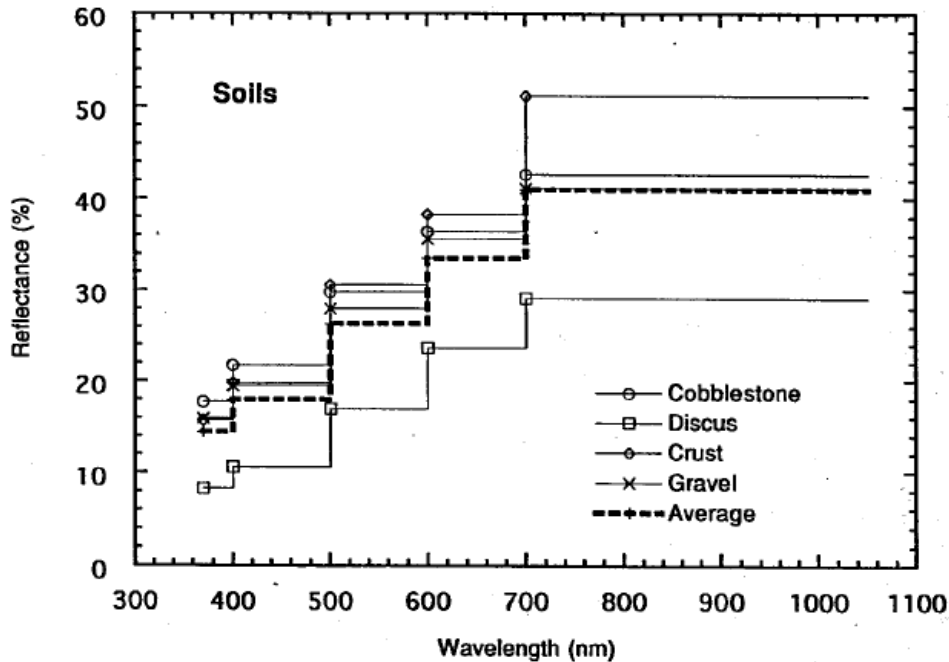


Figure 2.8: Spectrally-integrated values of reflectance for some typical surface types as observed at a wadi bed. From Pinker and Karnieli (1995).

Table 2.5: Minimum and maximum surface albedos used in the fitting of SBDART reflectance data to determine critical reflectance.

Wavelength ( $\mu\text{m}$ )	Minimum SFC Albedo	Maximum SFC Albedo
0.466	0.10	0.22
0.553	0.14	0.30
0.646	0.22	0.40
0.855	0.26	0.56
1.243	0.26	0.56
1.632	0.26	0.56
2.119	0.26	0.56

As a third determination of the critical reflectance, we simply use a routine to find the intersection of each TOA reflectance curve, plotted as a function of the simulated surface albedo, with the one-to-one line. No data fitting is performed on the simulated reflectances in this case. We call this method the TOA v SFC method, an example of which is shown in Figure 2.10.

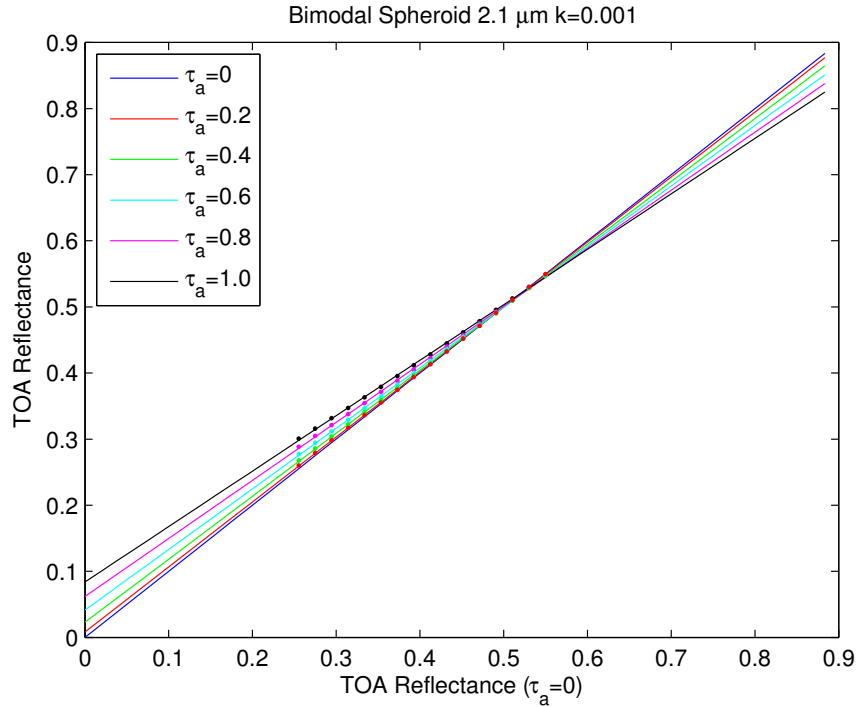


Figure 2.9: TOA reflectance for AOD = 0 (blue), 0.2 (red), 0.4 (green), 0.6 (cyan), 0.8 (magenta) and 1.0 (black) plotted against TOA reflectance for AOD = 0 for the bimodal spheroid model at 2.119  $\mu\text{m}$  and  $k = 0.001$ . The points represent simulated reflectance at surface albedos between 0.26 and 0.56, and the solid lines represent a linear fit to the simulated data.

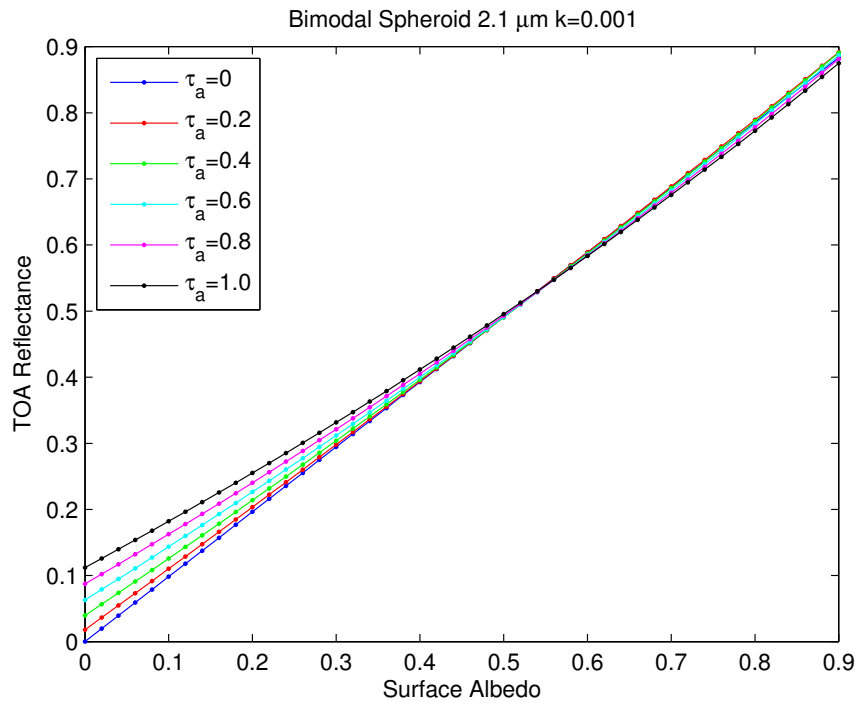


Figure 2.10: TOA reflectance for AOD = 0 (blue), 0.2 (red), 0.4 (green), 0.6 (cyan), 0.8 (magenta) and 1.0 (black) plotted against TOA reflectance for AOD = 0 for the bimodal spheroid model at 2.119  $\mu\text{m}$  and  $k = 0.001$ . The points represent simulated reflectance, and the solid lines simply connect the points together.

As mentioned above, the TOA reflectance curves exhibit some variability with AOD, which results in some uncertainty in determining the TOA critical reflectance from their intersections with the one-to-one line. We define the uncertainty in the average critical reflectance as the standard deviation of the intersections of these curves. Example results of the simulated critical reflectance ( $R_{crit}$ ) as a function of SSA for a fine and a coarse aerosol model are shown in Figure 2.11. The critical reflectance uncertainty, which is shown as the vertical error bars, generally increases as a function of SSA, and is also typically larger for the fine aerosol model.

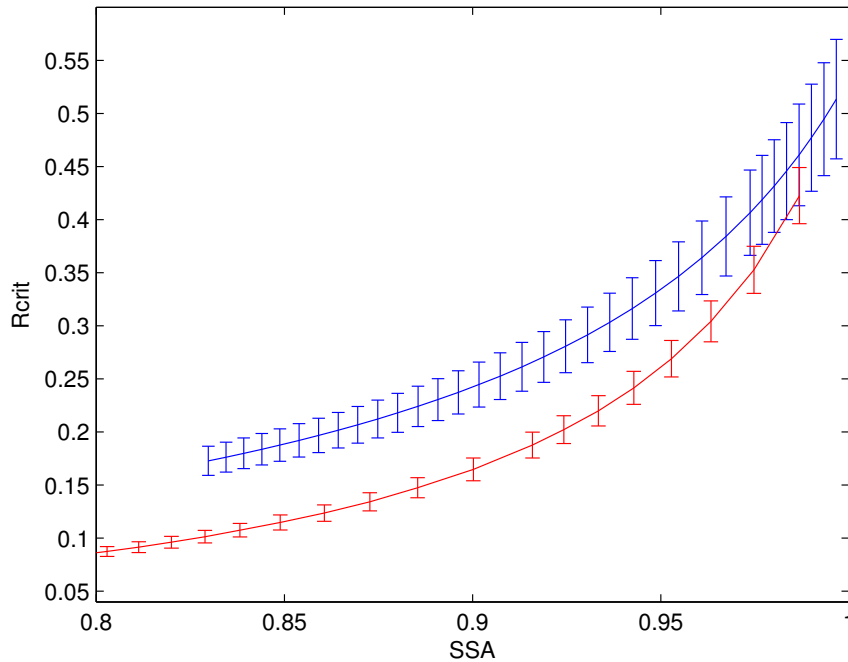


Figure 2.11:  $R_{crit}$ -SSA curves for fine (blue) and coarse (red) aerosol models at  $0.646 \mu\text{m}$ ,  $\text{SZA} = 24^\circ$ , view angle =  $60^\circ$ , and relative azimuth =  $120^\circ$ . Error bars represent the standard deviation of the intersections of the simulated TOA reflectance curves with the one-to-one line.

## 2.3 Inversion

The critical reflectance retrieved from MODIS is converted to SSA using the LUTs constructed for our aerosol models in SBDART. For each critical reflectance pixel, we perform a linear interpolation of the simulated critical reflectance in the LUT to the

appropriate solar zenith angle, view angle, and relative azimuth, and the resulting critical reflectance-SSA relationship is inverted to retrieve the SSA. We determine an error associated with the inversion by considering the uncertainty in the critical reflectance-SSA curve and the uncertainty in the MODIS critical reflectance due to data fitting (either using the standard deviation of the residuals or the uncertainties given by the robust regression). The intersection of the upper limit of the MODIS critical reflectance value with the lower limit of the LUT curve becomes the upper limit of the retrieved SSA value; the intersection of the lower limit of the MODIS critical reflectance value with the upper limit of the LUT curve becomes the lower limit of the retrieved SSA. The example in Figure 2.12 demonstrates this, assuming an observed critical reflectance of 0.3 with an uncertainty of  $\pm 0.03$ . For the coarse aerosol model LUT, this corresponds to a retrieved SSA of  $0.963 \pm 0.01$  at this particular wavelength, solar and viewing geometry.

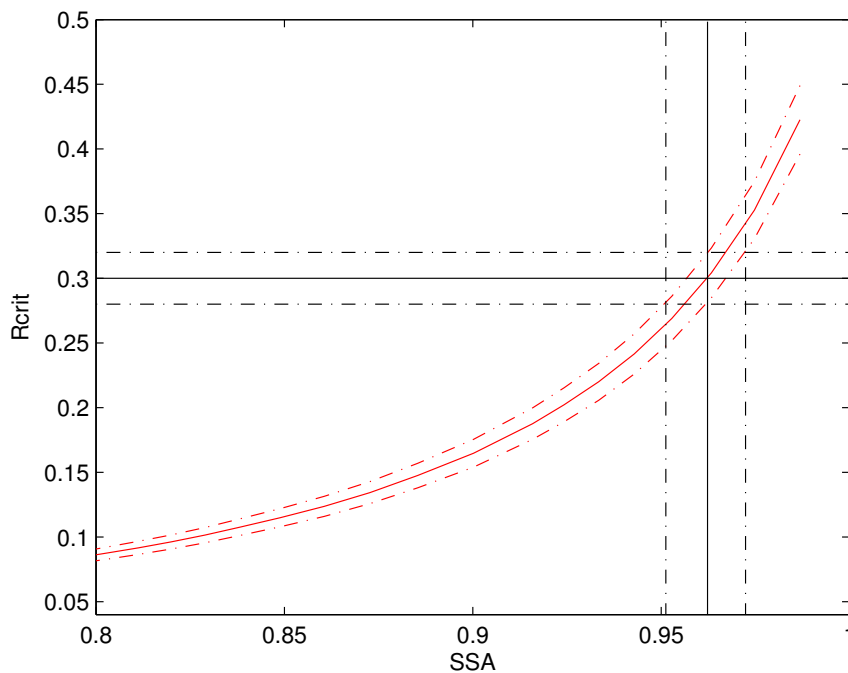


Figure 2.12: Example determination of the inversion uncertainty of the retrieved SSA for the coarse model at  $0.646 \mu\text{m}$ ,  $\text{SZA} = 24^\circ$ , view angle =  $60^\circ$ , and relative azimuth =  $120^\circ$ .

## 2.4 LUT results: Implications for Sensitivity to Aerosol Characteristics

LUT results for  $0.553\ \mu\text{m}$  are shown here in Figure 2.13 to Figure 2.15 for the fine aerosol model, Figure 2.16 to Figure 2.18 for the coarse aerosol model, and Figure 2.19 to Figure 2.21 for the bimodal spheroid model. Each figure contains contours of simulated critical reflectance (displayed as a function of satellite view angle and SSA) for a solar zenith angle (SZA) of  $12^\circ$ ,  $48^\circ$ , or  $66^\circ$ , and four relative sun-sensor azimuths ( $0^\circ$ ,  $60^\circ$ ,  $120^\circ$ , and  $180^\circ$ ). Results for the all albedo and albedo range fitting methods are shown; because the TOA v SFC produced similar results to one of the two fitting methods depending on the geometry, they are not displayed here, but we will still refer to them in the presentation of retrieval results. Results at all SZAs for the four aerosol models can be found in Appendix A. In the following sections we summarize the relationships between critical reflectance and solar/viewing geometry, particle size/shape, and data fitting method that are shown in the series of figures.

### 2.4.1 Sensitivity to Solar and Viewing Geometry

For each aerosol model and relative azimuth angle tested in this study, the sensitivity of the critical reflectance to changes in SSA is greatest for satellite view angles at and near the corresponding SZA. For small SZAs, this is the case for all relative azimuths, because the critical reflectance is nearly insensitive to changes in the relative azimuth at these angles. The latter result is due to the fact that only a small range of scattering angles is spanned over the range of relative azimuths when the SZA is small. At larger SZAs, however, more scattering angles are represented with the azimuth changes. The sensitivity of critical reflectance to SSA is largest at a relative azimuth of

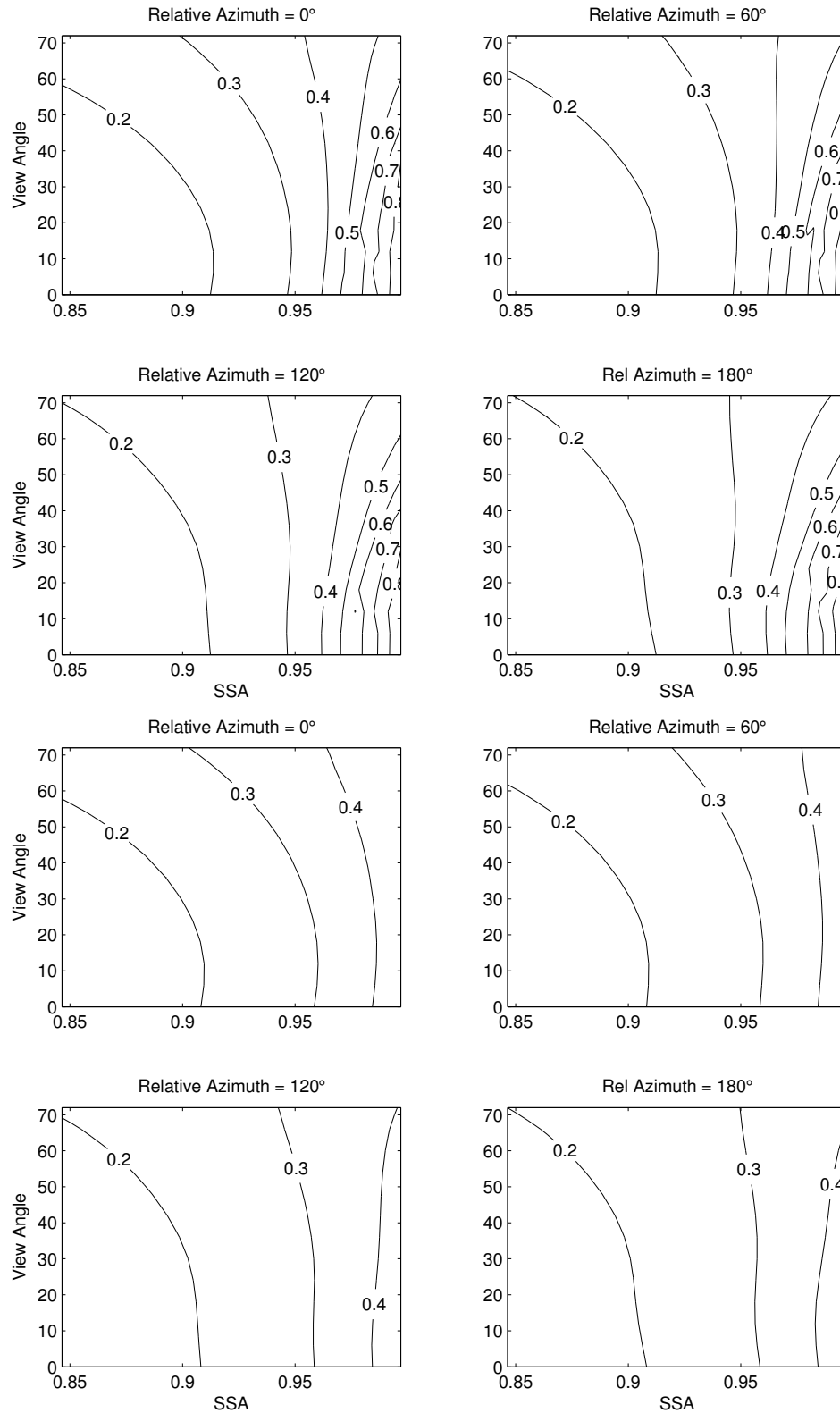


Figure 2.13: Critical reflectance LUT for the fine aerosol model at  $0.553 \mu\text{m}$  for  $\text{SZA} = 12^\circ$ , displayed as a function of satellite view and SSA for relative azimuth =  $0^\circ$  (upper left),  $60^\circ$  (upper right),  $120^\circ$  (lower left), and  $180^\circ$  (lower right). Upper panel is for the all albedo fitting method, lower panel is for the albedo range method.

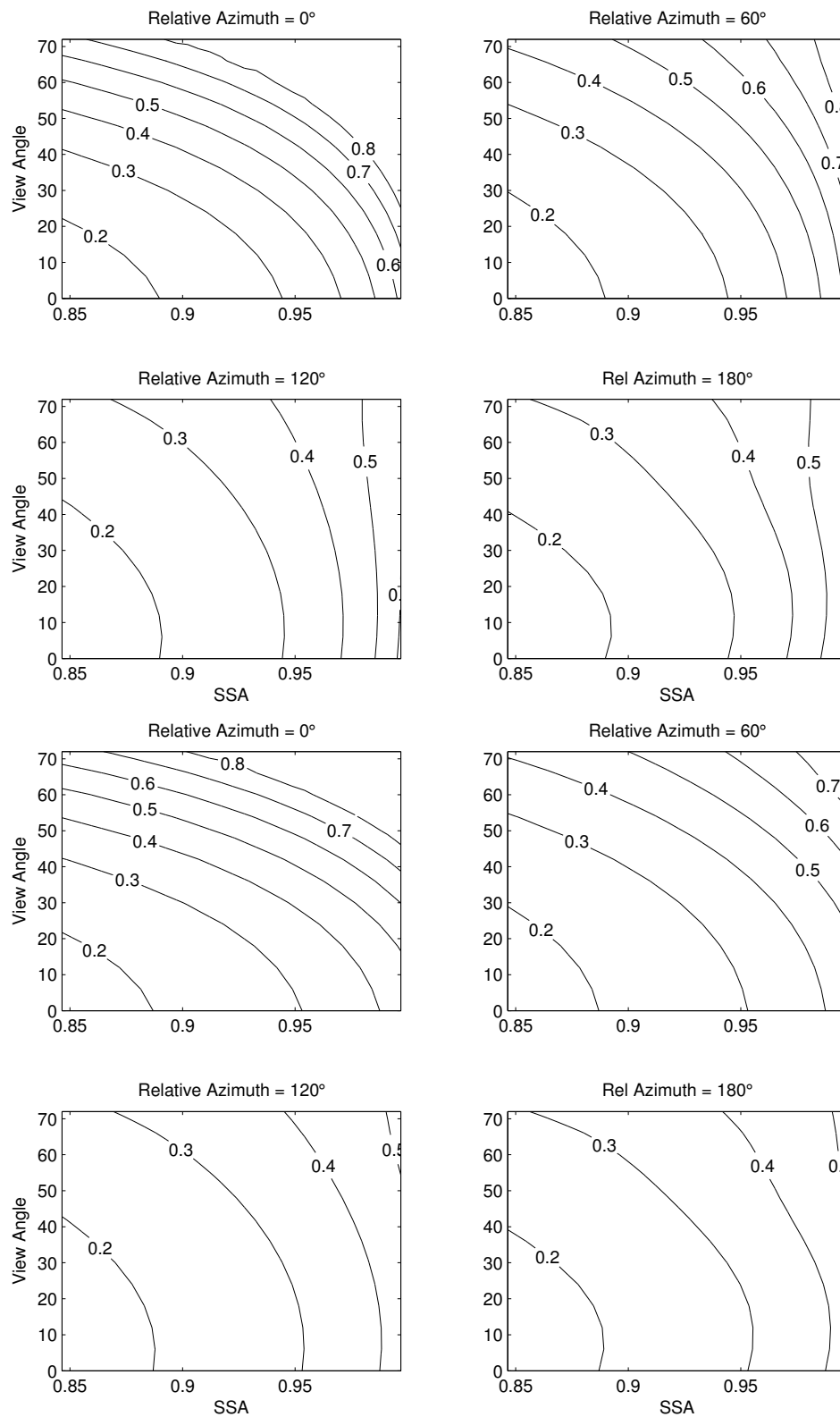


Figure 2.14: Critical reflectance LUT for the fine aerosol model at  $0.553 \mu\text{m}$  for  $\text{SZA} = 48^\circ$ , displayed as a function of satellite view and SSA for relative azimuth =  $0^\circ$  (upper left),  $60^\circ$  (upper right),  $120^\circ$  (lower left), and  $180^\circ$  (lower right). Upper panel is for the all albedo fitting method, lower panel is for the albedo range method.

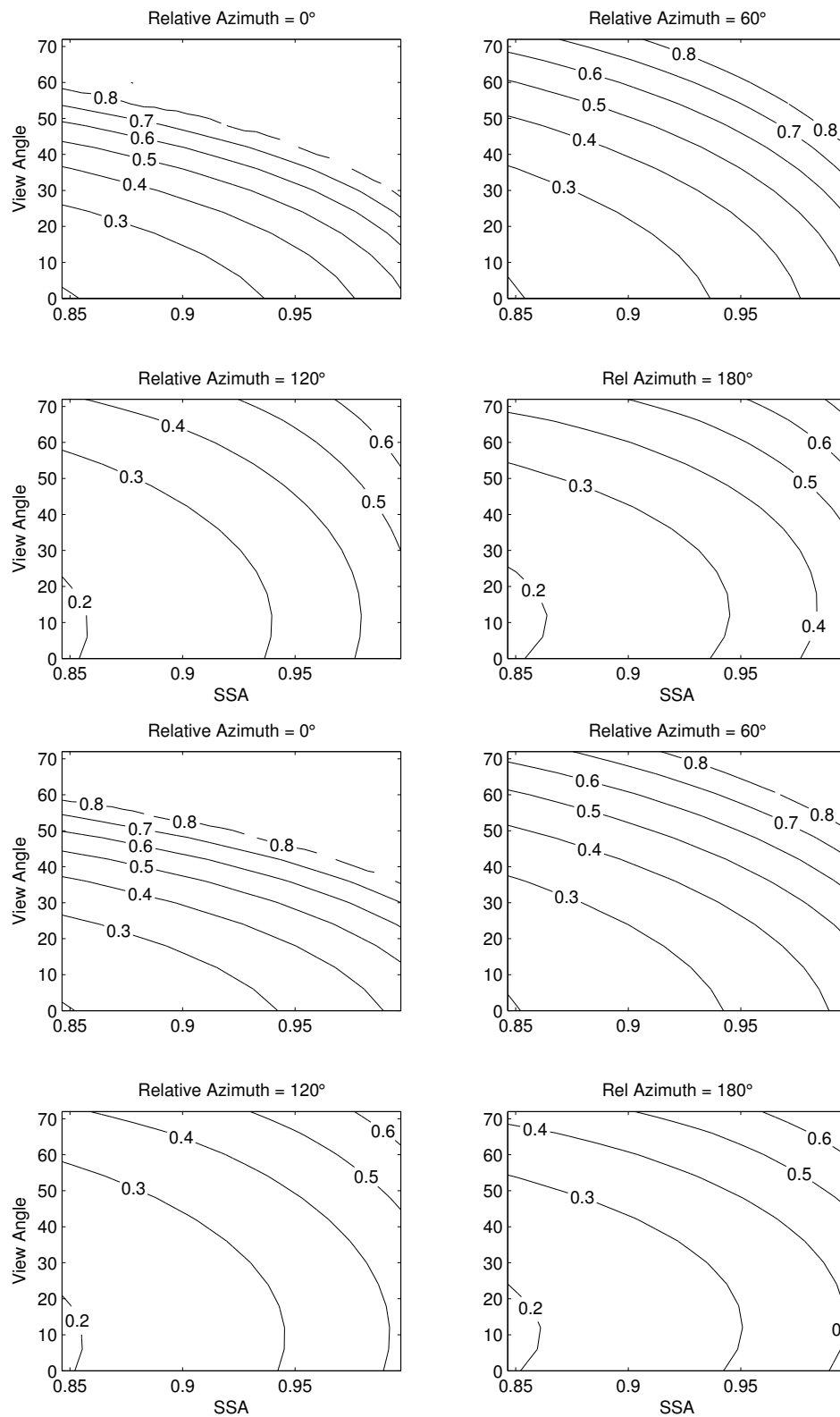


Figure 2.15: Critical reflectance LUT for the fine aerosol model at  $0.553 \mu\text{m}$  for  $\text{SZA} = 66^\circ$ , displayed as a function of satellite view and SSA for relative azimuth =  $0^\circ$  (upper left),  $60^\circ$  (upper right),  $120^\circ$  (lower left), and  $180^\circ$  (lower right). Upper panel is for the all albedo fitting method, lower panel is for the albedo range method.

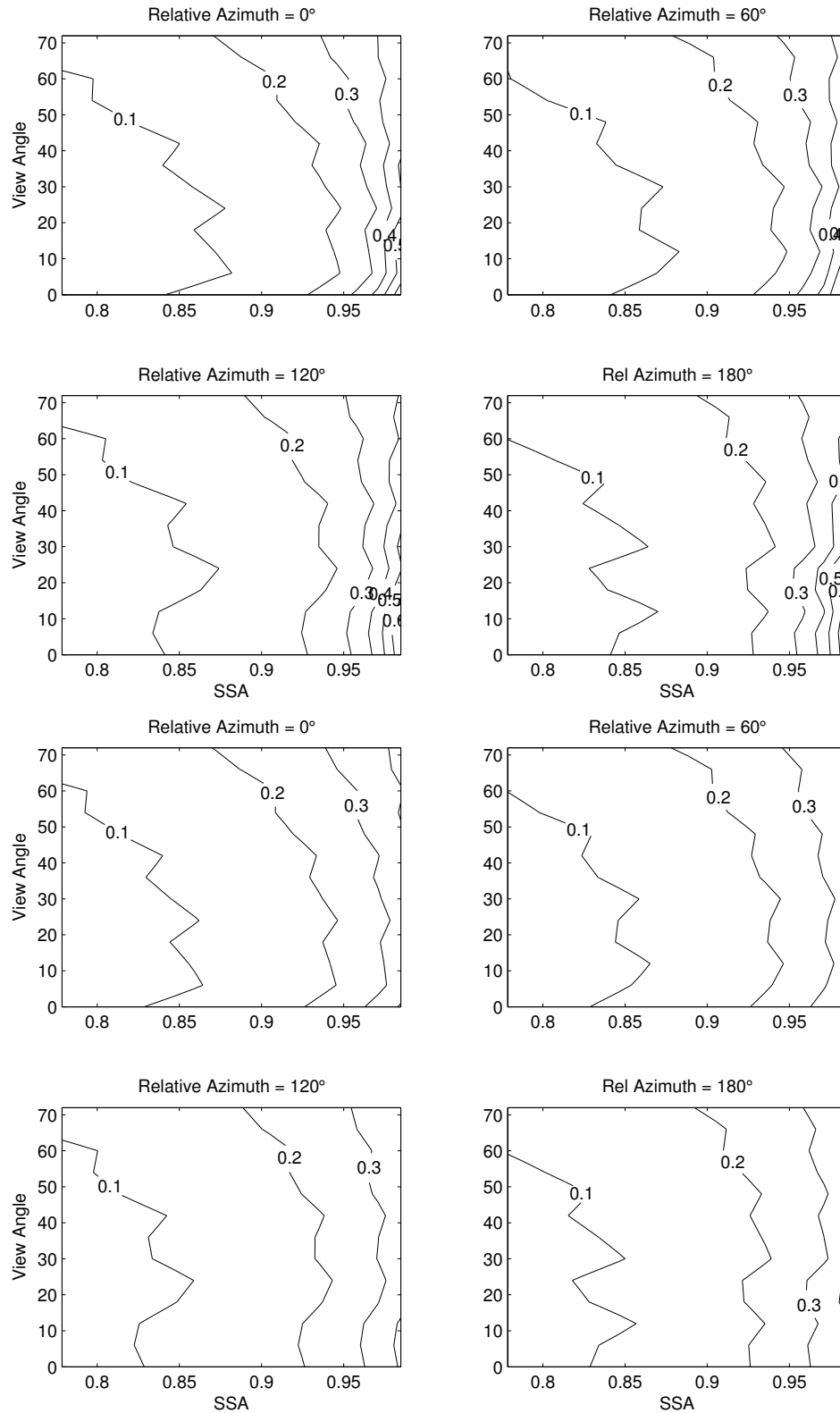


Figure 2.16: Critical reflectance LUT for the coarse aerosol model at  $0.553 \mu\text{m}$  for  $\text{SZA} = 12^\circ$ , displayed as a function of satellite view and SSA for relative azimuth =  $0^\circ$  (upper left),  $60^\circ$  (upper right),  $120^\circ$  (lower left), and  $180^\circ$  (lower right). Upper panel is for the all albedo fitting method, lower panel is for the albedo range method.

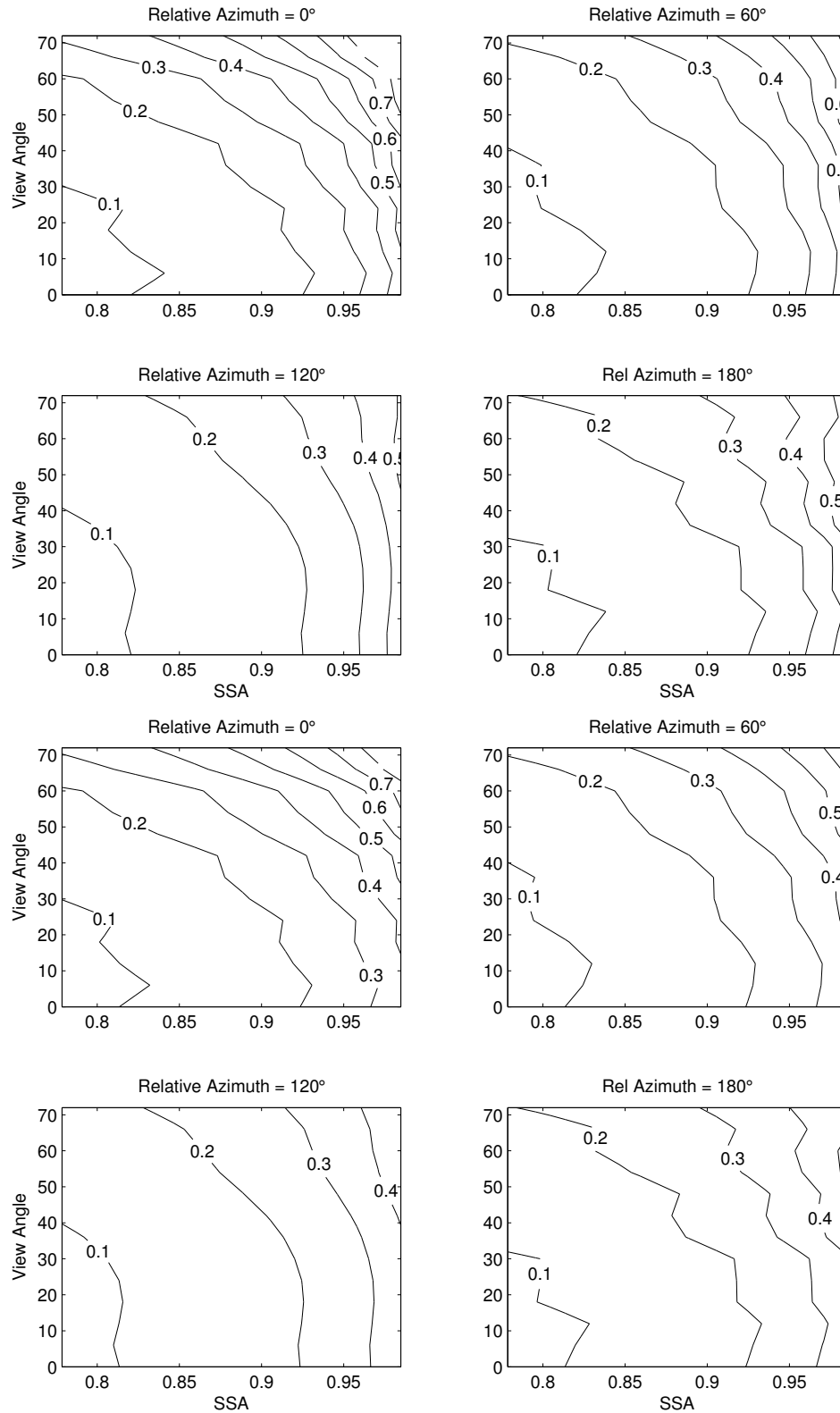


Figure 2.17: Critical reflectance LUT for the coarse aerosol model at  $0.553 \mu\text{m}$  for  $\text{SZA} = 48^\circ$ , displayed as a function of satellite view and SSA for relative azimuth =  $0^\circ$  (upper left),  $60^\circ$  (upper right),  $120^\circ$  (lower left), and  $180^\circ$  (lower right). Upper panel is for the all albedo fitting method, lower panel is for the albedo range method.

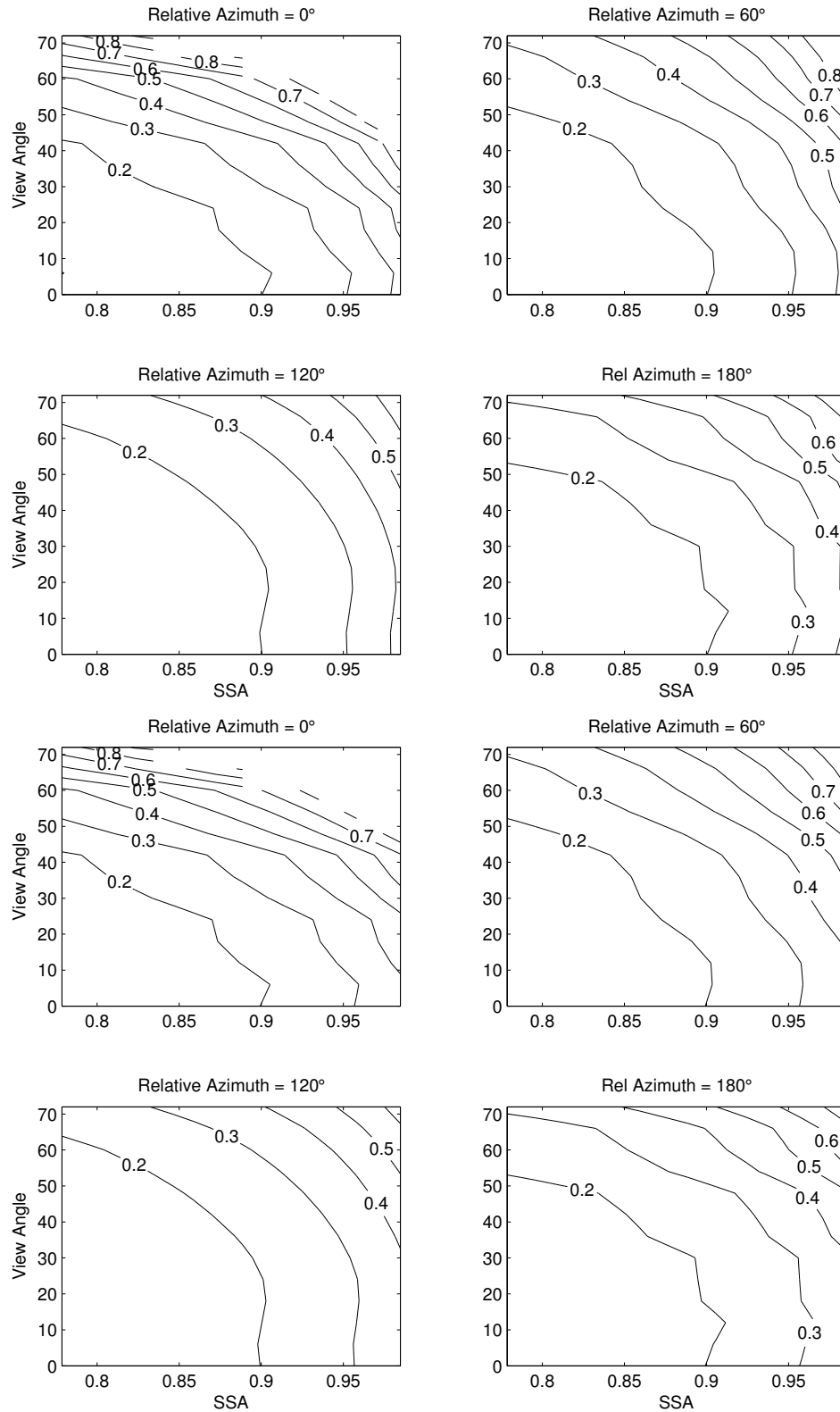


Figure 2.18: Critical reflectance LUT for the coarse aerosol model at  $0.553 \mu\text{m}$  for  $\text{SZA} = 66^\circ$ , displayed as a function of satellite view and SSA for relative azimuth =  $0^\circ$  (upper left),  $60^\circ$  (upper right),  $120^\circ$  (lower left), and  $180^\circ$  (lower right). Upper panel is for the all albedo fitting method, lower panel is for the albedo range method.

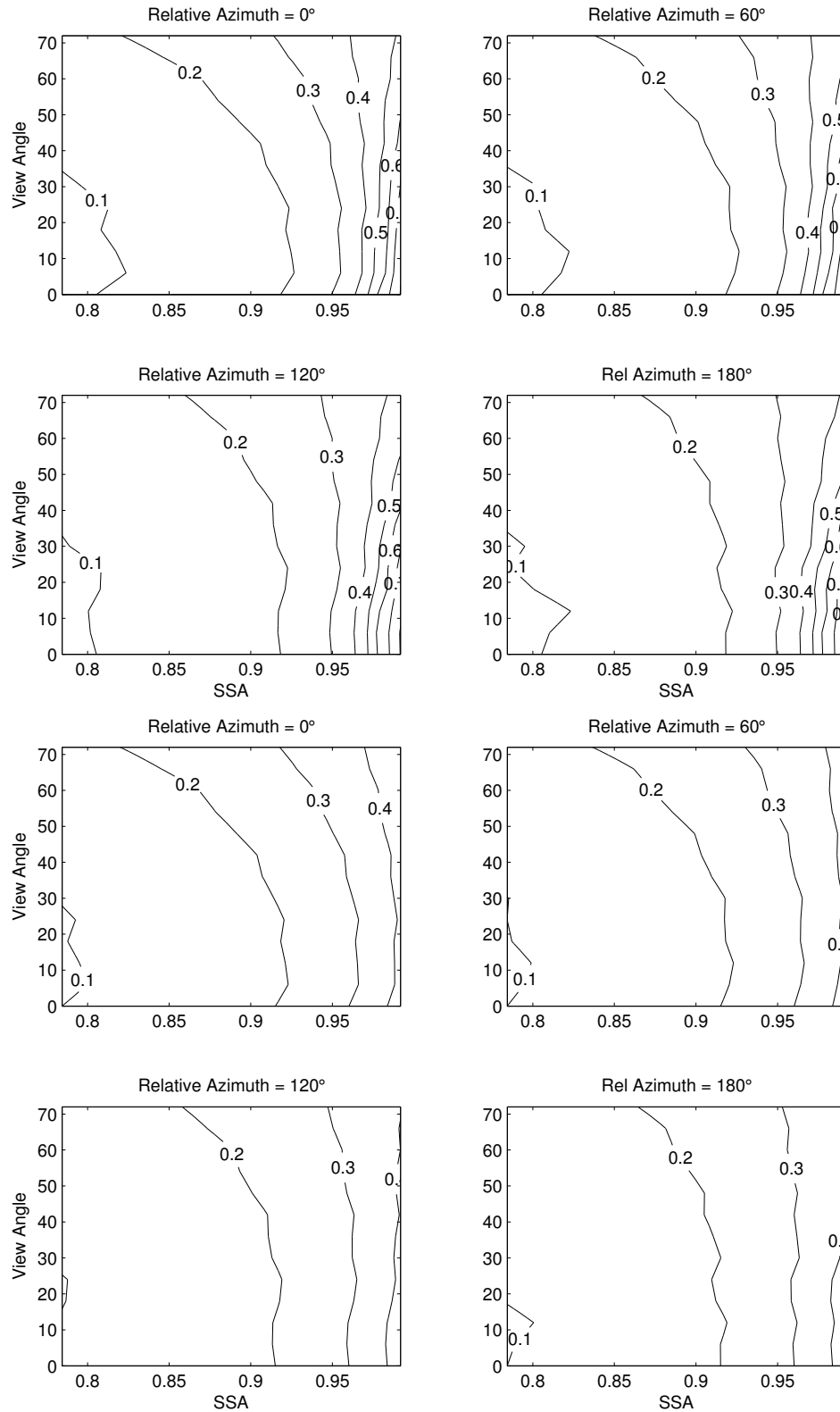


Figure 2.19: Critical reflectance LUT for the bimodal spheroid aerosol model at  $0.553 \mu\text{m}$  for  $\text{SZA} = 12^\circ$ , displayed as a function of satellite view and SSA for relative azimuth =  $0^\circ$  (upper left),  $60^\circ$  (upper right),  $120^\circ$  (lower left), and  $180^\circ$  (lower right). Upper panel is for the all albedo fitting method, lower panel is for the albedo range method.

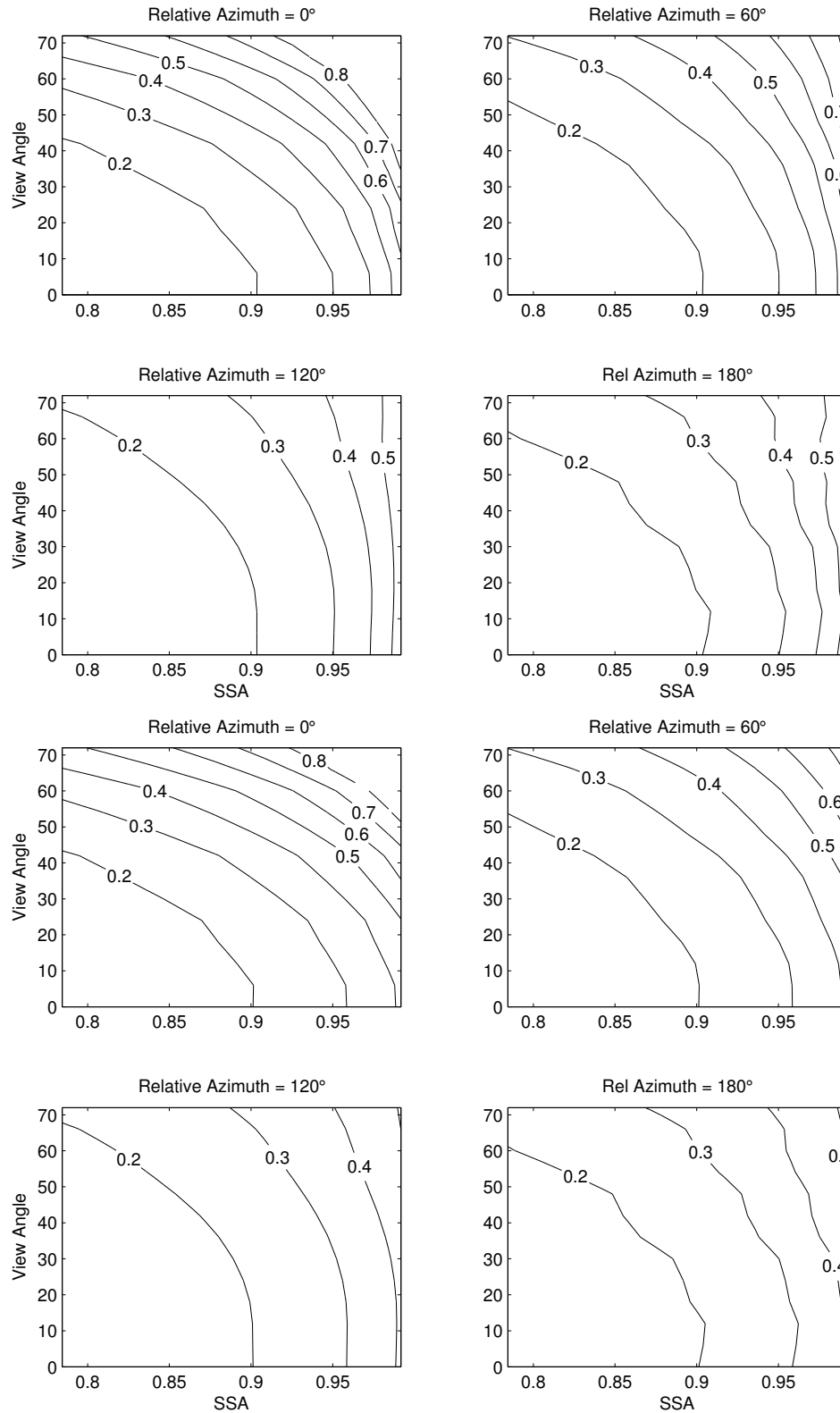


Figure 2.20: Critical reflectance LUT for the bimodal spheroid aerosol model at  $0.553 \mu\text{m}$  for  $\text{SZA} = 48^\circ$ , displayed as a function of satellite view and SSA for relative azimuth =  $0^\circ$  (upper left),  $60^\circ$  (upper right),  $120^\circ$  (lower left), and  $180^\circ$  (lower right). Upper panel is for the all albedo fitting method, lower panel is for the albedo range method.

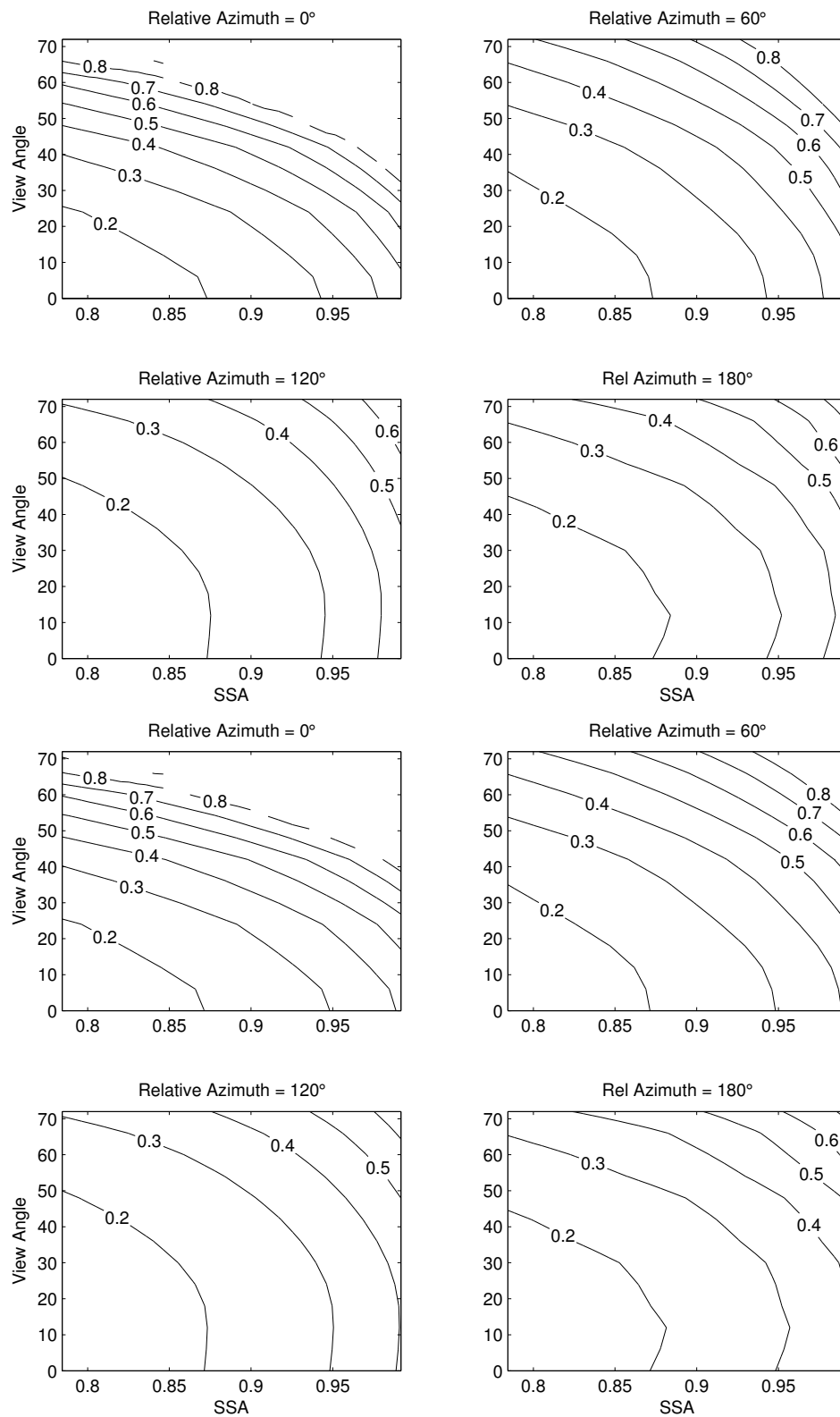


Figure 2.21: Critical reflectance LUT for the bimodal spheroid aerosol model at  $0.553 \mu\text{m}$  for  $\text{SZA} = 66^\circ$ , displayed as a function of satellite view and SSA for relative azimuth =  $0^\circ$  (upper left),  $60^\circ$  (upper right),  $120^\circ$  (lower left), and  $180^\circ$  (lower right). Upper panel is for the all albedo fitting method, lower panel is for the albedo range method.

180°, the geometry that corresponds to pure backscattering when SZA = view angle. At the larger SZAs the sensitivity of the critical reflectance to SSA drops off quickly with view angle for a relative azimuth of 0°; for SZA = 66°, the critical reflectance is nearly insensitive to changes in SSA as SSA approaches 1.0 at a relative azimuth of 0°.

#### **2.4.2 Sensitivity to Size and Shape**

In general, the critical reflectance exhibits a lower sensitivity to changes in SSA for the larger particles. For a given SSA, the fine aerosol model results in a higher critical reflectance value than the bimodal spheroid model, and the bimodal higher than the coarse model. The differences between the LUT results are more pronounced at high SSA values, indicating that the sensitivity to size is greater when the aerosol is only weakly-absorbing. The coarse model also exhibits a stronger drop off in the sensitivity to SSA at view angles corresponding to scattering angles  $< 180^\circ$  than the other aerosol models. The SBDART simulated critical reflectance is a smooth function of the satellite view angle for the fine model, whereas the coarse and bimodal spheroid aerosol models are more “spiky” functions of satellite view angle. This “spikiness” becomes less prominent as SZA increases, and as the particles become less absorbing (higher critical reflectance).

A comparison of the scattering phase functions for the aerosol models, shown in Figure 2.22 for two SSA values, may help explain these patterns. The coarse model exhibits the lowest scattering intensities at scattering angles greater than 90° and less than 170° of the four models, and thus the magnitude of the critical reflectance at a given SSA is lower for the coarse model, particularly at side scattering angles. Comparisons of the scattering phase functions for a SSA of 0.97 to those for an SSA of 0.85 reveal that the coarse and bimodal phase functions have a stronger forward scattering ( $\Theta = 0^\circ$ ) peak

when the SSA is more absorbing, which may contribute to the “spikier” nature of the critical reflectance LUT at lower SSAs. This effect is explored further in Section 2.5.4.

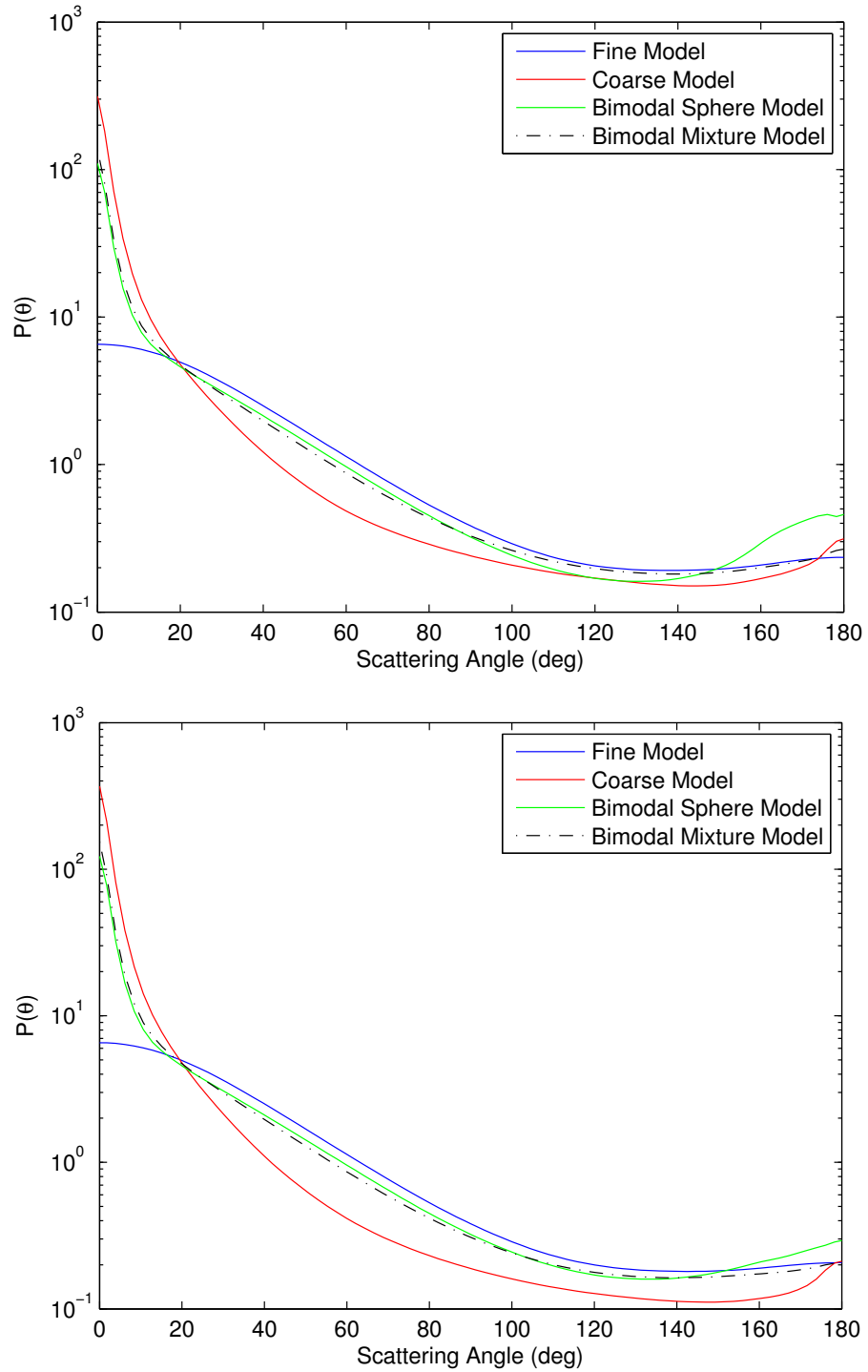


Figure 2.22: Scattering phase functions at  $0.553 \mu\text{m}$  from the T-matrix code for the four aerosol models for SSA = 0.97 (top panel) and SSA = 0.85 (bottom panel).

As with aerosol size, the critical reflectance sensitivity to shape is also strongest at backscattering angles, particularly for higher SSAs. The difference between LUTs for the bimodal sphere and spheroid models (Figure 2.23 to Figure 2.25, expressed as a percentage of the bimodal spheroid critical reflectance) reveals that, at lower SZAs, the critical reflectance uncertainty due to shape can exceed 30%. At SZAs of  $60^\circ$  or larger, however, the sensitivity to shape is very small, except at a relative azimuth of  $180^\circ$  when  $SZA = \text{view angle}$ . Figure 2.22 demonstrates that the backscattering angle is where the phase functions for the two models diverge, and this divergence is much more pronounced for the SSA of 0.97 for  $SSA = 0.85$ . The scattering intensities are higher for the spheroid model from  $100^\circ$  to  $140^\circ$  for  $SSA = 0.97$ , which is likely why it yields higher critical reflectances than the spherical model at larger view angles and higher SSAs.

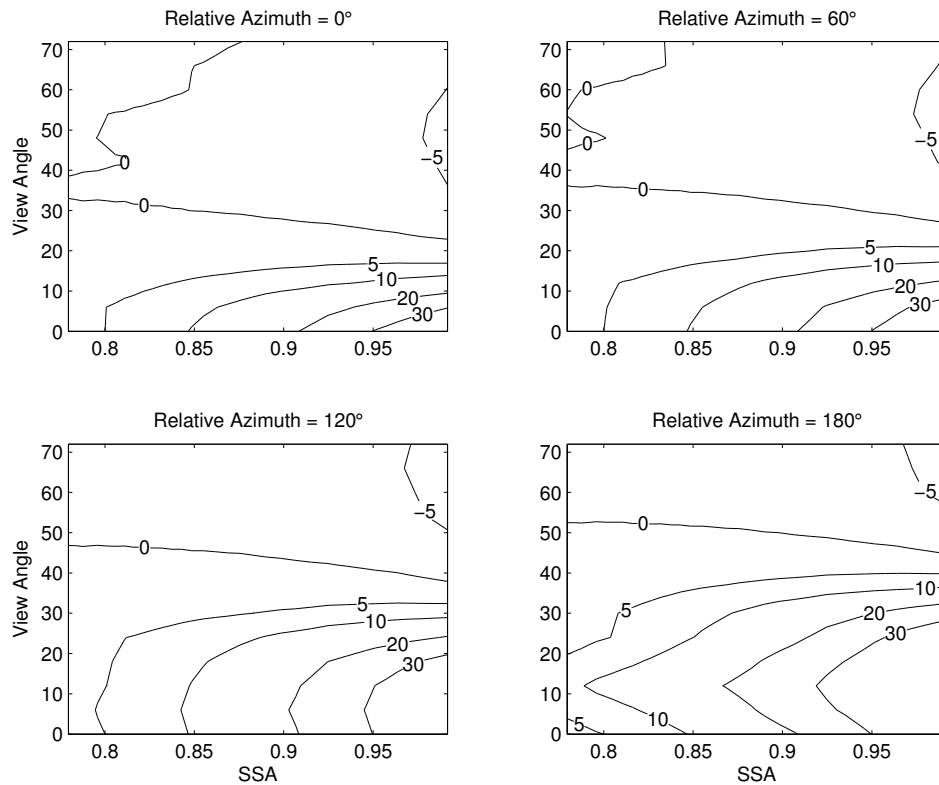


Figure 2.23: Difference between the bimodal sphere and bimodal spheroid model LUT, expressed as a percentage of the bimodal spheroid critical reflectance values, for  $0.553 \mu\text{m}$  and  $SZA = 12^\circ$ .

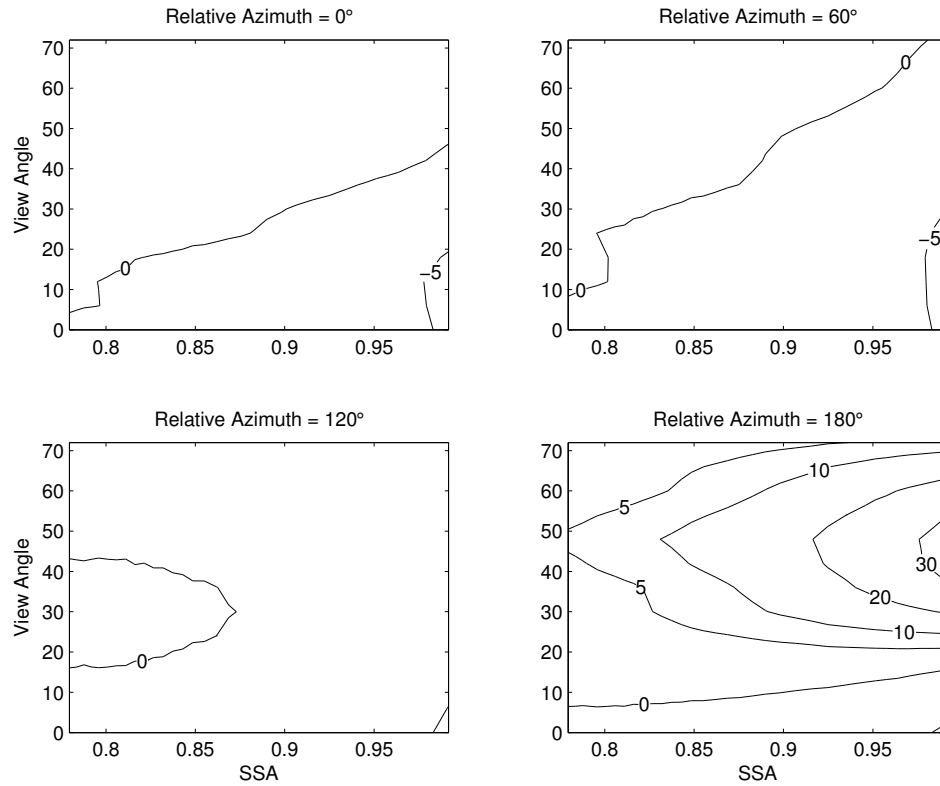


Figure 2.24: Difference between the bimodal sphere and bimodal spheroid model LUT, expressed as a percentage of the bimodal spheroid critical reflectance values, for 0.553  $\mu\text{m}$  and SZA = 48°.

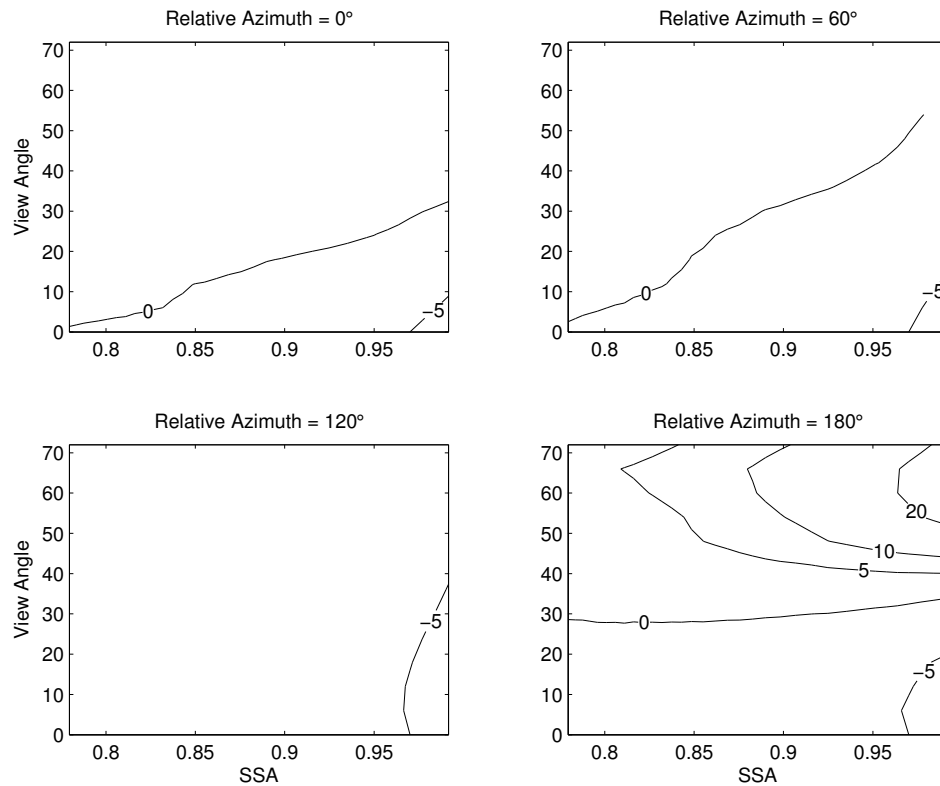


Figure 2.25: Difference between the bimodal sphere and bimodal spheroid model LUT, expressed as a percentage of the bimodal spheroid critical reflectance values, for 0.553  $\mu\text{m}$  and SZA = 66°.

### **2.4.3 Sensitivity to Fitting Method**

The sensitivity of the simulated critical reflectance to the fitting method used in its determination varies as a function of both the solar/viewing geometry, as well as the aerosol size and optical properties. For all aerosol models prescribed, the variability of the critical reflectance as a function of SSA is decreased when fitting to just the albedo range considered, primarily at smaller SZAs and for more scattering SSAs. At  $0.553\ \mu\text{m}$ , the sensitivity to choice of fitting method is most pronounced at SSAs at and above 0.95. This sensitivity is also more pronounced at view angles near the corresponding SZA, where the critical reflectance sensitivity to SSA is maximized. The critical reflectance is less sensitive to the fitting method at larger view angles, especially at relative azimuths of  $0^\circ$ . For SZAs greater than  $\sim 54^\circ$ , there is very little sensitivity to choice of fitting method for all aerosol models and SSAs.

## **2.5 Sensitivity Studies in SBDART: Implications for Forward Model Uncertainties**

In addition to simulating the full LUTs for our four aerosol models, we also perform studies of the sensitivity of the simulated critical reflectance to assumed aerosol real part of the refractive index, AOD, aerosol vertical profile, and the number of streams used in the SBDART model. As with the LUT results, we show only the simulation results here for  $\text{SZA} = 12^\circ, 48^\circ, \text{ and } 66^\circ$ . Results for all SZAs simulated can be found in Appendix B.

### **2.5.1 Sensitivity to Assumed Refractive Index**

Given that the refractive index of dust and biomass burning aerosol can vary based on mineralogy or source region, our assumed refractive index may not be

representative of the real aerosol present in the scene. In order to test the sensitivity of the critical reflectance to the assumed refractive index of the aerosol, we perform two test simulations in SBDART for the bimodal sphere model, one with a real refractive index of 1.43, and another with a real refractive index equal to 1.63. This range is probably more extreme than that found in nature, particularly at the values on the higher end, so this test represents the upper bound of uncertainty for the assumed refractive index. We vary the imaginary part of the refractive index over the same range as the standard bimodal LUT simulation. Contours of the difference between the two runs are shown in Figure 2.26 to Figure 2.28, expressed as the percentage of the values simulated for a real part of the refractive index equal to 1.53.

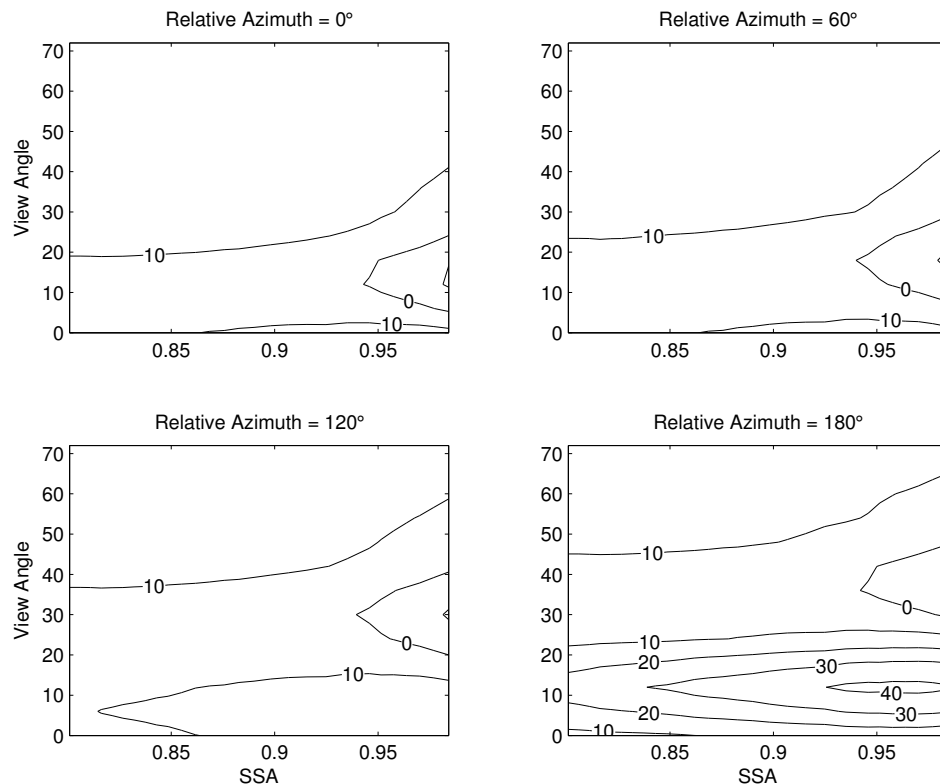


Figure 2.26: Difference between the  $n = 1.63$  and  $n = 1.43$  bimodal model LUT, expressed as a percentage of the  $n = 1.53$  critical reflectance values, for  $0.553 \mu\text{m}$  and  $\text{SZA} = 12^\circ$ .

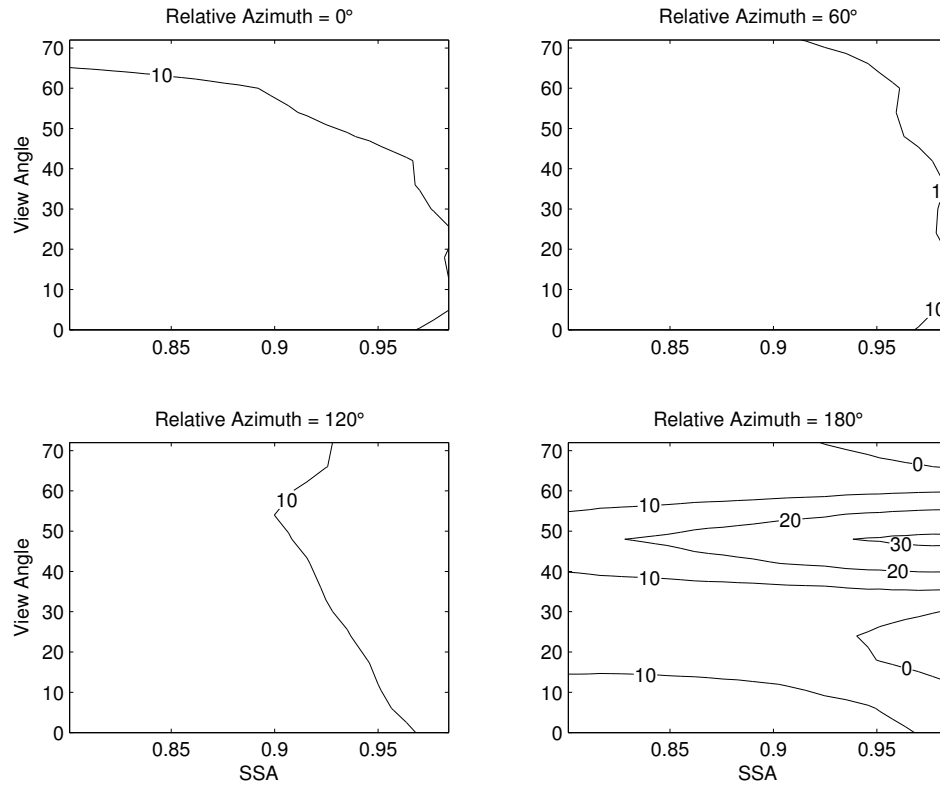


Figure 2.27: Difference between the  $n = 1.63$  and  $n = 1.43$  bimodal model LUT, expressed as a percentage of the  $n = 1.53$  critical reflectance values, for  $0.553 \mu\text{m}$  and  $\text{SZA} = 48^\circ$ .

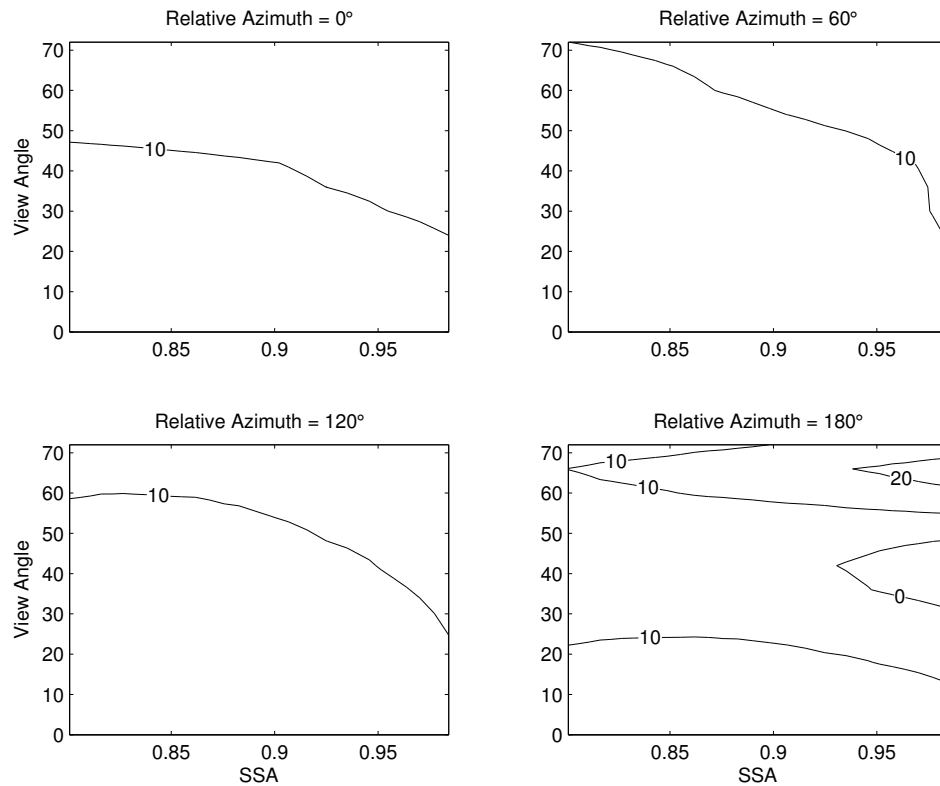


Figure 2.28: Difference between the  $n = 1.63$  and  $n = 1.43$  bimodal model LUT, expressed as a percentage of the  $n = 1.53$  critical reflectance values, for  $0.553 \mu\text{m}$  and  $\text{SZA} = 66^\circ$ .

The test results indicate that, for the bimodal aerosol model at least, the sensitivity to the refractive index is also greatest at backscattering angles. This sensitivity increases as SZA decreases and as the aerosol becomes less absorbing. For SZA = 6°, the difference between the two runs exceeds 40% of the  $n = 1.53$  critical reflectance (or,  $\pm 20\%$  of the assumed value) at SSA values larger than 0.9. For larger SZAs and relative azimuths less than 180°, the sensitivity is much lower. In general, the critical reflectance is always larger for  $n = 1.63$  than for  $n = 1.43$ , except for a range of scattering angles from 130° to 160° at SSAs higher than  $\sim 0.95$ .

### **2.5.2 Sensitivity to Varying AOD**

The critical reflectance principle represents the TOA reflectance that is roughly independent of AOD for an aerosol of fixed properties. However, we have shown our method of calculating critical reflectance to be at least somewhat sensitive to AOD, particularly at higher SSA values. Because we are using this method to retrieve aerosol properties over desert, we often do not have information about AOD. Thus, we calculate an average critical reflectance for an AOD range of 0 to 1.0 rather than assuming an AOD or trying to use ancillary information from another measurement platform. In order to test the sensitivity of our simulated results to the assumed range of AOD, we perform a test simulation for the coarse model in which we vary the AOD from 0 to 2.0. It is not uncommon to see such high AODs over the desert, especially in large dust storms. The results for the difference between the AOD = 0 to 2.0 and AOD = 0 to 1.0 simulations are shown in Figure 2.29 to Figure 2.31 for 0.553  $\mu\text{m}$ , displayed as a percentage of the critical reflectance for the AOD range of 0 to 1.0. The sensitivity is not found to be a function of fitting method, so only the albedo range results are shown.

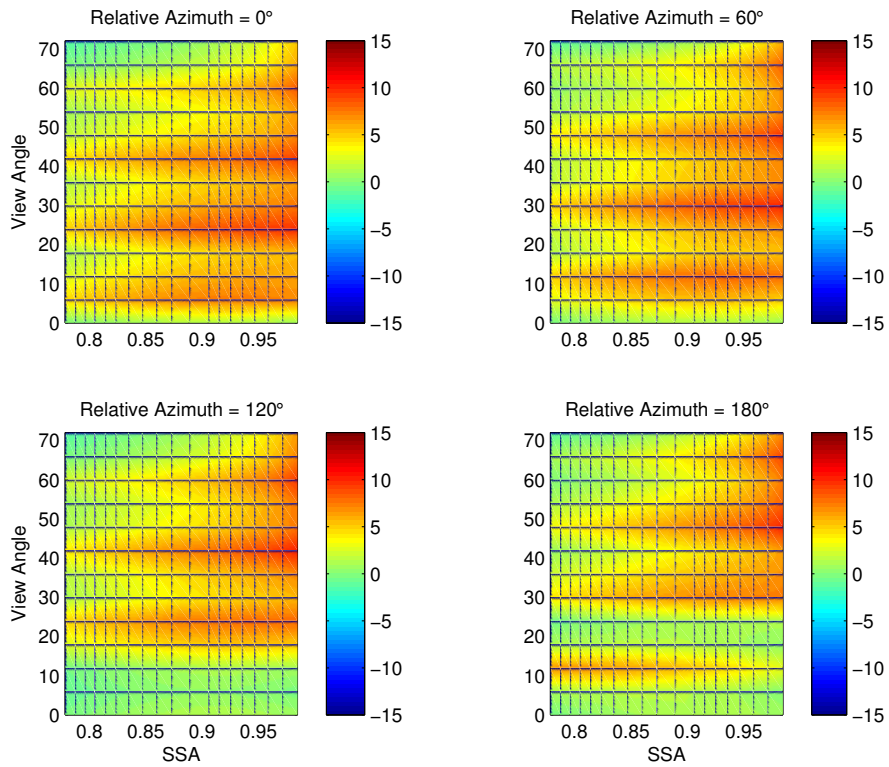


Figure 2.29: Difference between the AOD = 2.0 and AOD = 1.0 coarse model LUT, expressed as percentage of the AOD = 1.0 critical reflectance values, for 0.553  $\mu\text{m}$  and SZA = 12°.

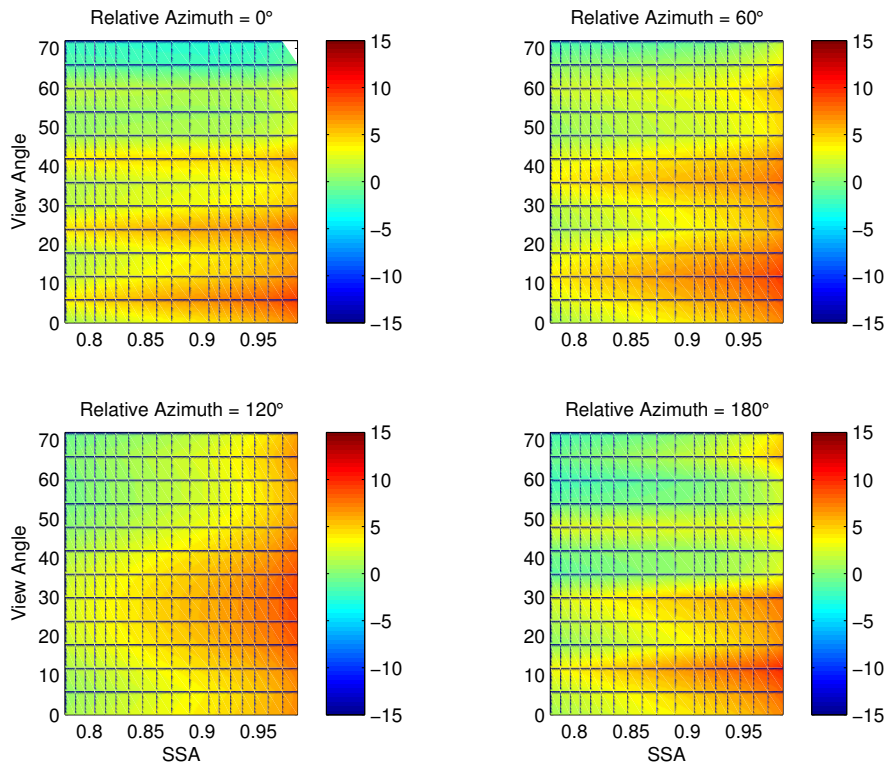


Figure 2.30: Difference between the AOD = 2.0 and AOD = 1.0 coarse model LUT, expressed as percentage of the AOD = 1.0 critical reflectance values, for 0.553  $\mu\text{m}$  and SZA = 48°.

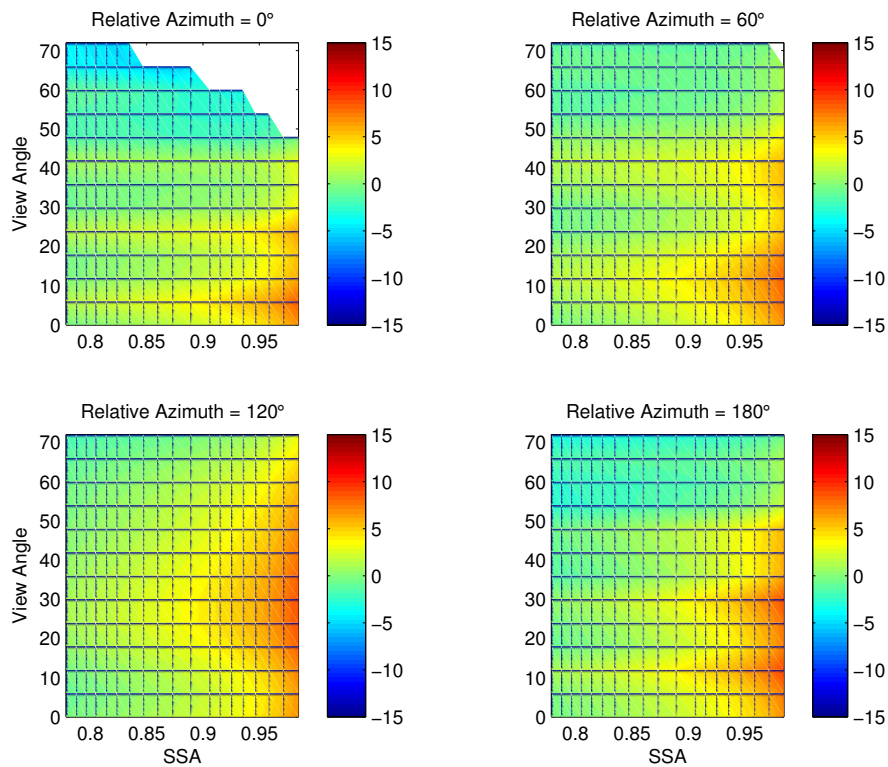


Figure 2.31: Difference between the AOD = 2.0 and AOD = 1.0 coarse model LUT, expressed as percentage of the AOD = 1.0 critical reflectance values, for 0.553  $\mu\text{m}$  and SZA = 66°.

We find the sensitivity to varying AOD to be a function of the aerosol optical properties, as well as the solar/viewing geometry. It increases as SSA increases, which is consistent with previous findings on the uncertainty of the simulated critical reflectance for the AOD = 1.0 simulation. There is some oscillatory behavior as a function of view angle, which reflects the oscillatory behavior of the coarse model LUT. The sensitivity is largest at side scattering angles (angles outside the range of the SZA), with a secondary maxima occurring at the backscattering angle at smaller SZAs. The AOD = 2.0 yields larger critical reflectances for a given SSA for smaller SZAs; for larger SZAs, the AOD = 2.0 run yields somewhat smaller critical reflectances than the AOD = 1.0 run for larger satellite view angles. In general, the sensitivity to AOD decreases as SZA increases. Differences between the two runs generally do not exceed 10%, however.

### 2.5.3 Sensitivity to Vertical Stratification

We test the SBDART code for the sensitivity of the TOA radiance to the assumed vertical profile of aerosol for both fine and coarse aerosol. We compare the TOA radiance output for the assumed vertical profile in Figure 2.5 to the radiance output when the aerosol layer is confined to the lowest 1 km of the atmosphere. The simulated TOA radiance is more sensitive to changes in vertical profile for the coarse aerosol model, so the LUT sensitivity of critical reflectance to the vertical profile is shown for the coarse model in Figure 2.32 to Figure 2.34. The critical reflectance is more sensitive to the vertical profile for more absorbing SSAs, and this sensitivity also increases somewhat with SZA and with relative azimuth. For the range of SSAs that are applicable to our region of study, however, we find that the critical reflectance variability is only 2-4%.

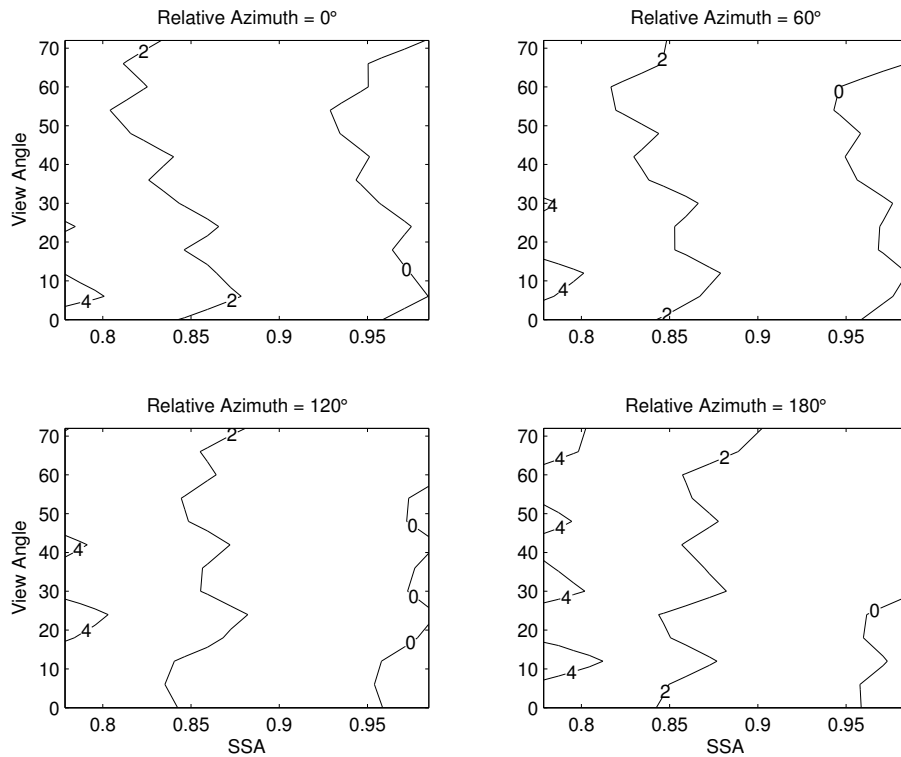


Figure 2.32: Difference between the coarse model LUTs for the assumed vertical distribution and a 1km aerosol layer height, expressed as percentage of the critical reflectance values for the assumed vertical distribution, for 0.553  $\mu\text{m}$  and SZA = 12°.

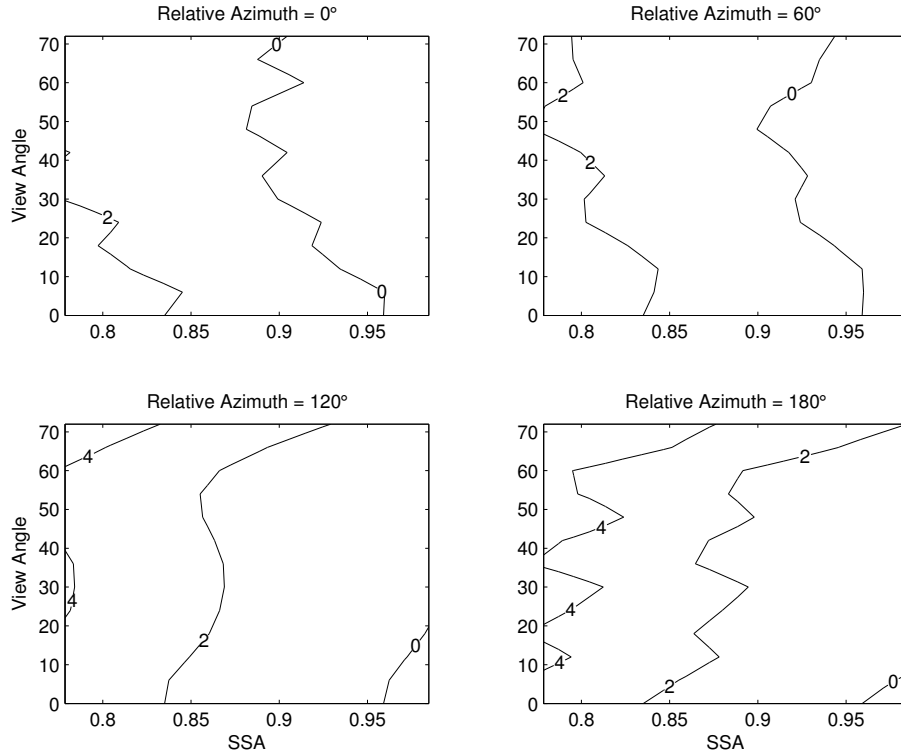


Figure 2.33: Difference between the coarse model LUTs for the assumed vertical distribution and a 1km aerosol layer height, expressed as percentage of the critical reflectance values for the assumed vertical distribution, for 0.553  $\mu\text{m}$  and SZA = 48°.

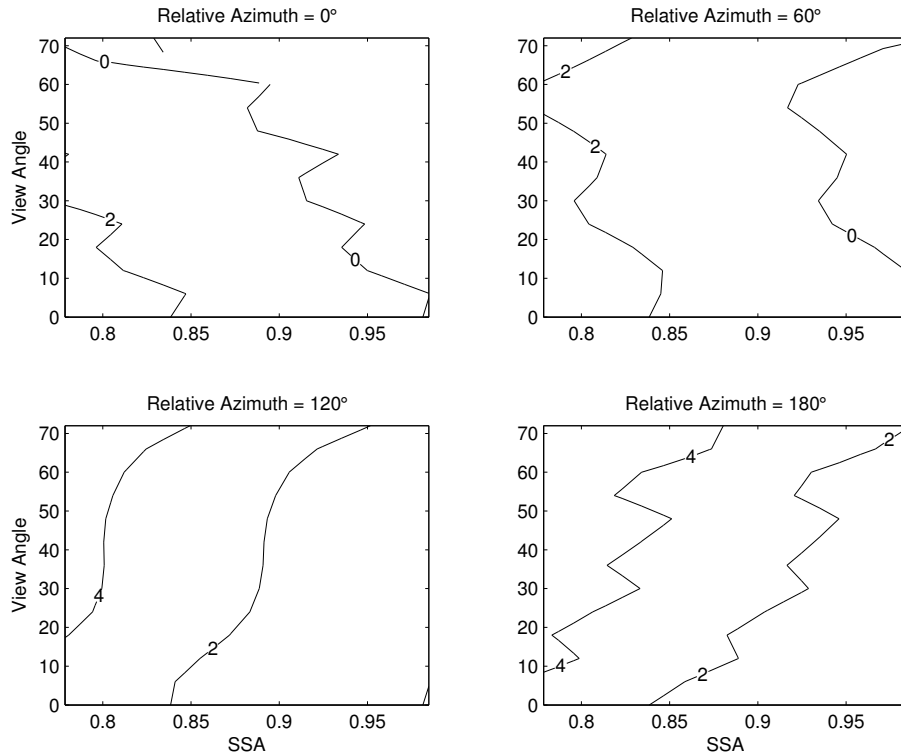


Figure 2.34: Difference between the coarse model LUTs for the assumed vertical distribution and a 1km aerosol layer height, expressed as percentage of the critical reflectance values for the assumed vertical distribution, for 0.553  $\mu\text{m}$  and SZA = 66°.

### 2.5.4 Sensitivity to Number of Streams Used in SBDART

The fact that the LUT results for the coarse model (and to a lesser degree the bimodal mixed model) are not a smooth function of the satellite viewing angle is somewhat disconcerting, and may point to the inability of the SBDART code to properly expand phase functions with a strong forward peak and very flat variation with scattering angle at side scattering angles. To test this, we run a full simulation using the coarse model with 40 streams, but only 80 expansion coefficients. Differences in the critical reflectance between the 40- and 20-stream run are shown in the following figures for  $0.553 \mu\text{m}$ . These differences were nearly insensitive to the fitting method used, so only results for the albedo range fitting method are shown in Figure 2.35 to Figure 2.37.

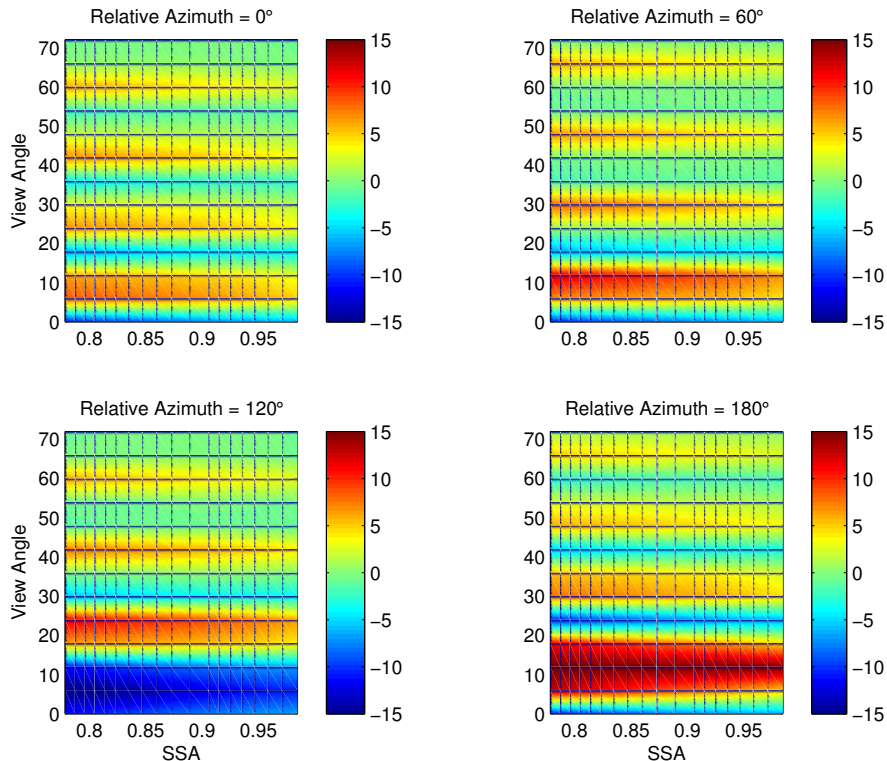


Figure 2.35: Difference between the 40- and 20-stream coarse model LUT, expressed as percentage of the 20-stream critical reflectance values, for  $0.553 \mu\text{m}$  and  $\text{SZA} = 12^\circ$ .

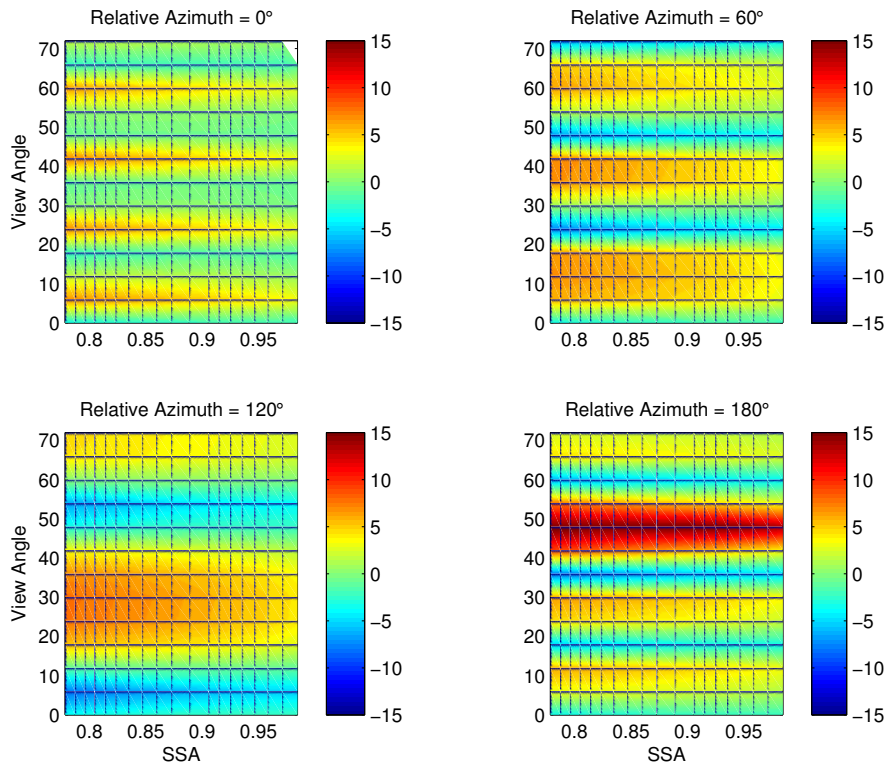


Figure 2.36: Difference between the 40- and 20-stream coarse model LUT, expressed as percentage of the 20-stream critical reflectance values, for  $0.553 \mu\text{m}$  and  $\text{SZA} = 42^\circ$ .

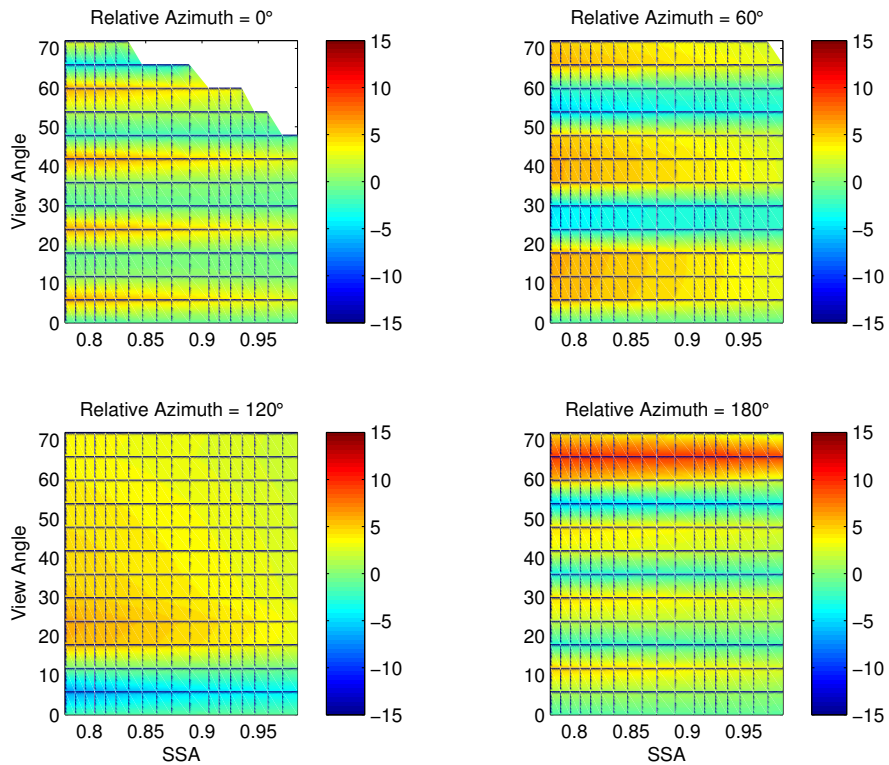


Figure 2.37: Difference between the 40- and 20-stream coarse model LUT, expressed as percentage of the 20-stream critical reflectance values, for  $0.553 \mu\text{m}$  and  $\text{SZA} = 66^\circ$ .

The differences between the two runs are nearly insensitive to the aerosol optical properties, but are a strong function of satellite view angle. This is a manifestation of the fact that the 40-stream LUT is a smoother function of view angle than the 20-stream run (although there are still some oscillations with view angle). Differences are largest for the backscattering angles; at an SZA of  $6^\circ$ , the difference at backscattering angles exceeds 20% of the 20-stream critical reflectance LUT. The sensitivity to number of streams decreases as SZA increases; resulting in uncertainties that are generally within 5% at all scattering angles less than backscattering.

### **2.5.5 Summary of Findings**

Based on the results presented here for the LUT simulations and sensitivity studies, we hypothesize that our application of the critical reflectance retrieval over North Africa may be subject to larger uncertainties due to assumptions of size, shape, refractive index, and AOD variability than if we applied the method in a region impacted by more absorbing aerosol. We find that the sensitivity of the critical reflectance to SSA is lower for coarse particles, so the inversion uncertainties of SSA for dust aerosol may be larger than for smaller particles. The sensitivity of the critical reflectance to changes in SSA is also greater for weakly-absorbing aerosol, and exhibits larger sensitivity to physical and optical properties of the aerosol. The sensitivity to shape and refractive index will have a more significant effect at backscattering angles, and thus may be reduced if we confine our retrieval to backscattering angles  $< \sim 170^\circ$ .

### 3 Case Study Results

To test the critical reflectance method of deriving SSA over bright desert surfaces, we perform retrievals over two North African AERONET sites that we assume to have a somewhat different regional aerosol influence: Tamanrasset INM, a site in the Algerian Sahara; and Banizoumbou, a Sahelian site located in Niger. Locations of the sites are mapped in Figure 3.1. In order to find cases with a 16-day separation that have different aerosol loadings, we utilize the Version 2 Level 2 AOD data from each site. Pairs of days are chosen so that the  $0.44 \mu\text{m}$  AOD is less than 0.2 on the clean day, and greater than 0.4 on the polluted day, resulting in 18 pairs of days at Tamanrasset, and 11 pairs of days at Banizoumbou. Some days have both Terra and Aqua data available, and a few days had clean cases for +16 and -16 days from the polluted day available for comparison, making a total of 27 cases at Tamanrasset, and 15 at Banizoumbou.

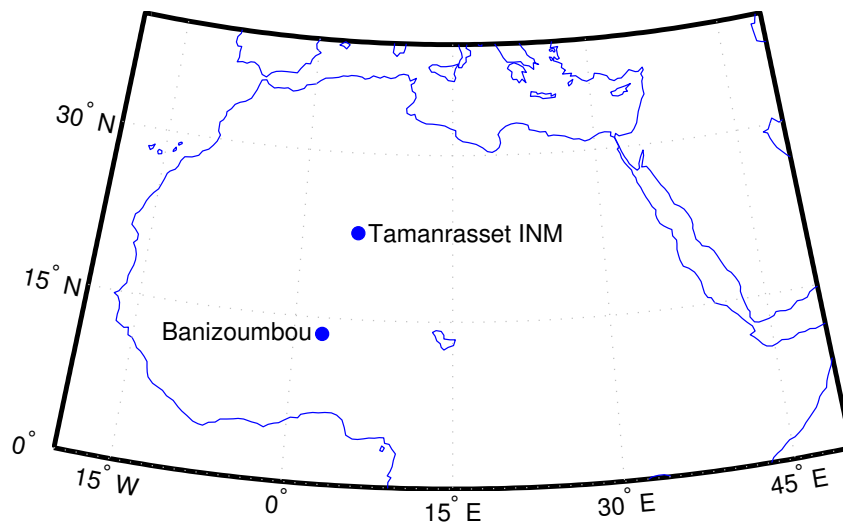


Figure 3.1: Locations of the two AERONET sites used for case study analysis.

### **3.1 Tamanrasset AERONET Site**

The Tamanrasset site is described as being in an area “free from industrial activities” ([http://aeronet.gsfc.nasa.gov/new\\_web/photo\\_db/Tamanrasset\\_INM.html](http://aeronet.gsfc.nasa.gov/new_web/photo_db/Tamanrasset_INM.html)) and, given its location, should thus be impacted primarily by soil dust aerosol. The average  $0.44 - 0.87 \mu\text{m}$  Angstrom exponent at this site is 0.16 for cases when the  $0.44 \mu\text{m}$  AOD exceeds 0.4, indicating that aerosol events at this site are dominated by coarse particles. Additionally, observations during a Saharan boundary layer study (Cuesta et al., 2008) note very clean conditions in the winter month at Tamanrasset, the season of peak northward transport of biomass burning from the Sahel. This site is also located at an elevation of 1377 meters—this elevation was assumed in the SBDART model when building a LUT for retrievals in this region.

#### **3.1.1 MODIS Reflectances**

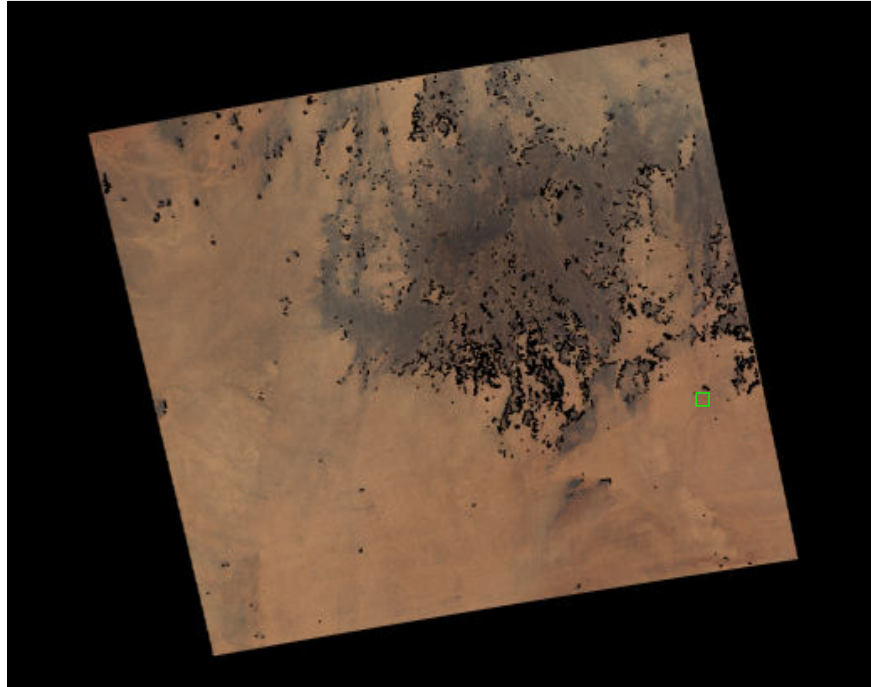
Before discussing the SSA results at Tamanrasset, a qualitative discussion of the RGB images and TOA reflectance scatter plots from MODIS is helpful in understanding the radiative effects of aerosol in this region. For a constant loading, aerosol can enhance (negative  $F_{\text{TOA}}$ ) or reduce (positive  $F_{\text{TOA}}$ ) the TOA reflectance near Tamanrasset, or a change in aerosol loading can result in little change in the TOA reflectance if the TOA reflectance is near the critical reflectance. The scatter plots of MODIS reflectances indicate that the brightening or darkening effect of the aerosol at visible wavelengths near Tamanrasset is primarily driven by the optical properties in the blue channel. Two pairs of images with a similar aerosol loading, one from 22 February/6 February 2007 and the

other from 28 February/15 March 2008, demonstrate this. Both 22 February 2007 and 28 February 2008 correspond to an AERONET reported AOD of  $\sim 0.7$  at  $0.44 \mu\text{m}$ .

On 22 February 2007, the brightness of the polluted RGB image (Figure 3.2, top) looks quite similar to that of the cleaner image (Figure 3.2, bottom), despite the aerosol loading. The reflectance scatter plots at the seven MODIS channels used in this study (Figure 3.3, corresponding to the area inside the green box in Figure 3.2) reveal that the polluted reflectances are quite close to the critical reflectances at each channel (very near the one-to-one line) for this case, with perhaps a small amount of brightening happening in the near-IR (where the reflectances start to rise above the one-to-one line). Thus, at this particular location and viewing geometry, the aerosol is exerting a near-zero TOA forcing in the visible channels, and a slightly negative TOA forcing in the near-IR.

The critical reflectance and y-intercept values from the scatter plots also tell us something about the predominant aerosol type that is present in this scene. The critical reflectance is lowest in the blue channel ( $\sim 0.2$ ), increasing strongly to a value near 0.4 in the red channel, and a value near 0.6 in the near-IR channels. This indicates that absorption is strongest in the blue channel, and decreases as a function of wavelength. Such a spectral dependence of absorption is typical of dust aerosol, because of the presence of iron oxides that are absorbing in the blue channel (Kaufman et al., 2001; Sokolik and Toon, 1999). The y-intercept in these plots is a measure of the difference in optical depth between the two days and, because the spectral dependence of optical depth contains information about aerosol size, the y-intercept (what we will call path radiance) should contain information about the aerosol size as well. For this case, the path radiance increases in magnitude from  $\sim 0.1$  in the blue to  $\sim 0.4$  at  $1.632 \mu\text{m}$ , decreasing by a small

2007053 1250 Aqua



2007037 1250 Aqua

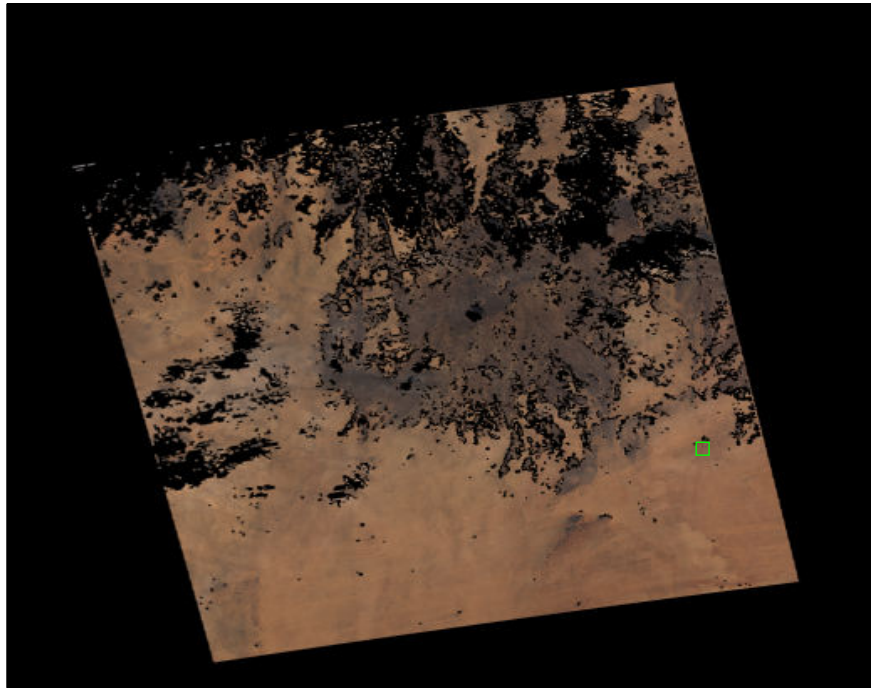


Figure 3.2: MODIS Aqua RGB images for a polluted day (22 Feb 2007 1250 UTC, top) and a cleaner day (6 Feb 2007 1250 UTC, bottom) near Tamanrasset.

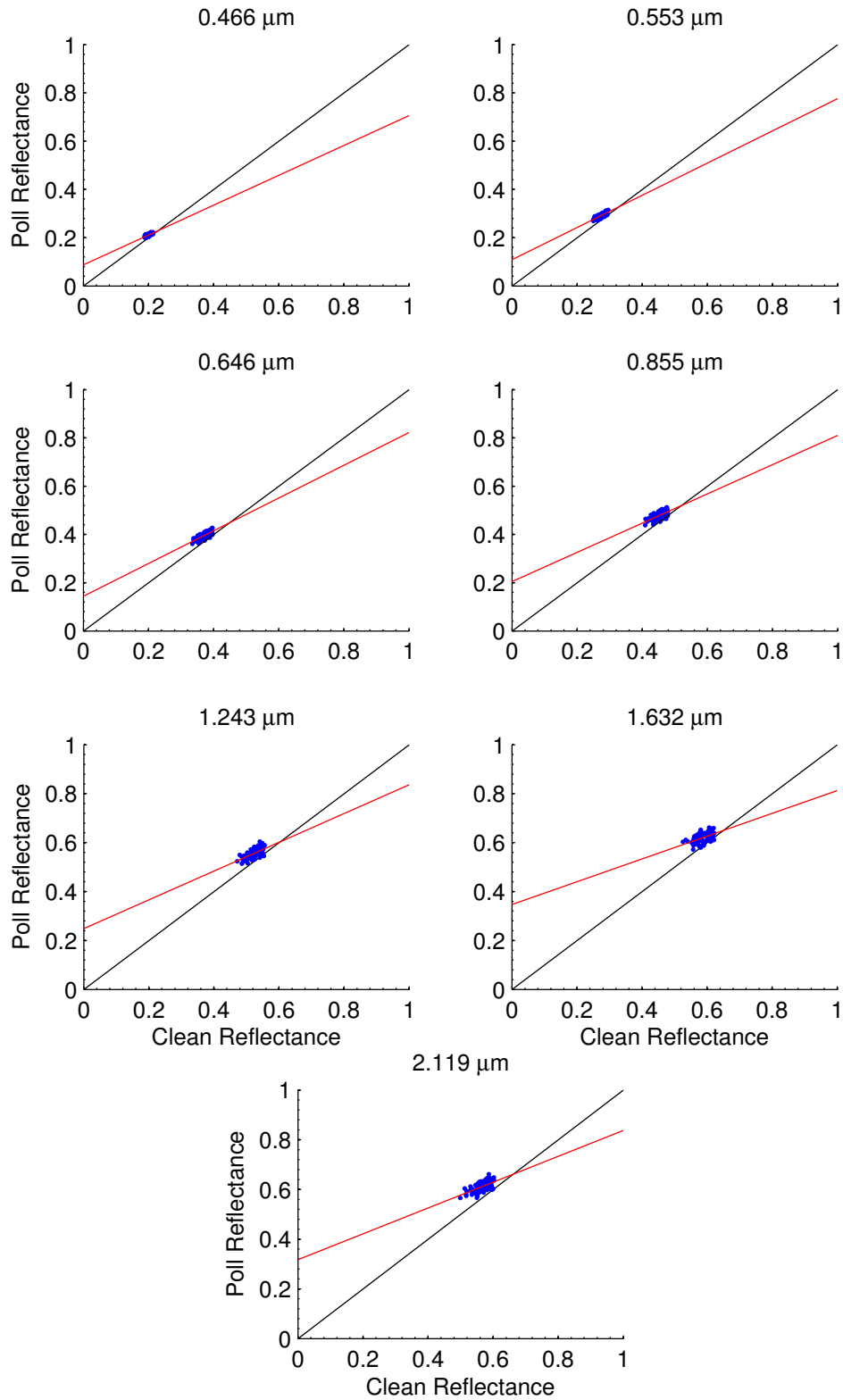
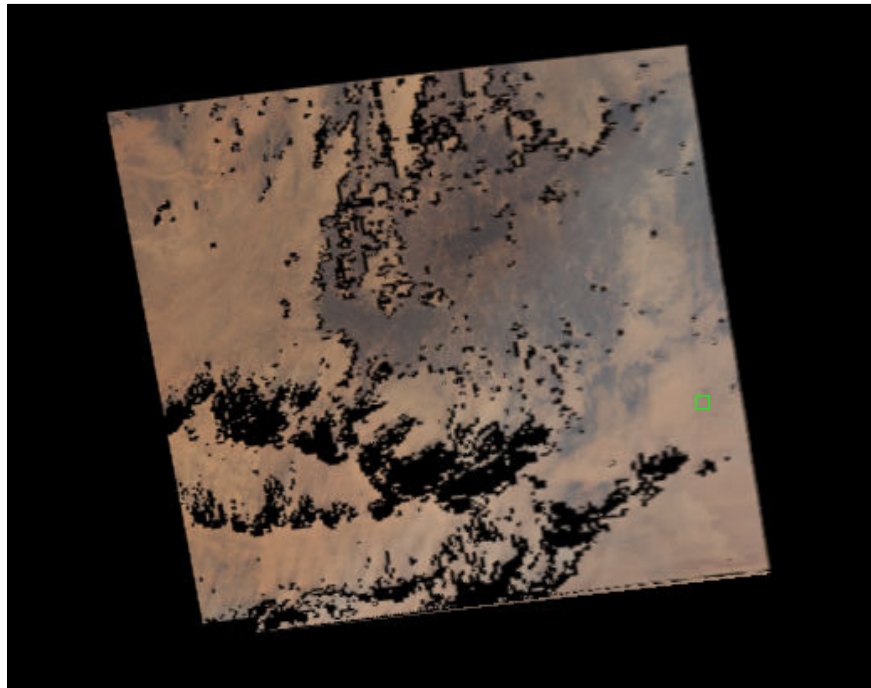


Figure 3.3: Scatter plots of the polluted versus clean reflectances for the 22 February 2007 case near Tamanrasset for each of the seven channels used in the retrieval. The red line is the robust linear fit to the reflectance data, and the black line is the one-to-one line.

amount at 2.119  $\mu\text{m}$ . An increase in the AOD with wavelength is indicative of the presence of large particles, as is the fact that there is still a significant aerosol signal in the near-IR. Thus, both the critical reflectance and path radiance for this case are consistent with what we might expect for dust aerosol. It should be noted, however, that the y-intercept value of the linear fits to the reflectance data will be sensitive to small changes in the slope of the fit line. Therefore, it probably does not represent a quantitative measure of the optical depth difference between the two days. The information content of the spectral dependence of path radiance and critical reflectance derived from the reflectance scatter plots will be explored further in Section 3.2.2.

In contrast to the aerosol in the first case presented, the aerosol on 28 February 2008 near Tamanrasset has enhanced the TOA reflectance in the visible channels, but has reduced the TOA reflectance in the near-IR. This can be seen in both the RGB images (Figure 3.4, particularly in the right half of the image) and in the scatter plots of the polluted versus clean reflectances (Figure 3.5, corresponding to the green box in Figure 3.4). In the blue and green channels, the polluted reflectances are higher than the clean values (resulting in a negative TOA effect at this geometry); in the red channel the reflectances are close to the critical reflectance value, and in the near-IR they are a bit lower than the critical reflectance (resulting in a positive TOA effect at these channels). The critical reflectance values for this case also increase with wavelength, and the y-intercept is almost spectrally-invariant. This again suggests that dust dominates the aerosol in this case, although perhaps with particles of a smaller mean size than in the first case. Compared to the first case, the critical reflectance values on this day are higher in the visible ( $\sim 0.4$  versus 0.2) and lower in the near-IR ( $\sim 0.5$  versus 0.6), resulting in a

2008059 1320 Aqua



2008075 1320 Aqua

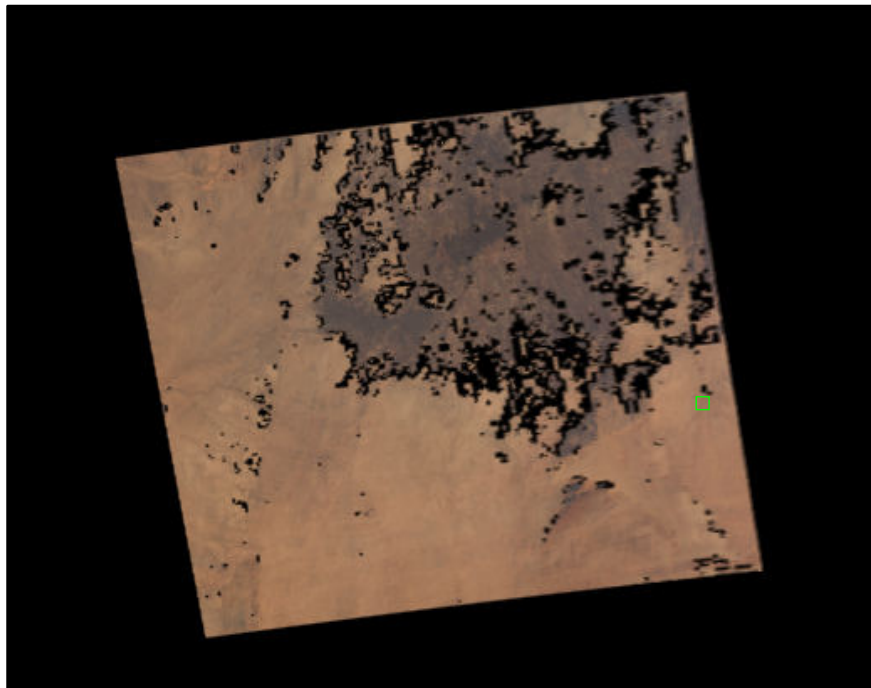


Figure 3.4: MODIS Aqua RGB images for a polluted day (28 Feb 2008 1320 UTC, top) and a cleaner day (15 March 2008 1320 UTC, bottom) near Tamanrasset.

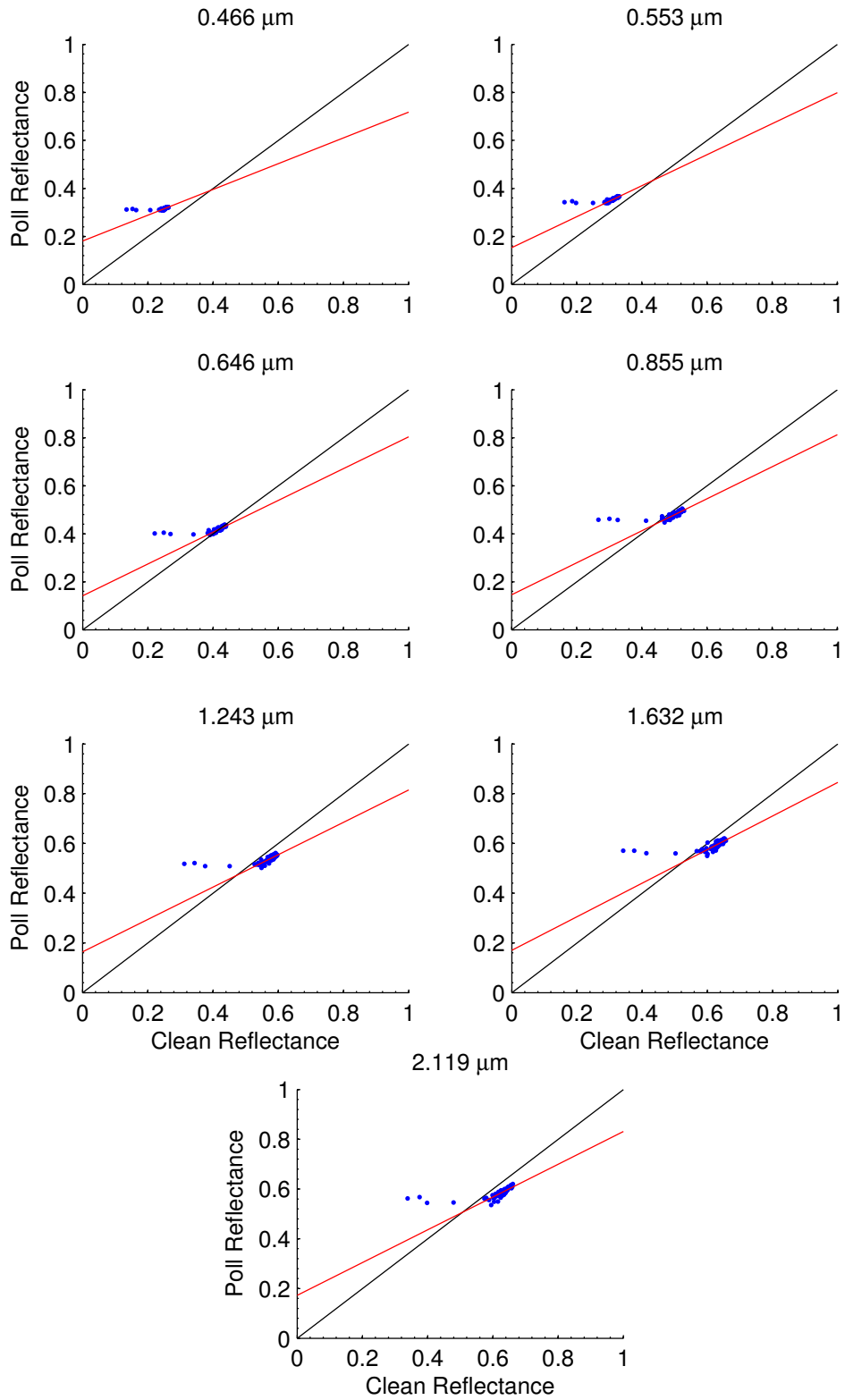


Figure 3.5: Scatter plots of the polluted versus clean reflectances for the 28 February 2008 case near Tamanrasset for each of the seven channels used in the retrieval. The red line is the robust linear fit to the reflectance data, and the black line is the one-to-one line.

weaker spectral dependence of the critical reflectance. It is important to recognize, however, that this does not necessarily mean that the SSA (or the spectral dependence of the SSA) will be different between these two days. The two polluted days have similar AODs but different satellite viewing geometries, so they may exhibit different critical reflectance-SSA relationships. Nevertheless, this image comparison demonstrates the potential of the critical reflectance to serve as a measure of the spectral direct radiative effect of aerosols over land at TOA, without having to make any assumptions about the physical or optical properties of the aerosol. It also indicates that the critical reflectance and path radiance may contain some information about the aerosol present in the scene—information that cannot be obtained from a single-image retrieval over this region.

### **3.1.2 Critical Reflectance and SSA Results**

#### ***3.1.2.1 SSA Image Retrievals***

Maps of the critical reflectance, path radiance, the radiative effect at TOA, and SSA at  $0.553\ \mu\text{m}$  are shown here for the two cases described in the previous section; results for all cases from Tamanrasset are displayed in Appendix C. The radiative effect at TOA was determined as the difference between the mean of the clean reflectances and the critical reflectance. If the value is positive, the aerosol causes a darkening of the scene (polluted reflectances are less than the clean reflectances); if the value is negative, the aerosol brightens the scene (polluted reflectances are greater than the clean reflectances). The SSA results shown are those determined using the TOA v SFC fitting method (discussed in Section 2.2.3). Missing pixels are due to the screening of clouds, missing reflectances within the retrieval pixel, or too much scatter as determined by the robust fitting routine. It should be noted that the area north of  $22^\circ\ \text{N}$  between  $5^\circ$  and  $7^\circ\ \text{E}$  often

yields poor fits to the reflectance data, despite the fact that many of the pixels are retained by the algorithm. The critical reflectances retrieved here are generally much lower than over the rest of the image, and are not representative of the actual critical reflectance based on a visual inspection of the scatter plots. Thus, we focus our attention on the portions of the image that are south and west of this area.

Results for the first case discussed, 22 February 2007, are shown in Figure 3.6. The critical reflectance values at  $0.553 \mu\text{m}$  are generally between 0.3 and 0.4, with some intermittent pixels exceeding 0.5 and 0.6. The path radiance contains more variability over the image, with patches of values ranging from 0.02 to 0.35. Values tend to be higher in the areas surrounding the cloud-cleared pixels along the western edge of the image, which could indicate incomplete removal of cloud contaminated pixels. The TOA effect was generally near zero over much of the image, as should be expected based on the appearance of the RGB image. Some pixels indicate stronger cooling, which corresponds with the higher critical reflectance values near the southern edge of the image.

The  $0.553 \mu\text{m}$  SSA values for this case fall mostly in the range between 0.97 and 0.98, although values are a bit lower near the cloudy area (which again could be due to incomplete removal of cloudy pixels) and a few have been set to a value of 1.0. As mentioned in Chapter 2, any pixel in which the critical reflectance exceeds the maximum value in the LUT is set to 1.0, and that is what has occurred in these pixels. The critical reflectance of these pixels is generally higher than the surrounding pixels, which could indicate that the background aerosol is varying across the image. The few pixels that remain in the area north of  $22^\circ \text{N}$  between  $5^\circ$  and  $7^\circ \text{E}$  have SSA values that appear much

more absorbing than the rest of the pixels in the image, again due to a poor determination of the critical reflectance. One reason for this poor determination may be the existence of complex terrain in the region, as Tamanrasset is located near the Ahaggar Mountains in southern Algeria.

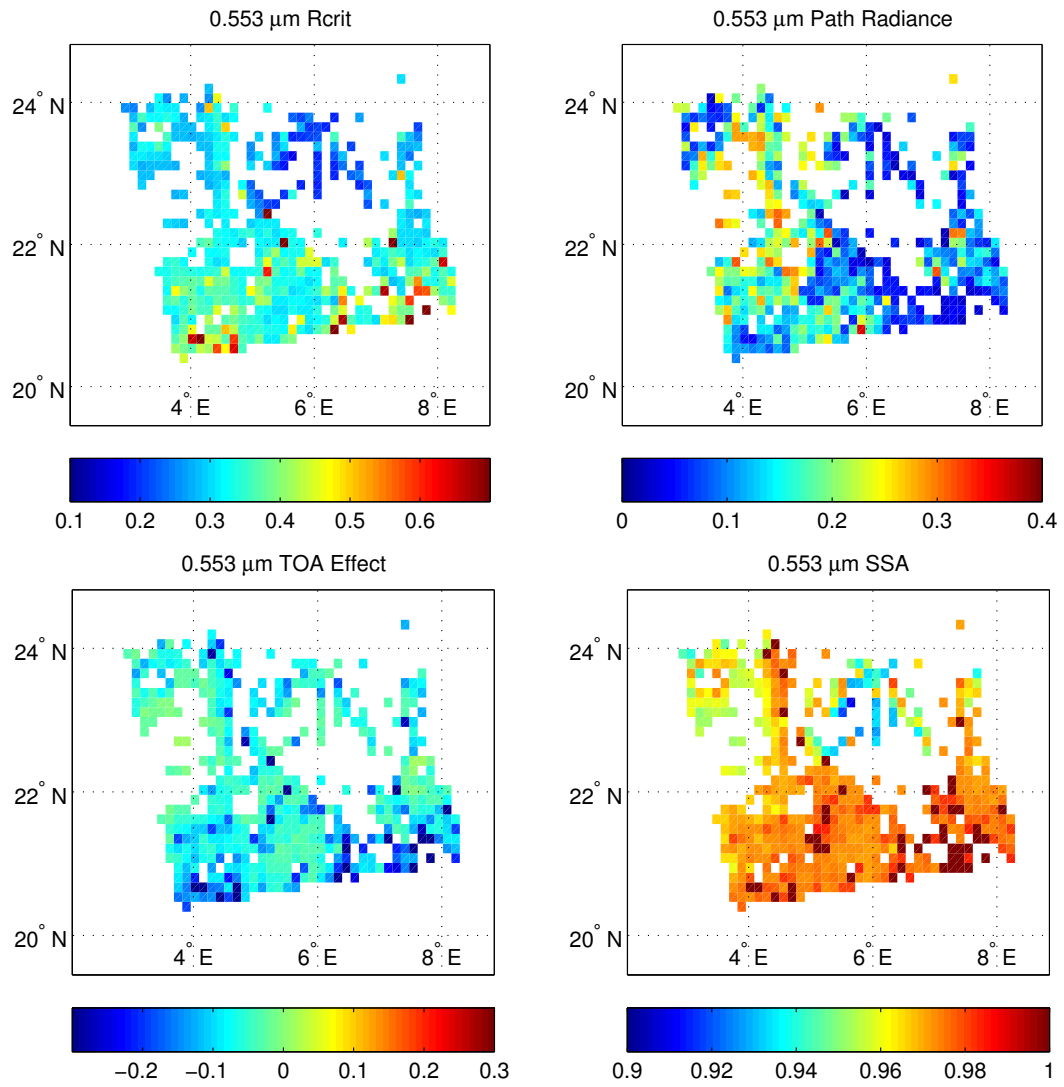


Figure 3.6: Image retrievals of critical reflectance (upper left), path radiance (upper right), TOA radiative effect (lower left), and SSA (lower right) at 0.553 μm for 22 February 2007 1250 UTC (compared to -16 days) near Tamanrasset.

Results for the second case, 28 February 2008, are shown in Figure 3.7. Due to the presence of clouds on the polluted day in this case, a large swath of the image has been removed. The critical reflectance values at 0.553 μm for this case are somewhat

higher than the first case, ranging from 0.4 to 0.5. The path radiance varies widely from pixel-to-pixel, which could indicate that the AOD is not constant in each pixel, or it could simply be due to the uncertainties associated with the robust fitting routine. There is a negative TOA effect over most of the image, particularly the eastern part that corresponds to the brightened region in the RGB image. SSA values in this region are a bit higher than they are in the first case ( $\sim 0.98$  with many pixels set to 1.0); SSAs are closer to 0.96 in the northwestern corner of the image, resulting in a near-zero TOA forcing here.

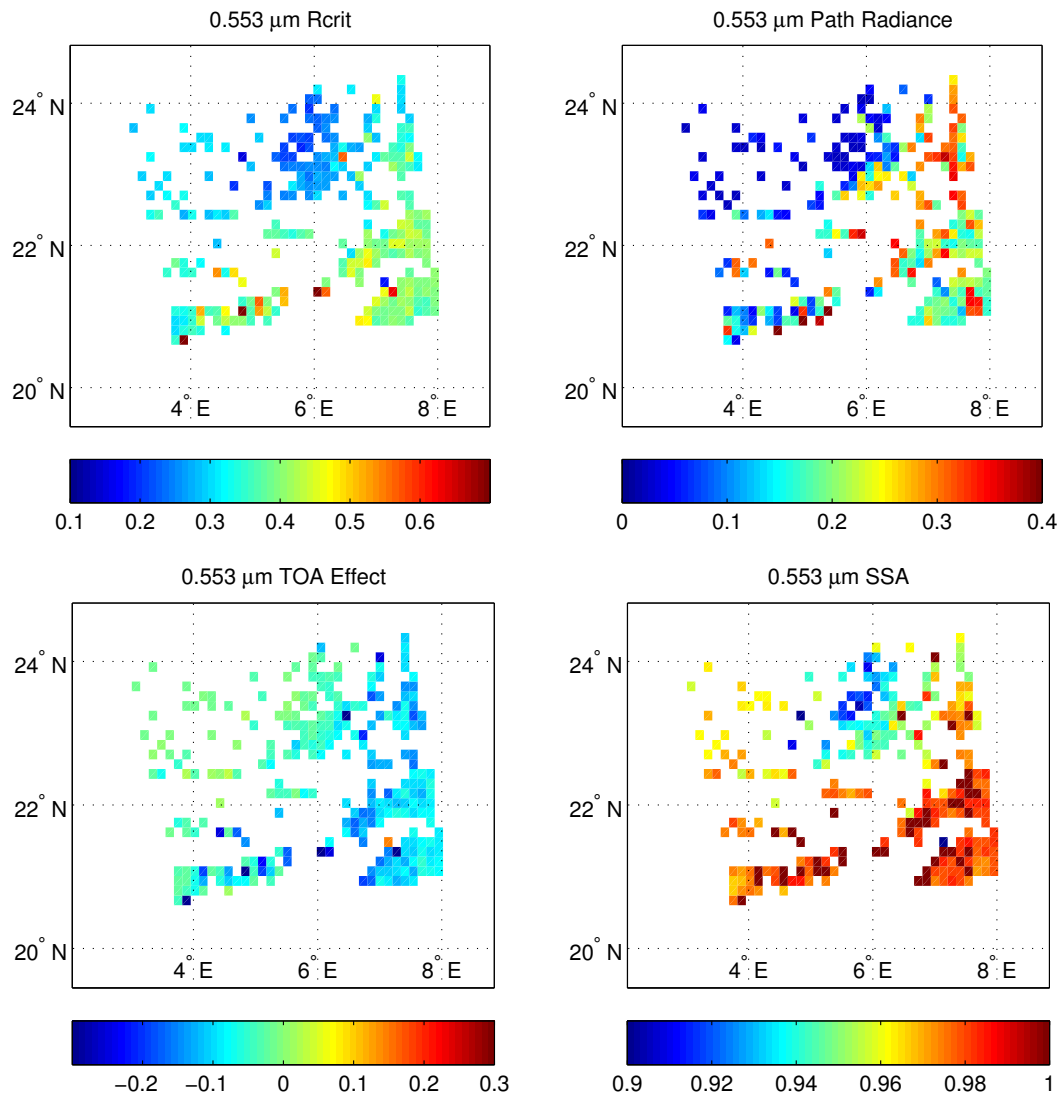


Figure 3.7: Image retrievals of critical reflectance (upper left), path radiance (upper right), TOA radiative effect (lower left), and SSA (lower right) at 0.553 μm for 28 February 2008 1320 UTC (compared to -16 days) near Tamanrasset.

### 3.1.2.2 Spectral SSA Retrievals near AERONET Site

In order to investigate the spectral behavior of the SSA, and to facilitate comparisons with the Tamanrasset AERONET station, we calculate 5 x 5 pixel (~75 x 75 km) averages of the critical reflectance, path radiance, and SSA near the Tamanrasset site. Because the site itself is located in the region where good retrievals could rarely be performed, all comparisons are to MODIS data located 1° latitude south of the station, where much better data regressions could be achieved and spatial variability of the results is much lower. The results are shown with error bars that represent either a spatial standard deviation of the critical reflectance ( $\sigma_{5 \times 5}$ ) or the average of the fitting uncertainties of each of the pixels that went into calculating the mean ( $\sigma_{mean}$ ). The latter uncertainty estimate is calculated as

$$\sigma_{mean} = \sqrt{\frac{\sum_{i=1}^N \sigma_{SSA,i}^2}{N^2}} \quad (3.1)$$

where  $\sigma_{SSA,i}$  is the fitting uncertainty of each individual pixel, and  $N$  is the number of pixels that went into the calculation of the spatial average (25 assuming there were no missing data in the vicinity). We find the average uncertainty of the individual pixels to generally be larger than the 5 x 5 pixel spatial variability of the SSA.

Spectral results for the critical reflectance, path radiance, and SSA near the site for the two example cases are located in Figure 3.8 and Figure 3.9. Plots on the left contain estimates of the uncertainty using Equation 3.1, and plots on the right contain error bars that are equal to  $\sigma_{5 \times 5}$ . Also shown are the Version 2 Level 1.5 AERONET SSA values for each day, as there were no Level 2 data yet available at the Tamanrasset site. Spectral plots for all 27 cases are shown in Appendix D.

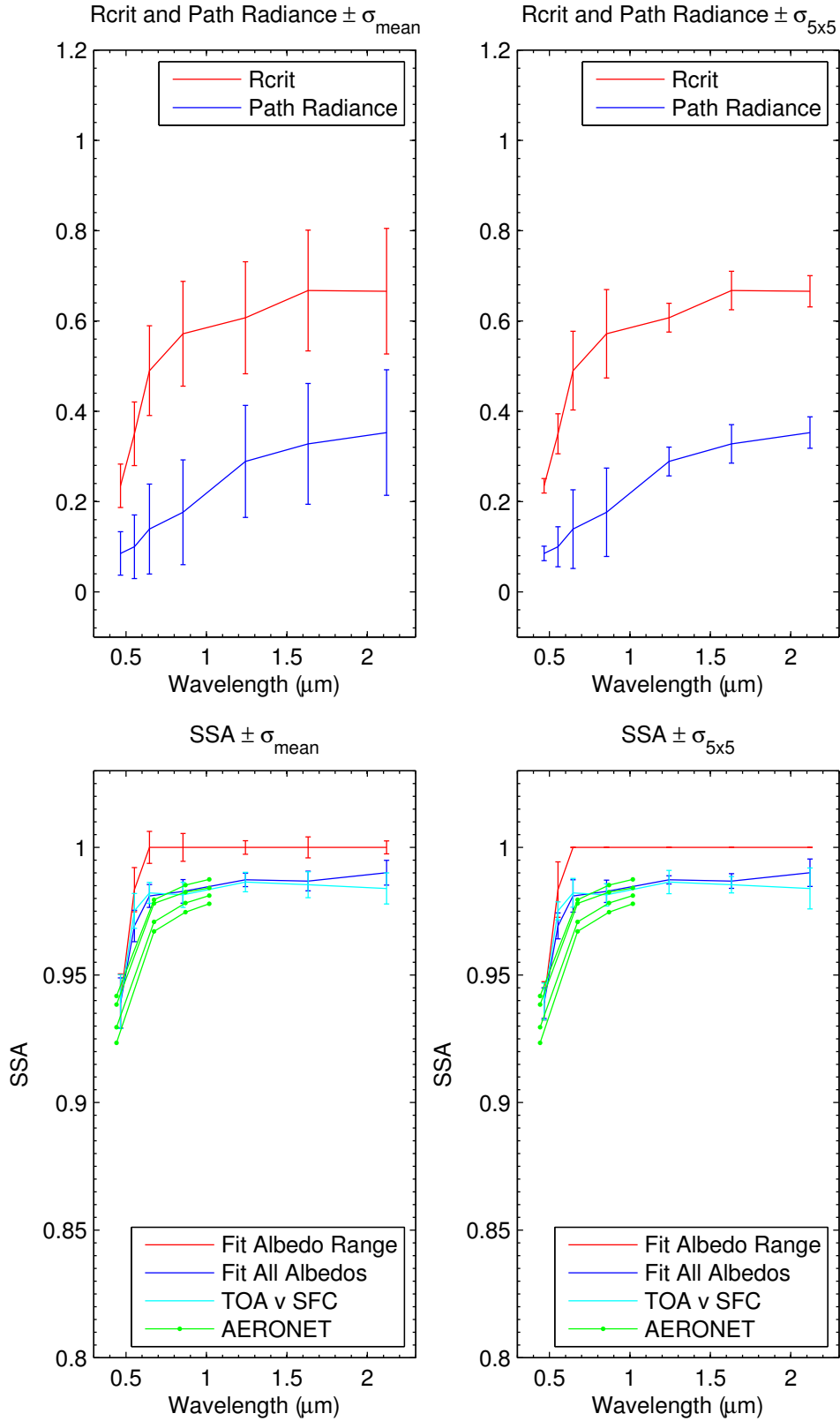


Figure 3.8: Spectral plots of critical reflectance and path radiance (upper panels) and SSA (lower panels) with error bars using the two error estimation methods, plus AERONET retrievals, for 22 February 2007 1250 UTC (compared to -16 days) for the Tamanrasset site.

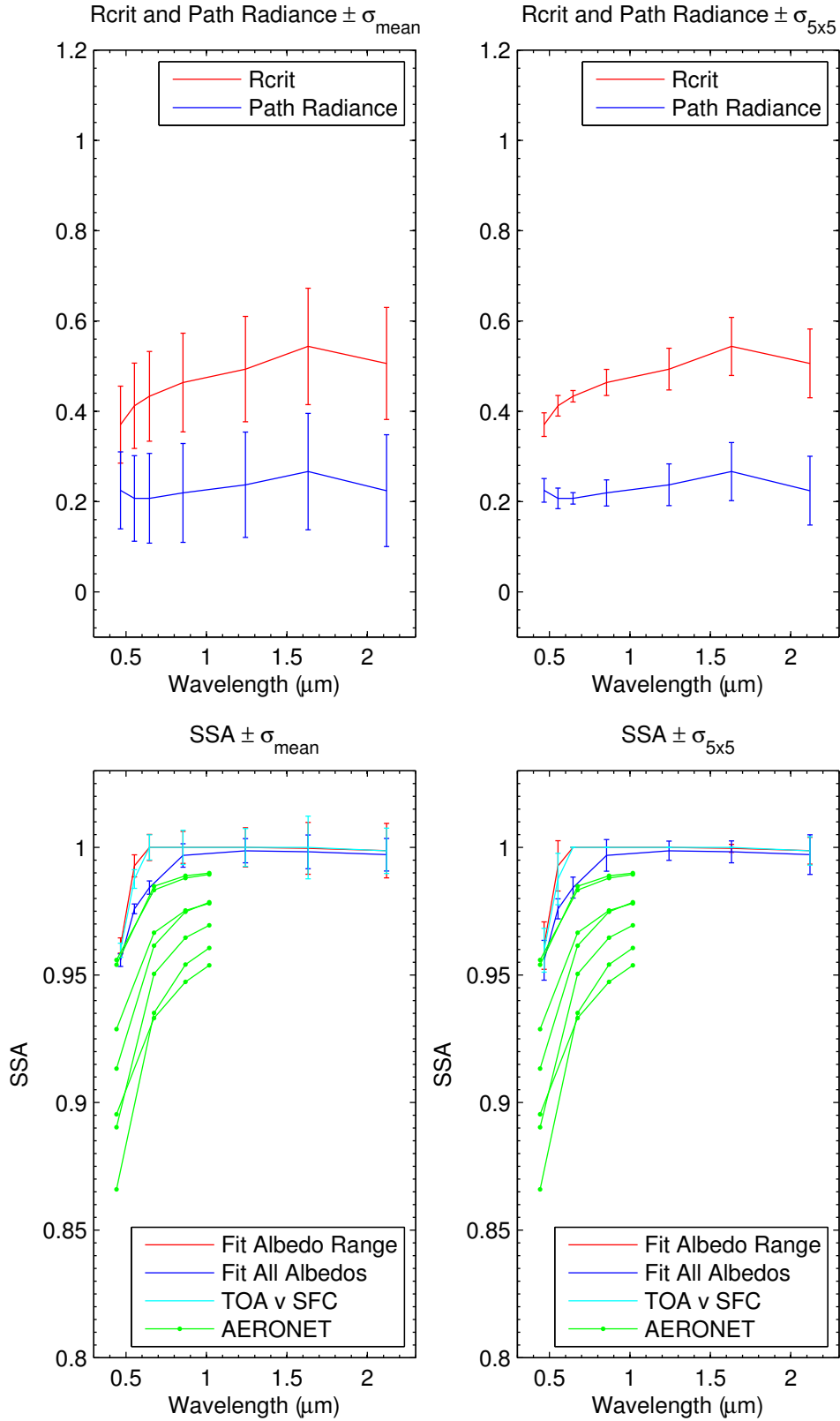


Figure 3.9: Spectral plots of critical reflectance and path radiance (upper panels) and SSA (lower panels) and error bars using the two error estimation methods, plus AERONET retrievals, for 28 February 2008 1320 UTC (compared to -16 days) for the Tamanrasset site.

Spectral SSA results for both cases look very much like dust aerosol, with the strongest absorption occurring in the blue channel, and very little absorption in the near-IR. Results for the 22 February 2007 case yield a somewhat more absorbing SSA at 0.466  $\mu\text{m}$  than the 28 February 2008 case. The SSA for the former case asymptotes to a value of 1.0 for the albedo range fitting method, and a value of 0.99 for the other two methods. SSA values for the latter case asymptote to 1.0 for all three fitting methods used. Uncertainty for both cases due to data fitting tends to be approximately  $\pm 0.01$  at each spectral band. It is important to remember that this does not yet represent a full uncertainty of the retrieved SSA value, only that due to the data fitting and inversion process.

For the 22 February 2007 case, agreement with the AERONET retrievals is quite good for the all albedo and TOA v SFC fitting methods. For the 28 February case, there is agreement in the shortwave channels between the least absorbing AERONET result and the all albedo fitting method; MODIS SSA values exceed the AERONET values at all other channels. There is more variability in the AERONET retrievals on this day, but the more absorbing ones correspond to SZA values less than 45°. Due to the mechanics of the AERONET scan, retrievals at lower SZAs often do not sample enough scattering angles to adequately reproduce the scattering phase function from which the SSA is retrieved.

The average SSA values for the 27 cases at Tamanrasset are shown in Figure 3.10. The results show that the average SSA is sensitive to the fitting method used at all channels except 0.466  $\mu\text{m}$ . The average SSA value at 0.466  $\mu\text{m}$  is 0.940 for all fitting methods; the average value for the TOA v SFC retrieval method at 0.553  $\mu\text{m}$  is 0.972. At

the other bands the values asymptote to  $\sim 1.0$  for the albedo range fitting method and a value of 0.99 for the other two fitting methods. The 0.466 and 0.553  $\mu\text{m}$  values are quite close to the values of 0.936 and 0.976 found by Yoshida and Murakami (2008) for the average SSA of Saharan dust. For all fitting methods used, the MODIS average values are less absorbing than the average of the AERONET results, although the AERONET data exhibit more variability. The average results for MODIS do fall within one standard deviation of the AERONET values for all fitting methods (except the albedo range fitting method in the red channel).

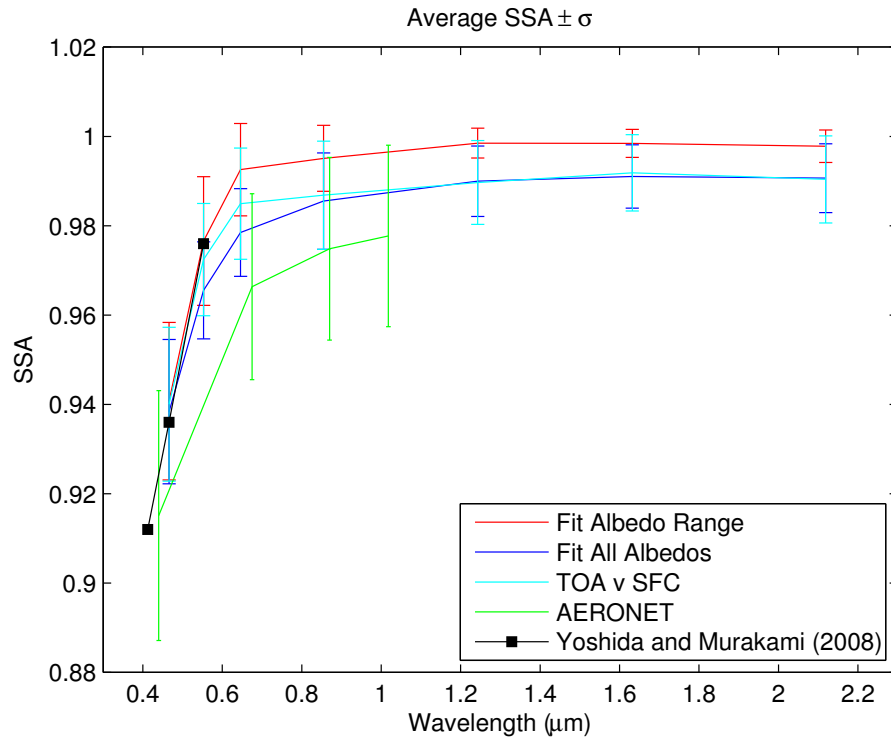


Figure 3.10: Spectral plots of the SSA mean and standard deviation for the 27 cases near Tamanrasset for both MODIS and AERONET. Black points are the Yoshida and Murakami (2008) results for average Saharan dust SSA.

To facilitate direct comparisons with the AERONET data on a case-by-case basis, we choose AERONET data that most closely meet the criteria of SZA greater than  $45^\circ$  and sky error (a measure of the goodness-of-fit of the retrieval to measured sky

radiances) less than 5%. At Tamanrasset, however, the retrieved SSA rarely corresponds to a sky error less than 5%. It should also be noted that the AERONET data are often from several hours before or after the actual overpass time because of the need to meet the  $\text{SZA} > 45^\circ$  criteria, which (depending upon the time of year) is only realized in the early morning and late afternoon. Given our criteria, there are three cases for which no valid AERONET SSA retrieval is available for comparison. The actual times, SZAs and sky errors of the AERONET retrievals chosen for comparison are listed in Table 3.1.

Table 3.1: MODIS overpass times, AERONET retrieval time, solar zenith angle and sky error corresponding to the AERONET retrievals at Tamanrasset.

Date	Overpass Time	AERONET time	SZA (deg)	Sky Error (%)
14 Dec 2006	1020 UTC	753 UTC	70.26	7.89
22 Feb 2007	945 UTC	739 UTC	69.96	5.02
22 Feb 2007	1250 UTC	1517 UTC	60.20	6.56
9 Mar 2007	1040 UTC	702 UTC	74.95	5.28
9 Mar 2007	1210 UTC	1500 UTC	54.18	9.72
19 Mar 2007	1245 UTC	828 UTC	53.45	6.52
20 Mar 2007	1020 UTC	712 UTC	70.01	5.36
20 Mar 2007	1330 UTC	1621 UTC	70.75	6.02
14 May 2007	1025 UTC	744 UTC	53.53	5.41
23 Jul 2007	950 UTC	752 UTC	53.69	5.68
4 Aug 2007	1015 UTC	755 UTC	53.65	5.01
6 Jan 2008	955 UTC	945 UTC	53.69	4.92
6 Jan 2008	1305 UTC	1553 UTC	75.76	6.52
28 Feb 2008	1015 UTC	822 UTC	59.50	6.98
28 Feb 2008	1320 UTC	1456 UTC	54.91	6.15
14 Apr 2008	1025 UTC	734 UTC	59.61	4.10
27 July 2008	935 UTC	727 UTC	59.69	6.56
3 Sep 2008	1040 UTC	651 UTC	70.02	8.86
29 Sep 2008	935 UTC	814 UTC	53.59	5.07
30 Sep 2008	1020 UTC	815 UTC	53.58	4.63
30 Sep 2008	1330 UTC	1512 UTC	60.56	6.46

Because AERONET does not take measurements at exactly the same spectral bands as MODIS, we linearly interpolated the data from each instrument for one-to-one comparison purposes. The Tamanrasset sunphotometer is a four-channel instrument with bands at 0.440, 0.675, 0.870, and 1.018  $\mu\text{m}$ . So, we interpolate the AERONET data to

0.466 and 0.855  $\mu\text{m}$  and the MODIS data to 0.675 and 1.018  $\mu\text{m}$ . We ascribe the AERONET-retrieved SSA a suggested error of  $\pm 0.03$  (Dubovik et al., 2000).

Scatter plots comparing the MODIS and AERONET SSA values at each of the four channels used for interpolation are shown in Figure 3.11, Figure 3.12, and Figure 3.13 for the albedo range, all albedo, and TOA v SFC fitting methods, respectively. For all channels and fitting methods considered, the MODIS retrieval produces a smaller range of SSA values than the AERONET retrieval, and the MODIS values are generally less absorbing than AERONET. The differences tend to be largest in the blue channel, where the results appear to be nearly insensitive to the fitting method used. The comparison at the other channels is more sensitive to fitting method, although many of the values at 0.855 and 1.018  $\mu\text{m}$  fall within the expected AERONET uncertainties.

The latter effect could simply be due to the fact that the SSA is capped at a value of 1.0, so the differences between MODIS and AERONET are automatically smaller in the near-IR channels where the SSA is less absorbing. Of the three fitting methods used, it appears that the TOA v SFC method results do best at capturing the variability of the SSA at 0.855 and 1.018  $\mu\text{m}$ , and thus it may be a better overall method of determining the SSA from MODIS critical reflectance measurements. This is not to say, however, that the AERONET SSA is the expected “true” value at Tamanrasset or Banizoumbou, as it is not a validated measurement of aerosol absorption and is also subject to retrieval uncertainties. Compared to satellite retrievals of absorption, however, the AERONET retrieval should be more straightforward and less impacted by assumptions, particularly assumptions related to surface reflectivity. Thus, it should provide reasonable estimates of aerosol SSA.

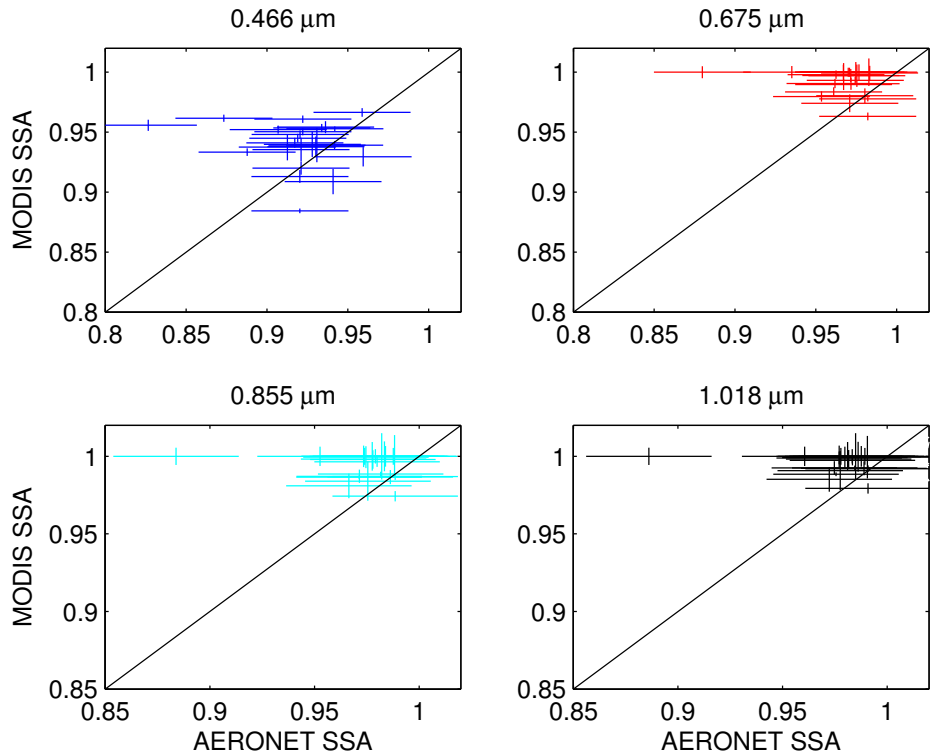


Figure 3.11: MODIS SSA retrieved using the albedo range fitting method compared to AERONET SSA for the 27 cases retrieved at Tamanrasset.

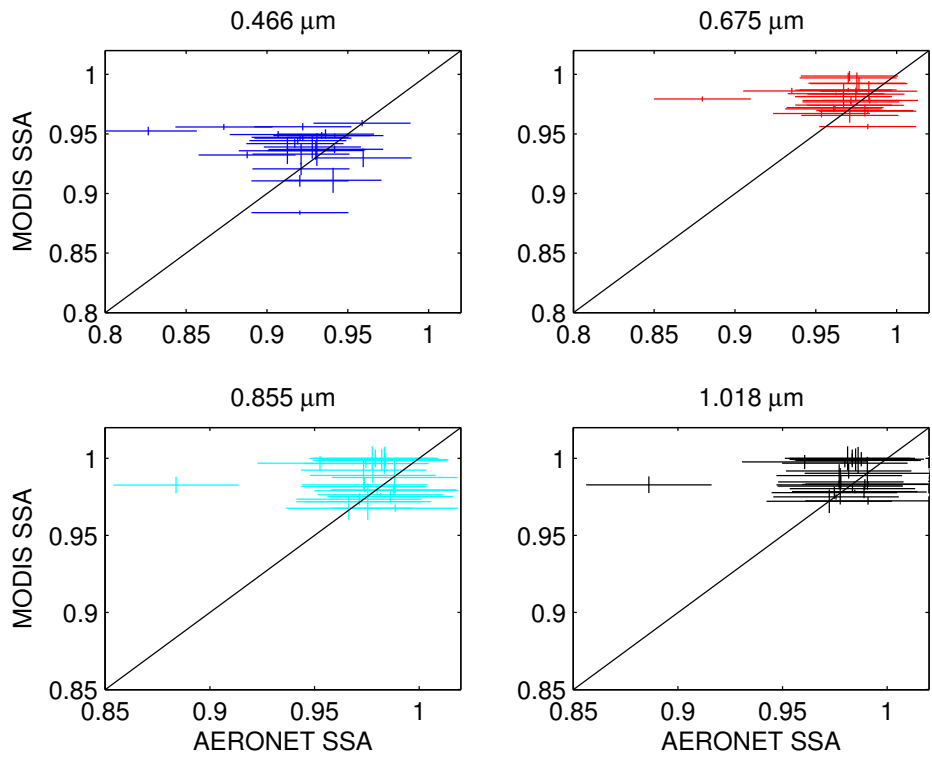


Figure 3.12: MODIS SSA retrieved using the all albedo fitting method compared to AERONET SSA for the 27 cases retrieved at Tamanrasset.

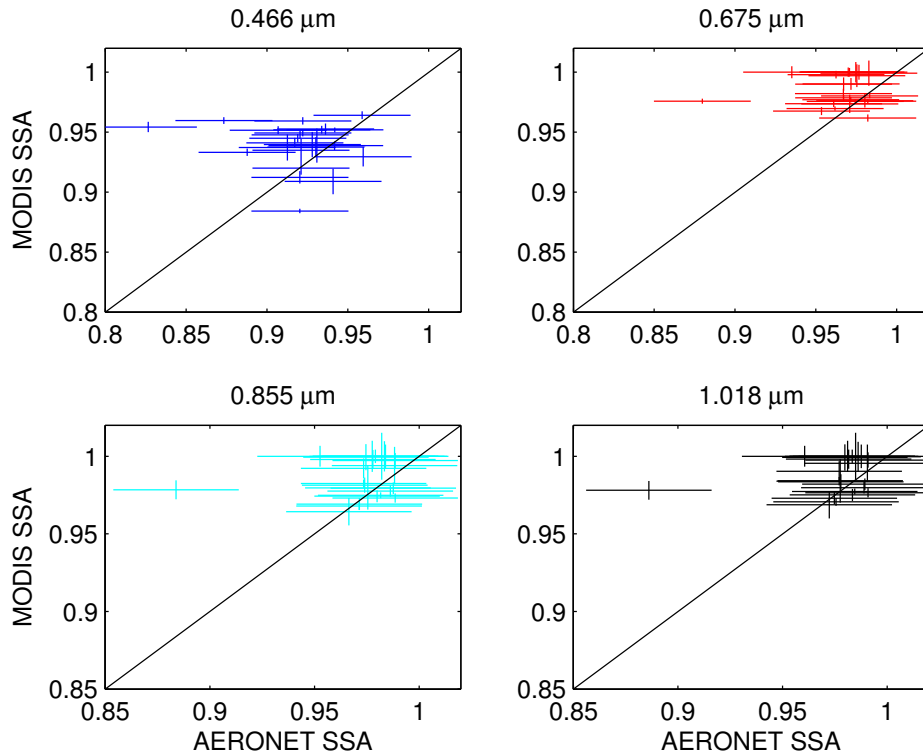


Figure 3.13: MODIS SSA retrieved using the TOA v SFC fitting method compared to AERONET SSA for the 27 cases retrieved at Tamanrasset.

To examine how the spectral dependence of the MODIS results compares to the AERONET spectral dependence, we take the difference between the interpolated MODIS and AERONET values for each case at each of the four interpolated channels. The results are shown in Figure 3.14, Figure 3.15, and Figure 3.16 for the three fitting methods. As suggested by the scatter plots, differences are often large in the blue channel, although 11 of the cases exhibit the largest differences at 0.675  $\mu\text{m}$ . The MODIS SSAs are usually less absorbing than the AERONET values and tend to exhibit a weaker spectral dependence of absorption, although there are a few cases (particularly Case 1, 5 and 21) where the AERONET spectral dependence is weaker than the MODIS estimate. SSA differences decrease with wavelength, and the differences at 0.855 and 1.018 are generally smaller for the TOA v SFC method than for the other two fitting methods.

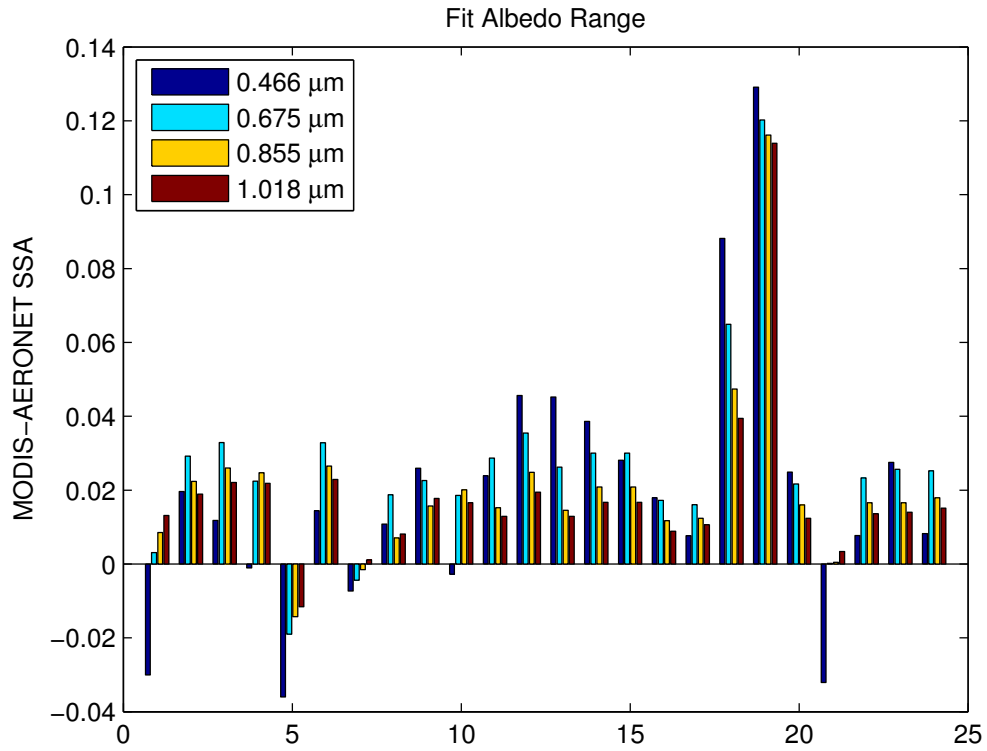


Figure 3.14: MODIS-AERONET SSA differences for each case and channel using the albedo range fitting method.

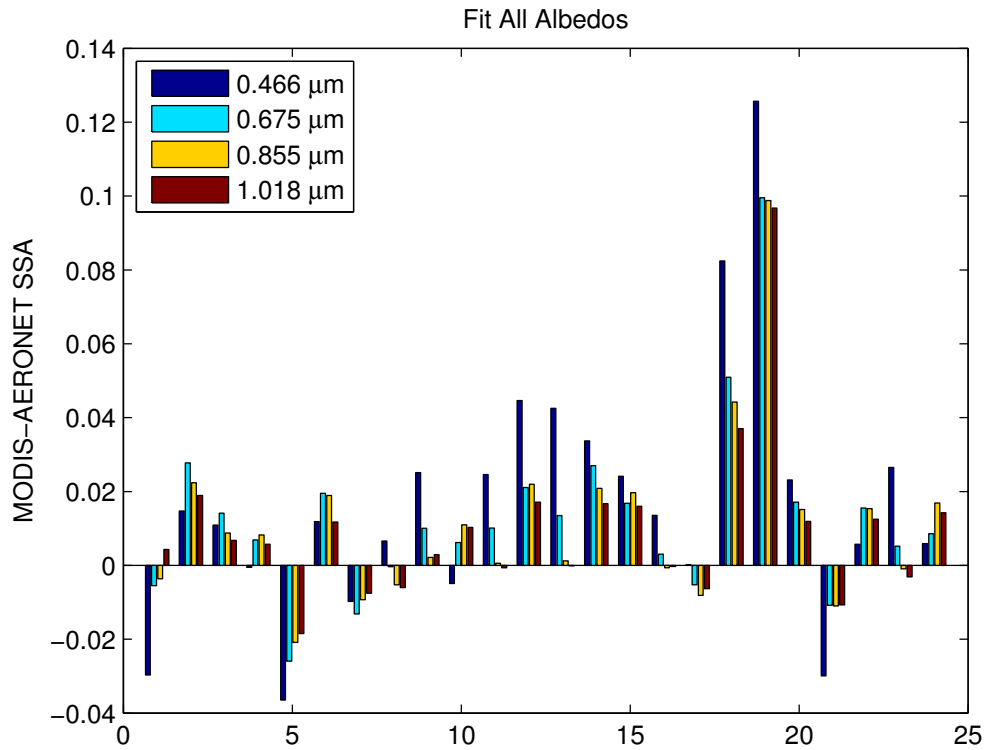


Figure 3.15: MODIS-AERONET SSA differences for each case and channel using the all albedo fitting method.

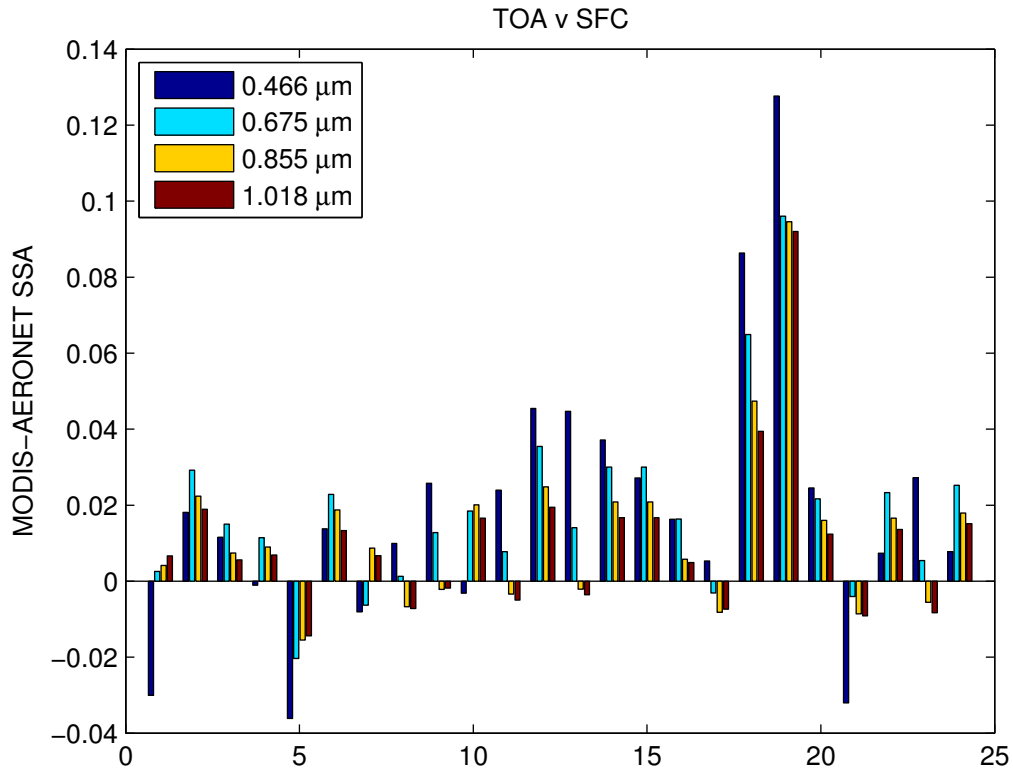


Figure 3.16: MODIS-AERONET SSA differences for each case and channel using the TOA v SFC fitting method.

Retrievals of DeepBlue MODIS SSA at  $0.466 \mu\text{m}$  are also available near Tamanrasset for most of the Aqua-retrieved cases. A comparison of the two datasets is shown in Figure 3.17 for individual pixels remapped to a  $0.03^\circ$  grid. A large number of pixels agree within 0.01 or 0.02, particularly in the SSA range of 0.94 to 0.96; however, MODIS critical reflectance results in a larger range of SSAs, many of which are more absorbing than the DeepBlue estimates. If we restrict the comparison to the  $5 \times 5$  pixel region over which the Tamanrasset AERONET comparison occurred, the two datasets appear to be in reasonable agreement, with the exception of one case in which the critical reflectance-retrieved SSA is much more absorbing. Like the AERONET data, DeepBlue is not a validate measurement of aerosol absorption, but the level of agreement with the critical reflectance SSA is encouraging.

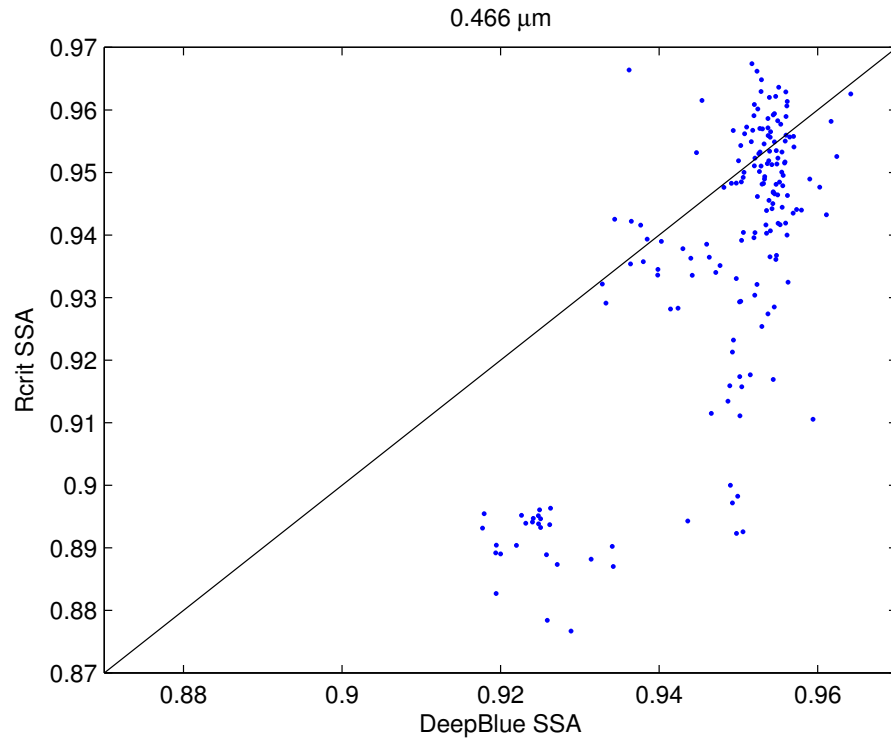


Figure 3.17: Pixel-to-pixel comparison of critical reflectance-retrieved SSA to DeepBlue SSA for Aqua-retrieved cases near Tamanrasset.

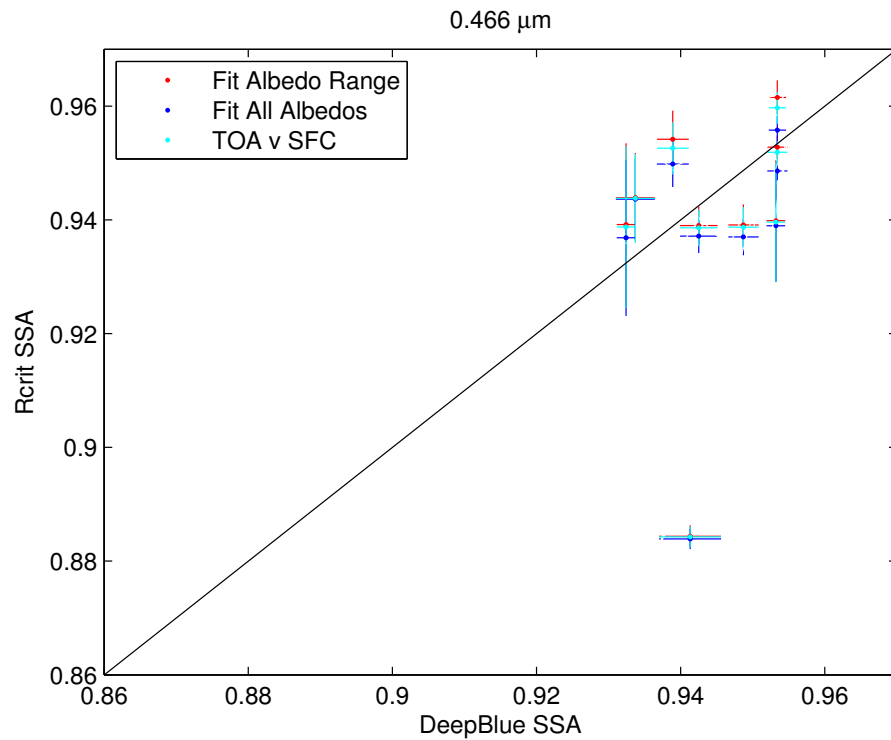


Figure 3.18: Comparison of critical reflectance-retrieved SSA to DeepBlue SSA for a 5 x 5 pixel region near the Tamanrasset comparison site.

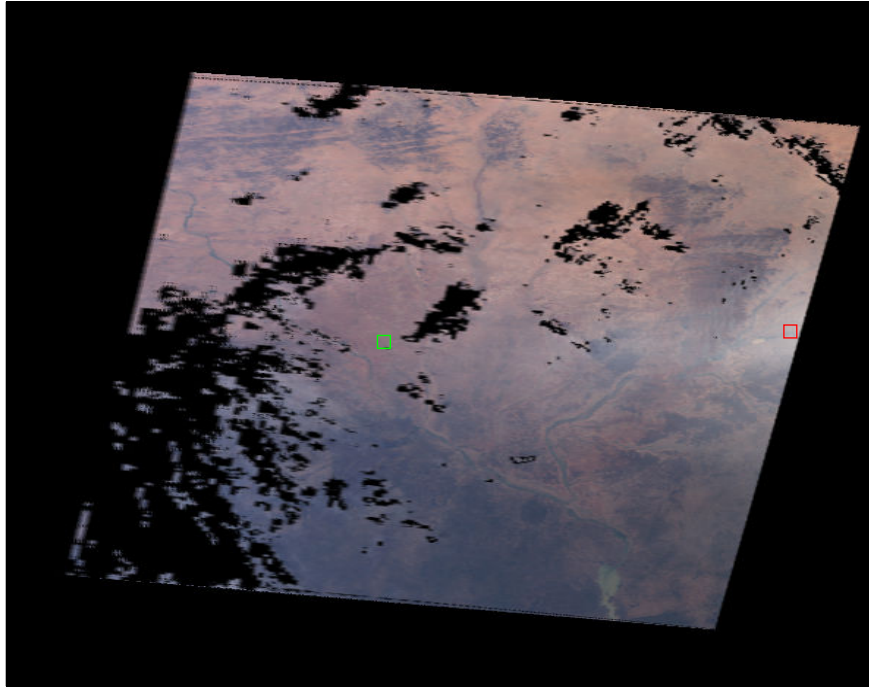
## **3.2 Banizoumbou AERONET Site**

The Banizoumbou site is located “on a small, isolated plateau in a cultivated sandy area 60 km east of Niamey, Niger” ([http://aeronet.gsfc.nasa.gov/new\\_web/photo\\_db/Banizoumbou.html](http://aeronet.gsfc.nasa.gov/new_web/photo_db/Banizoumbou.html)). The site elevation is 250 meters, so we assumed this elevation in SBDART for retrievals near this site. Banizoumbou is a more complicated site in terms of aerosol retrievals, because its location in the Sahelian region of Africa makes it prone to the influence of both dust and biomass burning aerosol, as discussed in Chapter 1. It is also impacted by convection from the West African monsoon, which limits the availability of both MODIS and AERONET data in the summer months due to cloud cover. The more persistent influence of dust aerosol during spring and summer also limits the ability to find pairs of days with high and low aerosol loading, respectively. Thus, the 15 cases from this site all occurred in the fall and winter months, with the exception of one day in March.

### **3.2.1 MODIS Reflectances**

Before SSA retrievals were performed at the Banizoumbou site, the critical reflectance in the region indicated a complicated aerosol mixture was sometimes present, which could vary in relative contributions of species across a MODIS image. RGB images for an example case from Banizoumbou, 11 December 2006, are contained in Figure 3.19. The polluted RGB image for this case shows an increase in brightness from west to east across the scene, indicating a change in the TOA aerosol effect which seems to be due to a variation in aerosol properties. Example TOA reflectance scatter plots for the pixel in the green box and the red box are shown in Figure 3.20 and Figure 3.21, respectively. The TOA reflectances in the green box are very near the critical reflectance

2006345 0950 Terra



2006361 0950 Terra

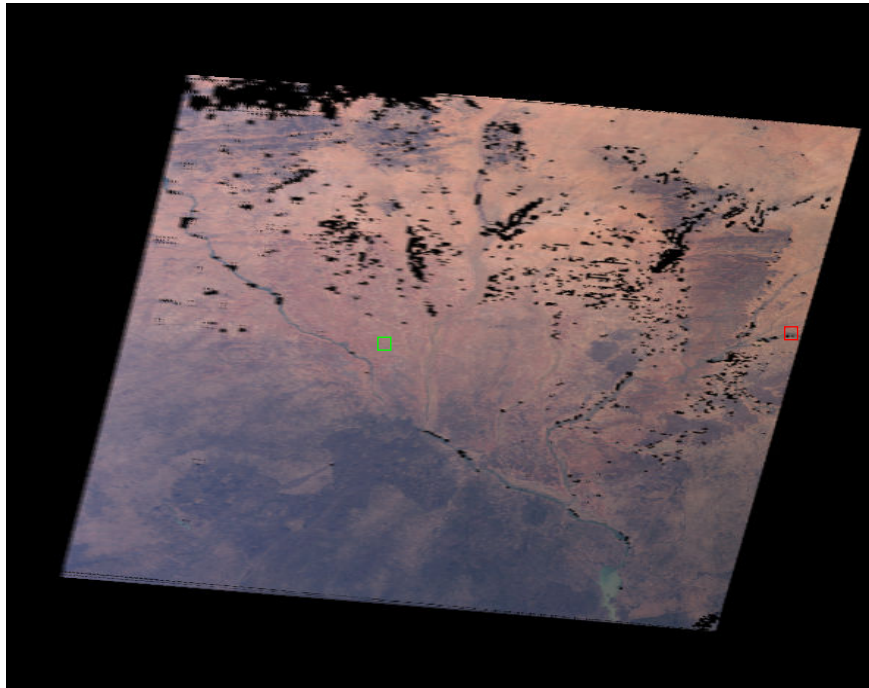


Figure 3.19: MODIS Aqua RGB images for a polluted day (11 December 2006 950 UTC, top) and a cleaner day (27 December 2006 950 UTC, bottom) near Banizoumbou.

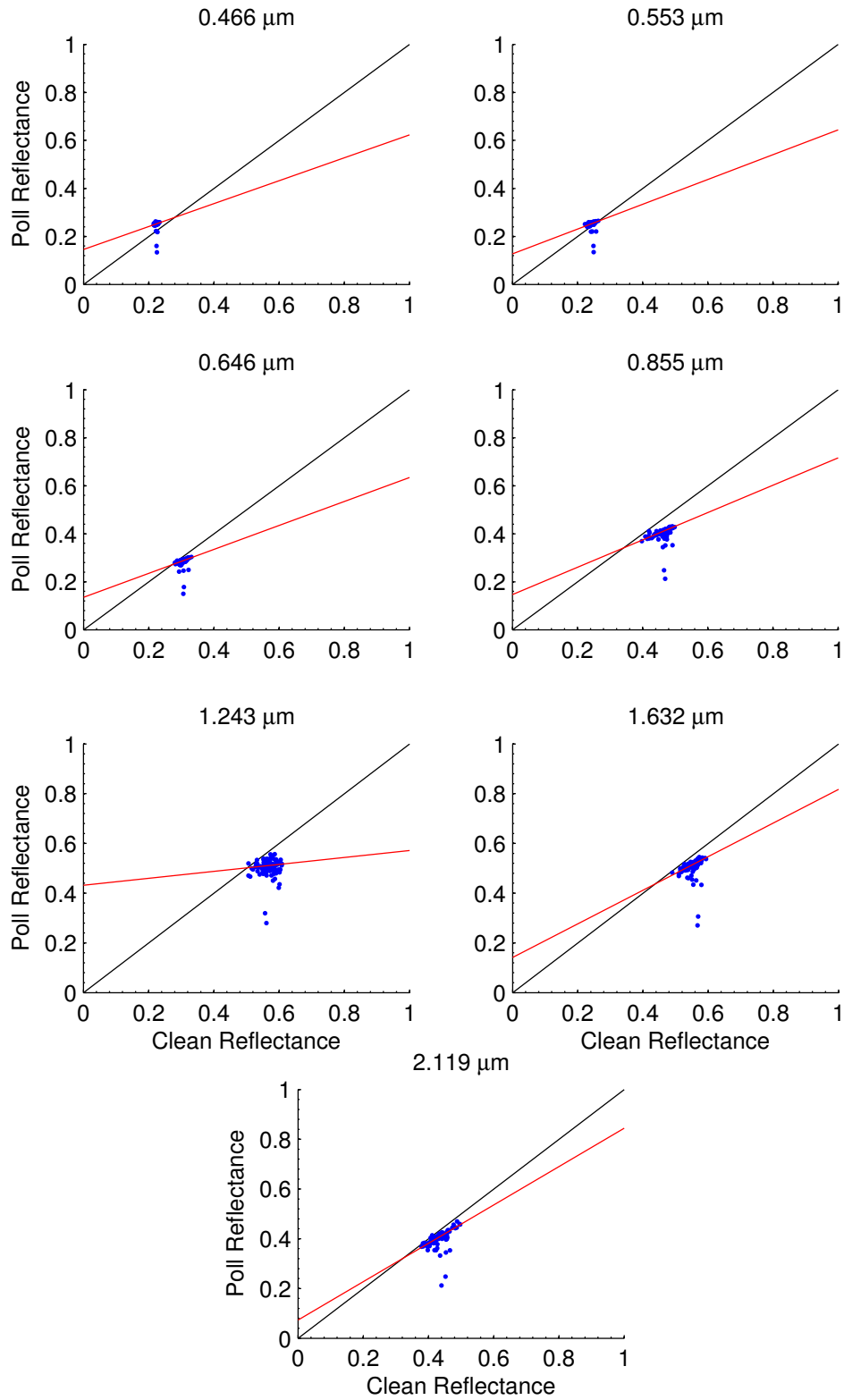


Figure 3.20: Scatter plots of the polluted versus clean reflectances for the 11 December 2006 (green box) case near Banizoumbou for each of the seven channels used in the retrieval. The red line is the robust linear fit to the reflectance data, and the black line is the one-to-one line.

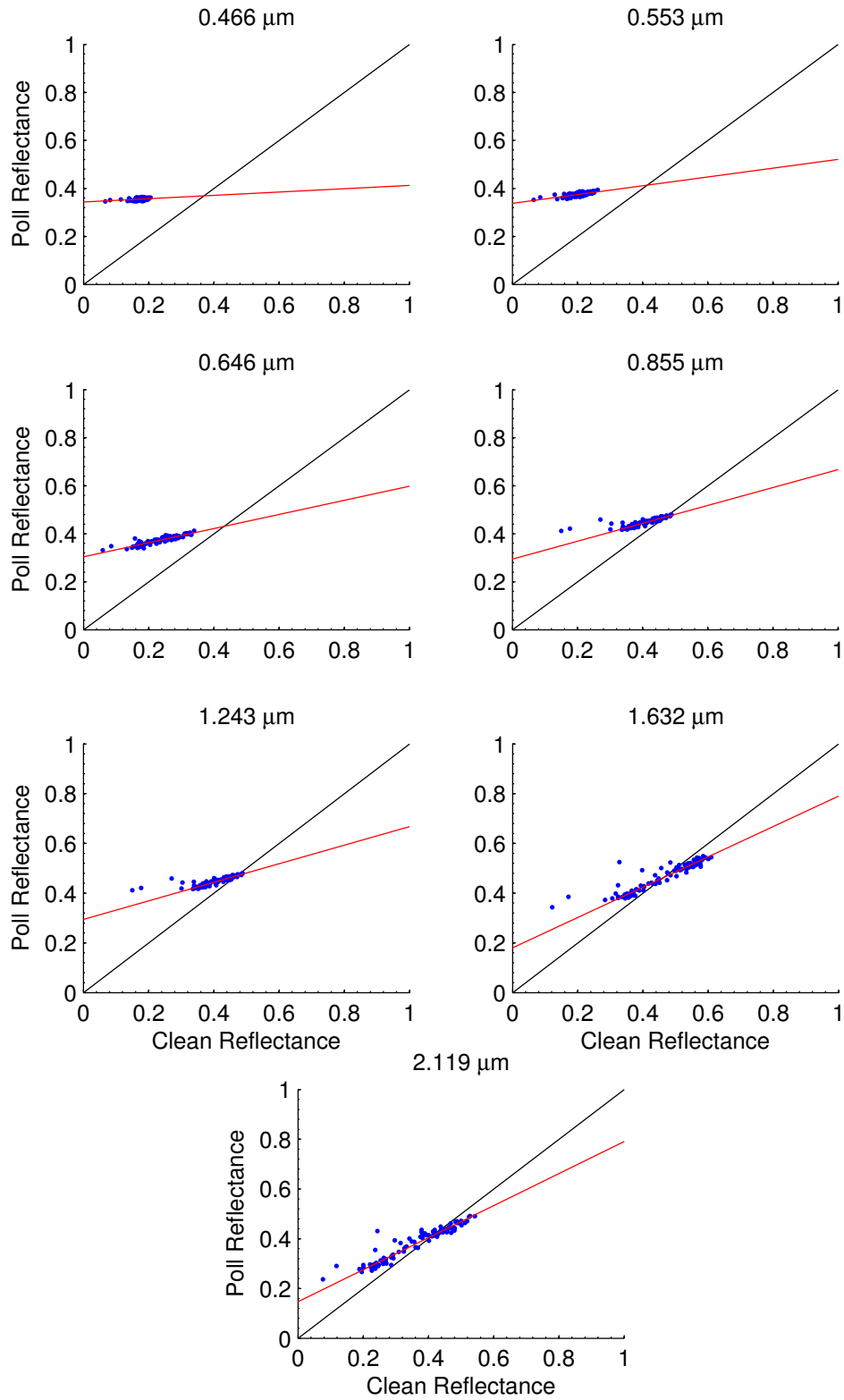


Figure 3.21: Scatter plots of the polluted versus clean reflectances for the 11 December 2006 (red box) case near Banizoumbou for each of the seven channels used in the retrieval. The red line is the robust linear fit to the reflectance data, and the black line is the one-to-one line.

in the visible channels, and just below the critical reflectance in the near-IR channels. Thus, there is very little change in the appearance of the RGB image at this location, and there is also evidence of aerosol absorption at all wavelengths. With the exception of the value at 1.243  $\mu\text{m}$ , the path radiances exhibit a slight decrease with wavelength, which could indicate the presence of some fine particles in the scene. In the red box on the right-hand side of the image, the critical reflectance values are higher, particularly at visible wavelengths ( $\sim 0.4$  versus 0.25). The TOA reflectance values are also larger than the critical reflectance in the visible here, resulting in TOA brightening. This suggests that the aerosol in this part of the image is predominantly scattering at these wavelengths, while the spectral decrease in the y-intercept indicates a mixture of particles may also be present.

### **3.2.2 Critical Reflectance and SSA Results**

#### **3.2.2.1 SSA Image Retrievals**

Maps of the critical reflectance, path radiance, the radiative effect at TOA, and SSA at 0.553  $\mu\text{m}$  are shown in Figure 3.22 for the 11 December 2007 case; results for the all cases at Banizoumbou are displayed in Appendix C. For this case, the critical reflectance varies smoothly across the image from values  $\sim 0.2$  to 0.3 – 0.4 in the brighter portion of the image to the east. As with the Tamanrasset cases, the path radiance is more spatially scattered, although it does exhibit some structure with higher values in the vicinity of the brighter aerosol plume. The variation in the TOA effect closely follows the variation in the critical reflectance, with positive forcing (TOA darkening) occurring where critical reflectance values are lower and negative forcing (TOA brightening) occurring where the critical reflectance values are higher.

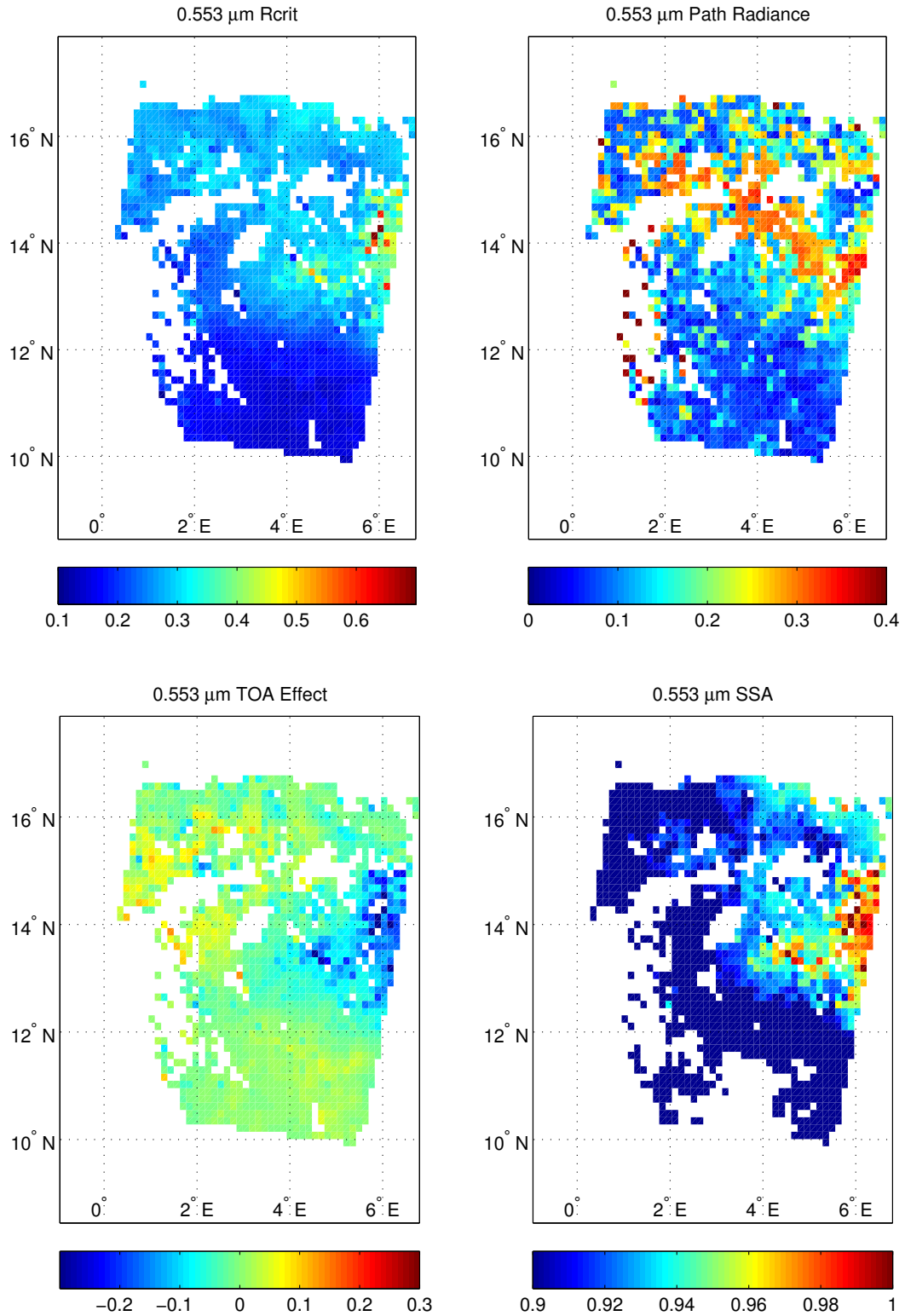


Figure 3.22: Image retrievals of critical reflectance (upper left), path radiance (upper right), TOA radiative effect (lower left), and SSA (lower right) at 0.553 μm for 11 December 2006 950 UTC (compared to +16 days) near Banizoumbou for the bimodal spheroid aerosol model.

Given the more complicated aerosol mixture present near Banizoumbou, we use both the coarse and bimodal spheroid LUTs to retrieve SSA for the 15 cases. The SSA results in Figure 3.22 are shown for the bimodal spheroid model retrieval, using the TOA v SFC fitting method. The choice of aerosol model mainly affects the magnitude of the SSA results, with some effect on the spectral dependence in the shorter wavelengths (and slightly in the near-IR), but does not change the relative variation of SSA over the scene. Just like the critical reflectance, the SSA for this case varies smoothly from west to east across this image, ranging from values below 0.9 in the south and west portions of the image to values near 1.0 in the vicinity of the bright plume.

### ***3.2.2.2 Spectral SSA Retrievals near AERONET Site***

Spectral results for the critical reflectance, path radiance, and SSA near the Banizoumbou site for the 11 December 2006 case are shown in Figure 3.23. The SSA results in the left panel are for the bimodal spheroid model and the result on the right is for the coarse mode model; the error bars in both plots are for the  $\sigma_{mean}$  estimation (Equation 3.1), as this results in a larger estimate of uncertainty than the 5 x 5 pixel standard deviation here. The only Level 2 Version 2 AERONET SSA retrieval for the day is also shown. Spectral plots for all cases at Banizoumbou are shown in Appendix D.

The SSA results for both aerosol models have a similar spectral shape, with strongest absorption in the blue, a peak in SSA at 1.243  $\mu\text{m}$ , and a decrease in SSA at 1.632  $\mu\text{m}$  and 2.119  $\mu\text{m}$ . The coarse model does yield a somewhat stronger spectral dependence in the visible channels and a slightly weaker spectral dependence in the near-IR. The SSA is relatively insensitive to the fitting method used for either model and at all channels; there are some small differences between fitting methods in the near-IR, but all

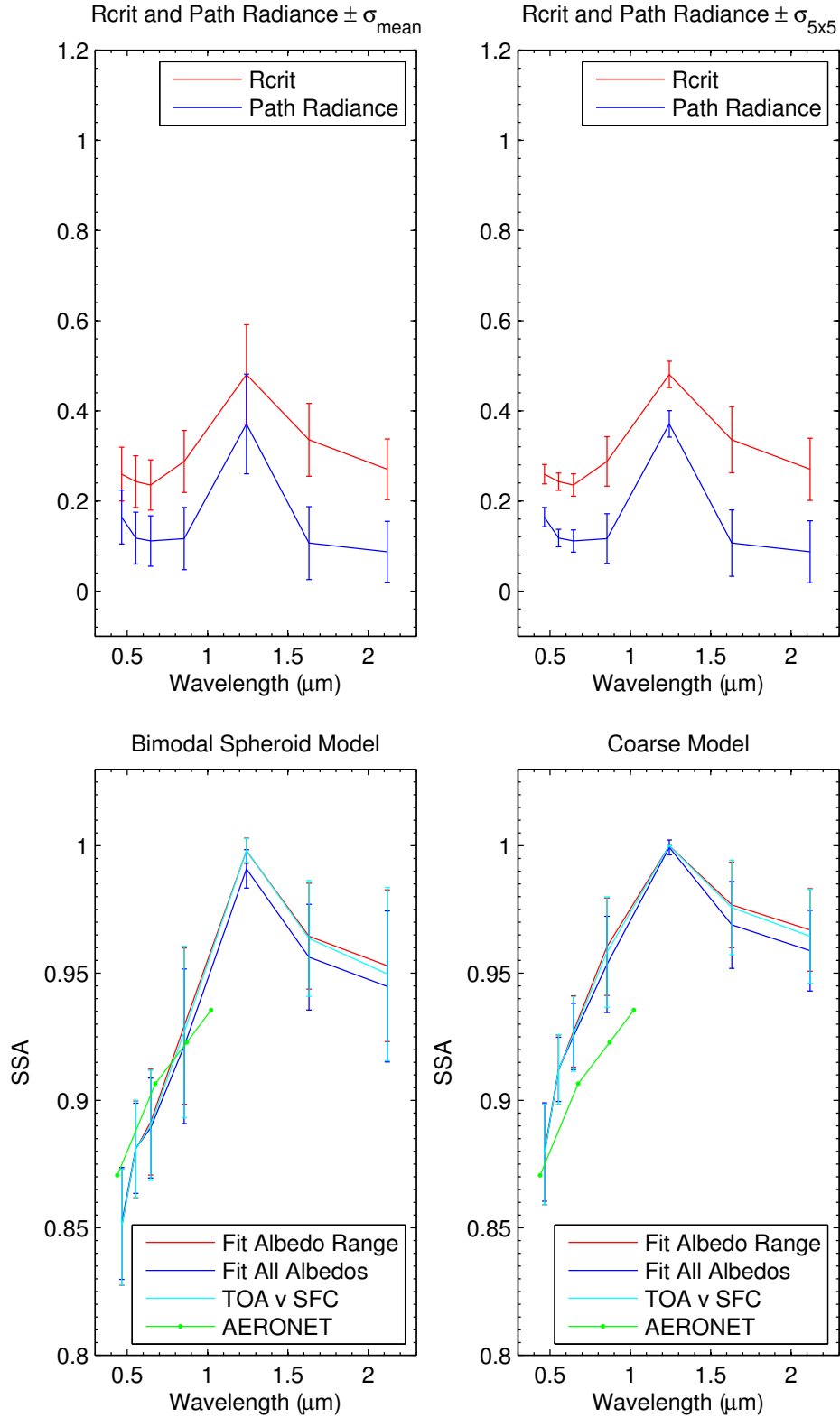


Figure 3.23: Spectral plots of critical reflectance and path radiance (upper panels) and SSA retrieved for the bimodal spheroid model (lower left) and coarse model (lower right) for 11 December 2006 950 UTC (compared to +16 days) at the Banizoumbou site. Error bars for the SSA are the  $\sigma_{\text{mean}}$  estimates. AERONET retrievals for the day are also shown.

of the SSA values are well within the uncertainties of the other estimates. The bimodal model yields more absorbing SSAs at all channels except 1.243, but the SSA differences between the two models are larger in the visible ( $\sim 0.4$ - $0.5$ ) than the near-IR ( $\sim 0.01$ ). The coarse model estimate at  $0.466 \mu\text{m}$  agrees well with the AERONET result, although the bimodal model yields better agreement at the other three AERONET channels. We note that the error bars for the Banizoumbou SSAs tend to be larger than those at Tamanrasset, which will influence our interpretation of the results and their comparison with AERONET.

The average and standard deviation of the MODIS and AERONET results are shown in Figure 3.24, for the bimodal spheroid model on the left, and the coarse model on the right. The spectral shape of the average results is very similar to that in the 11 December case, with a peak in SSA at  $1.243 \mu\text{m}$ . Both models yield very similar average results at  $1.632 \mu\text{m}$  and  $2.119 \mu\text{m}$ , whereas the bimodal spheroid model yields more absorbing average results in the visible and at  $0.855 \mu\text{m}$ . Compared to the average AERONET results, both models yield a more absorbing average SSA in the blue channel, but both also yield a steeper spectral dependence, resulting in values that are less absorbing than AERONET at  $1.020 \mu\text{m}$  (and  $0.675$  and  $0.870 \mu\text{m}$  for the coarse model retrieval). At Banizoumbou, the SSA results at channels beyond  $0.646 \mu\text{m}$  are more sensitive to the fitting method used for both models, but each method still results in an average SSA that is within the standard deviation of the values obtained using the other fitting methods.

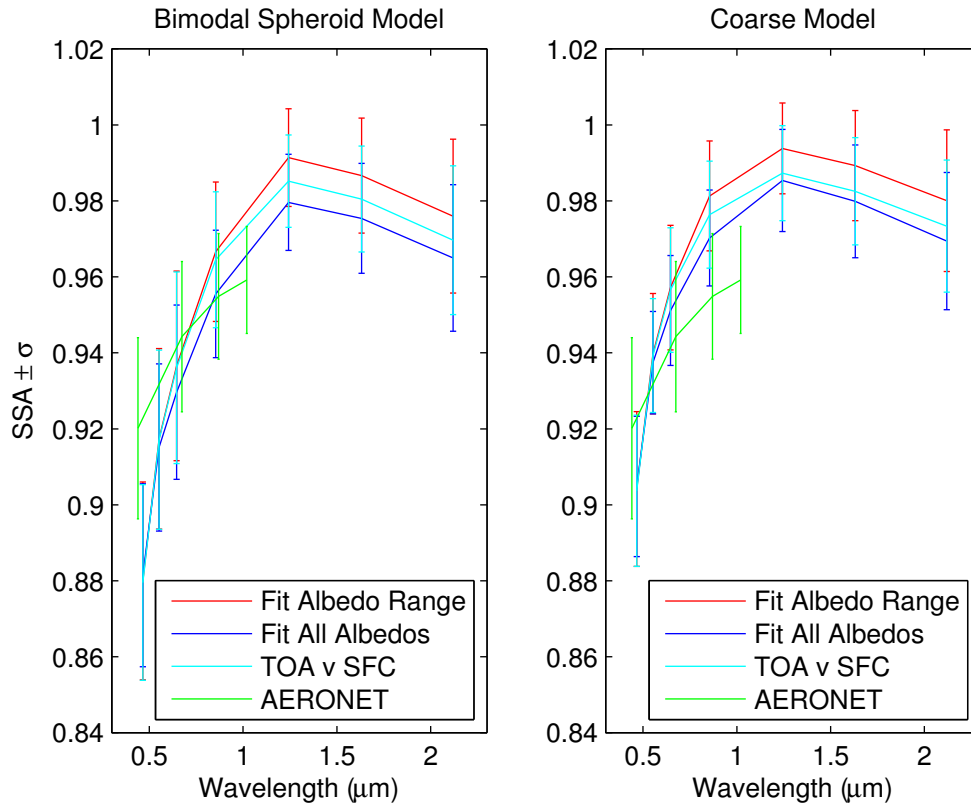


Figure 3.24: Spectral plots of the SSA mean and standard deviation of the 15 cases near Banizoumbou for both MODIS bimodal spheroid model (left) and coarse model (right) and AERONET.

The individual AERONET retrievals that were used for comparison at Banizoumbou are listed in Table 3.2. In general, the sky errors for these estimates were lower than at Tamanrasset, with only a few values exceeding the suggested 5% threshold. One value, the measurement taken on 11 December, was also taken at a slightly lower solar zenith angle than 45°, but had a reasonable corresponding sky error. Some measurements were several hours off of overpass time as they were at Tamanrasset, although many were available within one hour at this site, which could mean that the Banizoumbou AERONET retrievals will be more representative of the conditions at MODIS overpass.

Table 3.2: MODIS overpass times, AERONET retrieval time, solar zenith angle at time of AERONET retrieval, and sky error corresponding to the AERONET retrievals at Banizoumbou.

Date	Overpass Time	AERONET time	SZA (deg)	Sky Error (%)
13 Mar 2006	1045 UTC	725 UTC	69.79	5.13
16 Oct 2006	1345 UTC	1455 UTC	54.61	4.18
10 Nov 2006	1035 UTC	655 UTC	75.05	8.14
16 Nov 2006	955 UTC	835 UTC	54.48	5.80
16 Nov 2006	1300 UTC	1550 UTC	70.96	4.65
17 Nov 2006	1040 UTC	836 UTC	54.62	6.67
17 Nov 2006	1345 UTC	1613 UTC	75.93	6.38
18 Nov 2006	945 UTC	936 UTC	43.83	5.78
7 Dec 2006	1015 UTC	942 UTC	46.32	4.00
7 Dec 2006	1320 UTC	1342 UTC	46.83	3.81
11 Dec 2006	950 UTC	1044 UTC	39.23	4.52
13 Dec 2006	1245 UTC	1445 UTC	57.56	4.51
14 Dec 2006	1020 UTC	846 UTC	56.90	4.83
14 Dec 2006	1325 UTC	1346 UTC	47.36	4.52

Scatter plots comparing the interpolated MODIS and AERONET data are shown in Figure 3.25, Figure 3.26, and Figure 3.27. Top panels contain results for the bimodal spheroid model, and bottom panels contain results for the coarse model. Uncertainties for the AERONET data are again assumed to be  $\pm 0.03$ . Unlike at Tamanrasset, the MODIS values yield a similar dynamic range of SSA values as AERONET, at least at the 0.466 and 0.675  $\mu\text{m}$  channels. For all fitting methods used, the coarse model results yield better agreement with the AERONET values in the blue channel, whereas the bimodal model yields better results at all the other channels. Particularly good agreement is achieved in the red channel for the bimodal aerosol model. This channel serves as a “crossover point” of sorts between the two retrievals, as AERONET tends to report less absorbing SSAs than MODIS in the blue and more absorbing SSAs than MODIS at the longer wavelengths. The sensitivity to changes in absorption again seems to be strongest for the TOA v SFC fitting method, although absolute agreement may be a bit better for the all albedo fitting method.

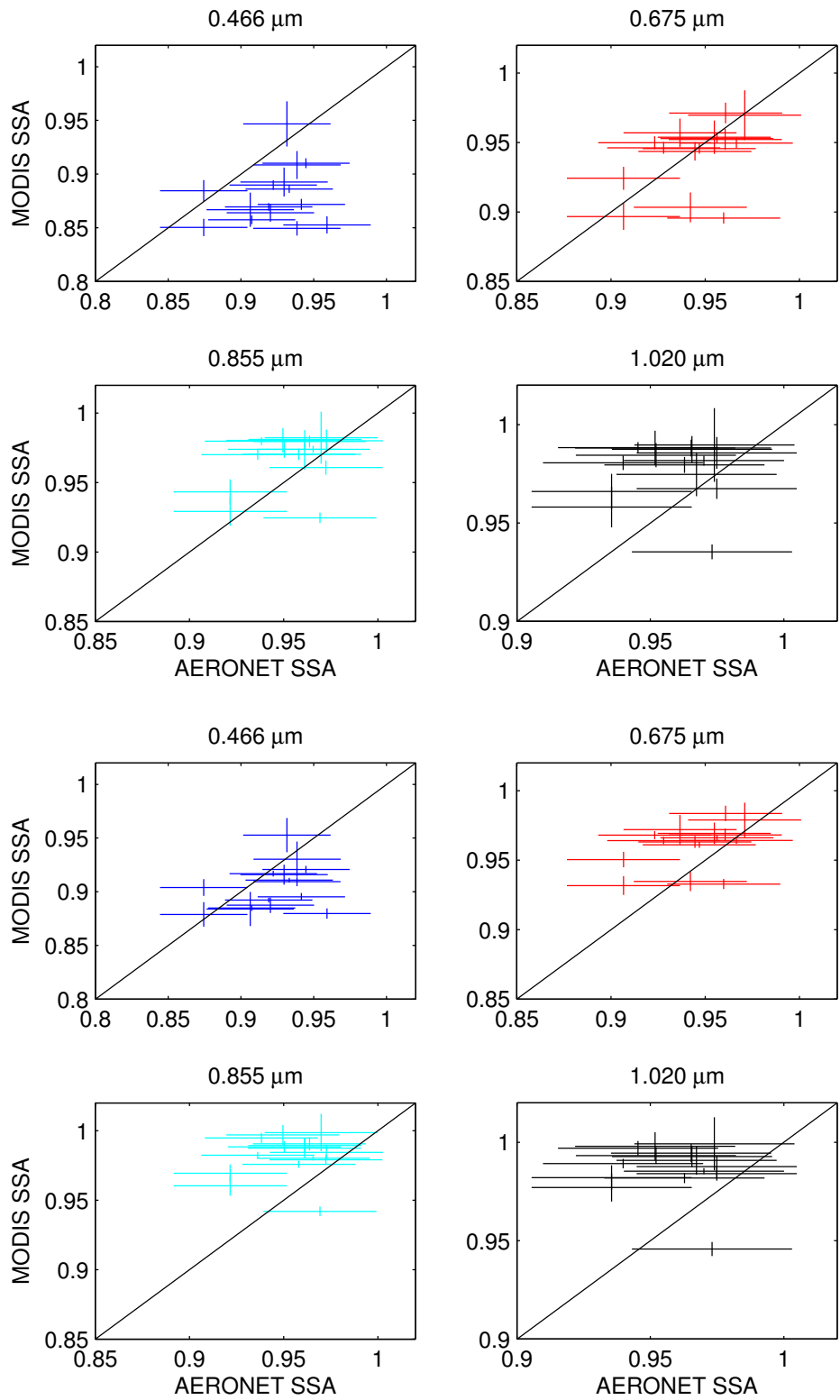


Figure 3.25: MODIS SSA retrieved using the albedo range fitting method for the bimodal spheroid model (upper) and coarse model (lower) compared to AERONET SSA for the 15 cases retrieved at Banizoumbou.

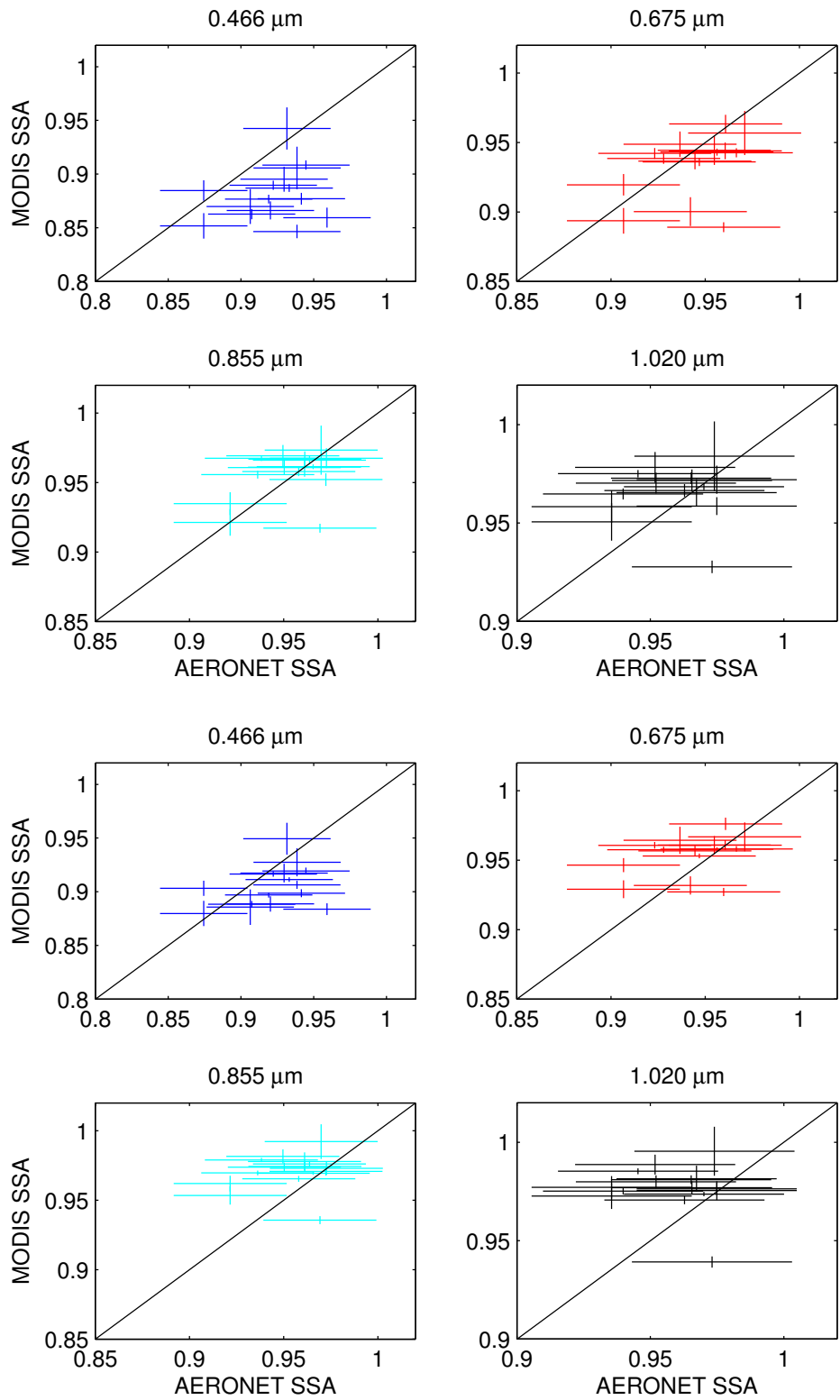


Figure 3.26: MODIS SSA retrieved using the all albedo fitting method for the bimodal spheroid model (upper) and coarse model (lower) compared to AERONET SSA for the 15 cases retrieved at Banizoumbou.

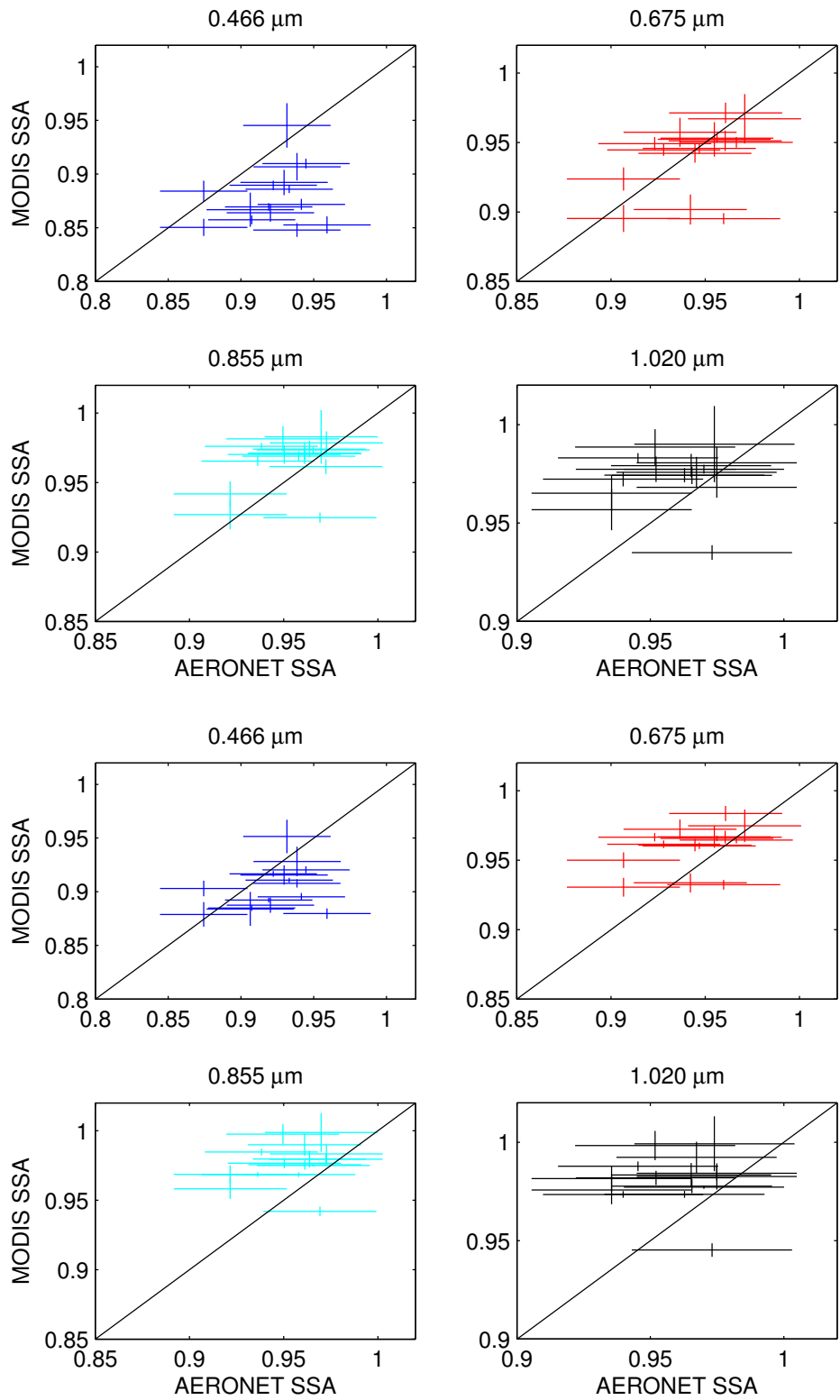


Figure 3.27: MODIS SSA retrieved using the TOA v SFC fitting method for the bimodal spheroid model (upper) and coarse model (lower) compared to AERONET SSA for the 15 cases retrieved at Banizoumbou.

The MODIS-AERONET differences by case shown in Figure 3.28, Figure 3.29, and Figure 3.30 confirm what the scatter plots suggest about how the spectral dependence compares between the two datasets: MODIS SSA is generally brighter than AERONET in the near-IR, and more absorbing than AERONET at 0.466  $\mu\text{m}$ . For the bimodal spheroid model (top plots) differences are largest in the blue channel, followed by 1.020  $\mu\text{m}$ , with the smallest differences occurring at 0.675  $\mu\text{m}$ . The coarse model yields better agreement in the blue channel, but worse agreement in the longer-wavelength channels.

Average and standard deviations of the absolute differences between MODIS and AERONET at both sites are listed in Table 3.3. In general, the absolute differences using the bimodal spheroid model at Banizoumbou are on the order of the differences found at Tamanrasset from 0.675-1.020, whereas the absolute differences using the coarse model are on the order of the differences found at Tamanrasset at 0.466  $\mu\text{m}$ . The variability of the absolute differences is lower at Banizoumbou, but the differences are more systematic at this site due to the differences in spectral dependence between the two datasets.

Table 3.3: Mean and standard deviation of the absolute difference between MODIS critical reflectance and AERONET SSAs at Tamanrasset and Banizoumbou (for both bimodal spheroid and coarse models) at the four interpolated channels.

Wavelength ( $\mu\text{m}$ ) and fitting method	Tamanrasset mean $\pm$ $\sigma$	Banizoumbou bimodal mean $\pm$ $\sigma$	Banizoumbou coarse mean $\pm$ $\sigma$
0.466	Albedo range	0.029 $\pm$ 0.028	0.046 $\pm$ 0.025
	All albedos	0.026 $\pm$ 0.027	0.044 $\pm$ 0.025
	TOA v SFC	0.028 $\pm$ 0.028	0.046 $\pm$ 0.026
0.675	Albedo range	0.028 $\pm$ 0.023	0.016 $\pm$ 0.017
	All albedos	0.018 $\pm$ 0.020	0.019 $\pm$ 0.017
	TOA v SFC	0.022 $\pm$ 0.021	0.016 $\pm$ 0.017
0.855	Albedo range	0.022 $\pm$ 0.022	0.020 $\pm$ 0.012
	All albedos	0.016 $\pm$ 0.020	0.012 $\pm$ 0.014
	TOA v SFC	0.017 $\pm$ 0.019	0.018 $\pm$ 0.012
1.020	Albedo range	0.019 $\pm$ 0.021	0.024 $\pm$ 0.012
	All albedos	0.014 $\pm$ 0.019	0.016 $\pm$ 0.012
	TOA v SFC	0.015 $\pm$ 0.018	0.020 $\pm$ 0.012

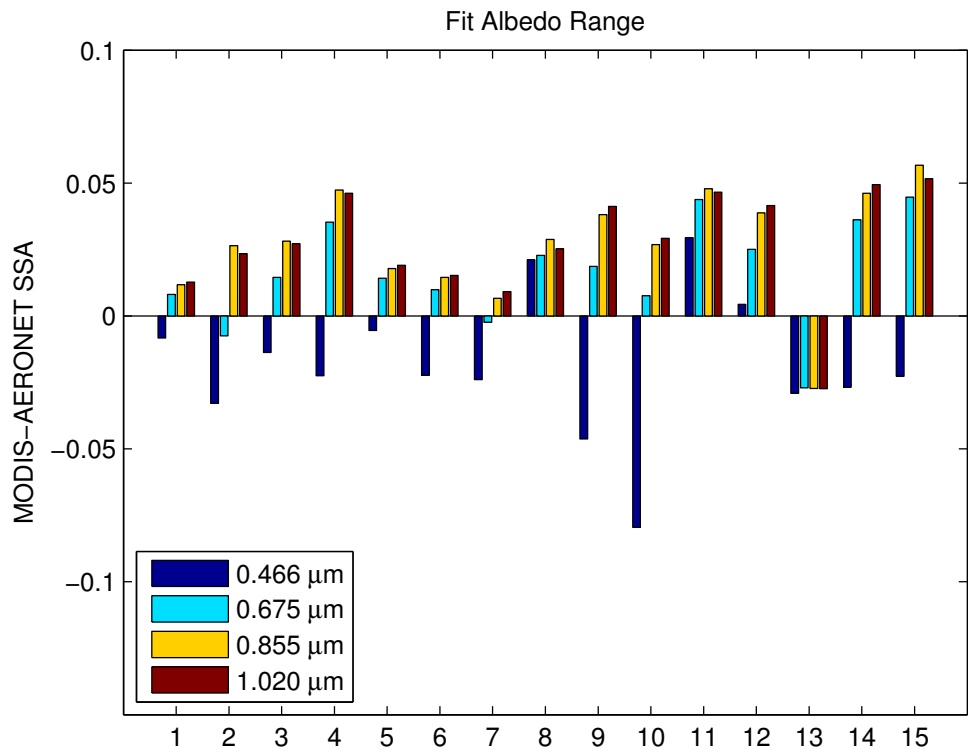
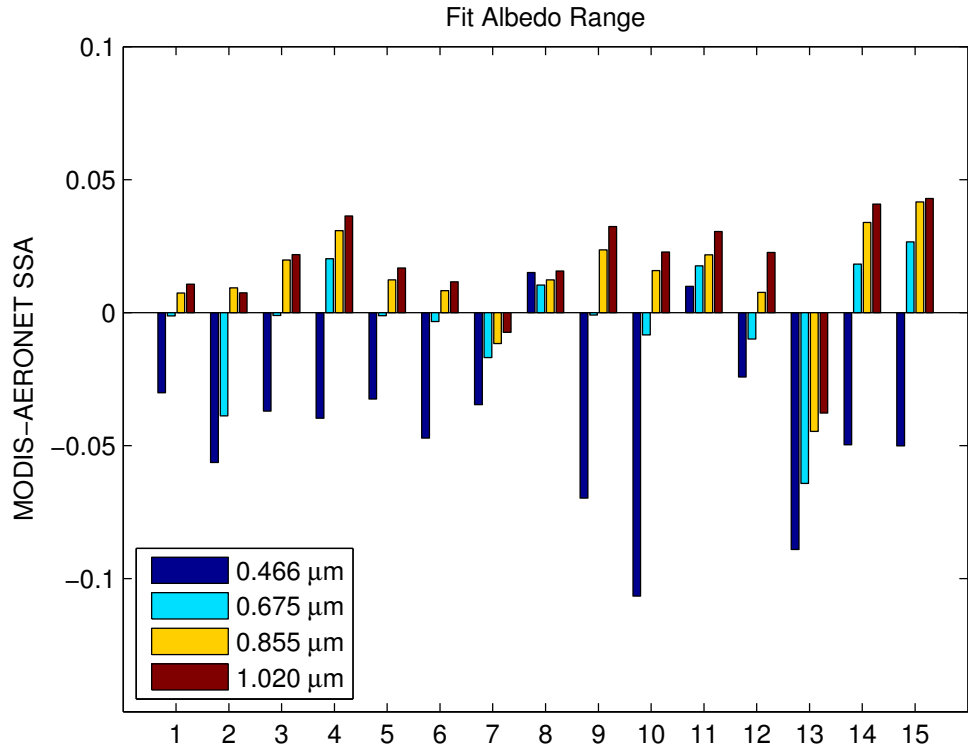


Figure 3.28: MODIS SSA retrieved using the albedo range fitting method compared to AERONET SSA for the 15 cases retrieved at Banizoumbou using the bimodal spheroid model (top) and the coarse model (bottom).

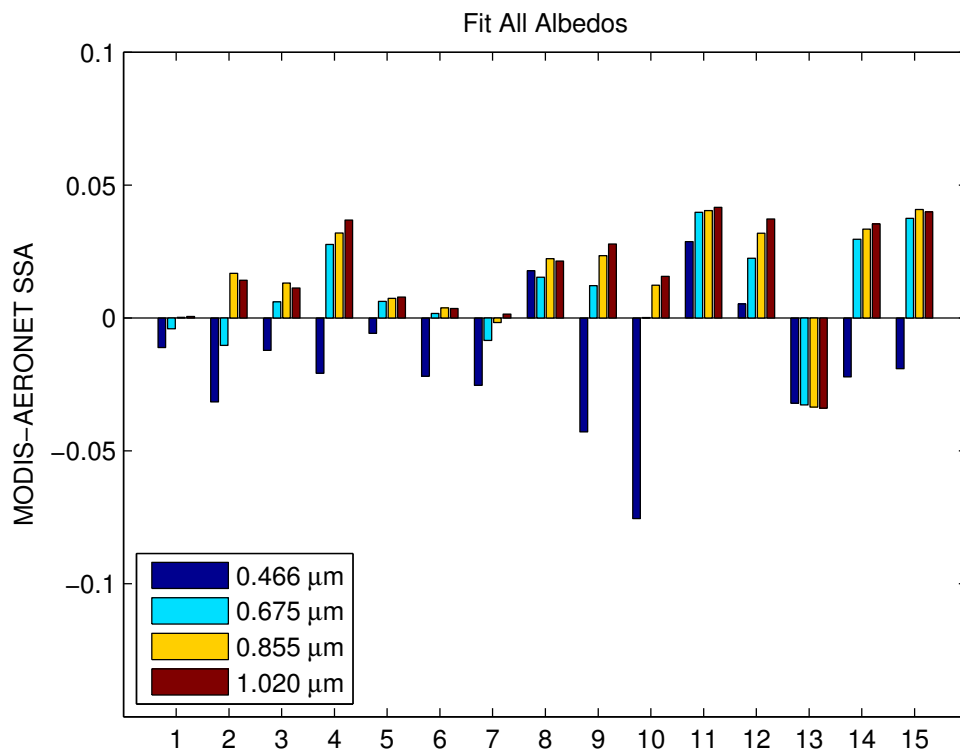
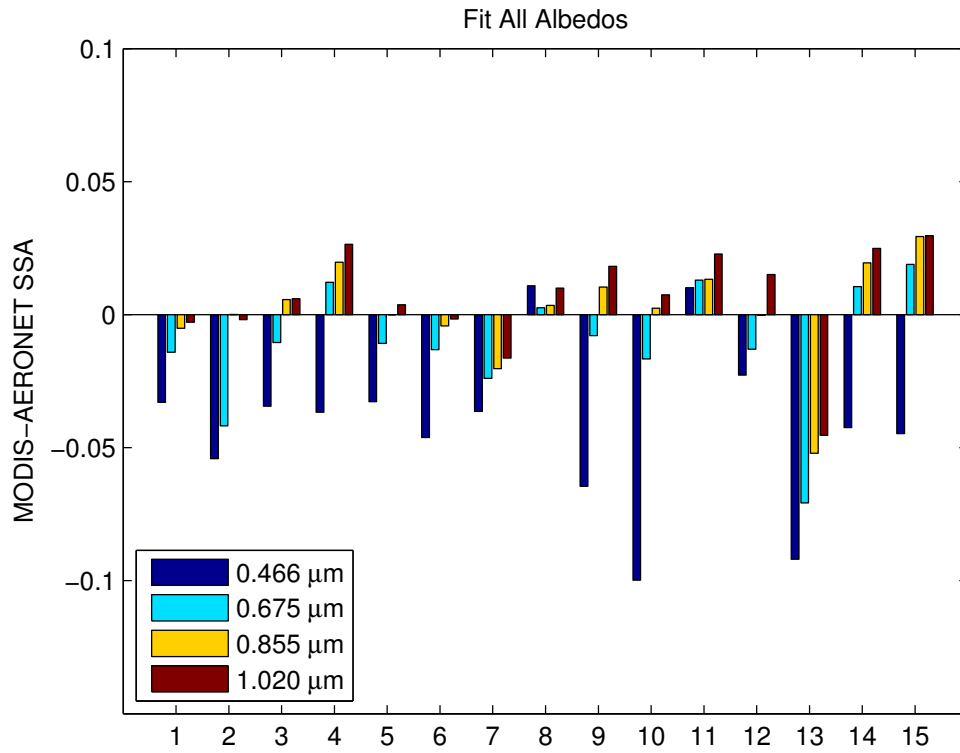


Figure 3.29: MODIS SSA retrieved using the all albedo fitting method compared to AERONET SSA for the 15 cases retrieved at Banizoumbou using the bimodal spheroid model (top) and the coarse model (bottom).

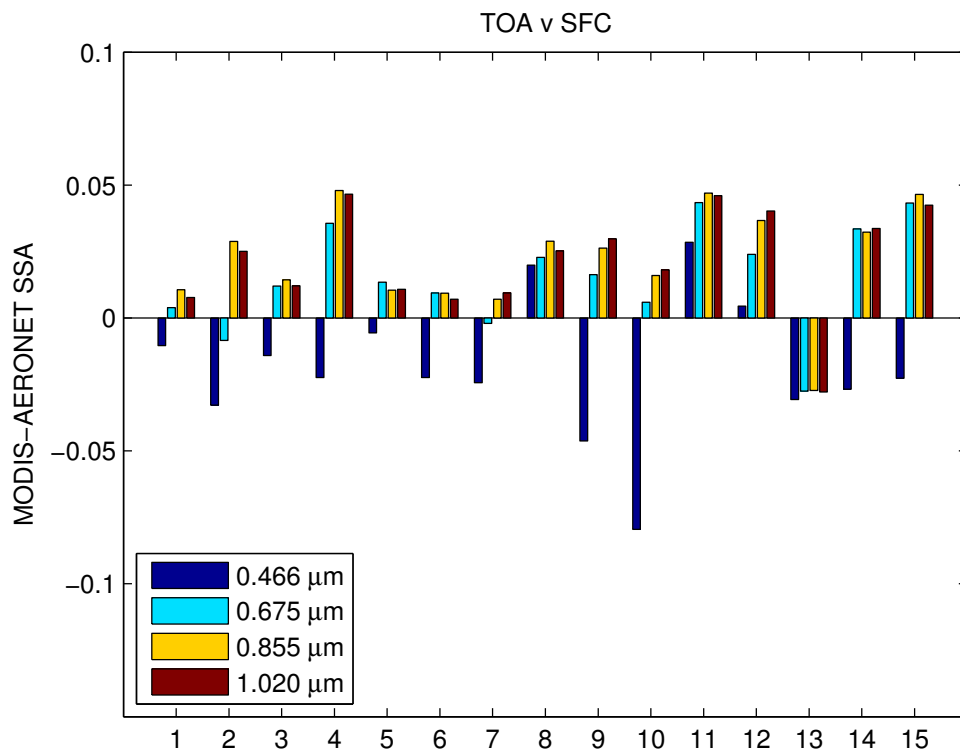
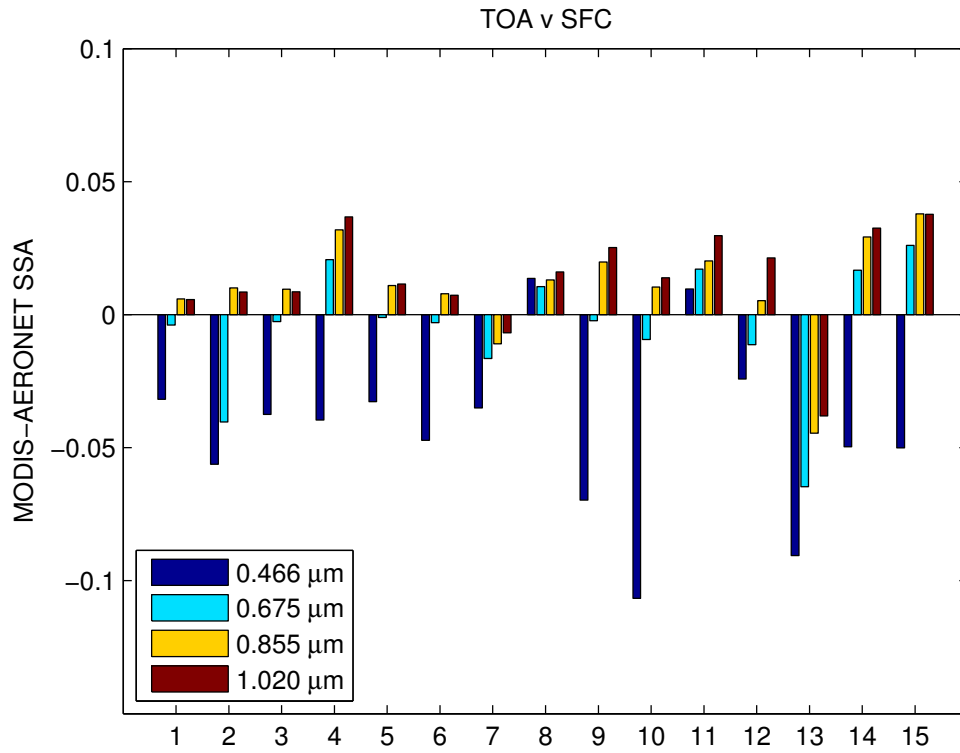


Figure 3.30: MODIS SSA retrieved using the TOA v SFC fitting method compared to AERONET SSA for the 15 cases retrieved at Banizoumbou using the bimodal spheroid model (top) and the coarse model (bottom).

The Banizoumbou results seem to indicate that the bimodal spheroid model yields better agreement with AERONET SSA, but the critical reflectance and AERONET-retrieved size distributions (see Chapter 4) are more consistent with an aerosol that is primarily dust-dominated. In our qualitative discussion of the critical reflectance and path radiance at Tamanrasset and Banizoumbou in Section 3.1.1 and 3.2.1, respectively, we noted that the spectral behavior of both parameters seems to contain some information about aerosol type. Thus, we are interested to see if the spectral dependence of critical reflectance and path radiance can be used to separate mixtures from more purely dust-dominated cases at Banizoumbou. We calculate the logarithmic spectral slope of critical reflectance and path radiance between 0.466 and 0.646  $\mu\text{m}$  at both sites; the frequency of both parameters at both sites for all cases is shown in Figure 3.31.

The histograms at the two sites look qualitatively like we might expect: a dominance of positive spectral dependence of critical reflectance with slightly larger values at Tamanrasset, and a dominance of positive spectral dependence of path radiance at Tamanrasset. Both of these should be consistent with the dominance of dust aerosol, whereas the higher frequency of negative spectral slopes at Banizoumbou should be consistent with the occasional influence of biomass burning particles mixed with the dust. When we calculate the frequency of negative path radiance and critical reflectance spectral slopes by case at Banizoumbou, we find that the two are reasonably well-correlated (Figure 3.32); however, we find that this behavior does not correlate with Angstrom exponent measured at the AERONET site. This is likely due to the fact that both parameters appear to drop off as a function of view angle (Figure 3.33), resulting in a higher frequency of negative values at view angles  $> 40^\circ$ .

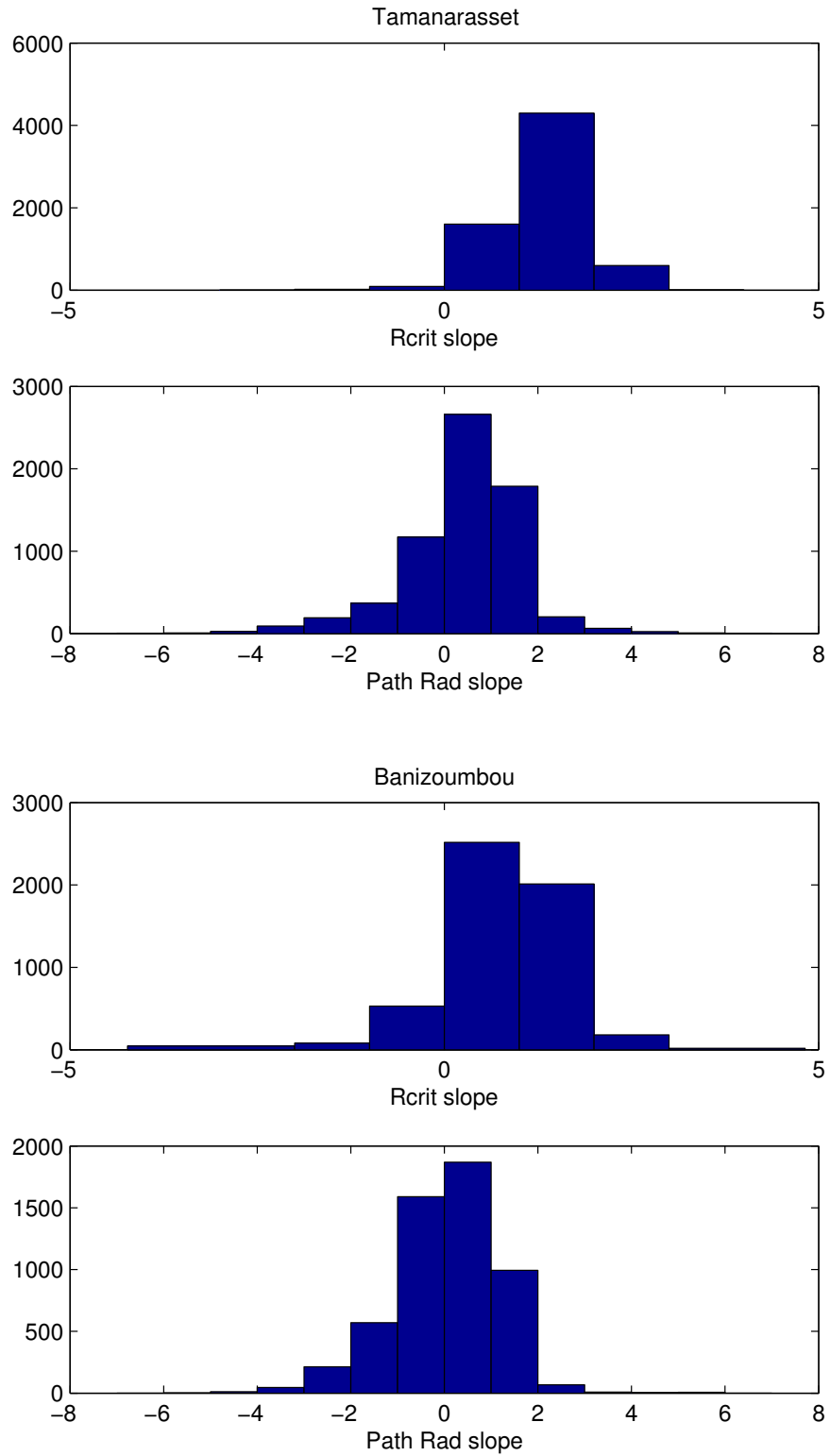


Figure 3.31: Histograms of the logarithmic slope of critical reflectance and path radiance between 0.466 and 0.646  $\mu\text{m}$  at Tamarasset (upper) and Banizoumbou (lower).

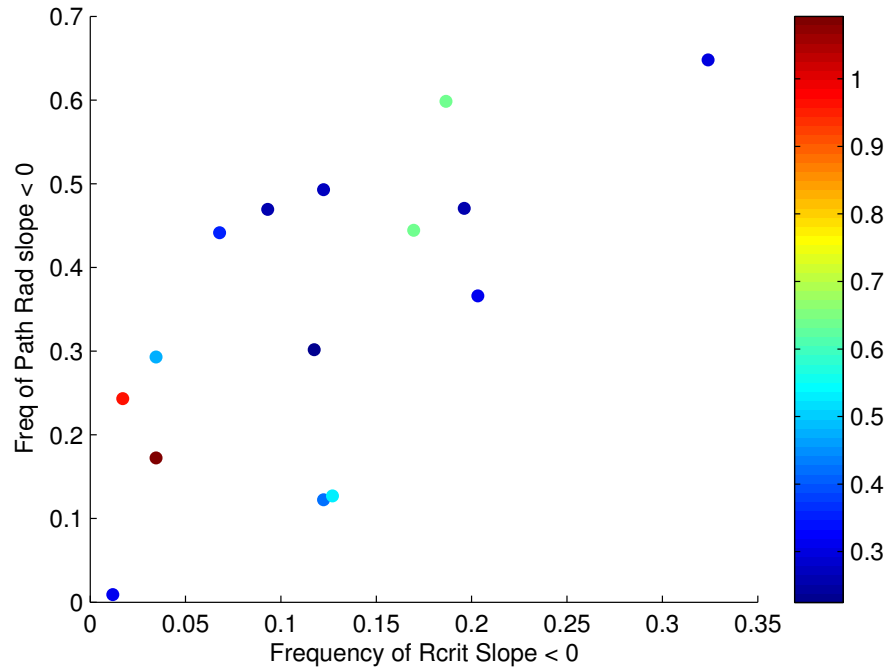


Figure 3.32: Frequency of negative 0.466 -0.646  $\mu\text{m}$  logarithmic path radiance spectral slope versus frequency of negative logarithmic critical reflectance spectral slope at Banizoumbou shaded by 0.44 – 0.87  $\mu\text{m}$  Angstrom exponent from AERONET.

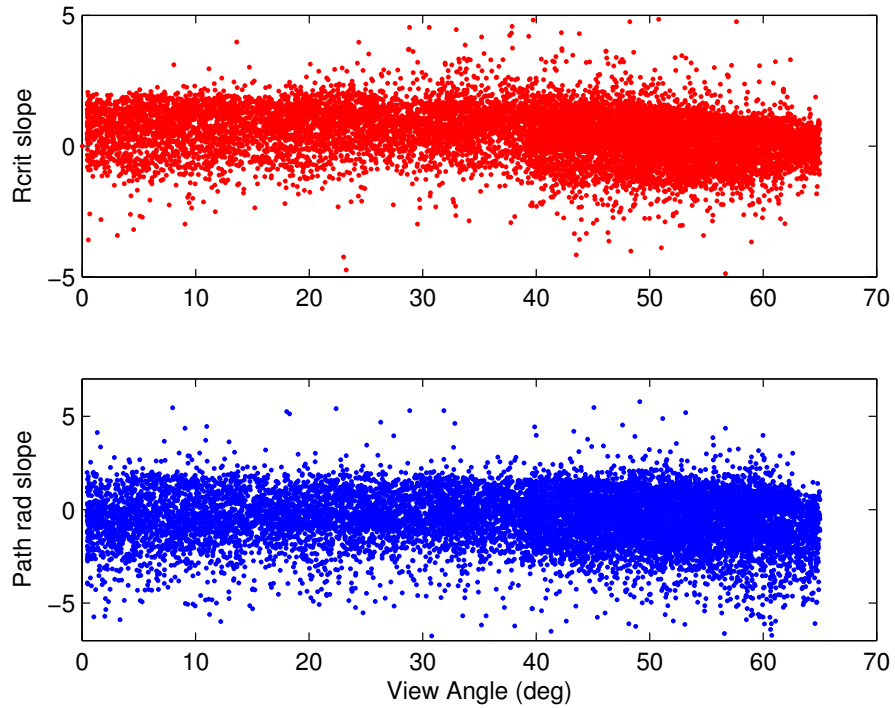


Figure 3.33: 0.466 -0.646  $\mu\text{m}$  logarithmic critical reflectance spectral slope (upper) and path radiance spectral slope as a function of view angle for retrievals near Banizoumbou.

Thus, we must be careful when using the spectral behavior of critical reflectance and path radiance to infer the type of aerosol present in the scene. The dependency of the logarithmic path radiance slope parameter on view angle is probably due to the spectral differences in SSA and AOD. For dust, the SSA is lowest in the blue channel, but the AOD is also highest in this channel (except in the case of very large particles). As the view angle increases, the relative impact of scattering versus absorption may decrease, due to the increase of multiple scattering with increased atmospheric path length. Thus, because absorption is higher in the blue channel, the relative path radiance at this channel may increase disproportionately to the other channels, causing a negative slope of path radiance that is not due to changes in aerosol size. The behavior of the spectral slope of critical reflectance is likely due to trends with view angle that we observe in SSA (which will be manifestations of trends in critical reflectance). Those trends are discussed in Section 3.3.2.

In a study of dust and biomass burning mixtures in Senegal from January to March 2006, Derimian et al. (2008) found that dust-biomass burning mixtures in the region were associated with 0.44 to 0.87  $\mu\text{m}$  Angstrom exponents of 0.5 to 1.2, depending on the relative contributions of each species. The two days on which the AERONET Angstrom exponents at Banizoumbou fall within this range are 7 December 2006 and 11 December 2006 (cases 9 – 12 in Figure 3.28 to Figure 3.30). All the others correspond to Angstrom exponents  $< 0.5$ . Although the mixture cases are not the ones which yield the best agreement with AERONET for the bimodal spheroid model, the bimodal model is most consistent with the ancillary data for size in these cases. So, the

results following will all be shown assuming the bimodal spheroid model for the 7 December and 11 December 2006 cases, and the coarse model for all other cases.

### **3.3 Discussion of Case Study Results**

#### **3.3.1 Terra-Aqua and Three-Day Comparisons**

Since some retrieval days had both Terra and Aqua data available, we compare results from the two instruments to evaluate whether a systematic difference between the two instruments is evident. The difference in the Terra and Aqua SSA for the nine days at Tamanrasset with both Terra and Aqua data available are shown in Figure 3.34, and the differences for the four at Banizoumbou are shown in Figure 3.35. Differences between the Terra and Aqua results tend to be larger at Tamanrasset from 0.855 to 1.243  $\mu\text{m}$ , although there are two cases where the differences are quite large at 0.466  $\mu\text{m}$  (near 0.04). The differences are also larger for the all albedo and TOA v SFC fitting method, although this is primarily due to the fact that the albedo range fitting method causes the SSA to be set to 1.0 at the near-IR channels in most cases.

If the differences between Terra and Aqua are not related to actual changes in the aerosol optical properties between the two times, they may result from differences in water vapor or background aerosol between the different overpass times. At Banizoumbou, Aqua-Terra differences are of a similar magnitude as those at Tamanrasset for the first case, but the differences for the other three cases are smaller. Because the Aqua-Terra differences change sign depending on the case, we conclude that there is no measurement bias between the two instruments; however, results at Tamanrasset may be more sensitive to variations in background aerosol or gases between overpass times.

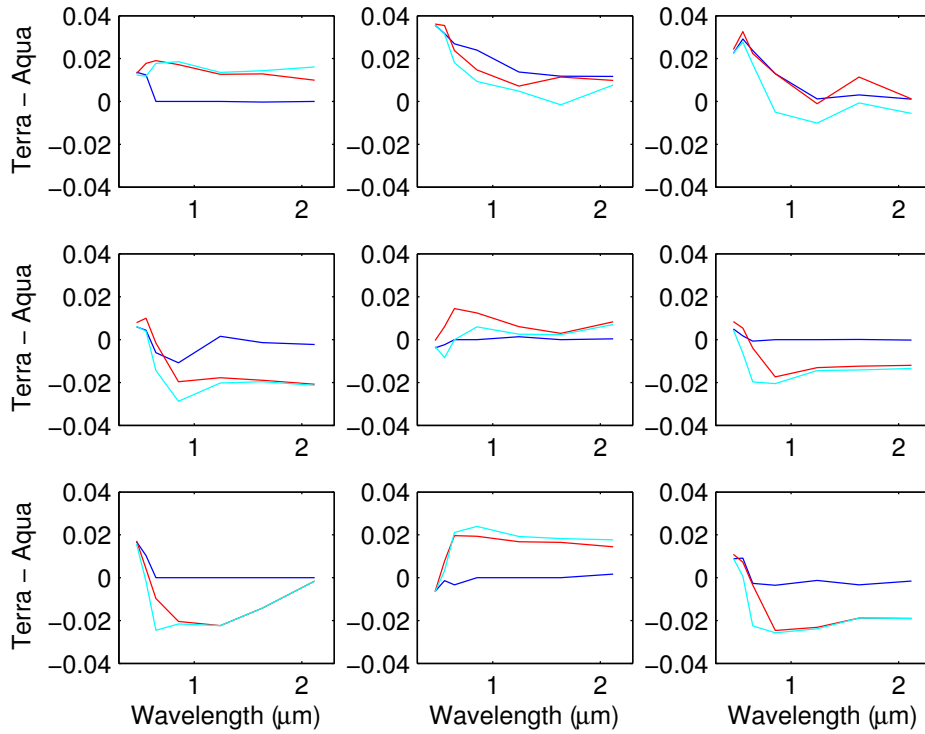


Figure 3.34: Difference in spectral SSA between Terra and Aqua retrievals for the same day at Tamanrasset. Results are shown for the albedo range fitting method (red), all albedo fitting method (blue), and TOA v SFC fitting (cyan).

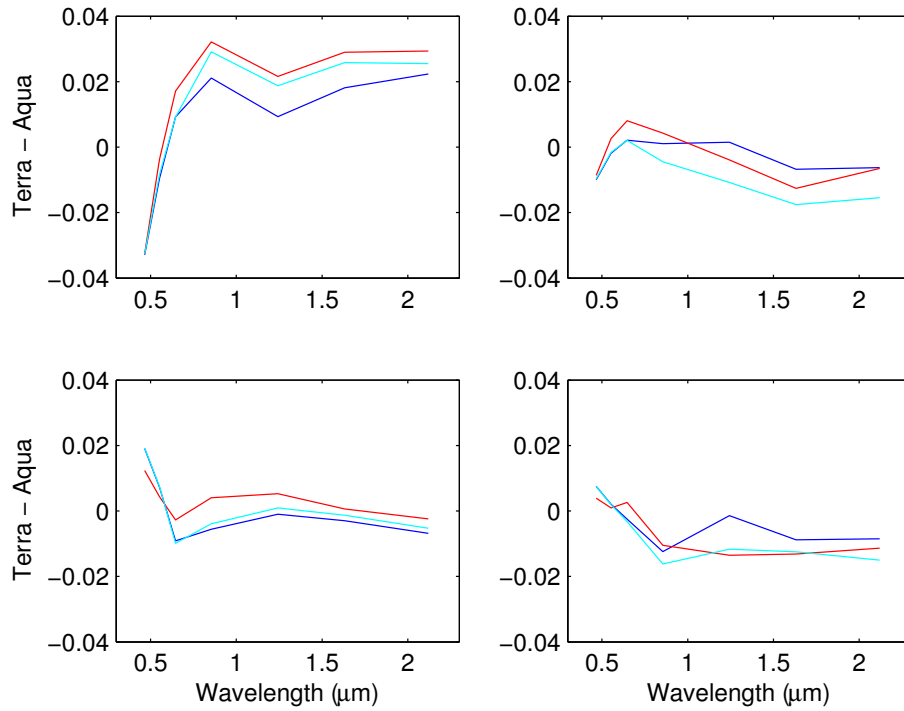


Figure 3.35: Difference in spectral SSA between Terra and Aqua retrievals for the same day at Banizoumbou. Results are shown for the albedo range fitting method (red), all albedo fitting method (blue), and TOA v SFC fitting (cyan).

There are also a few retrieval cases in which MODIS data for both -16 and +16 days were available. Differences between the two estimates can help to assess the effect of changes in the surface reflectance or background aerosol between the polluted and clean days. Three days at Tamanrasset have both +16 and -16 days that meet the  $0.44 \mu\text{m}$  AOD  $< 0.2$  criteria (Figure 3.36), but only one day at Banizoumbou (Figure 3.37). For the cases at both sites, differences between the comparison using -16 and +16 days generally exceed the inversion uncertainties of the individual estimates. At Tamanrasset, the values in the blue channel are most sensitive to the differences between the two cleaner days. There is evidence to suggest that this behavior is driven by differences in the aerosol properties between the two cleaner days. For the first case (upper left), the aerosol appears brighter when compared to the +16 day. The AOD difference between the +16 and -16 days for this case is zero, but the Angstrom exponent indicates that the particles on the +16 day are smaller than the particles on the -16 day. For the second case (upper right), particles also appear brighter when compared to the +16 day; the -16 day AOD is higher than the +16 day AOD for this case, but the particles appear smaller on the +16 day. For the third case (lower plot), the particles appear brighter when compared to the -16 day, which has a higher AOD. The large Angstrom exponents on the clean days indicate relatively small particles in both cases. Thus, although we assume the Tamanrasset site is dominated by dust aerosol in conditions with higher aerosol loading, this assumption does not seem to be valid for the cleaner days. It appears that many cleaner days are impacted by smaller particles that may contain absorbing black carbon, causing the dust to look brighter when the polluted day is compared to these days. The sensitivity to background aerosol at Tamanrasset is explored further in Chapter 4.

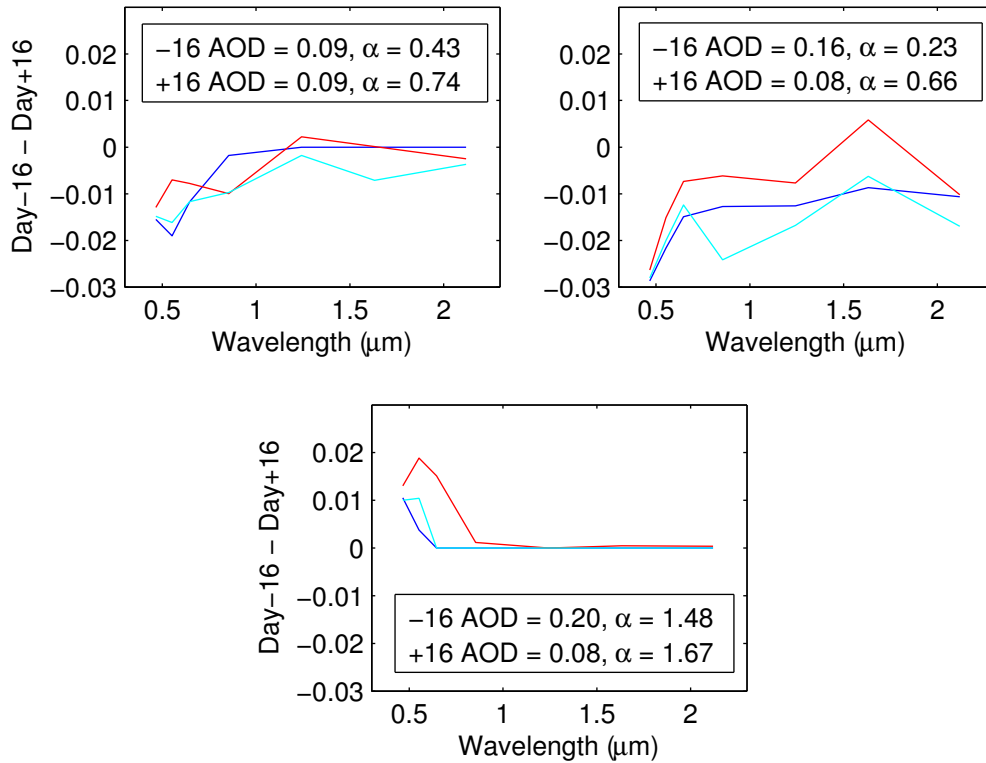


Figure 3.36: Difference in spectral SSA between cases in which both +16 and -16 days were available for comparison at Tamanrasset. Results are shown for the albedo range fitting method (red), all albedo fitting method (blue), and TOA v SFC fitting method (cyan).

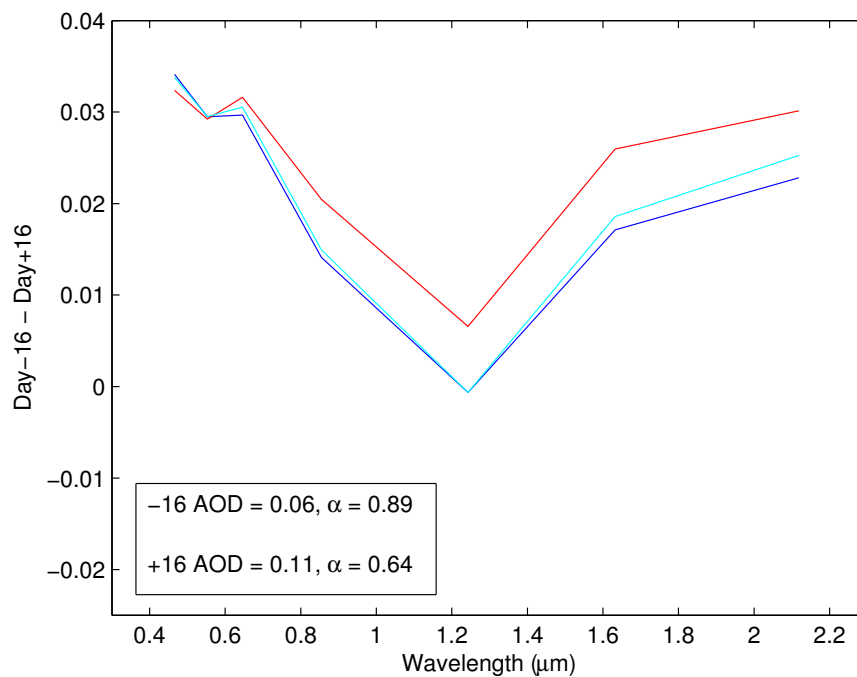


Figure 3.37: Difference in spectral SSA for 11 December 2006 compared to both +16 and -16 days at Banizoumbou. Results are shown for the albedo range fitting method (red), all albedo fitting method (blue), and TOA v SFC fitting method (cyan).

The case at Banizoumbou, from 11 December 2006, shows strong sensitivity to background aerosol in the visible and near-IR channels; the SSA appears insensitive at 1.243  $\mu\text{m}$ , but the retrieval sets the SSA to 1.0 for both cases for the albedo range and TOA v SFC fitting method. The AERONET Angstrom indicates a mixture of dust and biomass burning aerosol on this day, which means that a comparison to a cleaner day in which dust or biomass burning is the predominant species may cause the aerosol to look artificially brighter or darker, respectively. The retrieved SSA is brighter at all wavelengths for the -16 day comparison; the -16 day is somewhat cleaner, with slightly smaller particles. So, the aerosol on the -16 day may be more absorbing than the aerosol on the +16 day, causing the aerosol to appear brighter when using the -16 day as the clean day in the retrieval. Conversely, the fact that the conditions are cleaner on the -16 day may mean the comparison to this day is a better measure of the actual aerosol present on the polluted day. A case study of the effect of clean-day aerosol on SSA retrievals for mixtures near Banizoumbou will be presented in Chapter 4.

### **3.3.2 SSA Relationships with Geometry**

To further examine the robustness of the case study results, the full image retrievals are tested for a dependence on geometry. At each wavelength, SSA image results for all cases are sorted by solar zenith angle, satellite view angle, relative sun-sensor azimuth, and scattering angle. We confine our testing of geometry dependencies to pixels that have a SSA inversion error of less than  $\pm 0.01$ .

There is no discernable relationship between SSA and SZA or relative azimuth near either site (not shown), but we do find trends with view angle and scattering angle for the SSA results at both sites. Results for Tamanrasset as a function of view angle at

0.466 and 1.243  $\mu\text{m}$  are shown in Figure 3.38 as an example. For all three fitting methods used, we find a decrease in SSA at larger view angles in the visible channels. At Tamanrasset, this relationship is most pronounced at 0.466  $\mu\text{m}$ , where the range of SSA at nadir is approximately 0.92 to 0.98, reducing to a range of 0.85 to 0.95 at view angles  $> 60^\circ$ . In the near-IR channels, there is much less variability with view angle for the albedo range fitting method (save a drop-off in SSA at view angles  $> 60^\circ$ ), and the behavior for the other fitting methods is opposite to that observed at 0.466  $\mu\text{m}$ . For the other two fitting methods, particularly the TOA v SFC method, the SSA increases slightly and exhibits less variability at view angles  $> 10^\circ$ , asymptoting to a value of 0.98-0.99 at view angles near  $50^\circ$ . The SSA drops off again at view angles above  $60^\circ$ . Both of these patterns are observed at Banizoumbou as well, although there is more scatter in the SSA results near this site.

When we test for a dependence on scattering angle, we find a trend at both sites. We also find that this trend is driven by the combination of view angle and scattering angle. SSA as a function of scattering angle, shaded by the corresponding view angle, is displayed in Figure 3.39 for Tamanrasset and Figure 3.40 for Banizoumbou at 0.466 and 1.243  $\mu\text{m}$ . The results at 0.466  $\mu\text{m}$  serve to illustrate the behavior we observe at all of the visible channels: an arc-shaped pattern with maximum SSA values occurring between  $\sim 130^\circ$  and  $160^\circ$  and values dropping off at lower and higher scattering angles. There is also a secondary population of SSA values between scattering angles of  $130^\circ$  and  $160^\circ$  that are more absorbing than the other values in this range; these values correspond to larger view angles (generally greater than  $40^\circ$ ). The retrievals at which the SSA is set to 1.0 for the albedo range and TOA v SFC fitting method also appear most concentrated in

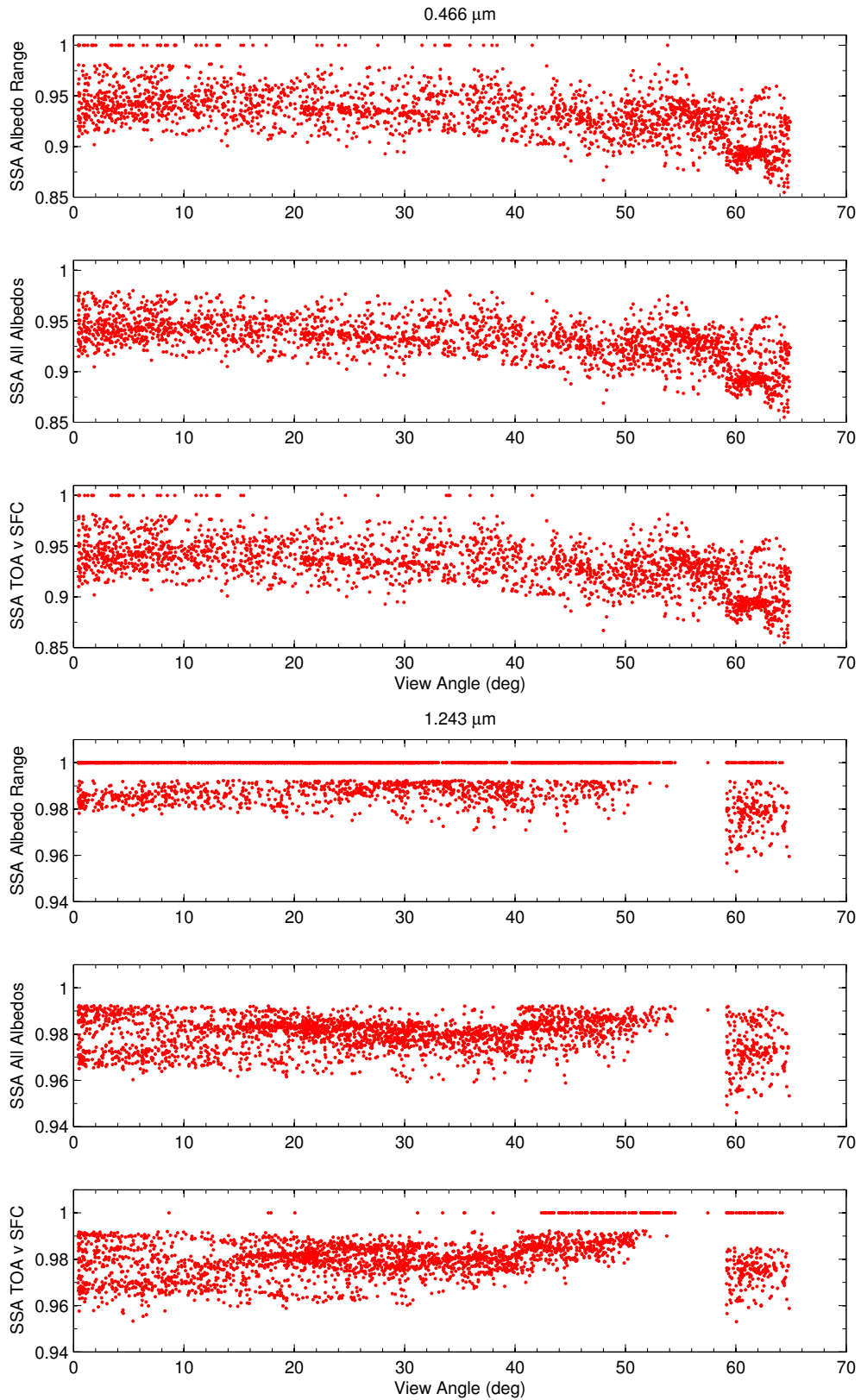


Figure 3.38: SSA results from all Tamanrasset images displayed as a function of view angle for  $0.466 \mu\text{m}$  (upper) and  $1.243 \mu\text{m}$  (lower). Data are confined to pixels with an inversion error less than  $\pm 0.01$ .

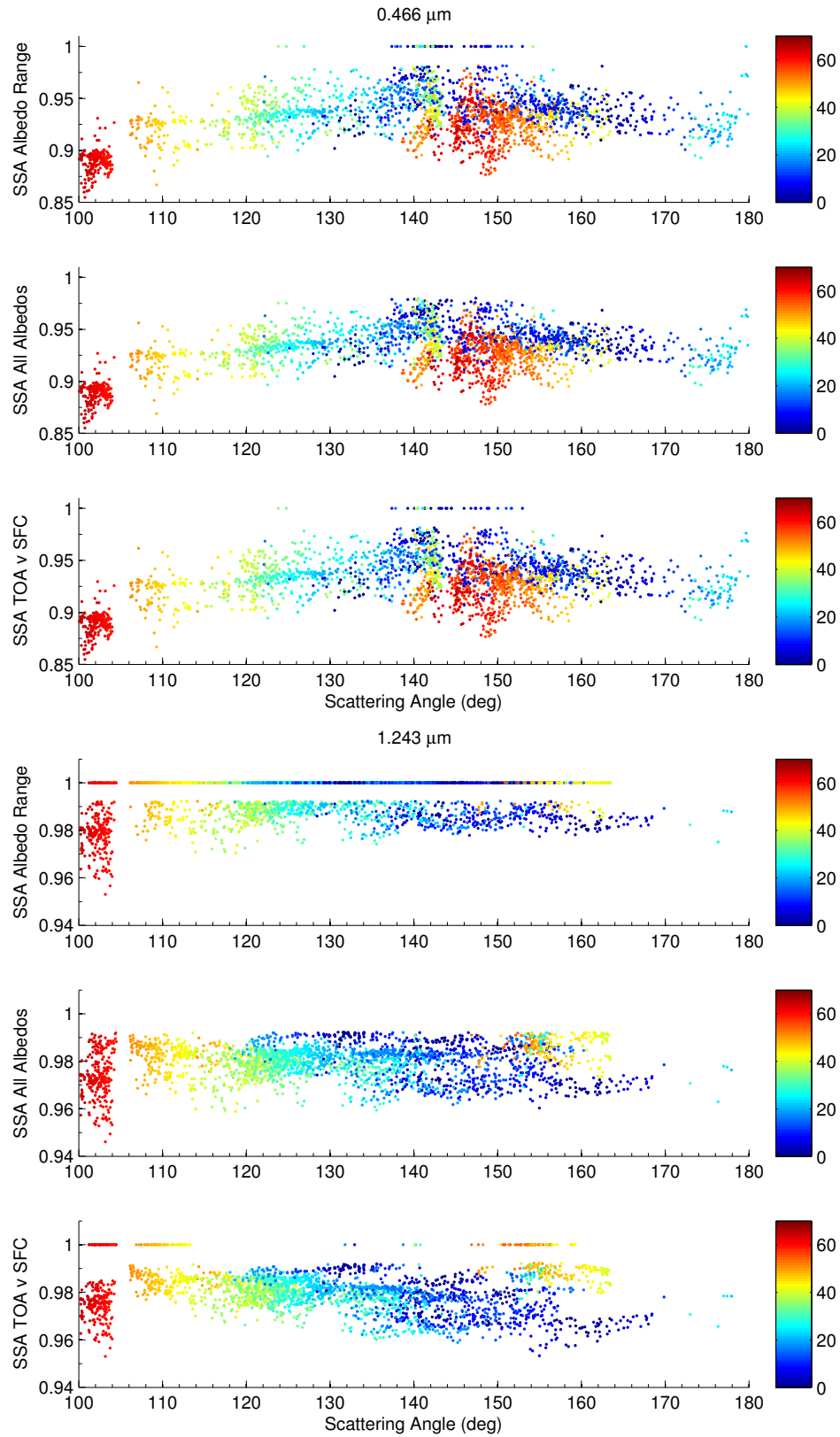


Figure 3.39: SSA results from all Tamanrasset images displayed as a function of scattering angle for 0.466 (upper) and 1.243  $\mu\text{m}$  (lower). Data are shaded based on the corresponding view angle, and confined to pixels with an inversion error less than  $\pm 0.01$ .

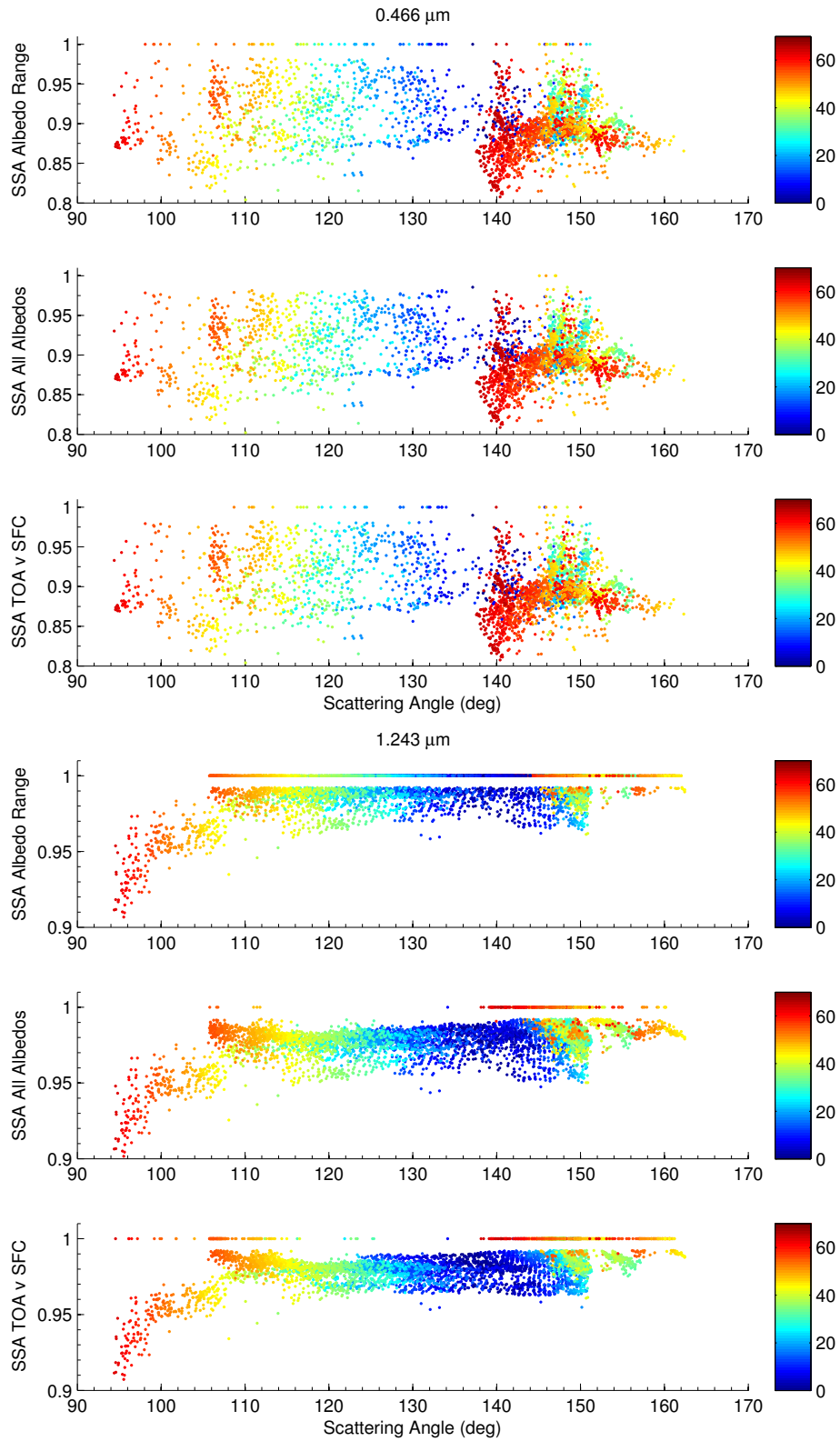


Figure 3.40: SSA results from all Banizoumbou images displayed as a function of scattering angle for 0.466 (upper) and 1.243  $\mu\text{m}$  (lower). Data are shaded based on the corresponding view angle, and confined to pixels with an inversion error less than  $\pm 0.01$ .

the 130° to 160° range of scattering angles at Tamanrasset, but this behavior is not apparent at Banizoumbou.

In the near-IR, there is a drop-off of SSA at scattering angles less than 110°. At other scattering angles, the SSA exhibits less variability than in the visible channels and the behavior is opposite to that observed at 0.466 μm. For the all albedo and TOA v SFC fitting method, the SSA appears slightly more absorbing in the 120° to 140° range of scattering angles, and slightly less absorbing just outside of this range. At Tamanrasset, the values within the 120° to 140° range also exhibit a slight negative trend with view angle, but this behavior is not apparent at Banizoumbou. The less absorbing values outside of this scattering angle range correspond to view angles > 40°. At both sites, the majority of SSA values that have been set to 1.0 by the TOA v SFC fitting method correspond to these larger view angles.

When Kaufman (1987) derived the theoretical conditions for determining the SSA from a given value of critical reflectance, he found the conditions to include:

$$P_a > 0.5P \quad (3.2)$$

where  $P_a$  is the average scattering phase function, and  $P$  is the phase function at a given scattering angle. In other words, the phase function at a given angle should be less than twice the value of the average phase function. Kaufman (1987) suggests that this may limit the critical reflectance application to scattering angles in the range of 120° to 160°, where the phase function values are relatively low compared to the values at higher and lower scattering angles.

Because our study area is impacted by primarily coarse, irregularly-shaped particles, the phase functions that represent the aerosol in our cases will tend to have

lower scattering phase function values in the side scattering range suggested by Kaufman et al, but the relative increase in the phase function values outside of this range should be lower than Mie theory predicts for spherical particles (Dubovik et al., 2002; Volten et al., 2001). Nonetheless, we see that the phase function does increase outside of the 120° to 160° range for our coarse and bimodal spheroid models (Figure 3.41). At 0.466  $\mu\text{m}$ , this increase may result in more multiple scattering at these scattering angles, which is likely the cause of the observed trend with scattering angle. Multiple scattering should also increase as a function of atmospheric path length, resulting in a group of more absorbing SSA values in the 120° to 160° range that correspond to larger view angle. At 1.243  $\mu\text{m}$ , the multiple scattering due to the combination of a higher phase function and larger view angle can explain the decrease in SSA at low scattering angles, but the behavior at other scattering angles is such that the larger view angles correspond to brighter SSAs. We hypothesize that this may be due to the influence of surface brightness on the retrievals, which we will explore further in Chapter 4.

The comparison of SSA with path radiance as a function of view angle also provides some evidence of multiple scattering effects at larger view angles and AODs (Figure 3.42, results shown for Tamanrasset). At 0.466  $\mu\text{m}$ , the more absorbing SSAs tend to be retrieved at higher path radiance values and large view angles, the conditions at which we expect multiple scattering effects to be most pronounced. We also note the tendency for the aerosol to look brighter at low path radiance values, where some values are set to 1.0. This could indicate the need for larger AOD differences when applying the critical reflectance to retrieve SSA, or it could indicate the presence of small particles at lower AODs that are not represented in our aerosol model. The comparison at 1.243  $\mu\text{m}$

also indicates that lower SSAs tend to be retrieved at higher path radiances and large view angles, but no trend at lower path radiance values is apparent.

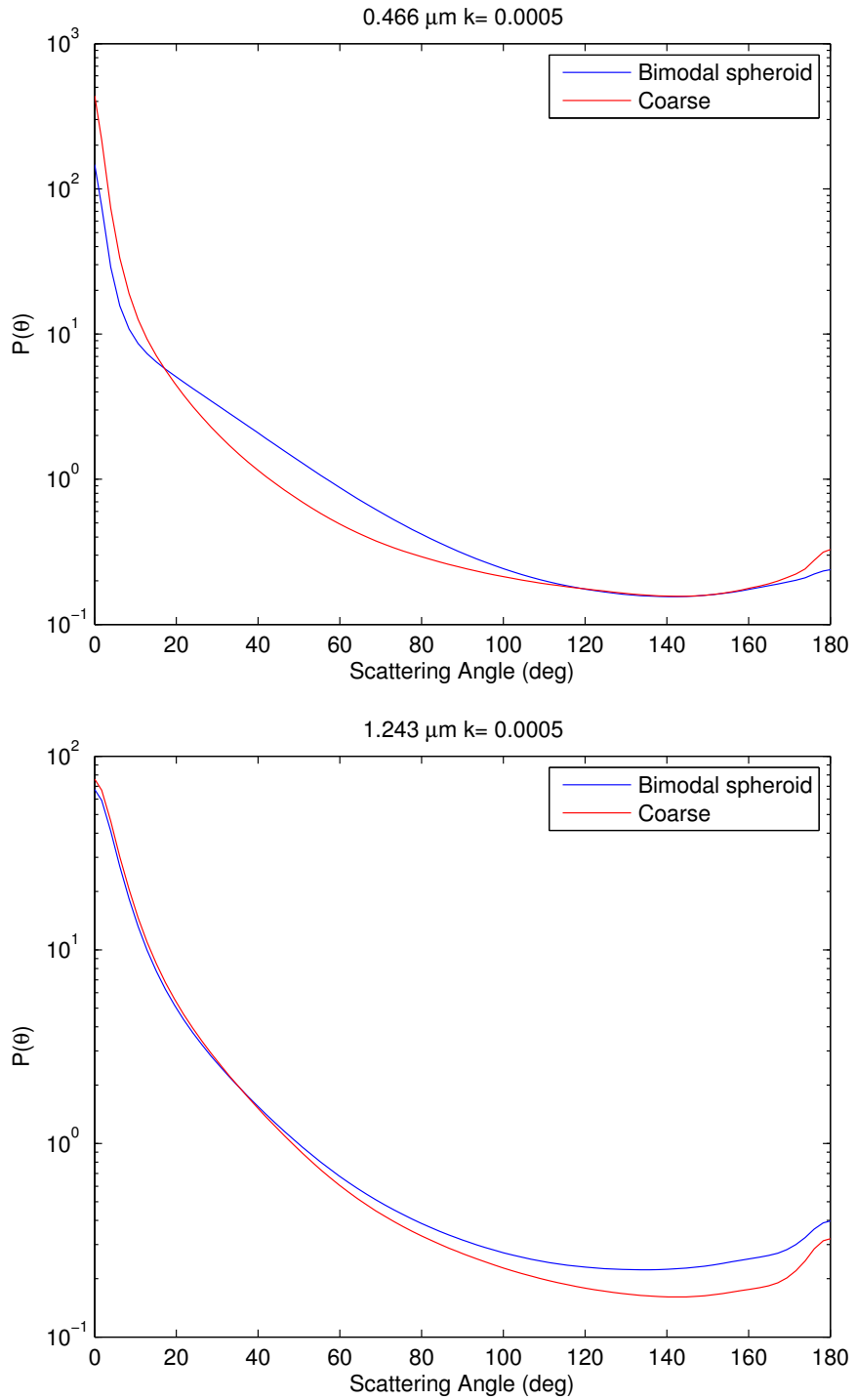


Figure 3.41: Phase functions for  $k = 0.0005$  at 0.466 (upper) and 1.243 μm (lower) for the bimodal spheroid and coarse aerosol models.

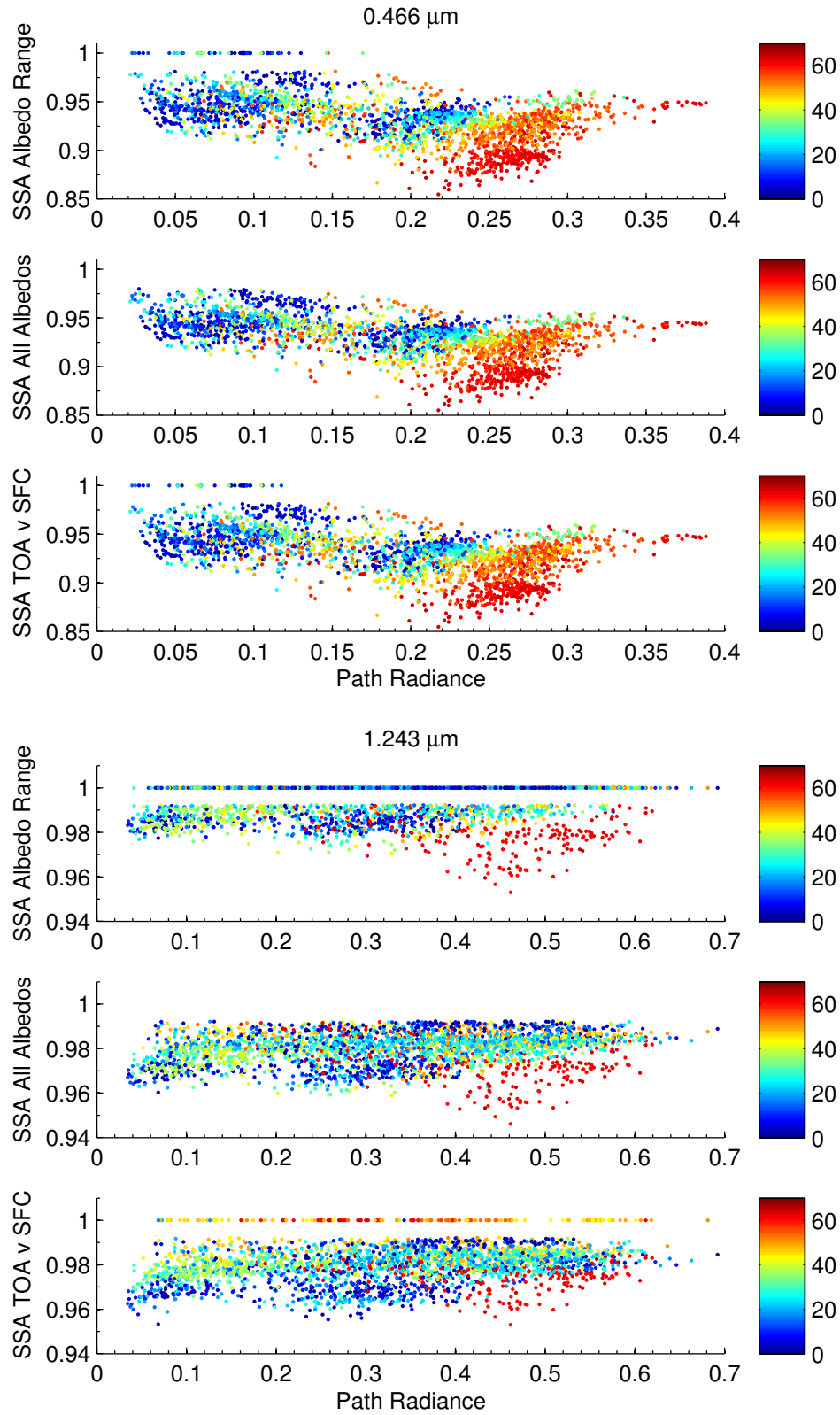


Figure 3.42: SSA results from all Tamanrasset cases displayed as a function of path radiance for  $0.466 \mu\text{m}$  (upper) and  $1.243 \mu\text{m}$  (lower). Data are shaded based on the corresponding view angle, and confined to pixels with an inversion error less than  $\pm 0.01$ .

It is somewhat apparent that the scattering angle trend affects the comparison between the MODIS and AERONET SSA results, although it is clearly only one factor contributing to differences in the two datasets. Results are shown in Figure 3.43 for Tamanrasset and Figure 3.44 for Banizoumbou. At Tamanrasset, there is a tendency for the MODIS values to be larger than AERONET at 0.466  $\mu\text{m}$  in the 130° to 160° scattering angle range, and slightly lower than AERONET at scattering angles near 100°. At 1.020  $\mu\text{m}$ , agreement between AERONET and MODIS may be slightly better for the smaller view angles for the all albedo and TOA v SFC fitting method, but this effect is hard to discern because the SSA in both datasets is approaching the maximum value of 1.0 in this spectral range. The effect of scattering angle at Banizoumbou is hard to discern at 0.466  $\mu\text{m}$ ; there is bit more of a trend at 1.020  $\mu\text{m}$ , with the higher SSA values occurring at scattering angles between 140° and 160°, and the more absorbing SSA occurs at the scattering angle near 100°.

With the exception of values at the smaller scattering angles (near  $\sim 100^\circ$ ), the effect of view angle is less apparent in the MODIS-AERONET SSA comparison, as the critical reflectance-derived SSA values corresponding to higher view angles in the scattering angle range of 120° to 160° are not necessarily lower than the AERONET measurements. Furthermore, we find no trend in the comparison at either site as a function of the AERONET AOD on the polluted day, the clean day, or the AOD difference between the two days (not shown). We also do not find a trend in agreement based upon AERONET sky-error, solar zenith angle, or time difference between the two measurements (also not shown).

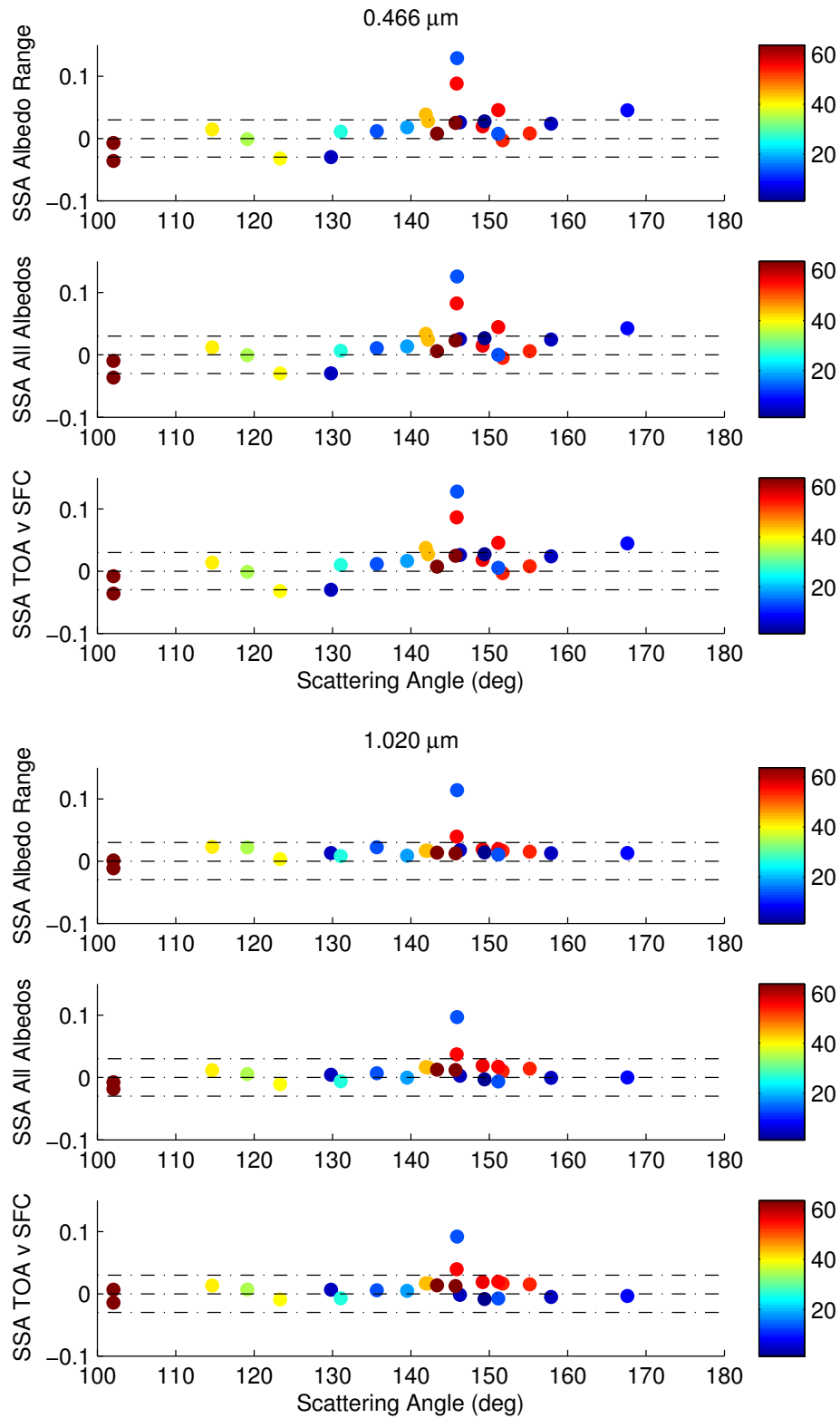


Figure 3.43: MODIS-AERONET differences at Tamanrasset as a function of scattering angle for the three fitting methods at 0.466  $\mu\text{m}$  (upper) and 1.020  $\mu\text{m}$  (lower). Data points are shaded by the corresponding view angle; the dashed lines indicate the bounds of the expected AERONET uncertainty.

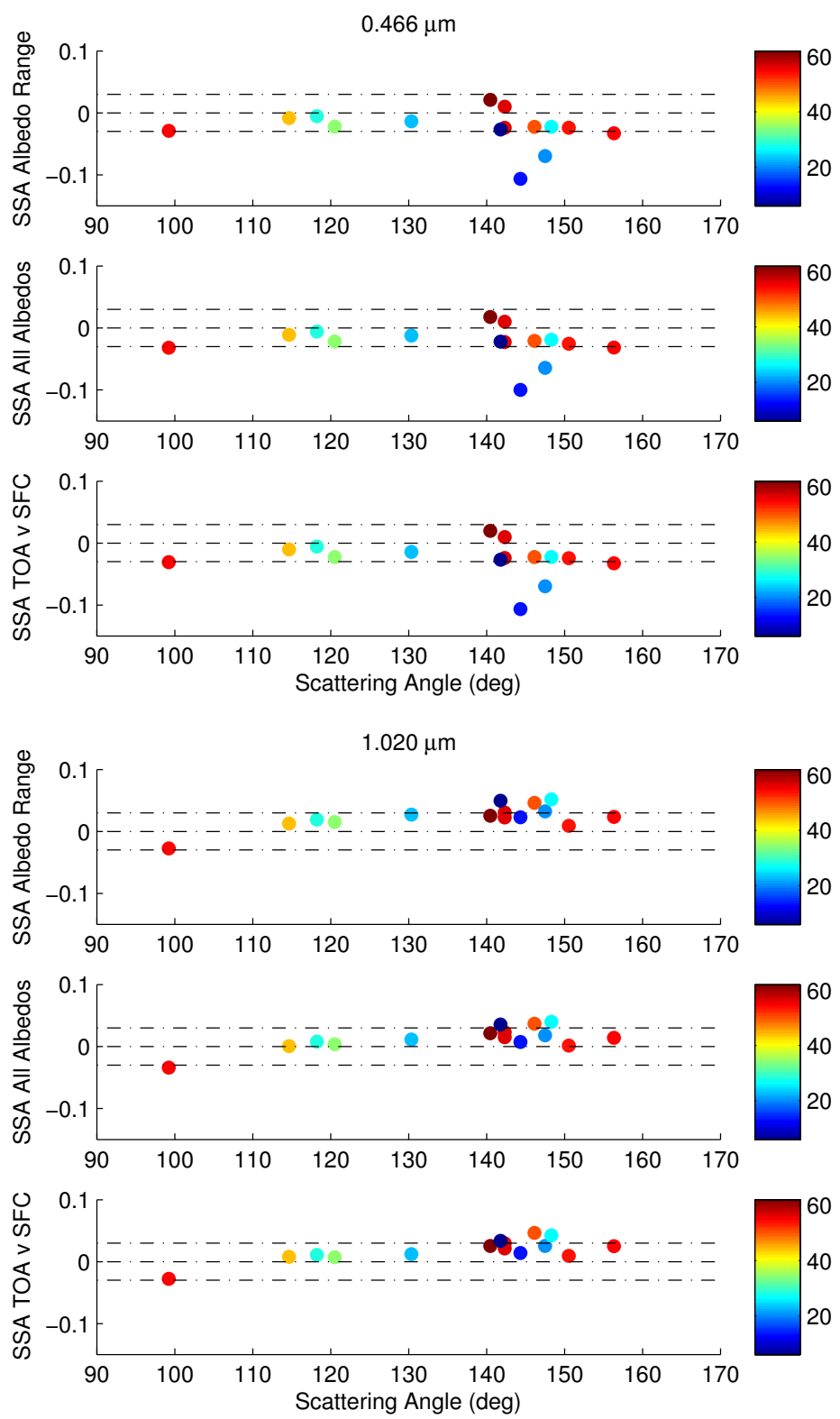


Figure 3.44: MODIS-AERONET differences at Banizoumbou as a function of scattering angle for the three fitting methods at 0.466 μm (upper) and 1.020 μm (lower). Data points are shaded by the corresponding view angle; the dashed lines indicate the bounds of the expected AERONET uncertainty.

The relationships shown here begin to highlight the complexities of using the critical reflectance to derive SSA from satellite measurements over desert, and of using ground-based measurements to validate the results. Our investigation of the full image results yields the following findings:

- The critical reflectance method shows skill in deriving the magnitude and spectral dependence of aerosol absorption over desert and desert transition regions.
- However, there are systematic geometrically-linked trends in critical reflectance-derived SSA that differ depending on the underlying terrain, type of aerosol in the region, and changing background aerosol conditions.
- There are systematic biases when comparing with AERONET, a retrieval that requires fewer assumptions and has well-characterized uncertainties. These are a tendency toward brighter aerosol at Tamanrasset and a stronger spectral dependence of SSA at Banizoumbou.

Given the observed trends in geometry, the method may be best applied within the scattering angle range of  $120^\circ$  to  $160^\circ$ , and at view angle  $< \sim 45^\circ$ . A full discussion of the other sources of uncertainty in our method, related to the assumptions made in the observations and modeling components, will be contained in Chapter 4.

## **4 Uncertainty Analysis and Forcing Estimation**

### **4.1 Observation Uncertainties**

The uncertainties associated with the determination of the critical reflectance from satellite observations arise primarily from the assumptions made when applying the method. Those assumptions, as outlined by Kaufman (1987), are listed in Chapter 1. We will address the effects of the four main assumptions on the retrieved SSA here.

#### **4.1.1 The AOD is Constant over the Retrieval Pixel**

This assumption is probably the most difficult to test, given that there are so few available observations of AOD over North Africa, especially at a resolution that is finer than our resolution scale of 15 km (10 x 10 Level 1B reflectance pixels). Small scale plumes (less than a few thousand meters across) should not affect the retrieval, as they would only change the reflectance of a few pixels and should not be given much weight in the robust fitting routine. The additional screening of 10 x 10 pixel boxes in which there are a larger number of outliers should also help to rule out cases where small plumes are present. If continuous changes in AOD exist across the 10 x 10 pixel area, however, the variability could affect the slope of the polluted versus clean reflectance, and thus affect the retrieved critical reflectance.

At Banizoumbou, the spatial variability of SSA tends to be larger than the uncertainty associated with data fitting. Thus, it is possible that the spatial variability in aerosol loading tends to be greater there, leading to larger uncertainties in the

determination of critical reflectance of a given pixel. To evaluate this effect, we calculate the standard deviation of the path radiance over a 3 x 3 pixel box and compare it to the fitting uncertainty of the SSA within each box. Results are shown in Figure 4.1. Because the SSA tends to peak at 1.243  $\mu\text{m}$  at Banizoumbou, we choose to look at the results at 2.119  $\mu\text{m}$  to assess the effect of AOD variability in the near-IR. We see no obvious trend in the SSA fitting uncertainty with path radiance variability; a higher frequency of higher fitting uncertainties actually occurs when the spatial variability of the path radiance is lower ( $\sigma < 0.1$ ), although this is probably due simply to the sheer number of observations that fall in that range. It should be noted that the spatial variability in path radiance is always higher in the near-IR, which could contain effects of variability in concentrations of absorbing gases in addition to aerosol.

If we confine the data to inversion errors less than 0.01 and compare the 3 x 3 pixel spatial variability in SSA to the 3 x 3 pixel spatial variability in the path radiance, we find that there is a slight tendency for increased SSA spatial variability with increased path radiance variability at 0.466  $\mu\text{m}$ . There are a few pixels for which this is true at 2.119  $\mu\text{m}$ , but the relationship is not nearly as pronounced. However, the spatial variability is already reduced in the near-IR due to the fact that the SSA values are often approaching the maximum value of 1.0. Thus, this comparison indicates that spatial variability in AOD may affect the SSA retrieval in the visible more than in the near-IR channels, even though the path radiance exhibits more variability in the longer wavelengths.

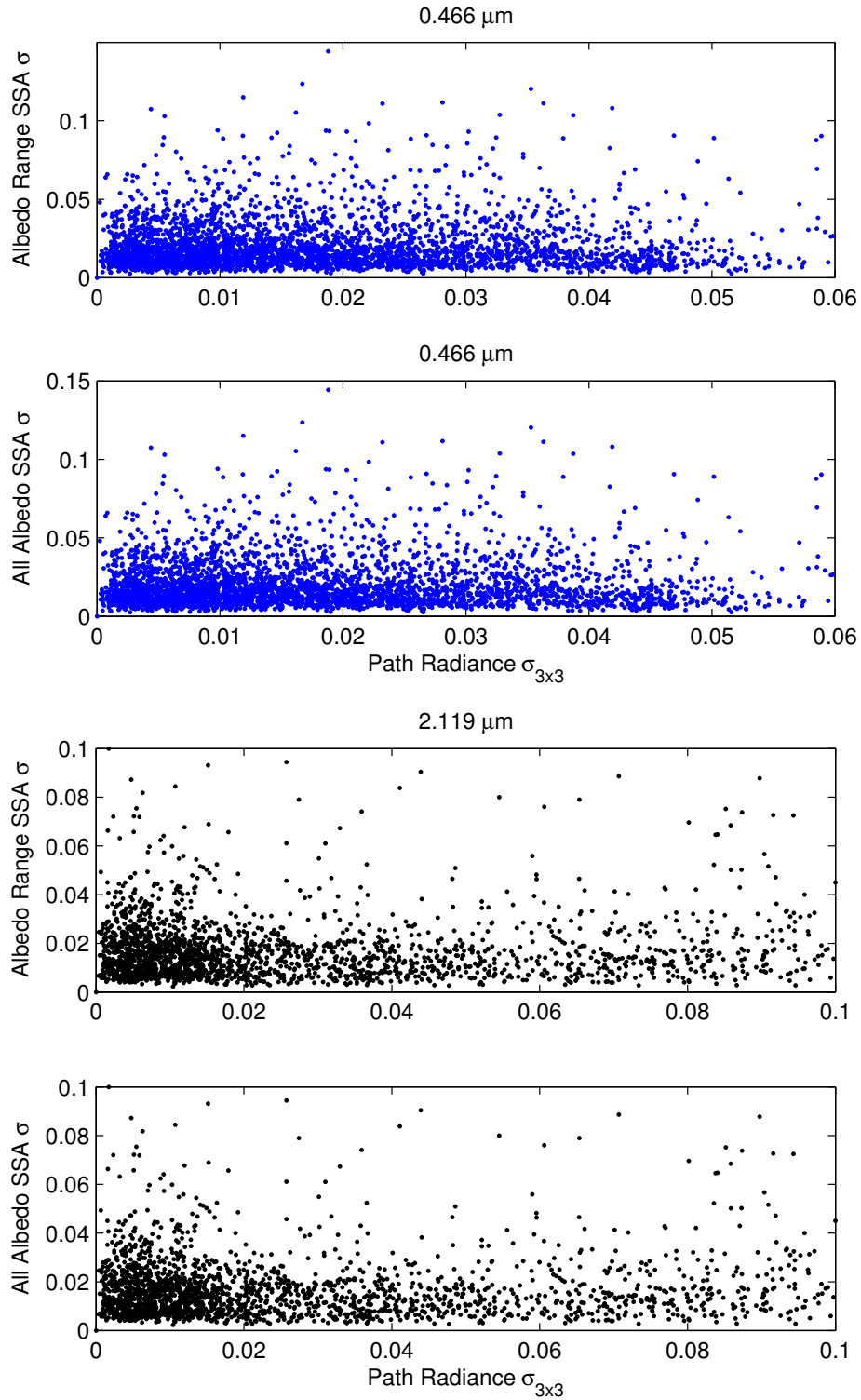


Figure 4.1: Fitting uncertainty of SSA versus  $3 \times 3$  retrieval pixel standard deviation of path radiance at Banizoumbou for the albedo range and all albedo fitting methods at 0.466 (upper) and 2.119  $\mu\text{m}$  (lower).

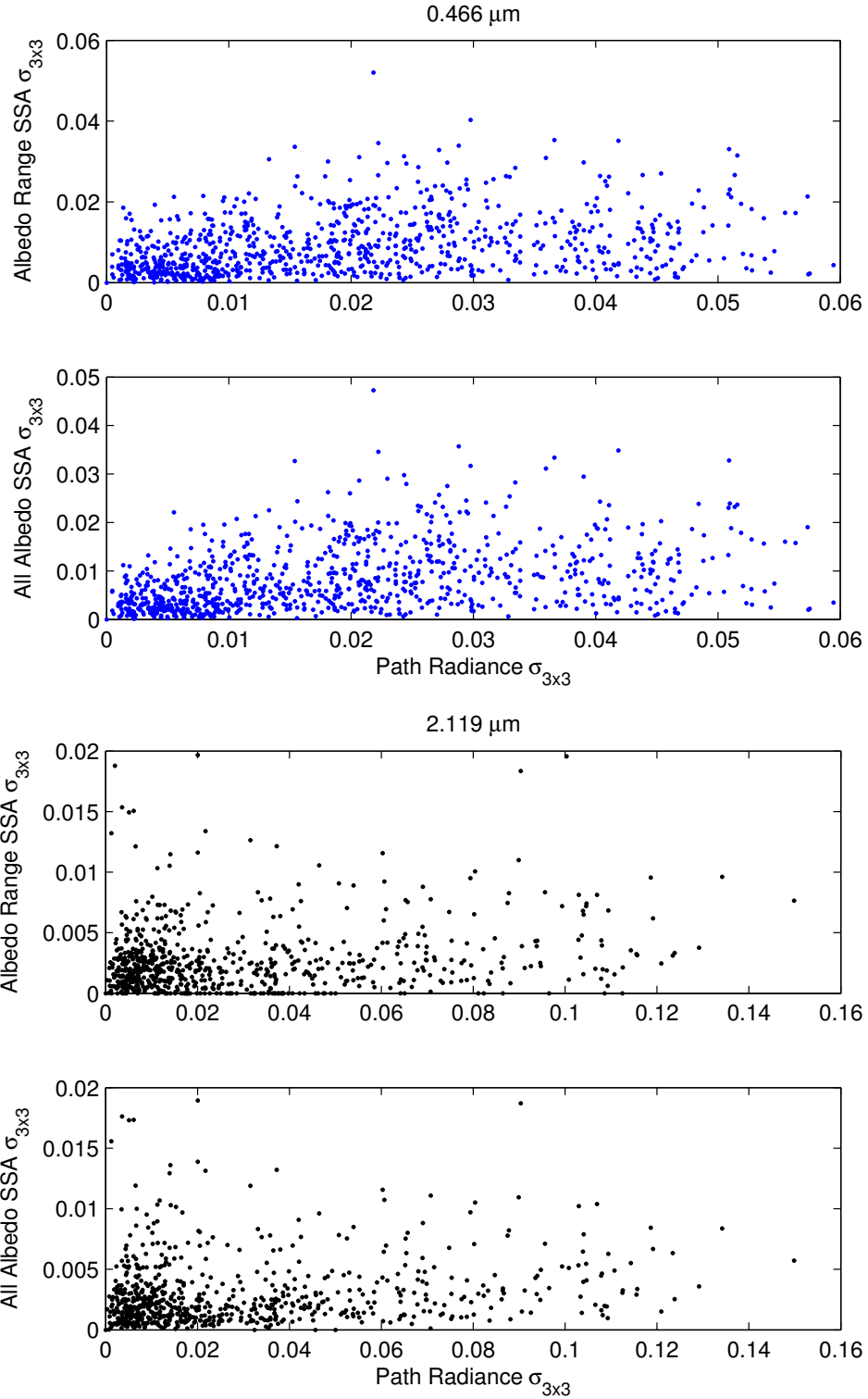


Figure 4.2: 3x3 pixel standard deviation of SSA versus 3x3 retrieval pixel standard deviation of path radiance at Banizoubou for the albedo range and all albedo fitting methods at 0.466 (upper) and 2.119  $\mu\text{m}$  (lower).

#### 4.1.2 Surface Reflectance is Invariant between the Polluted and Clean day

It is hoped that, because we limit our comparisons to clean days that are +16 or -16 days from the polluted day, our method is not affected by significant changes in the properties of the surface between the two days. To investigate the impact of the surface properties on the retrievals, we obtain the MODIS Terra + Aqua 16 day 0.05° gridded surface albedo product (MCD43C) from the Land Processes Distributed Active Archive Center (LPDAAC, <https://lpdaac.usgs.gov/>) for the years 2006 to 2008. A histogram of the broadband shortwave (SW) surface albedo at both sites for these years (Figure 4.3) reveals that the surface is darker and more variable at Banizoumbou; therefore, our assumption of invariant surface reflectivity between the polluted and clean days is likely to be a better one at Tamanrasset, and the variability of the surface may have more of an influence at Banizoumbou.

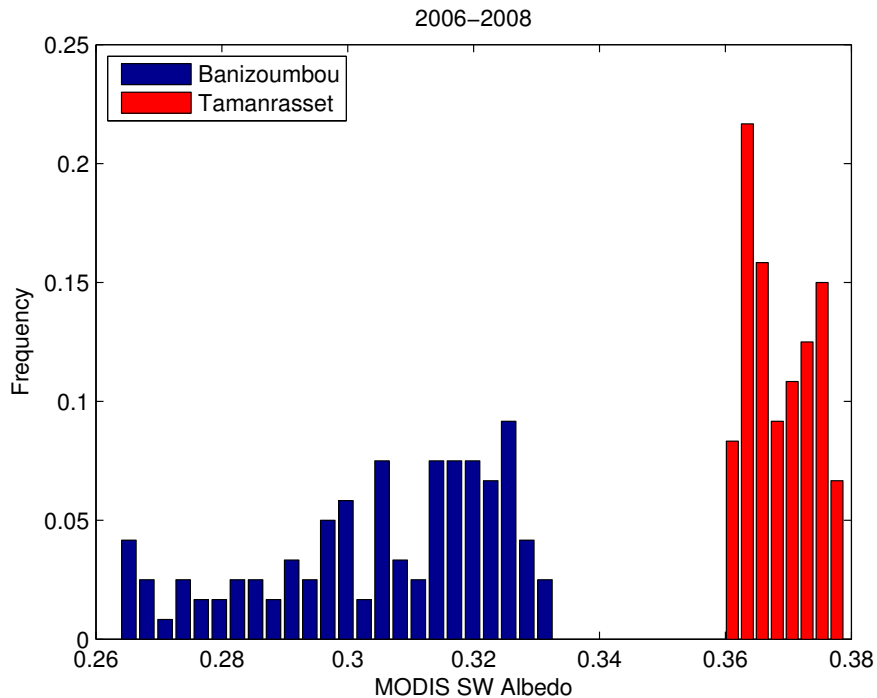


Figure 4.3: Histograms of MODIS broadband SW surface albedo for 2006-2008 at Banizoumbou (blue) and Tamanrasset (red).

However, our assumption is not just that the surface reflectivity between the clean and polluted day will remain unchanged, but that the surface reflectance (the normalized radiance leaving the earth's surface) will remain unchanged as well. Because we are comparing two days with different aerosol loadings, the amount of radiation reaching the earth's surface through the atmosphere will be different between the two days and, as a result, so will the amount of radiation reflected off of the surface. Since light extinction follows an exponential decay with increasing AOD in the atmosphere, the largest changes to the radiation incident upon the surface below the aerosol layer will occur at lower AOD values. Measurements of the downwelling shortwave flux near Banizoumbou as part of the RADAGAST campaign (see Section 4.3.2 for campaign description) demonstrate this effect, revealing a sharp decrease in the downwelling flux with AOD from 0.44  $\mu\text{m}$  AODs of 0 to  $\sim 0.6$ , with less attenuation per unit AOD increase at higher AODs.

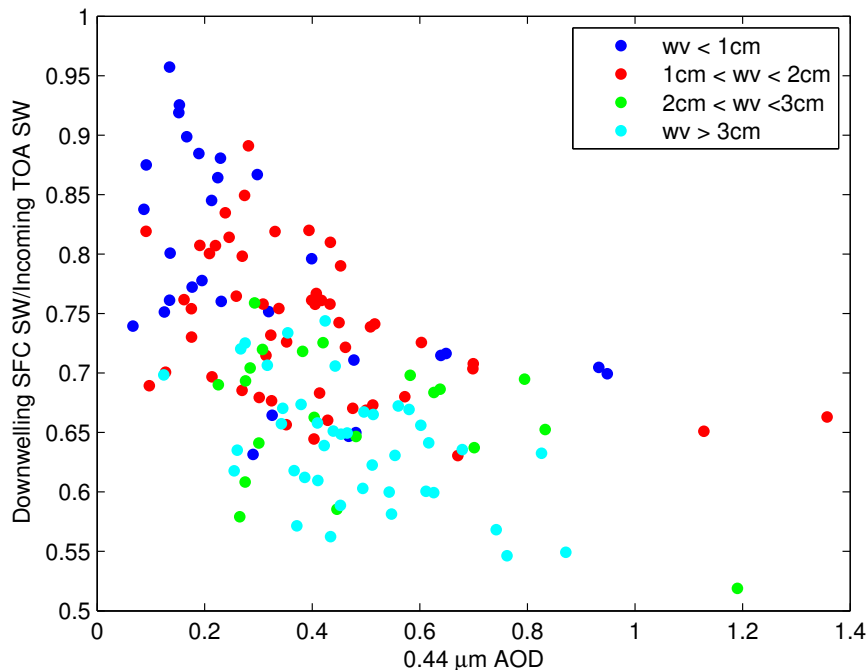


Figure 4.4: Surface downwelling shortwave radiation (normalized by incoming solar at TOA) measured at Niamey, Niger as a function of 0.44  $\mu\text{m}$  AOD at Banizoumbou and binned by water vapor concentration.

Therefore, although the critical reflectance is relatively insensitive to AOD in highly polluted conditions, it may be more sensitive to AOD changes in the presence of only moderate aerosol loadings. Comparisons of SSA retrieval results to AERONET SSA do not reveal an AOD dependence on the agreement between the two datasets, but a comparison to DeepBlue AOD retrieved from MODIS reflectances (available for the Aqua retrievals at Tamanrasset only) indicates that the range of SSA values retrieved using critical reflectance is larger at AODs  $< \sim 0.8$  at  $0.466 \mu\text{m}$  than at higher AODs (Figure 4.5). At the higher AODs, the SSA near Tamanrasset seems to be constrained to values between 0.93 and 0.97, whereas retrieved values have a larger range (and also appear more absorbing) as the AOD decreases. As with the DeepBlue SSA, it should be noted that the DeepBlue AOD product is experimental and has not been thoroughly validated, but the retrieval results near Tamanrasset have been shown to agree well with AERONET direct-sun measurements (Clare Salustro, personal communication).

Thus, if we assume the DeepBlue AOD to be a reasonable estimate of the AOD in the region, our decision to restrict our test cases to those with AODs greater than 0.4 in the blue channel may not be sufficient in order to assume changes in the surface reflectance will not affect the retrieved SSA. Or, since the satellite signal is noisier at lower AODs, it may simply be that our results are more impacted by noise in these cleaner conditions. The method would likely also be less impacted by surface reflectance changes when comparing two days with different but relatively high aerosol loading. In their application of the critical reflectance principle to derive the absorption of dust in a large dust plume over western Africa, Kaufman et al. (2001) compare a dusty day with a  $0.64 \mu\text{m}$  AOD of 2.6 to a less dusty day with a  $0.64 \mu\text{m}$  AOD of 0.8.

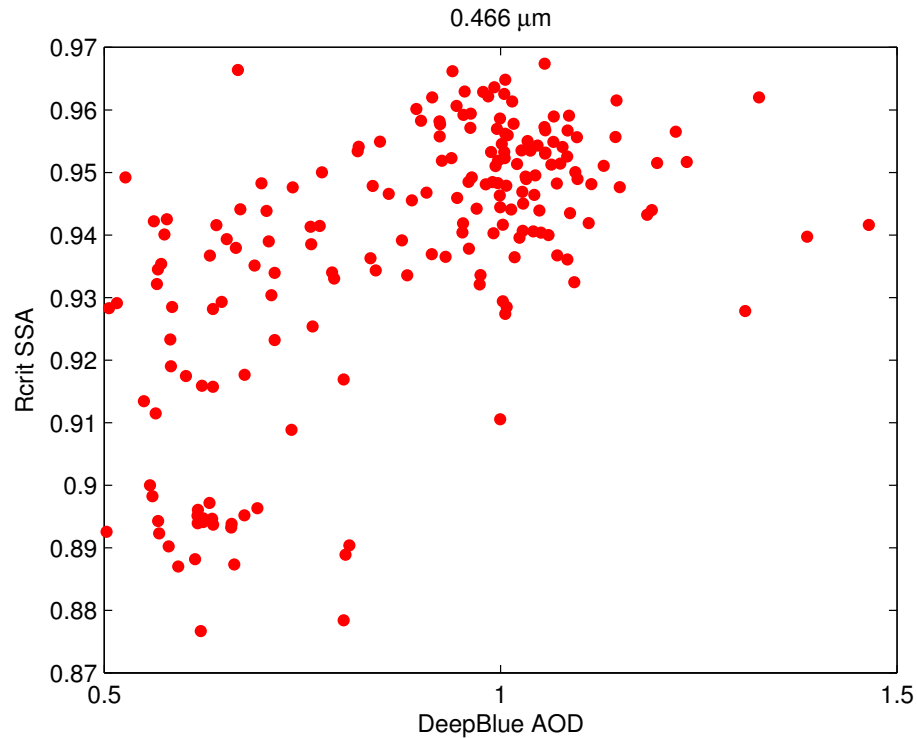


Figure 4.5: Critical reflectance-retrieved SSA compared to DeepBlue retrieved AOD at 0.466  $\mu\text{m}$  near Tamanrasset.

### 4.1.3 The Surface Reflectance is Lambertian

The assumption that the Earth’s surface is Lambertian, or, that the angular variability of the surface does not affect the comparison of the TOA reflectance on two different days, is made in both the observation and modeling components of this study. When we remap the spectral SW albedo data to the same spatial grid as the retrieved SSA and compare two datasets at each channel, we find a dependency of the retrieved SSA on surface albedo, but we do not find it to change as a function of viewing or solar geometry. Trends for all 27 image retrievals near Tamanrasset are shown in Figure 4.6 for the 0.466 and 1.243  $\mu\text{m}$  bands. Results for the 15 retrievals near Banizoumbou are shown in Figure 4.7 for the 0.553 and 1.243  $\mu\text{m}$  channels. The comparison is restricted to SSA values with an inversion error of less than 0.01, and results are shown for the albedo range and all albedo fitting method.

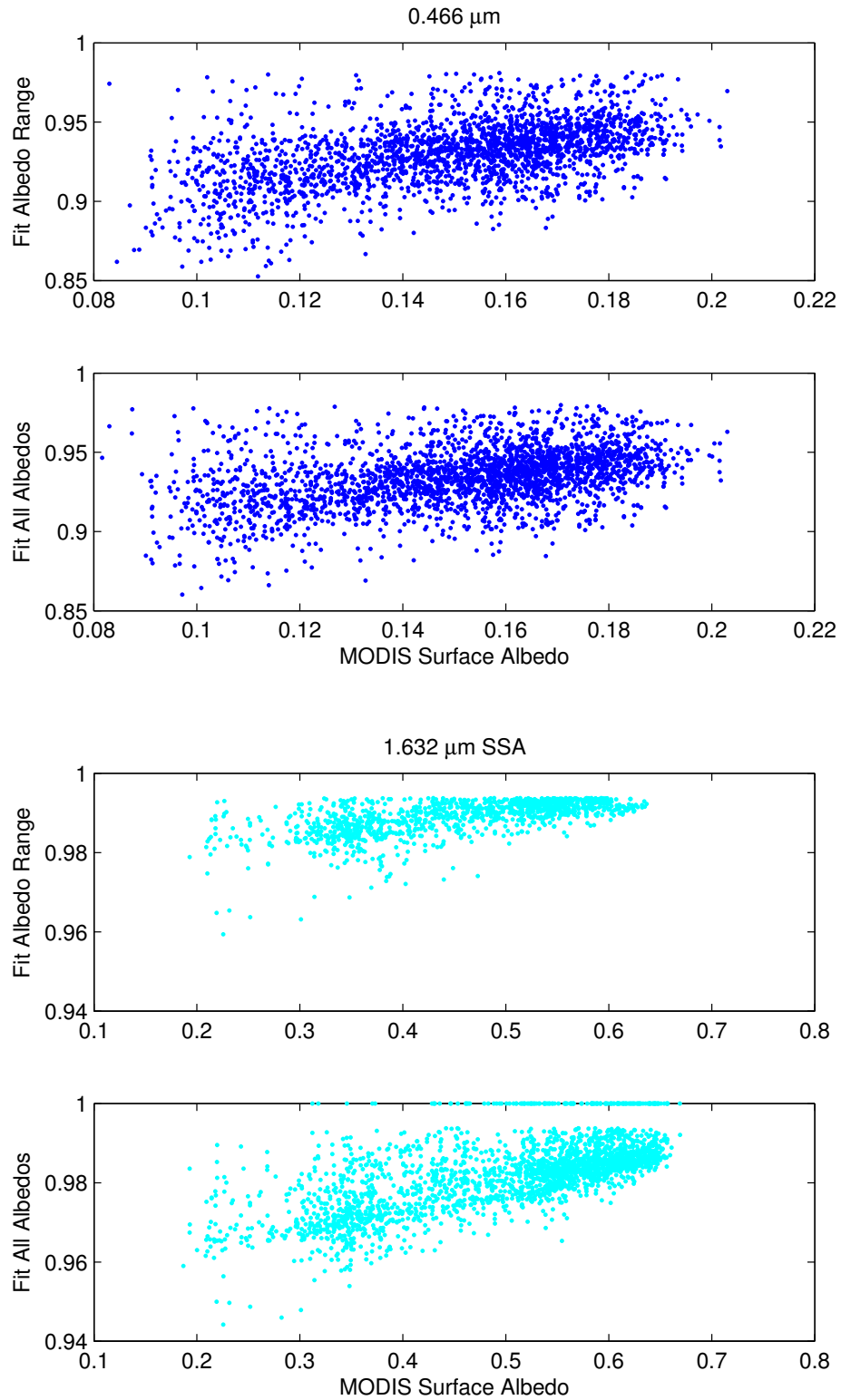


Figure 4.6: SSA near Tamanrasset at 0.466 (upper) and 1.632 (lower) versus MODIS 16-day surface albedo for the albedo range and all albedo fitting methods.

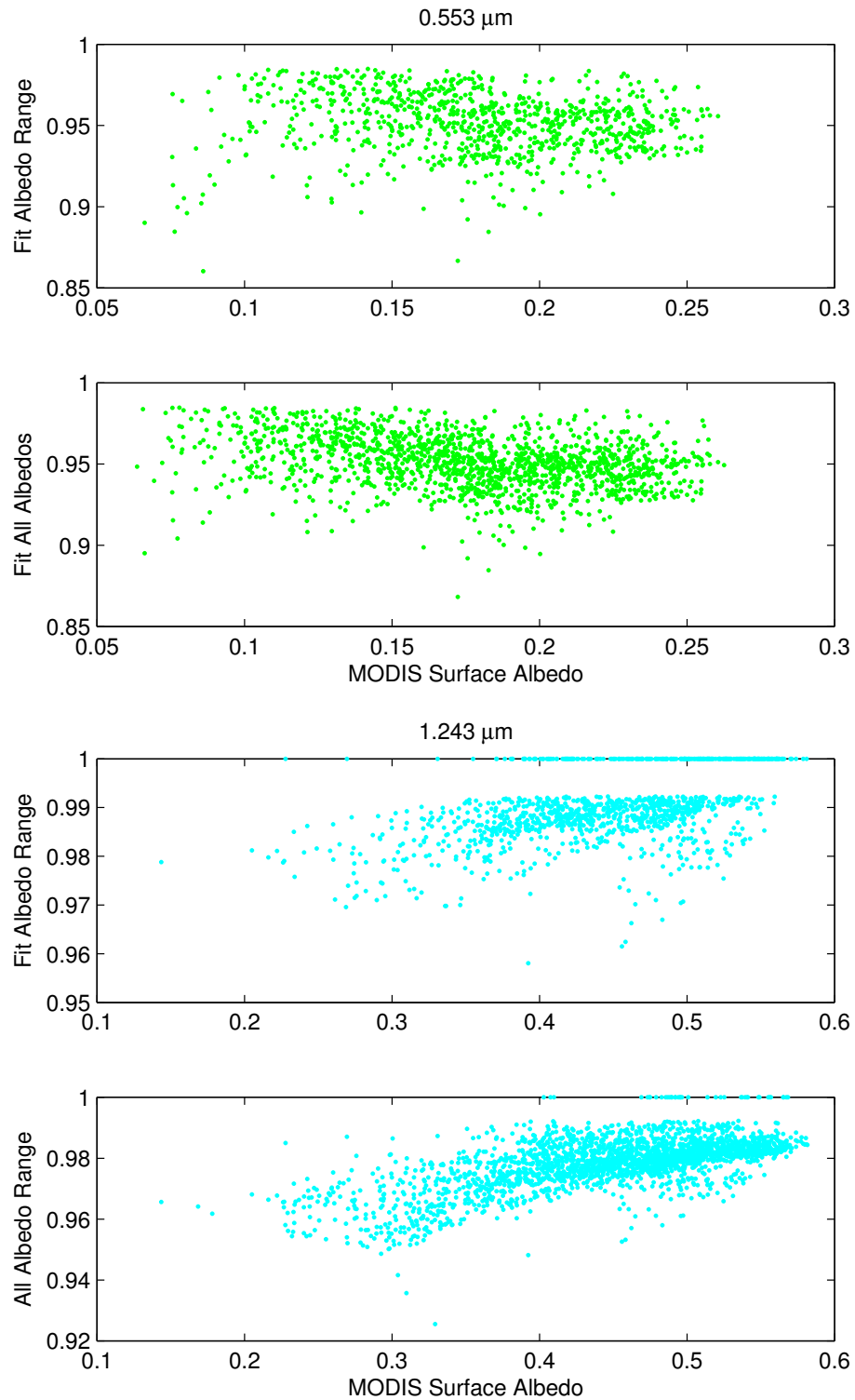


Figure 4.7: SSA near Banizoumbou at 0.553 (upper) and 1.632 (lower) versus MODIS 16-day surface albedo for the albedo range and all albedo fitting methods.

As demonstrated in the results shown in Figure 4.6, we find a positive trend of SSA with surface albedo at all wavelengths regardless of the fitting method used at Tamanrasset. In the visible channels, the trend is of similar magnitude for each fitting method; however, the trend is reduced for the albedo range fitting method at the longer-wavelength channels. Most of the cases at which the SSA was set to 1.0 due to the critical reflectance exceeding all values in the LUT occur at higher surface albedo values. The SSA results are also more variable at the lower surface albedo values; this could be due to the fact that more interpolation between the data and the one-to-one line is required to determine the critical reflectance when the surface reflectance is low. At Banizoumbou, the amount of scatter in the data at  $0.466 \mu\text{m}$  does not allow for a trend with surface albedo to be deduced. However, at  $0.553 \mu\text{m}$ , there is a slight negative trend of SSA with increasing surface brightness. In the near-IR, we find a positive trend of SSA with surface albedo, which levels off at higher surface albedos more rapidly than the SSA at Tamanrasset.

Although these trends do not directly demonstrate the effect of a non-Lambertian surface on the retrieval, nor do they indicate a directional dependence of the SSA dependence on surface albedo, they do reveal a relationship between SSA and surface brightness that could possibly explain observed relationships between SSA and viewing geometry that we see at both sites (Section 3.3.2, Figures 3.39 and 3.40). One model of the bidirectional reflectance distribution function (BRDF) over desert indicates that the surface reflectance increases with viewing and solar zenith angle (i.e. Figure 4.8, Capderou and Kandel, 1995), and that this increase is more pronounced at small relative azimuths. This reflectance distribution can explain the slight increases of SSA with view

angle that we observe in the near-IR, and perhaps also at Banizoumbou where we see a slight decrease of SSA with increasing surface reflectivity. But it does not explain the negative trend with view angle that is observed in the visible wavelengths at Tamanrasset. It also does not explain the absence of a trend in SSA with solar zenith angle at all wavelengths.

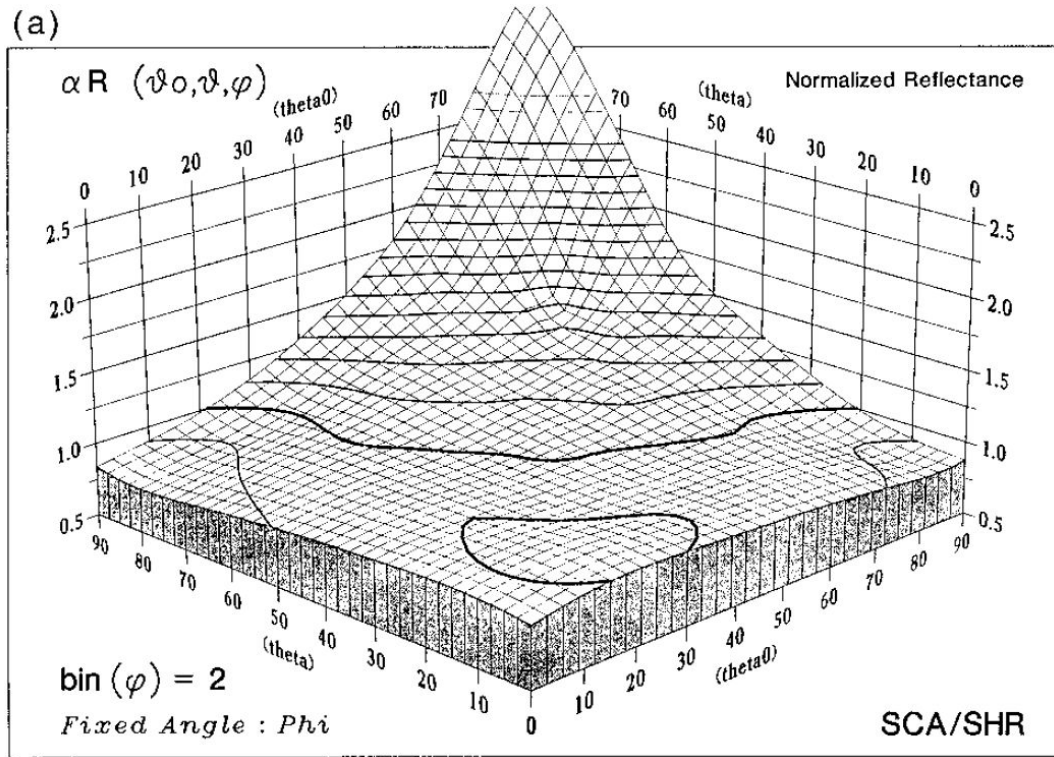


Figure 4.8: Normalized surface reflectance as a function of view ( $\theta$ ) and solar ( $\theta_0$ ) zenith angles for a Saharan surface model determined from satellite. From Capderou and Kandel (1995).

Thus, if the Capderou and Kandel (1995) model is representative of the BRDF at both AERONET sites, we infer that the effect of a non-Lambertian surface may be manifested as a tendency toward brighter aerosol in the near-IR at higher view angles (for scattering angles greater than  $110^\circ$ ) in our retrieval. Complicated BRDF effects are also likely to blame for the poor critical reflectance results in the vicinity of complex terrain near the Tamanrasset site.

Based on the SSA trend observed at Banizoumbou, a non-Lambertian surface may also have a small effect in the visible, but we hypothesize that the decrease in SSA with view angle in the visible is likely due more to an increase in the optical thickness at off-nadir angles than to changes in the surface reflectance with view angle. As discussed in Section 3.3.2, multiple scattering between the surface and the aerosol layer will increase at larger view angles, resulting in a decreased TOA reflectance which could then be interpreted as increased aerosol absorption in the retrieval. The reason that this effect is seen mainly in the visible channels could be simply due to the fact that the AOD is larger at these channels than in the near-IR.

We hypothesize further that the reason we observe trends in SSA as a function of surface brightness is related to a fundamental issue associated with the determination of the critical reflectance from satellite data, and the matching of the retrieved value to a modeled critical reflectance. As discussed in Chapter 2, our simulations suggest that the TOA reflectance begins to increase non-linearly at higher surface reflectances when the aerosol is only weakly absorbing. The simulated TOA reflectance assuming  $AOD = 1.0$  and  $k = 0.0015$  for the coarse model versus the TOA reflectance for  $AOD = 0$  is shown in Figure 4.9 (blue points). A linear fit to reflectance points over a relatively dark surface (red points) yields a critical reflectance that is represented by the crossover point of the red line and the one-to-one line, whereas the critical reflectance over a brighter surface (green points) is represented by the crossover point of the green line with the one-to-one line. The critical reflectance over the brighter surface is higher and, because there is no information about the actual surface albedo input into the retrieval, it produces a less-absorbing SSA as a result. The albedo range fitting method does help to reduce some of

the variability in retrieved SSA in the near-IR, but because it contains a wide assumed range of possible surface albedos that could be representative of desert surfaces in general, it is not able to account for pixel-to-pixel changes in the surface albedo.

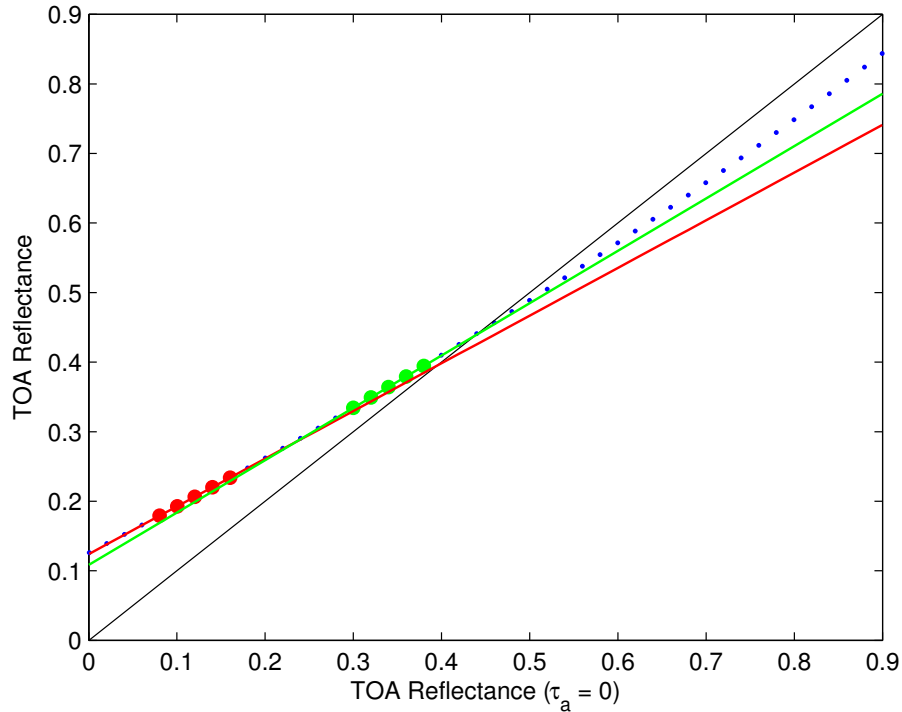


Figure 4.9: TOA reflectance data for AOD = 1.0 versus TOA reflectance for AOD = 0 for the coarse model ( $k = 0.0015$ ) at  $1.243 \mu\text{m}$  (blue points). A linear fit to data over a dark surface (red points, red line) and over a brighter surface (green points, green line) is shown.

#### 4.1.4 Background Aerosol and Gases are Similar between the Polluted and Clean Day

Our retrieval method includes the correction of the reflectance data for gaseous absorption by water vapor and ozone using ancillary data (see Chapter 2 for full description), but it is possible that this correction is incomplete. The stronger variability of path radiance in the near-IR channels could be indicative of this, but there is little other evidence to suggest that incomplete gas absorption is affecting the retrieved SSA in these channels. At Tamanrasset, there does appear to be a negative trend in the visible SSA with the AERONET column water vapor concentration (Figure 4.10, upper). This trend is

only apparent in the blue and green channels, however, which are not corrected for water vapor absorption. There may be a slight AERONET SSA trend at Tamanrasset (Figure 4.10, lower), but it is not nearly as apparent. The observed trend in the MODIS results could thus be a retrieval artifact, or it could be due to an increase in aerosol size. If dust particles are taking up water at Tamanrasset, the increase in size beyond that represented by our coarse aerosol model could mean that the modeled  $R_{crit}$ -SSA curve is too steep to represent the aerosol being observed. As a result, the retrieved SSA would be lower than the “true” SSA of the particles in the scene.

A larger source of uncertainty that affects the SSA results at both sites is the impact of different background aerosol composition (and aerosol mixtures) between the polluted and clean days. We will discuss the impact of background aerosol at Tamanrasset here; a case study examining the effect of aerosol mixtures at Banizoumbou is contained in Section 4.2.2. The comparison of +16 and -16 day retrievals at Tamanrasset (see Chapter 3) suggests that the cleaner days at the site are sometimes dominated by smaller particles (as indicated by AERONET Angstrom exponent) that result in brighter SSAs, particularly in the blue channel. This could be due to absorbing background aerosol from an anthropogenic source in the region. To investigate the sensitivity of the coarse model critical reflectance to clean-day aerosol composition, we perform two tests in SBDART: one with dust in the polluted day and a primarily-scattering fine aerosol ( $k = 0.0005$  at all wavelengths) in the clean day, and another with dust in the polluted day and a more absorbing fine aerosol ( $k = 0.03$ , corresponding to a  $0.466 \mu\text{m}$  SSA  $\sim 0.8$ ). For each test we calculated the critical reflectance that would be observed for a clean day AOD of 0.05 and 0.2, and a polluted AOD of 0.6.

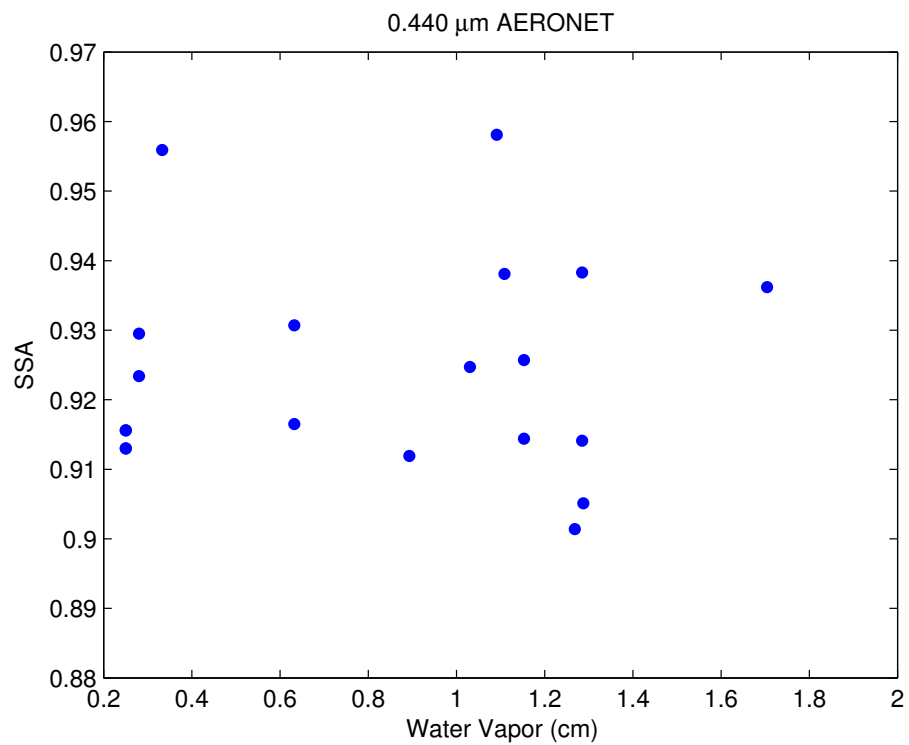
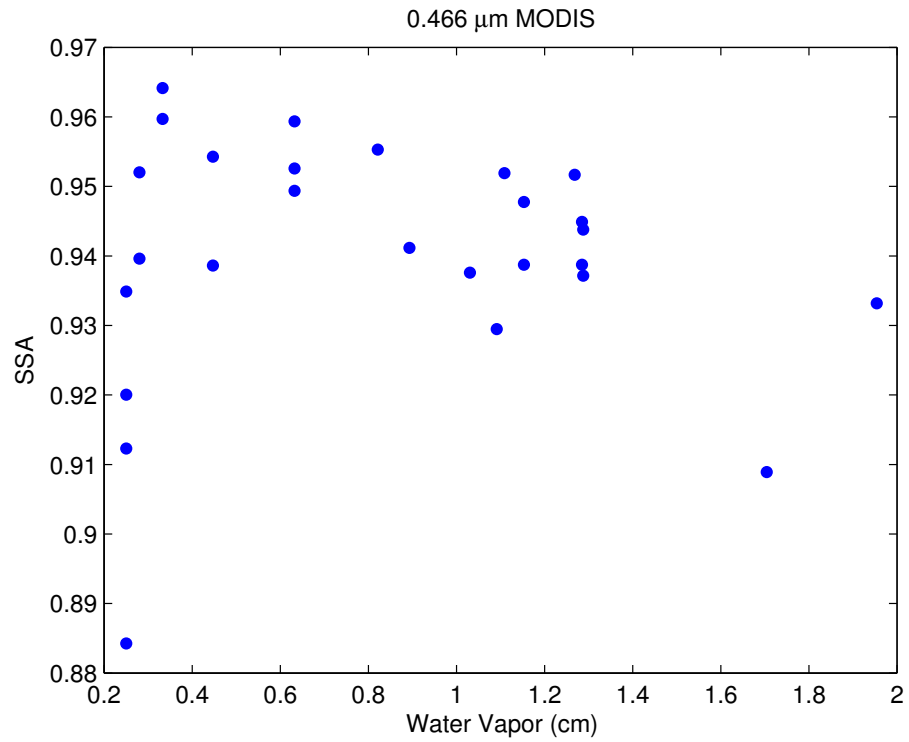


Figure 4.10: SSA at Tamanrasset as a function of AERONET column water vapor at 0.466  $\mu\text{m}$  for MODIS critical reflectance results (upper) and AERONET results (lower).

Example results of the test are shown for  $\text{SZA} = 36^\circ$  in Figure 4.11 for the scattering background aerosol, and Figure 4.12 for the more absorbing background aerosol. Because the sensitivity to background aerosol at Tamanrasset is most apparent at  $0.466 \mu\text{m}$ , we will limit our discussion to the results at this channel. We find very little change in the critical reflectance between the coarse LUT (see Appendix A) and the coarse LUT calculated with the scattering fine background aerosol at either simulated AOD. With the more absorbing background aerosol, however, we find an increased sensitivity of critical reflectance to changes in SSA (steeper  $R_{\text{crit}}$ -SSA relationship) that is more pronounced at higher SSAs and smaller view angles. This sensitivity increases when the clean day AOD is higher.

This behavior is consistent with the SSA observations at Tamanrasset. In the presence of an absorbing background aerosol on the clean day, the measured critical reflectance would be higher than on a day in which only coarse aerosol was present on both the clean and polluted days. The use of our original coarse model LUT to retrieve SSA will thus result in a brighter SSA than the “true” SSA of the aerosol in the scene. At Tamanrasset, we find that this can lead to uncertainties in our retrieved SSA on the order of 0.03. If we compare the lower left panels (clean day AOD = 0.2 and relative azimuth =  $120^\circ$ ) in Figure 4.11 and Figure 4.12 for a view angle =  $0^\circ$ , we find a similar magnitude of uncertainty. For a measured critical reflectance of 0.03, the coarse LUT with only scattering fine mode background aerosol results in a  $0.466 \mu\text{m}$  of  $\sim 0.98$ , whereas the LUT with a more absorbing fine mode background aerosol results in a SSA value closer to 0.95.

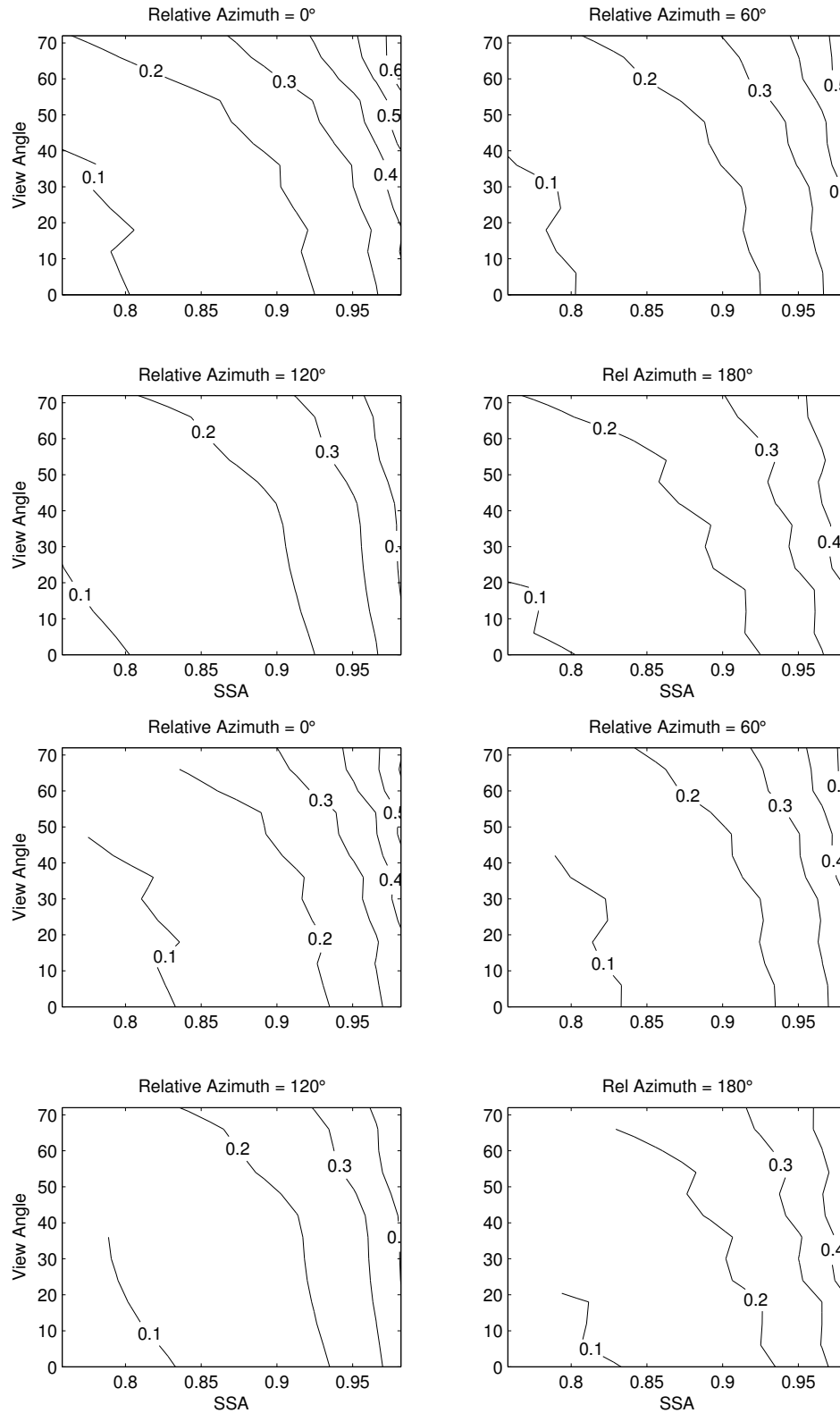


Figure 4.11: Critical reflectance LUT for the coarse aerosol model with scattering fine mode aerosol ( $k = 0.005$ ) on the clean day at  $0.466 \mu\text{m}$  for  $\text{SZA} = 36^\circ$ , displayed as a function of satellite view angle and SSA for relative azimuth =  $0^\circ$  (upper left),  $60^\circ$  (upper right),  $120^\circ$  (lower left), and  $180^\circ$  (lower right). Upper panel is for a  $0.466 \mu\text{m}$  clean day AOD of 0.05 and lower panel is for a clean day AOD of 0.2.

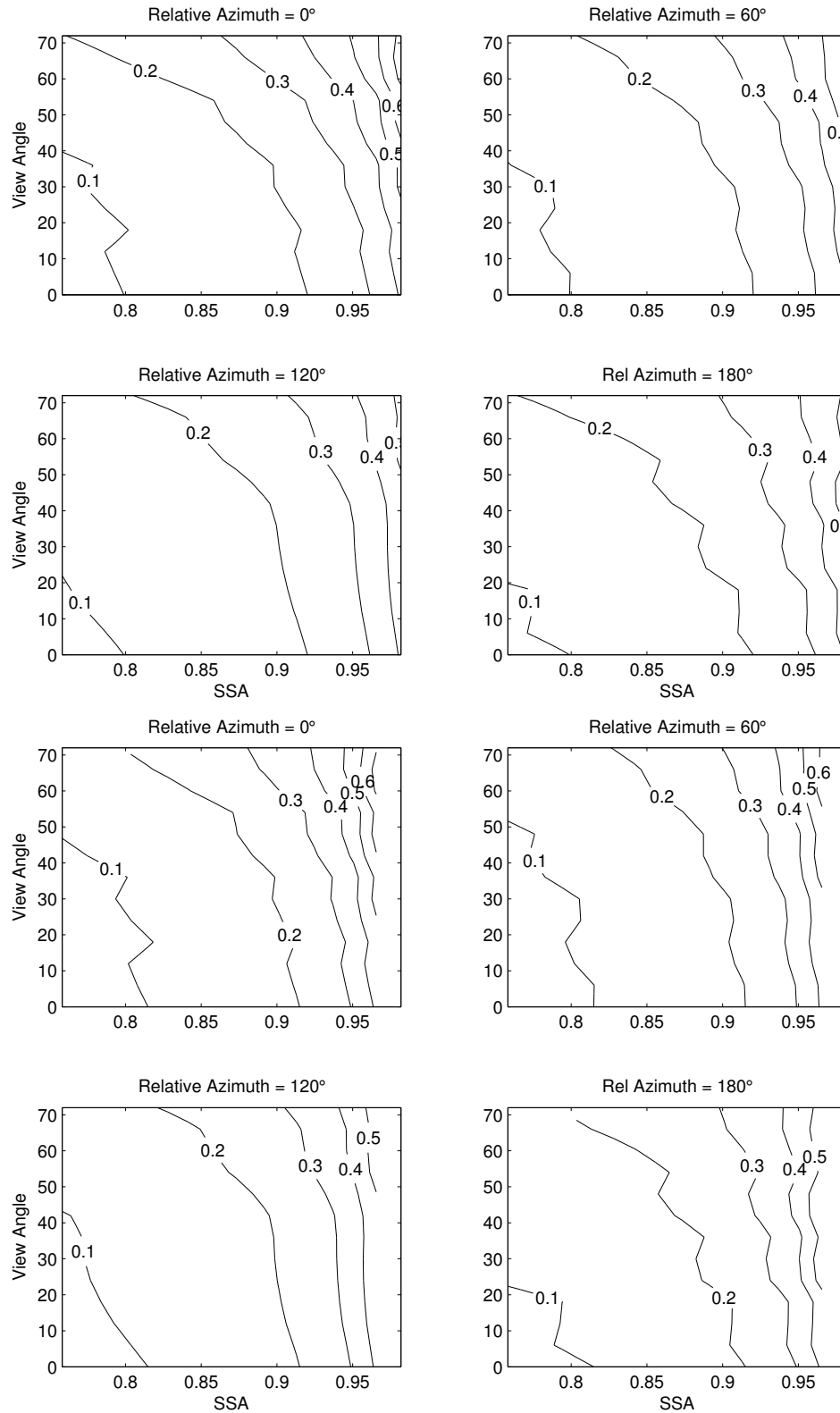


Figure 4.12: Critical reflectance LUT for the coarse aerosol model with absorbing fine aerosol ( $k = 0.03$ ) on the clean day at  $0.466 \mu\text{m}$  for  $\text{SZA} = 36^\circ$ , displayed as a function of satellite view angle and SSA for relative azimuth =  $0^\circ$  (upper left),  $60^\circ$  (upper right),  $120^\circ$  (lower left), and  $180^\circ$  (lower right). Upper panel is for a  $0.466 \mu\text{m}$  clean day AOD of 0.05 and lower panel is for a clean day AOD of 0.2.

## 4.2 Forward Model Uncertainties

While the uncertainties in the observations lead to uncertainties in the critical reflectance derivation, the forward model uncertainties lead to errors in the conversion of critical reflectance to SSA. The effects of major assumptions about particle properties and the atmospheric profile of aerosol and gases will be discussed in more detail here.

### 4.2.1 Assumed Particle Properties

#### 4.2.1.1 *Size*

The sensitivity of the critical reflectance to changes in aerosol absorption generally increases as particle size decreases and, for SSA values above 0.8, the critical reflectance magnitude is higher for smaller particles at a given SSA (see Chapter 2). Thus, an overestimation of the aerosol size can consequently lead to an overestimation in SSA (and vice versa) and will also affect the retrieval of the spectral dependence of the SSA. To investigate the dependence of the agreement of our retrieval results with AERONET on the particle size, we compare the AERONET retrieved size distributions to our model distribution for each retrieval case. Results for Tamanrasset are shown in Figure 4.13, and results for Banizoumbou are shown in Figure 4.14 and Figure 4.15 for the bimodal and coarse model, respectively. Each size distribution is normalized to the total particle volume retrieved for that case. Cases where the MODIS SSA exceeds the AERONET SSA by more than 0.03 are shaded in red, cases where the AERONET SSA exceeds the MODIS SSA by more than 0.03 are shaded in blue, and cases where the two estimates agree within 0.03 are shaded in green. Data for both 0.466 and 0.855  $\mu\text{m}$  are shown.

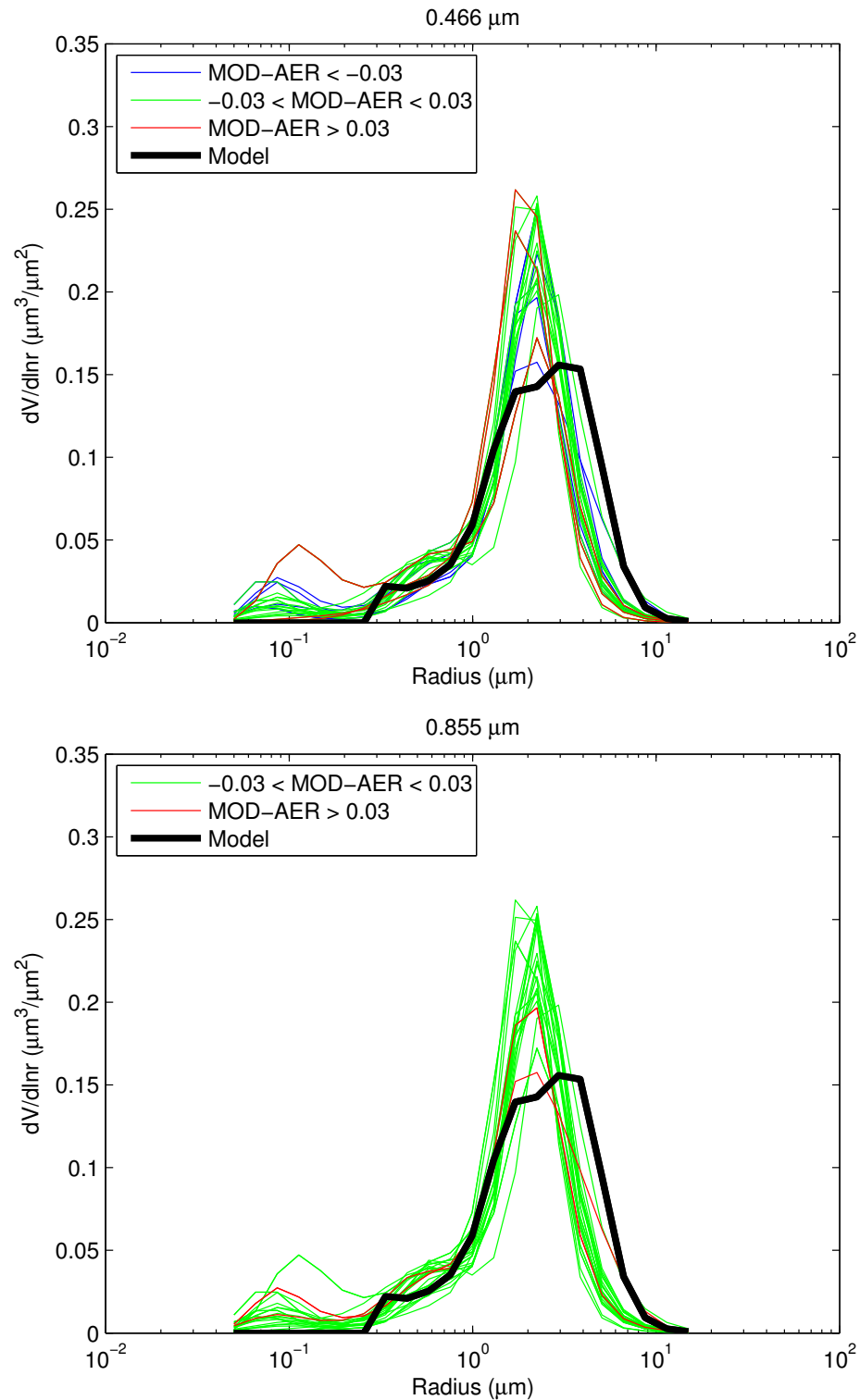


Figure 4.13: AERONET Version 2 retrievals of the particle size distribution for the 27 cases at Tamanrasset at 0.466 (upper) and 0.855  $\mu\text{m}$  (lower), colored based on the difference between the MODIS critical reflectance and AERONET retrieved SSA for that case. All distributions have been normalized by the total particle volume for that case.

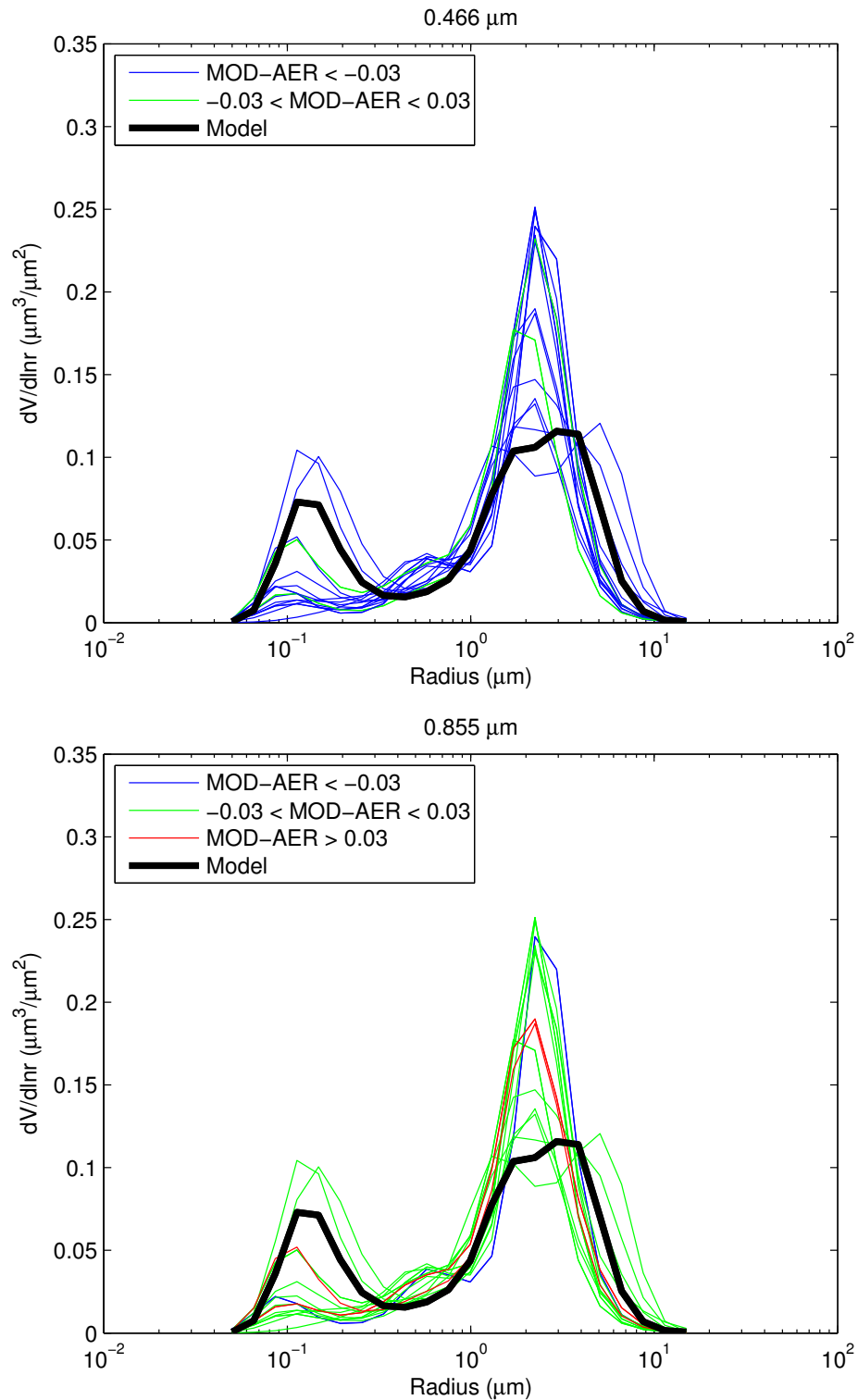


Figure 4.14: AERONET Version 2 retrievals of the particle size distribution for the 15 cases at Banizoumbou at 0.466 (upper) and 0.855  $\mu\text{m}$  (lower), colored based on the difference between the MODIS critical reflectance (bimodal spheroid model) and AERONET retrieved SSA for that case. All distributions have been normalized by the total particle volume for that case.

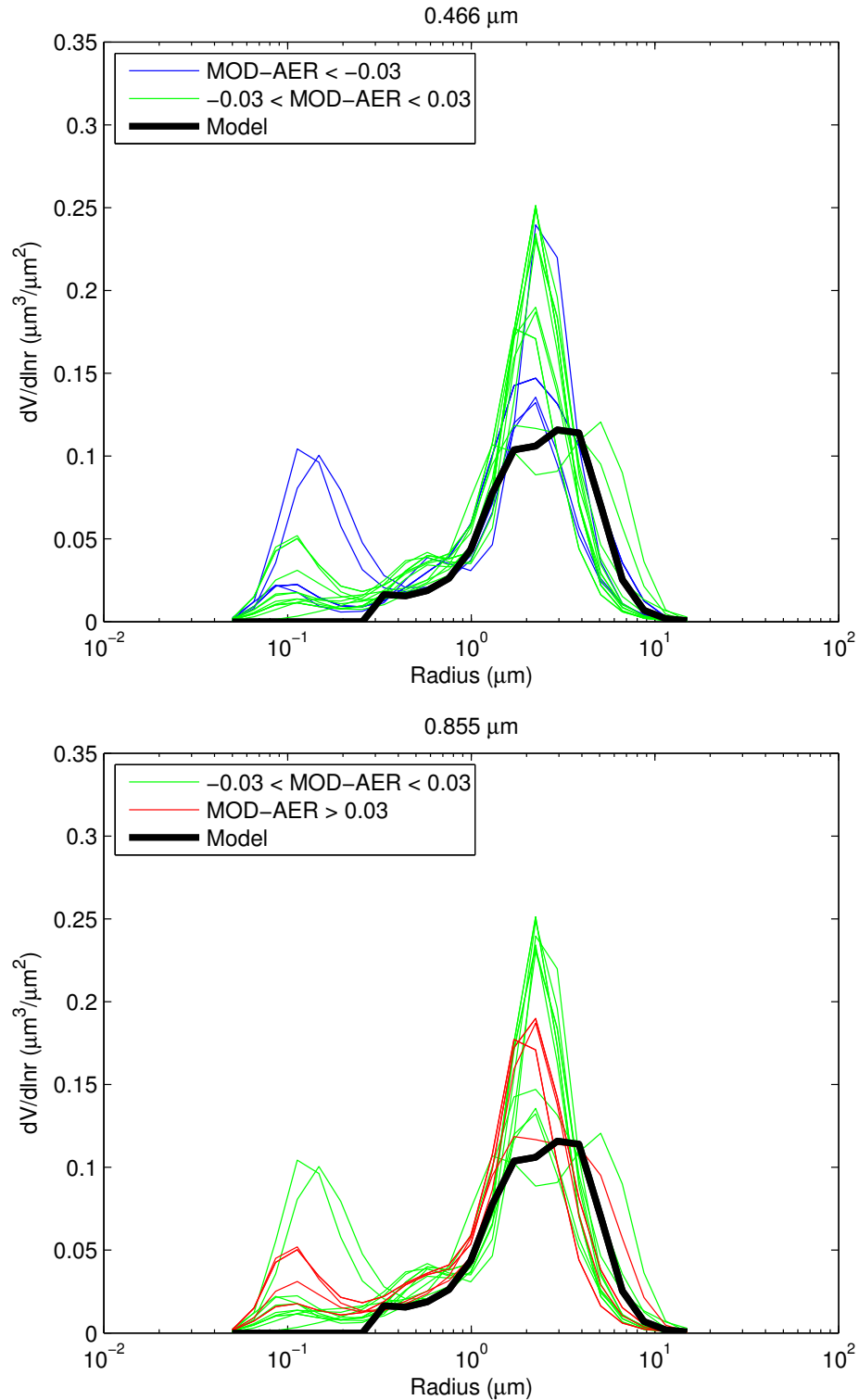


Figure 4.15: AERONET Version 2 retrievals of the particle size distribution for the 15 cases at Banizoumbou at 0.466 (upper) and 0.855  $\mu\text{m}$  (lower), colored based on the difference between the MODIS critical reflectance (coarse model) and AERONET retrieved SSA for that case. All distributions have been normalized by the total particle volume for that case.

At Tamanrasset, the median radius of the retrieved coarse modes is smaller and more sharply peaked than our coarse model median radius for all 27 cases, which could partially explain why the critical reflectance SSAs are generally less absorbing than the AERONET SSAs retrieved at this site. Of the three cases in which the AERONET SSA is greater than MODIS by at least 0.03 at 0.466  $\mu\text{m}$ , two have median coarse mode radii that are on the smaller range, and one has a more significant fine mode contribution than the rest of the cases, but these differences are quite small. There are also a few cases in which the MODIS SSA exceeds the AERONET SSA by more than 0.03 that have a more significant fine mode, so it does not seem likely that the presence of more fine particles is driving the differences between the two retrievals. At 0.855  $\mu\text{m}$  there are only two cases in which the MODIS SSA exceeds the AERONET SSA by more than 0.03, neither of which has the smallest median size according to AERONET. Many of the AERONET retrieved size distributions have a small intermediate size mode that is not represented by our aerosol model. A previous study ascribes this mode to the presence of stratospheric aerosol (Remer and Kaufman, 1998), but it is unclear what this mode may represent in more recent years over North Africa, or why it is necessary in order to reproduce measured sky radiances.

At Banizoumbou, the impact of our assumptions about aerosol size is a bit clearer, although size differences do not explain the MODIS-AERONET SSA differences in full. When a bimodal size distribution is assumed for all cases at Banizoumbou, the critical reflectance-determined MODIS estimates are generally much more absorbing than AERONET in the blue channel. The size distributions indicate that most of the cases are more coarse-dominated than the bimodal model, which could explain the higher SSAs in

the blue channel; however, the AERONET SSA also exceeds the MODIS SSA for the two cases with the largest retrieved fine mode. The use of the coarse mode model improves agreement between the two datasets for most of the coarse-dominated cases, but, it still results in more absorbing 0.466  $\mu\text{m}$  SSAs than AERONET for the two cases with the most volume in the fine mode. For these cases, assumptions about size are clearly not the most important contribution to the SSA uncertainty. At 0.855  $\mu\text{m}$ , the coarse model results in an overestimation of SSA (relative to AERONET) for some of the cases with a more significant fine mode fraction, but not for the two cases with the largest fine mode fraction.

The analysis of the effect of size on the retrieval results at Banizoumbou serves to highlight the complicated nature of capturing the optical properties of aerosol mixtures with critical reflectance. While pure dust exhibits a positive spectral dependence of SSA, biomass burning aerosol tends to result in a negative spectral dependence of absorption (e.g. Eck et al., 2001). Dust-biomass burning mixtures in the Sahelian region tend to have a very moderate spectral dependence of SSA compared to their individual counterparts. Such behavior was observed by Derimian et al. (2008) in Senegal during the AMMA campaign. The individual AERONET SSA retrievals and their corresponding size distribution retrievals (normalized by the total aerosol volume in each distribution) are shown in Figure 4.16. The cases for which AERONET retrieves a bimodal distribution at Banizoumbou also correspond to the retrievals with a flatter spectral dependence of SSA. The cases with the largest fine mode contribution have the flattest spectral dependence of SSA, but the retrieved SSAs are not necessarily more absorbing than the other coarse-dominated cases. The 0.44  $\mu\text{m}$  SSA ranges from 0.87 to 0.96 for the bimodal mixture

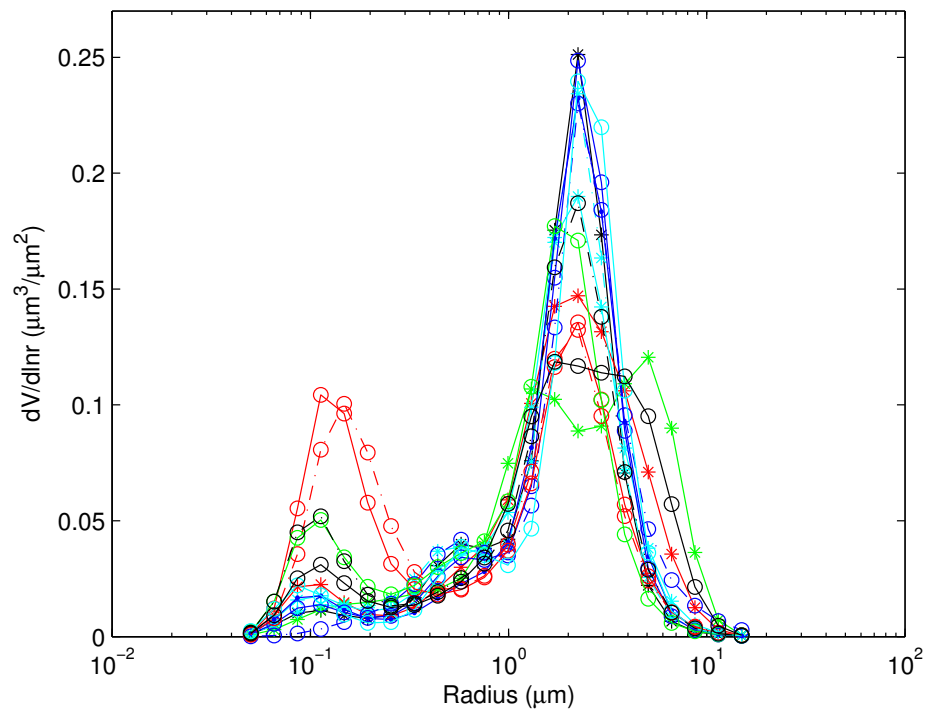
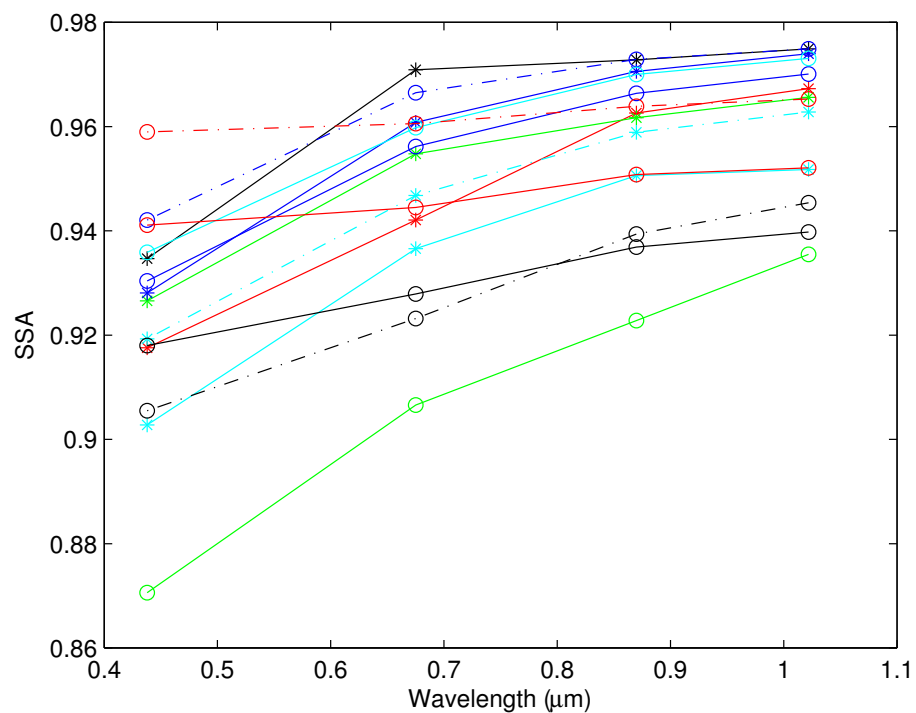


Figure 4.16: Version 2 spectral SSA (upper) and corresponding size distribution (lower) retrieved at the Banizoumbou AERONET station for the 15 cases used in this study. Days with both Terra and Aqua have Terra data in solid lines and Aqua data in dashed lines.

cases, all less absorbing values than the 0.8 to 0.84 measured in dust-biomass burning mixtures by Derimian et al (2008). This could indicate that the retrieval cases at Banizoumbou are more dust-dominated than those observed by Derimian et al (2008), as many of our cases are from the months preceding the period of maximum biomass burning during the Sahel dry season.

#### ***4.2.1.2 Refractive Index and Sphericity***

While we assume a fixed real part of the refractive index for our aerosol models, the refractive index will vary based on the aerosol composition. We assume a real refractive index of 1.53 at all wavelengths for our aerosol models. The LUT results reveal that the sensitivity to assumed real refractive index (in the range of 1.43 to 1.63) is mainly confined to the backscattering direction, and thus does not represent a significant source of uncertainty for the retrieved SSA at other viewing/solar geometries. Real refractive indices throughout our tested range are retrieved from AERONET, however, and there is no systematic relationship between the AERONET retrieved real refractive index and the level of agreement between AERONET and MODIS SSA at either site. Although the refractive index is not an independently-retrieved piece of information in the AERONET algorithm (Dubovik et al., 2002), it could possibly indicate actual changes in the particle composition that are not captured in our model assumptions. One behavior we observe in the AERONET SSA is a relationship between retrieved real refractive index and particle sphericity; we find that the retrieved real refractive index decreases as the percent sphericity of the particle population increases. This correlation may simply arise due to assumptions in the AERONET retrieval, but it is consistent with

the behavior that would be observed if water uptake were occurring on the particles. This process is not one that is accounted for in our forward model assumptions.

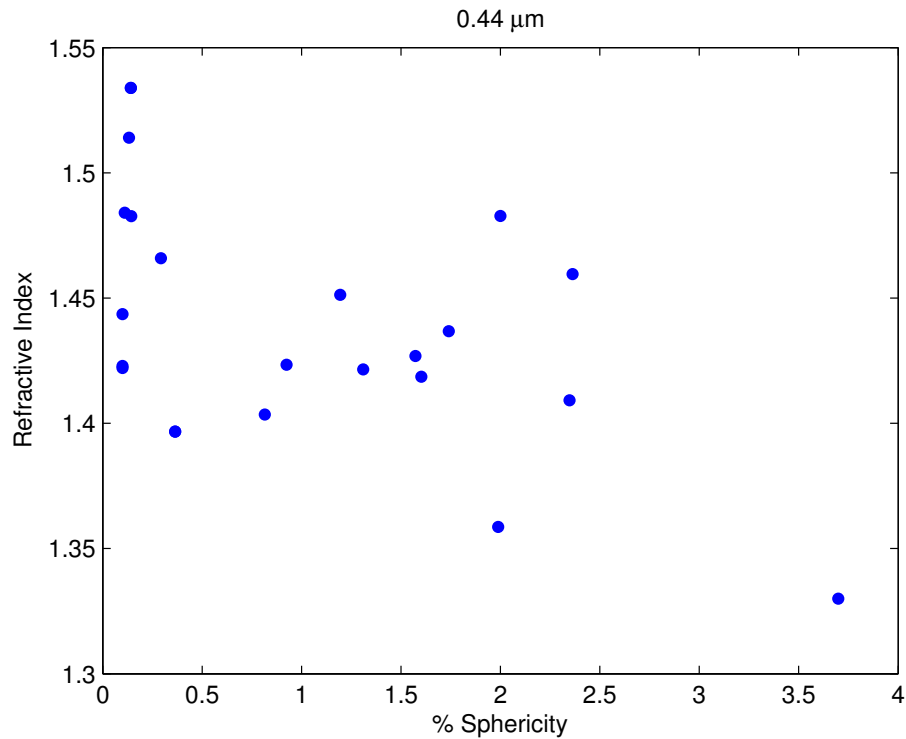


Figure 4.17: The real part of the refractive index at  $0.44 \mu\text{m}$  retrieved from AERONET as a function of the retrieved percent sphericity for the 27 cases at Tamanrasset.

Figure 4.17 also indicates that the AERONET retrieved real refractive index is lower than our assumed value for nearly all of the 27 retrieval cases at Tamanrasset. To test whether the AERONET retrieved particle size and refractive index constitute a more appropriate aerosol model at Tamanrasset than our coarse model, we build an aerosol model using the average size distribution and refractive index of all cases at Tamanrasset in which the SZA exceeds  $45^\circ$  and the AOD at  $0.44 \mu\text{m}$  exceeds 0.4. The average size distribution for Tamanrasset cases is shown in Figure 4.18, with our coarse aerosol model size distribution for comparison. The average real part of the refractive index retrieved by AERONET is 1.44, which we ascribe to all seven MODIS channels. After building a full LUT based on this model and conducting all 27 retrievals at Tamanrasset with it, we find

that the results are quite insensitive to the change in refractive index and size. The differences between the SSA retrieved using the new and original aerosol models are shown in Figure 4.19. The AERONET-based model results in slightly higher (less-absorbing) SSAs than the original coarse mode model at Tamanrasset (particularly in the blue channel) which slightly worsens the agreement between the critical reflectance and AERONET SSAs at the site. These differences are all less than 0.01, however, which is generally less than the inversion uncertainty for the SSA. Since the average size distribution at Tamanrasset turns out to be quite similar to the coarse model size distribution, the results mainly demonstrate the insensitivity of the SSA to the real refractive index, which is consistent with our sensitivity study findings in Chapter 2.

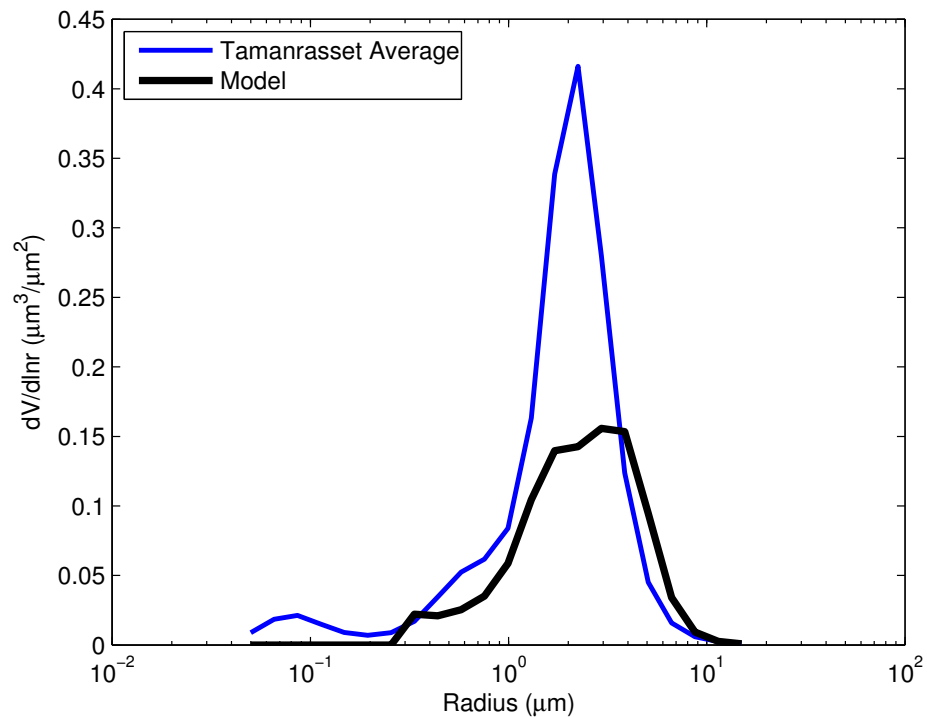


Figure 4.18: Average aerosol size distribution retrieved at Tamanrasset for all cases with SZA > 45° and AOD > 0.4 at 0.466 μm, compared to the coarse mode aerosol model.

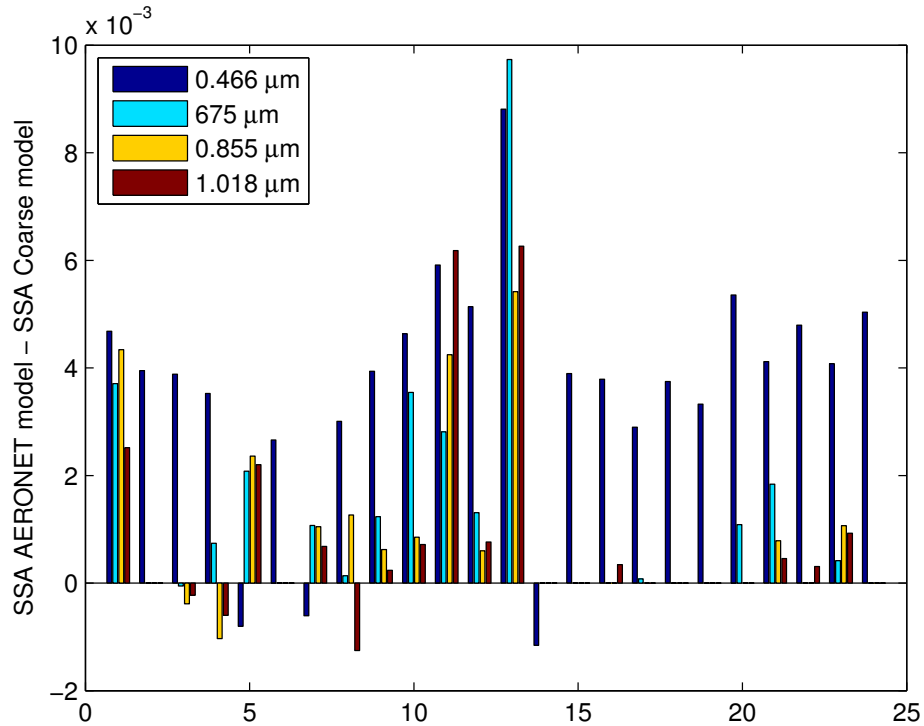


Figure 4.19: Spectral difference between SSA retrieved using the AERONET-based aerosol model at Tamanrasset and the original coarse mode model.

#### 4.2.1.3 *Aerosol Properties are Independent of AOD*

The assumption of an aerosol size model that is independent of AOD is another source of uncertainty in our forward model. A fixed size model may not be representative of dust, as other studies have shown SSA to have an AOD dependence that is indicative of the presence of larger particles at higher dust loadings (e.g Kaufman et al., 2001). An analysis of the entire time series of SSA from the Tamanrasset AERONET site indicates a dependence of SSA on size is present at the site, and also a tendency for higher-AOD conditions to be dominated by larger aerosol particles. Figure 4.20 shows the relationship between SSA and 0.441  $\mu\text{m}$  AOD at all four AERONET channels at Tamanrasset. The data are restricted to retrievals with  $\text{SZA} > 45^\circ$  and the symbols are shaded by their corresponding 0.44-0.87  $\mu\text{m}$  Angstrom exponent value. For the largest particles (lowest

Angstrom exponents), the retrieved SSA is always near 0.9 at 0.441  $\mu\text{m}$ , 0.97 at 0.65  $\mu\text{m}$ , and 0.98-0.99 at 0.87 and 1.018  $\mu\text{m}$ . The SSA asymptotes to these values at AODs greater than 1.0. Also, Angstrom exponents  $> 0.25$  do not occur at 0.44  $\mu\text{m}$  AODs greater than  $\sim 0.6$ , indicating a dominance of larger particles at higher AOD conditions.

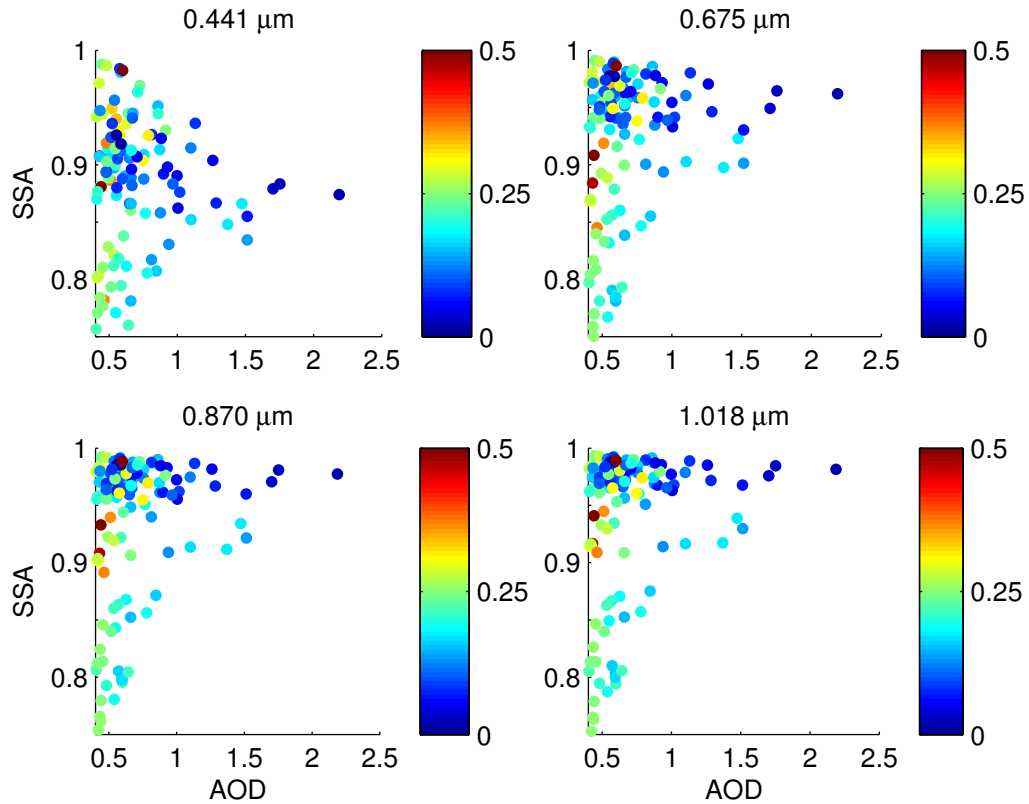


Figure 4.20: SSA versus 0.44  $\mu\text{m}$  AOD, shaded by 0.44-0.87  $\mu\text{m}$  Angstrom exponent from AERONET retrievals at Tamanrasset from 2006-2008.

Results presented in Section 4.1.2 indicate a tendency for the critical reflectance retrieval to produce more variable SSA values at lower AODs near Tamanrasset, which is consistent with the general tendency of the AERONET retrieval results shown in Figure 4.20. Although there is more signal noise at lower aerosol loadings, our results could also be an indication that smaller particles are present at lower AODs. We also find possible evidence for the existence of smaller particles at lower AODs in cases where the MODIS critical reflectance exceeds the maximum value in the coarse model LUT. The difference

between the MODIS 2.119  $\mu\text{m}$  critical reflectance and the maximum critical reflectance value in the LUT, expressed as the percentage of the MODIS critical reflectance, is compared to AERONET AOD in Figure 4.21. We find a general decrease in the difference with increasing AOD, which indicates that the modeled Rcrit-SSA slope may not be steep enough to represent the particles that are present at lower AODs. Because the critical reflectance-SSA slope is steeper for smaller particles, the observed behavior indicates that the contribution of smaller particles to the total dust aerosol is likely larger at these lower AODs, and our coarse model is not representative of the aerosol in these cases.

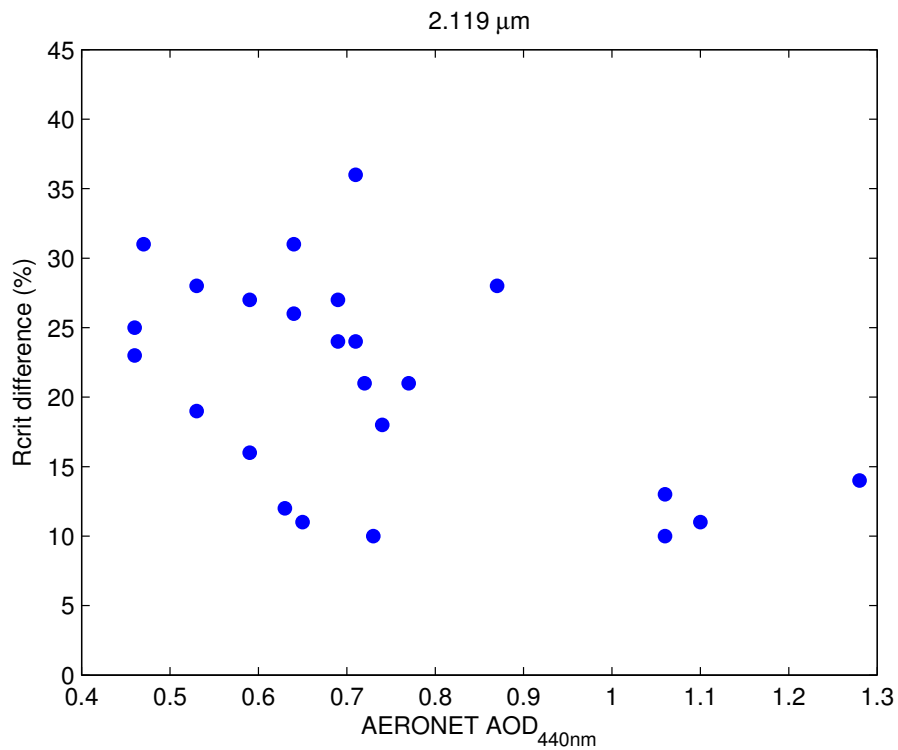


Figure 4.21: Difference between the observed MODIS critical reflectance and the maximum critical reflectance in the LUT at 2.119  $\mu\text{m}$  for the albedo range fitting method. Values are displayed as a percentage of the observed values.

The AERONET data at Banizoumbou (Figure 4.22) also reveal relationships between SSA and AOD that are a function of aerosol size, although there are two modes

of aerosol influence at this site. Many of the higher AOD cases are dominated by coarse particles that have high SSA values (near 1.0 from 0.675 to 1.020  $\mu\text{m}$ ), but there is a secondary impact by smaller, more absorbing particles on high aerosol loading days. The SSAs of dust and biomass burning dominated samples are distinct, but there is a transition zone between the two modes with intermediate SSA and Angstrom exponent values that indicates a mixture of the two particle types. The AERONET data also suggest the dust may be less absorbing at Banizoumbou than the dust at Tamanrasset, which could indicate a difference in mean size or in dust mineralogy between the two sites. Variability in the relative contributions of dust and biomass burning is the main contributing factor to the retrieved SSA uncertainty at Banizoumbou, which will be further addressed in the following section.

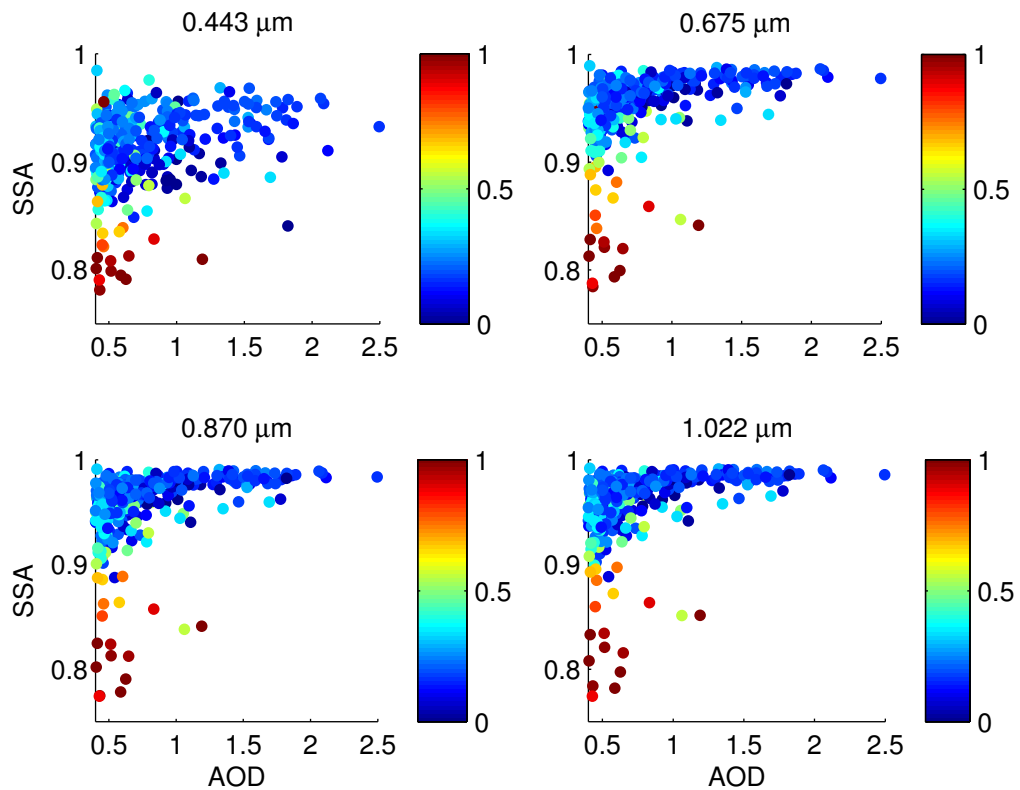


Figure 4.22: SSA versus 0.44  $\mu\text{m}$  AOD, shaded by 0.44-0.87  $\mu\text{m}$  Angstrom exponent from AERONET retrievals at Banizoumbou from 2006-2008.

#### 4.2.2 Aerosol Mixtures and Vertical Stratification: 19 January 2006 Case Study

Since many of our retrieval cases at Banizoumbou are from November-December, it is not surprising that a few of the cases exhibit evidence of a mixture of biomass burning and dust aerosol. In situ and ground-based measurements have shown that the vertical profile of aerosol in the Sahel during this season can be dominated by dust in the boundary layer, with biomass burning aerosol lofted above. We perform a retrieval corresponding to the 19 January 2006 flight from the DABEX campaign, which encountered elevated aerosol concentrations near Banizoumbou. A detailed analysis of the campaign data for this day can be found in Johnson et al. (2009). Data for -16 and +16 days were available for this case, although neither day met our “clean” day criterion of  $0.44 \mu\text{m AOD} < 0.2$  set forth for our case studies. SSA results for the comparison to both days are shown in Figure 4.23. The bimodal spheroid aerosol model was assumed for both retrievals.

The results for the -16 day comparison exhibit a stronger spectral dependence in the visible than from 0.855 to 1.022  $\mu\text{m}$ , whereas the +16 day comparison SSA increases strongly through this entire spectral range. The SSA results for the +16 day comparison are more absorbing than the -16 day estimates, indicating that the background aerosol may be different between the two cleaner days. Both estimates agree reasonably well with the SSA value at 0.55  $\mu\text{m}$  retrieved from the flight profile ( $0.877 \pm 0.04$ , Ben Johnson, personal communication). The +16 day comparison yields good agreement with AERONET in the visible, although it does not exhibit the flat/slightly negative spectral dependence retrieved by AERONET in the longer-wavelength channels. This could be

due to a combination of different background aerosol and an incorrect representation of the vertical profile of aerosol in our model.

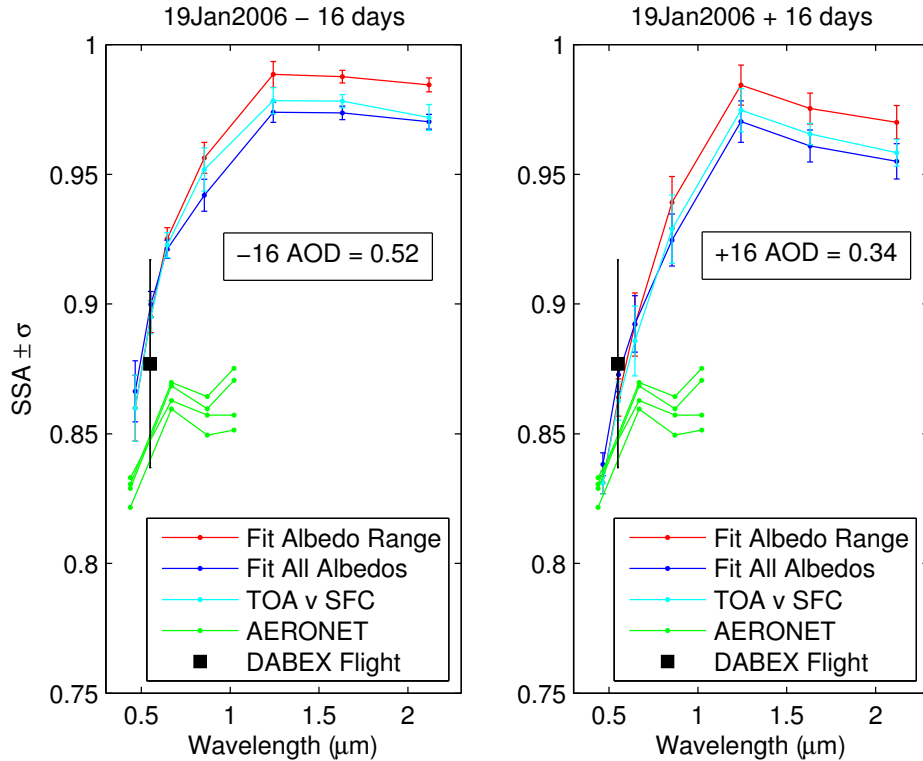


Figure 4.23: Spectral plots of SSA plus AERONET retrievals for 19 January 2006 950 UTC, compared to -16 days (left) and +16 days (right) at the Banizoumbou site using the bimodal spheroid model. The black data point corresponds to the 0.55  $\mu\text{m}$  SSA estimated from the in situ flight profiles.

Aircraft measurements from 19 January 2006 near Banizoumbou show that the particle volume is dominated by coarse aerosol below 1 km, with a mixture of coarse and fine aerosol from 1 – 4 km above (see Chapter 1 Figure 1.10, Johnson et al., 2008a). The retrieved size distribution from AERONET for this day is consistent with these measurements, indicating a bimodal aerosol with a large coarse mode contribution. The fact that the retrieved SSAs for this day look more absorbing when compared to the image from +16 days (4 February) suggests the aerosol on the latter day may be more coarse-dominated than the aerosol on -16 days (3 January). The retrieved size distributions from AERONET for both days (Figure 4.24) confirm this behavior.

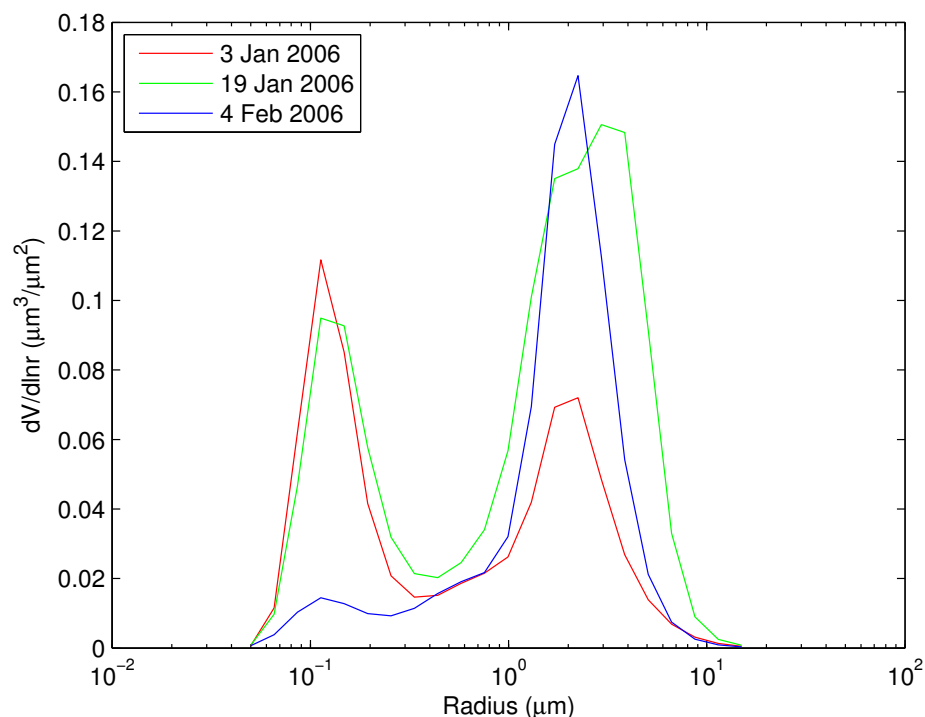


Figure 4.24: AERONET size distributions retrieved at Banizoumbou on 3 January 2006, 19 January 2006, and 4 February 2006.

In order to see how *a priori* knowledge of the vertical distribution of aerosol mixtures on the polluted day (and of the aerosol size and AOD on the clean day) affects the retrieval, we use the ancillary data from DABEX and AERONET to model the 19 January case. AERONET AOD indicates that 4 February was cleaner than 3 January, so we focus our attention on the +16 day comparison as it is more representative of the conditions of our standard retrieval framework. To model the clean day, we assume the AOD to be that measured by AERONET (interpolated to the MODIS wavelengths) and assume purely dust aerosol that is confined to a 1 km-deep boundary layer. Because we are retrieving the optical properties of the aerosol on the polluted day, we must assume the optical properties of the aerosol on the clean day. We set the SSA for the dust to the average SSA retrieved at Tamanrasset (see Chapter 3, Figure 3.10) using critical reflectance. On the polluted day, we assume dust in the 1 km –deep boundary layer, with

the same optical properties as we assume for the cleaner day. Above the dust we ascribe a second aerosol layer from 1 to 4 km in height. We perform one simulation in which this layer contains bimodal aerosol, and another in which it contains only fine mode aerosol. The fractional aerosol optical depths assumed for each layer are shown in Figure 4.25.

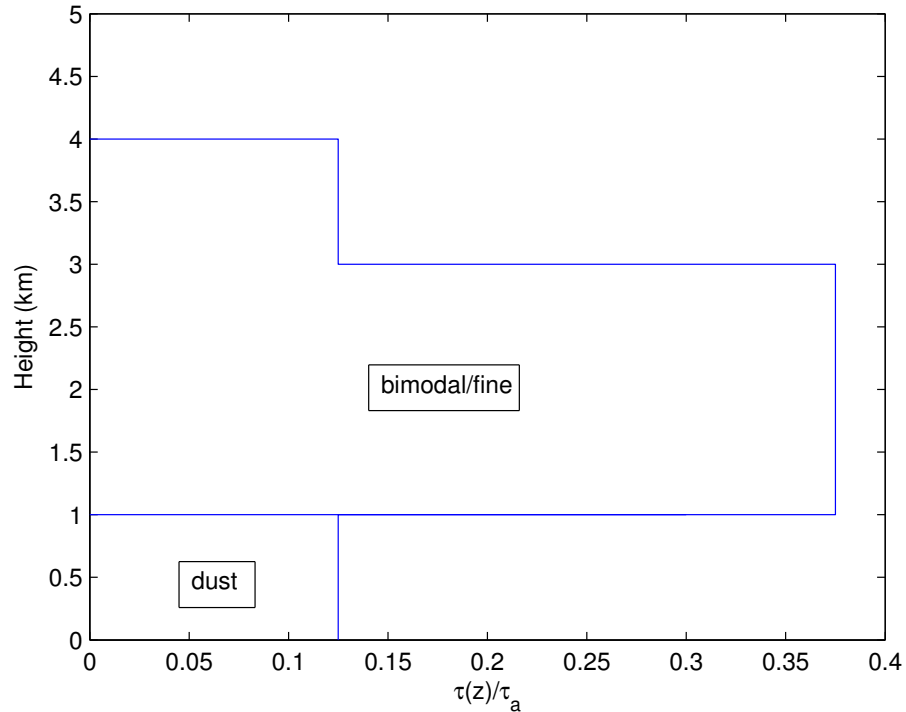


Figure 4.25: Vertical profile of fractional aerosol optical depth and aerosol type assumed for the polluted day of the 19 January 2006 case at Banizoumbou.

The retrieved SSAs assuming both the bimodal and fine aerosol lofted above the dust (compared to the dust-dominated cleaner day) are shown in Figure 4.26. We average the retrieved upper layer SSAs with the assumed lower layer dust SSAs, weighted by their fractional AOD contributions, to get the columnar SSA. The assumption of a bimodal aerosol lofted over the dust increases the SSAs slightly relative to the assumption of bimodal aerosol throughout the column (with bimodal aerosol assumed on the clean day), particularly in the visible channels. The assumption of fine aerosol lofted over the dust leads to a reduction in the retrieved SSAs in the near-IR and also reduces

the spectral dependence somewhat in the visible (although a solution could not be found at 0.466  $\mu\text{m}$ ), but not to the degree that the AERONET data exhibit past 0.675  $\mu\text{m}$ . The new bimodal retrieval is similar in shape and magnitude to the standard retrieval for the -16 day comparison, indicating that perhaps the original retrieval on this -16 day comparison was a better measure of the aerosol SSA. Even though the AOD was higher on the day 16 days prior to the polluted day, AERONET retrieved size distributions (Figure 4.24) indicate that the aerosol on this day may have been more similar to the aerosol on the polluted day.

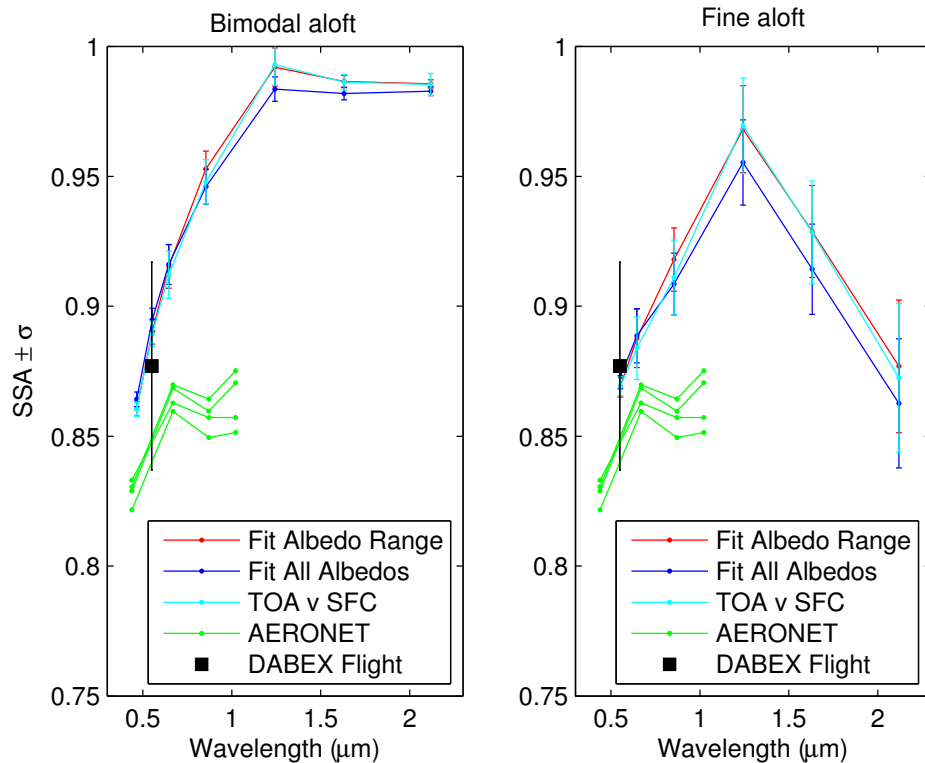


Figure 4.26: Spectral plots of total columnar SSA plus AERONET retrievals for 19 January 2006 950 UTC, for bimodal aerosol aloft (left) and fine aerosol aloft (right) compared to a dust-dominated clean day at the Banizoumbou site. The black data point corresponds to the 0.55  $\mu\text{m}$  SSA estimated from the in situ flight profiles.

## 4.3 Aerosol Forcing Estimation

### 4.3.1 Tamanrasset

To obtain an independent measure of aerosol absorption to compare to our estimates at Tamanrasset, as well as to gain some insight on the role of absorption in aerosol forcing near the site, we use ES-4 data from the CERES (Clouds and Earth's Radiant Energy System) instrument (<http://eosweb.larc.nasa.gov>). Like MODIS, CERES is also mounted on both the Terra and Aqua satellites. ES-4 data contain daily-average global shortwave TOA flux and albedo estimates for clear-sky and all-sky conditions on a 2.5° grid. We compare the CERES TOA clear-sky SW albedo to the 0.44 μm AERONET measured AOD at Tamanrasset for the years 2006-2008. Results are shown in Figure 4.27, binned by column water vapor concentration. Aerosol events clearly act to reduce the TOA albedo in nearly all cases near Tamanrasset, indicating that absorption is dominating the TOA aerosol effect. Higher average AODs at the site also seem to correspond to higher water vapor concentrations, which provides more possible evidence for the uptake of water on particles at Tamanrasset.

A key question is the following: can the average spectral absorption that we retrieve using critical reflectance from MODIS explain the sign and magnitude of the TOA albedo at Tamanrasset as a function of AOD? To test this, we input the average spectral SSA results determined from critical reflectance for the 27 cases at Tamanrasset into SBDART. The average spectral values are listed in Table 4.1. We use our standard coarse mode model to represent the aerosol size.

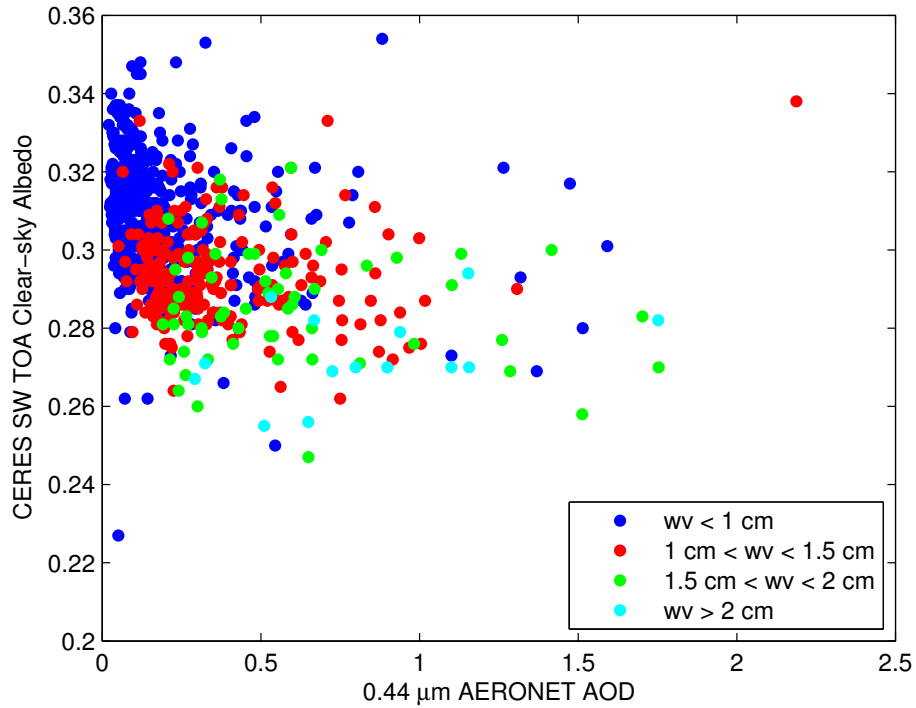


Figure 4.27: 2006-2008 CERES ES-4 shortwave clear-sky albedo near Tamanrasset compared to AERONET AOD at  $0.44 \mu\text{m}$ .

Table 4.1: Average critical reflectance-retrieved SSA for the 27 cases at Tamanrasset.

Wavelength ( $\mu\text{m}$ )	Average Rcrit SSA
0.466	0.940
0.553	0.972
0.646	0.985
0.855	0.987
1.243	0.989
1.632	0.992
2.119	0.990

For each simulation, we vary the  $0.466 \mu\text{m}$  AOD from 0 to 2.4 in increments of 0.2, assuming an Angstrom exponent at all wavelength ranges of 0.16 (the average  $0.44\text{-}0.87 \mu\text{m}$  Angstrom at Tamanrasset from AERONET data) to estimate the spectral AOD. We perform one simulation each for a high and low albedo scenario at Tamanrasset, using the MODIS spectral surface albedo from the days when the broadband MODIS surface albedo was at a minimum and a maximum for 2006-2008 at Tamanrasset, respectively. The spectral surface albedo values used are listed in Table 4.2. We also

simulate four different column water vapor amounts: 0.75 cm, 1.25 cm, 1.75 cm, and 2.25 cm.

Table 4.2: Spectral surface albedo corresponding to the minimum and maximum broadband surface albedo at Tamanrasset from 2006-2008.

Wavelength ( $\mu\text{m}$ )	Min SFC Albedo	Max SFC Albedo
0.466	0.165	0.160
0.553	0.270	0.269
0.646	0.380	0.390
0.855	0.455	0.458
1.243	0.524	0.562
1.632	0.587	0.622
2.119	0.544	0.569

The resulting SBDART TOA albedos are shown as a function of AOD for the critical reflectance-determined spectral SSA, overlaid on top of the CERES observations (Figure 4.27). The results indicate a decline in TOA albedo that is driven by AOD, whereas the water vapor concentration affects the albedo magnitude. The TOA albedo curves for the darker surface are only offset by about 0.01 from the curves for the brighter surface, as the variability of surface albedo at Tamanrasset is quite small. The curves seem to capture the general trend of TOA albedo with AOD, but they overestimate the vast majority of the CERES TOA albedo values in each corresponding water vapor bin. There is a lot of scatter in the CERES data, which could be driven by a number of factors. The AOD may vary across the  $2.5^\circ \times 2.5^\circ$  CERES pixel, as could the concentrations of absorbing gases, or the clearing of clouds within the grid may also be incomplete. The Tamanrasset data also suggest that the aerosol on cleaner days is sometimes dominated by fine mode particles that are more absorbing than the dust; many of the points at lower AOD in Figure 4.27 could result from the impact of these particles.

Despite the aforementioned caveats, we conclude that the average retrieved spectral SSA at Tamanrasset is likely an underestimate of the average spectral absorption

of the dust that impacts the site. However, this result does not tell us how the retrieval is doing on a case-by-case basis. Since we are most interested in the use of critical reflectance for real-time monitoring of aerosol absorption changes over North Africa, rather than large scale or long-term averages of SSA, we turn to modeling individual cases at Tamanrasset.

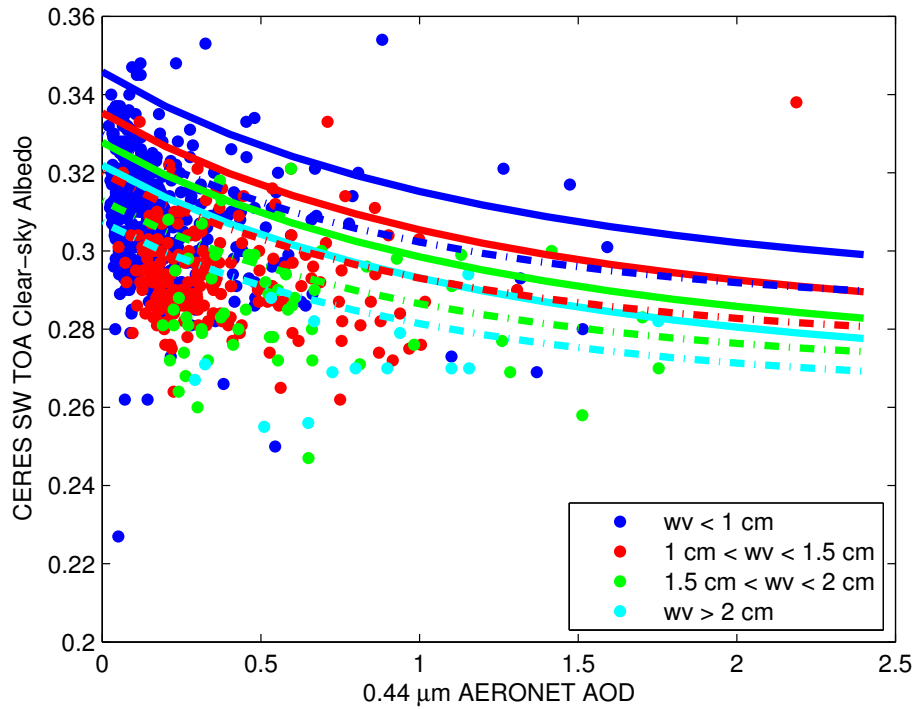


Figure 4.28: SBDART simulated TOA albedos for the average critical reflectance-derived SSA at Tamanrasset, overlaid on the clear-sky TOA albedo values from CERES.

To simulate individual cases at Tamanrasset, we choose the five days with the lowest all-sky AERONET retrieval error at the site. We use SBDART to simulate the TOA albedo on these days, for both the retrieved spectral SSA from critical reflectance and from AERONET. We interpolate the AERONET SSAs to the MODIS wavelengths, assuming that the SSA is constant in the near-IR and equal to the retrieved value at 1.018  $\mu\text{m}$ . For each date we input the spectral MODIS surface albedo for the corresponding 16 day period, the daily average water vapor and 0.44  $\mu\text{m}$  AOD retrieved by AERONET,

and the O<sub>3</sub> concentration from the corresponding TOAST dataset. We use the daily average AERONET 0.44 – 0.87 μm Angstrom exponent to interpolate the 0.44 μm AOD to the seven MODIS wavelengths for each case. We also simulate each case for AOD = 0 in order to estimate the TOA forcing that the aerosol exerts. The dates, MODIS broadband surface albedos, AODs, Angstrom exponents, water vapor, and O<sub>3</sub> concentrations for the cases are listed in Table 4.3.

Table 4.3: Dates, 16-day MODIS broadband SW surface albedo, daily 0.44 μm AOD, 0.44-0.87 μm Angstrom exponent, daily water vapor concentration, and daily average O<sub>3</sub> concentration for the simulated cases at Tamanrasset.

Date	SW Albedo	0.44 μm AOD	0.44-0.87 μm Angstrom	Water vapor (cm)	O <sub>3</sub> (DU)
22 Feb 2007	0.378	0.671	0.107	0.28	280.0
23 July 2007	0.363	1.286	0.076	1.95	282.9
6 Jan 2008	0.377	0.675	0.145	0.63	294.4
14 Apr 2008	0.370	0.659	0.447	0.24	290.7
30 Sep 2008	0.375	0.861	0.203	1.15	310.2

The results for the five simulated cases are displayed in Figure 4.29. The 6 January 2008 case has estimates for both a -16 day comparison and a +16 day comparison; they are displayed as 6Jan08 1 and 6Jan08 2, respectively. Results for all three fitting methods for critical reflectance are shown, along with the simulated result for AERONET, the measured clear-sky albedo value from CERES, and the simulated TOA albedo for AOD = 0. All of the cases indicate darkening of the TOA albedo relative to the AOD = 0 conditions, but the magnitude of this darkening varies between the MODIS and AERONET results. Results using the MODIS critical reflectance-derived SSAs follow the same pattern as the CERES data, but they all indicate a brighter TOA albedo than CERES. This difference tends to be slightly larger for the albedo range fitting method than for the other two fitting methods. Thus, like the average SSA results at the site, all the retrieved spectral SSA values for these cases may represent an underestimation of the

spectral absorption of the dust. Furthermore, the agreement between the simulated and measured TOA albedo values seems to be driven by the absorption values in the visible channels, indicating that the characterization of absorption at these spectral bands is most important for estimating SW aerosol forcing. For the 6 Jan 2008 estimate, the +16 day was cleaner than the -16 day ( $0.44 \mu\text{m}$  AOD of 0.08 versus 0.2), so the uncertainty in the retrieved SSA for the 6Jan08 2 case is reduced. The SSA values are a bit lower in the visible for this case (Figure 4.30), which results in slightly better agreement with the CERES data.

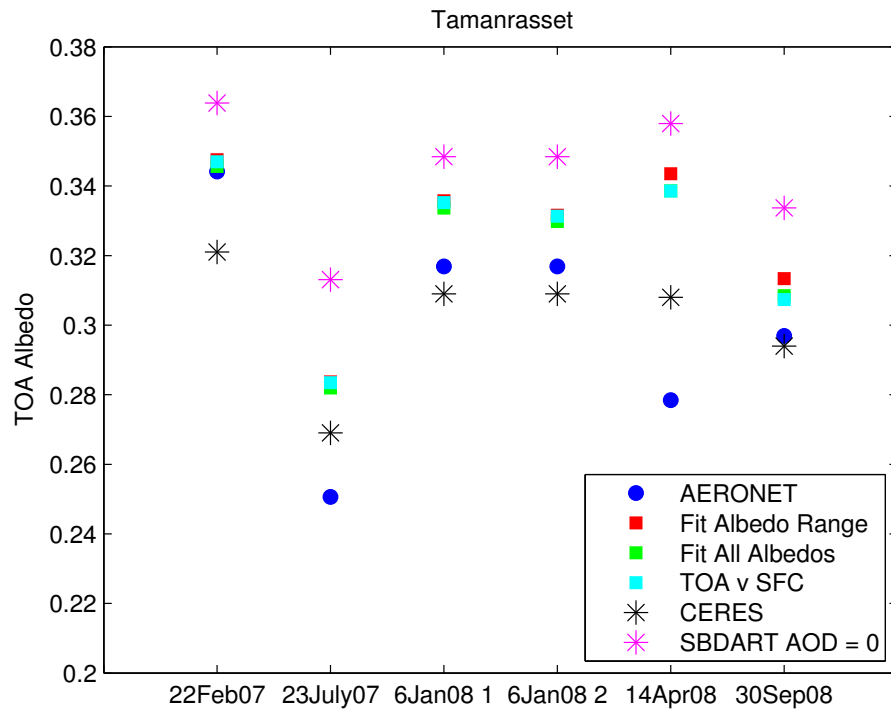


Figure 4.29: Simulated SW TOA albedo using AERONET retrieved SSA, critical reflectance-retrieved SSA (for all three fitting methods), measured TOA albedo from CERES, and SBDART simulated albedo for AOD = 0 at Tamanrasset.

The AERONET data, on the other hand, result in TOA values that are above or below the measured values depending on the case, and yields quite good agreement with CERES on 6 January 2008 and 30 September 2008. The spectral SSA retrieved on these two days (Figure 4.30) is very similar, and thus may be more representative of the “true”

spectral SSA for dust near Tamanrasset. AERONET retrieves less absorption on 22 February 2007, resulting in a TOA albedo that is very close to the critical reflectance value, but brighter than the CERES measurement. AERONET retrieves more absorption on 23 July 2007 and 14 April 2008, resulting in a darker albedo than that measured by CERES TOA albedo.

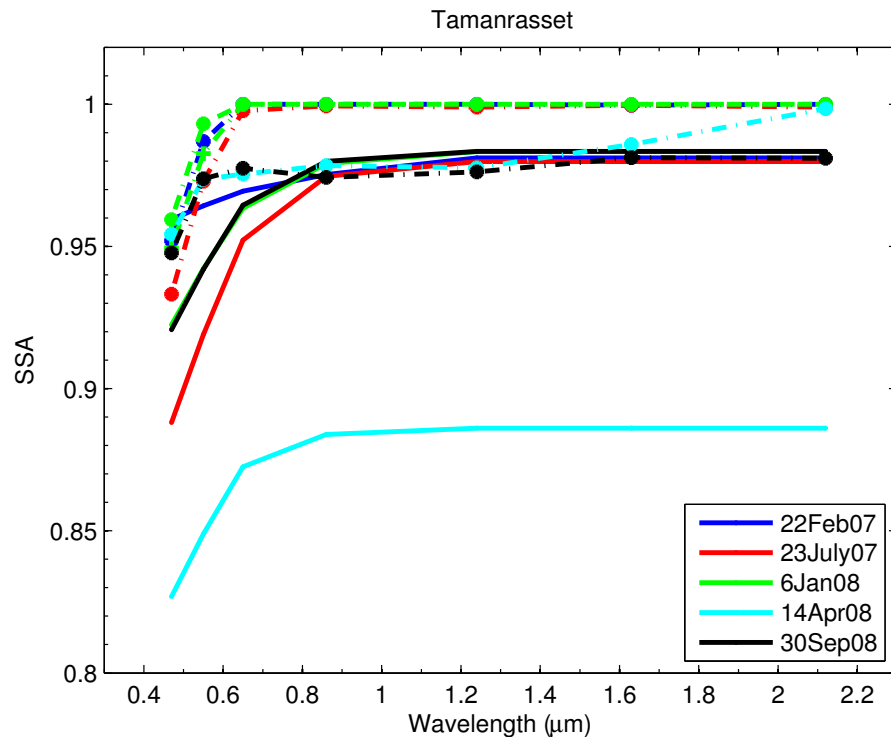


Figure 4.30: Spectral SSA retrieved for the five cases used in the TOA albedo simulation. The solid lines correspond to the AERONET retrieval and the dashed lines correspond to the MODIS critical reflectance retrieval (TOA v SFC method). The critical reflectance derivation for 6Jan08 1 is represented by the closed circles and the derivation for 6Jan08 2 is represented by the plus signs (+).

To see if the AERONET spectral SSA of dust retrieved at Tamanrasset on 30 September 2008 is a good measure of the spectral absorption of dust that typically impacts the site, we ascribe the retrieved spectral SSA from this day to the other four days in SBDART. The simulation results are shown in Figure 4.31, along with all other estimates. The 30 September 2008 AERONET retrieval results in improved agreement with CERES for all four cases, particularly on 22 February 2007 and 6 January 2008. The

AOD of the case on 23 July 2007 is higher than the others, so there may be larger particles present that result in somewhat more absorption on this day than the 30 September 2008 case.

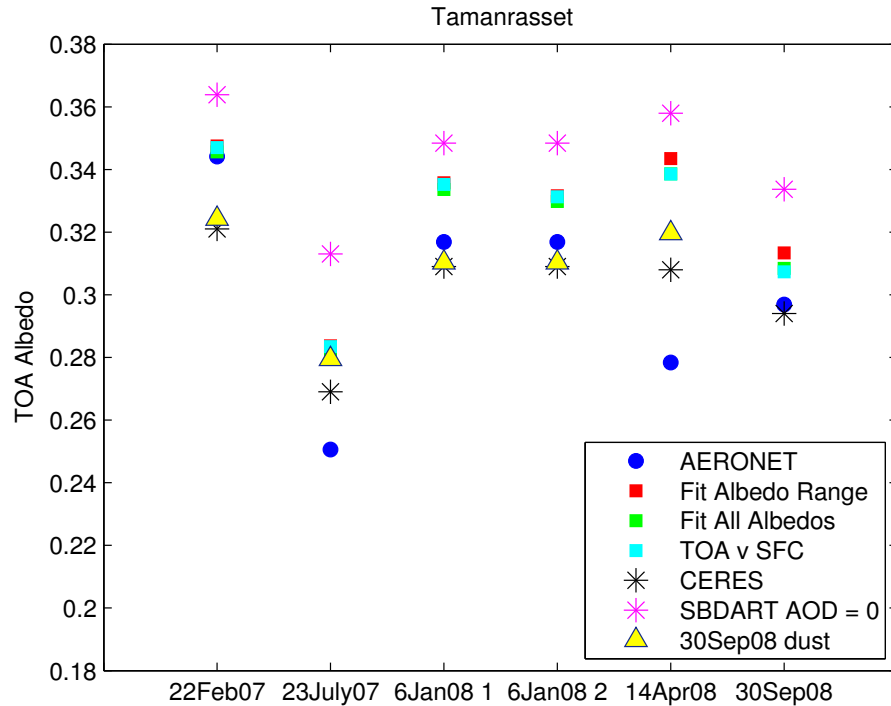


Figure 4.31: Simulated SW TOA albedo as shown in Figure 4.29, but with additional estimates assuming the 30 September 2008 AERONET spectral SSA for the other four cases.

To estimate what range of TOA forcing values correspond to the range of TOA albedo values simulated for the AERONET and MODIS critical reflectance SSAs, we take daily TOA incoming flux data from CERES and multiply these values by the difference between the simulated AOD = 0 albedo and the TOA albedos from AERONET, MODIS and CERES. The results correspond to a large range of TOA forcing estimates (Figure 4.32). The critical reflectance SSA results in TOA forcing values between 4 and 14  $\text{Wm}^{-2}$ , the AERONET SSA results in TOA forcing values that range from 7 to 35  $\text{Wm}^{-2}$ , and the CERES estimates fall in the 10 to 22  $\text{Wm}^{-2}$  range. For

each individual case the resulting variability in the TOA forcing is 8 to 15  $\text{W m}^{-2}$ , and nearly 30  $\text{W m}^{-2}$  for the 14 April 2008 case.

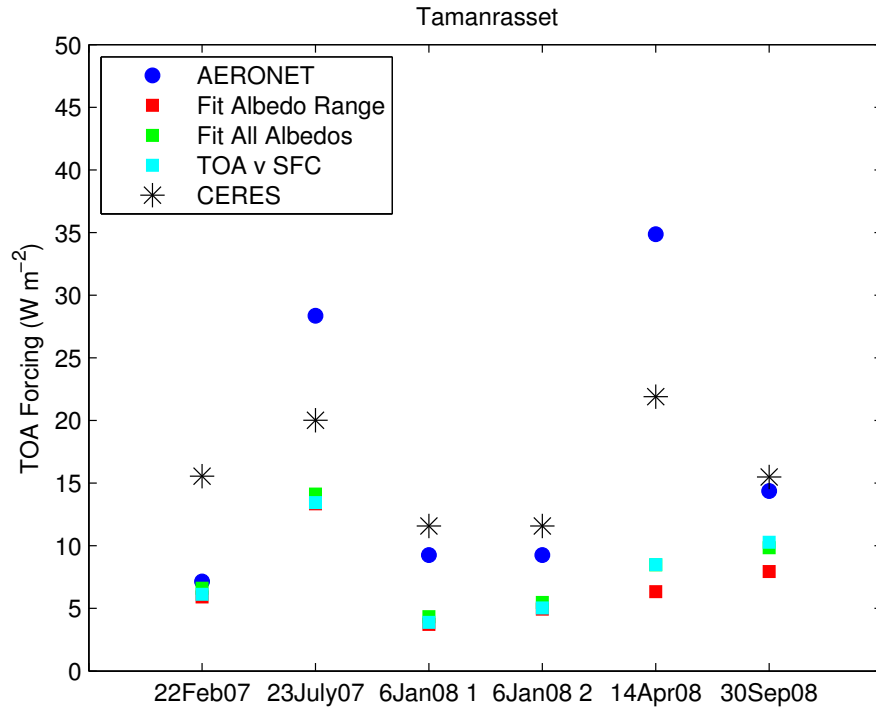


Figure 4.32: Simulated TOA forcing ( $\text{W m}^{-2}$ ) for the five Tamanrasset cases.

When the TOA forcing results are displayed as a function of AOD (Figure 4.33), the critical reflectance estimates exhibit a relatively linear, small increase of TOA forcing with AOD. If we disregard the retrieval from AERONET on 14 April 2008, which results in an anomalously-high TOA forcing at low AOD, the AERONET data indicate a more pronounced TOA forcing efficiency (forcing per unit AOD) than MODIS. The CERES data show more variability at lower AOD, but the slope of TOA forcing with AOD appears possibly more consistent with the MODIS critical reflectance results. Thus, the critical reflectance may be a reasonable measure of changes in the TOA aerosol effect, even if the relative magnitude may be too low.

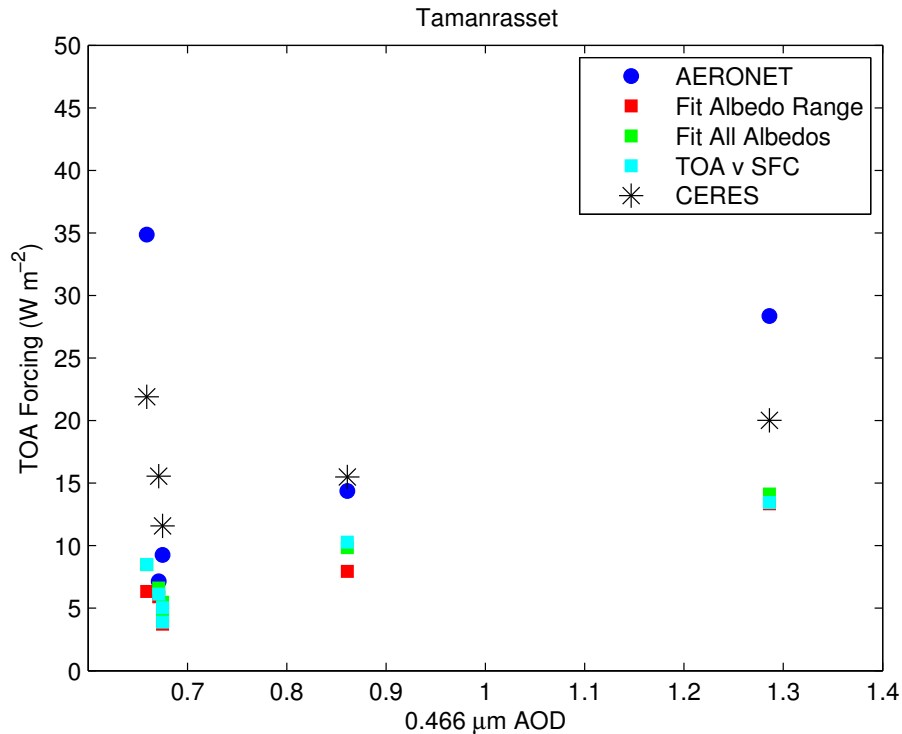


Figure 4.33: Simulated TOA forcing ( $\text{W m}^{-2}$ ) for the five Tamanrasset cases displayed as a function of  $0.466 \mu\text{m}$  AERONET AOD.

We must point out in this discussion that the comparison of point measurements, such as those from AERONET and small geographical averages from MODIS, to measurements with a larger footprint like CERES can be problematic due to the differences in spatial sampling between the two datasets. The CERES data represent a measurement over a larger area in which variations in surface reflectance, AOD, and gaseous concentrations are likely. The AERONET measured SSA, AOD, and water vapor concentration may not be representative of average conditions across the CERES footprint. Additionally, the CERES data may have uncertainty associated with instrument calibration and with the models used to convert the measured radiances to TOA flux. The use of SBDART for the broadband flux estimates introduces another source of uncertainty in the comparison. In their analysis of a major Saharan dust outbreak in March 2006, Slingo et al (2006) found that the use of SBDART to simulate the event

resulted in an underestimate of the measured forcing in the atmospheric column when they input absorption properties estimated from ground-based measurements.

#### 4.3.2 Banizoumbou

Our results from Banizoumbou coincide with a year-long period of radiation measurements taken close to the AERONET site in Niamey, Niger in 2006 as part of the African Monsoon Multidisciplinary Analysis (AMMA) campaign. This particular component of AMMA, known as RADAGAST (Radiative Atmospheric Divergence using Atmospheric Radiation Measurement Mobile facility, Geostationary Earth Radiation Budget data, and African Monsoon Multidisciplinary Analysis stations), involved measurements of surface downwelling and upwelling radiation using the suite of radiometers that make up the DOE Atmospheric Radiation Measurement (ARM, Ackerman and Stokes, 2003) mobile facility, and time-resolved measurements of TOA fluxes from the Geostationary Earth Radiation Budget (GERB, Sandford et al., 2003) instrument (Slingo et al., 2009). The addition of the surface flux data allows an estimation of the divergence of radiation in the column, which gives an estimate of the atmospheric forcing due to the aerosol absorption. Without the surface data we can only estimate the TOA aerosol forcing, which is proportional to the total aerosol extinction. The divergence of radiation in the atmospheric column is simply the difference between the radiation entering the atmospheric column and the radiation that is exiting it:

$$Div = (F_{TOA} \downarrow + F_{SFC} \uparrow) - (F_{TOA} \uparrow + F_{SFC} \downarrow) \quad (4.1)$$

where the first term represents the fluxes entering the atmospheric column (downwelling at TOA and upwelling at the surface) and the second term represents the radiation leaving the column (upward flux at TOA and downwelling flux at the surface).

An analysis of the entire dataset available from the RADAGAST campaign gives us an idea of the relationship between atmospheric column divergence and aerosol absorption that we might expect at Banizoumbou. We calculate the daily average fractional broadband SW divergence using the GERB TOA fluxes and the ARM surface fluxes for the entire campaign (2006), normalized by the daily incoming flux as reported in the GERB data. Because the column divergence is driven by the aerosol absorption (and not total extinction), we compare our calculations to AERONET daily average absorption aerosol optical depth (AAOD), calculated as  $AOD \cdot (1 - SSA)$ , rather than the total AOD. We confine the comparison to days on which the (GERB-indicated) daily average cloud fraction is less than 0.1. Results are shown in Figure 4.34, compared to  $0.44 \mu\text{m}$  AAOD and binned by column water vapor concentration retrieved from the ARM surface measurements. We find a linear increase in daily average column SW divergence with AERONET  $0.44 \mu\text{m}$  AAOD; the two datasets are especially well-correlated at  $0.44 \mu\text{m}$  AAOD values greater than 0.06, which correspond to higher total aerosol loadings. This could indicate that the contribution of absorption at  $0.44 \mu\text{m}$  to the broadband SW divergence is more variable at lower AAOD values, or it could simply confirm that the AERONET retrieval has better sensitivity to absorption at higher AOD.

Although the comparison in Figure 4.34 does not validate the individual magnitudes of the AERONET-retrieved SSA, we can conclude that the AERONET SSA retrieval is sensitive to aerosol absorption changes at Banizoumbou. The retrieved SSAs at the site capture the dynamic range of divergence values as indicated by the RADAGAST data, particularly at higher aerosol loadings where the retrieved AERONET SSAs have been shown to have smaller errors (Sinyuk et al., 2007). Thus, if the MODIS

critical reflectance is also a good measure of changes in aerosol absorption, we should expect a linear relationship when comparing our AAOD results with the RADAGAST observations.

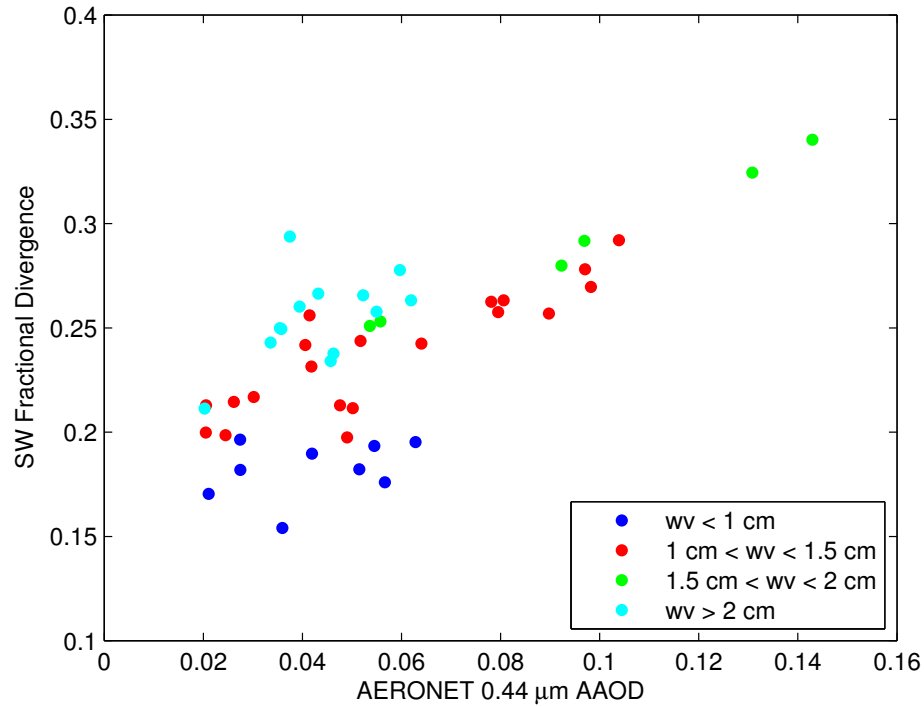


Figure 4.34: Daily SW fractional divergence for days with GERB cloud fraction < 0.1 compared to AERONET 0.44 μm AAOD.

Because nearly all of our retrieval cases at Banizoumbou occur on days in which there is some cloud cover near the site, the RADAGAST surface flux data often exhibit sharp changes over a short time interval due to the passing of clouds overhead (example shown in Figure 4.35). Because the GERB data have a larger footprint (~44 km at nadir) than the ground-based radiometer at the ARM site, the sharp reductions in downwelling surface flux do not correspond to sharp increases in the upwelling TOA flux in the GERB time series. Thus, the divergence calculated at these times is more a measure of the reduction in surface flux due to the cloud overpass, rather than the actual column divergence due to aerosol absorption. Therefore, we calculate the SW divergence from

GERB and ARM for the specific times corresponding to the MODIS overpass for each of our retrieval cases at Banizoumbou, and normalize these by the incoming flux as reported by GERB at that time.

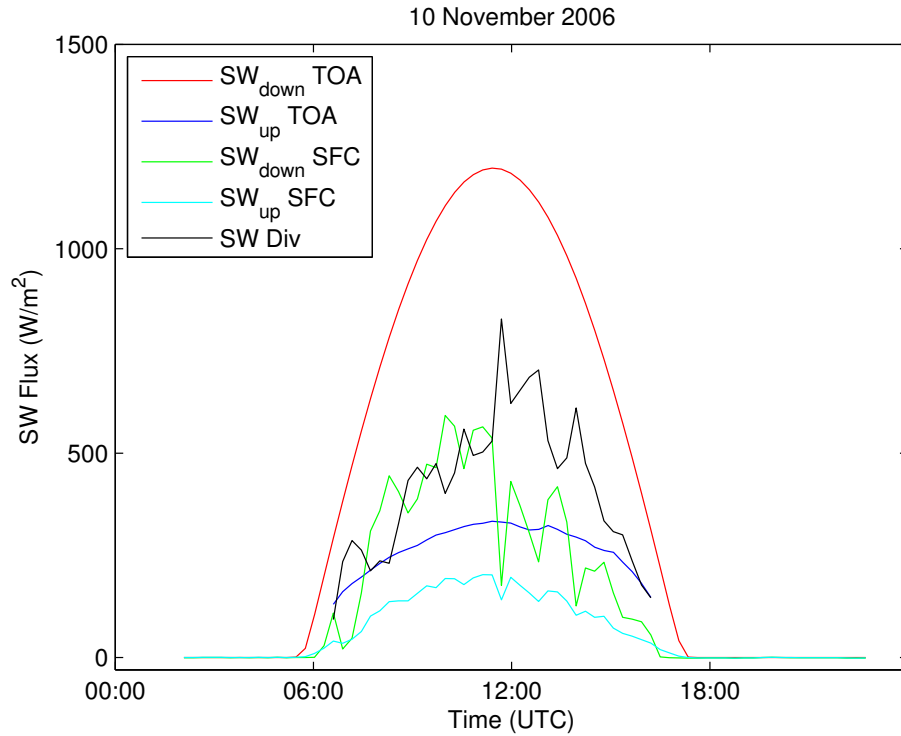


Figure 4.35: Timeline of SW fluxes measured at the surface and TOA, and SW divergence calculated from the measurements, at Niamey, Niger on 10 November 2008.

The divergences are compared in Figure 4.36 to the  $0.44 \mu\text{m}$  AAOD calculated using the MODIS critical reflectance SSA (left panel) and the AERONET SSA (right panel), binned by column water vapor. The estimates do not correlate well with the  $0.44 \mu\text{m}$  AAOD for either dataset. There are a number of points with high divergence values at the lower end of the AAOD range, which could be the result of cloud impacts at the surface, but it is likely due to solar zenith angle variability of the shortwave divergence. We find that the fractional divergence (column divergence normalized by incoming flux at TOA) estimates calculated from the ARM and GERB data have a solar zenith angle dependence, an example of which is shown in Figure 4.37 for a relatively cloud-free day.

Therefore, we cannot combine measurements at different times to investigate the overall goodness of fit between the MODIS or AERONET AAOD and the RADAGAST SW divergence measurements. We normalize the divergence data by the incoming solar zenith angle, and compare again to the MODIS and AERONET AAOD (Figure 4.38). The SZA variation may have accounted for some of the scatter in the data, but the existence of a linear relationship of AAOD with SW divergence is still hard to discern. It does appear that the AERONET data are a bit less scattered with AAOD than the critical reflectance-derived estimates from MODIS, but we may still have residual cloud effects, or we may simply have too few cases to clearly ascertain their level of agreement with the GERB-ARM measurements.

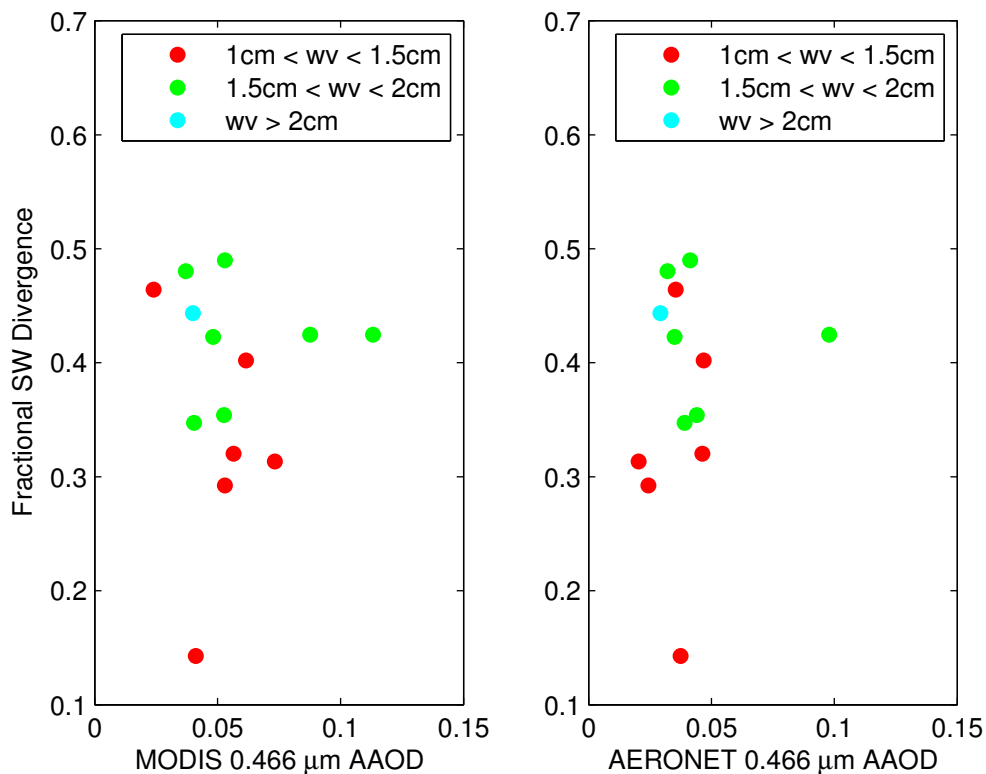


Figure 4.36: SW fractional divergence versus 0.44 μm AAOD for the 15 Banizoumbou cases using either the bimodal spheroid (left) or coarse (right) aerosol model.

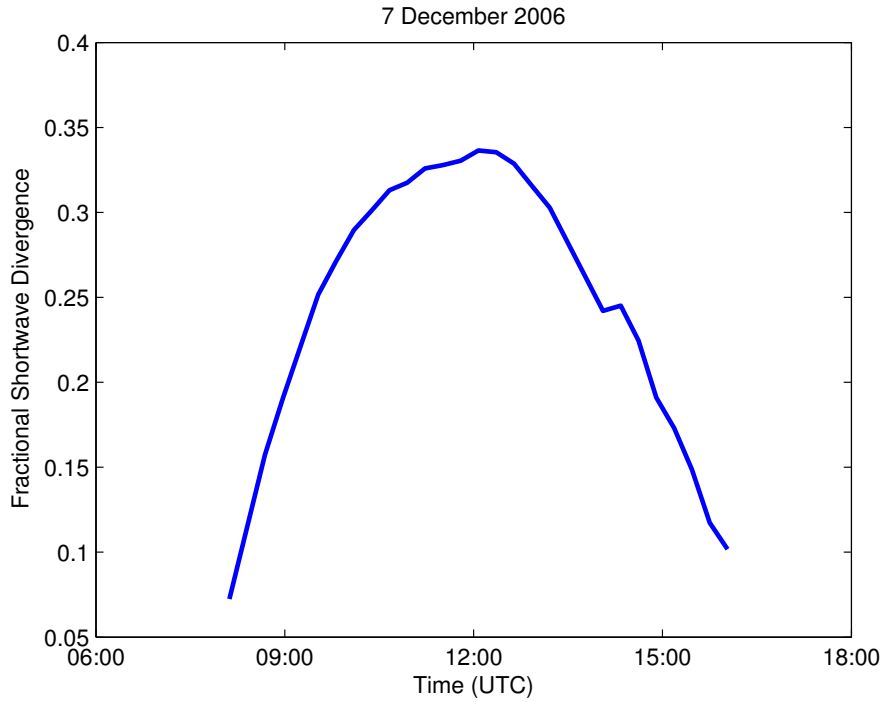


Figure 4.37: Timeline of SW fractional divergence measured at Niamey on 7 December 2006.

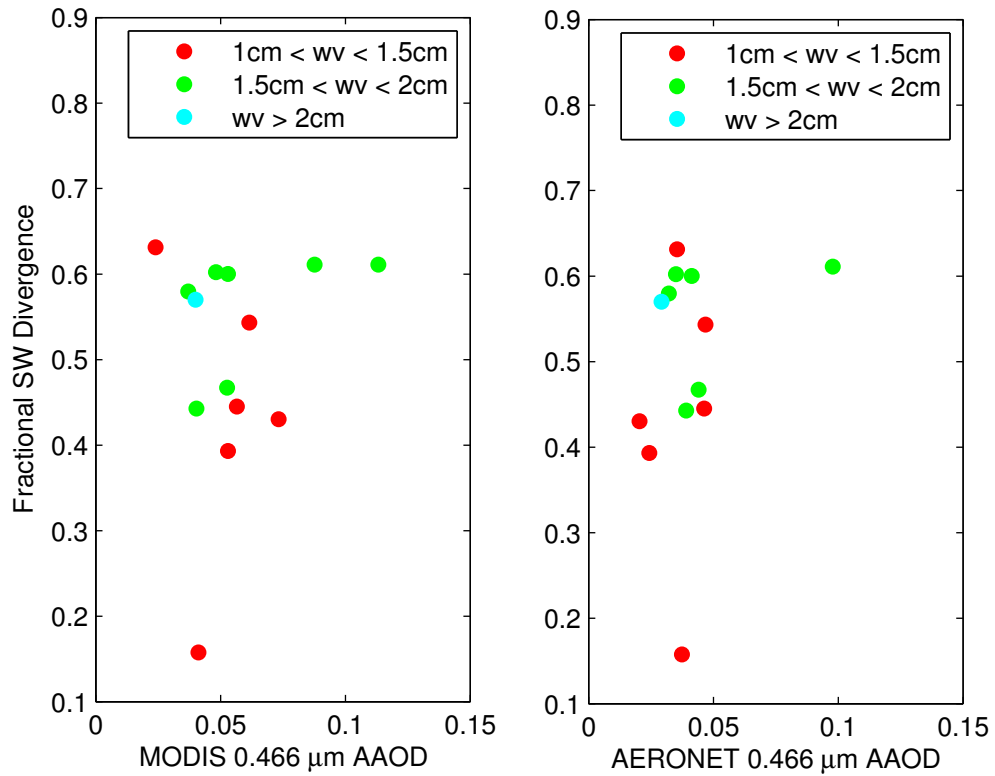


Figure 4.38: SW fractional divergence normalized by cosine of SZA versus  $0.44 \mu\text{m}$  AAOD for the 15 Banizoubou cases using either the bimodal spheroid (left) or coarse (right) aerosol model.

As at Tamanrasset, we next investigate the TOA aerosol effect at Banizoumbou using the CERES clear-sky albedo data. A comparison of the TOA albedo as a function of AOD for the years 2006-2008 (not shown) yields a lot of scatter in the data, which is not surprising given the complicated aerosol mixtures that are sometimes present at the site. So, we again focus on modeling individual cases here. We choose four cases to highlight at Banizoumbou, two with an apparent dust-dominated aerosol (17 November 2006 and 13 December 2006), and two with an aerosol mixture present (19 January 2006 and 11 December 2006). The cases chosen are listed in Table 4.4 along with the corresponding shortwave surface albedo, AOD, Angstrom exponent, and concentrations of water vapor and ozone. The 11 December case had both +16 and -16 days available.

Table 4.4: 16-day MODIS broadband SW surface albedo, daily 0.44  $\mu\text{m}$  AOD, 0.44-0.87  $\mu\text{m}$  Angstrom exponent, daily water vapor concentration, and daily  $\text{O}_3$  concentration for the simulated cases at Banizoumbou.

Date	SW Albedo	0.44 $\mu\text{m}$ AOD	0.44-0.87 $\mu\text{m}$ Angstrom	Water vapor (cm)	$\text{O}_3$ (DU)
19 Jan 2006	0.2844	0.833	0.897	2.55	258.9
17 Nov 2006	0.2966	0.699	0.280	1.53	261.6
11 Dec 2006	0.3031	0.853	0.626	1.60	250.9
13 Dec 2006	0.3058	1.528	0.292	2.38	253.2

The TOA albedo simulation results for Banizoumbou compared to the CERES measurements are shown in Figure 4.39. As at Tamanrasset, the AERONET and MODIS critical reflectance SSA both lead to a reduction in the TOA albedo relative to aerosol-free conditions. However, the CERES data only show this behavior at 17 November and 11 December; on 19 January and 13 December they indicate almost no change in TOA albedo. Both the AERONET and critical reflectance SSA result in much lower TOA albedos than the CERES measured values, except on 17 November where all three datasets agree well. With the exception of this day, neither dataset follows the same trend as CERES, which exhibits very little change on a case-by-case basis. The surface albedo

near Banizoumbou is darker here than at Tamanrasset, so the aerosol at this site is likely closer to the critical SSA at which little change in TOA reflectance would be realized.

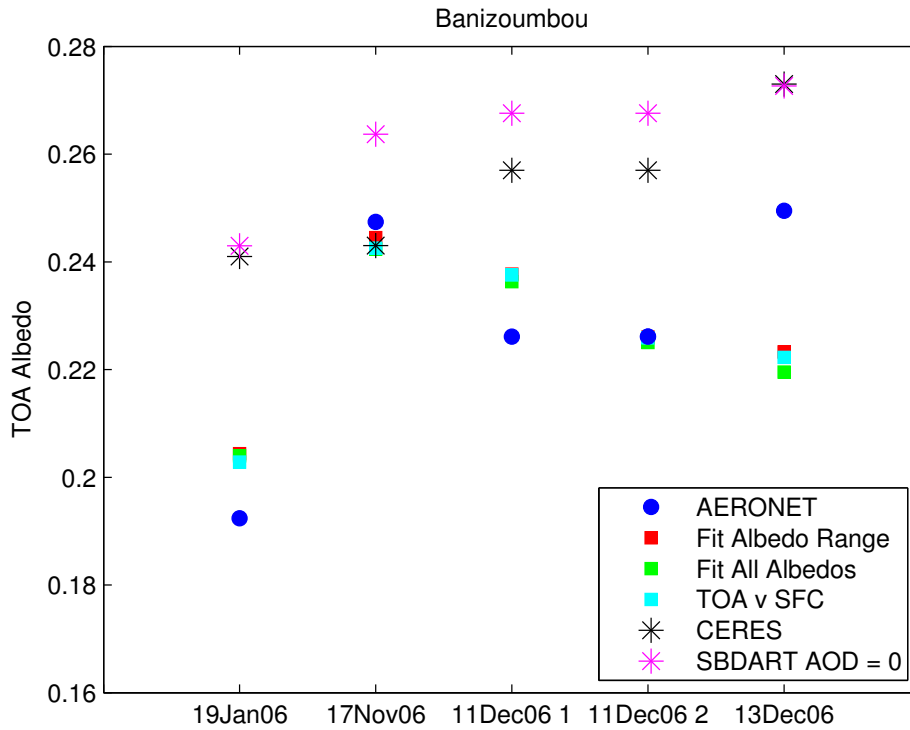


Figure 4.39: Simulated SW TOA albedo using AERONET retrieved SSA, critical reflectance retrieved SSA (for all three fitting methods), measured TOA albedo from CERES, and SBDART simulated albedo for AOD = 0 at Banizoumbou.

The corresponding spectral SSAs retrieved for AERONET and from MODIS are shown in Figure 4.40. The 19 January and 11 December cases were retrieved with the bimodal spheroid model and the 17 November and 13 December cases were retrieved with the coarse model. The spectral SSA retrieved from AERONET on 17 November and 13 December are very similar, although only the 17 November case corresponds well with the CERES TOA albedo estimate, as does the MODIS estimate for that day. The MODIS SSA for this day exhibits a stronger spectral dependence than the AERONET retrieval, with a lower SSA in the blue channel and higher SSA at all other wavelengths. This corresponds to a TOA albedo that is slightly lower than the AERONET estimate,

which again indicates that absorption in the blue channel is a key driver of the shortwave TOA forcing. The SSA results for MODIS and AERONET on 13 December have similar spectral shapes, but the values are more absorbing for the critical reflectance estimate. Both spectral values lead to a much lower TOA albedo than CERES, despite the fact that the AERONET SSA results on this day are nearly identical to the 17 November case. This could indicate that a brighter dust (lower mass fraction of iron oxides or smaller mean size) may be present near Banizoumbou.

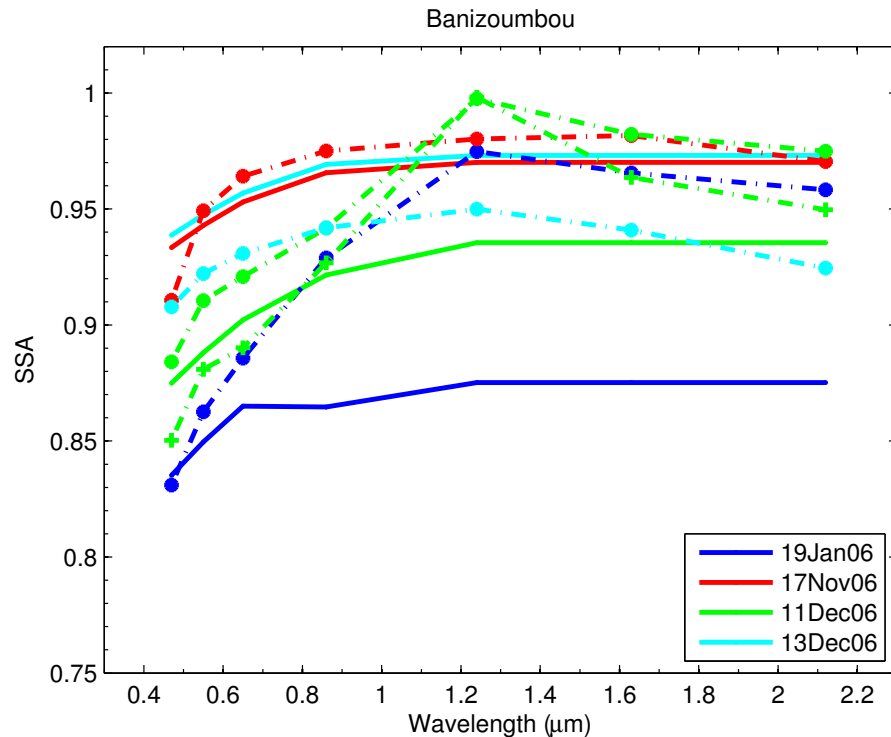


Figure 4.40: Spectral SSA retrieved for the four cases used in the TOA albedo simulation at Banizoumbou. The solid lines correspond to the AERONET retrieval and the dashed lines correspond to the MODIS critical reflectance retrieval (TOA v SFC method). The critical reflectance derivation for 11Dec06 1 is represented by the closed circles and the derivation for 11Dec06 2 is represented by the plus signs (+).

For the two mixture cases, the critical reflectance from MODIS still results in a stronger spectral dependence of SSA than the AERONET case. For the 11 December case, the -16 day is cleaner than the +16 day, so the 11Dec2006 1 SSA may be a better estimate than 11Dec2006 2. Thus, the critical reflectance on both days indicates a

brighter aerosol than the AERONET estimate at all channels except 0.466  $\mu\text{m}$ . These both result in TOA albedos that are closer to CERES than AERONET, but still much lower than the measured values. This could be due to the assumption of a well-mixed vertical profile of aerosol, when in situ data indicate that biomass burning aerosol is often lofted above dust when a mixture of aerosol is present near Banizoumbou in the dry season. When we test this, however, we find that the simulated TOA albedo is quite insensitive to the assumed vertical profile. The TOA albedo results for the 19 January 2006 case change from 0.2028 to 0.2025 when we assume the vertical profile shown in Figure 4.25 with bimodal aerosol lofted over dust. Thus, the difference is likely due to the optical properties retrieved from MODIS, in addition to the other caveats associated with the comparison that were discussed in 4.3.1.

The uncertainty in the TOA albedo at Banizoumbou translates into a large range of TOA forcing (Figure 4.41). The CERES estimates indicate that the TOA forcing is not very sensitive to the presence of the aerosol for these cases, with values ranging from 0 to  $7 \text{ W m}^{-2}$ . The values corresponding to the critical reflectance-retrieved SSA values exhibit the opposite trend of CERES, with the largest TOA forcing values ( $14 - 17 \text{ W m}^{-2}$ ) corresponding to the near-zero values from CERES, and the lowest value ( $7 \text{ W m}^{-2}$ ) corresponding to the highest CERES value. The variability in the AERONET-retrieved values does not follow the same trend as the critical reflectance estimates, but it does have roughly the same magnitude of variability (indicating more TOA albedo sensitivity than CERES).

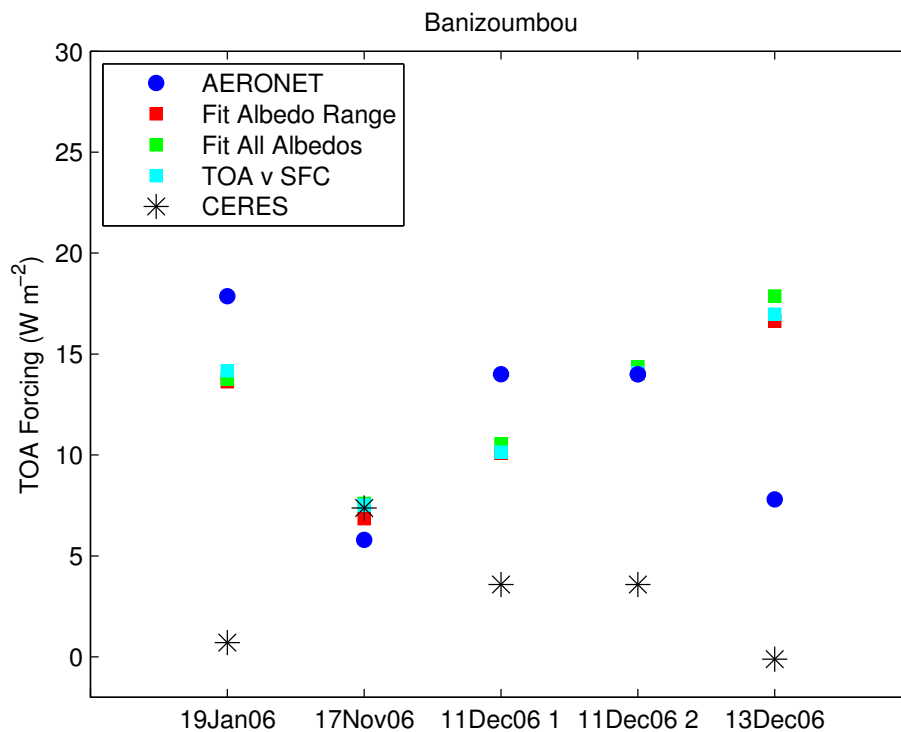


Figure 4.41: Simulated TOA forcing ( $\text{W m}^{-2}$ ) for the four Banizoumbou cases.

On closer inspection of the MODIS data, however, we find that some of the cases chosen for comparison with CERES correspond to large view angles or low scattering angles, resulting in more absorbing SSAs and much darker TOA albedos that are not representative of the true aerosol absorption. Thus, the comparison at this site helps to illustrate how the retrieval uncertainties translate to a large uncertainty in radiative forcing. If we choose only cases that correspond to scattering angles between  $120^\circ$  and  $160^\circ$  and view angles less than  $40^\circ$ , the comparison between the two datasets is much improved and the MODIS SSAs no longer result in a low bias in TOA albedo with respect to CERES (Figure 4.42). With the exception of the 19 January case with the aerosol mixture, the rest of the cases appear predominantly impacted by dust. Our retrieved spectral SSAs for the dust result in TOA forcing values that agree with CERES within  $\pm 5 \text{ W m}^{-2}$ .

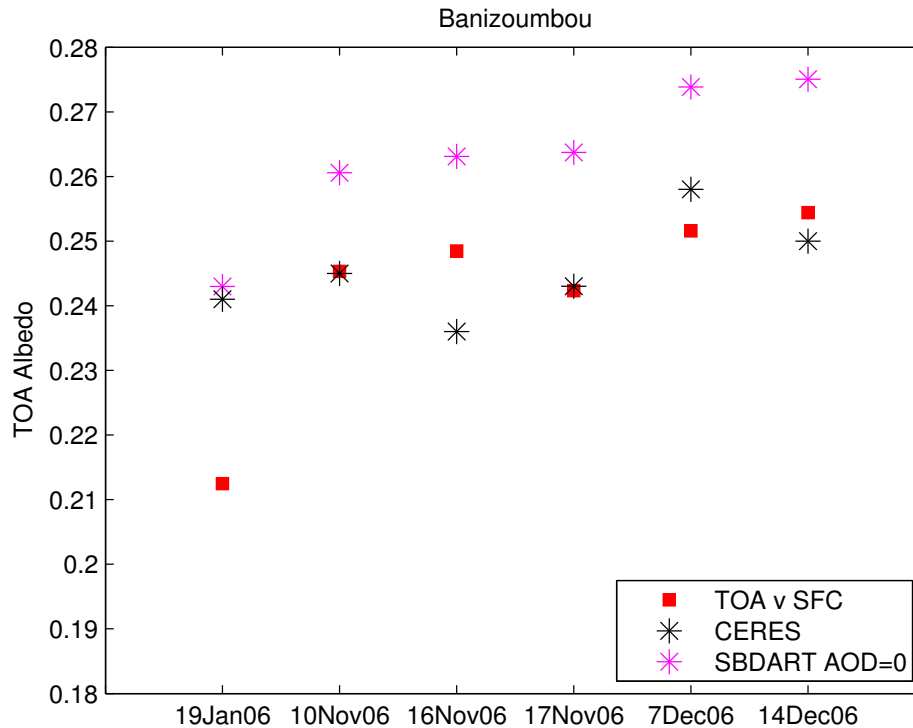


Figure 4.42: Simulated TOA albedo for Banizoumbou cases with scattering angles between 120° and 160°, and view angles < 40°.

By simply accounting for the variability in the critical reflectance-retrieved SSA with scattering and view angle, we are able to account for much of the uncertainty in the SSA that drives the TOA forcing at Banizoumbou in dusty conditions. Based on our analysis presented here, the remaining uncertainty in the dust SSA is likely due to:

- Changes in surface reflectance due to relatively low AODs on both the polluted and clean days.
- Brightness of the surface resulting in a non-linear increase in TOA reflectance that cannot be accurately captured with a linear fitting routine.
- Changing background aerosol on the cleaner day.

The main sources of uncertainty in the presence of dust-biomass burning mixtures, however, are somewhat more elusive. Even with information about the aerosol vertical profile, as well as polluted and clean day AODs and aerosol size, our SSA results for one

mixture case do not exhibit the same spectral behavior as AERONET, and they correspond to a TOA albedo that is much darker than the CERES measurement. This could suggest that water uptake is occurring on the particles in these cases, resulting in a brightening of the TOA reflectance that would not be captured by the bimodal spheroid LUT. It could also suggest that the relative contributions of the two species are not well represented by our aerosol model for our particular case. More work on characterizing mixtures will be crucial to ascertain whether critical reflectance can provide spectral SSA information in the presence of both biomass burning and dust over North Africa.

## 5 Summary and Future Work

Over desert surfaces, the sign and magnitude of the top-of-atmosphere aerosol radiative forcing is sensitive to small changes in aerosol absorption. Thus, the accurate determination of the spectral absorption properties of aerosol is critical for the determination of the TOA aerosol radiative forcing over desert regions. Accurate information on the aerosol forcing over desert is critical to quantifying the regional effects of aerosols on surface and atmospheric heating rates and, ultimately, how those effects will change atmospheric stability and the location and intensity of rainfall in areas where water is a scarce resource. In this study, we focus on determining aerosol properties over North Africa, a desert region impacted by absorbing dust and biomass burning aerosols, using critical reflectance derived from MODIS reflectances. The application of the critical reflectance has been used in a few studies to estimate the absorbing properties of aerosol for specific species or events; however, the method has not been applied for the purposes of daily monitoring of aerosol absorption (and subsequent estimation of the daily top-of-atmosphere aerosol forcing) over desert. The feasibility of applying the principle in this manner has also not been rigorously investigated to date.

We use the SBDART model to explore the sensitivity of the TOA critical reflectance to aerosol physical and optical properties for a range of solar and viewing geometries that are representative of MODIS observations. A T-matrix code provides

phase function and SSA estimates for fine, coarse, and bimodal aerosol models for a range of imaginary refractive indices and assumed size, shape, and real refractive index. Our results provide us with look-up tables that we use to retrieve spectral aerosol SSA in the vicinity of two AERONET stations: Tamanrasset, a site in the Algerian Sahara that is impacted primarily by dust aerosol, and Banizoumbou, a Sahelian site in Niger that is impacted by dust throughout the year, and by biomass burning aerosol from agricultural burning activities during the winter dry season. Our LUTs and SSA retrieval results help us to determine the major sources of uncertainty associated with the application of this method, and to determine the conditions at which we can be most confident in the critical reflectance-retrieved SSA. We use our findings to address the implications for the uncertainty of aerosol forcing over the North African region.

## **5.1 Key Findings**

- **Sensitivity to size, shape and real refractive index is maximized at higher SSAs and backscattering angles; coarse mode model may result in an overestimate of size in cleaner conditions**

The SBDART simulations indicate that the sensitivity of the critical reflectance to SSA is greater as aerosol size decreases, with variations as a function of solar and viewing geometry. Thus, since we are focusing on a region that is regularly impacted by coarse dust particles, the uncertainties associated with retrieving SSA for an assumed size may be somewhat larger for our application than for critical reflectance retrievals of more absorbing fine mode aerosol. Our results also suggest that the sensitivity to assumed real refractive index is low; assuming that the real refractive index varies from 1.43 to 1.63 results in an uncertainty of generally less than 10% of the critical reflectance, although

larger uncertainties exist at angles close to backscattering. The sensitivity to shape is also largest at backscattering angles and at higher SSAs; the difference in critical reflectance for a bimodal size distribution assuming 100% sphericity versus 4% sphericity can exceed 40% at backscattering angles as SSA approaches 1.0.

A test of the retrieval cases at Tamanrasset using the AERONET-retrieved real refractive index of 1.44 confirms a very low sensitivity of the SSA to assumed real refractive index; however, our case study results may contain evidence of the need to include fine particles in the dust model. Although the agreement between MODIS and AERONET SSA is not dependent on the size of the fine mode as indicated by the AERONET-retrieved size distribution, incidences where the measured critical reflectance exceeds the maximum value in the coarse model look-up table are more common at lower path radiance differences, and the difference between the measured critical reflectance in the near-IR and the maximum LUT value is higher at lower AERONET AOD. The full AERONET dataset at Tamanrasset contains more variable SSA and higher Angstrom exponents at lower AODs; thus, the mean aerosol size in cases of moderate aerosol loading in the region may be overestimated by our coarse model.

- **Retrieved SSA decreases at larger view angles and depends on scattering angle**

At both sites, the retrieved SSA in the visible channels exhibit a drop-off at high and low scattering angle ( $> \sim 160^\circ$  and  $< \sim 120^\circ$ ) and also at larger view angles ( $> \sim 45^\circ$ ) within the intermediate scattering angle range. This behavior is likely the result of multiple scattering due to higher scattering phase function values outside of the  $120^\circ$  to  $160^\circ$  scattering angle range, and longer atmospheric path lengths at larger satellite view angles. In the near-IR, a drop-off in SSA still occurs at the smallest scattering angles

(~100°), but the trend beyond this range is the opposite of what we observe in the visible bands. Because AOD tends to be lower at these channels, whereas the spectral surface albedo tends to be brighter, we hypothesize that the near-IR trend is an effect of surface brightness on the retrieval.

TOA albedo simulations for cases originally chosen at Banizoumbou for comparison to CERES have a tendency to produce much darker results than the observations (which indicate low sensitivity of TOA albedo to aerosol near this site). However, we find that most of these cases correspond to either low scattering angle or larger view angles; when we compare CERES to retrieval cases that correspond to a scattering angle range of 120° to 160° and a view angle less than 40°, the MODIS spectral SSA produces TOA forcing estimates that are within  $\pm 5 \text{ W m}^{-2}$  of the CERES measurements when dust aerosol is the dominant species.

- **Variable background aerosol increases the uncertainty in critical reflectance-retrieved SSA**

Although we assume that the Tamanrasset site is dominated by dust aerosol, AERONET Angstrom exponents sometimes indicate the presence of fine particles on cleaner days. Retrievals performed on comparisons to these days result in higher SSA values, particularly in the blue channel (resulting in SSA uncertainties ~0.03 for our cases). The same is found for one case at Banizoumbou. A sensitivity study of the dependence of the coarse aerosol critical reflectance on the presence of fine aerosol on the clean day suggests that an absorbing fine aerosol on the clean day would result in a retrieved SSA that is biased in the direction consistent with our observations (positive). It also suggests that the magnitude of this effect would depend on the clean day AOD

(higher clean day AOD = higher polluted day SSA). There is little sensitivity to the presence of fine aerosol that is non-absorbing, however, so the presence of a background aerosol containing black carbon should have a larger impact on the retrieval than one dominated by sulfate aerosol.

- **Surface reflectance changes between the clean and polluted day may be greater at lower AOD; higher surface reflectance corresponds to higher SSAs and also may provide evidence of BRDF effects**

There is no direct evidence that the properties of the surface are changing between the clean and polluted day in our retrieval cases, although the MODIS 16-day albedo data indicate that the chances of surface variability are greater at Banizoumbou than Tamanrasset. We do find greater variability in retrieved SSA at 0.466  $\mu\text{m}$  when the aerosol loading is lower as indicated by DeepBlue AOD. This demonstrates the effect of increased noise at lower aerosol loadings on the retrievals, but it could also indicate that changes in the surface reflectance between the clean and polluted day impact the retrieval more when the polluted day has only a moderate aerosol loading (AOD <  $\sim 0.7$ ).

We also find trends with surface albedo at both sites: a positive trend with SSA at Tamanrasset at all spectral bands and a positive trend in the near-IR at Banizoumbou. We believe these trends to be related to data fitting issues at brighter surface reflectance. Simulation results suggest that the TOA reflectance increases non-linearly with surface reflectance for a weakly-absorbing aerosol; thus, when we apply a linear regression to the data, the slope increases with increasing surface reflectance and results in a positive trend of critical reflectance with surface albedo. This issue may be somewhat unique to retrievals of dust aerosol over North Africa, given the combination of weakly absorbing

aerosol and high surface reflectance that exists in the region. Because the surface is brighter and less variable near Tamanrasset, the surface effect is a bit more apparent for all channels near this site.

These SSA trends with surface albedo do not appear to be a function of solar or viewing geometry, but they do suggest that the effects of the BRDF could be important to the retrieval. One BRDF model for desert surfaces exhibits an increase in surface reflectance with viewing and solar zenith angle, so we might expect higher SSAs at these angles given the tendency for retrieved SSA to increase with surface brightness. We hypothesize that this effect may result in the tendency for the retrieved SSA to be brighter at larger view angles in the near-IR.

- **Aerosol mixtures are not well-represented in the current retrieval framework, resulting in SSA values that underestimate the TOA albedo**

The presence of aerosol mixtures is itself a retrieval complication at Banizoumbou, however, the retrieval of SSA for mixtures is also complicated by a lack of knowledge of the vertical profile of the aerosol and of whether the same relative contributions of dust and biomass burning aerosol are present on the cleaner day. The use of ancillary data on the vertical profile of dust and biomass burning aerosol from a DABEX flight profile on 19 January 2006, combined with information on the aerosol type and AOD at Banizoumbou on the cleaner day, results in a retrieved spectral SSA that is brighter than that retrieved when our standard assumptions are applied. The results indicate a much stronger spectral dependence of SSA than the AERONET retrieval, which is the general tendency of the critical reflectance results at Banizoumbou, particularly when the impact of dust-biomass mixtures is evident. Both AERONET and

critical reflectance SSA estimates for the 19 January 2006 case result in a much lower TOA albedo than CERES indicates, so it is unclear which spectral dependence is more representative of the aerosol for this case, or what sources of uncertainty are most important in the retrieval for dust-biomass burning mixtures.

- **Dust absorption results in darkening the TOA albedo over very bright desert, but the retrieved SSA for dust may be too bright**

The results for simulations of TOA albedo for average critical reflectance-retrieved SSA and for individual cases reveal that the TOA effect near Tamanrasset is driven mainly by the absorption properties in the blue channel, and nearly all spectral SSA results at the site result in a higher TOA albedo than CERES indicates. The data do follow the same CERES trend with AOD, however. The SSA retrieval from AERONET is more variable, however, it achieves excellent agreement with CERES on 30 September 2008. When we apply this spectral SSA to other cases, the TOA albedo agreement with CERES data is improved. Thus, this particular retrieval from AERONET may be a good measure of the typical spectral absorption of dust that impacts the site, which is somewhat more absorbing than most of the critical reflectance results near Tamanrasset.

## **5.2 Suggestions for Critical Reflectance Application**

Given the findings in our case study results, testing of the method assumptions, and TOA forcing simulations, we conclude that the critical reflectance can be used to retrieve SSA from MODIS reflectances over North Africa, provided the following conditions are met:

- Scattering angle lies between  $120^\circ$  and  $160^\circ$
- Satellite view angle  $< \sim 45^\circ$

- A clean day aerosol phase function that can be confirmed to be the same as the polluted day, or can at least be confirmed to be non-absorbing if the clean day AOD is low. Or, a relatively high aerosol loading of the same type of aerosol on both days may also suffice.

The first two conditions will allow multiple scattering effects to be avoided, limit the sensitivity of the retrieval to assumptions about refractive index and shape, and should also help to restrict the effect of surface albedo somewhat. Of course, there is also a need for realistic assumed aerosol models, but our very basic, fixed models produce results that suggest particle size information is secondary to the above considerations.

### **5.3 Future Work**

Based on the critical reflectance retrieval results and the comparison of the results with AERONET, we find a number of possible retrieval additions that might be useful for retrieving SSA from critical reflectance over North Africa. In addition, the retrieval results potentially contain some information about aerosol impacts in the region that warrants further investigation.

- **Dynamic aerosol models**

The full AERONET dataset at both sites indicates that aerosol size and SSA vary in this region as a function of AOD. For dust events, higher AOD corresponds to a larger mean aerosol size and vice versa. Since many of our cases take place on days with moderate AODs ( $0.4 \mu\text{m} < 0.6$ ) our coarse model may not contain a sufficient contribution of fine particles to represent the measured critical reflectance. Therefore, an aerosol model that contains a dynamic size-AOD relationship may result in a better representation of SSA at lower aerosol loadings. Of course, the application of an AOD-

dependent aerosol model requires information about AOD (which is scarce in this region), so it may not be a feasible addition for aerosol monitoring over North Africa.

- **Size information from the critical reflectance and path radiance**

The statistics on the spectral dependence of critical reflectance and path radiance seem consistent with the dominance of dust aerosol at Tamanrasset, and of some dust-biomass burning aerosol mixtures at Banizoumbou. However, the translation of this behavior into quantitative information about the relative aerosol size is complicated due to the variation of the spectral slope of critical reflectance and path radiance with view angle. Clear patterns of either parameter with view angle do not emerge from the critical reflectance retrieved from MODIS; therefore, we suggest simulating the spectral slope assuming a range of relative contributions of dust and biomass-burning aerosol (or relative changes in size in the case of pure dust) in order to determine whether the retrieved critical reflectance or path radiance spectral slope can be used to constrain choices of aerosol models in the retrieval.

- **Surface albedo information over the brightest areas of the region**

The high bias of the simulated TOA albedo for critical reflectance-retrieved SSAs at Tamanrasset is likely due in part to the effect of the higher surface albedo near this site. The albedo range fitting method was designed to address this issue in the retrieval, but the SSA results for this fitting method still exhibit a trend with surface albedo. This may indicate a need to include surface albedo information when retrieving SSA over the brightest desert regions, where the TOA reflectance cannot be approximated by a linear relationship with surface reflectance.

- **Spectral dependence of SSA for dust-biomass burning mixtures**

Our SSA retrievals exhibit a stronger spectral dependence of SSA than AERONET at Banizoumbou, particularly in cases where the AERONET-retrieved size distribution indicates a mixture of dust and biomass burning aerosol is present. Even when ancillary data from DABEX and AERONET are used to simulate a mixture, the results still exhibit a strong spectral dependence of SSA. More work is needed to ascertain the reasons for the differences, and also to determine a representative aerosol mixture for this region.

- **Improved estimates of shortwave divergence for retrieval validation**

The daily average shortwave divergence, as calculated from RADAGAST data, is reasonably well-correlated with the daily AOD calculated from the AERONET AOD and SSA retrievals at Banizoumbou. However, the comparison of the retrieval results to the shortwave divergence at specific MODIS overpass times does not reveal a good correlation with MODIS or AERONET results. The reason for this is not known, but it could indicate a need to more carefully consider the differences in resolution between surface point measurements and TOA measurements with a larger footprint when combining the two for shortwave divergence estimates.

- **Investigations of the effects of water uptake on dust**

Retrieved SSA results and CERES TOA albedo measurements contain some evidence that dust may be hygroscopic near Tamanrasset. The CERES data indicates some AOD dependence on column water vapor, and the critical reflectance-retrieved SSA at Tamanrasset is correlated with column water vapor in the visible channels in a manner that suggests the aerosols are larger at higher water vapor concentrations. It is

unclear whether the critical reflectance parameter could be used to confirm the uptake of water by the dust, but further study of the evidence mentioned above could add to the general understanding of aerosol processes in this region.

## References

- Ackerman, T. P. and G. M. Stokes, 2003: The Atmospheric Radiation Measurement program. *Physics Today*, **56**, 38-44.
- Alfaro, S. C., S. Lafon, J. L. Rajot, P. Formenti, A. Gaudichet, and M. Maille, 2004: Iron oxides and light absorption by pure desert dust: An experimental study. *Journal of Geophysical Research-Atmospheres*, **109**, doi:10.1029/2003JD004374.
- Anderson, T. L., R. J. Charlson, N. Bellouin, O. Boucher, M. Chin, S. A. Christopher, J. Haywood, Y. J. Kaufman, S. Kinne, J. A. Ogren, L. A. Remer, T. Takemura, D. Tanré, O. Torres, C. R. Trepte, B. A. Wielicki, D. M. Winker, and H. B. Yu, 2005: An "A-Train" strategy for quantifying direct climate forcing by anthropogenic aerosols. *Bulletin of the American Meteorological Society*, **86**, 1795-1809.
- Capderou, M. and R. Kandel, 1995: Determination of the Shortwave Anisotropic Function for Clear-Sky Desert Scenes from Meteosat Data. *Journal of Applied Meteorology*, **34**, 1349-1374.
- Carrico, C. M., M. D. Petters, S. M. Kreidenweis, A. P. Sullivan, G. R. McMeeking, E. J. T. Levin, G. Engling, W. C. Malm, and J. L. Collett, 2010: Water uptake and chemical composition of fresh aerosols generated in open burning of biomass. *Atmospheric Chemistry and Physics*, **10**, 5165-5178.
- Colarco, P. R., O. B. Toon, O. Torres, and P. J. Rasch, 2002: Determining the UV imaginary index of refraction of Saharan dust particles from Total Ozone Mapping Spectrometer data using a three-dimensional model of dust transport. *Journal of Geophysical Research-Atmospheres*, **107**, doi:10.1029/2001JD000903.
- Cuesta, J., D. Edouart, M. Mimouni, P. H. Flamant, C. Loth, F. Gibert, F. Marnas, A. Bouklila, M. Kharef, B. Ouchene, M. Kadi, and C. Flamant, 2008: Multiplatform observations of the seasonal evolution of the Saharan atmospheric boundary layer in Tamanrasset, Algeria, in the framework of the African Monsoon Multidisciplinary Analysis field campaign conducted in 2006. *Journal of Geophysical Research-Atmospheres*, **113**, doi:10.1029/2007JD009417.
- Derimian, Y., J. F. Leon, O. Dubovik, I. Chiapello, D. Tanré, A. Sinyuk, F. Auriol, T. Podvin, G. Brogniez, and B. N. Holben, 2008: Radiative properties of aerosol mixture observed during the dry season 2006 over M'Bour, Senegal (African Monsoon Multidisciplinary Analysis campaign). *Journal of Geophysical Research-Atmospheres*, **113**, doi:10.1029/2008JD009904.
- Dubovik, O. and M. D. King, 2000: A flexible inversion algorithm for retrieval of aerosol optical properties from Sun and sky radiance measurements. *Journal of Geophysical Research-Atmospheres*, **105**, 20673-20696.

- Dubovik, O., A. Smirnov, B. N. Holben, M. D. King, Y. J. Kaufman, T. F. Eck, and I. Slutsker, 2000: Accuracy assessments of aerosol optical properties retrieved from Aerosol Robotic Network (AERONET) Sun and sky radiance measurements. *Journal of Geophysical Research-Atmospheres*, **105**, 9791-9806.
- Dubovik, O., B. N. Holben, T. Lapyonok, A. Sinyuk, M. I. Mishchenko, P. Yang, and I. Slutsker, 2002: Non-spherical aerosol retrieval method employing light scattering by spheroids. *Geophysical Research Letters*, **29**, doi:10.1029/2001GL014506.
- Dubovik, O., B. Holben, T. F. Eck, A. Smirnov, Y. J. Kaufman, M. D. King, D. Tanré, and I. Slutsker, 2002: Variability of absorption and optical properties of key aerosol types observed in worldwide locations. *Journal of the Atmospheric Sciences*, **59**, 590-608.
- Eck, T. F., B. N. Holben, J. S. Reid, O. Dubovik, A. Smirnov, N. T. O'Neill, I. Slutsker, and S. Kinne, 1999: Wavelength dependence of the optical depth of biomass burning, urban, and desert dust aerosols. *Journal of Geophysical Research-Atmospheres*, **104**, 31333-31349.
- Eck, T. F., B. N. Holben, D. E. Ward, O. Dubovik, J. S. Reid, A. Smirnov, M. M. Mukelabai, N. C. Hsu, N. T. O'Neill, and I. Slutsker, 2001: Characterization of the optical properties of biomass burning aerosols in Zambia during the 1997 ZIBBEE field campaign. *Journal of Geophysical Research-Atmospheres*, **106**, 3425-3448.
- Formenti, P., J. L. Rajot, K. Desboeufs, S. Caquineau, S. Chevaillier, S. Nava, A. Gaudichet, E. Journet, S. Triquet, S. Alfaro, M. Chiari, J. Haywood, H. Coe, and E. Highwood, 2008: Regional variability of the composition of mineral dust from western Africa: Results from the AMMA SOP0/DABEX and DODO field campaigns. *Journal of Geophysical Research-Atmospheres*, **113**, doi:10.1029/2008JD009903.
- Fraser, R. S. and Y. J. Kaufman, 1985: The Relative Importance of Aerosol Scattering and Absorption in Remote-Sensing. *Ieee Transactions on Geoscience and Remote Sensing*, **23**, 625-633.
- Giglio, L., I. Csiszar, and C. O. Justice, 2006: Global distribution and seasonality of active fires as observed with the Terra and Aqua Moderate Resolution Imaging Spectroradiometer (MODIS) sensors. *Journal of Geophysical Research-Biogeosciences*, **111**, doi:10.1029/2005JG000142.
- Hansen, J., M. Sato, and R. Ruedy, 1997: Radiative forcing and climate response. *Journal of Geophysical Research-Atmospheres*, **102**, 6831-6864.
- Haywood, J. M., R. P. Allan, I. Culverwell, T. Slingo, S. Milton, J. Edwards, and N. Clerbaux, 2005: Can desert dust explain the outgoing longwave radiation anomaly over the Sahara during July 2003? *Journal of Geophysical Research-Atmospheres*, **110**, doi:10.1029/2004JD005232.
- Haywood, J. M., J. Pelon, P. Formenti, N. Bharmal, M. Brooks, G. Capes, P. Chazette, C. Chou, S. Christopher, H. Coe, J. Cuesta, Y. Derimian, K. Desboeufs, G. Greed, M.

- Harrison, B. Heese, E. J. Highwood, B. Johnson, M. Mallet, B. Marticorena, J. Marsham, S. Milton, G. Myhre, S. R. Osborne, D. J. Parker, J. L. Rajot, M. Schulz, A. Slingo, D. Tanré, and P. Tulet, 2008: Overview of the Dust and Biomass-burning Experiment and African Monsoon Multidisciplinary Analysis Special Observing Period-0. *Journal of Geophysical Research-Atmospheres*, **113**, doi:10.1029/2008JD010077.
- Herman, J. R., P. K. Bhartia, O. Torres, C. Hsu, C. Seftor, and E. Celarier, 1997: Global distribution of UV-absorbing aerosols from Nimbus 7/TOMS data. *Journal of Geophysical Research-Atmospheres*, **102**, 16911-16922.
- Holben, B. N., T. F. Eck, I. Slutsker, D. Tanré, J. P. Buis, A. Setzer, E. Vermote, J. A. Reagan, Y. J. Kaufman, T. Nakajima, F. Lavenu, I. Jankowiak, and A. Smirnov, 1998: AERONET - A federated instrument network and data archive for aerosol characterization. *Remote Sensing of Environment*, **66**, 1-16.
- Hsu, N. C., S. C. Tsay, M. D. King, and J. R. Herman, 2004: Aerosol properties over bright-reflecting source regions. *Ieee Transactions on Geoscience and Remote Sensing*, **42**, 557-569.
- Hsu, N. C., S. C. Tsay, M. D. King, and J. R. Herman, 2006: Deep blue retrievals of Asian aerosol properties during ACE-Asia. *Ieee Transactions on Geoscience and Remote Sensing*, **44**, 3180-3195.
- Hsu, N. C., J. R. Herman, P. K. Bhartia, C. J. Seftor, O. Torres, A. M. Thompson, J. F. Gleason, T. F. Eck, and B. N. Holben, 1996: Detection of biomass burning smoke from TOMS measurements. *Geophysical Research Letters*, **23**, 745-748.
- Hu, R. M., R. V. Martin, and T. D. Fairlie, 2007: Global retrieval of columnar aerosol single scattering albedo from space-based observations. *Journal of Geophysical Research-Atmospheres*, **112**, doi:10.1029/2005JD006832.
- IPCC, 2007: *Climate Change 2007: The Physical Science Basis. Contribution of Working Group I to the Fourth Assessment Report of the Intergovernmental Panel on Climate Change*. Cambridge University Press.
- Johnson, B. T., S. R. Osborne, J. M. Haywood, and M. A. J. Harrison, 2008a: Aircraft measurements of biomass burning aerosol over West Africa during DABEX. *Journal of Geophysical Research-Atmospheres*, **113**, doi:10.1029/2007JD009451.
- Johnson, B. T., B. Heese, S. A. McFarlane, P. Chazette, A. Jones, and N. Bellouin, 2008b: Vertical distribution and radiative effects of mineral dust and biomass burning aerosol over West Africa during DABEX. *Journal of Geophysical Research-Atmospheres*, **113**, doi:10.1029/2008JD009848.
- Johnson, B. T., S. Christopher, J. M. Haywood, S. R. Osborne, S. McFarlane, C. Hsu, C. Salustro, and R. Kahn, 2009: Measurements of aerosol properties from aircraft, satellite and ground-based remote sensing: A case-study from the Dust and Biomass-burning

Experiment (DABEX). *Quarterly Journal of the Royal Meteorological Society*, **135**, 922-934.

Kaufman, Y. J., 1987: Satellite Sensing of Aerosol Absorption. *Journal of Geophysical Research-Atmospheres*, **92**, 4307-4317.

Kaufman, Y. J., D. Tanré, O. Dubovik, A. Karnieli, and L. A. Remer, 2001: Absorption of sunlight by dust as inferred from satellite and ground-based remote sensing. *Geophysical Research Letters*, **28**, 1479-1482.

Kaufman, Y. J., A. E. Wald, L. A. Remer, B. C. Gao, R. R. Li, and L. Flynn, 1997: The MODIS 2.1- $\mu$  m channel - Correlation with visible reflectance for use in remote sensing of aerosol. *Ieee Transactions on Geoscience and Remote Sensing*, **35**, 1286-1298.

Kaufman, Y. J., D. Tanré, L. A. Remer, E. F. Vermote, A. Chu, and B. N. Holben, 1997: Operational remote sensing of tropospheric aerosol over land from EOS moderate resolution imaging spectroradiometer. *Journal of Geophysical Research-Atmospheres*, **102**, 17051-17067.

Koren, I., Y. J. Kaufman, R. Washington, M. C. Todd, Y. Rudich, J. V. Martins, and D. Rosenfeld, 2006: The Bodele depression: a single spot in the Sahara that provides most of the mineral dust to the Amazon forest. *Environmental Research Letters*, **1**, doi:10.1088/1748-9326/1/1/014005.

Liao, H. and J. H. Seinfeld, 1998: Radiative forcing by mineral dust aerosols: sensitivity to key variables. *Journal of Geophysical Research-Atmospheres*, **103**, 31637-31645.

Maring, H., D. L. Savoie, M. A. Izaguirre, L. Custals, and J. S. Reid, 2003: Mineral dust aerosol size distribution change during atmospheric transport. *Journal of Geophysical Research-Atmospheres*, **108**, doi:10.1029/2002JD002536.

Martins, J. V., D. Tanré, L. Remer, Y. Kaufman, S. Mattoo, and R. Levy, 2002: MODIS Cloud screening for remote sensing of aerosols over oceans using spatial variability. *Geophysical Research Letters*, **29**, doi:10.1029/2001GL013252.

Mbourou, G. N., J. J. Bertrand, and S. E. Nicholson, 1997: The diurnal and seasonal cycles of wind-borne dust over Africa north of the equator. *Journal of Applied Meteorology*, **36**, 868-882.

McConnell, C. L., E. J. Highwood, H. Coe, P. Formenti, B. Anderson, S. Osborne, S. Nava, K. Desboeufs, G. Chen, and M. A. J. Harrison, 2008: Seasonal variations of the physical and optical characteristics of Saharan dust: Results from the Dust Outflow and Deposition to the Ocean (DODO) experiment. *Journal of Geophysical Research-Atmospheres*, **113**, doi:10.1029/2007JD009606.

McMeeking, G. R., S. M. Kreidenweis, S. Baker, C. M. Carrico, J. C. Chow, J. L. Collett, W. M. Hao, A. S. Holden, T. W. Kirchstetter, W. C. Malm, H. Moosmuller, A. P. Sullivan, and C. E. Wold, 2009: Emissions of trace gases and aerosols during the open

- combustion of biomass in the laboratory. *Journal of Geophysical Research-Atmospheres*, **114**, doi:10.1029/2009JD011836.
- Parker, D. J., C. D. Thorncroft, R. R. Burton, and A. Diongue-Niang, 2005: Analysis of the African easterly jet, using aircraft observations from the JET2000 experiment. *Quarterly Journal of the Royal Meteorological Society*, **131**, 1461-1482.
- Perry, K. D., T. A. Cahill, R. A. Eldred, D. D. Dutcher, and T. E. Gill, 1997: Long-range transport of North African dust to the eastern United States. *Journal of Geophysical Research-Atmospheres*, **102**, 11225-11238.
- Pinker, R. T. and A. Karnieli, 1995: Characteristic Spectral Reflectance of a Semiarid Environment. *International Journal of Remote Sensing*, **16**, 1341-1363.
- Prospero, J. M., R. A. Glaccum, and R. T. Nees, 1981: Atmospheric Transport of Soil Dust from Africa to South-America. *Nature*, **289**, 570-572.
- Prospero, J. M., P. Ginoux, O. Torres, S. E. Nicholson, and T. E. Gill, 2002: Environmental characterization of global sources of atmospheric soil dust identified with the Nimbus 7 Total Ozone Mapping Spectrometer (TOMS) absorbing aerosol product. *Reviews of Geophysics*, **40**, doi:10.1029/2000RG000095.
- Reid, J. S. and P. V. Hobbs, 1998: Physical and optical properties of young smoke from individual biomass fires in Brazil. *Journal of Geophysical Research-Atmospheres*, **103**, 32013-32030.
- Remer, L., D. Tanré, R. Levy, Y. Kaufman, and S. Mattoo, 2006: Algorithm for Remote Sensing of Tropospheric Aerosol from MODIS: Collection 5.
- Remer, L. A. and Y. J. Kaufman, 1998: Dynamic aerosol model: Urban/industrial aerosol. *Journal of Geophysical Research-Atmospheres*, **103**, 13859-13871.
- Remer, L. A., Y. J. Kaufman, D. Tanré, S. Mattoo, D. A. Chu, J. V. Martins, R. R. Li, C. Ichoku, R. C. Levy, R. G. Kleidman, T. F. Eck, E. Vermote, and B. N. Holben, 2005: The MODIS aerosol algorithm, products, and validation. *Journal of the Atmospheric Sciences*, **62**, 947-973.
- Ricchiazzi, P., S. R. Yang, C. Gautier, and D. Sowle, 1998: SBDART: A research and teaching software tool for plane-parallel radiative transfer in the Earth's atmosphere. *Bulletin of the American Meteorological Society*, **79**, 2101-2114.
- Sandford, M. C. W., P. M. Allan, M. E. Caldwell, J. Delderfield, M. B. Oliver, E. Sawyer, J. E. Harries, J. Ashmall, H. Brindley, S. Kellock, R. Mossavati, R. Wrigley, D. Llewellyn-Jones, O. Blake, G. Butcher, R. Cole, N. Nelms, S. DeWitte, P. Gloesener, and F. Fabbrizzi, 2003: The geostationary Earth radiation budget (GERB) instrument on EUMETSAT's MSG satellite. *Acta Astronautica*, **53**, 909-915.

- Satheesh, S. K. and J. Srinivasan, 2005: A method to infer short wave absorption due to aerosols using satellite remote sensing. *Geophysical Research Letters*, **32**, doi:10.1029/2005GL023064.
- Satheesh, S. K., O. Torres, L. A. Remer, S. S. Babu, V. Vinoj, T. F. Eck, R. G. Kleidman, and B. N. Holben, 2009: Improved assessment of aerosol absorption using OMI-MODIS joint retrieval. *Journal of Geophysical Research-Atmospheres*, **114**, doi:10.1029/2008JD011024.
- Sinyuk, A., O. Dubovik, B. Holben, T. F. Eck, F. M. Breon, J. Martonchik, R. Kahn, D. J. Diner, E. F. Vermote, J. C. Roger, T. Lapyonok, and I. Slutsker, 2007: Simultaneous retrieval of aerosol and surface properties from a combination of AERONET and satellite data. *Remote Sensing of Environment*, **107**, 90-108.
- Slingo, A., H. E. White, N. A. Bharmal, and G. J. Robinson, 2009: Overview of observations from the RADAGAST experiment in Niamey, Niger: 2. Radiative fluxes and divergences. *Journal of Geophysical Research-Atmospheres*, **114**, doi:10.1029/2008JD010497.
- Slingo, A., T. P. Ackerman, R. P. Allan, E. I. Kassianov, S. A. McFarlane, G. J. Robinson, J. C. Barnard, M. A. Miller, J. E. Harries, J. E. Russell, and S. Dewitte, 2006: Observations of the impact of a major Saharan dust storm on the atmospheric radiation balance. *Geophysical Research Letters*, **33**, doi:10.1029/2006GL027869.
- Sokolik, I. N. and O. B. Toon, 1999: Incorporation of mineralogical composition into models of the radiative properties of mineral aerosol from UV to IR wavelengths. *Journal of Geophysical Research-Atmospheres*, **104**, 9423-9444.
- Sokolik, I. N., O. B. Toon, and R. W. Bergstrom, 1998: Modeling the radiative characteristics of airborne mineral aerosols at infrared wavelengths. *Journal of Geophysical Research-Atmospheres*, **103**, 8813-8826.
- Solmon, F., M. Mallet, N. Elguindi, F. Giorgi, A. Zakey, and A. Konare, 2008: Dust aerosol impact on regional precipitation over western Africa, mechanisms and sensitivity to absorption properties. *Geophysical Research Letters*, **35**, doi:10.1029/2008GL035900.
- Stamnes, K., S. C. Tsay, W. Wiscombe, and K. Jayaweera, 1988: Numerically Stable Algorithm for Discrete-Ordinate-Method Radiative-Transfer in Multiple-Scattering and Emitting Layered Media. *Applied Optics*, **27**, 2502-2509.
- Tanré, D., J. Haywood, J. Pelon, J. F. Leon, B. Chatenet, P. Formenti, P. Francis, P. Goloub, E. J. Highwood, and G. Myhre, 2003: Measurement and modeling of the Saharan dust radiative impact: Overview of the Saharan Dust Experiment (SHADE). *Journal of Geophysical Research-Atmospheres*, **108**, doi:10.1029/2002JD003273.
- Torres, O., P. K. Bhartia, J. R. Herman, Z. Ahmad, and J. Gleason, 1998: Derivation of aerosol properties from satellite measurements of backscattered ultraviolet radiation: Theoretical basis. *Journal of Geophysical Research-Atmospheres*, **103**, 17099-17110.

- Vermote, E. F., J. C. Roger, A. Sinyuk, N. Saleous, and O. Dubovik, 2007: Fusion of MODIS-MISR aerosol inversion for estimation of aerosol absorption. *Remote Sensing of Environment*, **107**, 81-89.
- Volten, H., O. Munoz, E. Rol, J. F. de Haan, W. Vassen, J. W. Hovenier, K. Muinonen, and T. Nousiainen, 2001: Scattering matrices of mineral aerosol particles at 441.6 nm and 632.8 nm. *Journal of Geophysical Research-Atmospheres*, **106**, 17375-17401.
- Volz, F. E., 1973: Infrared Optical-Constants of Ammonium Sulfate, Sahara Dust, Volcanic Pumice, and Flyash. *Applied Optics*, **12**, 564-568.
- Washington, R. and M. C. Todd, 2005: Atmospheric controls on mineral dust emission from the Bodele Depression, Chad: The role of the low level jet. *Geophysical Research Letters*, **32**, doi:10.1029/2005GL023597.
- Washington, R., M. C. Todd, S. Engelstaedter, S. Mbainayel, and F. Mitchell, 2006: Dust and the low-level circulation over the Bodele Depression, Chad: Observations from BoDEx 2005. *Journal of Geophysical Research-Atmospheres*, **111**, doi:10.1029/2005JD006502.
- WMO, 1983: Radiation commission of IAMAP meeting of experts on aerosol and their climatic effects. *WCP55*, Williamsburg, VA, 28-30.
- Yoshida, M. and H. Murakami, 2008: Dust absorption averaged over the Sahara inferred from moderate resolution imaging spectroradiometer. *Applied Optics*, **47**, 1995-2003.
- Yu, H., Y. J. Kaufman, M. Chin, G. Feingold, L. A. Remer, T. L. Anderson, Y. Balkanski, N. Bellouin, O. Boucher, S. Christopher, P. DeCola, R. Kahn, D. Koch, N. Loeb, M. S. Reddy, M. Schulz, T. Takemura, and M. Zhou, 2006: A review of measurement-based assessments of the aerosol direct radiative effect and forcing. *Atmospheric Chemistry and Physics*, **6**, 613-666.
- Zhang, J. L. and S. A. Christopher, 2003: Longwave radiative forcing of Saharan dust aerosols estimated from MODIS, MISR, and CERES observations on Terra. *Geophysical Research Letters*, **30**, doi:10.1029/2003GL018479.

## **Appendix A LUT Results at 0.553 $\mu\text{m}$**

The following pages contain the full LUT results at 0.553  $\mu\text{m}$  results that were highlighted in Chapter 2. Each figure contains contours of the critical reflectance for a single solar zenith angle as a function of view angle and SSA for four relative azimuths ( $0^\circ$ ,  $60^\circ$ ,  $120^\circ$  and  $180^\circ$ ). The upper plots contain values determined using for the all albedo fitting range, the lower plots contain values determined using the albedo range fitting method. Results are shown for each of the simulated solar zenith angles ( $6^\circ$ ,  $12^\circ$ ,  $24^\circ$ ,  $36^\circ$ ,  $48^\circ$ ,  $54^\circ$ ,  $60^\circ$ ,  $66^\circ$ ,  $72^\circ$ ). The first nine figures are for the fine aerosol model, the next nine figures are for the coarse aerosol model, the next set are for the bimodal spheroid model, and the final nine figures are for the bimodal sphere model.

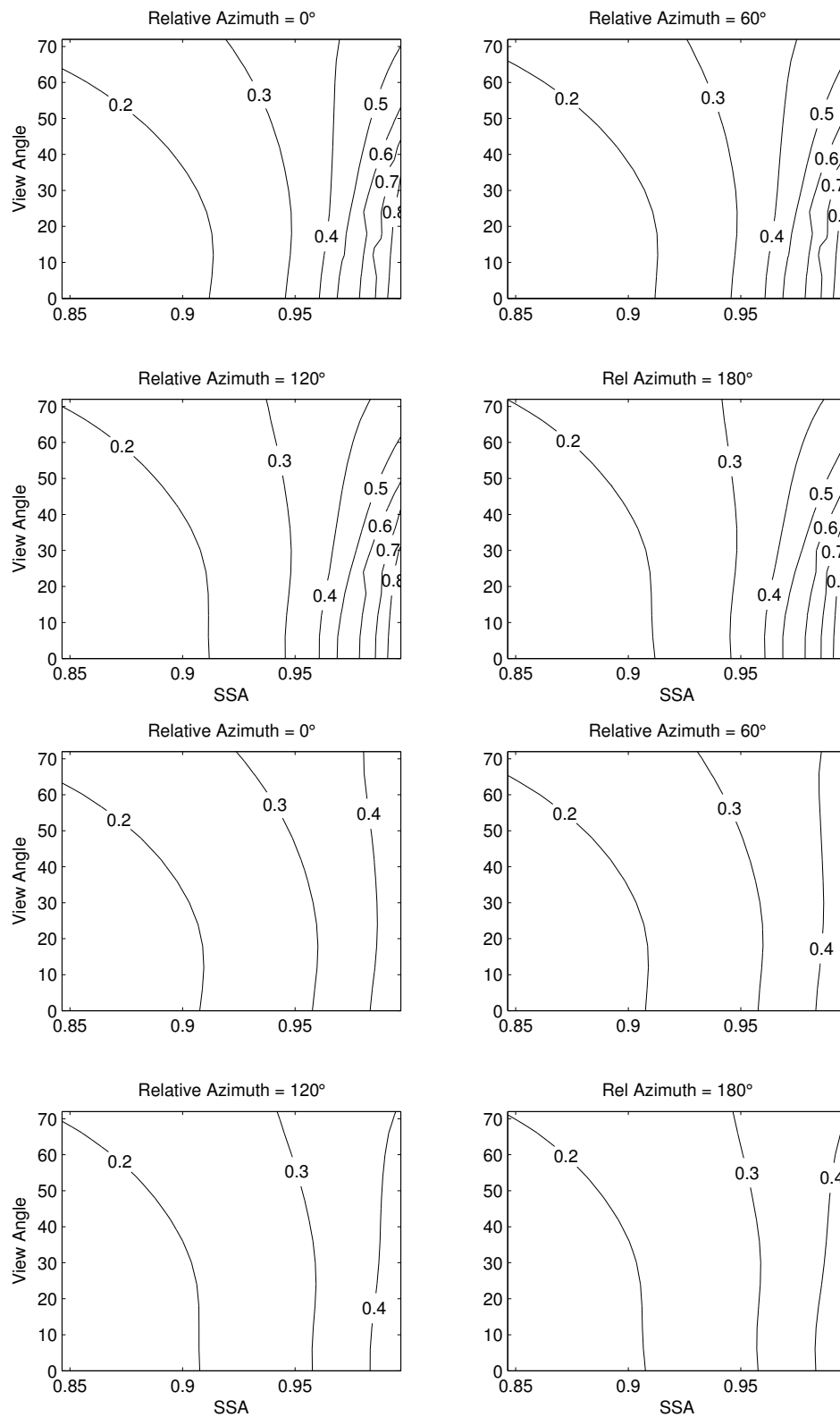


Figure A.1: Critical reflectance LUT for the fine aerosol model at  $0.553 \mu\text{m}$  for  $\text{SZA} = 6^\circ$ , displayed as a function of satellite view and SSA for relative azimuth =  $0^\circ$  (upper left),  $60^\circ$  (upper right),  $120^\circ$  (lower left), and  $180^\circ$  (lower right). Upper panel is for fitting all albedos, lower panel is for fitting an albedo range.

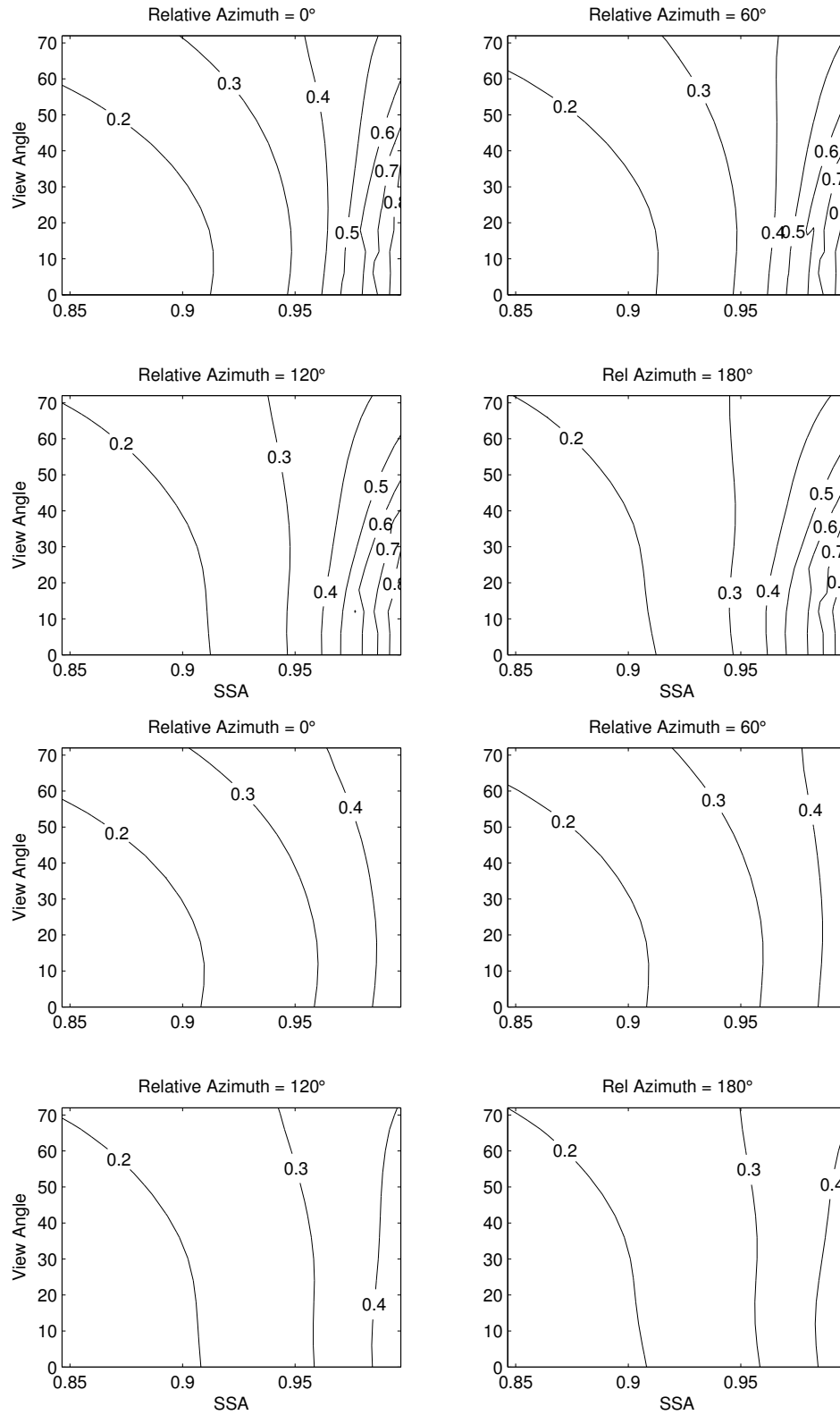


Figure A.2: Critical reflectance LUT for the fine aerosol model at  $0.553 \mu\text{m}$  for  $\text{SZA} = 12^\circ$ , displayed as a function of satellite view and SSA for relative azimuth =  $0^\circ$  (upper left),  $60^\circ$  (upper right),  $120^\circ$  (lower left), and  $180^\circ$  (lower right). Upper panel is for fitting all albedos, lower panel is for fitting an albedo range.

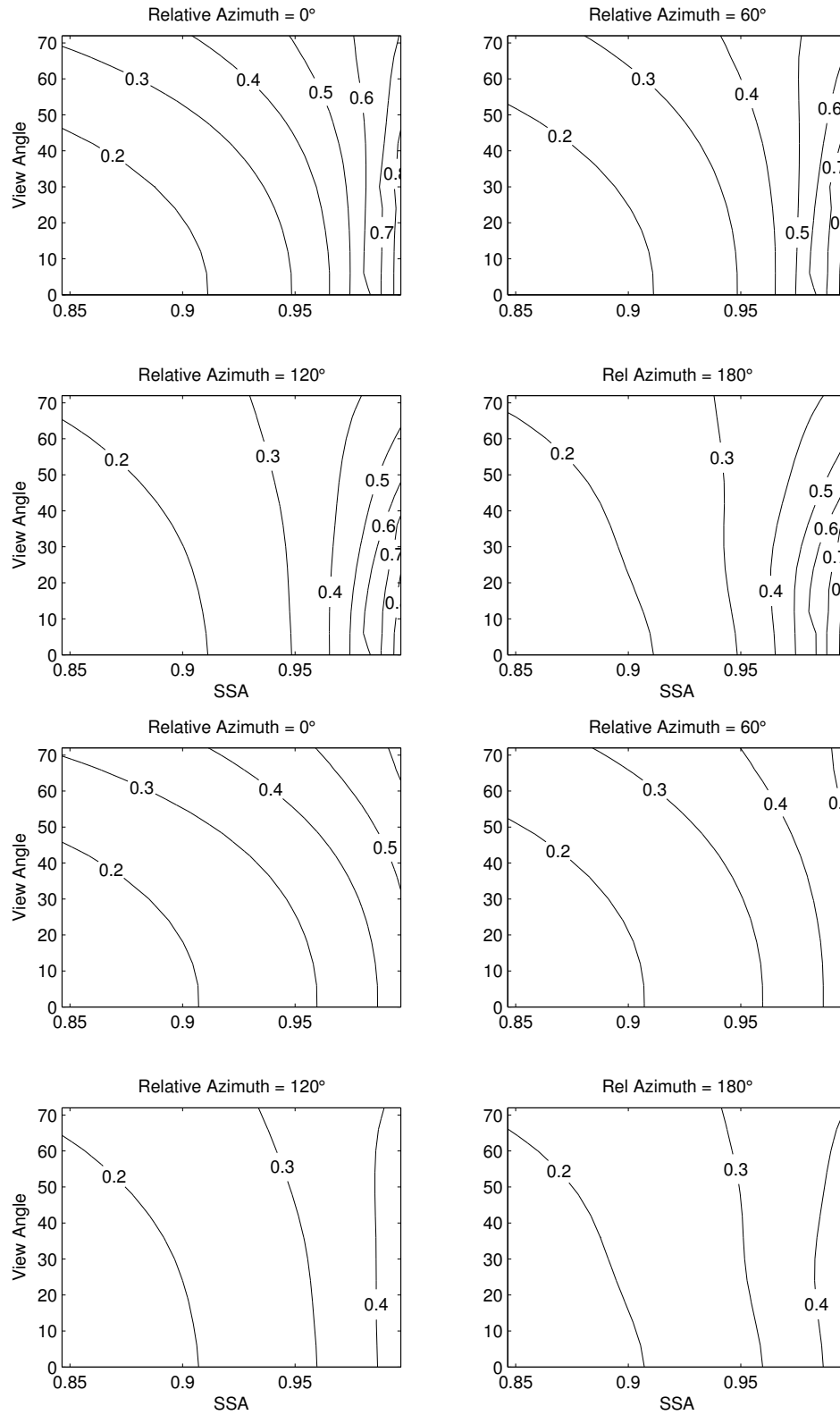


Figure A.3: Critical reflectance LUT for the fine aerosol model at  $0.553 \mu\text{m}$  for  $\text{SZA} = 24^\circ$ , displayed as a function of satellite view and SSA for relative azimuth =  $0^\circ$  (upper left),  $60^\circ$  (upper right),  $120^\circ$  (lower left), and  $180^\circ$  (lower right). Upper panel is for fitting all albedos, lower panel is for fitting an albedo range.

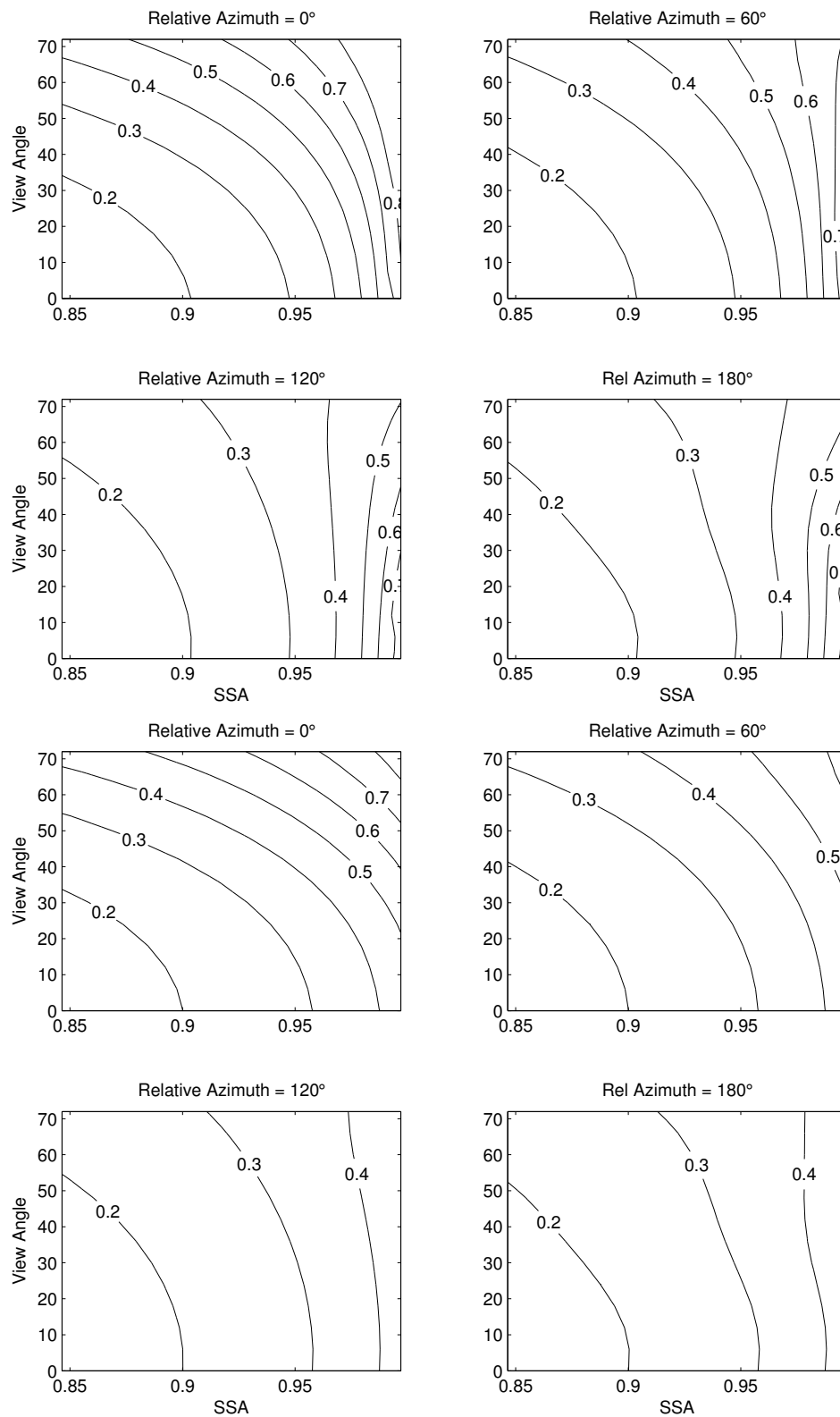


Figure A.4: Critical reflectance LUT for the fine aerosol model at  $0.553 \mu\text{m}$  for  $\text{SZA} = 36^\circ$ , displayed as a function of satellite view and SSA for relative azimuth =  $0^\circ$  (upper left),  $60^\circ$  (upper right),  $120^\circ$  (lower left), and  $180^\circ$  (lower right). Upper panel is for fitting all albedos, lower panel is for fitting an albedo range.

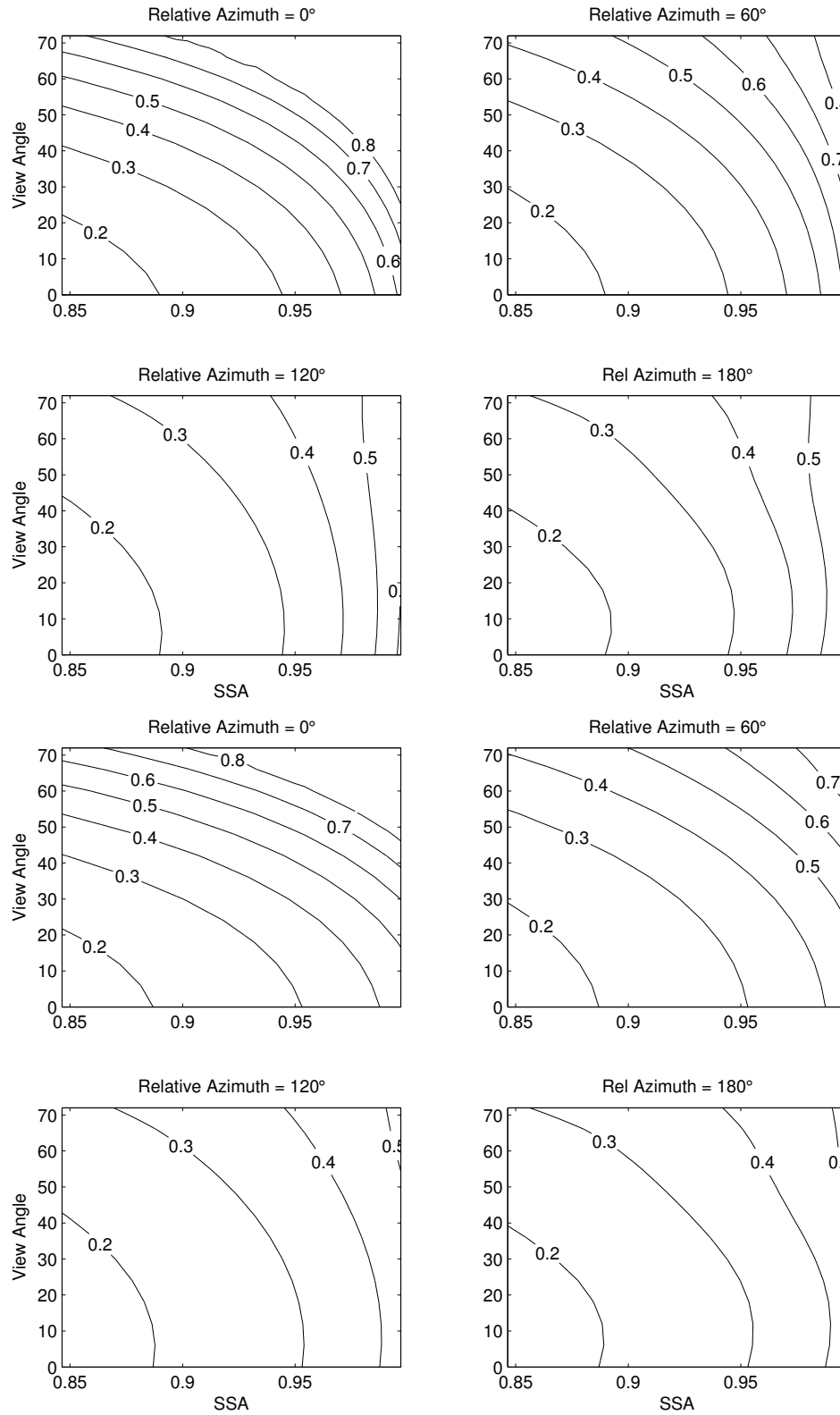


Figure A.5: Critical reflectance LUT for the fine aerosol model at  $0.553 \mu\text{m}$  for  $\text{SZA} = 48^\circ$ , displayed as a function of satellite view and SSA for relative azimuth =  $0^\circ$  (upper left),  $60^\circ$  (upper right),  $120^\circ$  (lower left), and  $180^\circ$  (lower right). Upper panel is for fitting all albedos, lower panel is for fitting an albedo range.

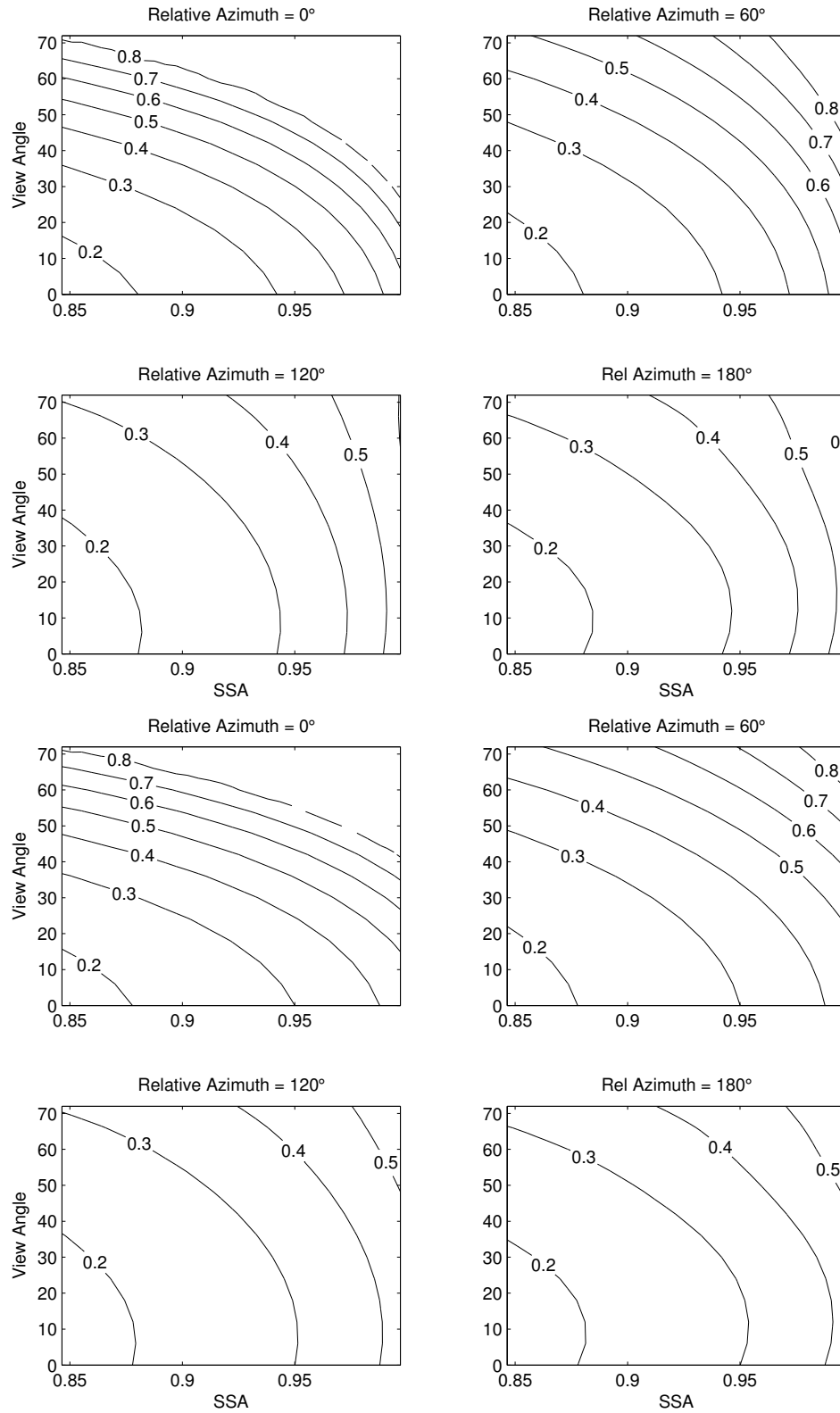


Figure A.6: Critical reflectance LUT for the fine aerosol model at  $0.553 \mu\text{m}$  for  $\text{SZA} = 54^\circ$ , displayed as a function of satellite view and SSA for relative azimuth =  $0^\circ$  (upper left),  $60^\circ$  (upper right),  $120^\circ$  (lower left), and  $180^\circ$  (lower right). Upper panel is for fitting all albedos, lower panel is for fitting an albedo range.

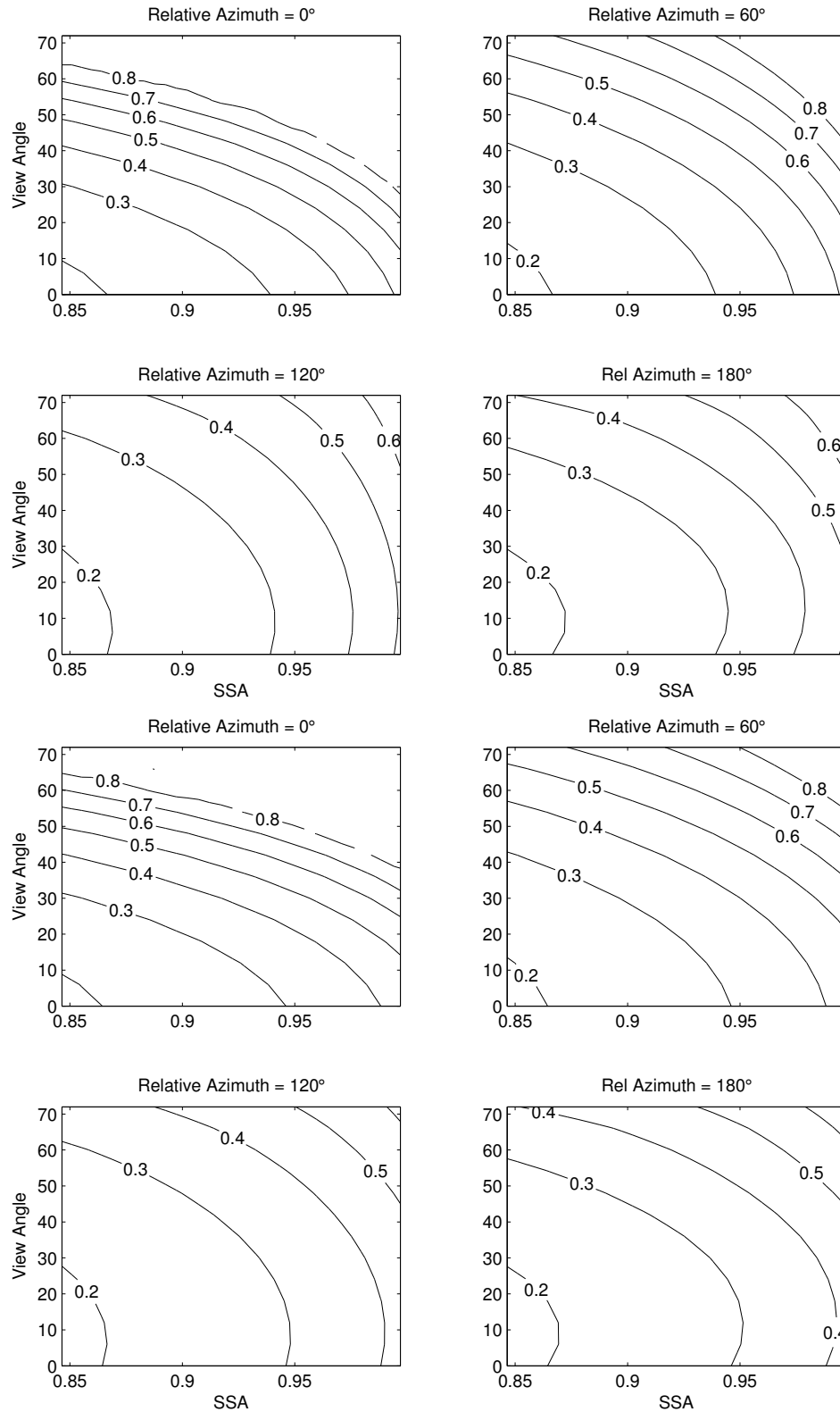


Figure A.7: Critical reflectance LUT for the fine aerosol model at  $0.553 \mu\text{m}$  for  $\text{SZA} = 60^\circ$ , displayed as a function of satellite view and SSA for relative azimuth =  $0^\circ$  (upper left),  $60^\circ$  (upper right),  $120^\circ$  (lower left), and  $180^\circ$  (lower right). Upper panel is for fitting all albedos, lower panel is for fitting an albedo range.

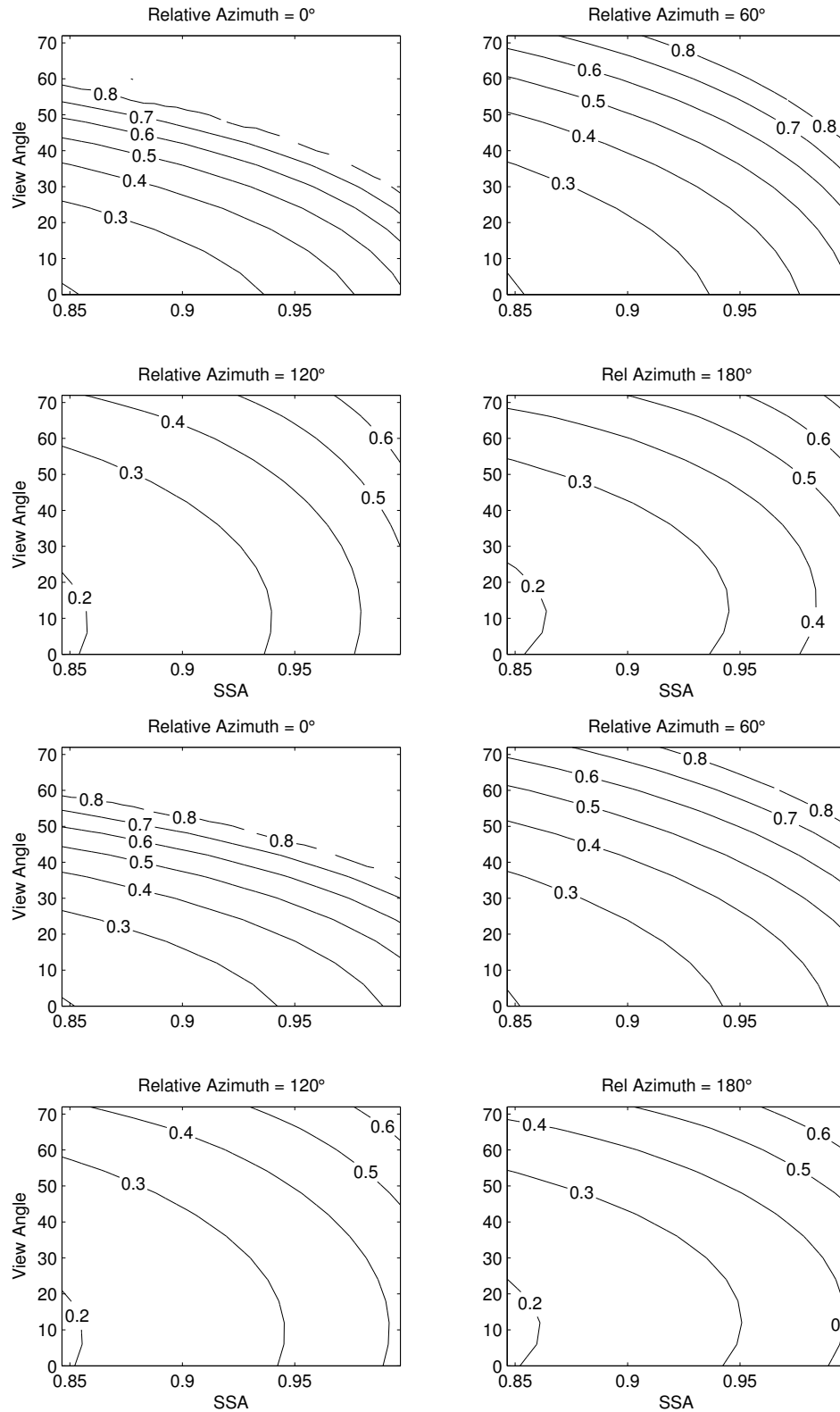


Figure A.8: Critical reflectance LUT for the fine aerosol model at  $0.553 \mu\text{m}$  for  $\text{SZA} = 66^\circ$ , displayed as a function of satellite view and SSA for relative azimuth =  $0^\circ$  (upper left),  $60^\circ$  (upper right),  $120^\circ$  (lower left), and  $180^\circ$  (lower right). Upper panel is for fitting all albedos, lower panel is for fitting an albedo range.

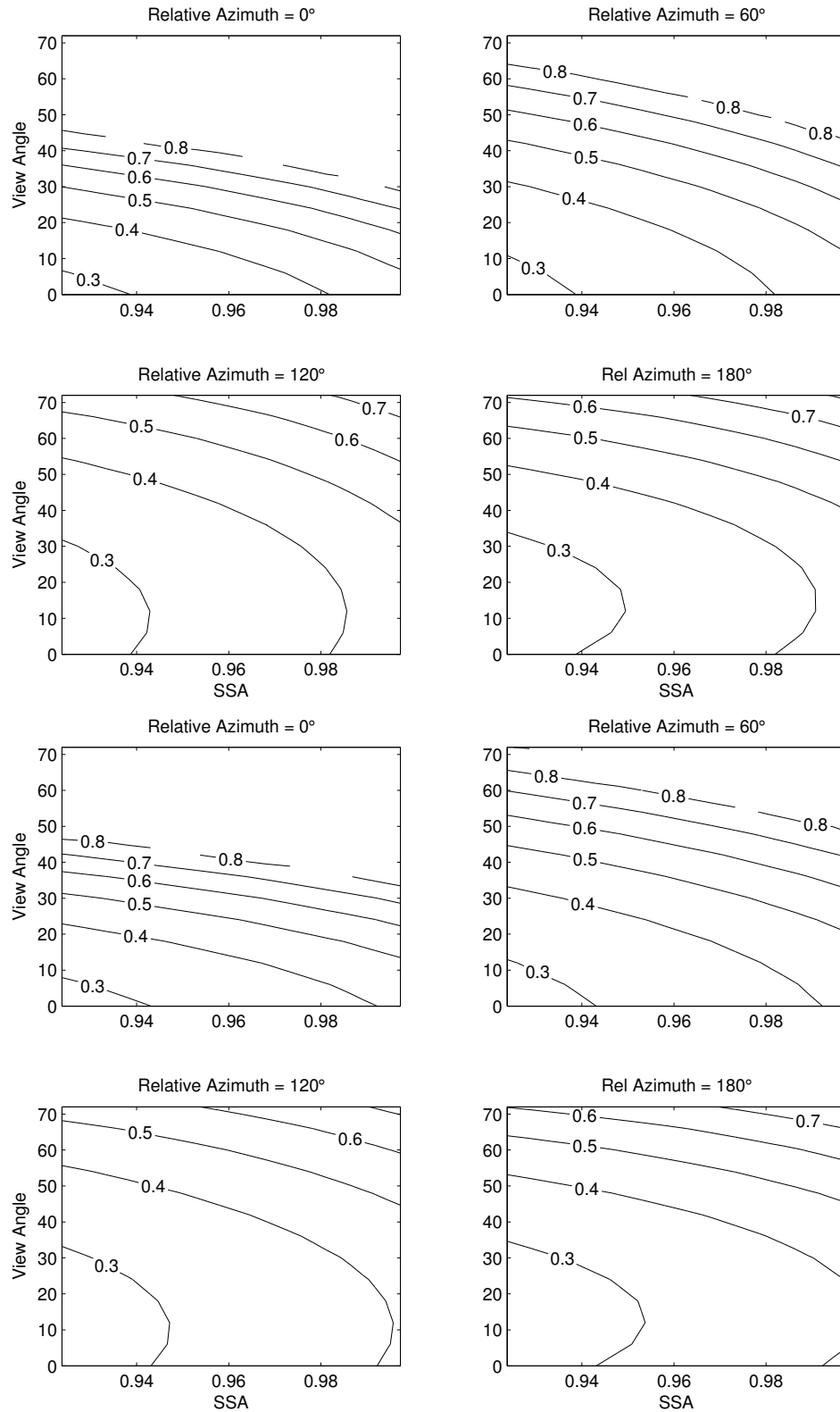


Figure A.9: Critical reflectance LUT for the fine aerosol model at  $0.553 \mu\text{m}$  for  $\text{SZA} = 72^\circ$ , displayed as a function of satellite view and SSA for relative azimuth =  $0^\circ$  (upper left),  $60^\circ$  (upper right),  $120^\circ$  (lower left), and  $180^\circ$  (lower right). Upper panel is for fitting all albedos, lower panel is for fitting an albedo range.

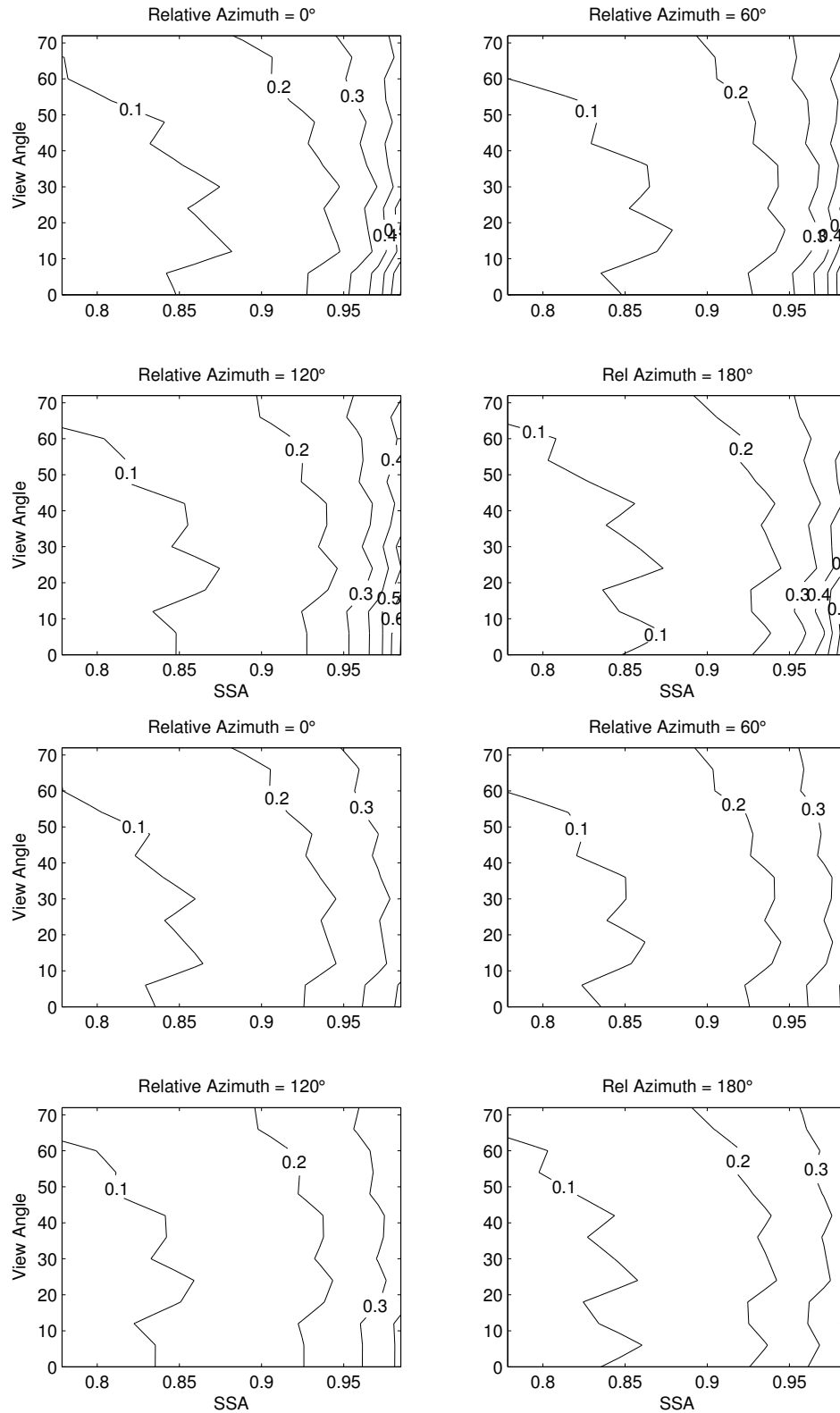


Figure A.10: Critical reflectance LUT for the coarse aerosol model at  $0.553 \mu\text{m}$  for  $\text{SZA} = 6^\circ$ , displayed as a function of satellite view and SSA for relative azimuth =  $0^\circ$  (upper left),  $60^\circ$  (upper right),  $120^\circ$  (lower left), and  $180^\circ$  (lower right). Upper panel is for fitting all albedos, lower panel is for fitting an albedo range.

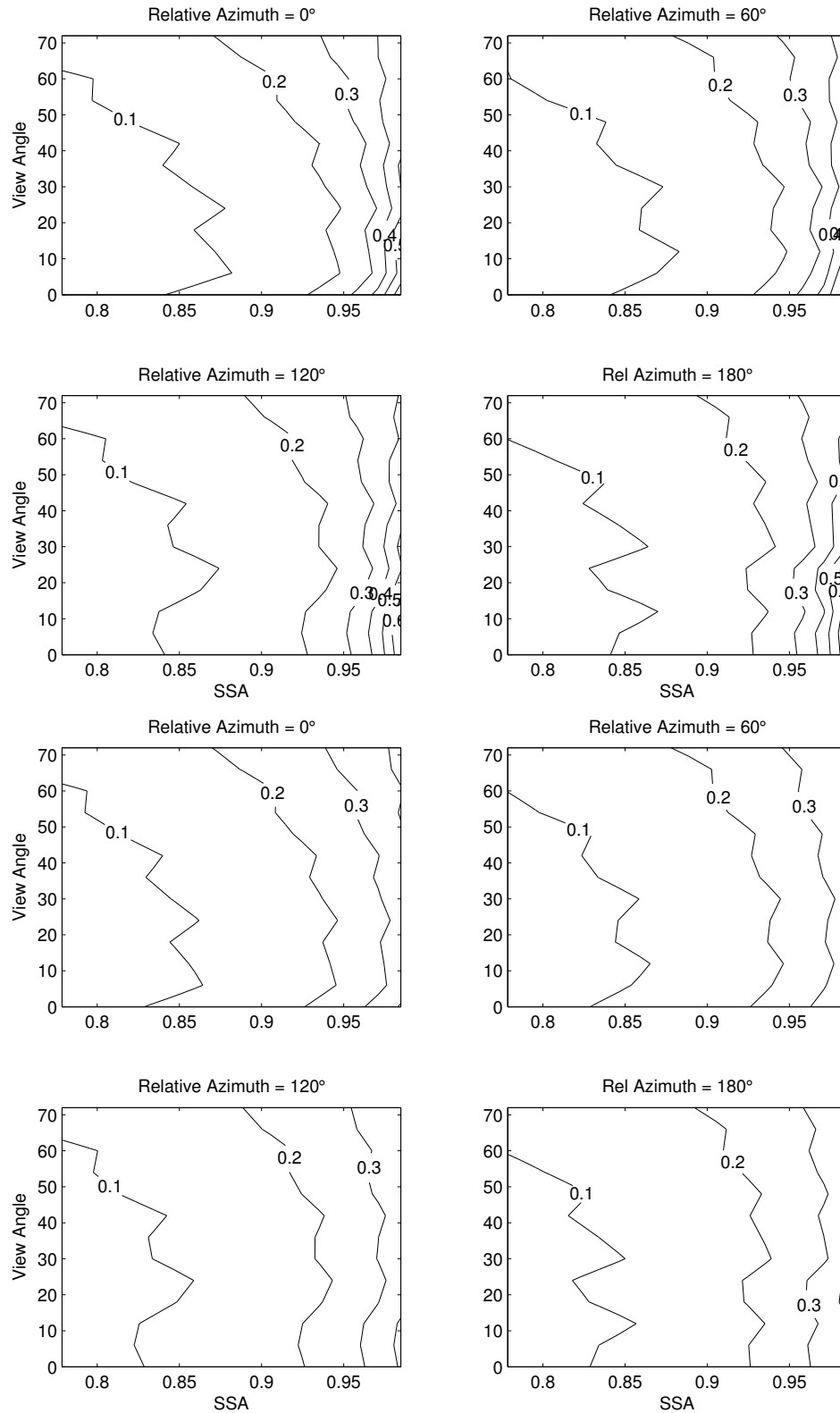


Figure A.11: Critical reflectance LUT for the coarse aerosol model at  $0.553 \mu\text{m}$  for  $\text{SZA} = 12^\circ$ , displayed as a function of satellite view and SSA for relative azimuth =  $0^\circ$  (upper left),  $60^\circ$  (upper right),  $120^\circ$  (lower left), and  $180^\circ$  (lower right). Upper panel is for fitting all albedos, lower panel is for fitting an albedo range.

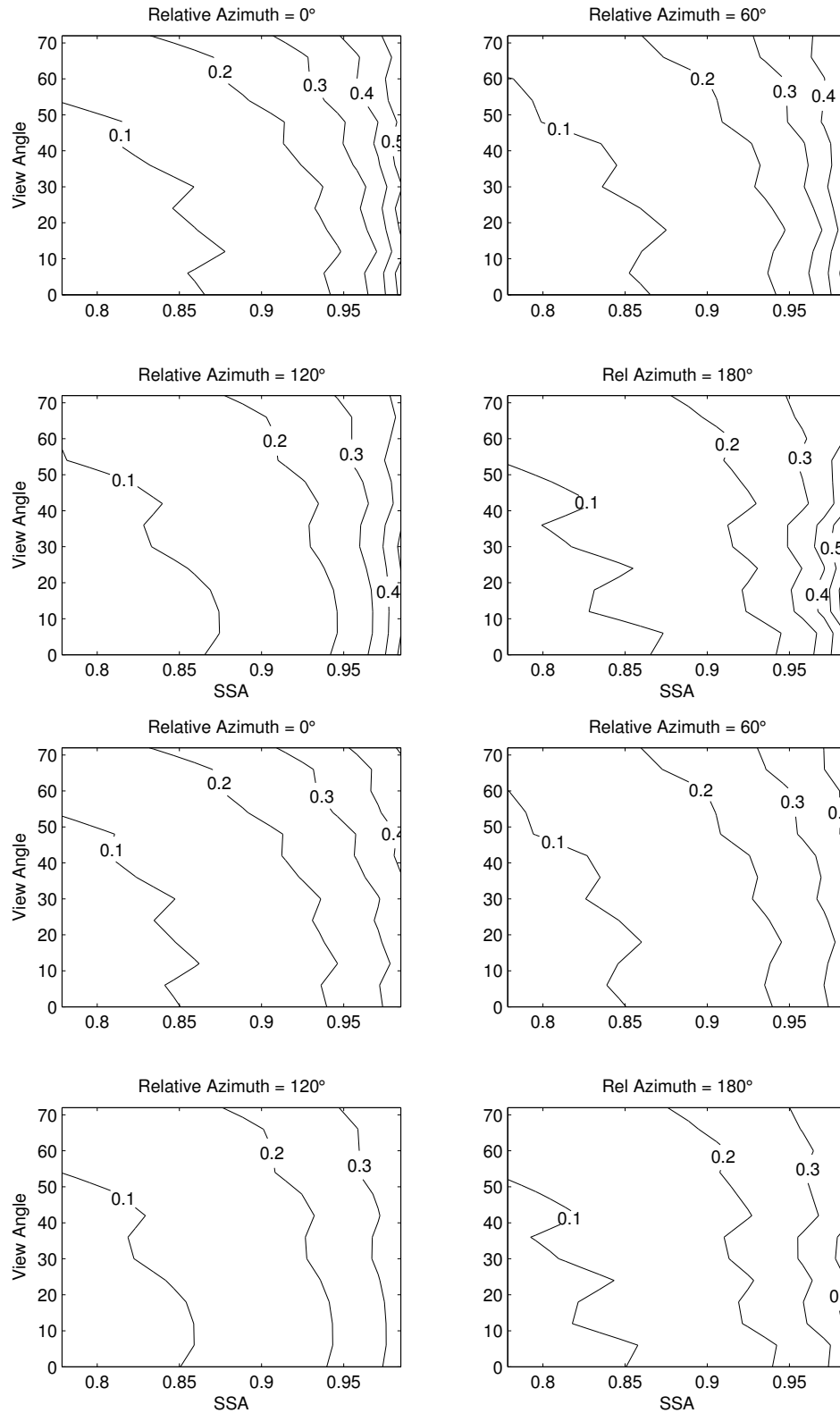


Figure A.12: Critical reflectance LUT for the coarse aerosol model at  $0.553 \mu\text{m}$  for  $\text{SZA} = 24^\circ$ , displayed as a function of satellite view and SSA for relative azimuth =  $0^\circ$  (upper left),  $60^\circ$  (upper right),  $120^\circ$  (lower left), and  $180^\circ$  (lower right). Upper panel is for fitting all albedos, lower panel is for fitting an albedo range.

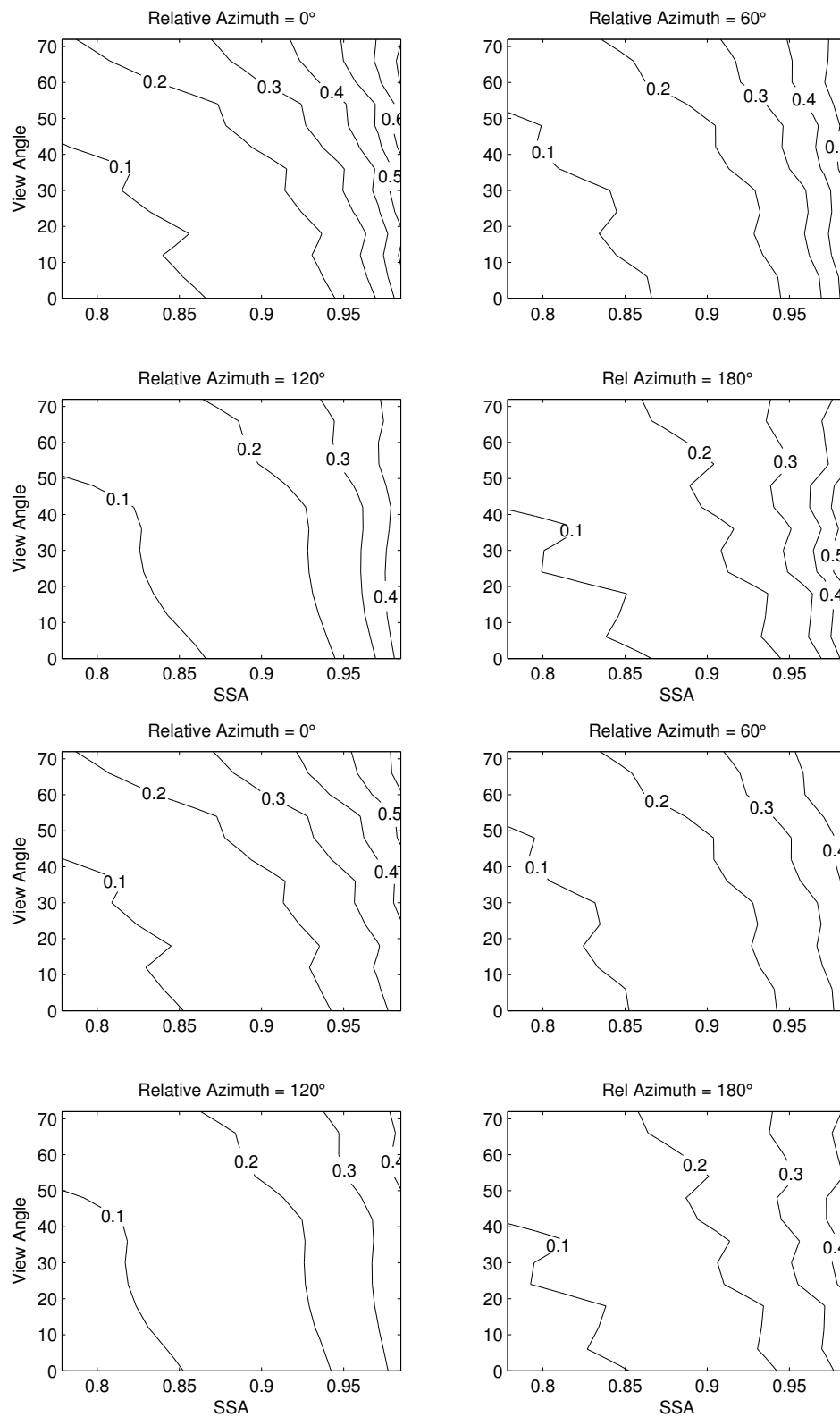


Figure A.13: Critical reflectance LUT for the coarse aerosol model at  $0.553 \mu\text{m}$  for  $\text{SZA} = 36^\circ$ , displayed as a function of satellite view and SSA for relative azimuth =  $0^\circ$  (upper left),  $60^\circ$  (upper right),  $120^\circ$  (lower left), and  $180^\circ$  (lower right). Upper panel is for fitting all albedos, lower panel is for fitting an albedo range.

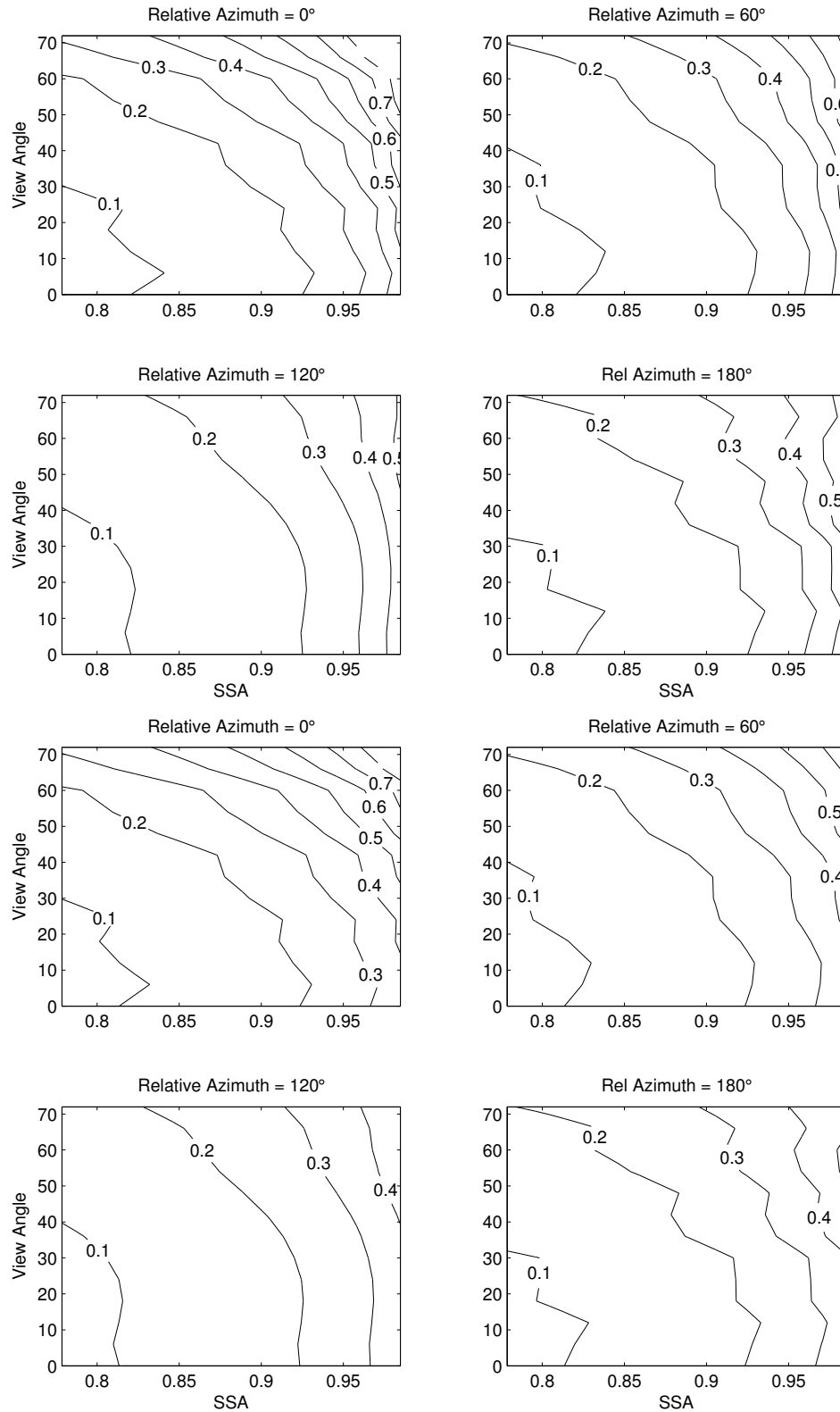


Figure A.14: Critical reflectance LUT for the coarse aerosol model at  $0.553 \mu\text{m}$  for  $\text{SZA} = 48^\circ$ , displayed as a function of satellite view and SSA for relative azimuth =  $0^\circ$  (upper left),  $60^\circ$  (upper right),  $120^\circ$  (lower left), and  $180^\circ$  (lower right). Upper panel is for fitting all albedos, lower panel is for fitting an albedo range.

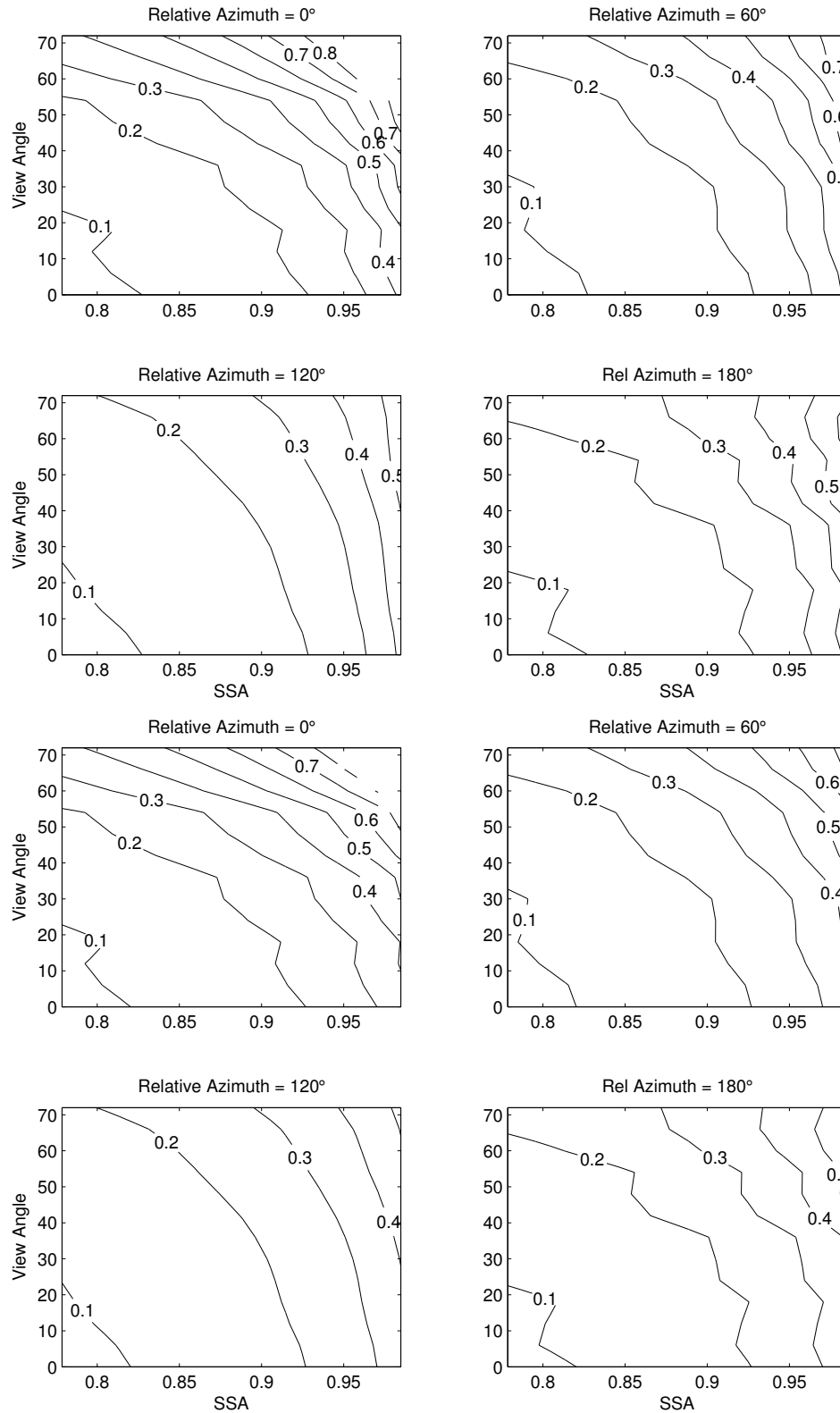


Figure A.15: Critical reflectance LUT for the coarse aerosol model at  $0.553 \mu\text{m}$  for  $\text{SZA} = 54^\circ$ , displayed as a function of satellite view and SSA for relative azimuth =  $0^\circ$  (upper left),  $60^\circ$  (upper right),  $120^\circ$  (lower left), and  $180^\circ$  (lower right). Upper panel is for fitting all albedos, lower panel is for fitting an albedo range.

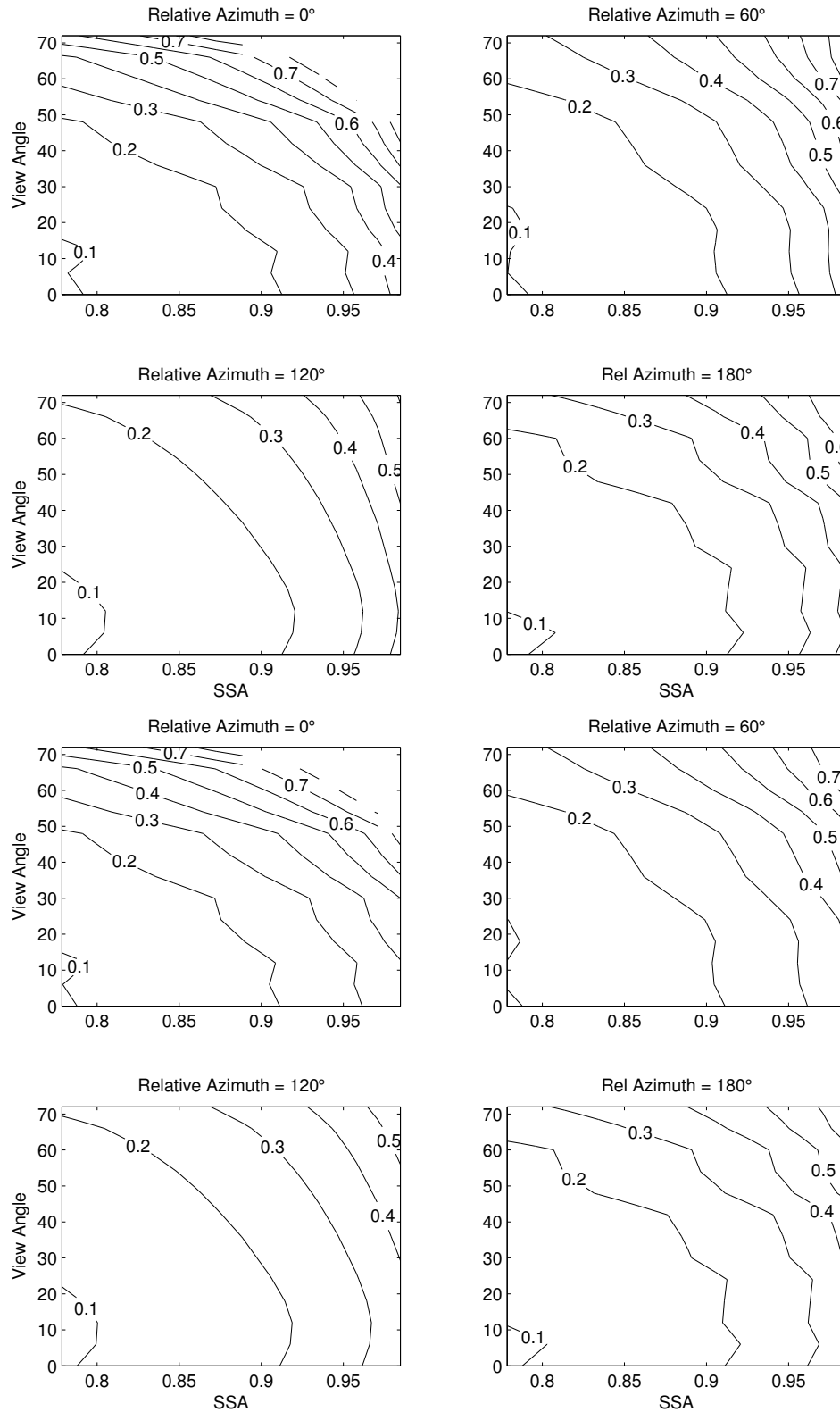


Figure A.16: Critical reflectance LUT for the coarse aerosol model at  $0.553 \mu\text{m}$  for  $\text{SZA} = 60^\circ$ , displayed as a function of satellite view and SSA for relative azimuth =  $0^\circ$  (upper left),  $60^\circ$  (upper right),  $120^\circ$  (lower left), and  $180^\circ$  (lower right). Upper panel is for fitting all albedos, lower panel is for fitting an albedo range.

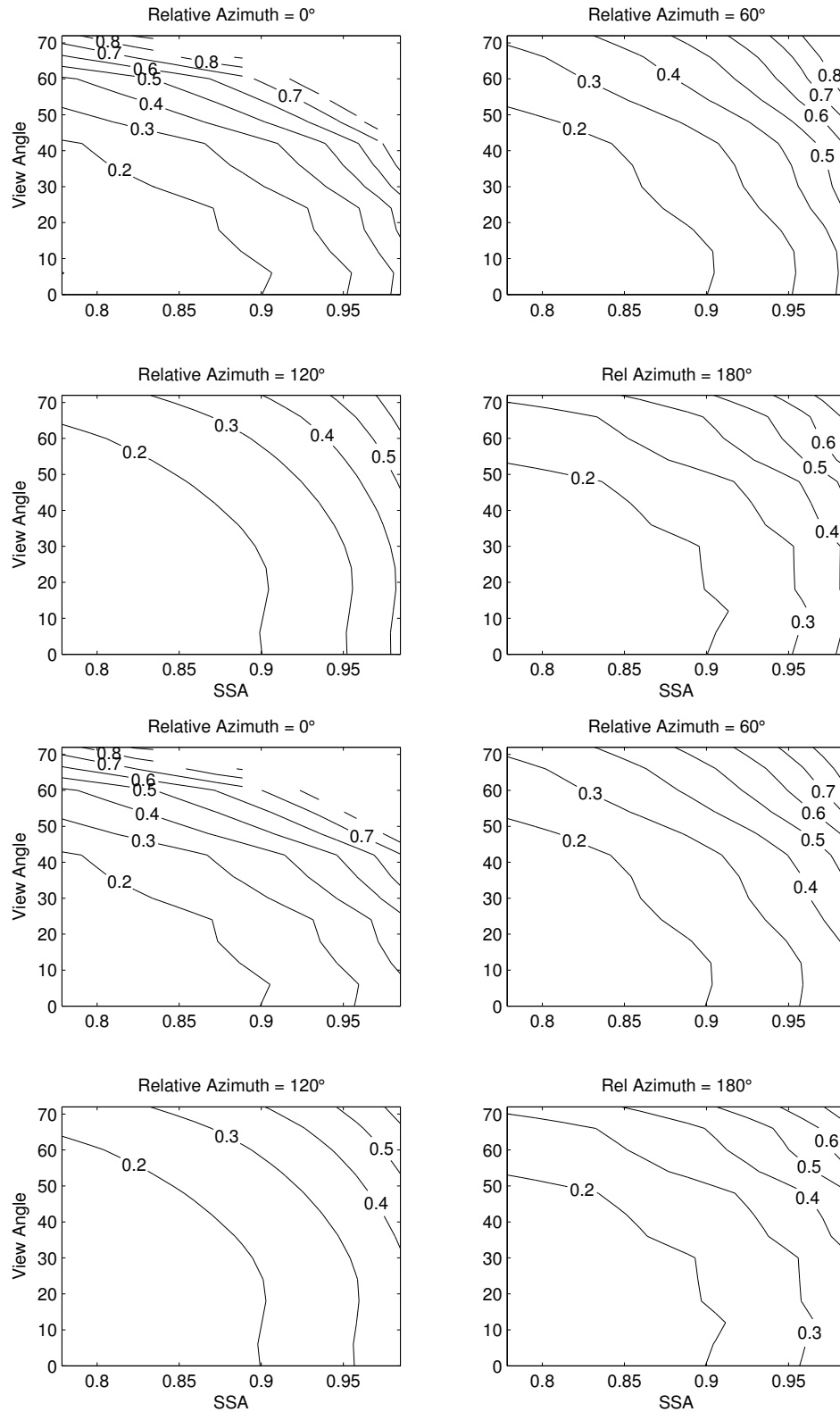


Figure A.17: Critical reflectance LUT for the coarse aerosol model at  $0.553 \mu\text{m}$  for  $\text{SZA} = 66^\circ$ , displayed as a function of satellite view and SSA for relative azimuth =  $0^\circ$  (upper left),  $60^\circ$  (upper right),  $120^\circ$  (lower left), and  $180^\circ$  (lower right). Upper panel is for fitting all albedos, lower panel is for fitting an albedo range.

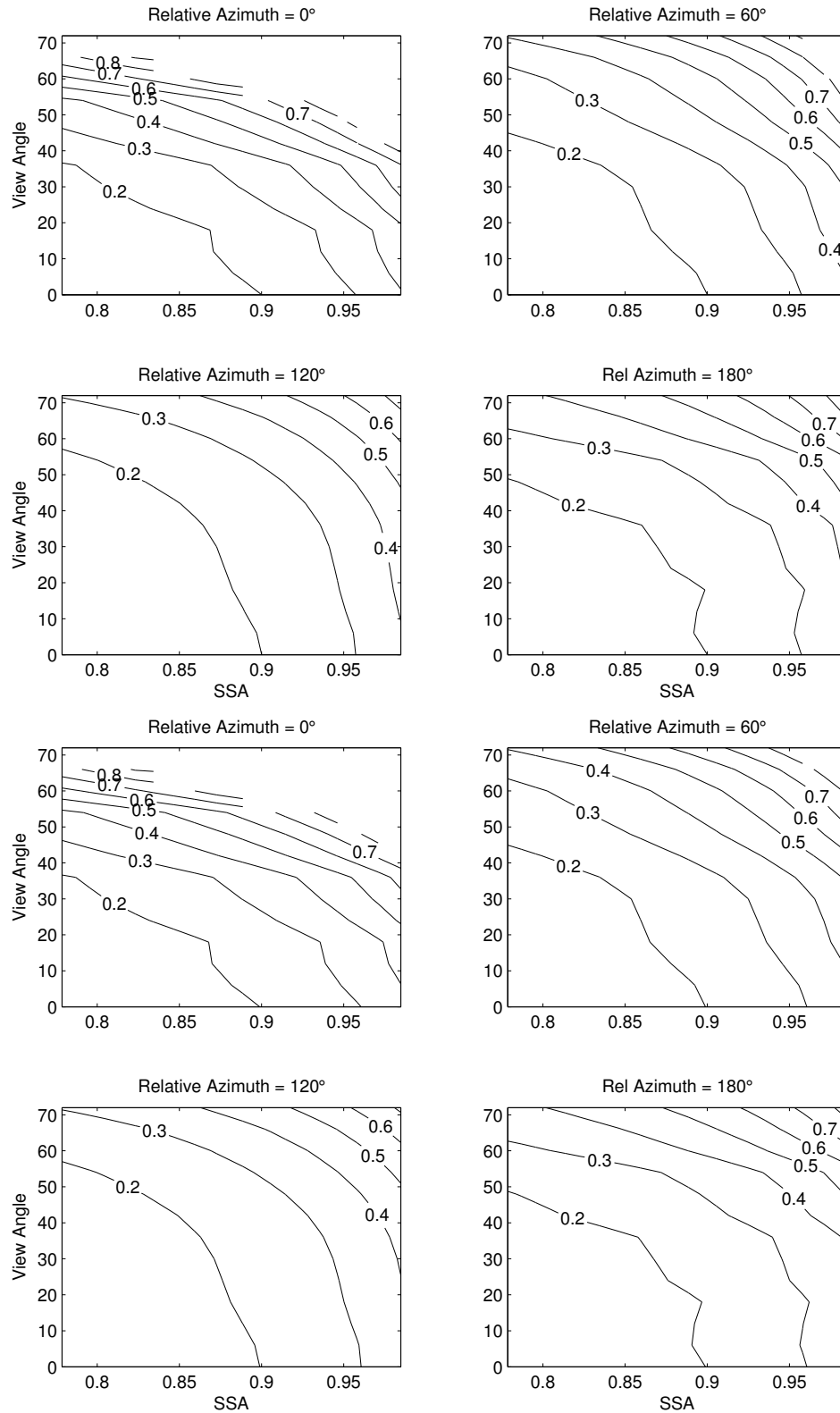


Figure A.18: Critical reflectance LUT for the coarse aerosol model at  $0.553 \mu\text{m}$  for  $\text{SZA} = 72^\circ$ , displayed as a function of satellite view and SSA for relative azimuth =  $0^\circ$  (upper left),  $60^\circ$  (upper right),  $120^\circ$  (lower left), and  $180^\circ$  (lower right). Upper panel is for fitting all albedos, lower panel is for fitting an albedo range.

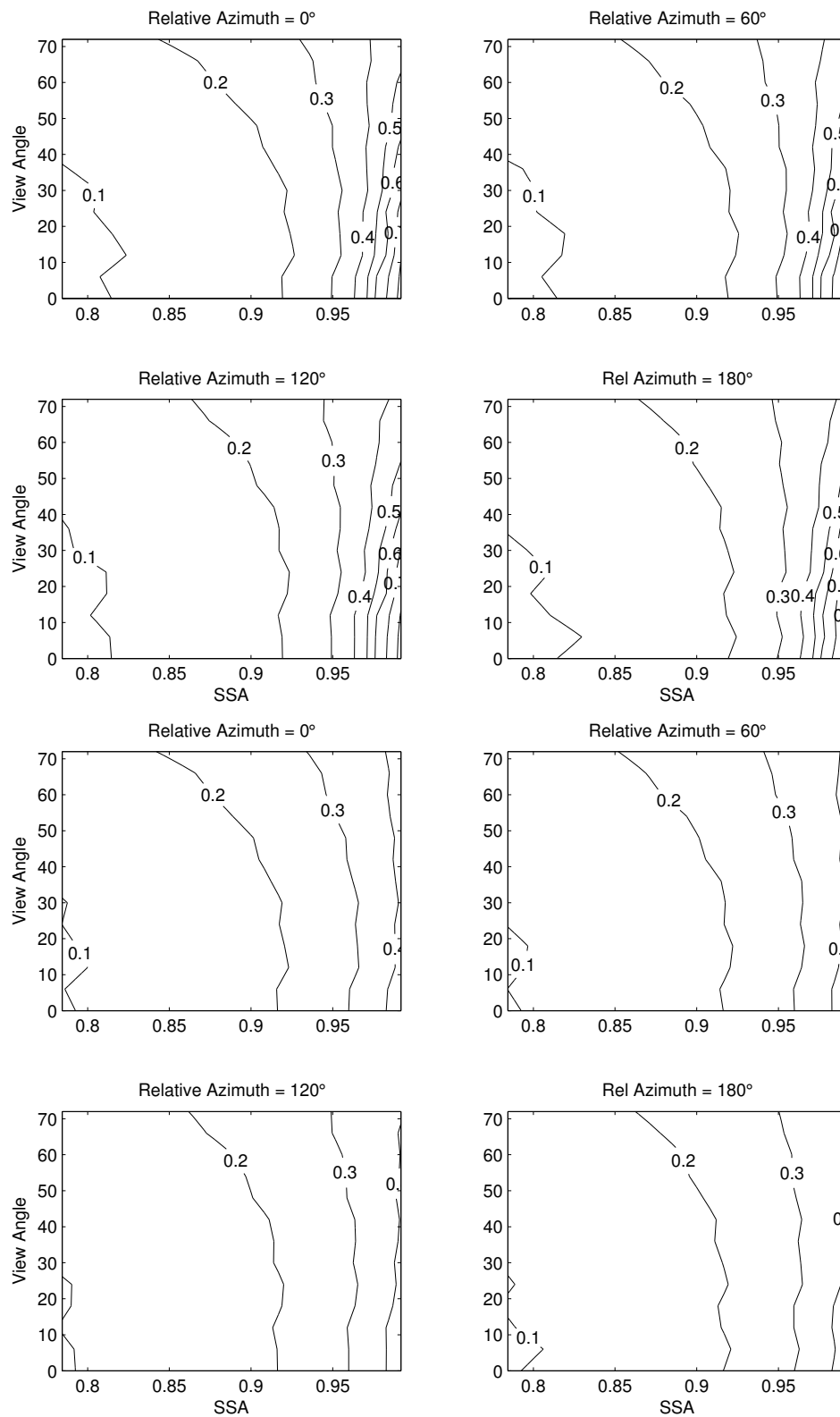


Figure A.19: Critical reflectance LUT for the bimodal spheroid aerosol model at  $0.553 \mu\text{m}$  for  $\text{SZA} = 6^\circ$ , displayed as a function of satellite view and SSA for relative azimuth =  $0^\circ$  (upper left),  $60^\circ$  (upper right),  $120^\circ$  (lower left), and  $180^\circ$  (lower right). Upper panel is for fitting all albedos, lower panel is for fitting an albedo range.

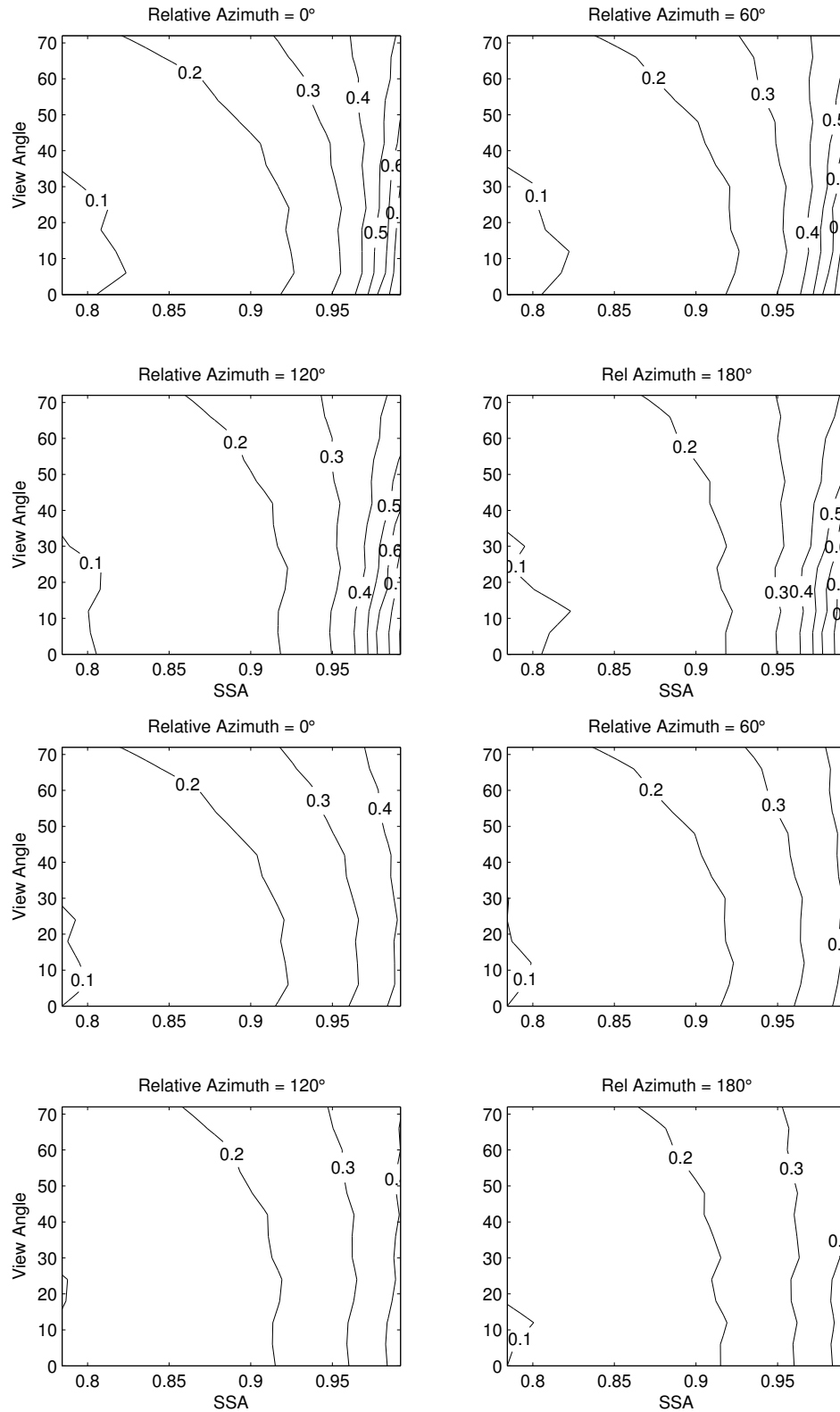


Figure A.20: Critical reflectance LUT for the bimodal spheroid aerosol model at  $0.553 \mu\text{m}$  for  $\text{SZA} = 12^\circ$ , displayed as a function of satellite view and SSA for relative azimuth =  $0^\circ$  (upper left),  $60^\circ$  (upper right),  $120^\circ$  (lower left), and  $180^\circ$  (lower right). Upper panel is for fitting all albedos, lower panel is for fitting an albedo range.

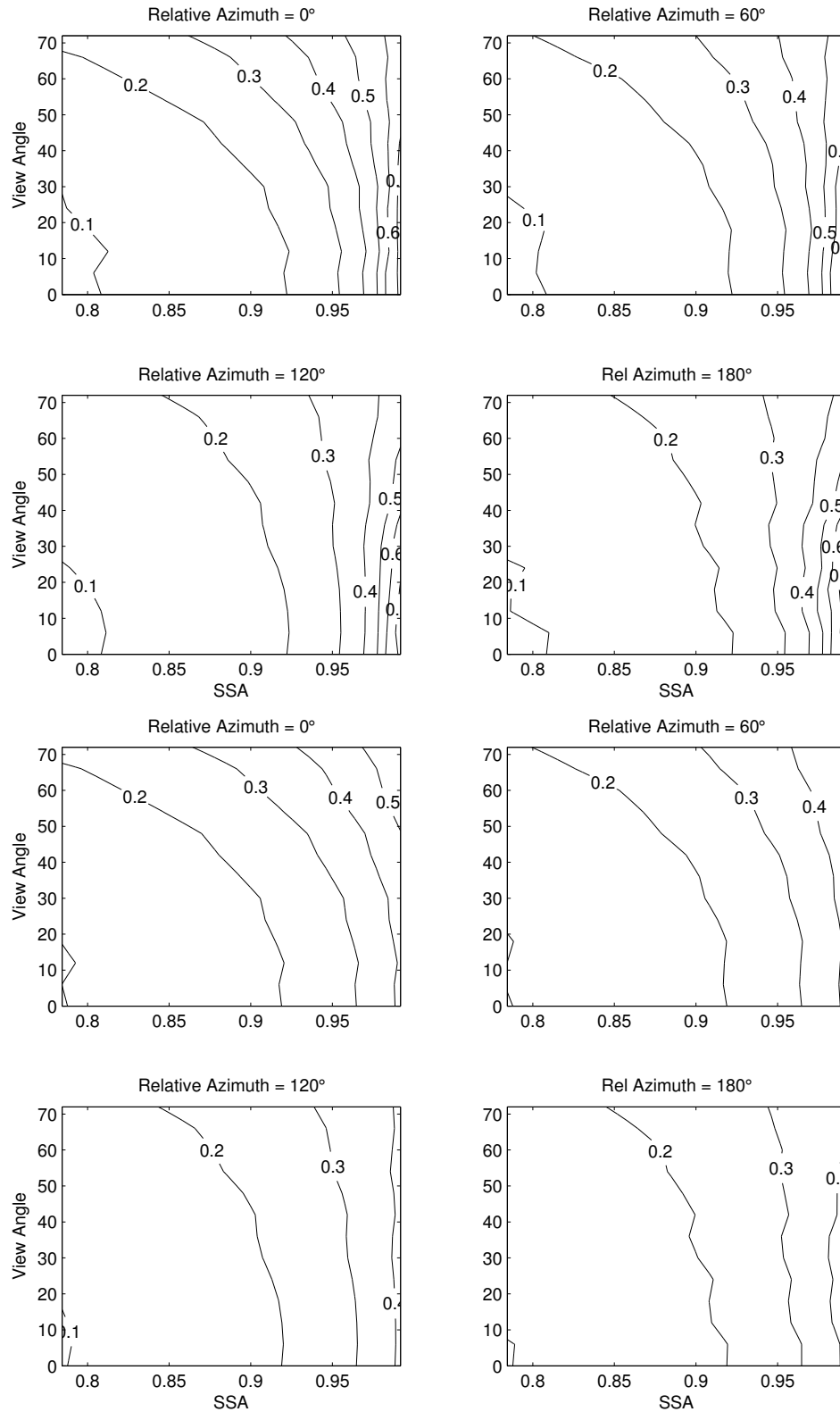


Figure A.21: Critical reflectance LUT for the bimodal spheroid aerosol model at  $0.553 \mu\text{m}$  for  $\text{SZA} = 24^\circ$ , displayed as a function of satellite view and SSA for relative azimuth =  $0^\circ$  (upper left),  $60^\circ$  (upper right),  $120^\circ$  (lower left), and  $180^\circ$  (lower right). Upper panel is for fitting all albedos, lower panel is for fitting an albedo range.

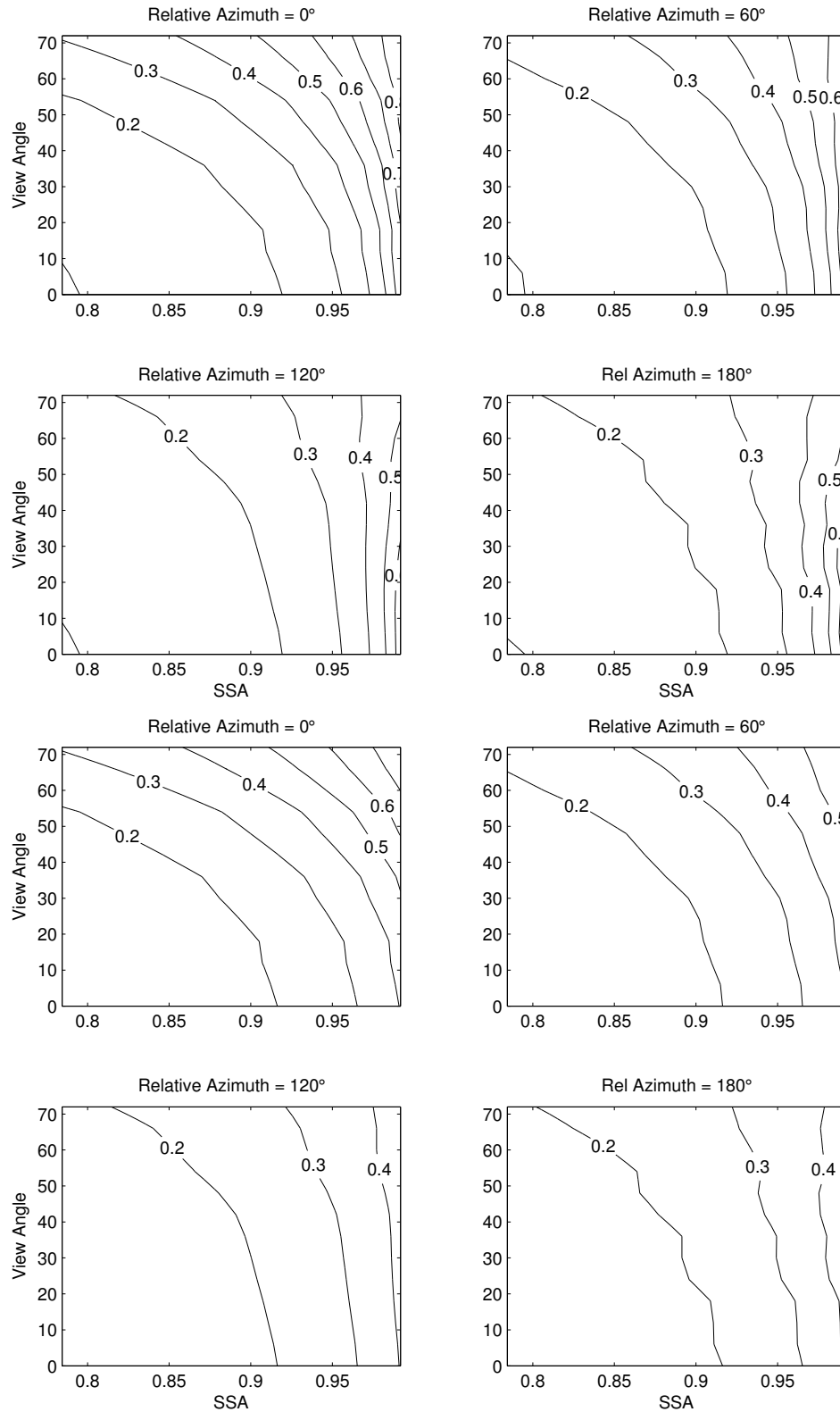


Figure A.22: Critical reflectance LUT for the bimodal spheroid aerosol model at  $0.553 \mu\text{m}$  for  $\text{SZA} = 36^\circ$ , displayed as a function of satellite view and SSA for relative azimuth =  $0^\circ$  (upper left),  $60^\circ$  (upper right),  $120^\circ$  (lower left), and  $180^\circ$  (lower right). Upper panel is for fitting all albedos, lower panel is for fitting an albedo range.

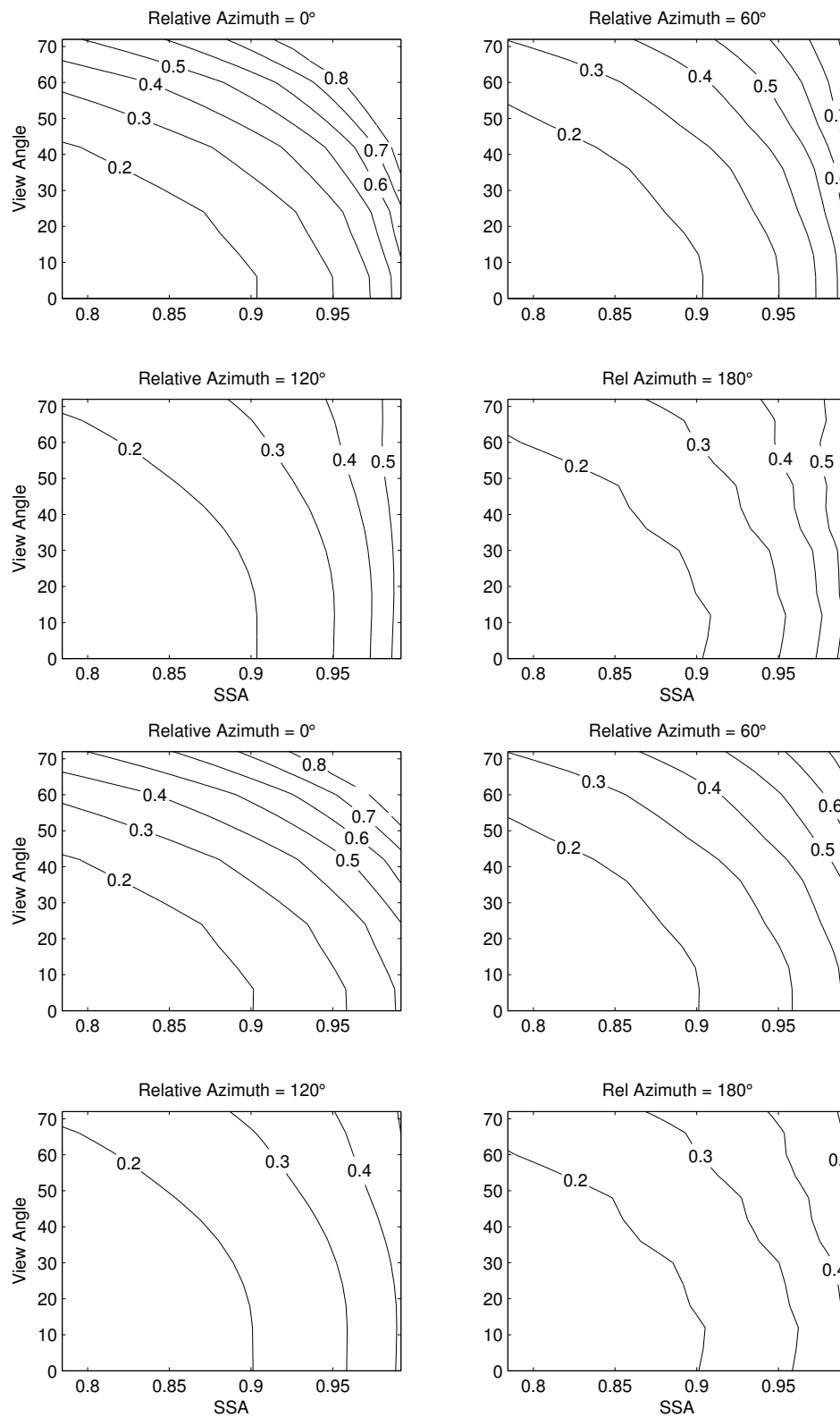


Figure A.23: Critical reflectance LUT for the bimodal spheroid aerosol model at  $0.553 \mu\text{m}$  for  $\text{SZA} = 48^\circ$ , displayed as a function of satellite view and SSA for relative azimuth =  $0^\circ$  (upper left),  $60^\circ$  (upper right),  $120^\circ$  (lower left), and  $180^\circ$  (lower right). Upper panel is for fitting all albedos, lower panel is for fitting an albedo range.

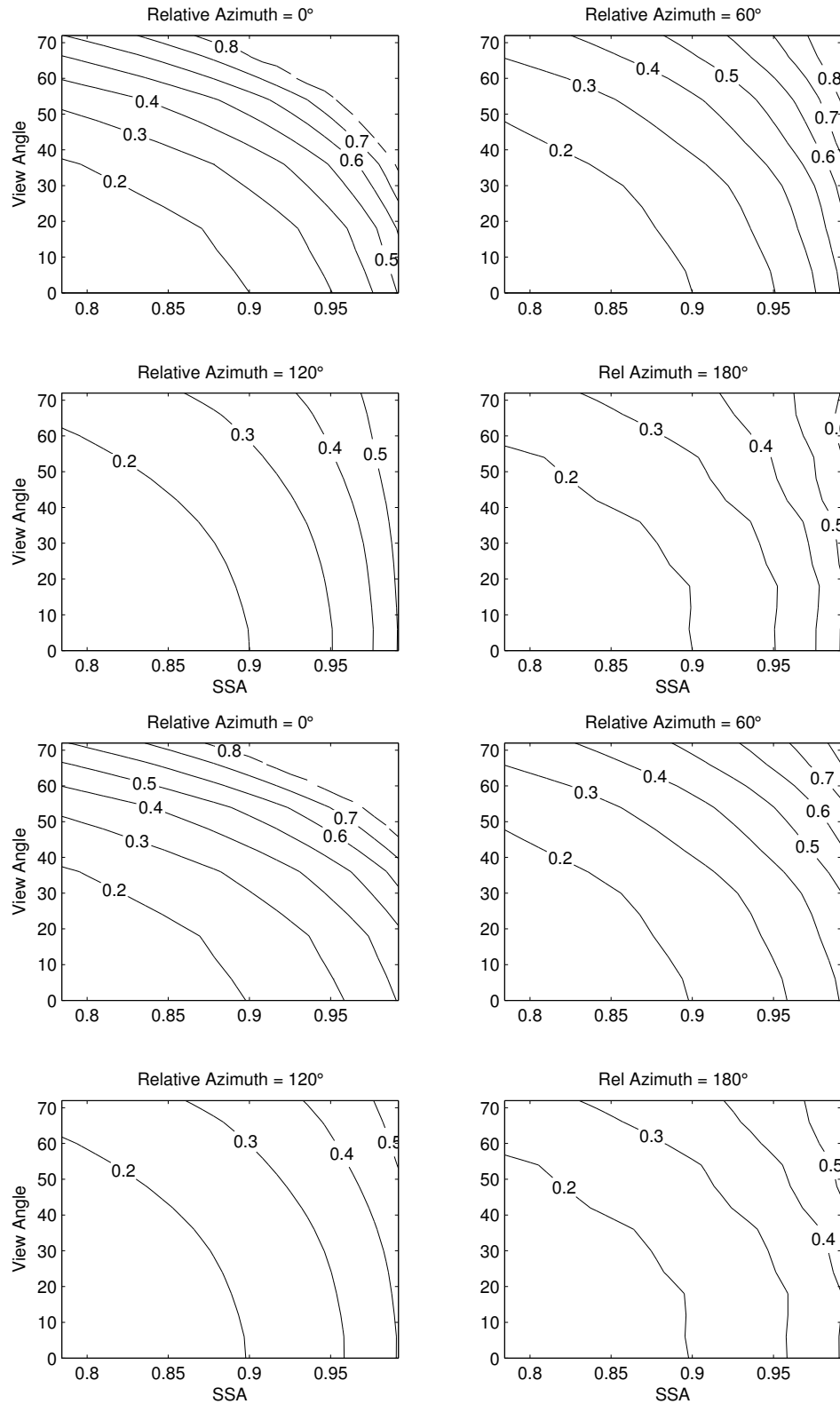


Figure A.24: Critical reflectance LUT for the bimodal spheroid aerosol model at  $0.553 \mu\text{m}$  for  $\text{SZA} = 54^\circ$ , displayed as a function of satellite view and SSA for relative azimuth =  $0^\circ$  (upper left),  $60^\circ$  (upper right),  $120^\circ$  (lower left), and  $180^\circ$  (lower right). Upper panel is for fitting all albedos, lower panel is for fitting an albedo range.

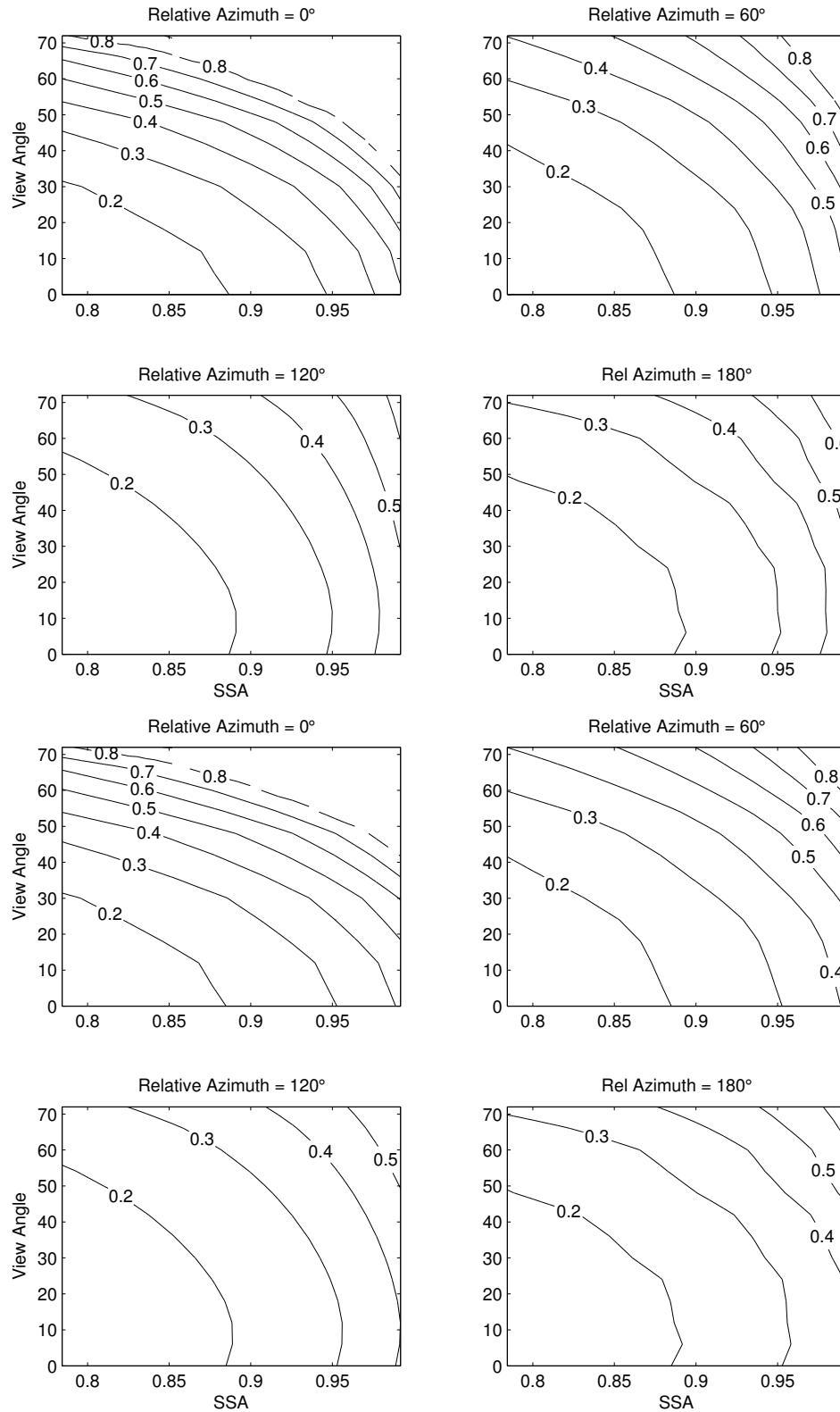


Figure A.25: Critical reflectance LUT for the bimodal spheroid aerosol model at  $0.553 \mu\text{m}$  for  $\text{SZA} = 60^\circ$ , displayed as a function of satellite view and SSA for relative azimuth =  $0^\circ$  (upper left),  $60^\circ$  (upper right),  $120^\circ$  (lower left), and  $180^\circ$  (lower right). Upper panel is for fitting all albedos, lower panel is for fitting an albedo range.

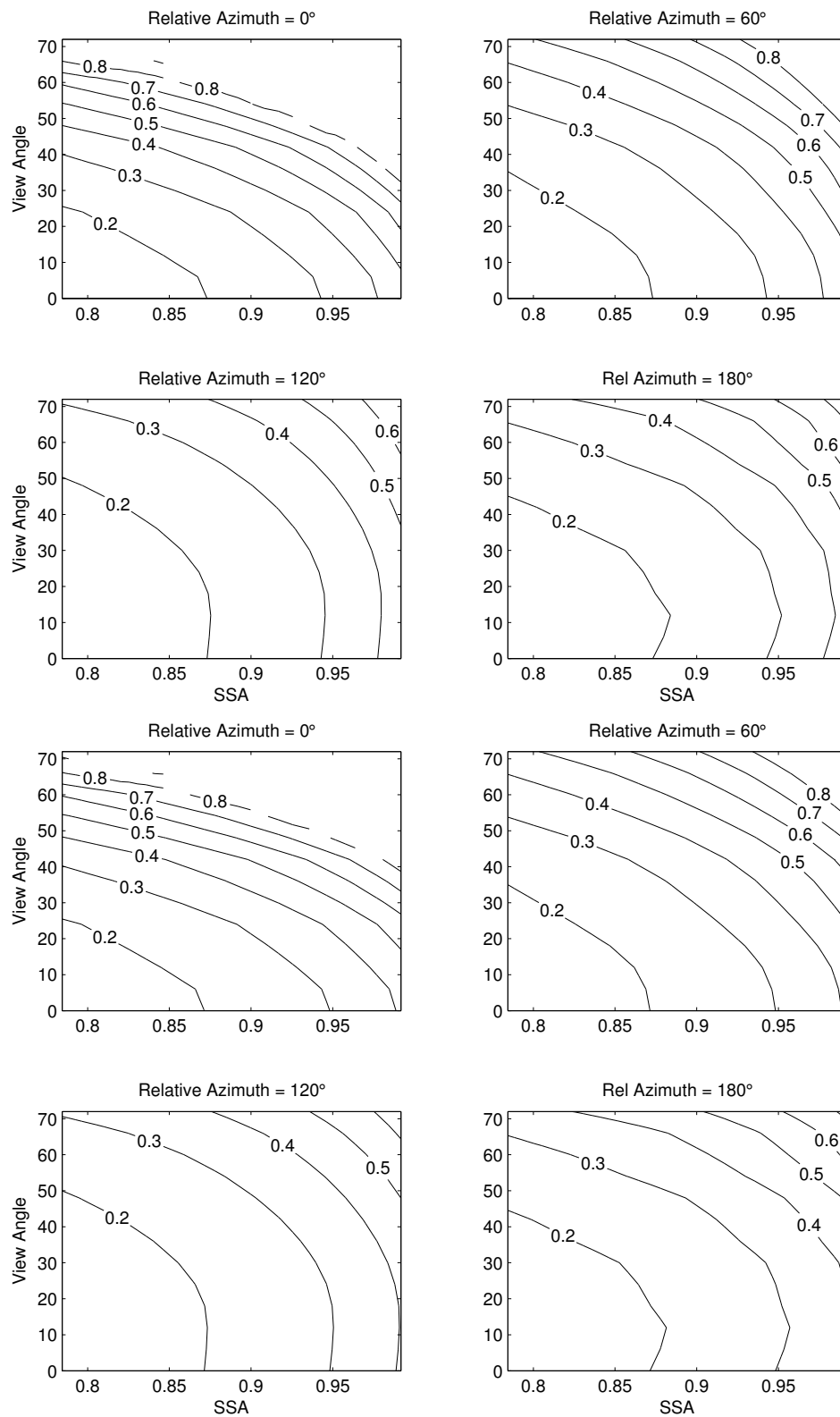


Figure A.26: Critical reflectance LUT for the bimodal spheroid aerosol model at  $0.553 \mu\text{m}$  for  $\text{SZA} = 66^\circ$ , displayed as a function of satellite view and SSA for relative azimuth =  $0^\circ$  (upper left),  $60^\circ$  (upper right),  $120^\circ$  (lower left), and  $180^\circ$  (lower right). Upper panel is for fitting all albedos, lower panel is for fitting an albedo range.

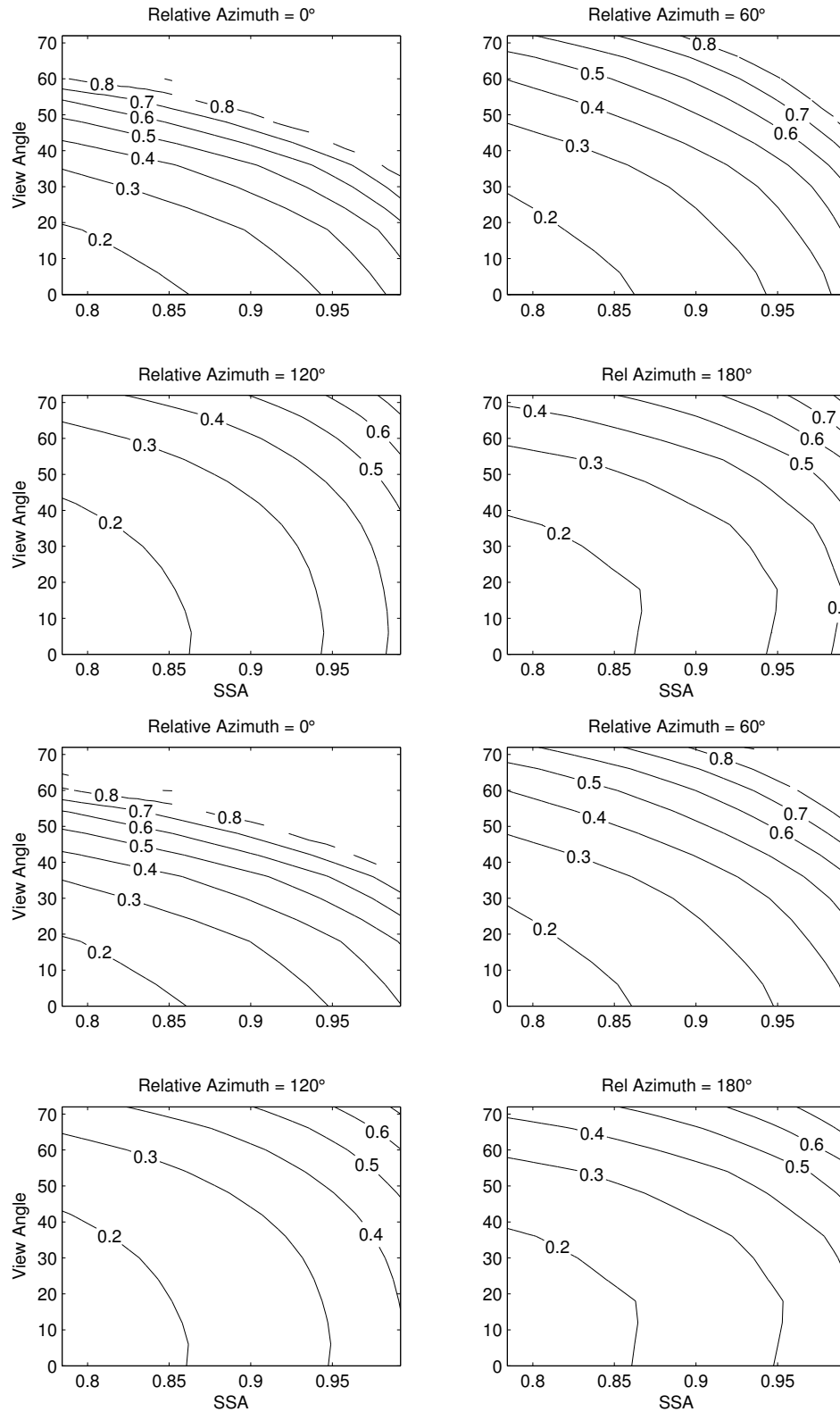


Figure A.27: Critical reflectance LUT for the bimodal spheroid aerosol model at  $0.553 \mu\text{m}$  for  $\text{SZA} = 72^\circ$ , displayed as a function of satellite view and SSA for relative azimuth =  $0^\circ$  (upper left),  $60^\circ$  (upper right),  $120^\circ$  (lower left), and  $180^\circ$  (lower right). Upper panel is for fitting all albedos, lower panel is for fitting an albedo range.

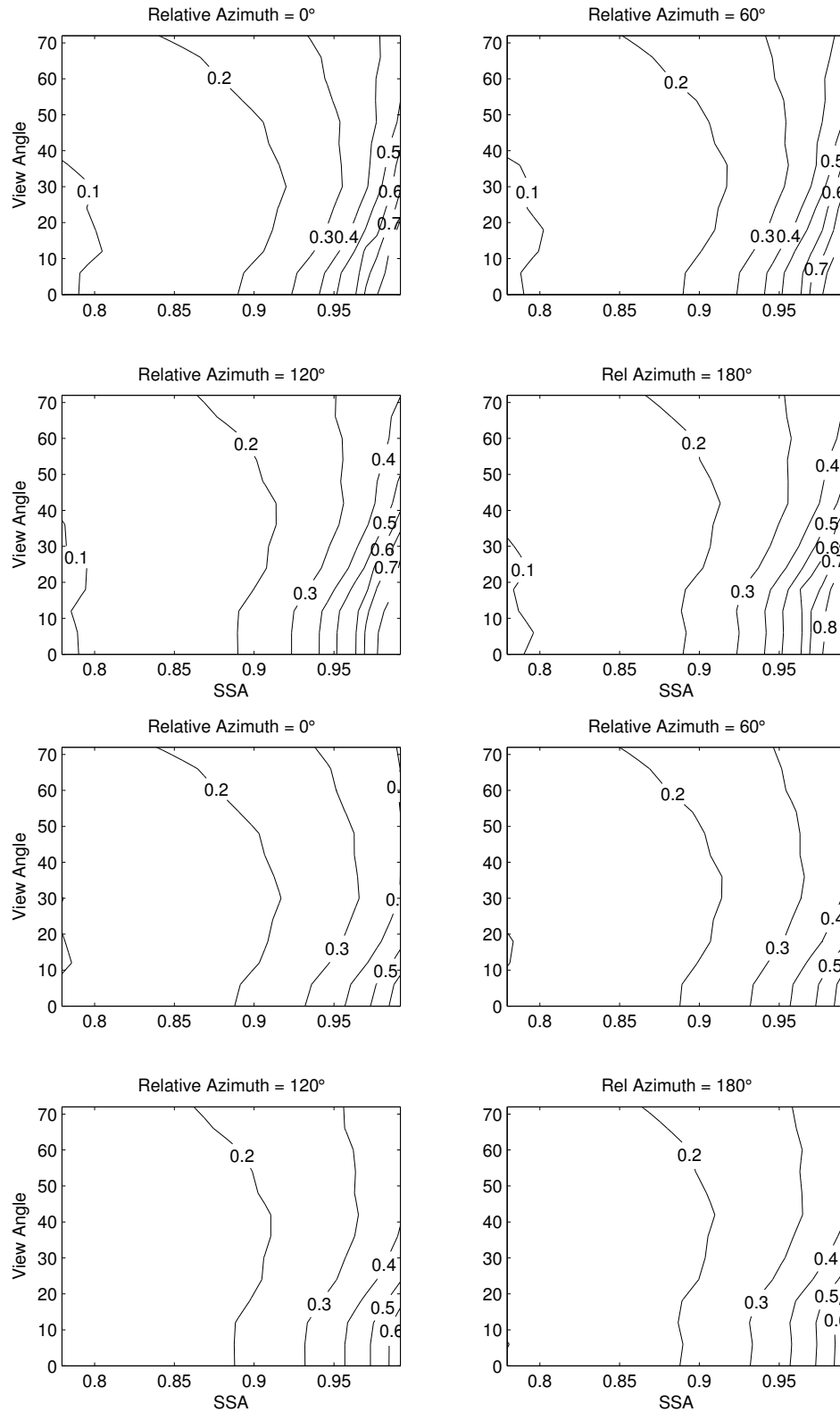


Figure A.28: Critical reflectance LUT for the bimodal sphere aerosol model at  $0.553 \mu\text{m}$  for  $\text{SZA} = 6^\circ$ , displayed as a function of satellite view and SSA for relative azimuth =  $0^\circ$  (upper left),  $60^\circ$  (upper right),  $120^\circ$  (lower left), and  $180^\circ$  (lower right). Upper panel is for fitting all albedos, lower panel is for fitting an albedo range.

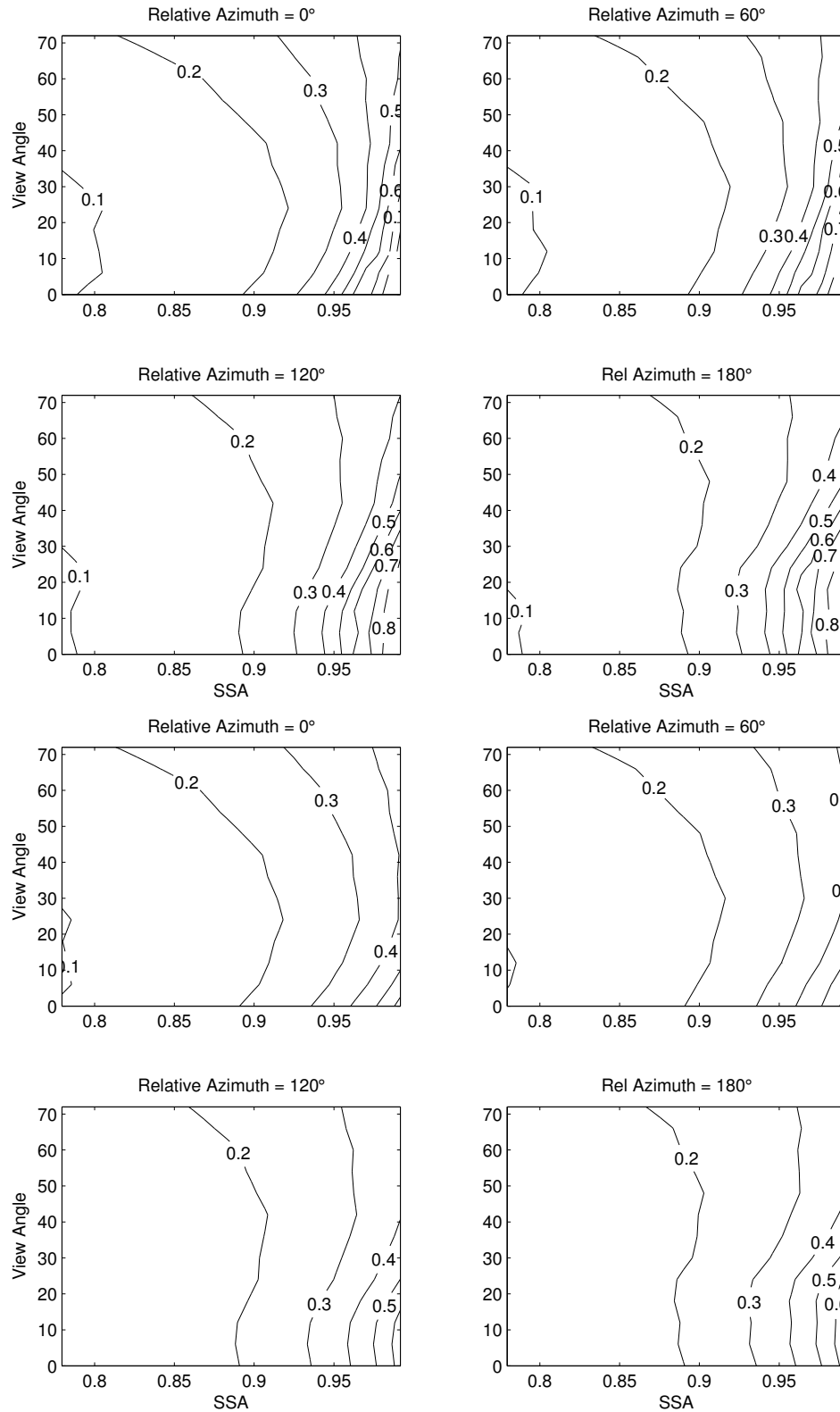


Figure A.29: Critical reflectance LUT for the bimodal sphere aerosol model at  $0.553 \mu\text{m}$  for  $\text{SZA} = 12^\circ$ , displayed as a function of satellite view and SSA for relative azimuth =  $0^\circ$  (upper left),  $60^\circ$  (upper right),  $120^\circ$  (lower left), and  $180^\circ$  (lower right). Upper panel is for fitting all albedos, lower panel is for fitting an albedo range.

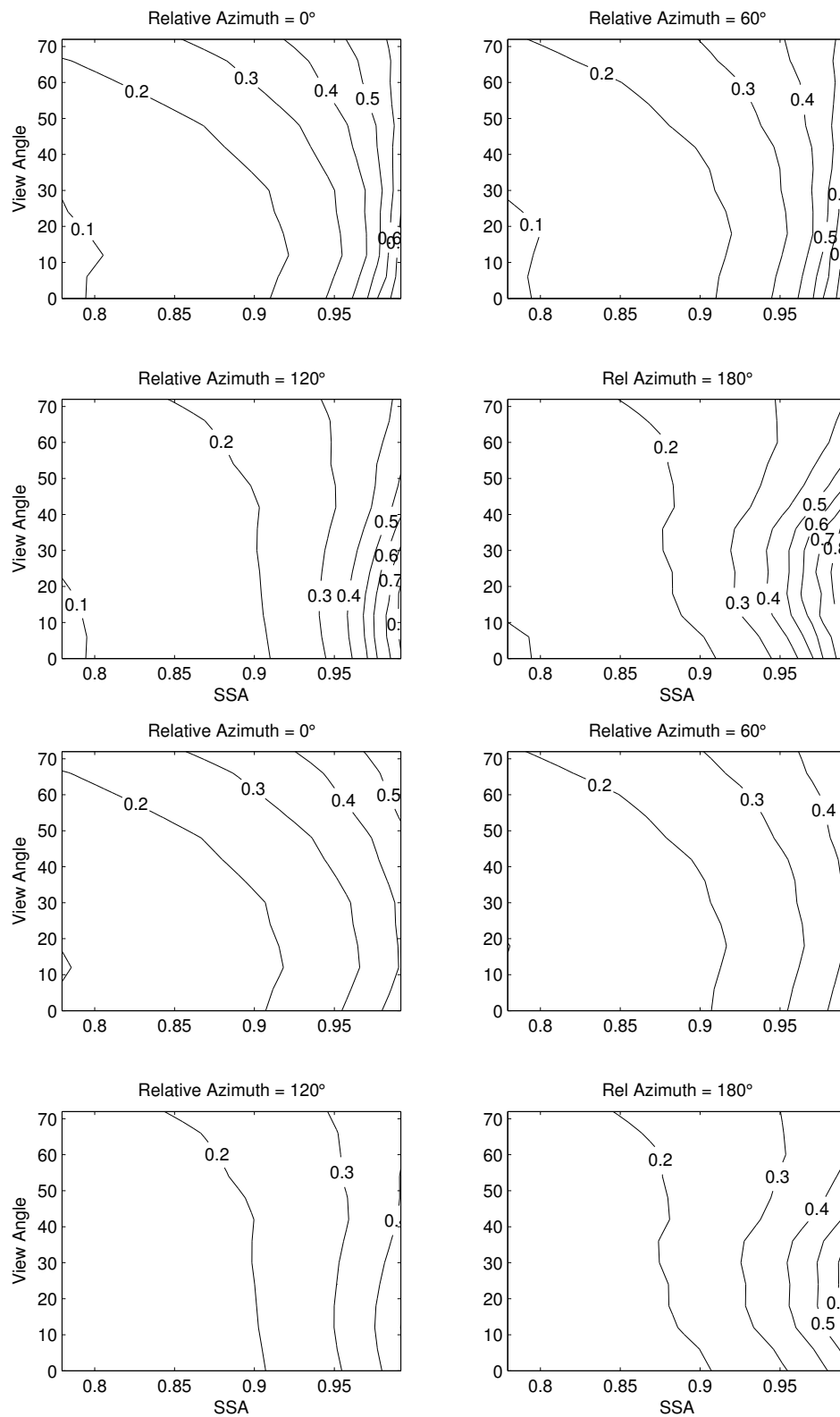


Figure A.30: Critical reflectance LUT for the bimodal sphere aerosol model at  $0.553 \mu\text{m}$  for  $\text{SZA} = 24^\circ$ , displayed as a function of satellite view and SSA for relative azimuth =  $0^\circ$  (upper left),  $60^\circ$  (upper right),  $120^\circ$  (lower left), and  $180^\circ$  (lower right). Upper panel is for fitting all albedos, lower panel is for fitting an albedo range.

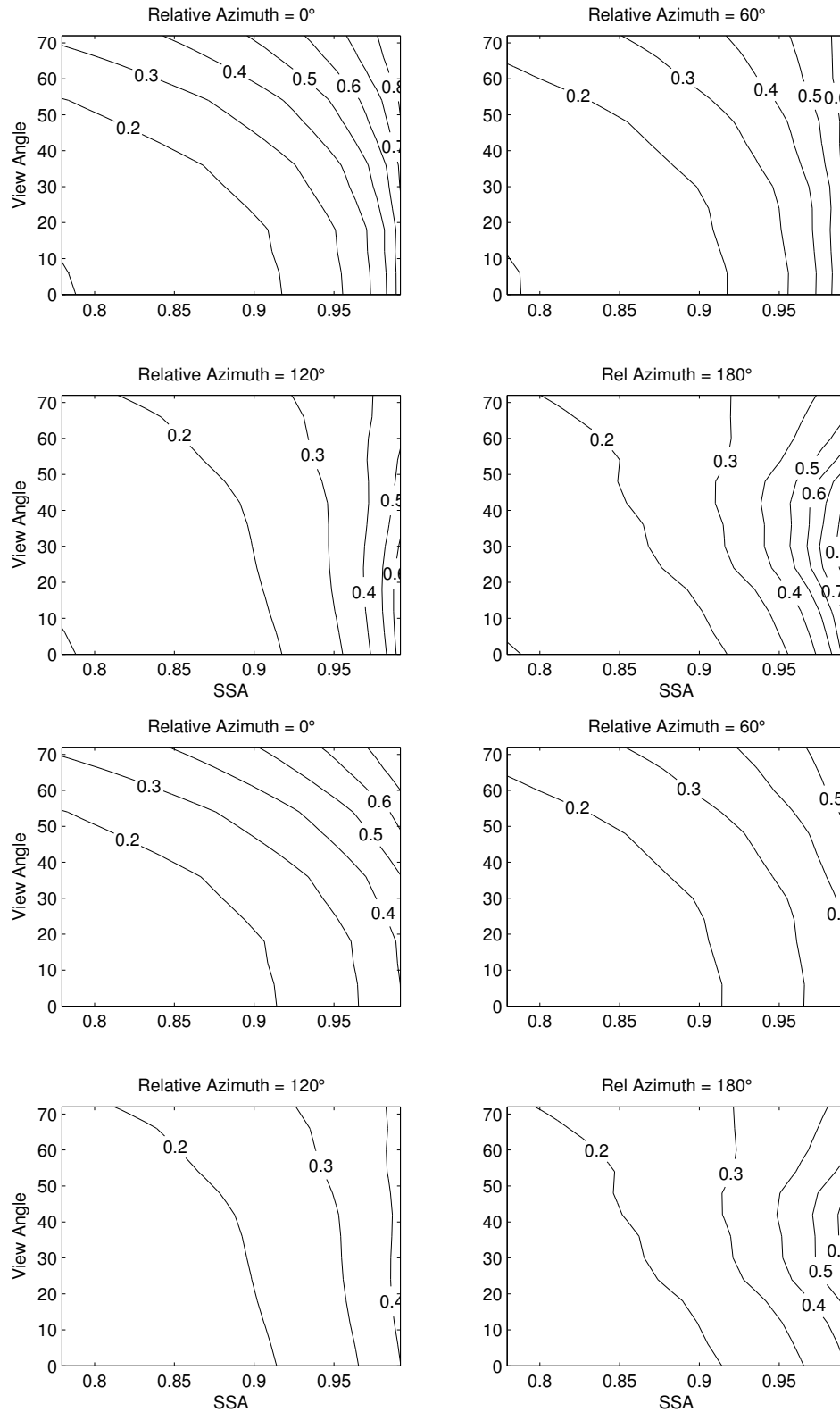


Figure A.31: Critical reflectance LUT for the bimodal sphere aerosol model at  $0.553 \mu\text{m}$  for  $\text{SZA} = 36^\circ$ , displayed as a function of satellite view and SSA for relative azimuth =  $0^\circ$  (upper left),  $60^\circ$  (upper right),  $120^\circ$  (lower left), and  $180^\circ$  (lower right). Upper panel is for fitting all albedos, lower panel is for fitting an albedo range.

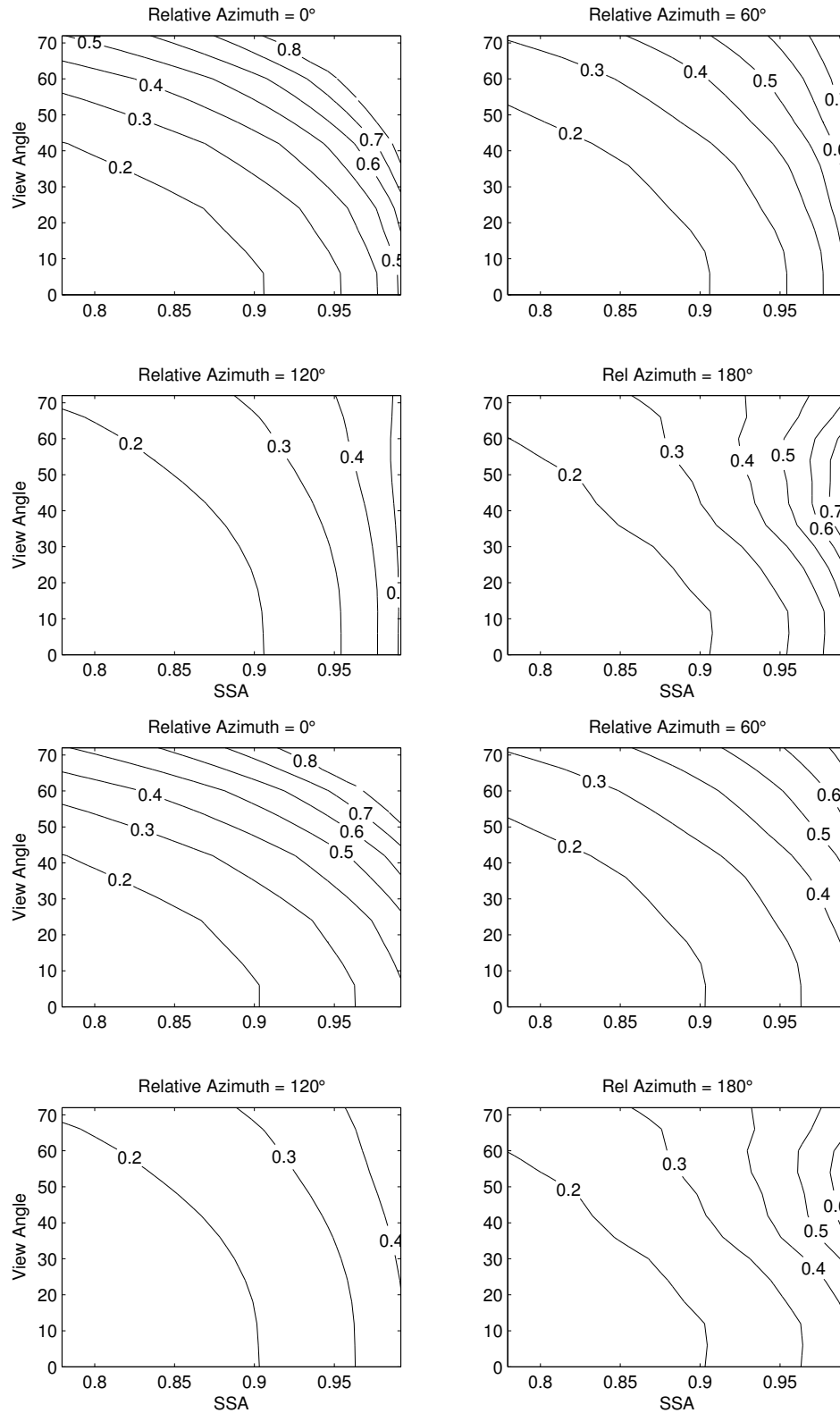


Figure A.32: Critical reflectance LUT for the bimodal sphere aerosol model at  $0.553 \mu\text{m}$  for  $\text{SZA} = 48^\circ$ , displayed as a function of satellite view and SSA for relative azimuth =  $0^\circ$  (upper left),  $60^\circ$  (upper right),  $120^\circ$  (lower left), and  $180^\circ$  (lower right). Upper panel is for fitting all albedos, lower panel is for fitting an albedo range.

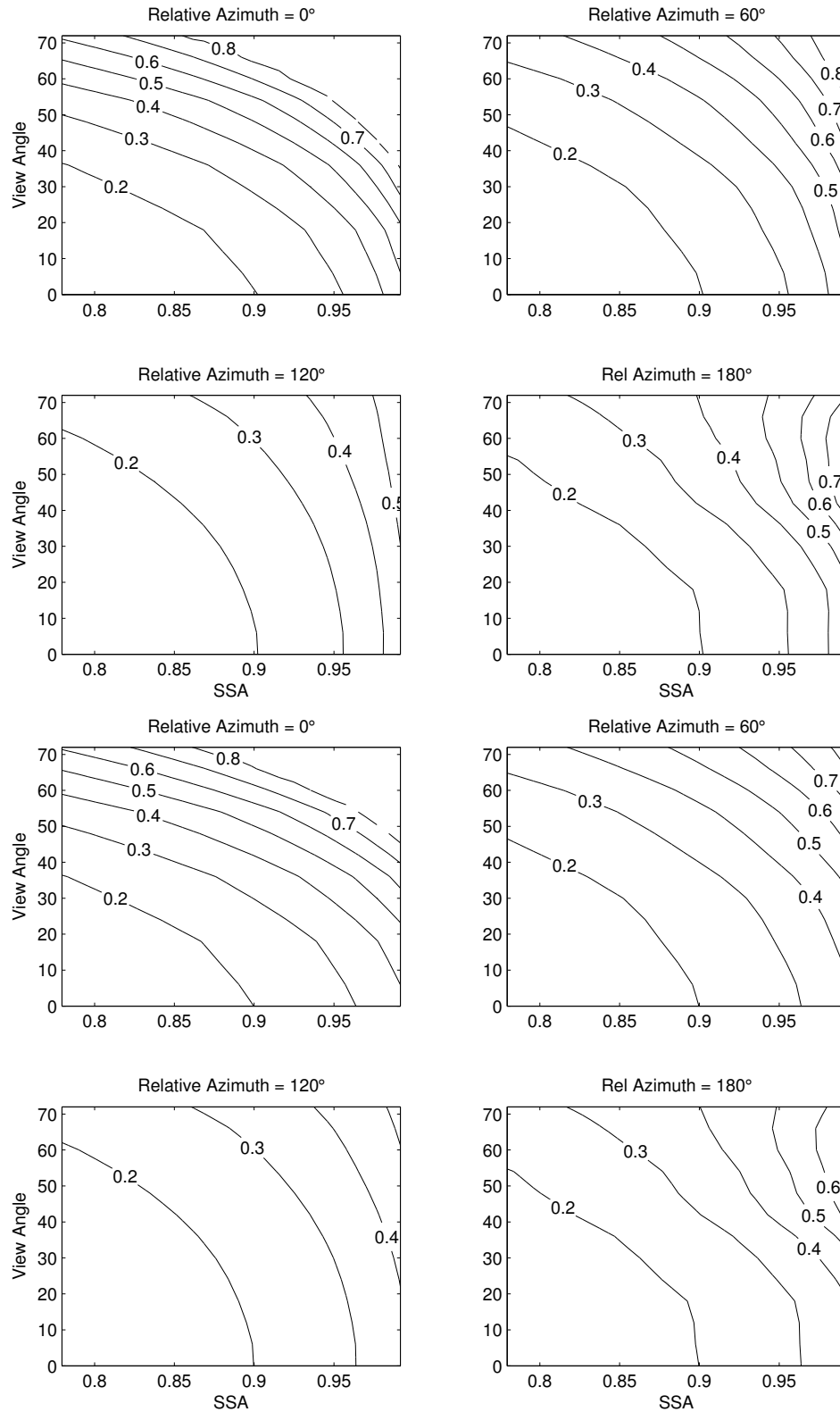


Figure A.33: Critical reflectance LUT for the bimodal sphere aerosol model at  $0.553 \mu\text{m}$  for  $\text{SZA} = 54^\circ$ , displayed as a function of satellite view and SSA for relative azimuth =  $0^\circ$  (upper left),  $60^\circ$  (upper right),  $120^\circ$  (lower left), and  $180^\circ$  (lower right). Upper panel is for fitting all albedos, lower panel is for fitting an albedo range.

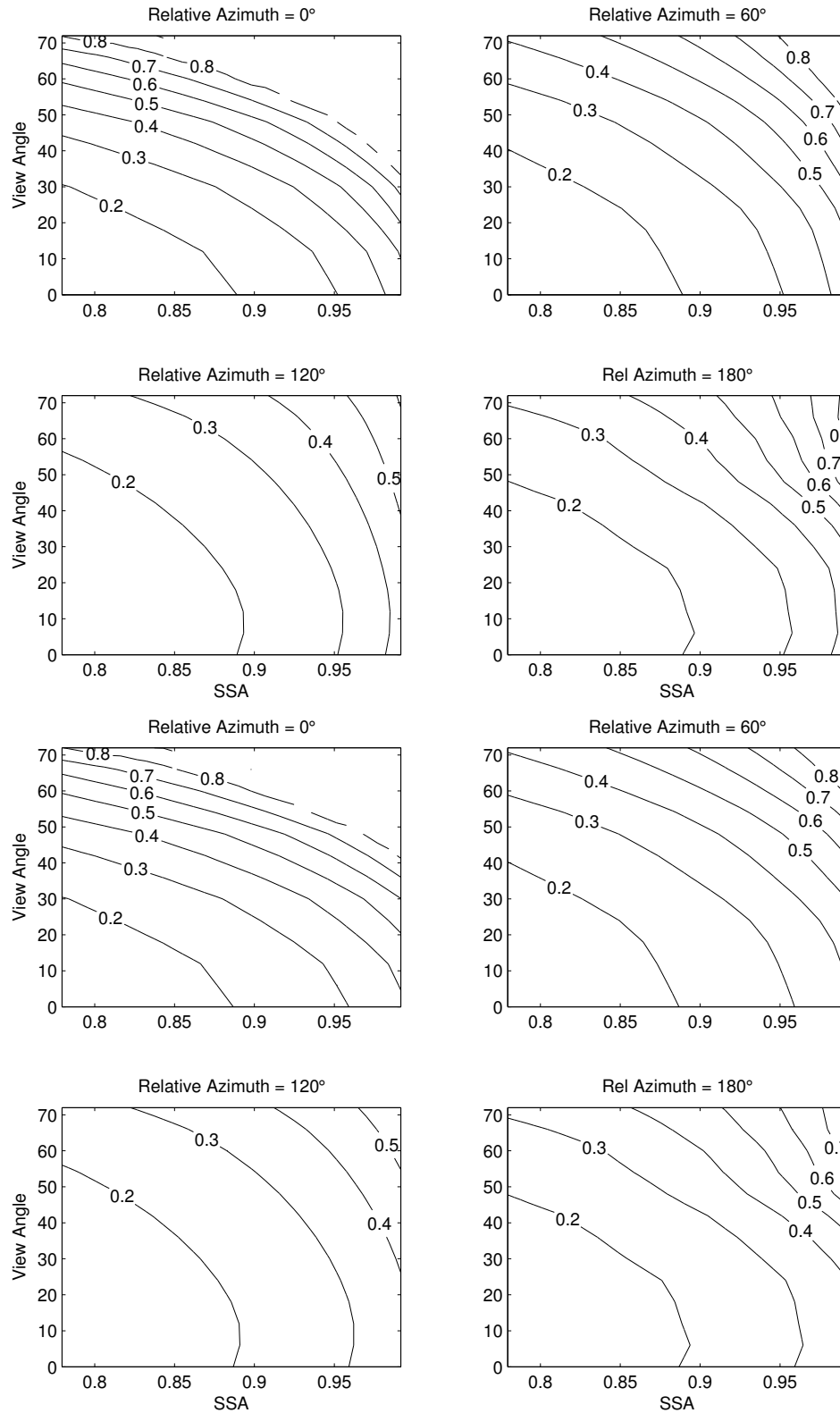


Figure A.34: Critical reflectance LUT for the bimodal sphere aerosol model at  $0.553 \mu\text{m}$  for  $\text{SZA} = 60^\circ$ , displayed as a function of satellite view and SSA for relative azimuth =  $0^\circ$  (upper left),  $60^\circ$  (upper right),  $120^\circ$  (lower left), and  $180^\circ$  (lower right). Upper panel is for fitting all albedos, lower panel is for fitting an albedo range.

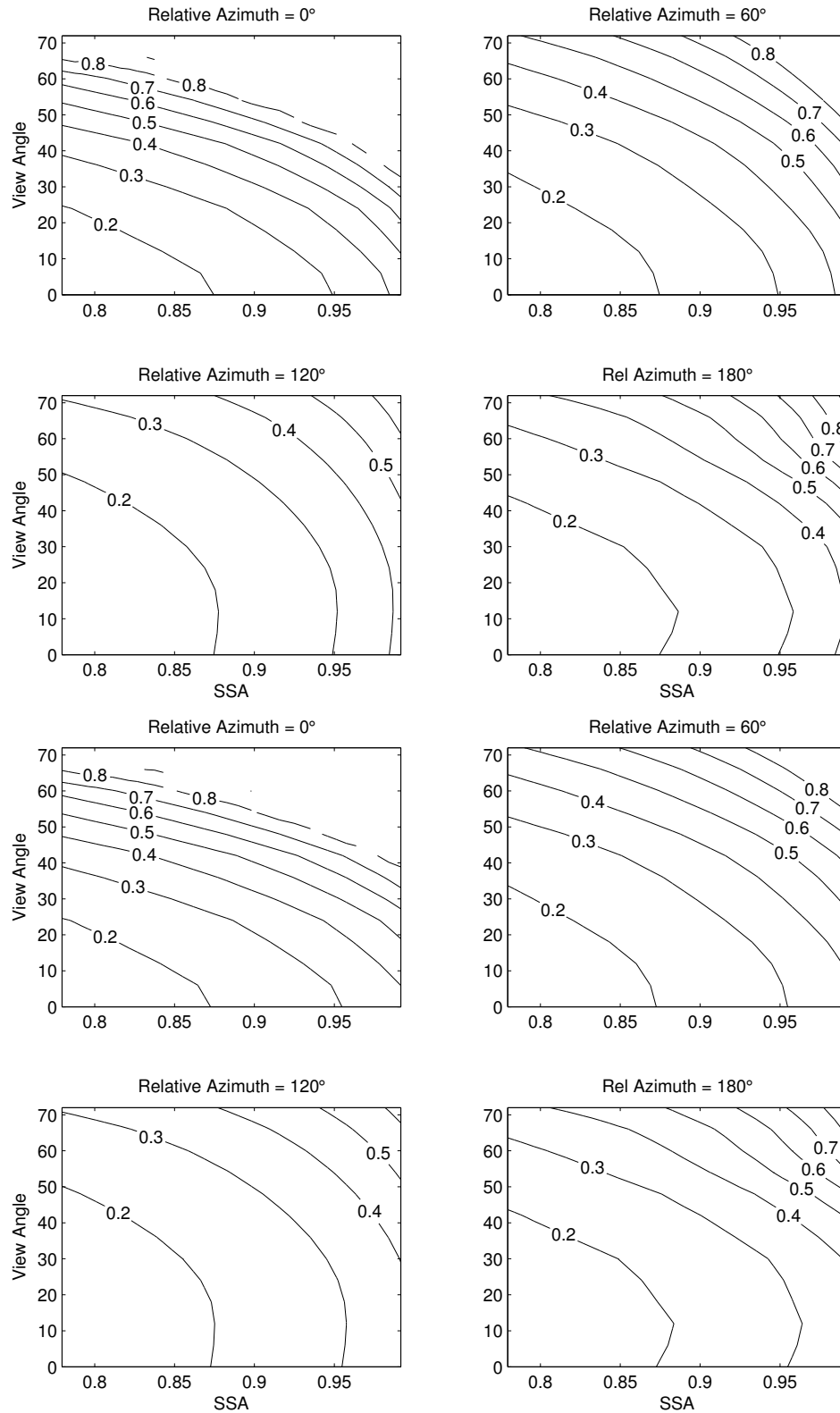


Figure A.35: Critical reflectance LUT for the bimodal sphere aerosol model at  $0.553 \mu\text{m}$  for  $\text{SZA} = 66^\circ$ , displayed as a function of satellite view and SSA for relative azimuth =  $0^\circ$  (upper left),  $60^\circ$  (upper right),  $120^\circ$  (lower left), and  $180^\circ$  (lower right). Upper panel is for fitting all albedos, lower panel is for fitting an albedo range.

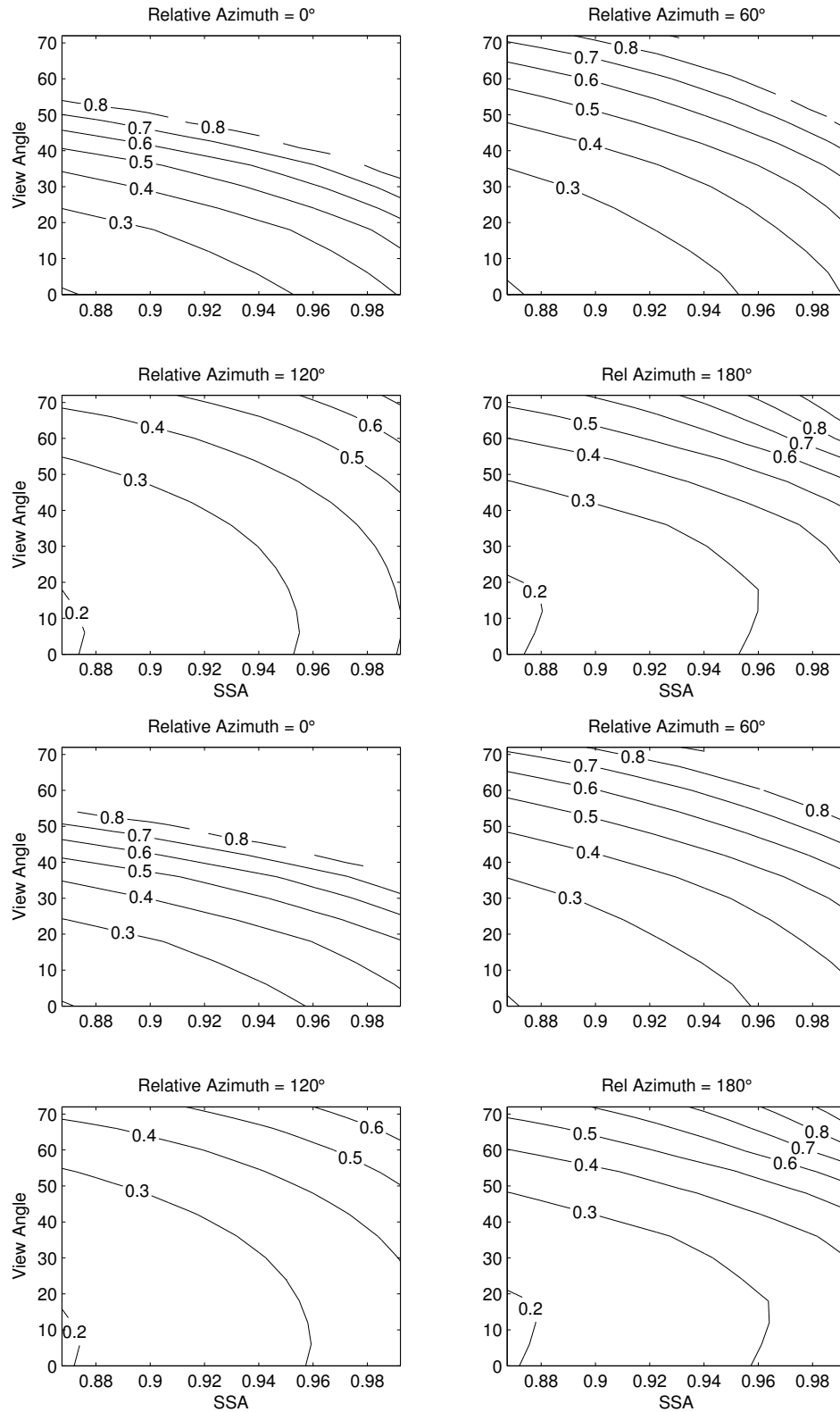


Figure A.36: Critical reflectance LUT for the bimodal sphere aerosol model at  $0.553 \mu\text{m}$  for  $\text{SZA} = 72^\circ$ , displayed as a function of satellite view and SSA for relative azimuth =  $0^\circ$  (upper left),  $60^\circ$  (upper right),  $120^\circ$  (lower left), and  $180^\circ$  (lower right). Upper panel is for fitting all albedos, lower panel is for fitting an albedo range.

## Appendix B Sensitivity Test Results at 0.553 $\mu\text{m}$

The following pages contain the sensitivity test results at 0.553  $\mu\text{m}$  results that were highlighted in Chapter 2. Results are shown for each of the simulated solar zenith angles ( $6^\circ$ ,  $12^\circ$ ,  $24^\circ$ ,  $36^\circ$ ,  $48^\circ$ ,  $54^\circ$ ,  $60^\circ$ ,  $66^\circ$ ,  $72^\circ$ ). The first nine figures are for the refractive index sensitivity study, the next nine figures are for AOD variability, the next set are for the vertical profile sensitivity, and the final nine figures are for the 40-stream sensitivity.

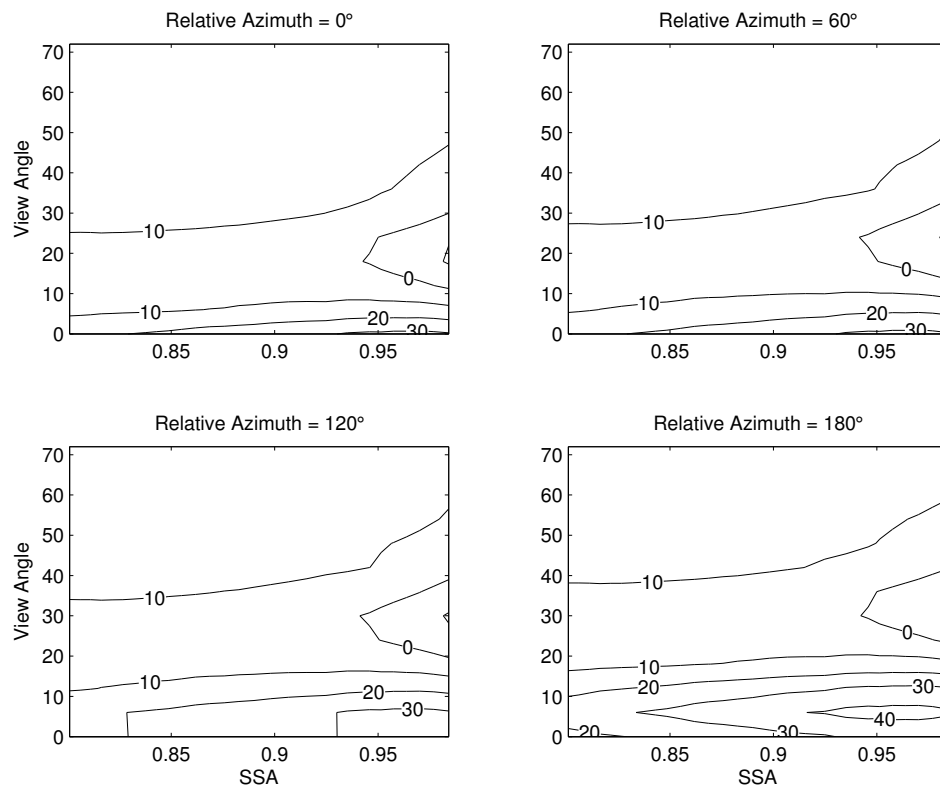


Figure B.1: Difference between the  $n = 1.63$  and  $n = 1.43$  bimodal model LUT, expressed as a percentage of the  $n = 1.53$  critical reflectance values, for 0.553  $\mu\text{m}$  and SZA =  $6^\circ$ .

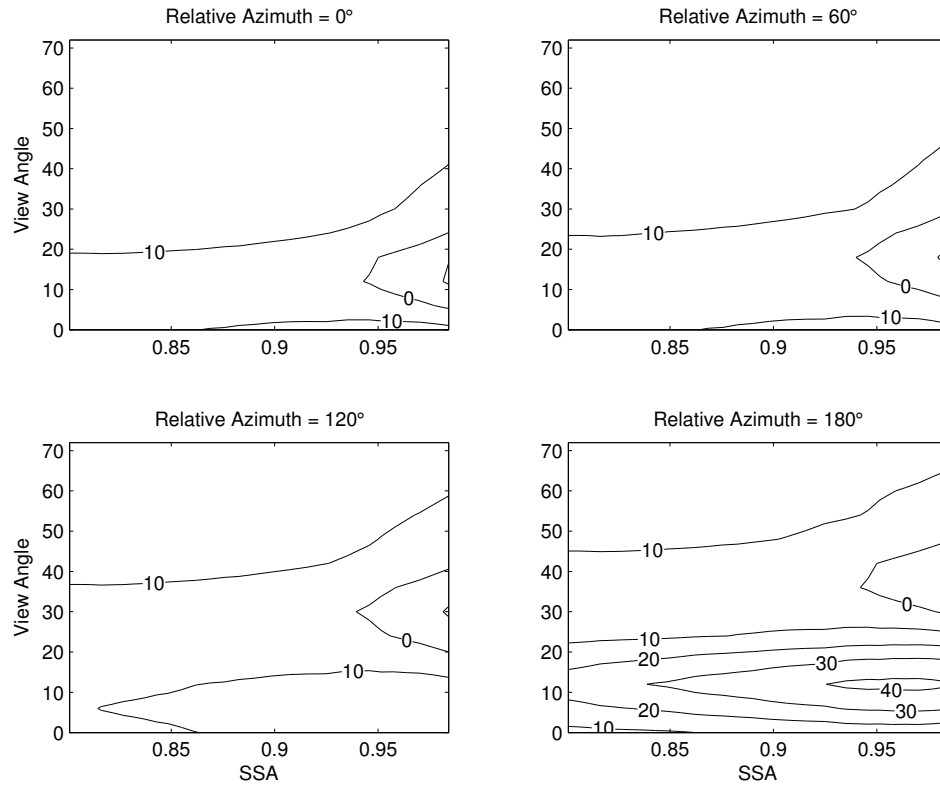


Figure B.2: Difference between the  $n = 1.63$  and  $n = 1.43$  bimodal model LUT, expressed as a percentage of the  $n = 1.53$  critical reflectance values, for  $0.553 \mu\text{m}$  and  $\text{SZA} = 12^\circ$ .

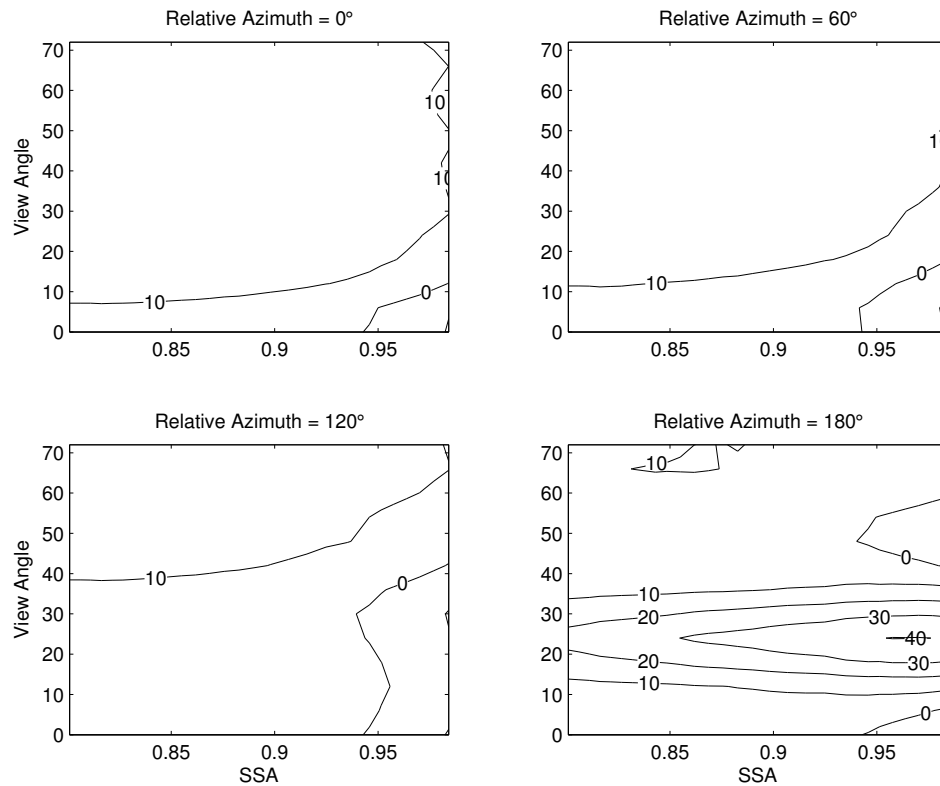


Figure B.3: Difference between the  $n = 1.63$  and  $n = 1.43$  bimodal model LUT, expressed as a percentage of the  $n = 1.53$  critical reflectance values, for  $0.553 \mu\text{m}$  and  $\text{SZA} = 24^\circ$ .

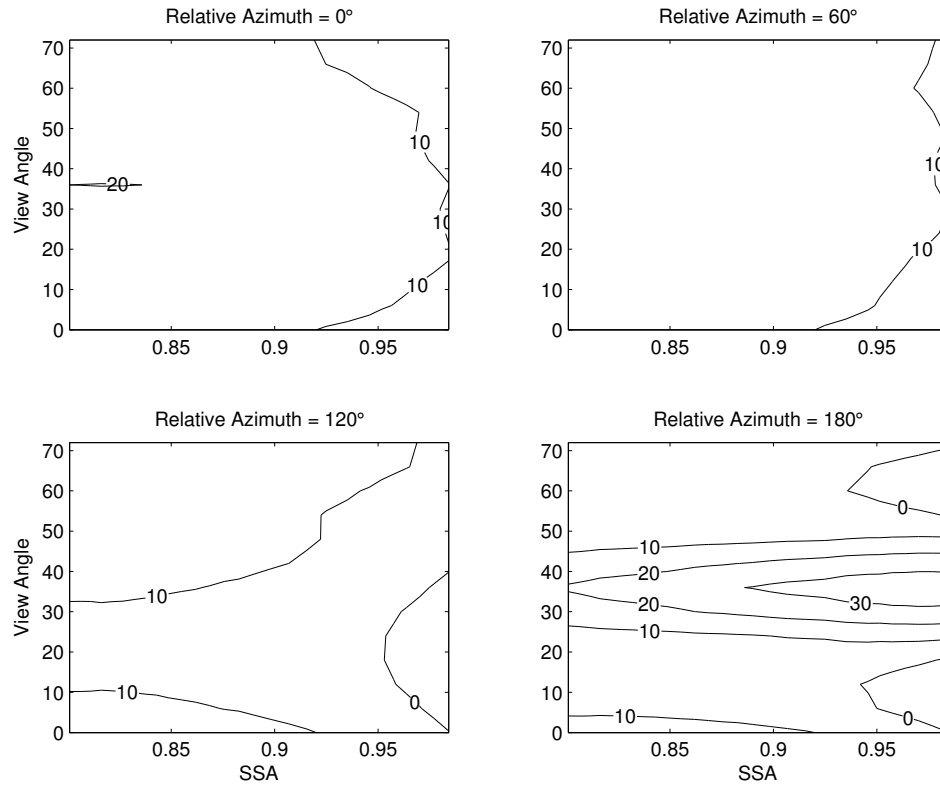


Figure B.4: Difference between the  $n = 1.63$  and  $n = 1.43$  bimodal model LUT, expressed as a percentage of the  $n = 1.53$  critical reflectance values, for  $0.553 \mu\text{m}$  and  $\text{SZA} = 36^\circ$ .

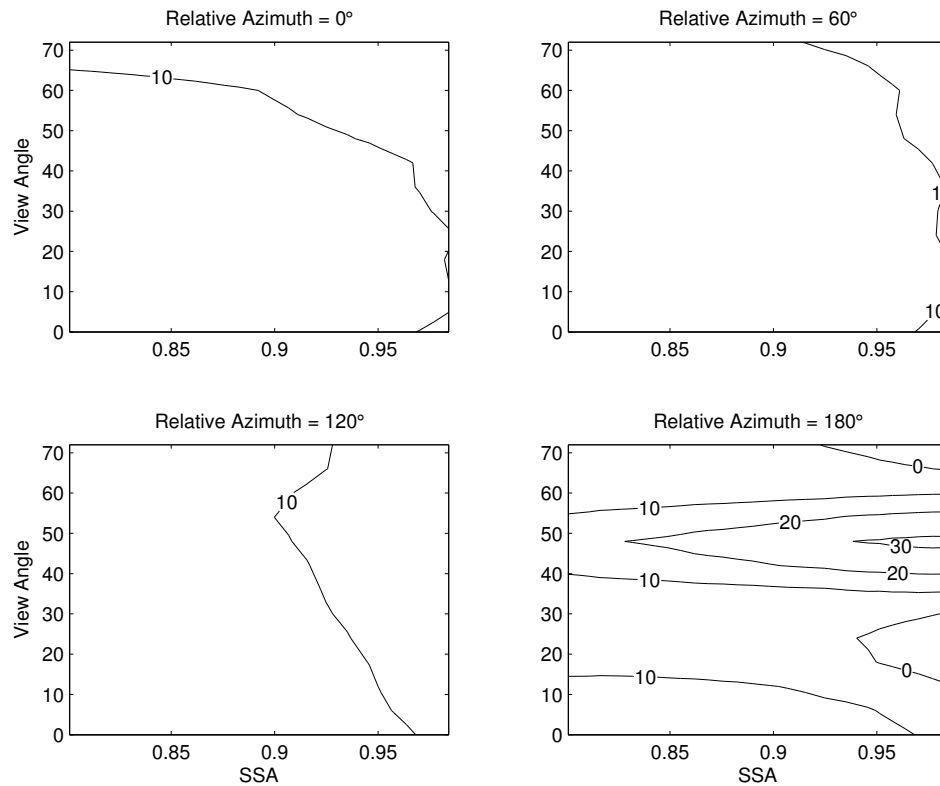


Figure B.5: Difference between the  $n = 1.63$  and  $n = 1.43$  bimodal model LUT, expressed as a percentage of the  $n = 1.53$  critical reflectance values, for  $0.553 \mu\text{m}$  and  $\text{SZA} = 48^\circ$ .

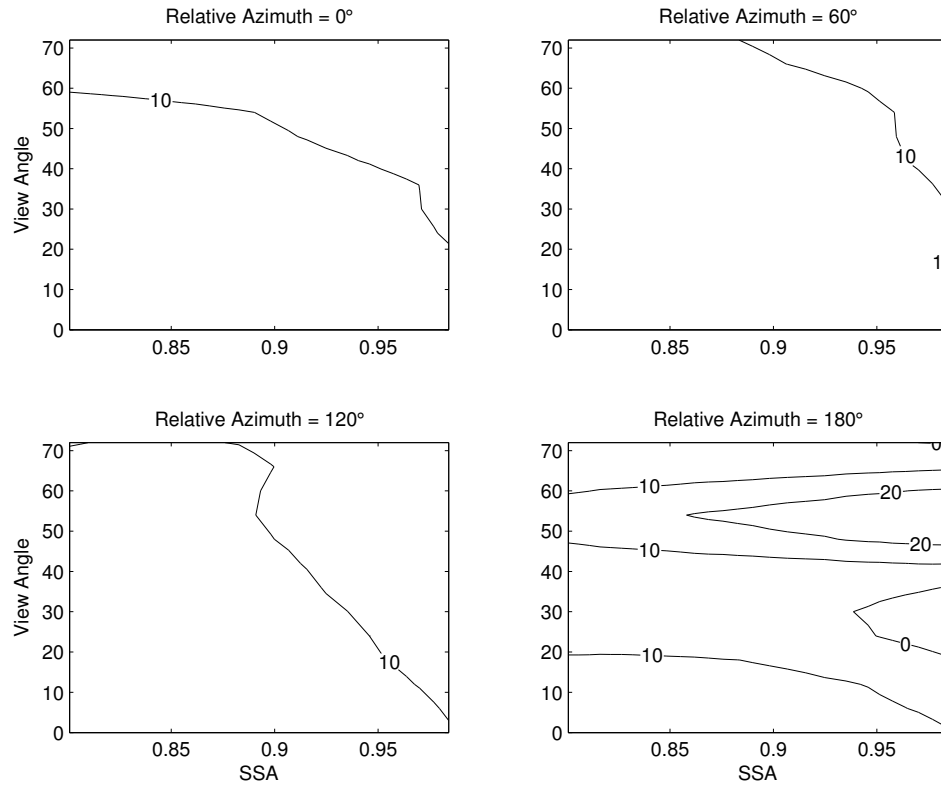


Figure B.6: Difference between the  $n = 1.63$  and  $n = 1.43$  bimodal model LUT, expressed as a percentage of the  $n = 1.53$  critical reflectance values, for  $0.553 \mu\text{m}$  and  $\text{SZA} = 54^\circ$ .

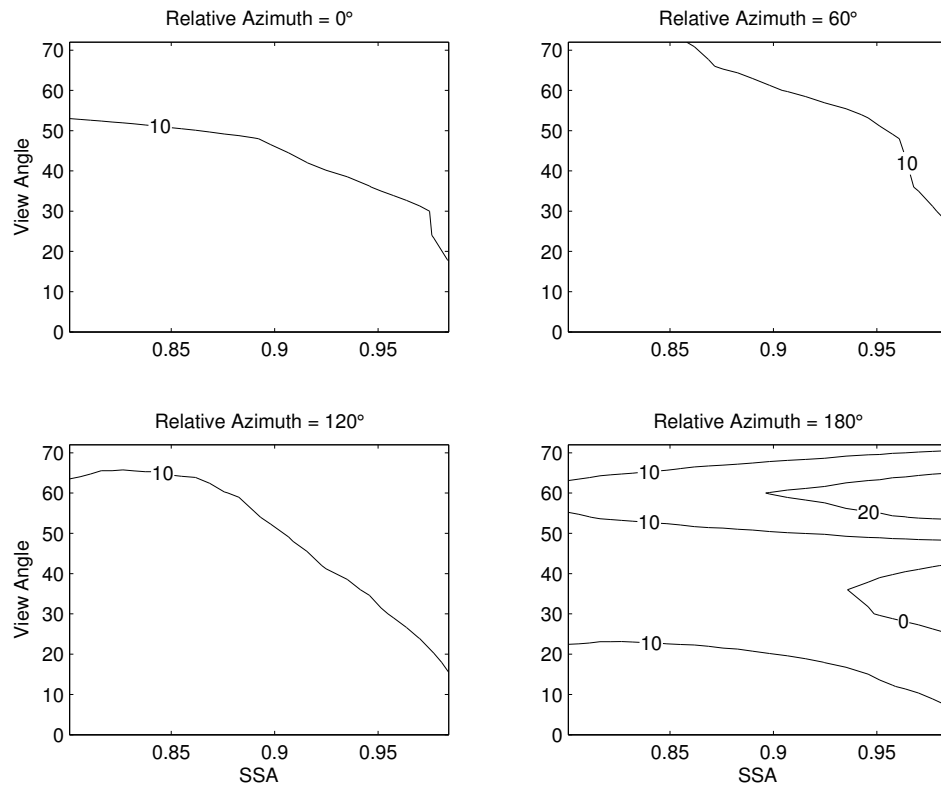


Figure B.7: Difference between the  $n = 1.63$  and  $n = 1.43$  bimodal model LUT, expressed as a percentage of the  $n = 1.53$  critical reflectance values, for  $0.553 \mu\text{m}$  and  $\text{SZA} = 60^\circ$ .

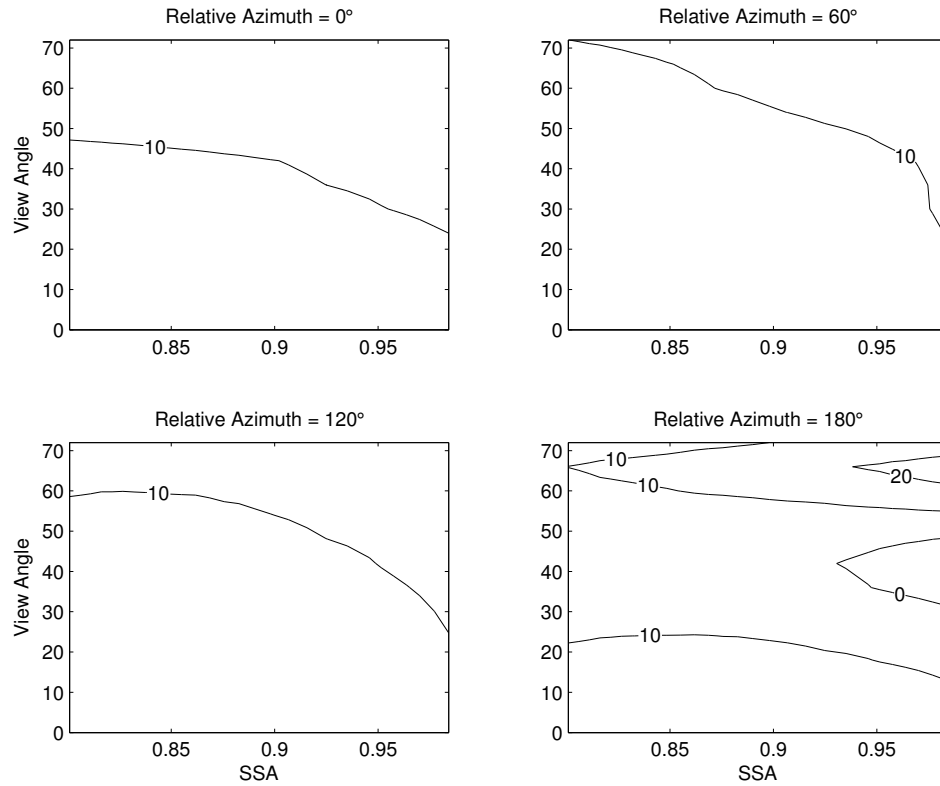


Figure B.8: Difference between the  $n = 1.63$  and  $n = 1.43$  bimodal model LUT, expressed as a percentage of the  $n = 1.53$  critical reflectance values, for  $0.553 \mu\text{m}$  and  $\text{SZA} = 66^\circ$ .

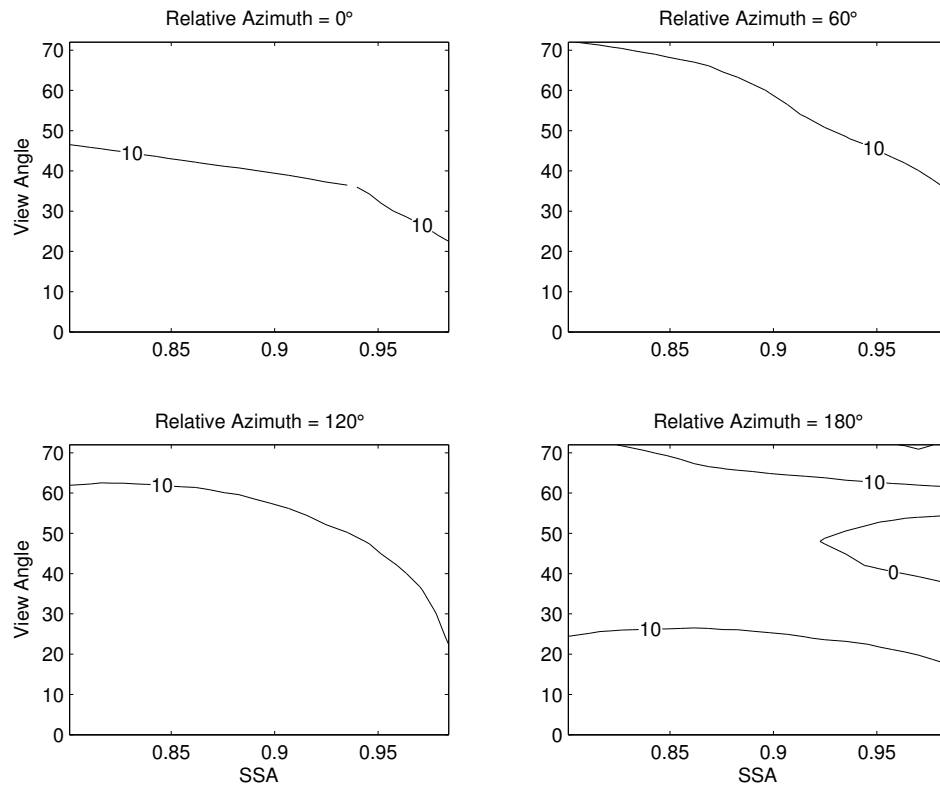


Figure B.9: Difference between the  $n = 1.63$  and  $n = 1.43$  bimodal model LUT, expressed as a percentage of the  $n = 1.53$  critical reflectance values, for  $0.553 \mu\text{m}$  and  $\text{SZA} = 72^\circ$ .

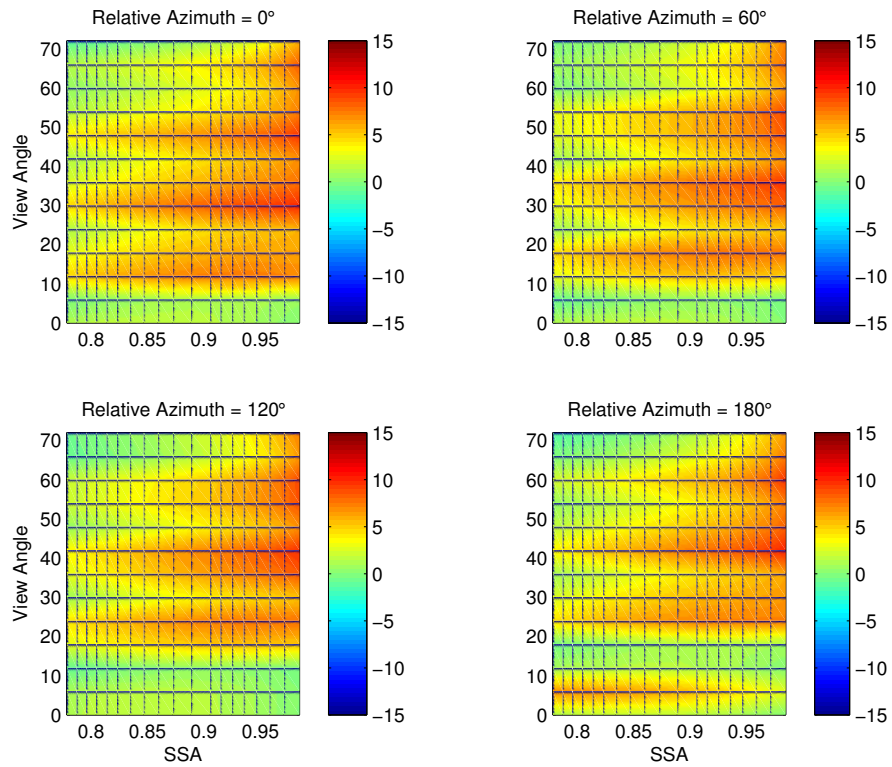


Figure B.10: Difference between the AOD = 2.0 and AOD = 1.0 coarse model LUT, expressed as percentage of the AOD = 1.0 critical reflectance values, for 0.553  $\mu\text{m}$  and SZA = 6°.

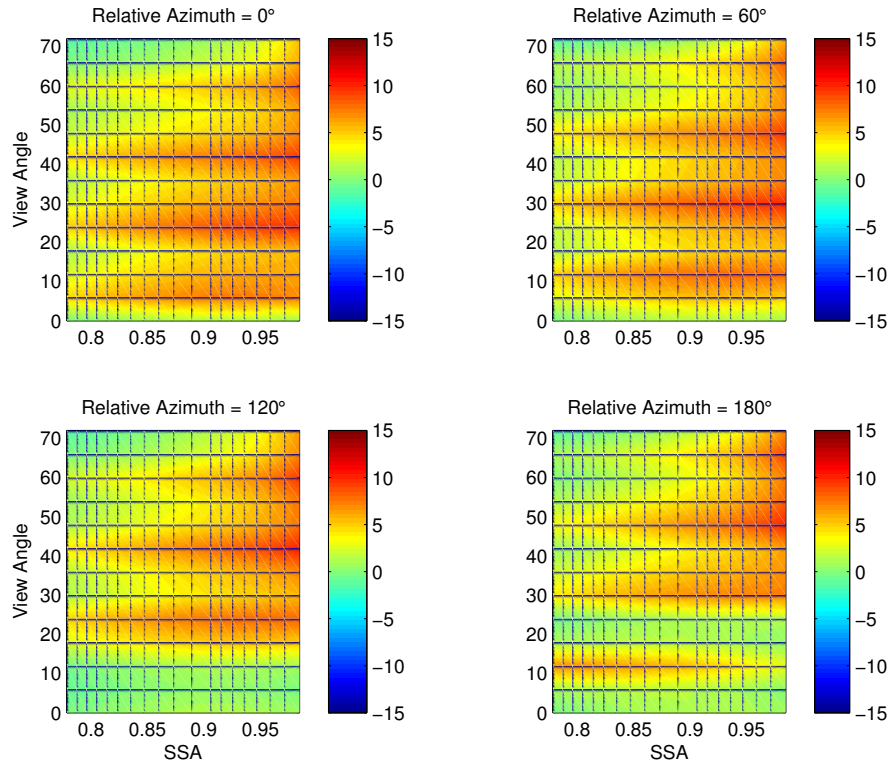


Figure B.11: Difference between the AOD = 2.0 and AOD = 1.0 coarse model LUT, expressed as percentage of the AOD = 1.0 critical reflectance values, for 0.553  $\mu\text{m}$  and SZA = 12°.

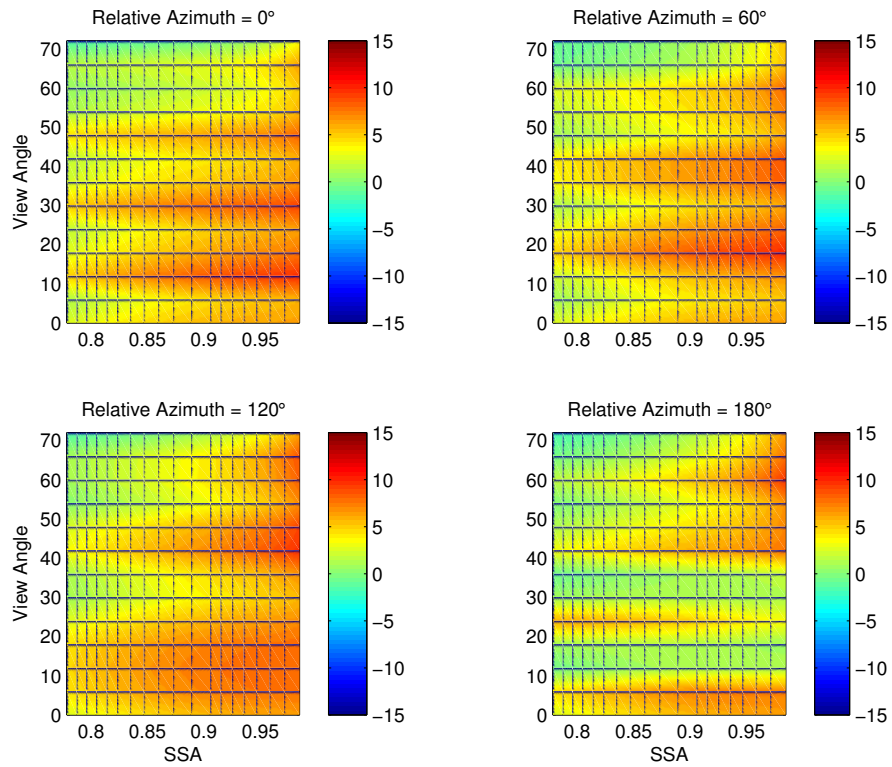


Figure B.12: Difference between the AOD = 2.0 and AOD = 1.0 coarse model LUT, expressed as percentage of the AOD = 1.0 critical reflectance values, for 0.553  $\mu\text{m}$  and SZA = 24°.

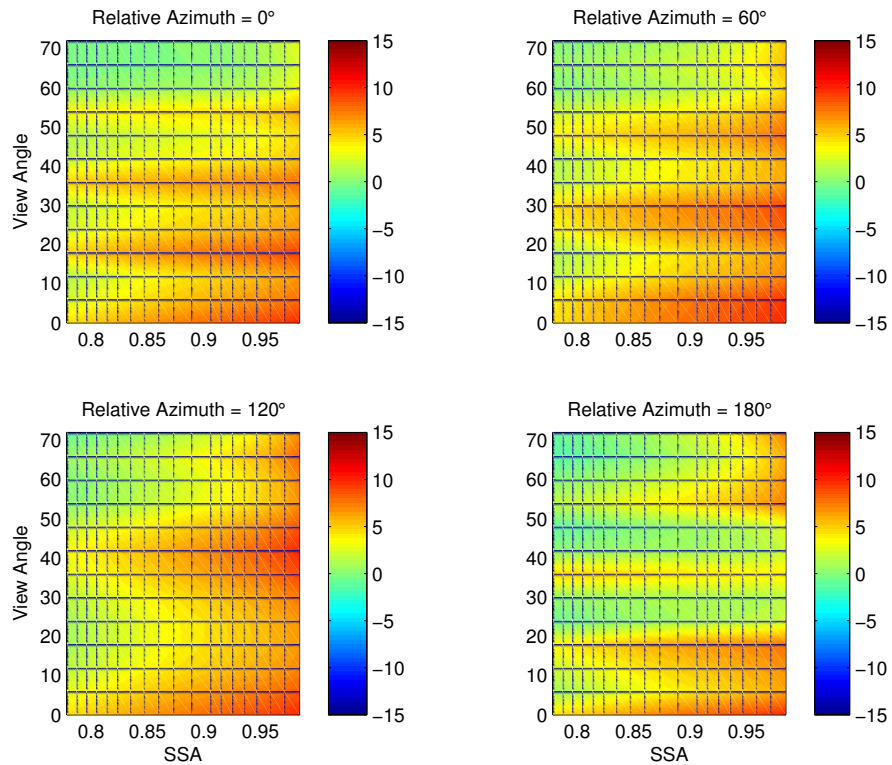


Figure B.13: Difference between the AOD = 2.0 and AOD = 1.0 coarse model LUT, expressed as percentage of the AOD = 1.0 critical reflectance values, for 0.553  $\mu\text{m}$  and SZA = 36°.

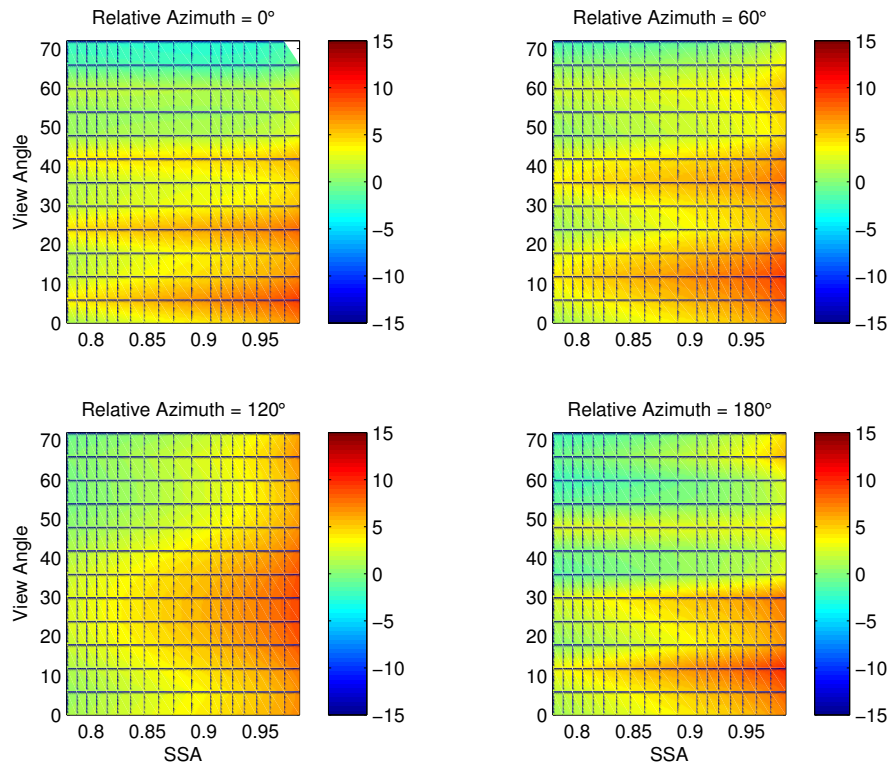


Figure B.14: Difference between the AOD = 2.0 and AOD = 1.0 coarse model LUT, expressed as percentage of the AOD = 1.0 critical reflectance values, for 0.553  $\mu\text{m}$  and SZA = 48°.

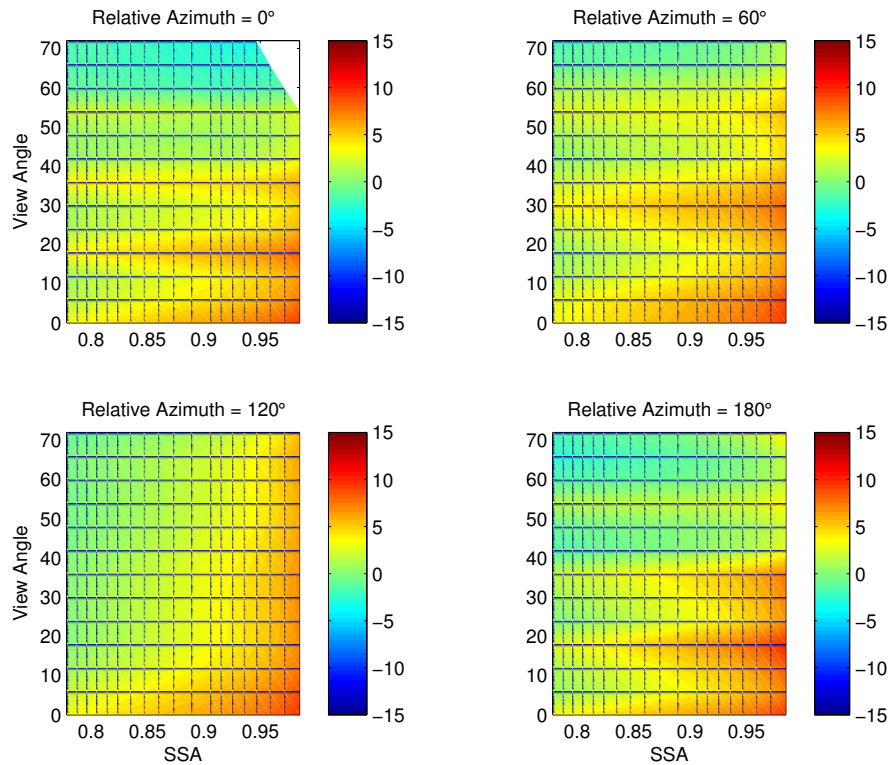


Figure B.15: Difference between the AOD = 2.0 and AOD = 1.0 coarse model LUT, expressed as percentage of the AOD = 1.0 critical reflectance values, for 0.553  $\mu\text{m}$  and SZA = 54°.

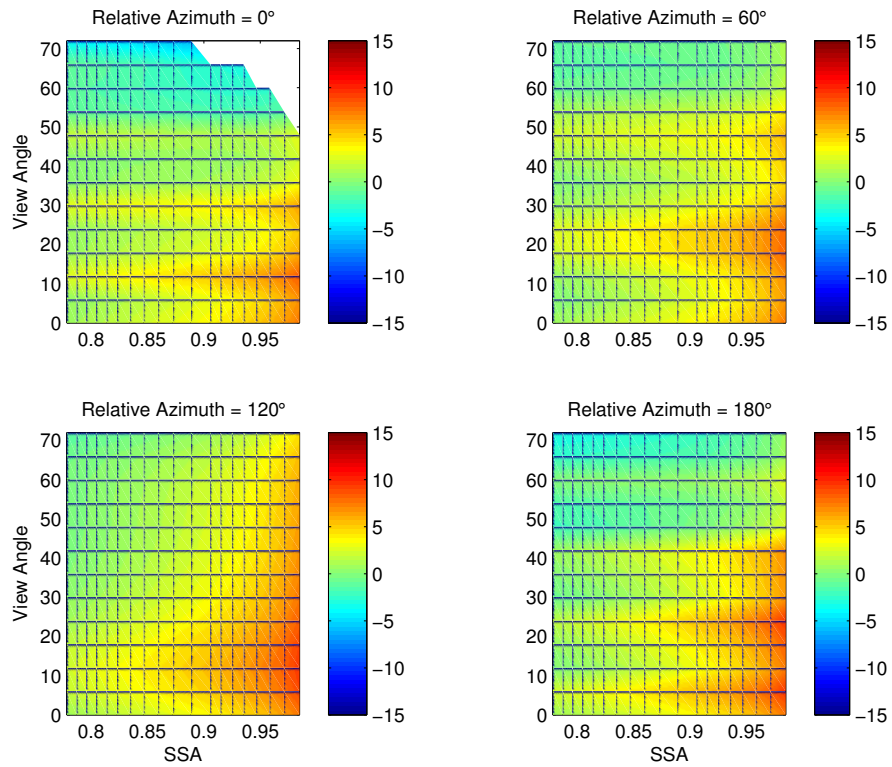


Figure B.16: Difference between the AOD = 2.0 and AOD = 1.0 coarse model LUT, expressed as percentage of the AOD = 1.0 critical reflectance values, for 0.553 μm and SZA = 60°.

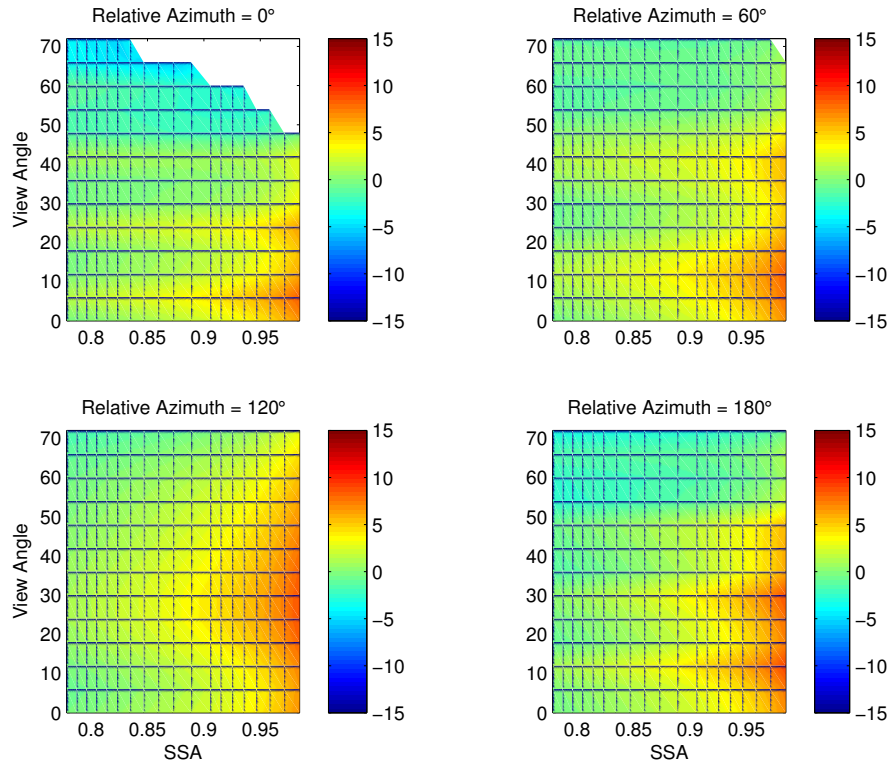


Figure B.17: Difference between the AOD = 2.0 and AOD = 1.0 coarse model LUT, expressed as percentage of the AOD = 1.0 critical reflectance values, for 0.553 μm and SZA = 66°.

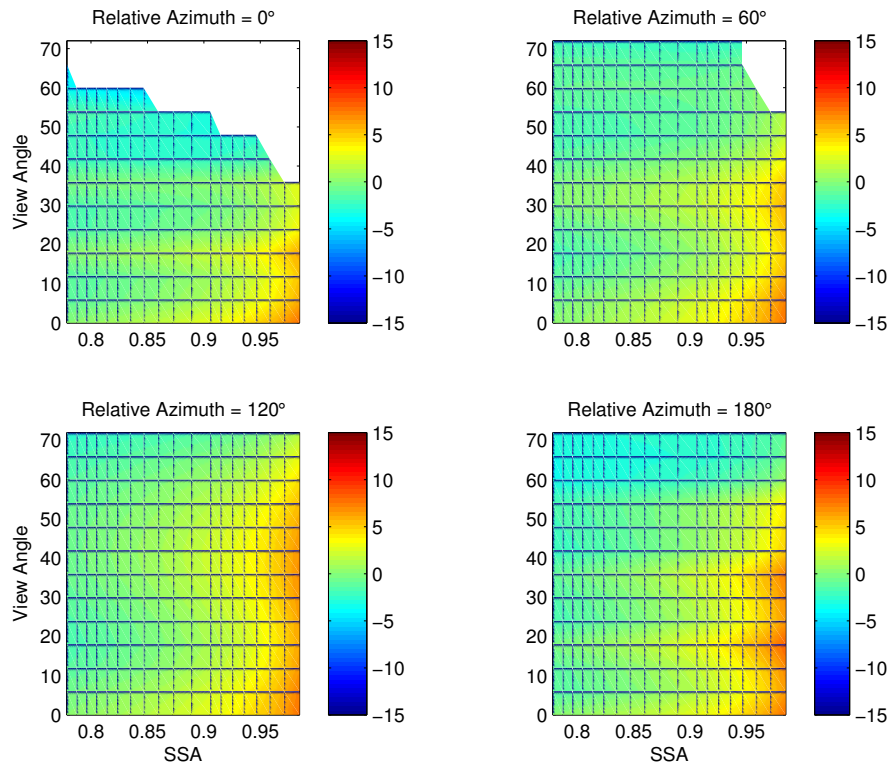


Figure.B.18: Difference between the AOD = 2.0 and AOD = 1.0 coarse model LUT, expressed as percentage of the AOD = 1.0 critical reflectance values, for 0.553  $\mu\text{m}$  and SZA = 72°.

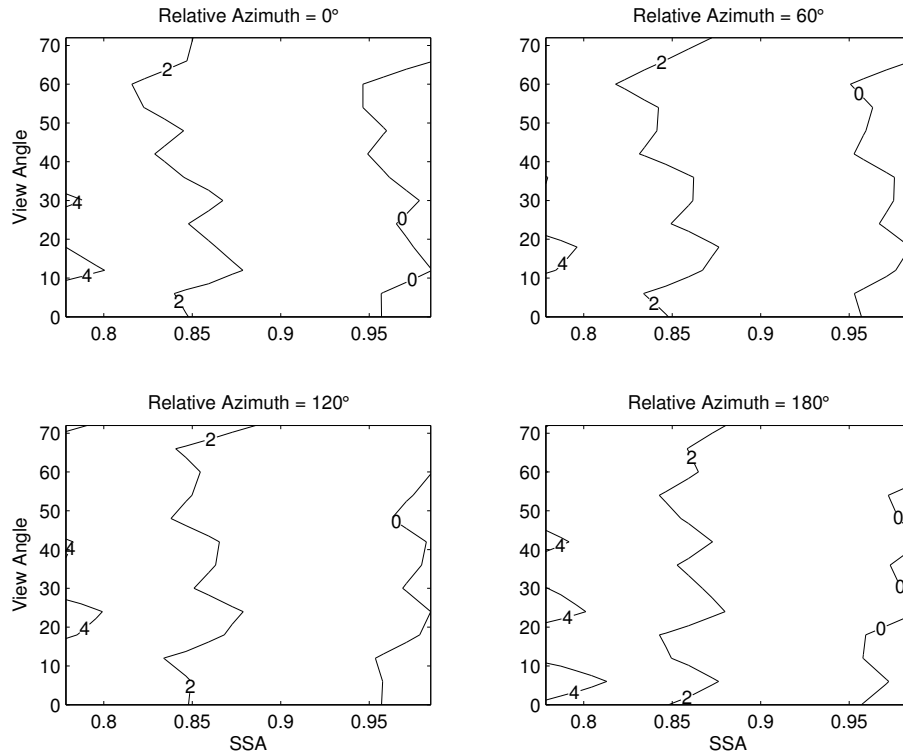


Figure B.19: Difference between the coarse model LUTs for the assumed vertical distribution and a 1km aerosol layer height, expressed as percentage of the critical reflectance values for the assumed vertical distribution, for 0.553  $\mu\text{m}$  and SZA = 6°.

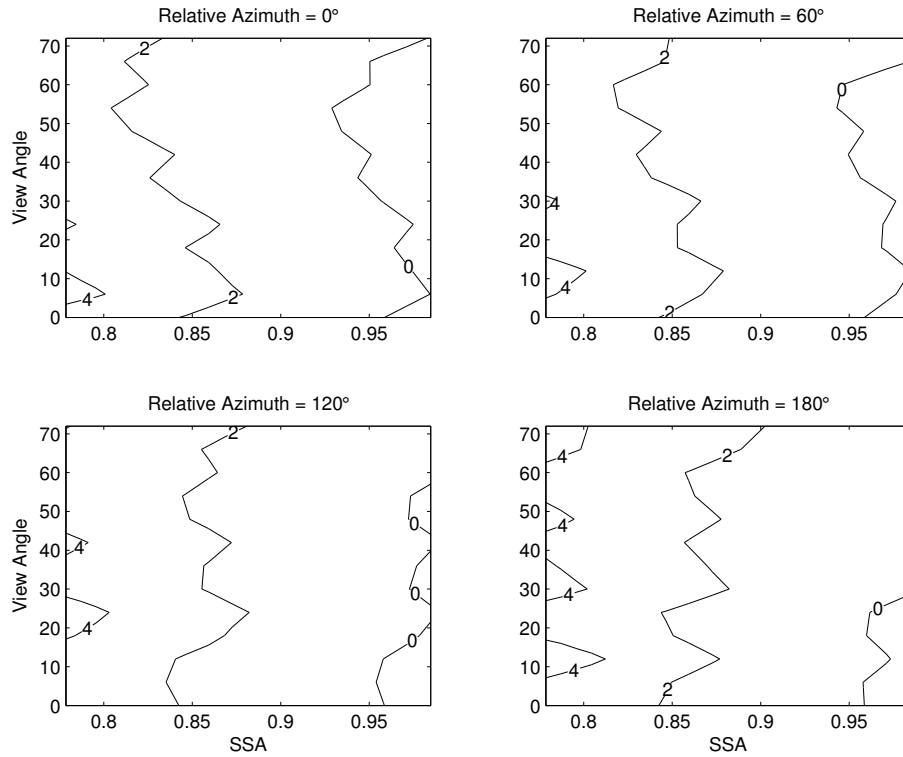


Figure B.20: Difference between the coarse model LUTs for the assumed vertical distribution and a 1km aerosol layer height, expressed as percentage of the critical reflectance values for the assumed vertical distribution, for 0.553  $\mu\text{m}$  and SZA = 12°.

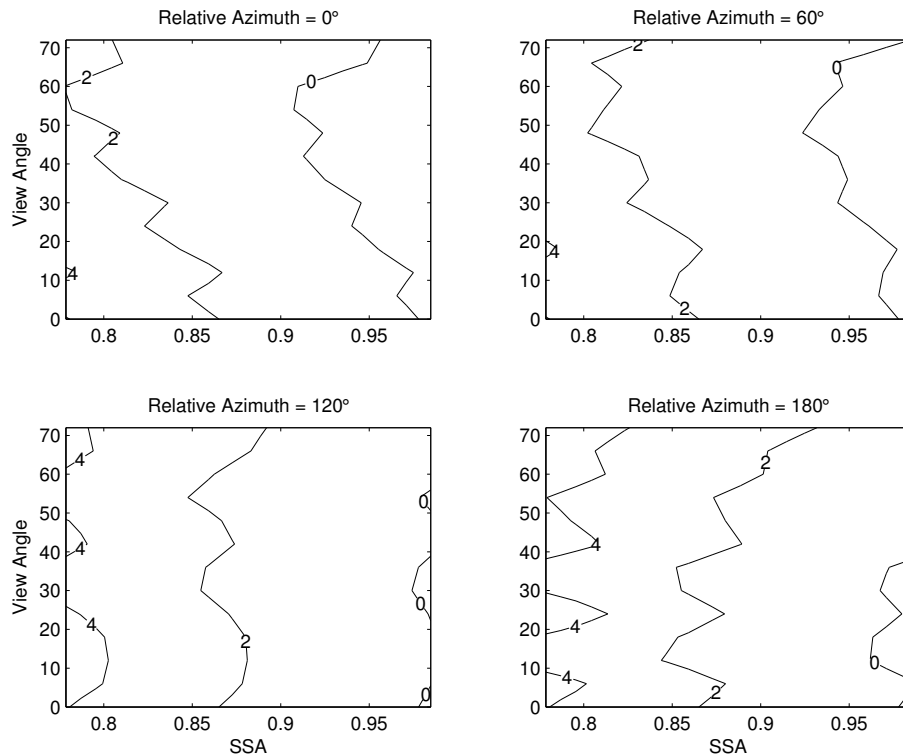


Figure B.21: Difference between the coarse model LUTs for the assumed vertical distribution and a 1km aerosol layer height, expressed as percentage of the critical reflectance values for the assumed vertical distribution, for 0.553  $\mu\text{m}$  and SZA = 24°.

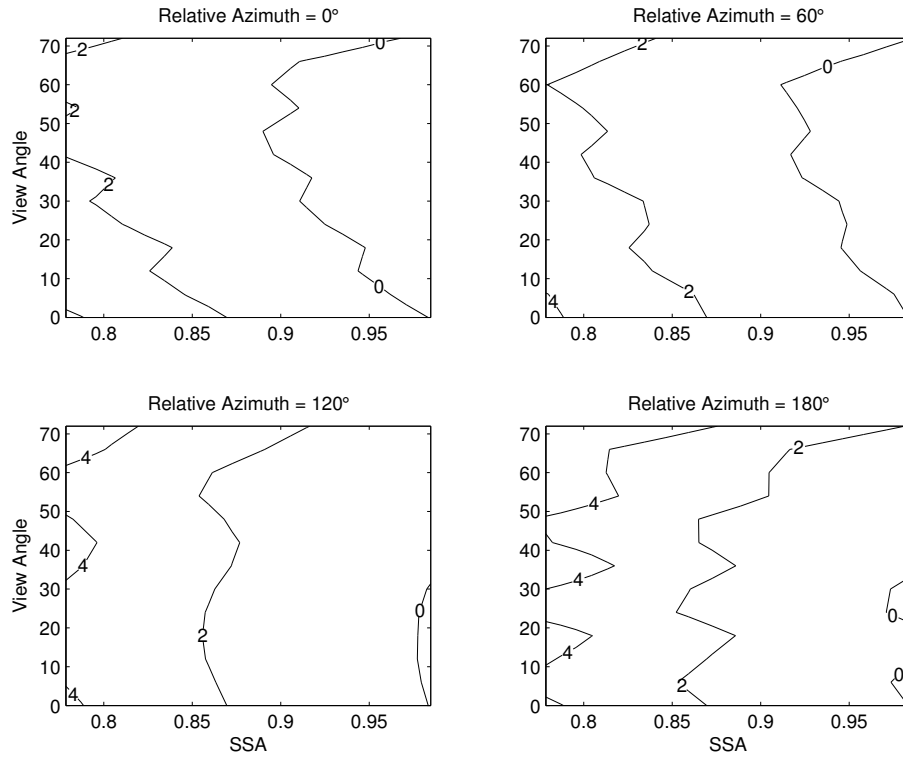


Figure B.22: Difference between the coarse model LUTs for the assumed vertical distribution and a 1km aerosol layer height, expressed as percentage of the critical reflectance values for the assumed vertical distribution, for 0.553  $\mu\text{m}$  and SZA = 36°.

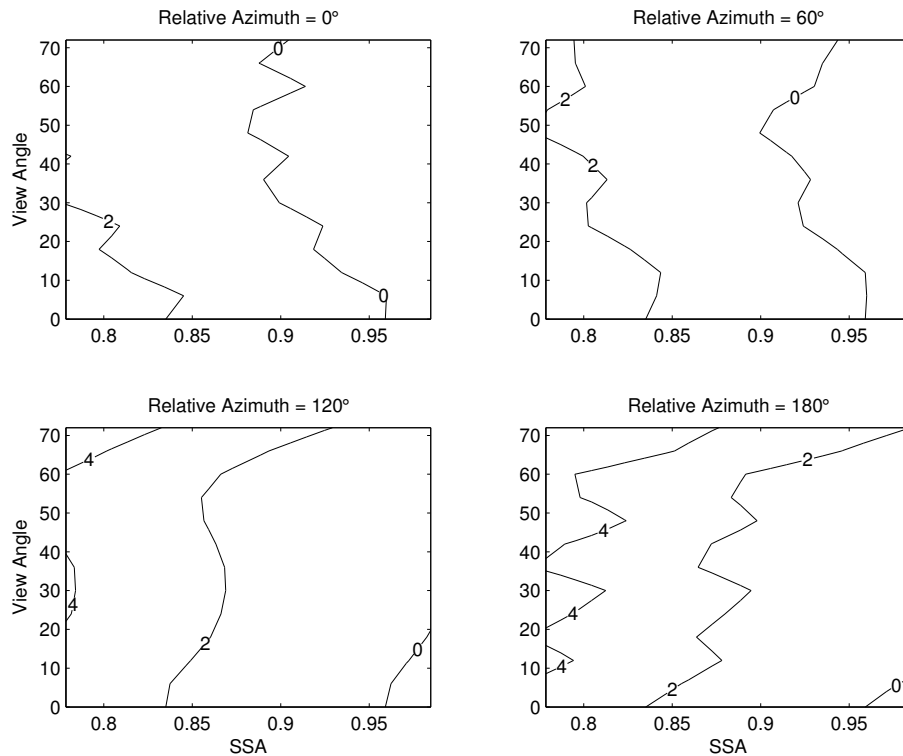


Figure B.23: Difference between the coarse model LUTs for the assumed vertical distribution and a 1km aerosol layer height, expressed as percentage of the critical reflectance values for the assumed vertical distribution, for 0.553  $\mu\text{m}$  and SZA = 48°.

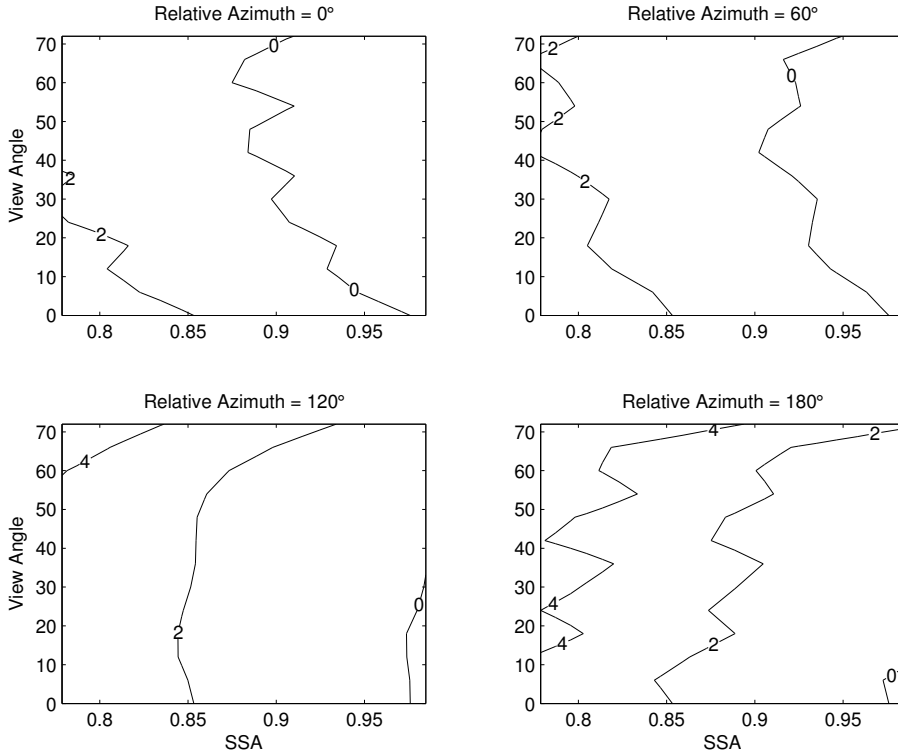


Figure B.24: Difference between the coarse model LUTs for the assumed vertical distribution and a 1km aerosol layer height, expressed as percentage of the critical reflectance values for the assumed vertical distribution, for 0.553  $\mu\text{m}$  and SZA = 54°.

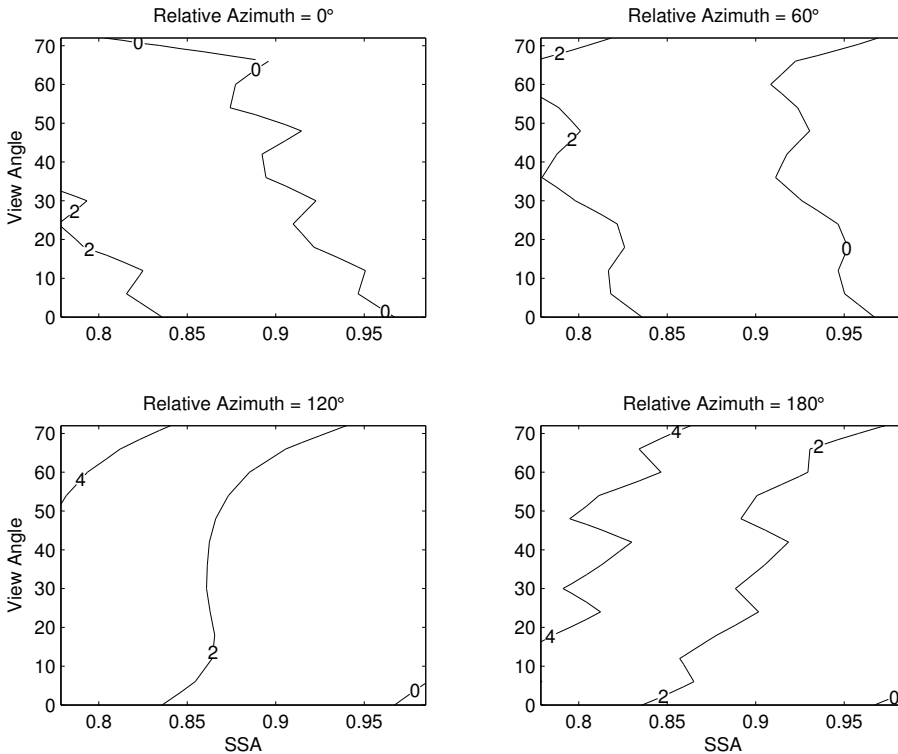


Figure B.25: Difference between the coarse model LUTs for the assumed vertical distribution and a 1km aerosol layer height, expressed as percentage of the critical reflectance values for the assumed vertical distribution, for 0.553  $\mu\text{m}$  and SZA = 60°.

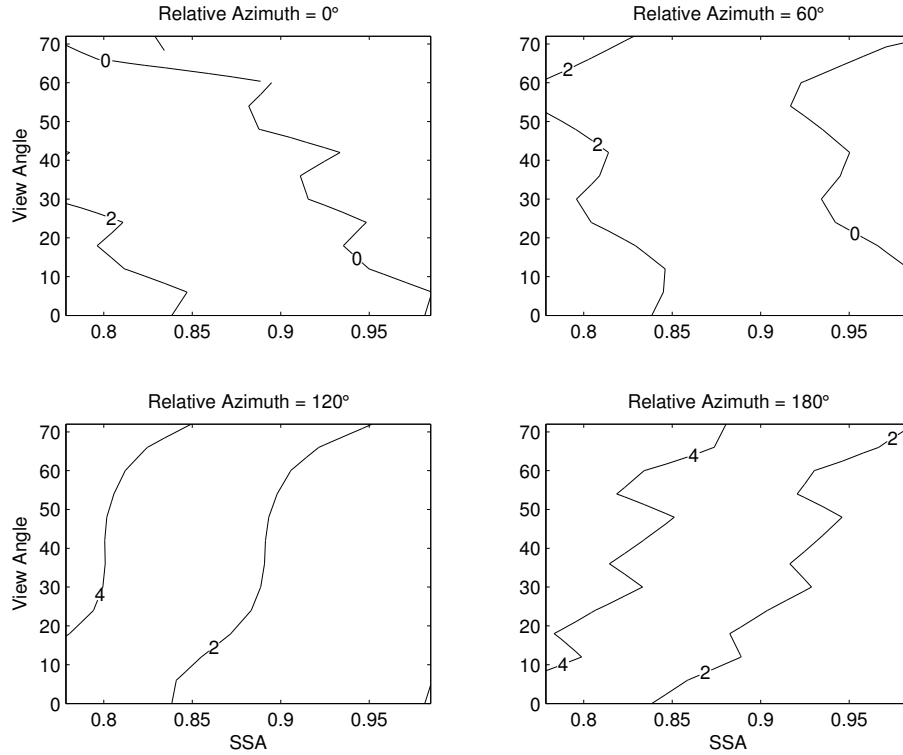


Figure B.26: Difference between the coarse model LUTs for the assumed vertical distribution and a 1km aerosol layer height, expressed as percentage of the critical reflectance values for the assumed vertical distribution, for 0.553  $\mu\text{m}$  and SZA = 66°.

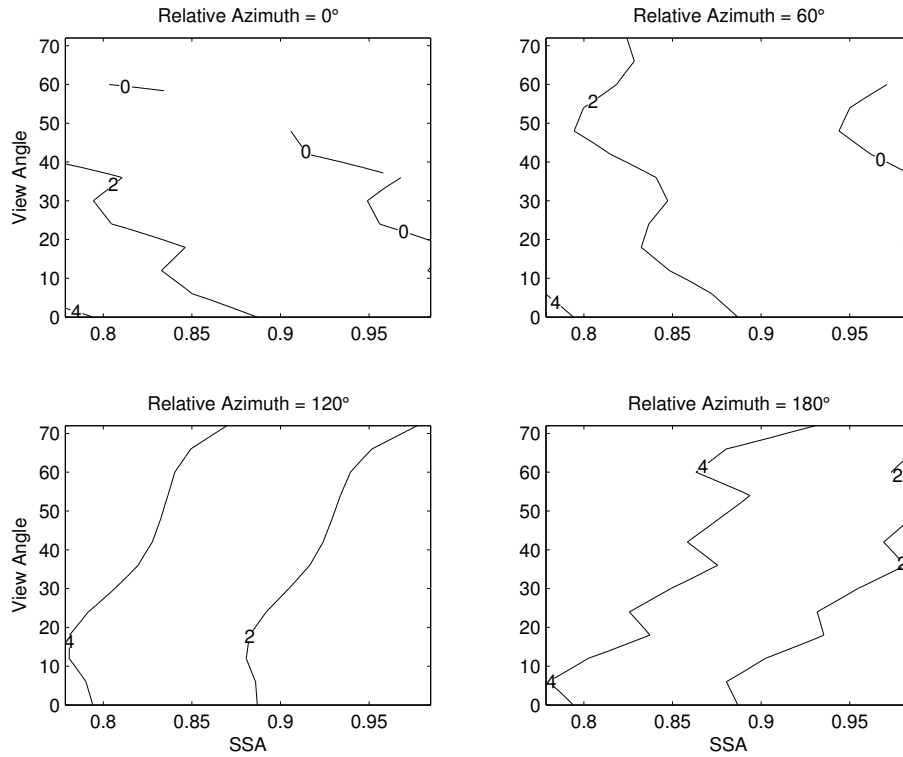


Figure B.27: Difference between the coarse model LUTs for the assumed vertical distribution and a 1km aerosol layer height, expressed as percentage of the critical reflectance values for the assumed vertical distribution, for 0.553  $\mu\text{m}$  and SZA = 72°.

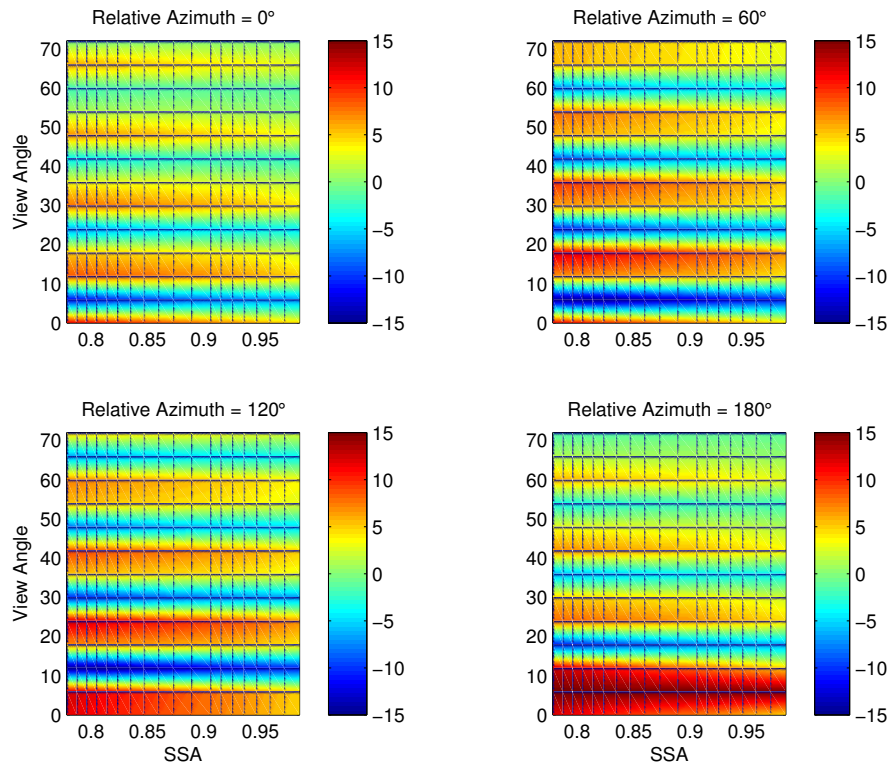


Figure B.28: Difference between the 40 and 20 stream coarse model LUT, expressed as percentage of the 20 stream critical reflectance values, for 0.553  $\mu\text{m}$  and SZA = 6°.

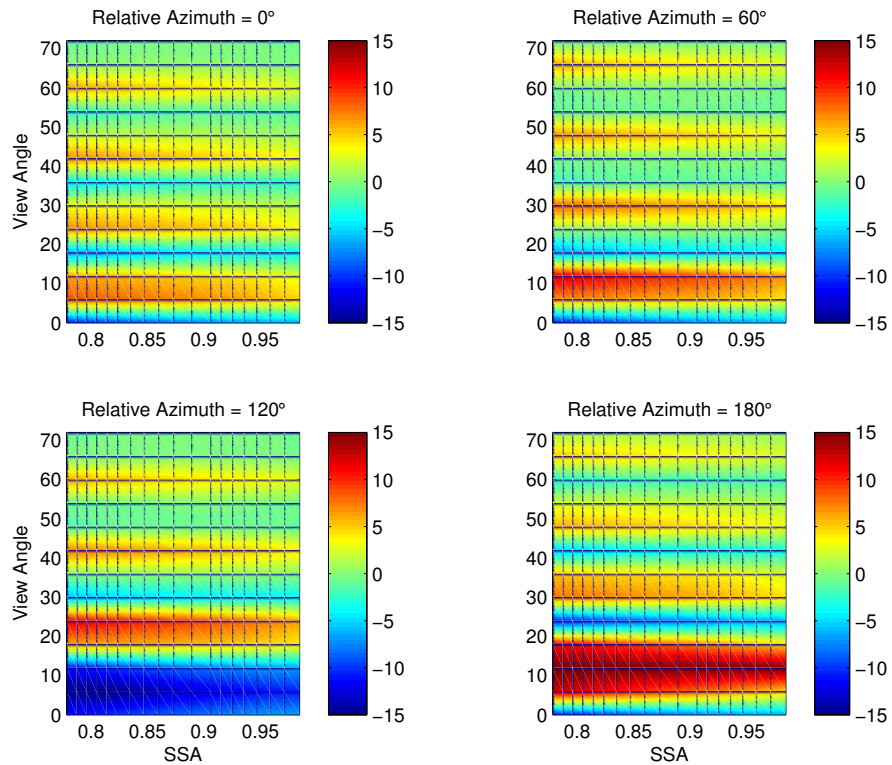


Figure B.29: Difference between the 40 and 20 stream coarse model LUT, expressed as percentage of the 20 stream critical reflectance values, for 0.553  $\mu\text{m}$  and SZA = 12°.

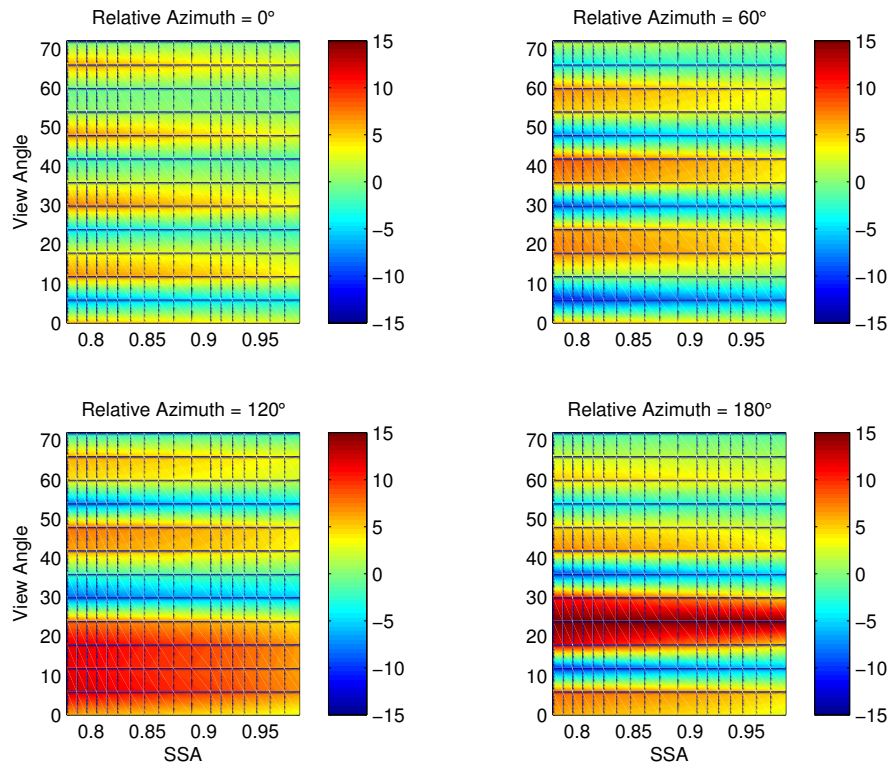


Figure B.30: Difference between the 40 and 20 stream coarse model LUT, expressed as percentage of the 20 stream critical reflectance values, for 0.553  $\mu\text{m}$  and SZA = 24°

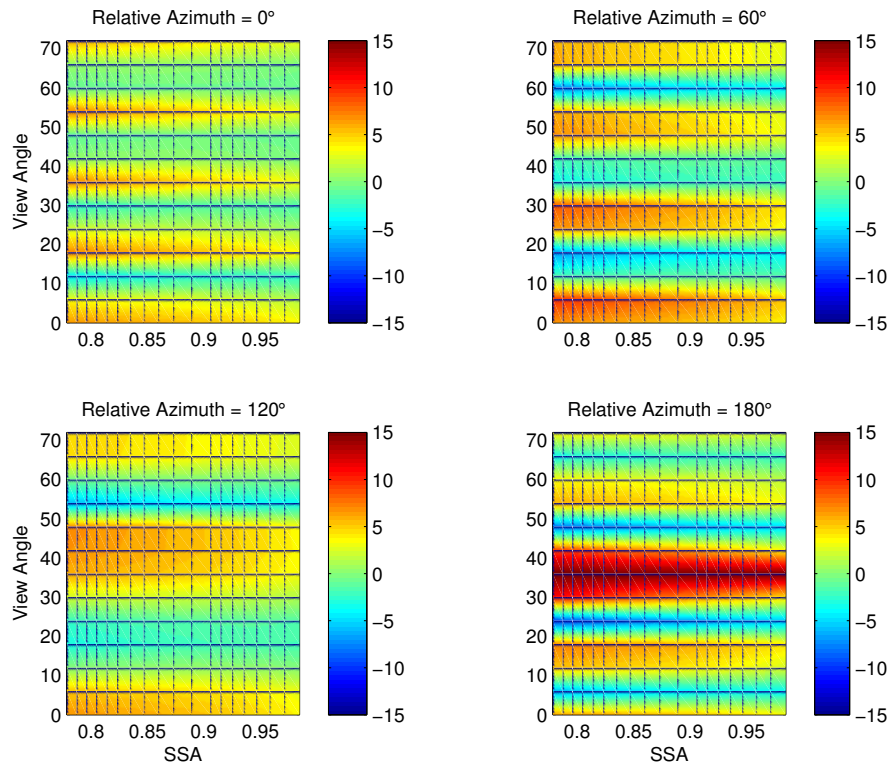


Figure B.31: Difference between the 40 and 20 stream coarse model LUT, expressed as percentage of the 20 stream critical reflectance values, for 0.553  $\mu\text{m}$  and SZA = 36°.

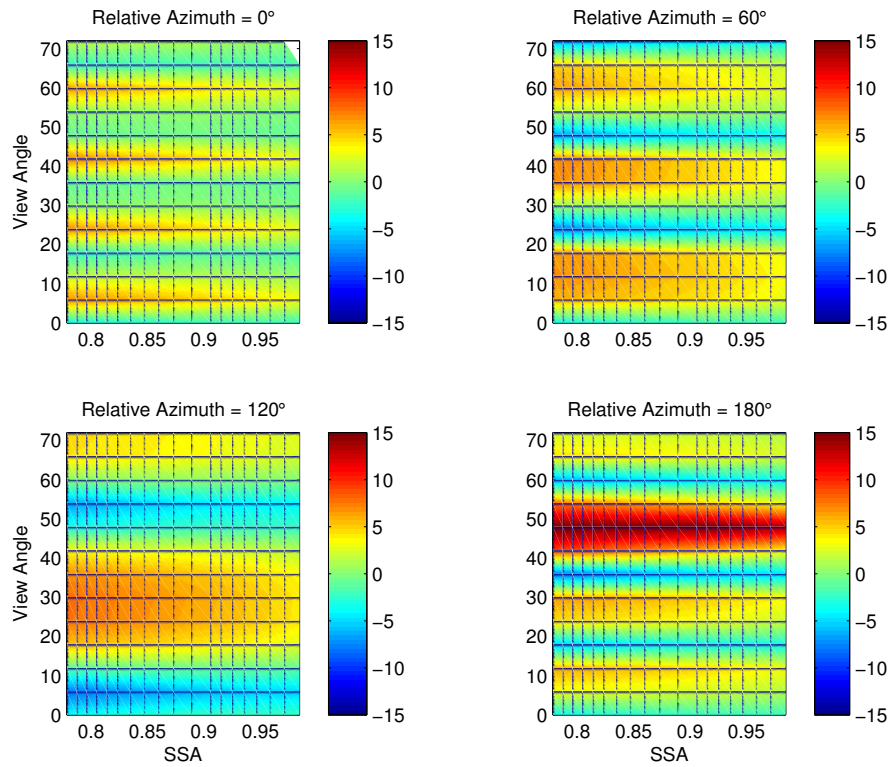


Figure B.32: Difference between the 40 and 20 stream coarse model LUT, expressed as percentage of the 20 stream critical reflectance values, for 0.553  $\mu\text{m}$  and SZA = 48°.

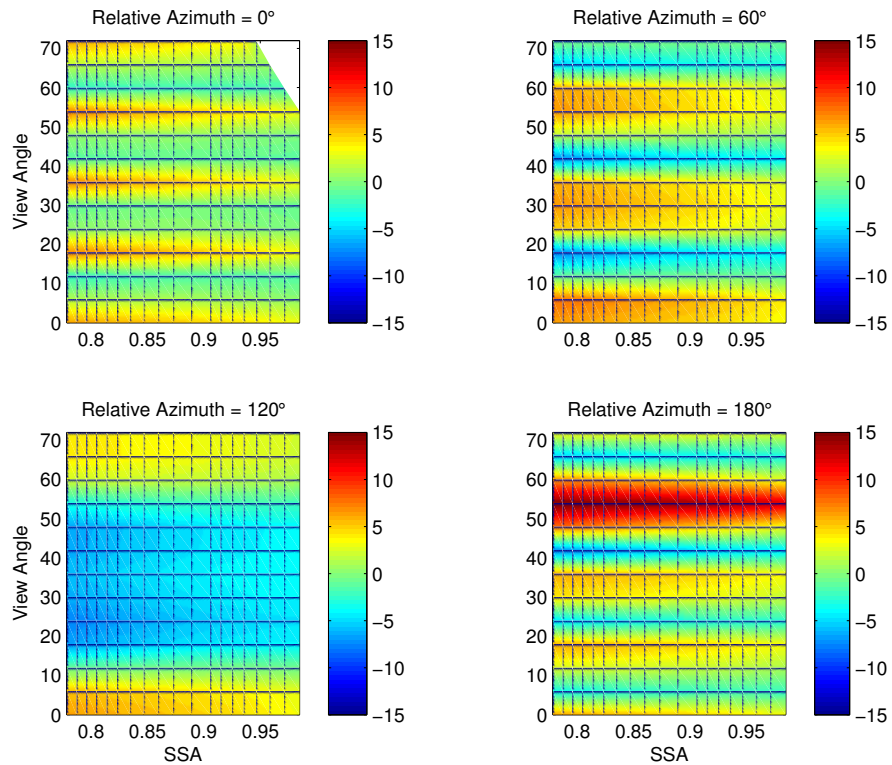


Figure B.33: Difference between the 40 and 20 stream coarse model LUT, expressed as percentage of the 20 stream critical reflectance values, for 0.553  $\mu\text{m}$  and SZA = 54°.

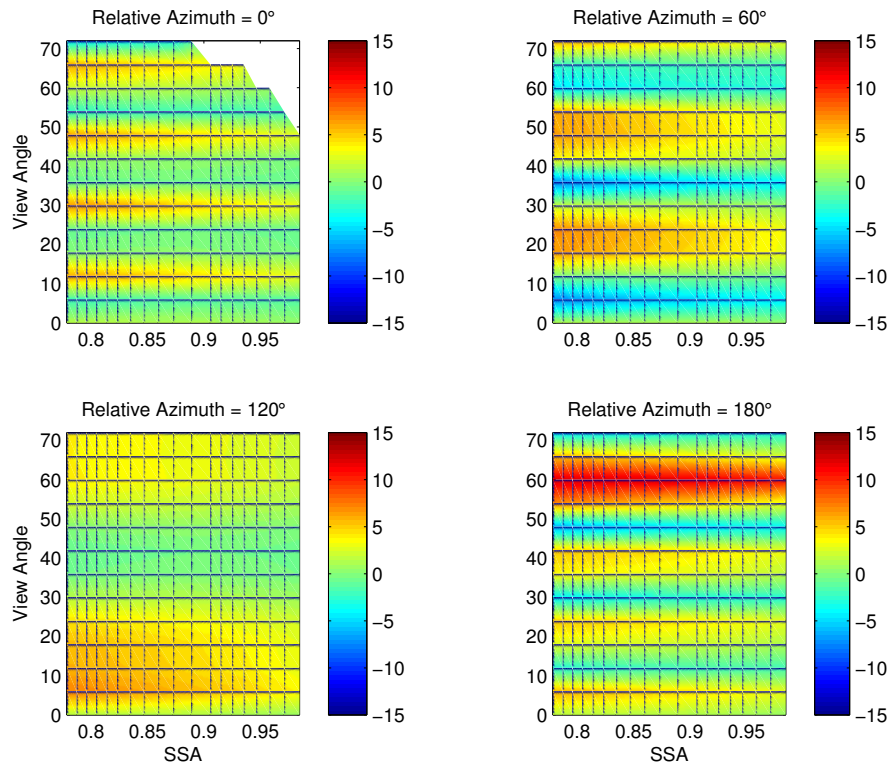


Figure B.34: Difference between the 40 and 20 stream coarse model LUT, expressed as percentage of the 20 stream critical reflectance values, for 0.553  $\mu\text{m}$  and SZA = 60°.

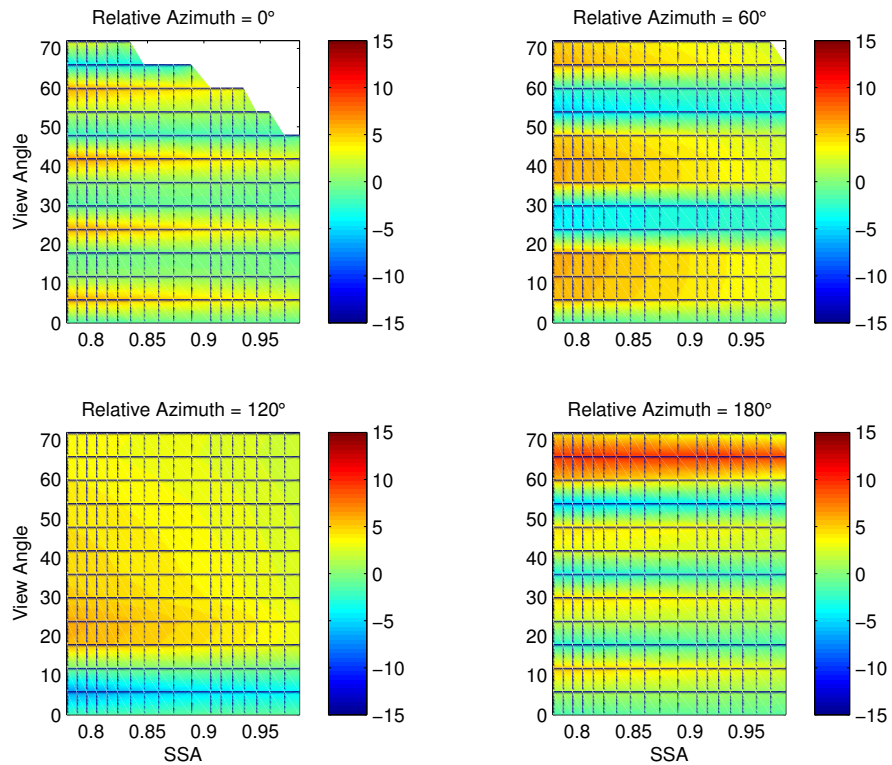


Figure B.35: Difference between the 40 and 20 stream coarse model LUT, expressed as percentage of the 20 stream critical reflectance values, for 0.553  $\mu\text{m}$  and SZA = 66°.

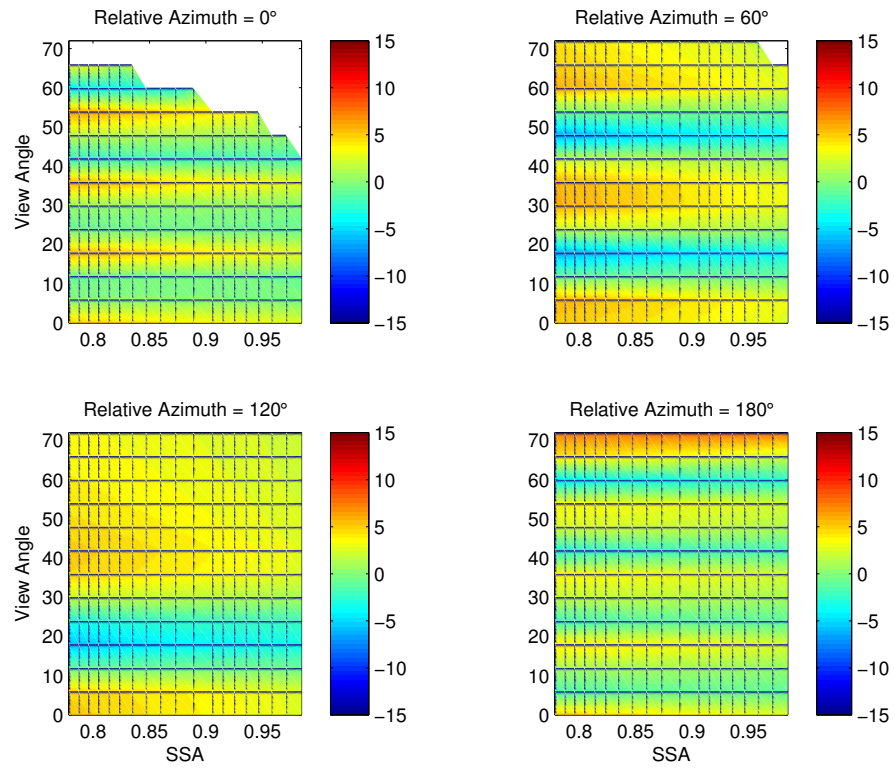


Figure B.36: Difference between the 40 and 20 stream coarse model LUT, expressed as percentage of the 20 stream critical reflectance values, for  $0.553 \mu\text{m}$  and  $\text{SZA} = 72^\circ$ .

## **Appendix C Image retrievals at 0.553 $\mu\text{m}$**

The following pages contain the image retrieval results for the 27 cases at Tamanrasset, and 15 cases at Banizoumbou that were discussed in Chapter 3. Results are shown for critical reflectance and path radiance at 0.553  $\mu\text{m}$  in the top panels, and the TOA effect and retrieved SSA in the lower panels. The radiative effect at TOA was determined as the difference between the average of the clean reflectances and the critical reflectance; positive values correspond to positive TOA forcing at the particular sun solar geometry of a scene, and vice versa. SSA values shown are for the TOA v SFC retrieval method. All Tamanrasset cases were retrieved using the coarse aerosol model, the model used for each Banizoumbou case will be indicated in the figure caption.

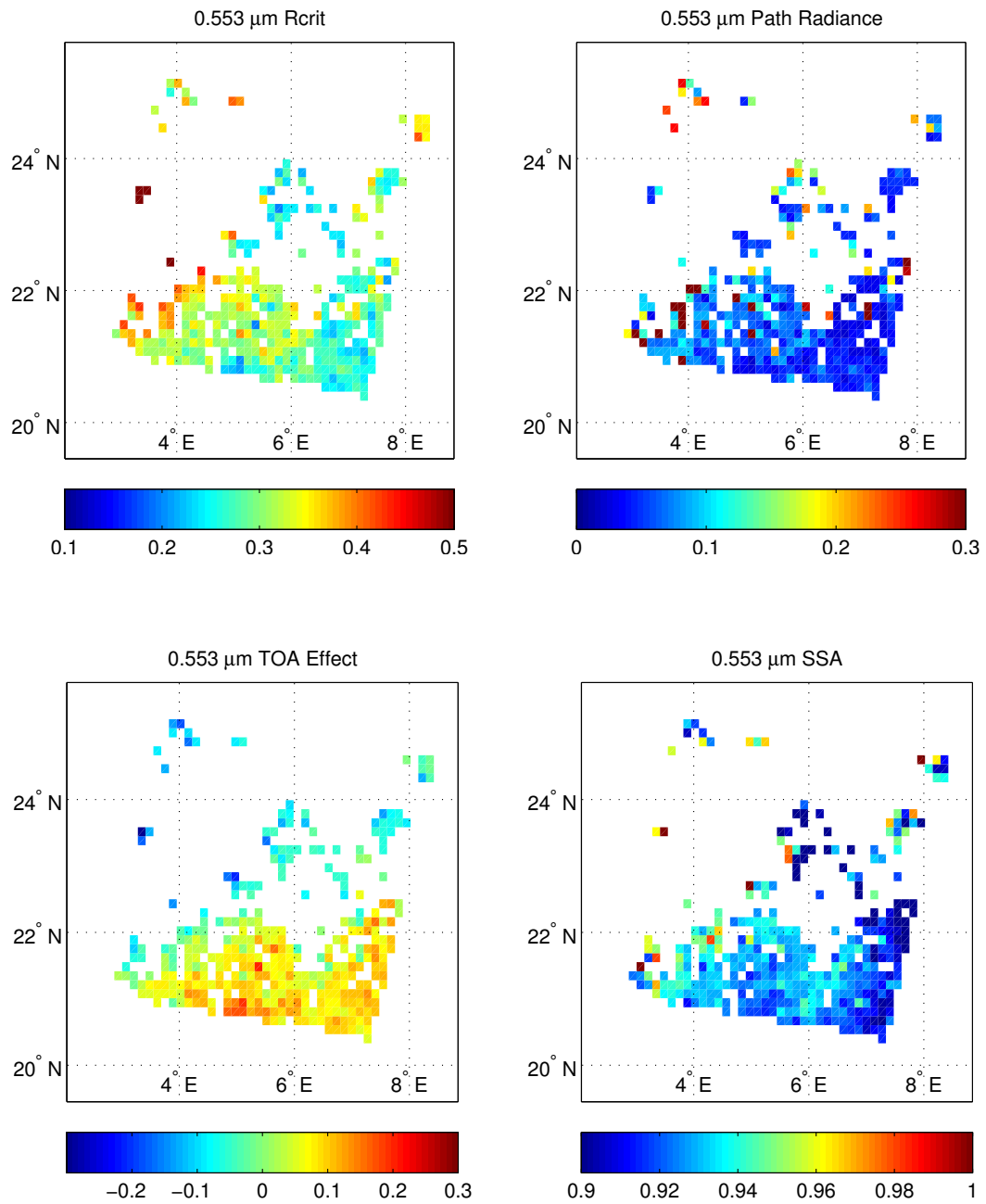


Figure C.1: Image retrievals of critical reflectance (upper left), path radiance (upper right), TOA radiative effect (lower left), and SSA (lower right) at 0.553  $\mu\text{m}$  for 14 December 2006 1020 UTC (compared to -16 days) near Tamanrasset.

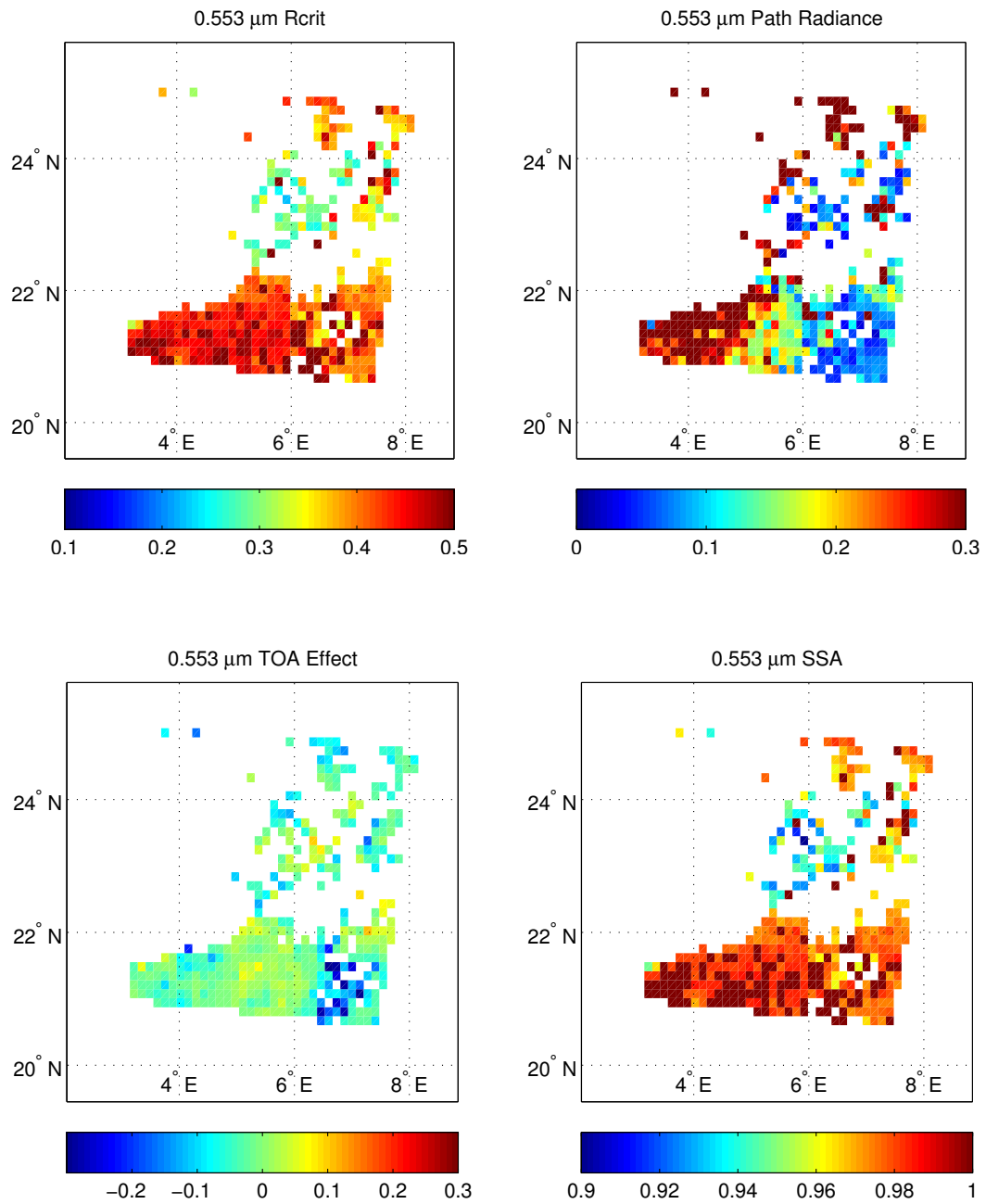


Figure C.2: Image retrievals of critical reflectance (upper left), path radiance (upper right), TOA radiative effect (lower left), and SSA (lower right) at 0.553  $\mu\text{m}$  for 22 February 2007 945 UTC (compared to -16 days) near Tamanrasset.

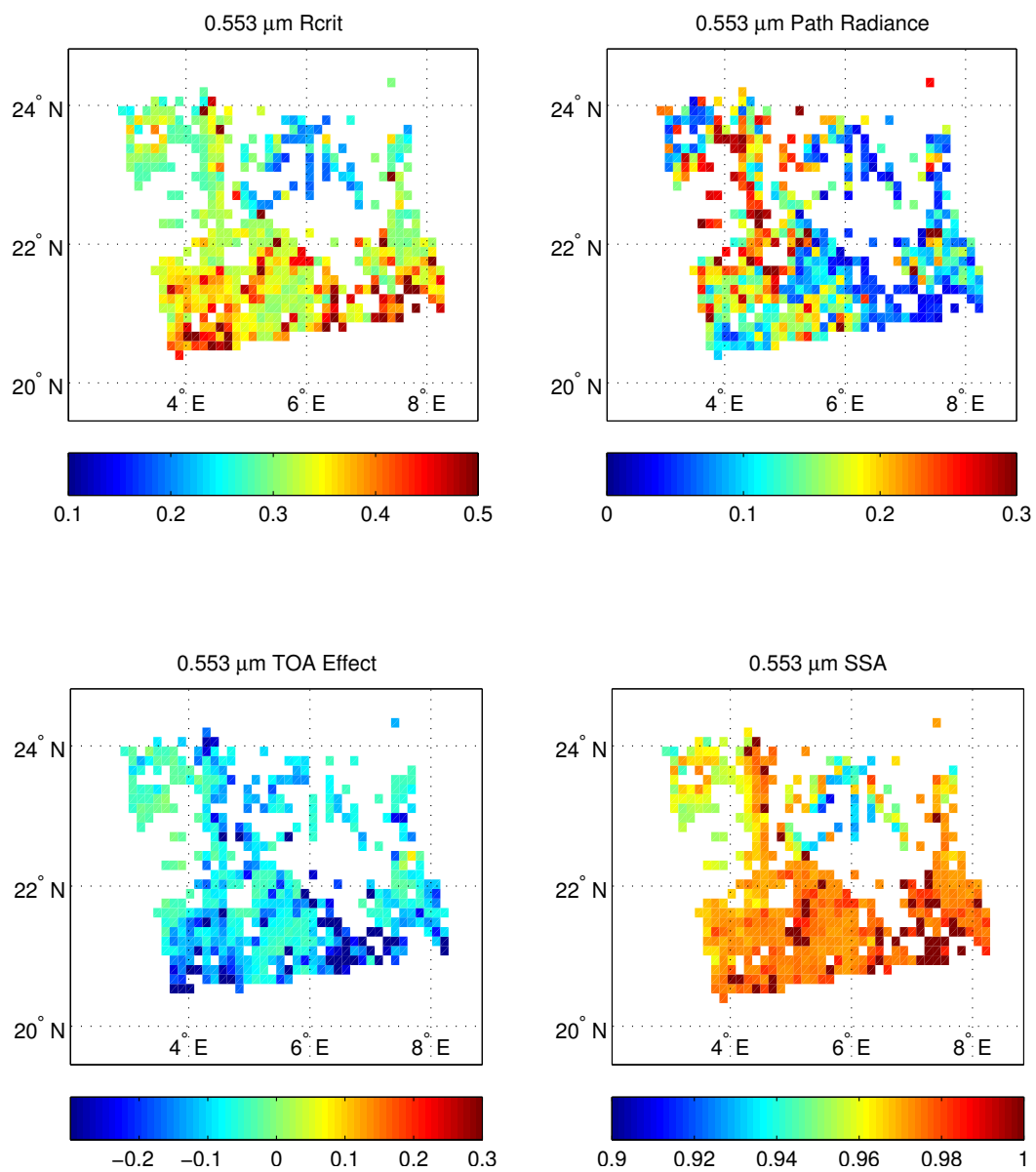


Figure C.3: Image retrievals of critical reflectance (upper left), path radiance (upper right), TOA radiative effect (lower left), and SSA (lower right) at 0.553  $\mu\text{m}$  for 22 February 2007 1250 UTC (compared to -16 days) near Tamanrasset.

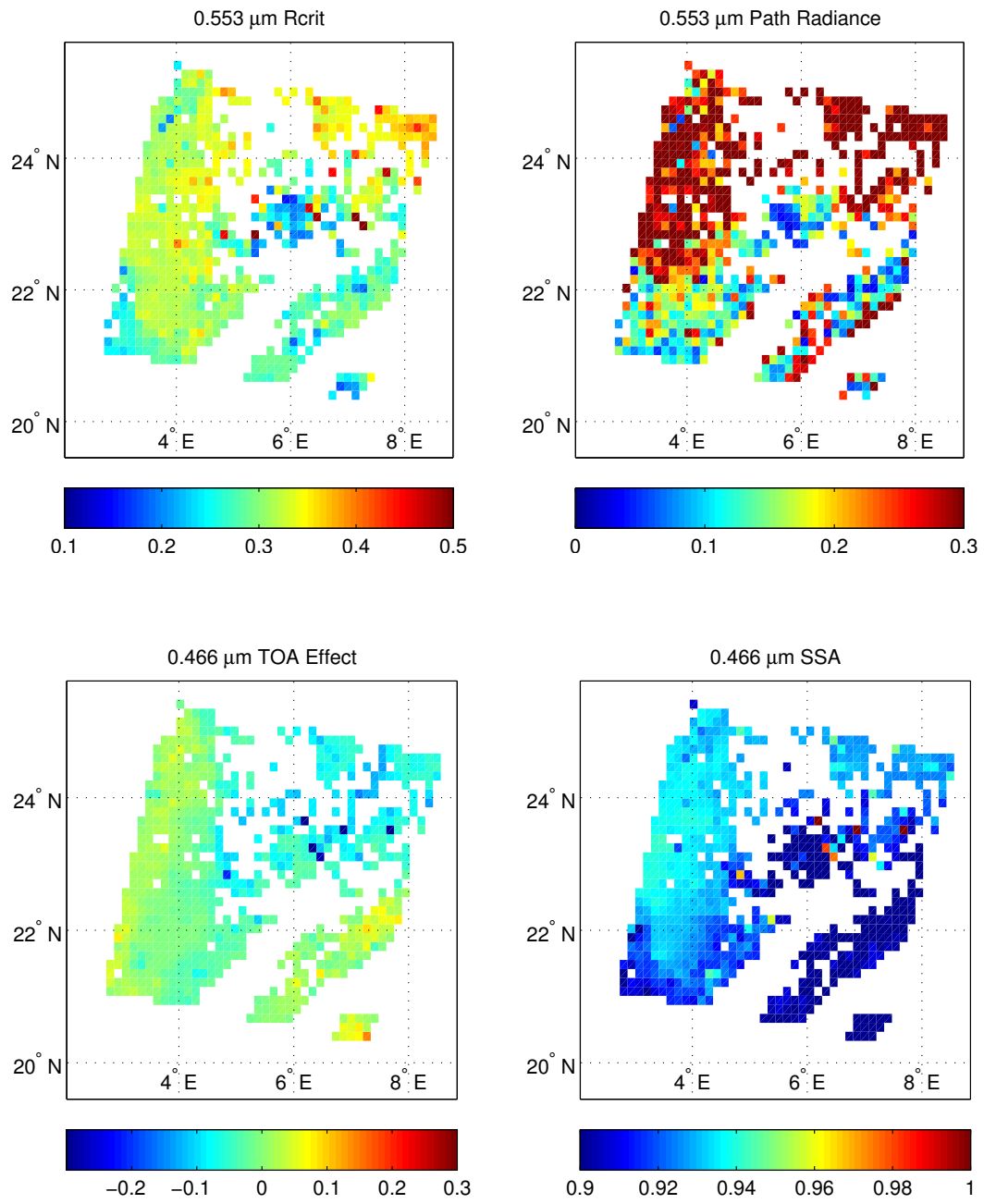


Figure C.4: Image retrievals of critical reflectance (upper left), path radiance (upper right), TOA radiative effect (lower left), and SSA (lower right) at 0.553  $\mu\text{m}$  for 9 March 2007 1040 UTC (compared to -16 days) near Tamanrasset.

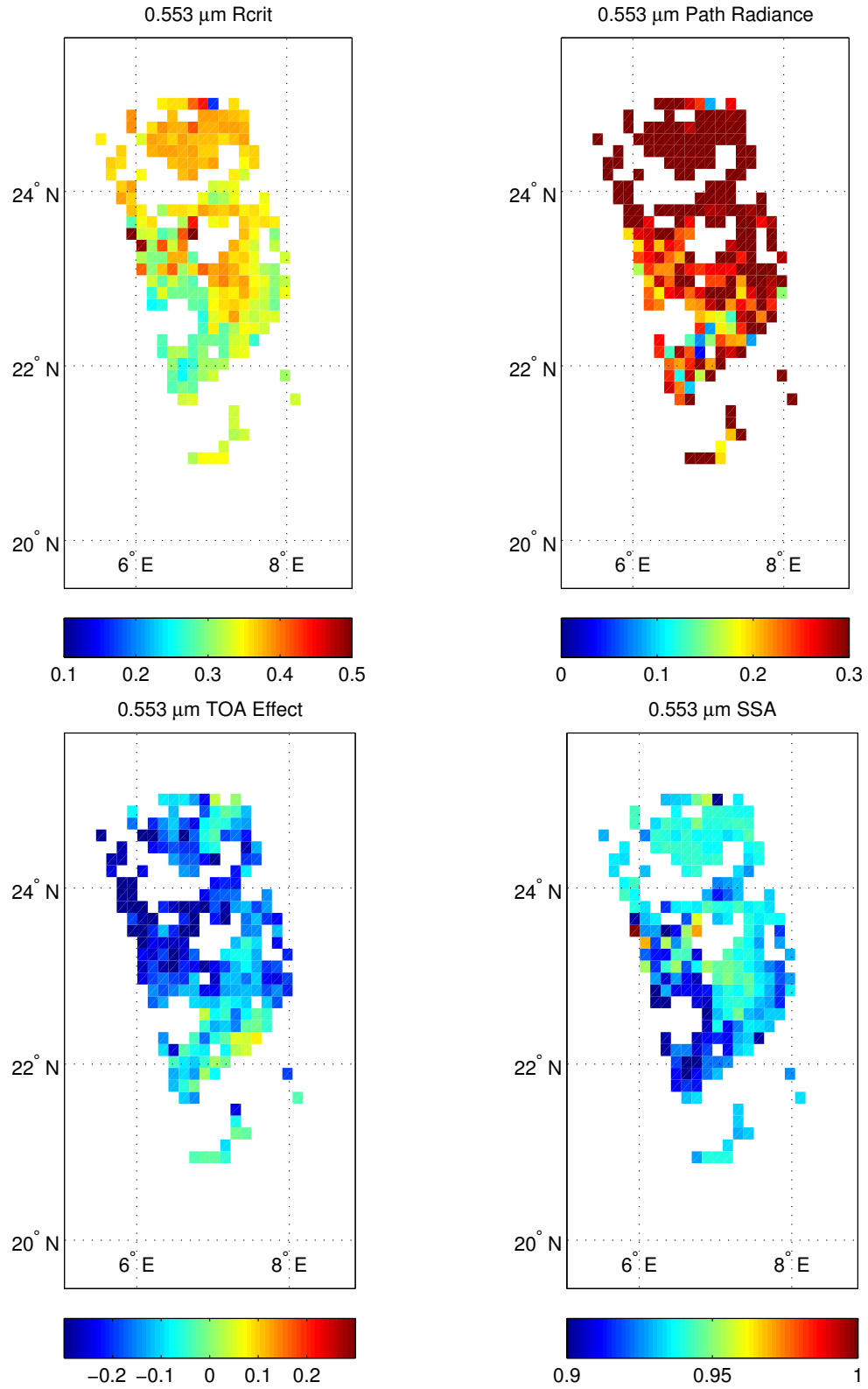


Figure C.5: Image retrievals of critical reflectance (upper left), path radiance (upper right), TOA radiative effect (lower left), and SSA (lower right) at 0.553 μm for 9 March 2007 1210 UTC (compared to -16 days) near Tamanrasset.

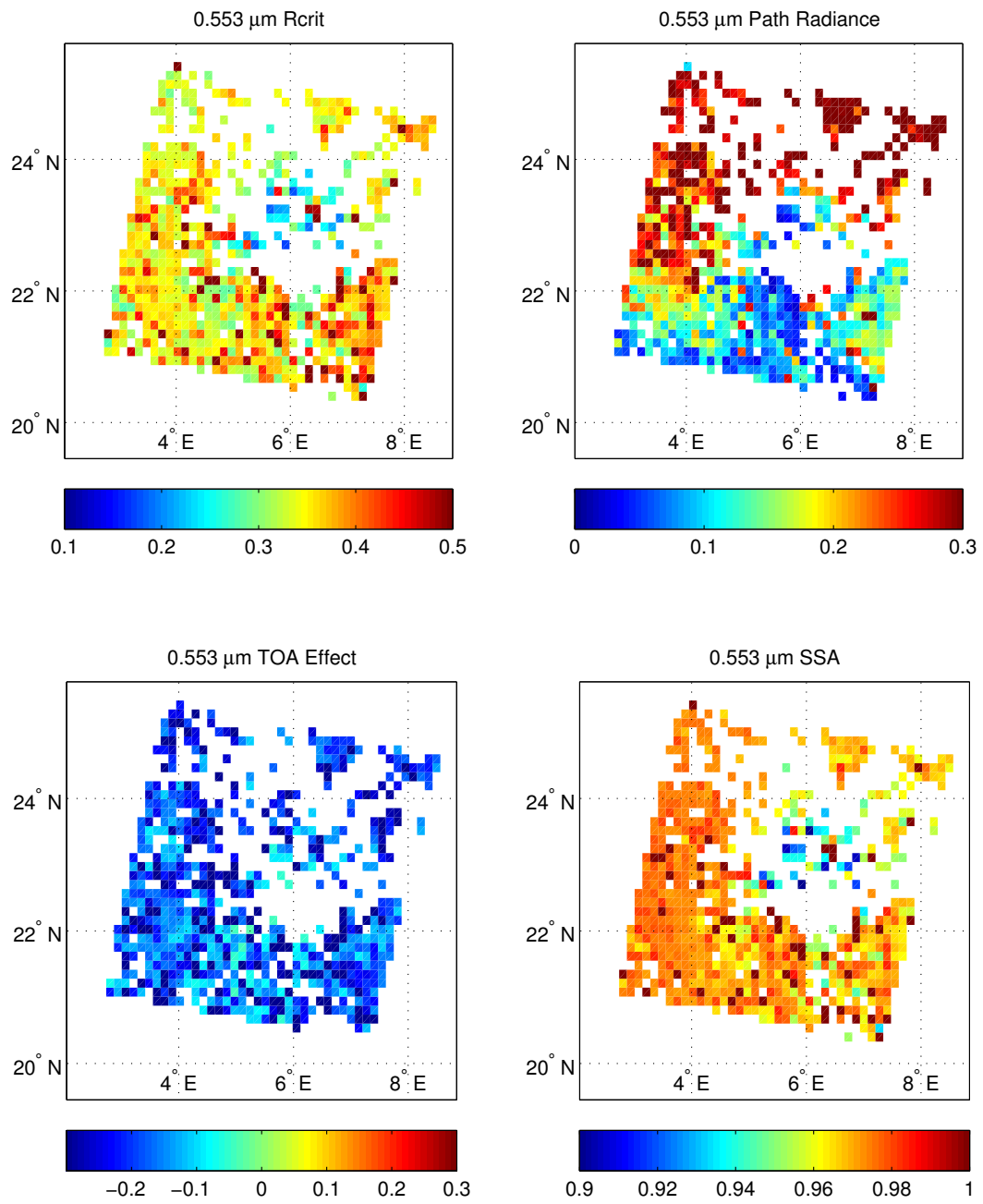


Figure C.6: Image retrievals of critical reflectance (upper left), path radiance (upper right), TOA radiative effect (lower left), and SSA (lower right) at 0.553 μm for 9 March 2007 1040 UTC (compared to +16 days) near Tamanrasset.

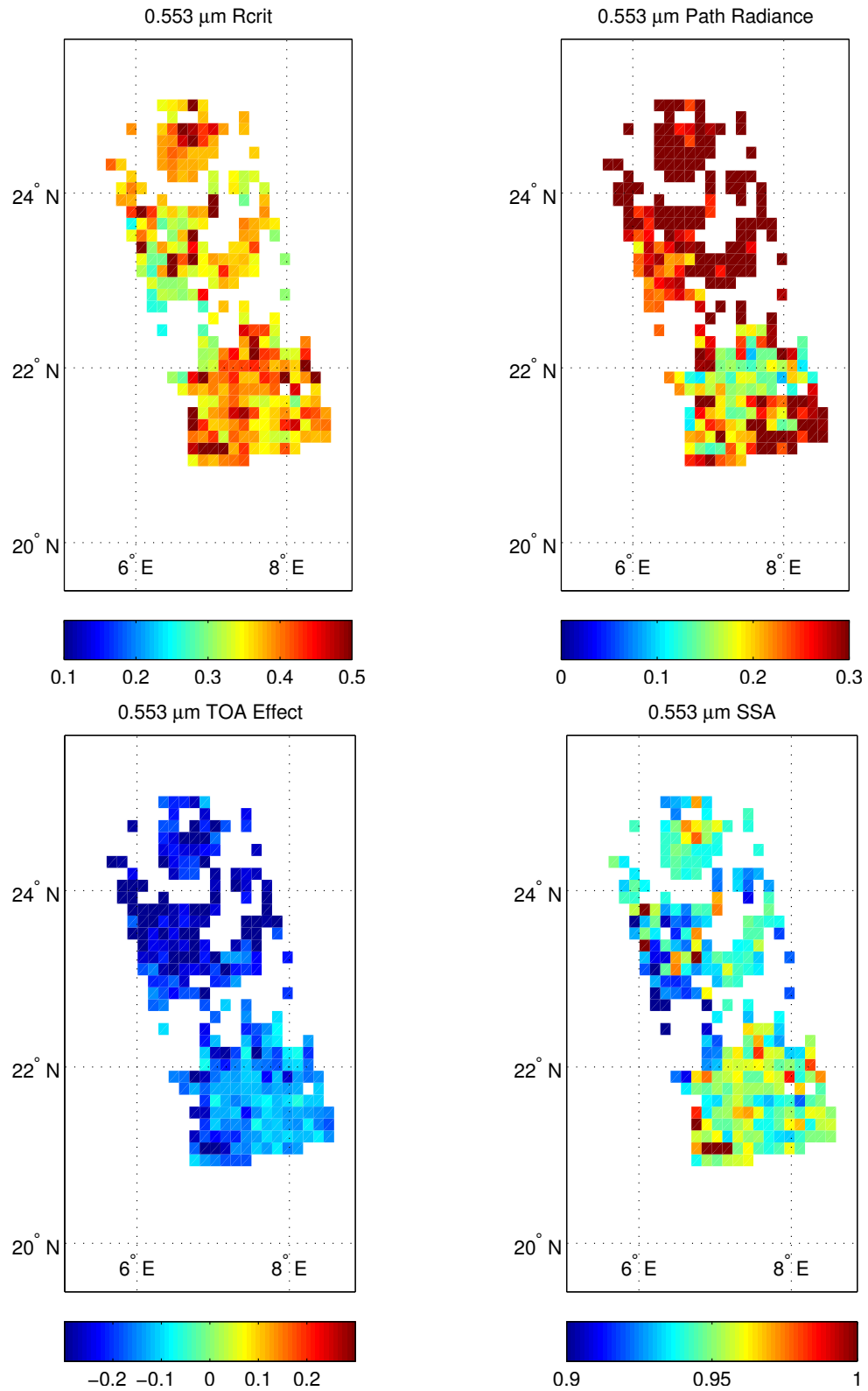


Figure C.7: Image retrievals of critical reflectance (upper left), path radiance (upper right), TOA radiative effect (lower left), and SSA (lower right) at 0.553 μm for 9 March 2007 1210 UTC (compared to +16 days) near Tamanrasset.

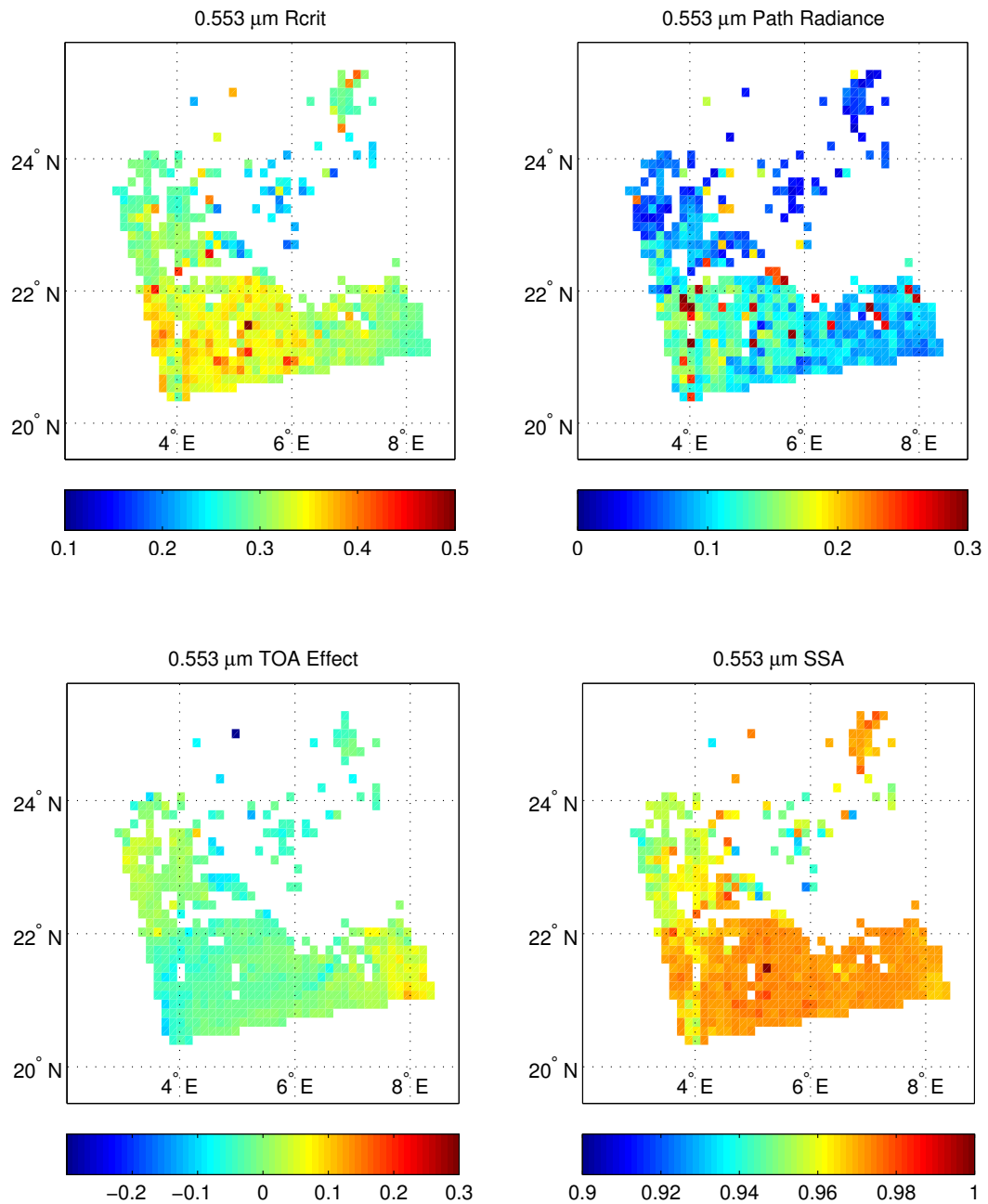


Figure C.8: Image retrievals of critical reflectance (upper left), path radiance (upper right), TOA radiative effect (lower left), and SSA (lower right) at 0.553 μm for 19 March 2007 1245 UTC (compared to -16 days) near Tamanrasset.

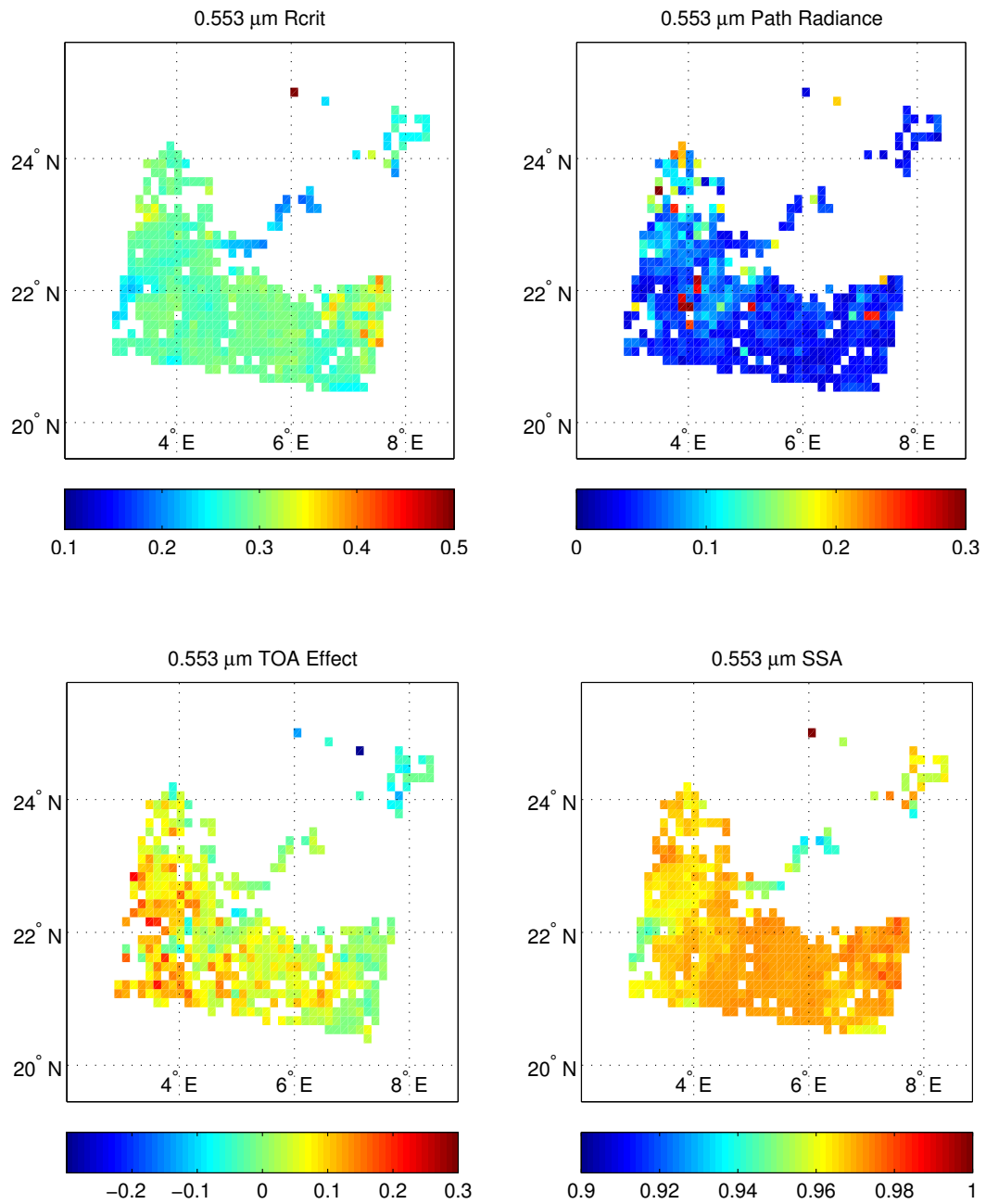


Figure C.9: Image retrievals of critical reflectance (upper left), path radiance (upper right), TOA radiative effect (lower left), and SSA (lower right) at 0.553 μm for 20 March 2007 1020 UTC (compared to +16 days) near Tamanrasset.

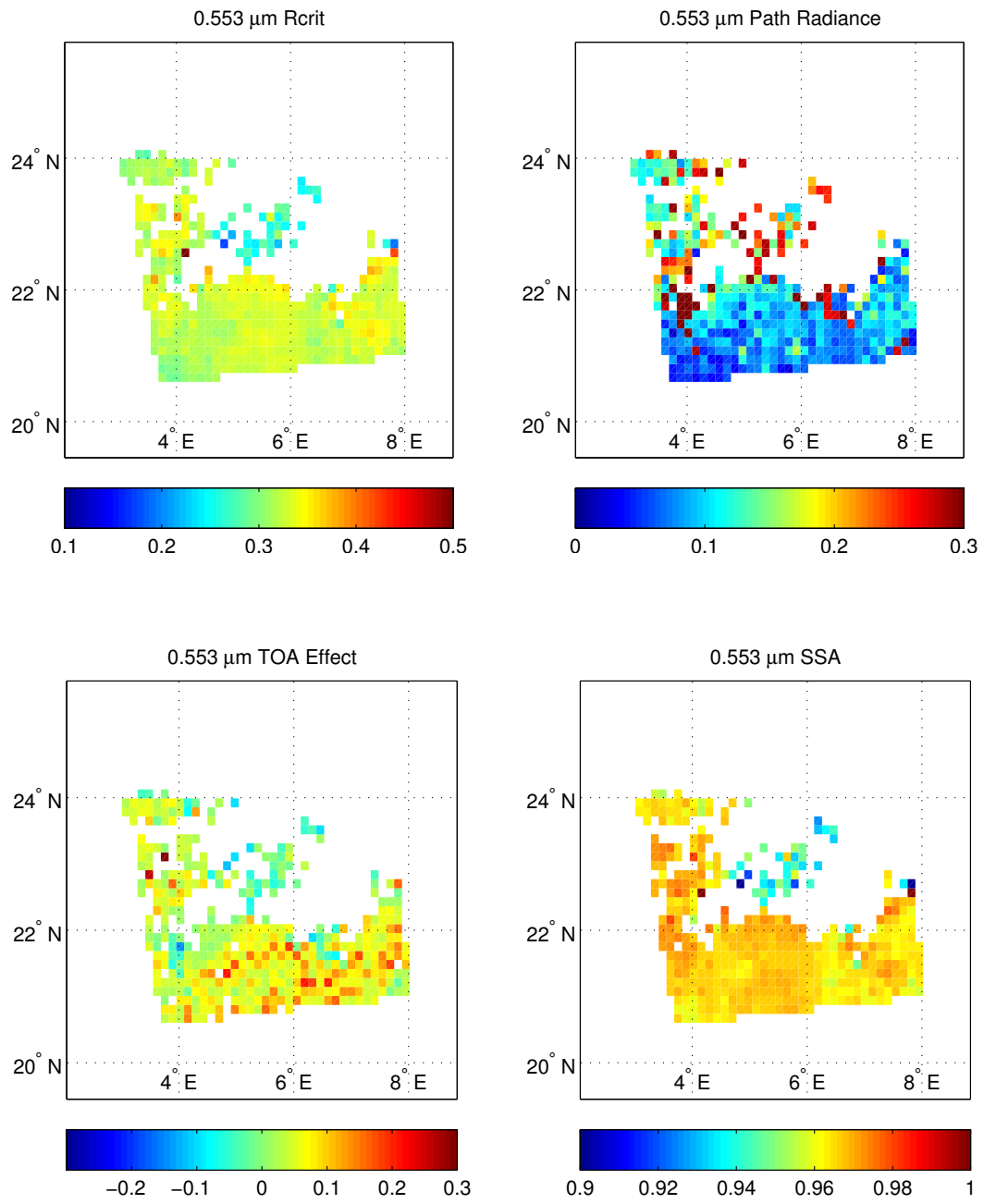


Figure C.10: Image retrievals of critical reflectance (upper left), path radiance (upper right), TOA radiative effect (lower left), and SSA (lower right) at 0.553  $\mu\text{m}$  for 20 March 2007 1330 UTC (compared to +16 days) near Tamanrasset.

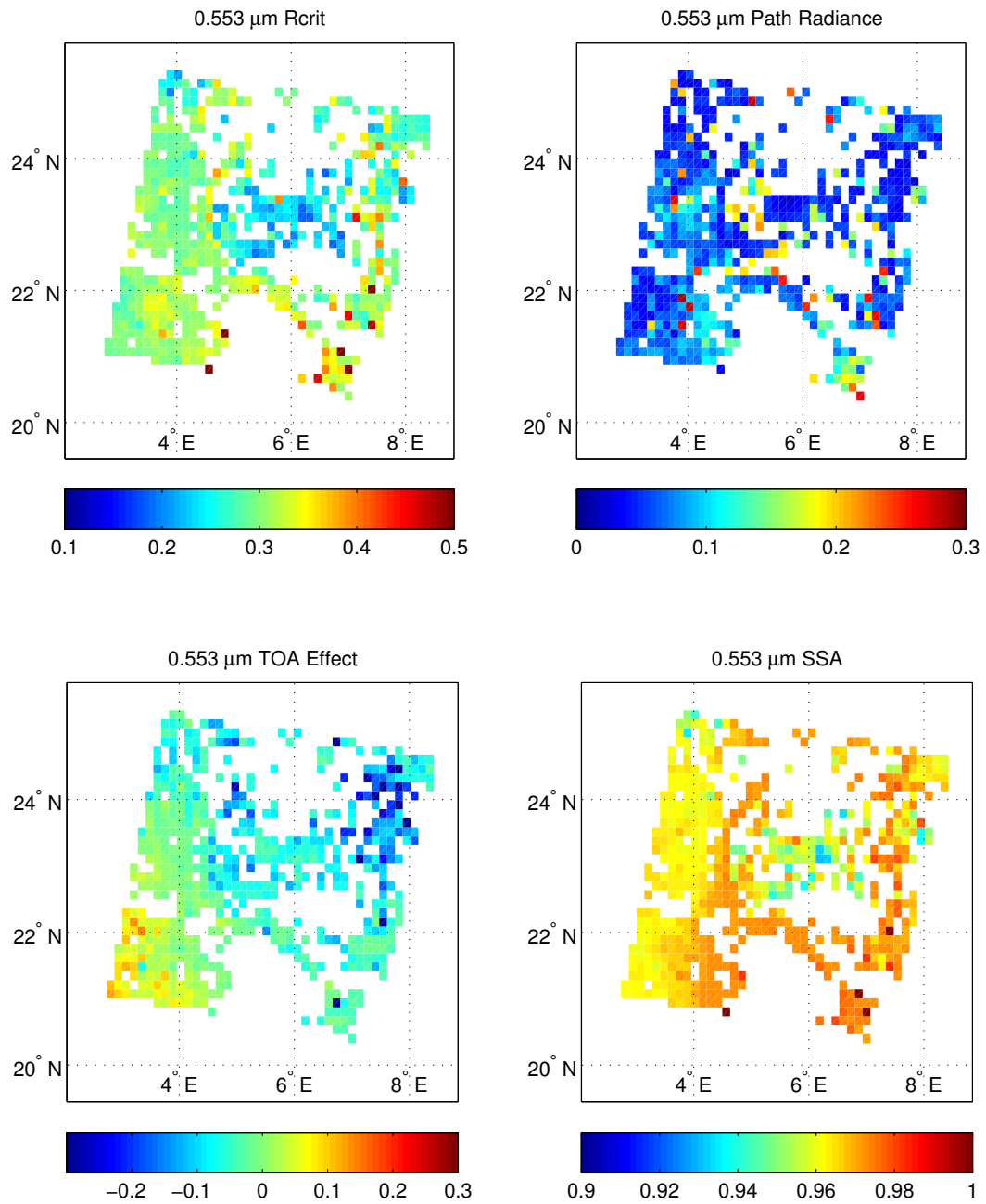


Figure C.11: Image retrievals of critical reflectance (upper left), path radiance (upper right), TOA radiative effect (lower left), and SSA (lower right) at 0.553  $\mu\text{m}$  for 14 May 2007 1025 UTC (compared to -16 days) near Tamanrasset.

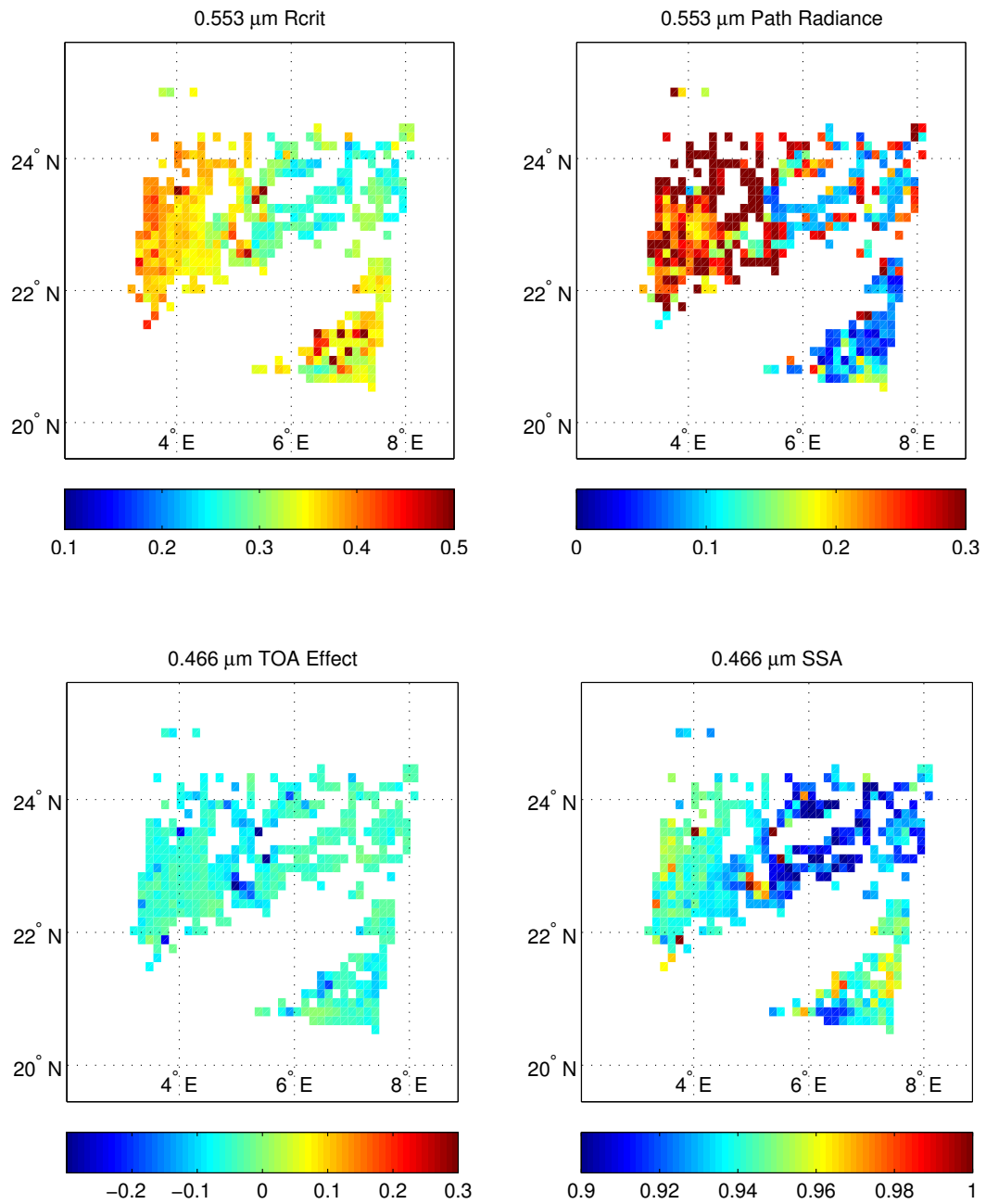


Figure C.12: Image retrievals of critical reflectance (upper left), path radiance (upper right), TOA radiative effect (lower left), and SSA (lower right) at 0.553  $\mu\text{m}$  for 23 July 2007 950 UTC (compared to -16 days) near Tamanrasset.

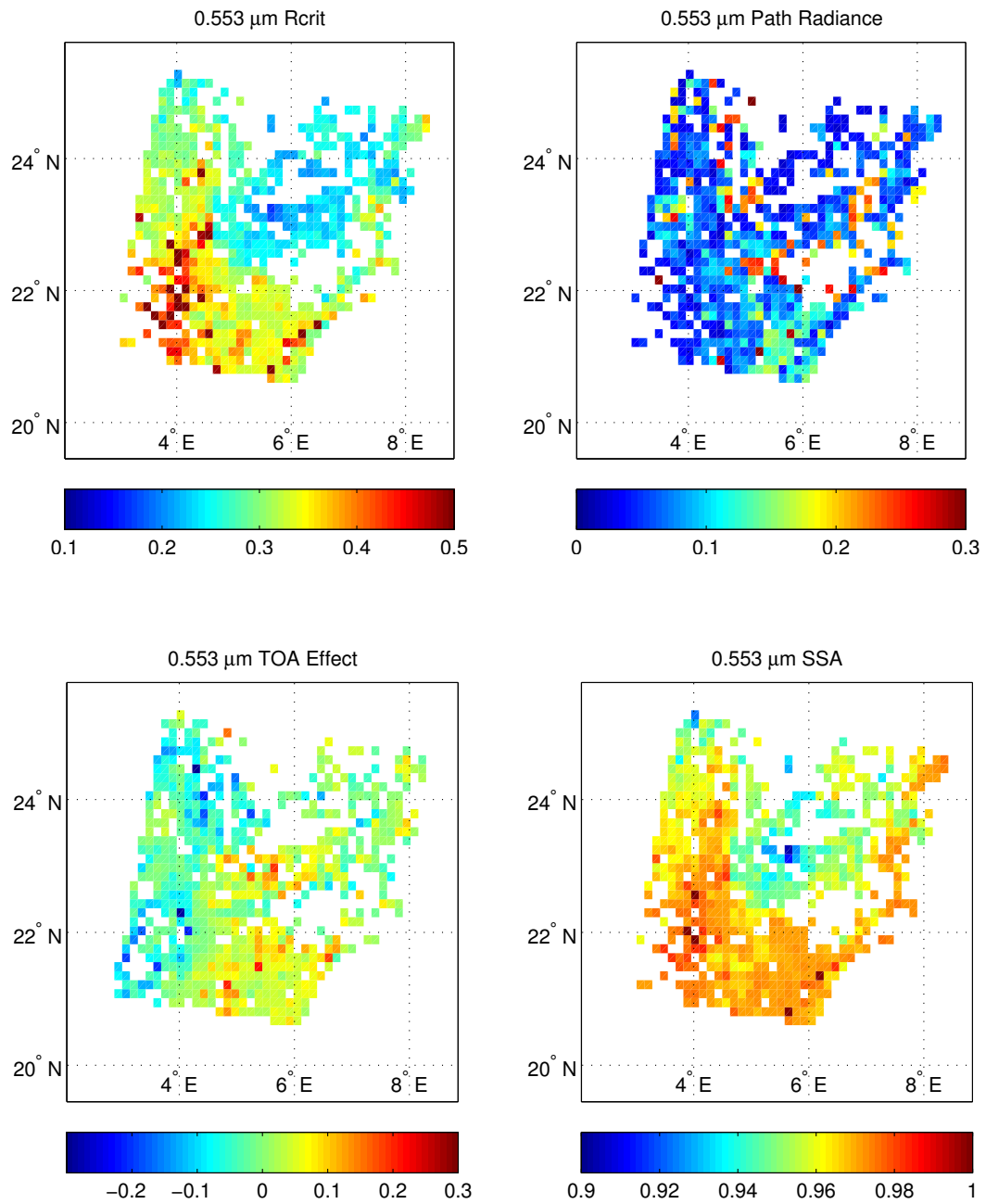


Figure C.13: Image retrievals of critical reflectance (upper left), path radiance (upper right), TOA radiative effect (lower left), and SSA (lower right) at 0.553  $\mu\text{m}$  for 4 August 2007 1015 UTC (compared to -16 days) near Tamanrasset.

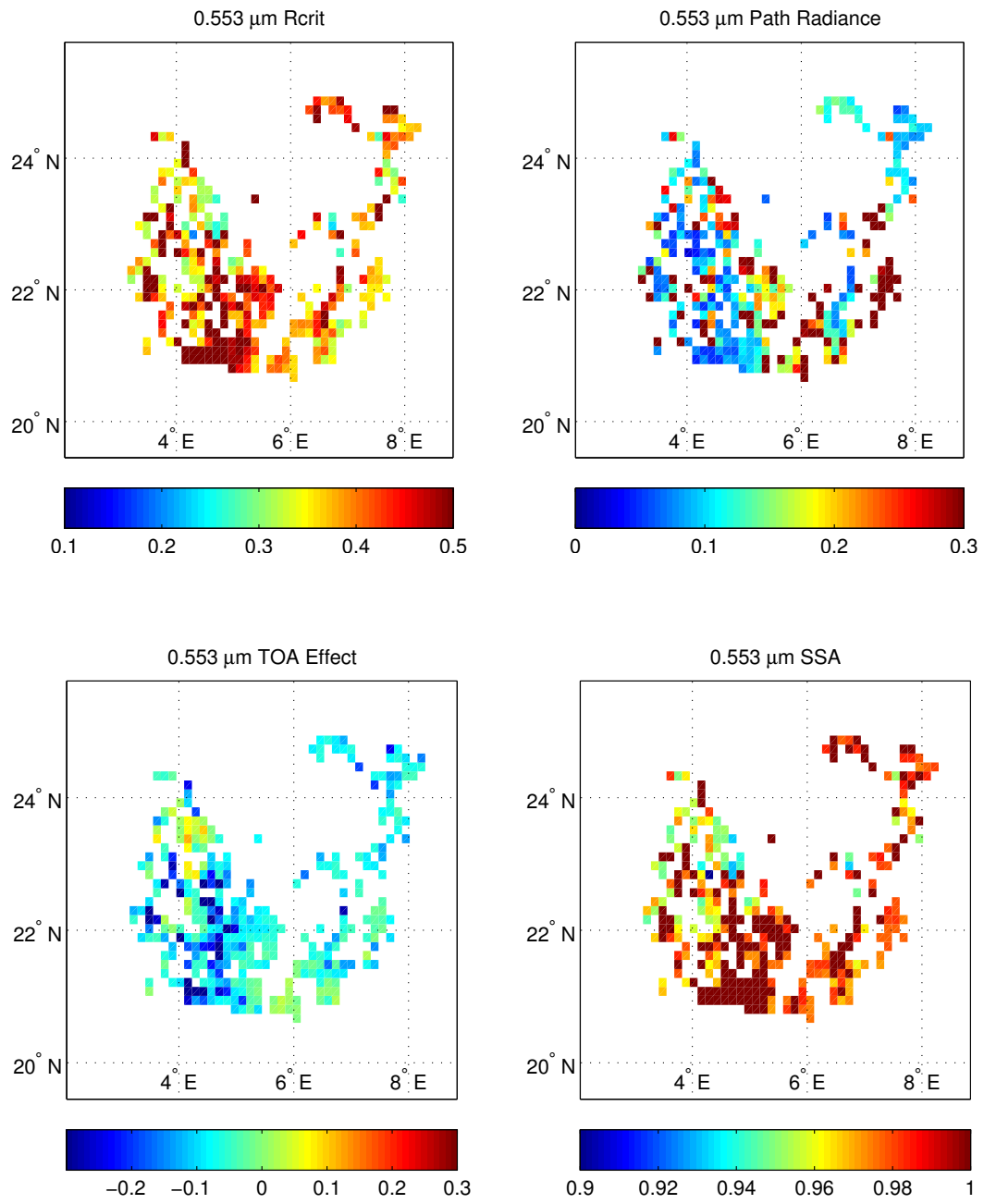


Figure C.14: Image retrievals of critical reflectance (upper left), path radiance (upper right), TOA radiative effect (lower left), and SSA (lower right) at 0.553 μm for 6 January 2008 955 UTC (compared to -16 days) near Tamanrasset.

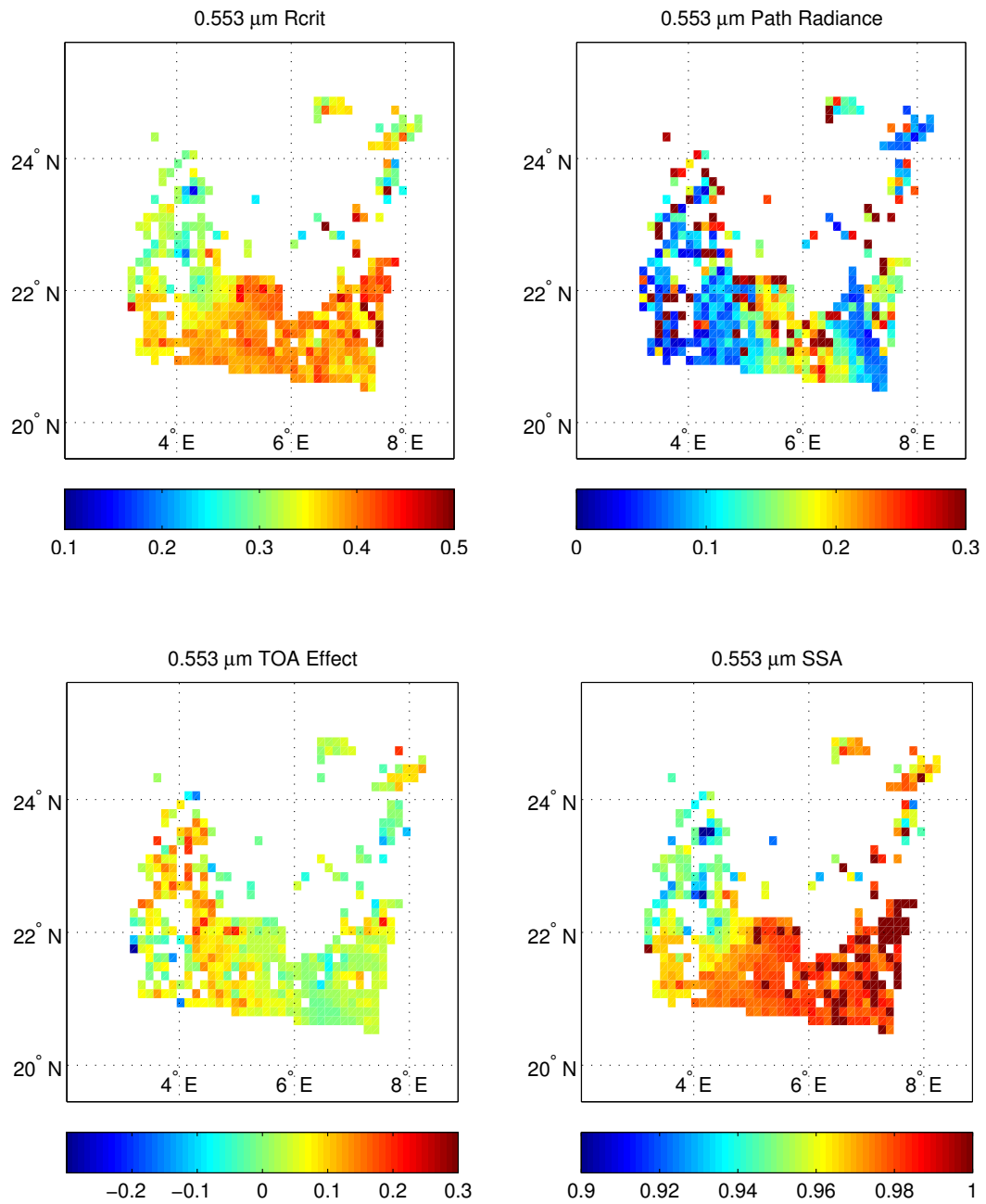


Figure C.15: Image retrievals of critical reflectance (upper left), path radiance (upper right), TOA radiative effect (lower left), and SSA (lower right) at 0.553 μm for 6 January 2008 955 UTC (compared to +16 days) near Tamanrasset.

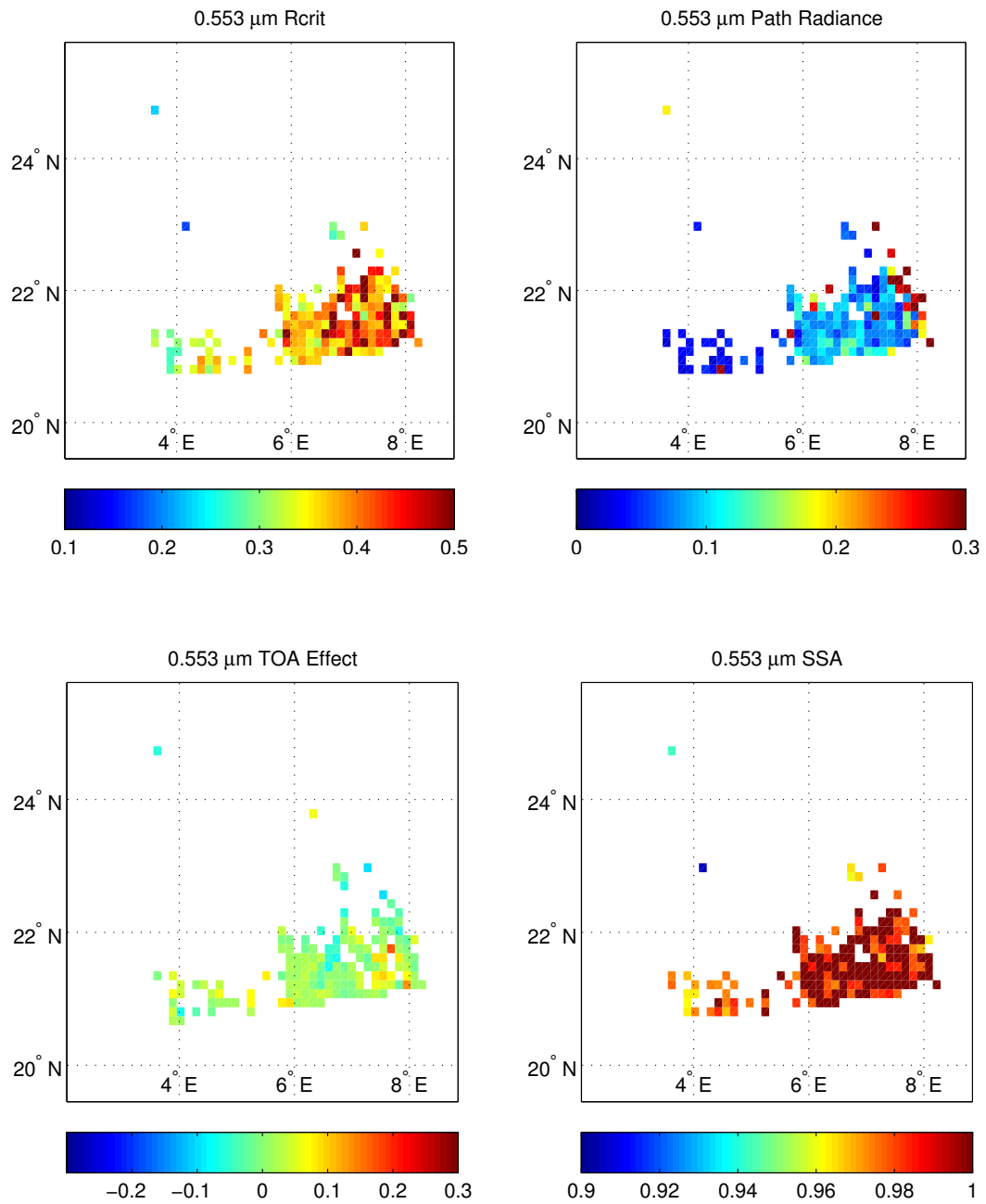


Figure C.16: Image retrievals of critical reflectance (upper left), path radiance (upper right), TOA radiative effect (lower left), and SSA (lower right) at 0.553 μm for 6 January 2008 1305 UTC (compared to +16 days) near Tamanrasset.

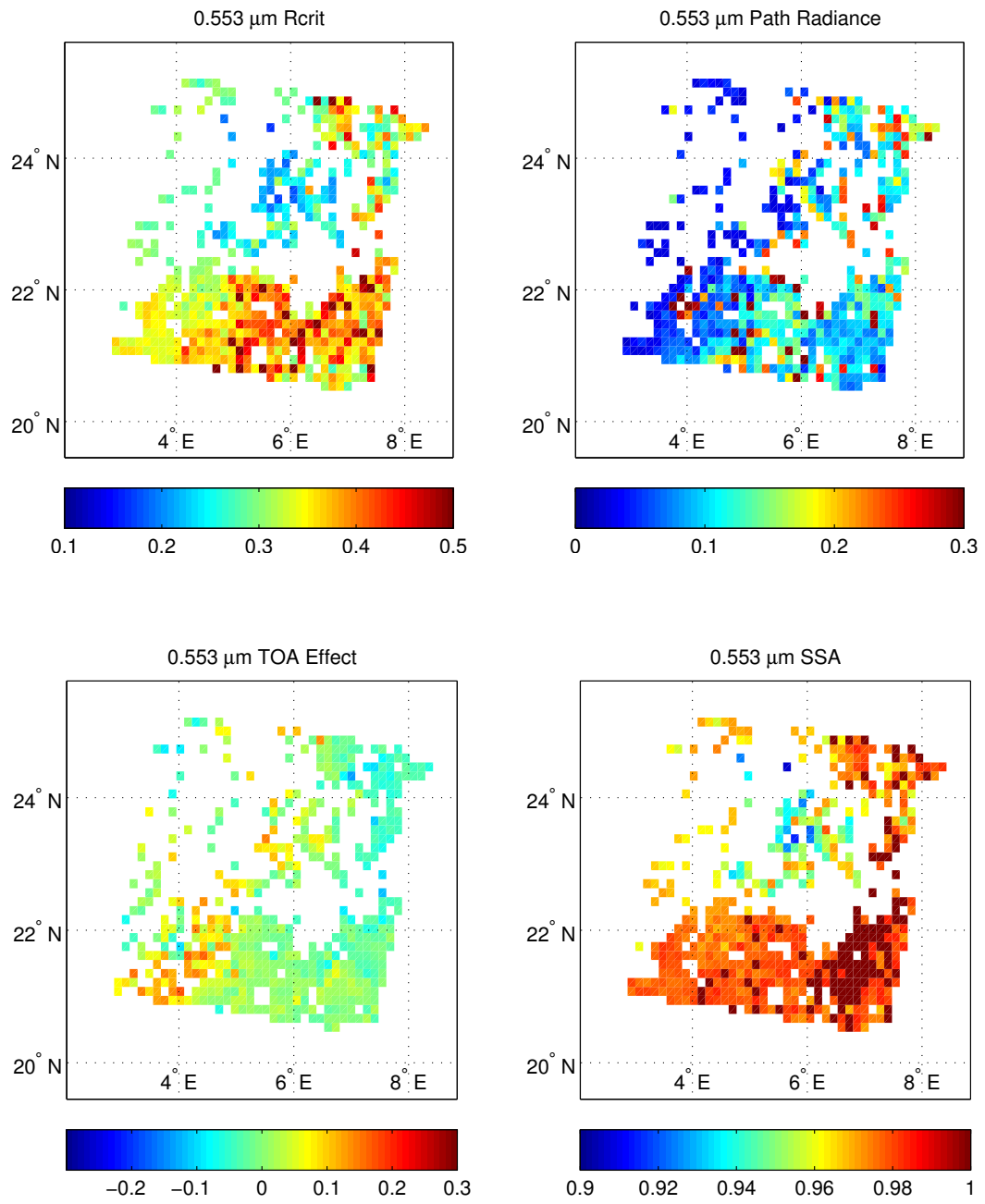


Figure C.17: Image retrievals of critical reflectance (upper left), path radiance (upper right), TOA radiative effect (lower left), and SSA (lower right) at 0.553 μm for 28 February 2008 1015 UTC (compared to +16 days) near Tamanrasset.

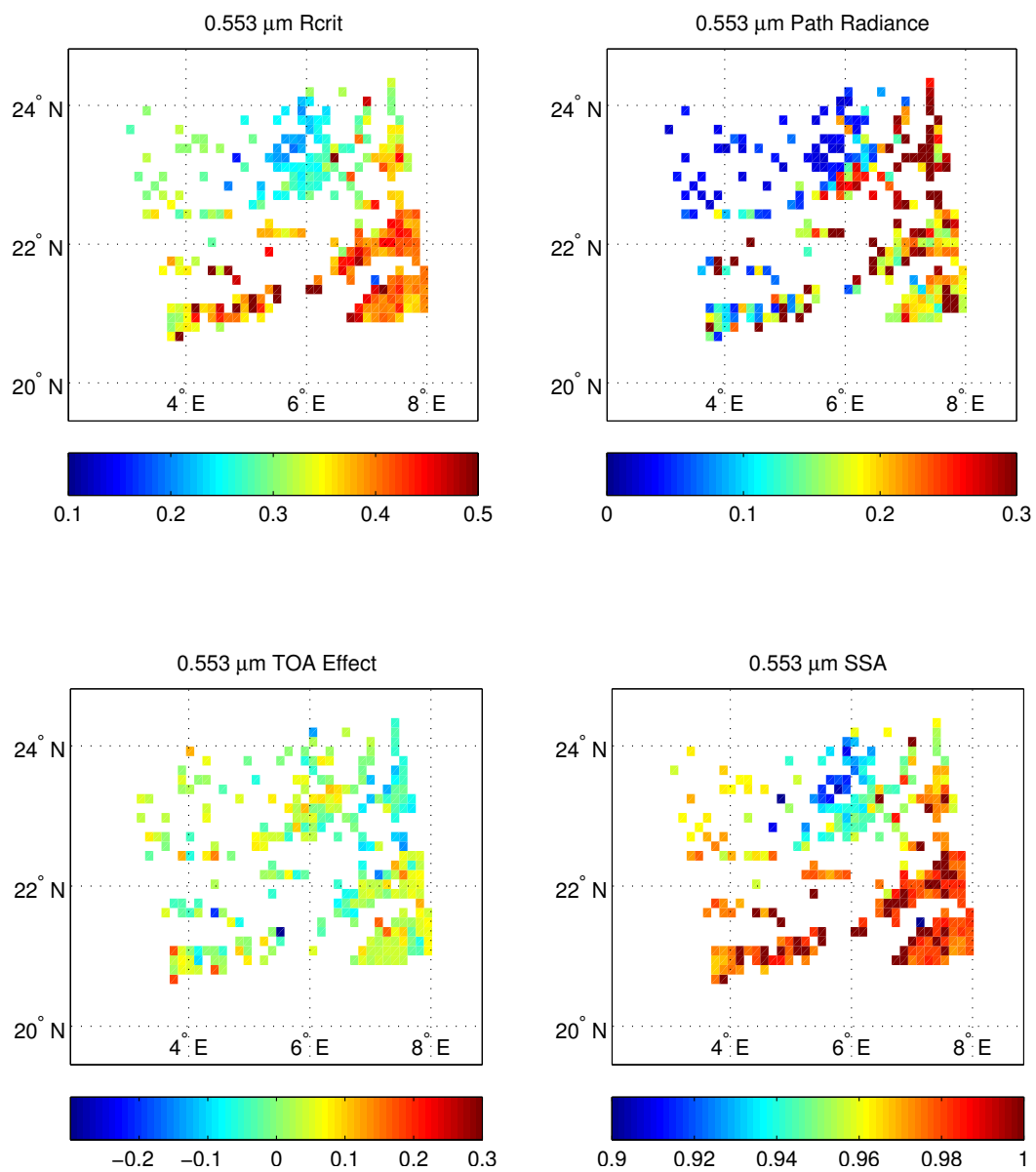


Figure C.18: Image retrievals of critical reflectance (upper left), path radiance (upper right), TOA radiative effect (lower left), and SSA (lower right) at 0.553 μm for 28 February 2008 1320 UTC (compared to +16 days) near Tamanrasset.

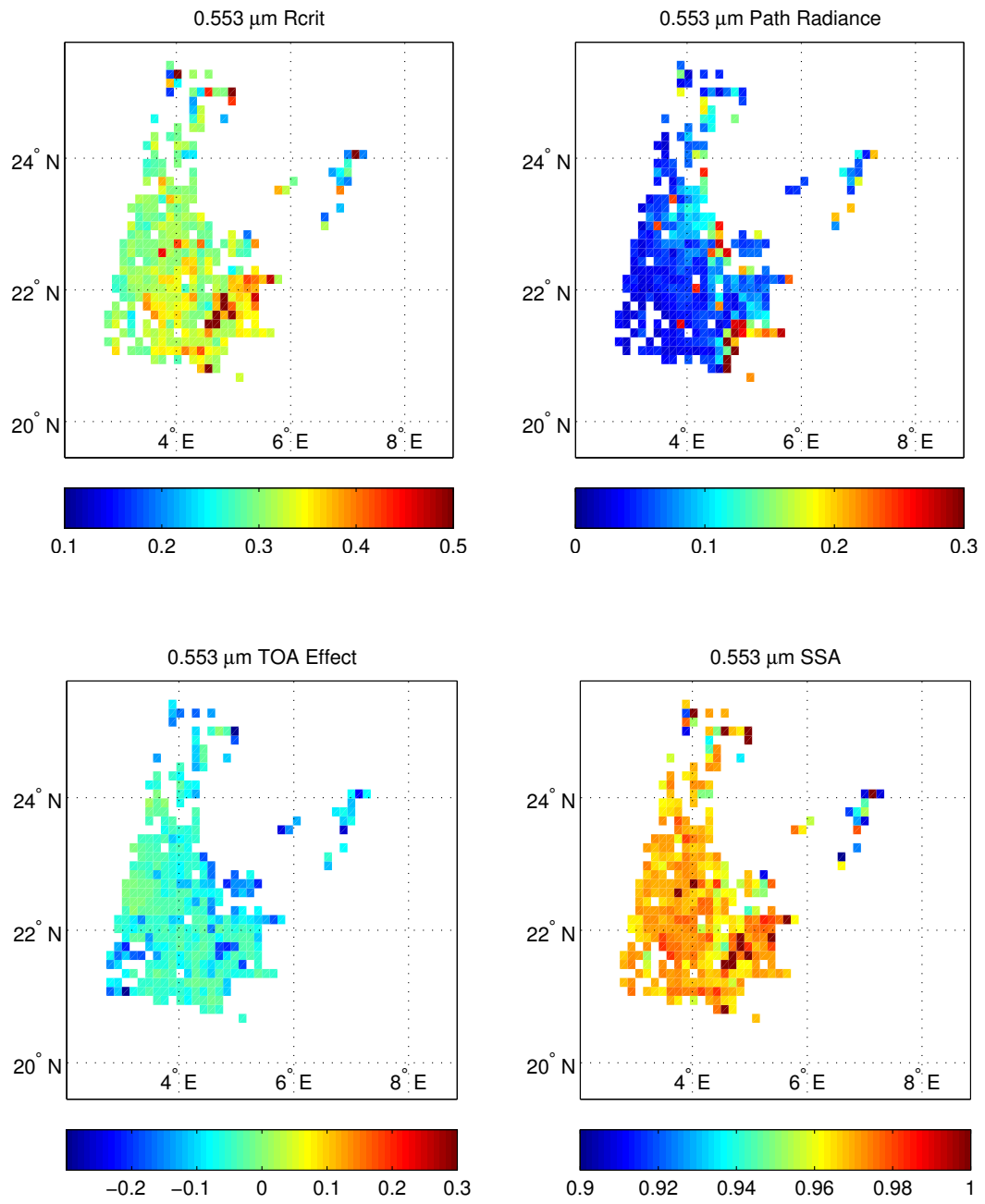


Figure C.19: Image retrievals of critical reflectance (upper left), path radiance (upper right), TOA radiative effect (lower left), and SSA (lower right) at 0.553  $\mu\text{m}$  for 3 April 2008 1045 UTC (compared to -16 days) near Tamanrasset.

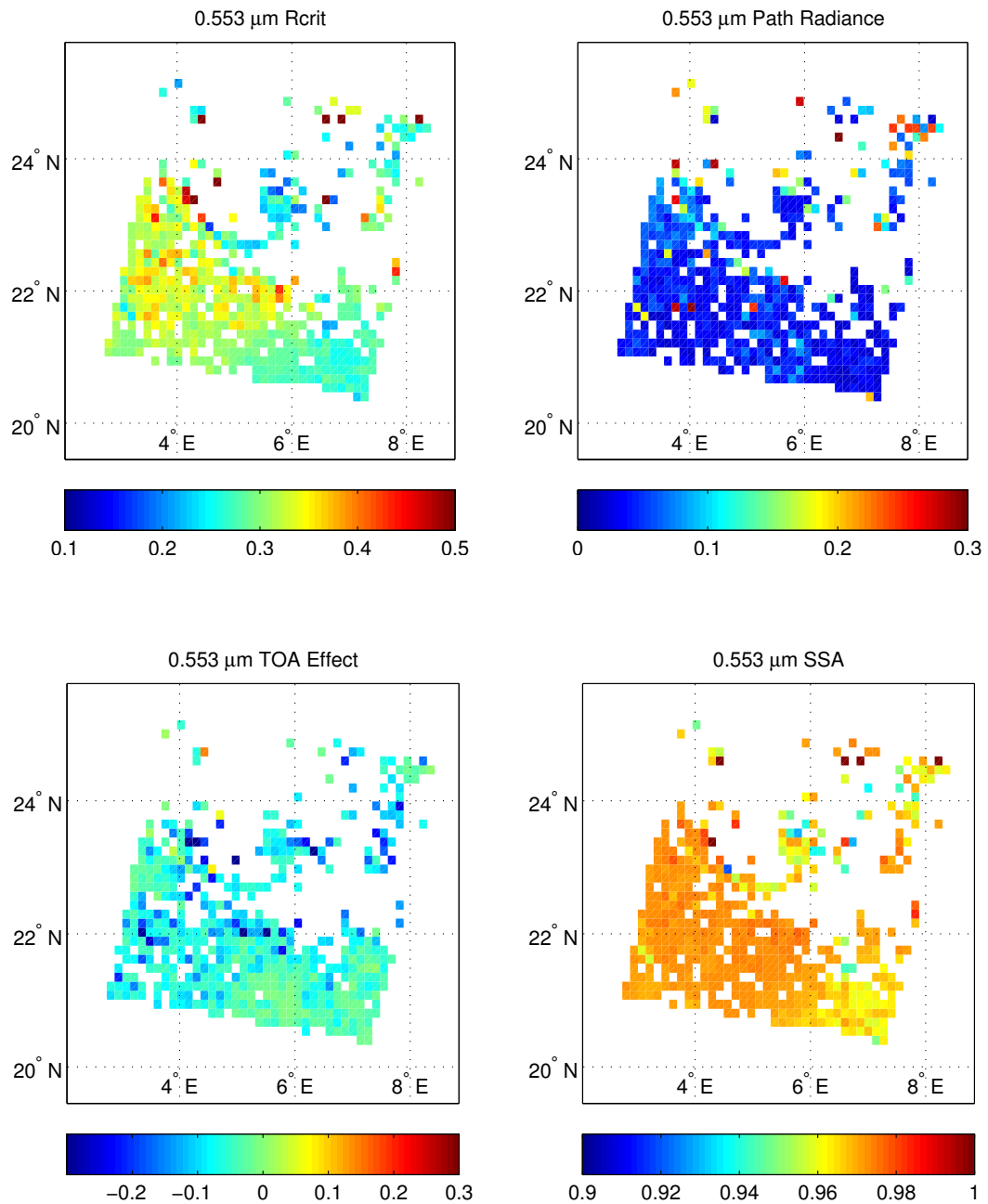


Figure C.20: Image retrievals of critical reflectance (upper left), path radiance (upper right), TOA radiative effect (lower left), and SSA (lower right) at 0.553 μm for 14 April 2008 1025 UTC (compared to -16 days) near Tamanrasset.

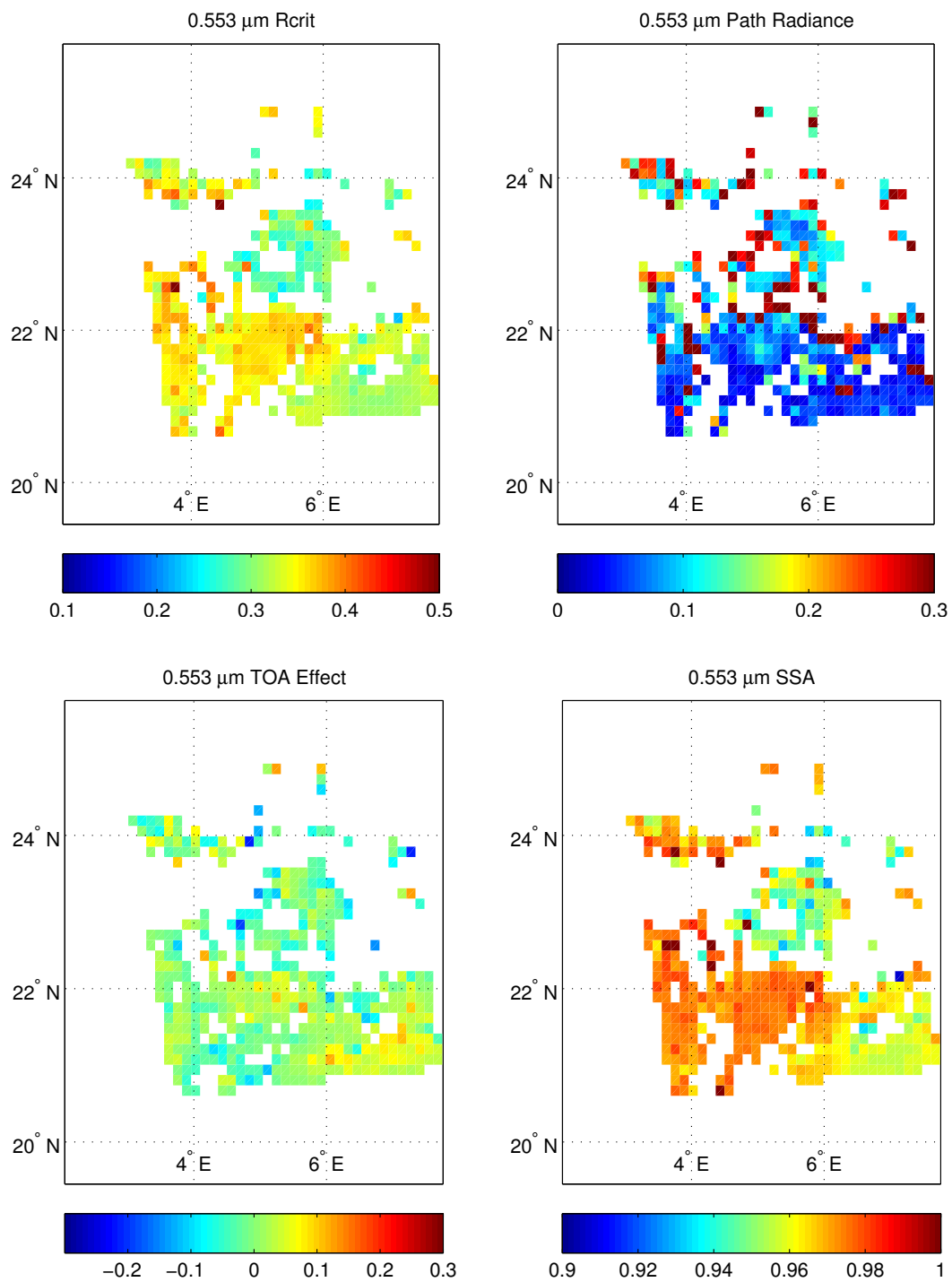


Figure C.21: Image retrievals of critical reflectance (upper left), path radiance (upper right), TOA radiative effect (lower left), and SSA (lower right) at 0.553 μm for 14 April 2008 1335 UTC (compared to -16 days) near Tamanrasset.

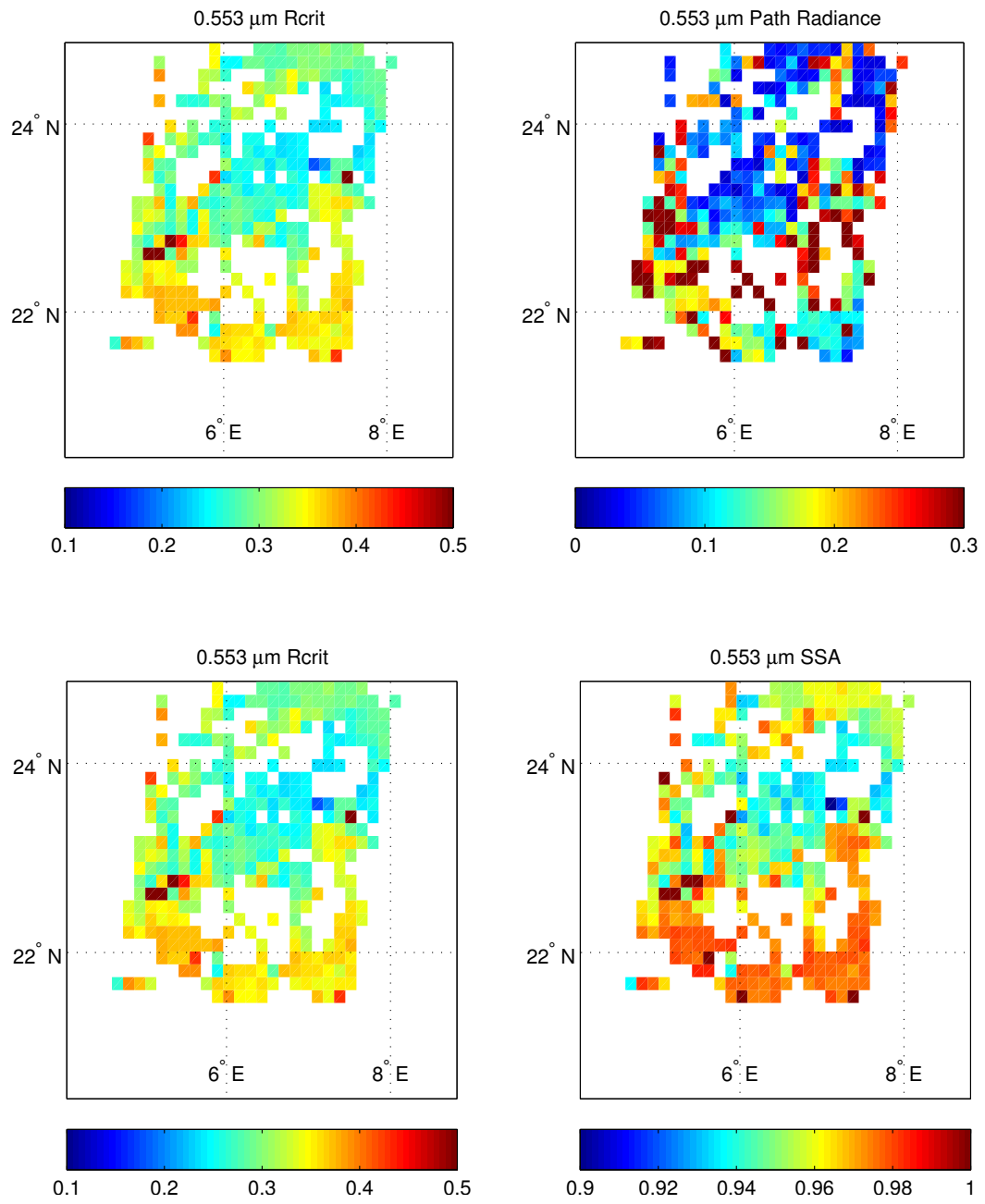


Figure C.22: Image retrievals of critical reflectance (upper left), path radiance (upper right), TOA radiative effect (lower left), and SSA (lower right) at 0.553 μm for 27 July 2008 935 UTC (compared to +16 days) near Tamanrasset.

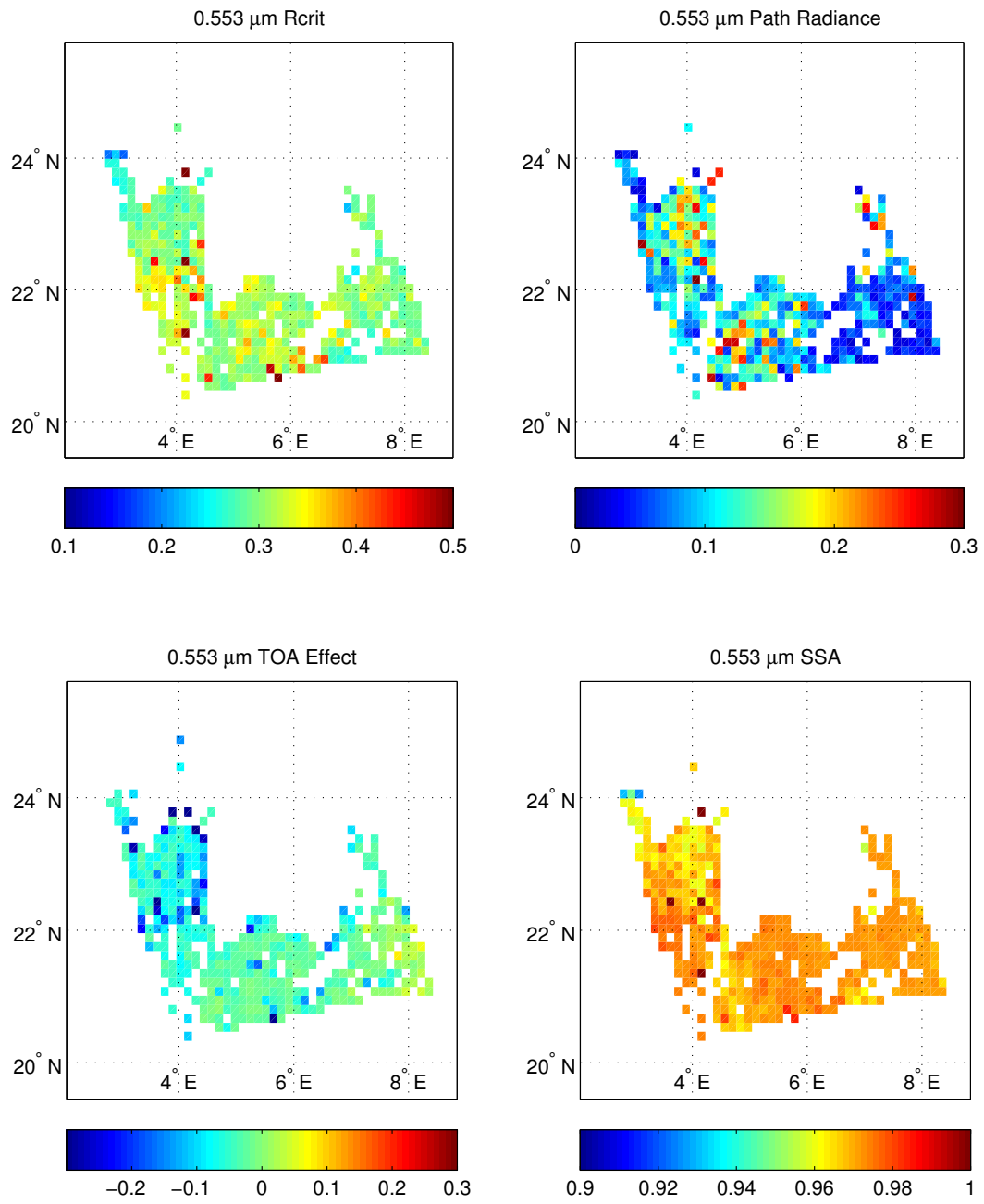


Figure C.23: Image retrievals of critical reflectance (upper left), path radiance (upper right), TOA radiative effect (lower left), and SSA (lower right) at 0.553 μm for 27 July 2008 1245 UTC (compared to +16 days) near Tamanrasset.

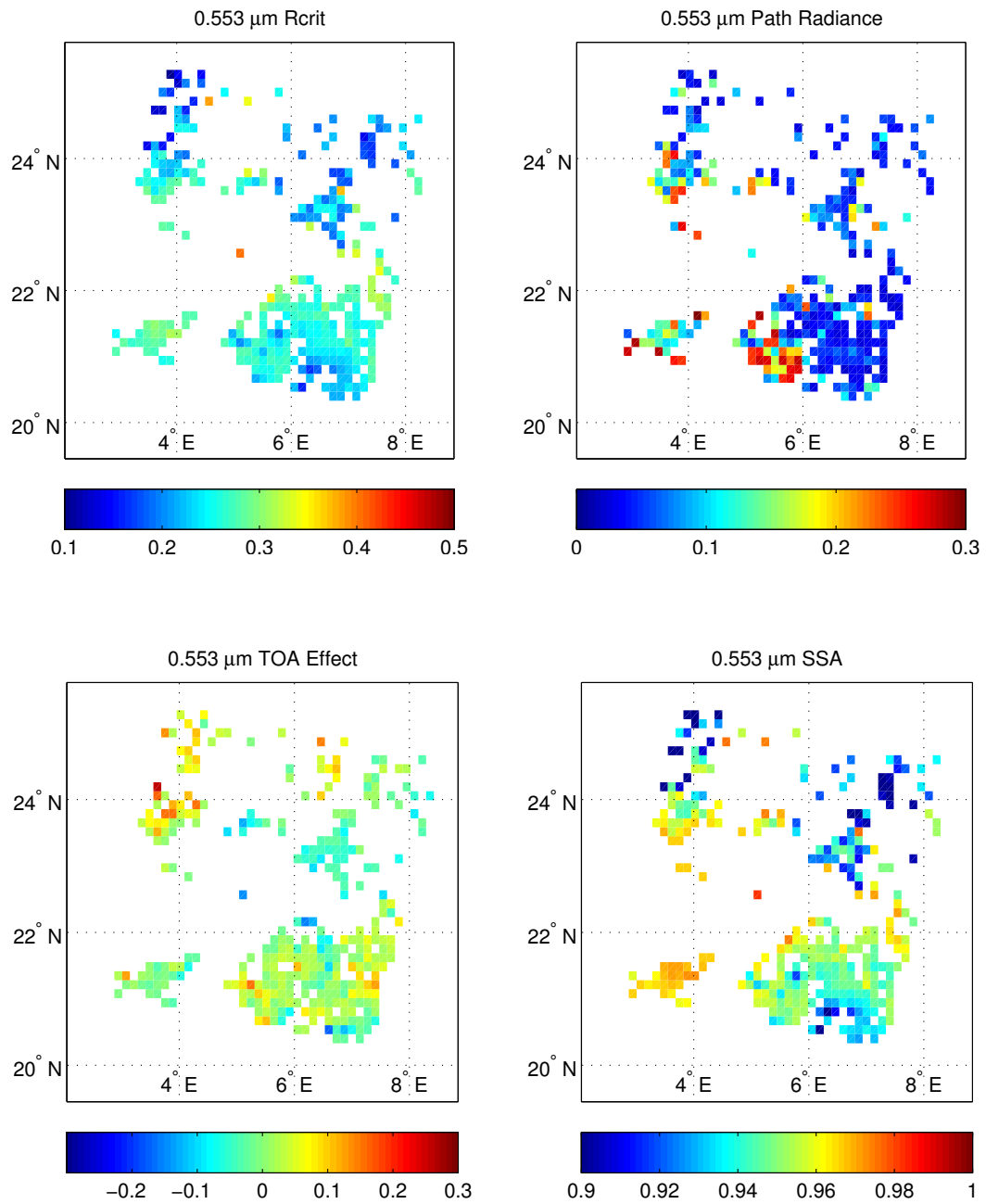


Figure C.24: Image retrievals of critical reflectance (upper left), path radiance (upper right), TOA radiative effect (lower left), and SSA (lower right) at 0.553 μm for 3 September 2008 1040 UTC (compared to -16 days) near Tamanrasset.

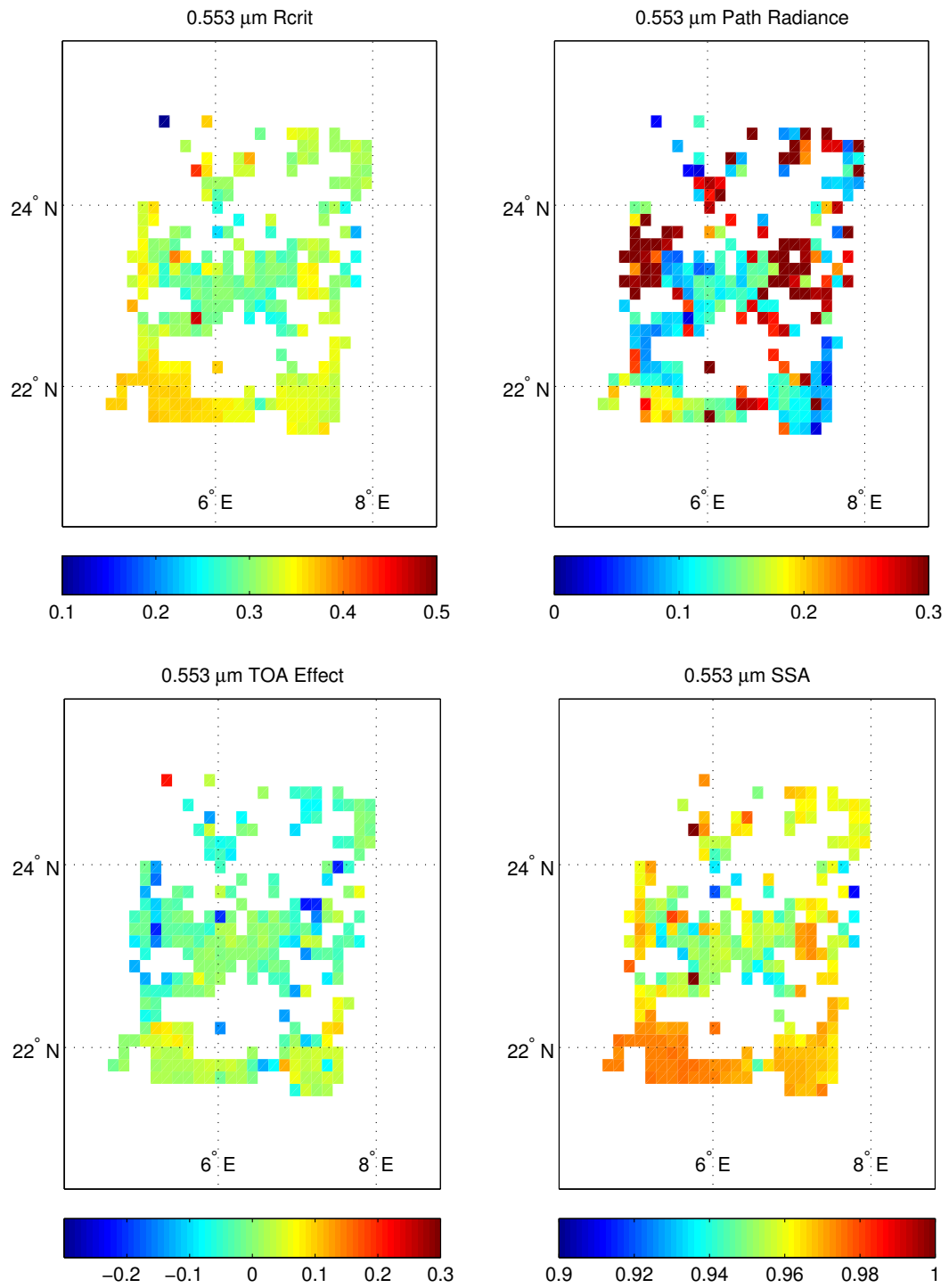


Figure C.25: Image retrievals of critical reflectance (upper left), path radiance (upper right), TOA radiative effect (lower left), and SSA (lower right) at 0.553  $\mu\text{m}$  for 29 September 2008 935 UTC (compared to +16 days) near Tamanrasset.

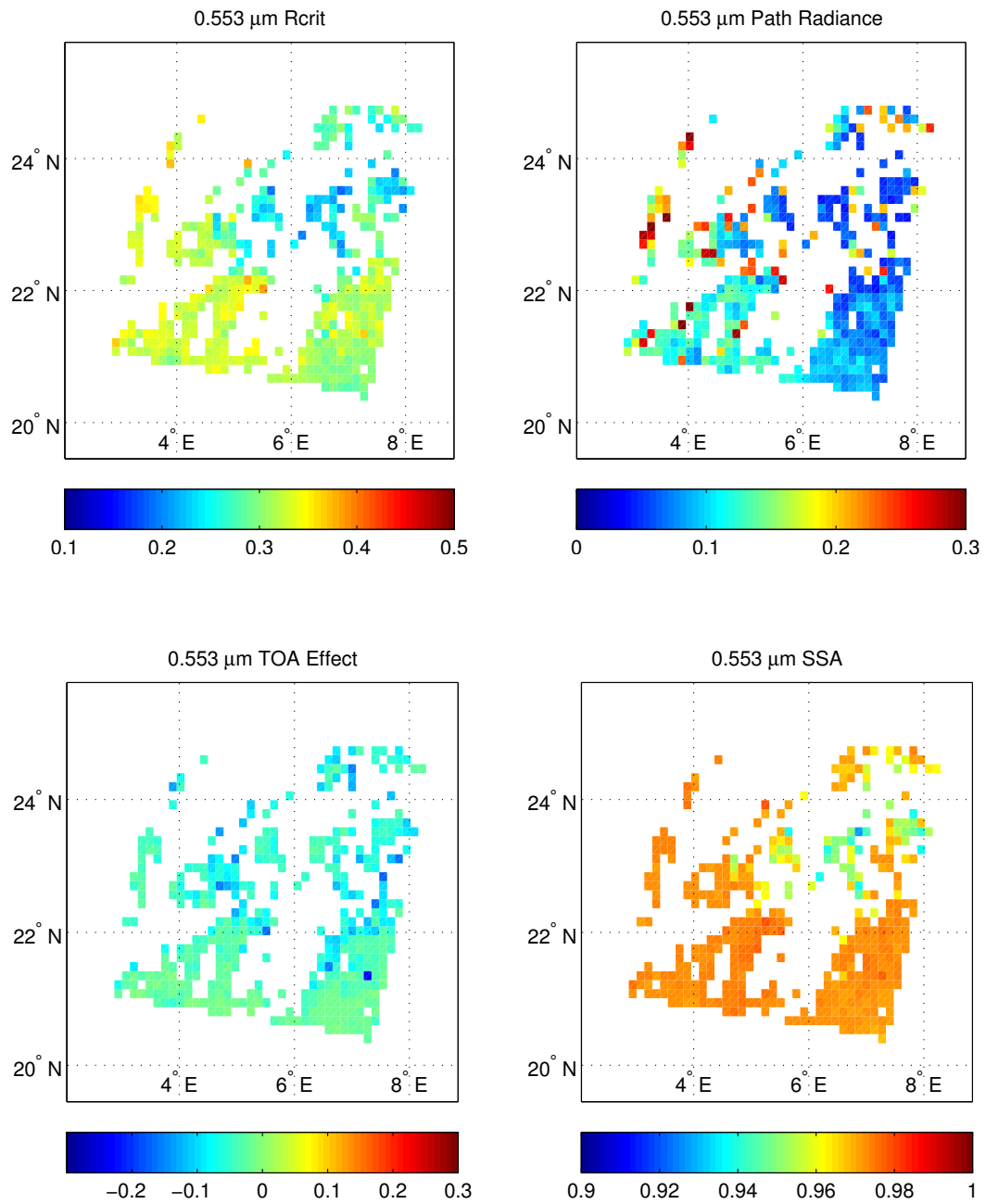


Figure C.26: Image retrievals of critical reflectance (upper left), path radiance (upper right), TOA radiative effect (lower left), and SSA (lower right) at 0.553 μm for 30 September 2008 1020 UTC (compared to +16 days) near Tamanrasset.

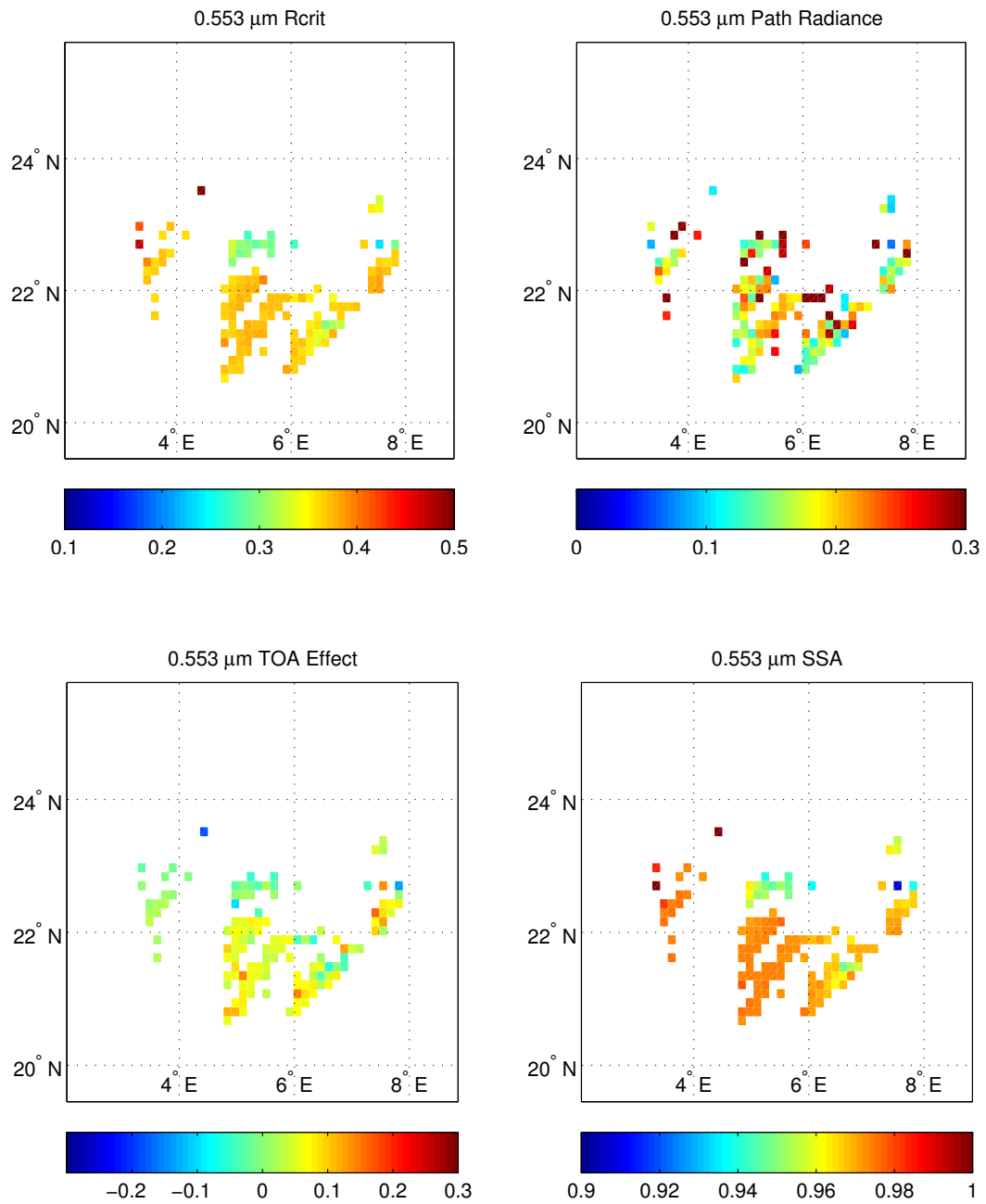


Figure C.27: Image retrievals of critical reflectance (upper left), path radiance (upper right), TOA radiative effect (lower left), and SSA (lower right) at 0.553 μm for 30 September 2008 1330 UTC (compared to +16 days) near Tamanrasset.

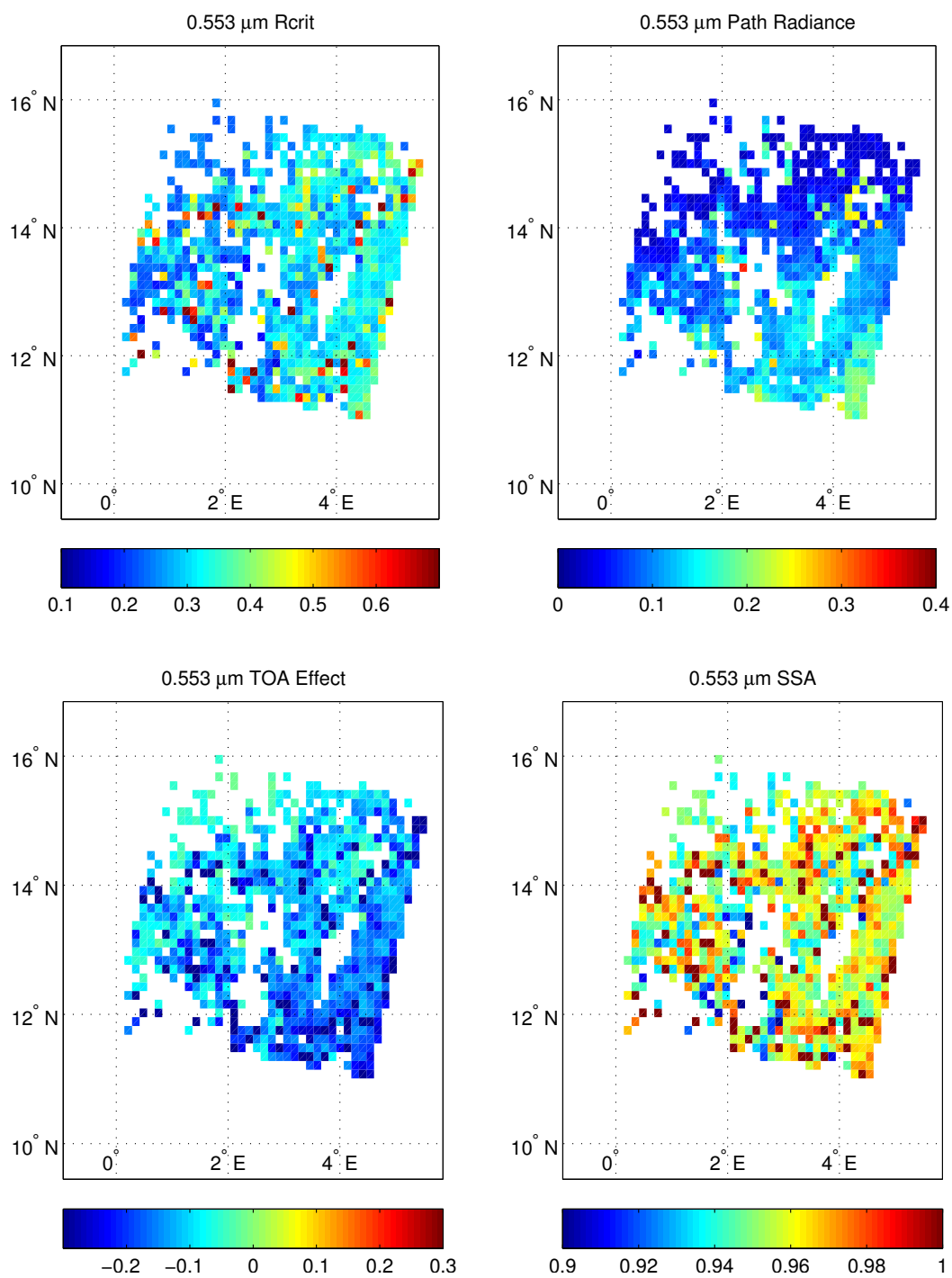


Figure C.28: Image retrievals of critical reflectance (upper left), path radiance (upper right), TOA radiative effect (lower left), and SSA (lower right) at 0.553 μm for 13 March 2006 1045 UTC (compared to -16 days) near Banizoumbou for the coarse aerosol model.

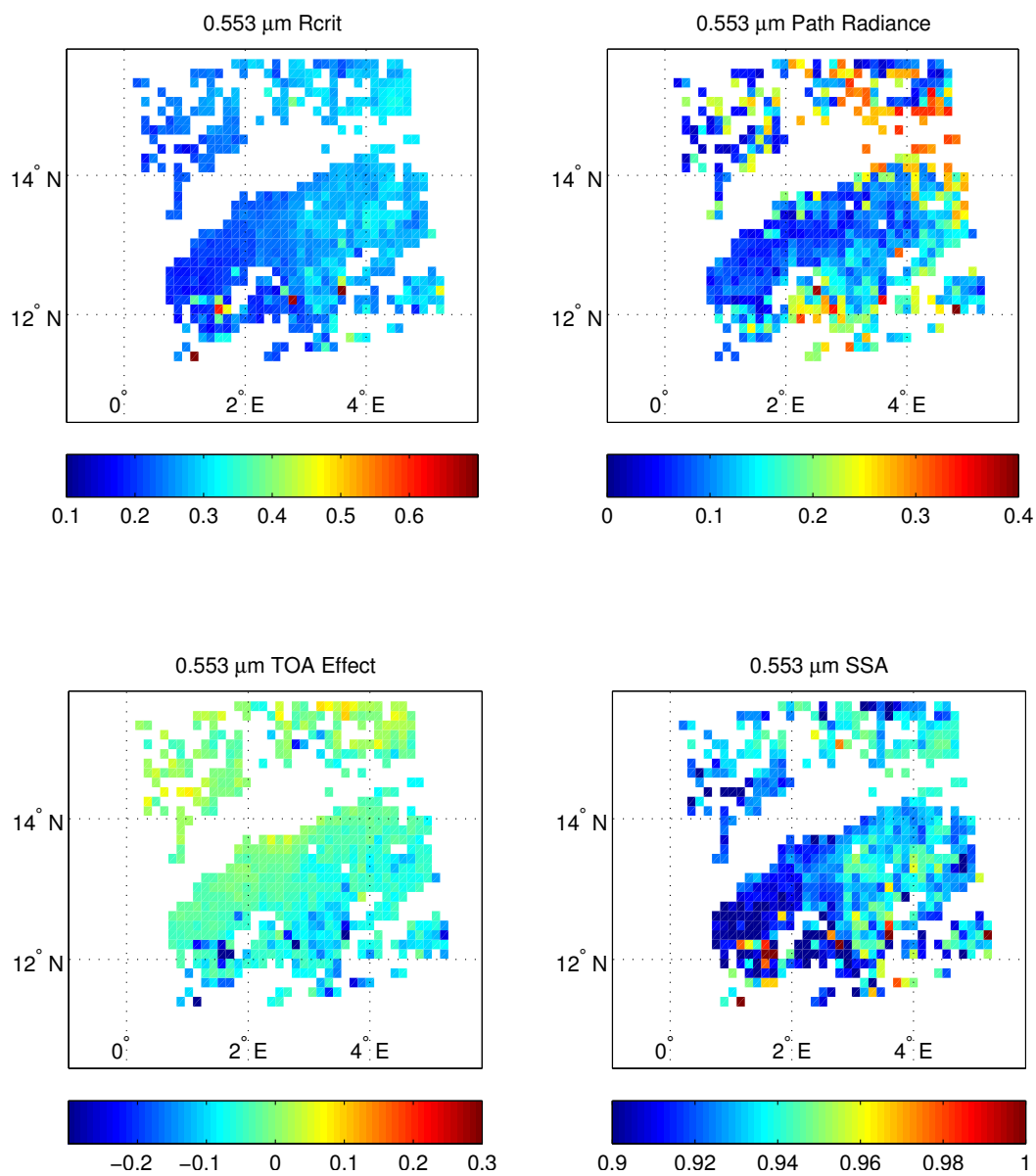


Figure C.29: Image retrievals of critical reflectance (upper left), path radiance (upper right), TOA radiative effect (lower left), and SSA (lower right) at 0.553  $\mu\text{m}$  for 16 October 2006 1345 UTC (compared to +16 days) near Banizoumbou for the coarse aerosol model.

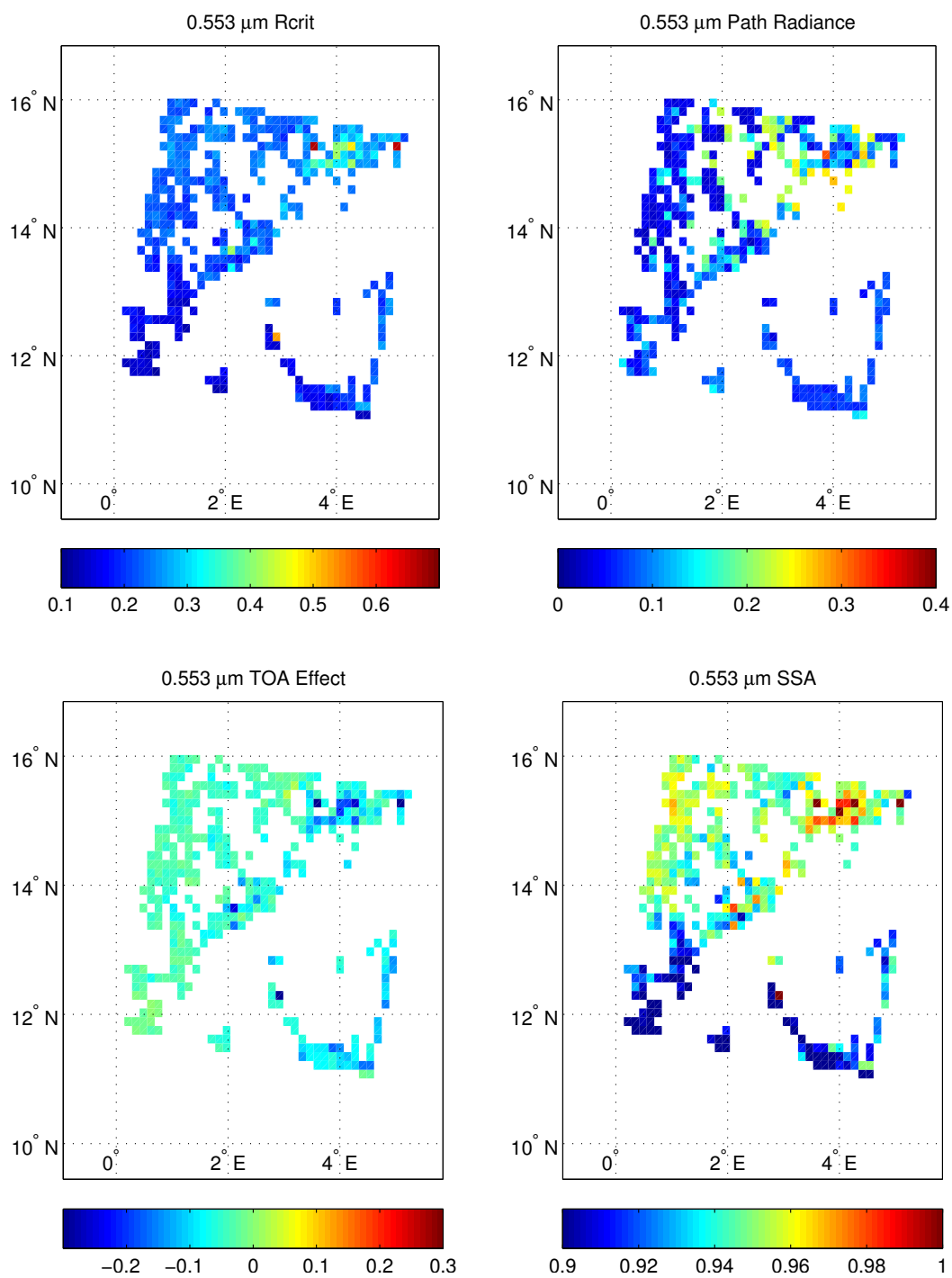


Figure C.30: Image retrievals of critical reflectance (upper left), path radiance (upper right), TOA radiative effect (lower left), and SSA (lower right) at 0.553  $\mu\text{m}$  for 10 November 2006 1035 UTC (compared to +16 days) near Banizoumbou for the coarse aerosol model.

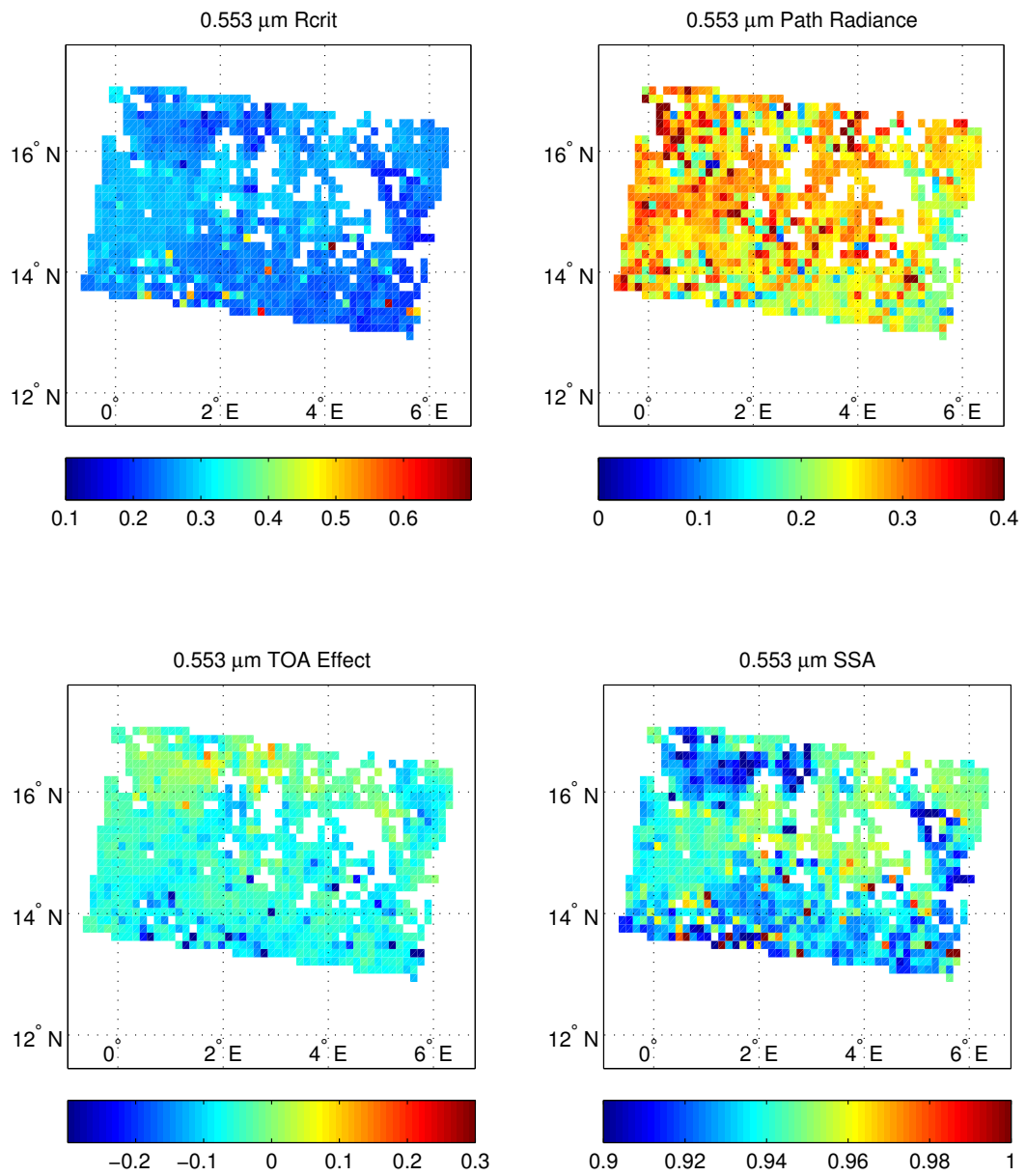


Figure C.31: Image retrievals of critical reflectance (upper left), path radiance (upper right), TOA radiative effect (lower left), and SSA (lower right) at 0.553  $\mu\text{m}$  for 16 November 2006 955 UTC (compared to -16 days) near Banizoumbou for the coarse aerosol model.

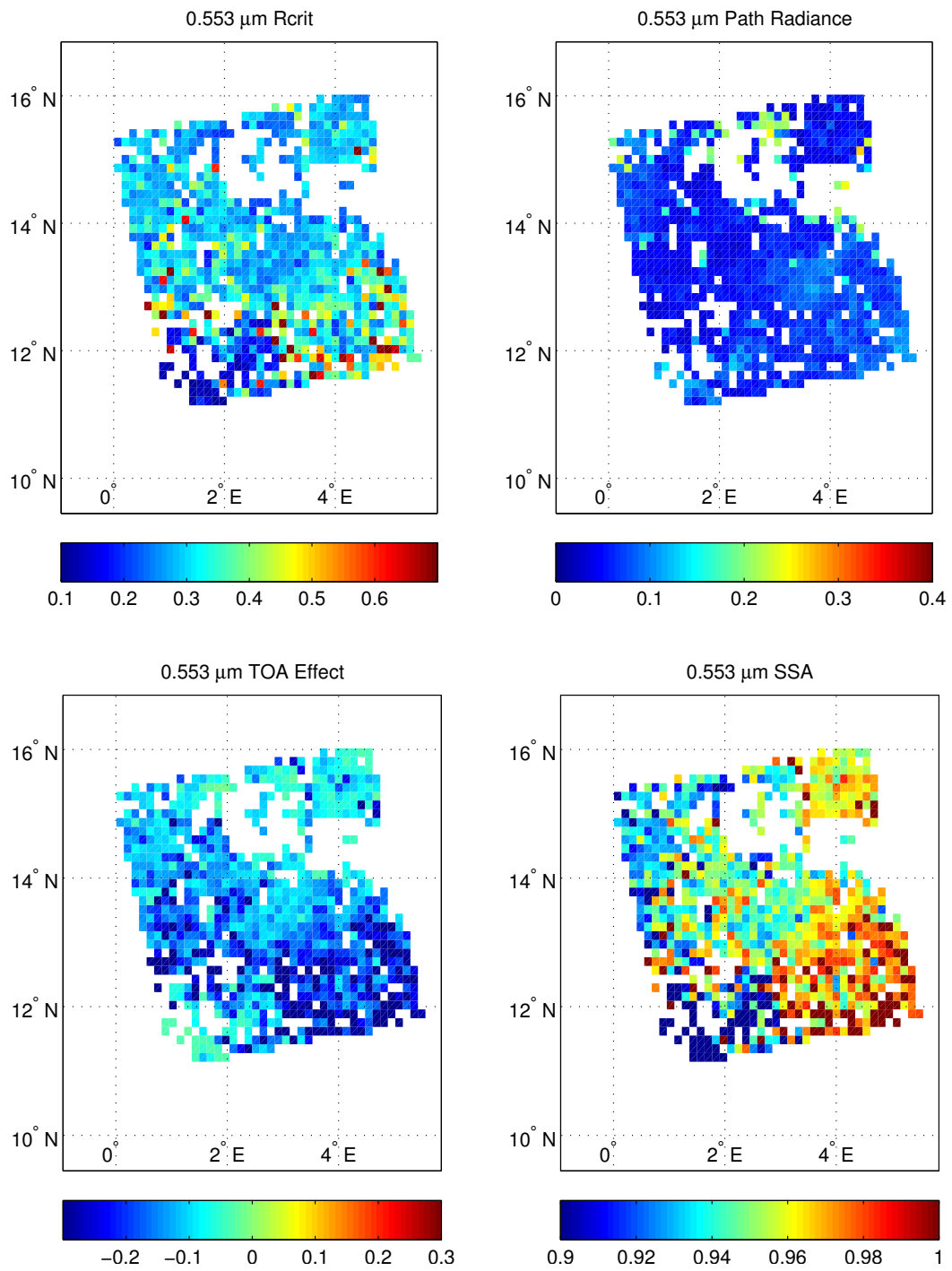


Figure C.32: Image retrievals of critical reflectance (upper left), path radiance (upper right), TOA radiative effect (lower left), and SSA (lower right) at 0.553 μm for 16 November 2006 1300 UTC (compared to -16 days) near Banizoumbou for the coarse aerosol model.

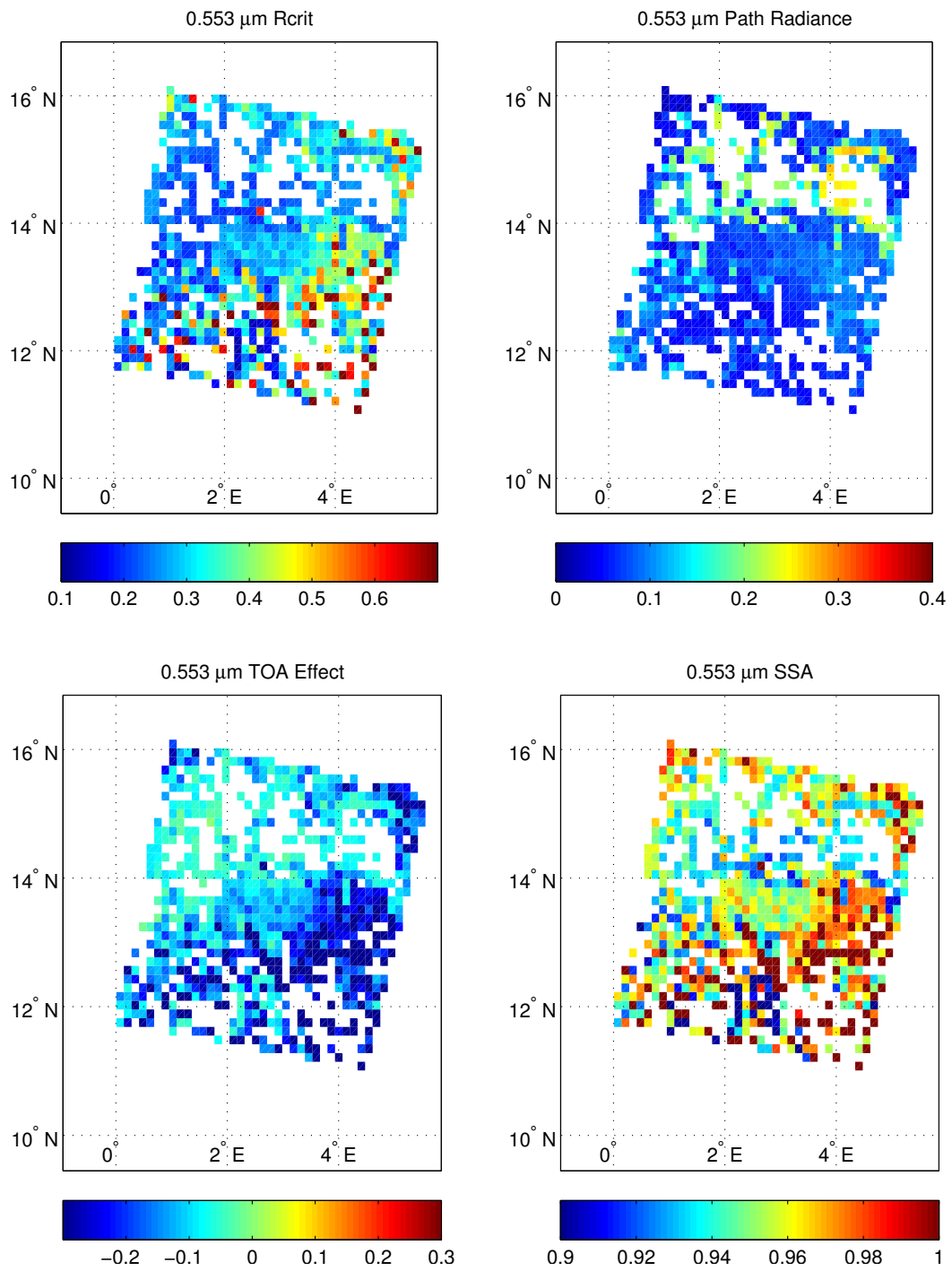


Figure C.33: Image retrievals of critical reflectance (upper left), path radiance (upper right), TOA radiative effect (lower left), and SSA (lower right) at 0.553  $\mu\text{m}$  for 17 November 2006 1040 UTC (compared to -16 days) near Banizoumbou for the coarse aerosol model.

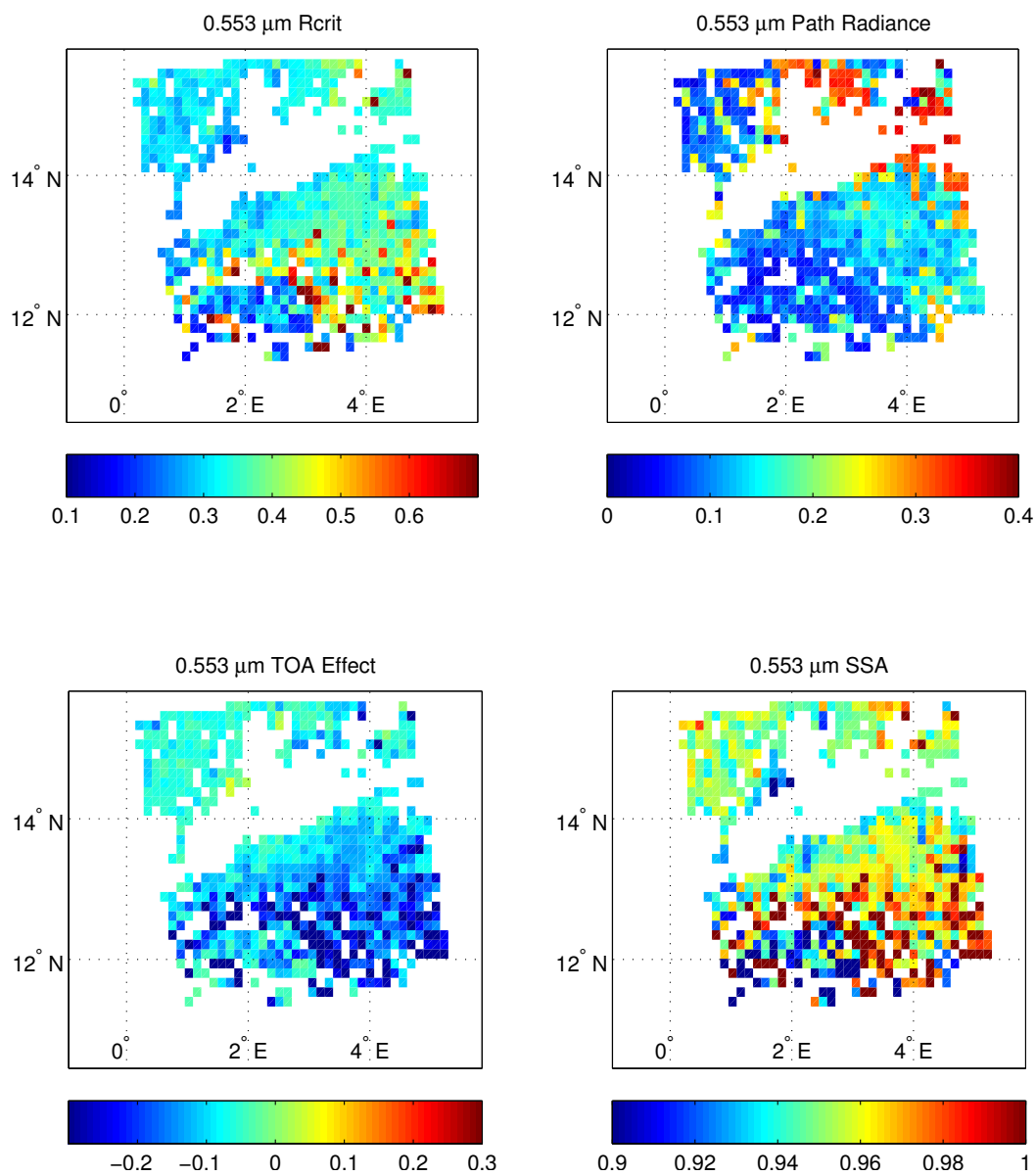


Figure C.34: Image retrievals of critical reflectance (upper left), path radiance (upper right), TOA radiative effect (lower left), and SSA (lower right) at 0.553 μm for 17 November 2006 1345 UTC (compared to -16 days) near Banizoumbou for the coarse aerosol model.

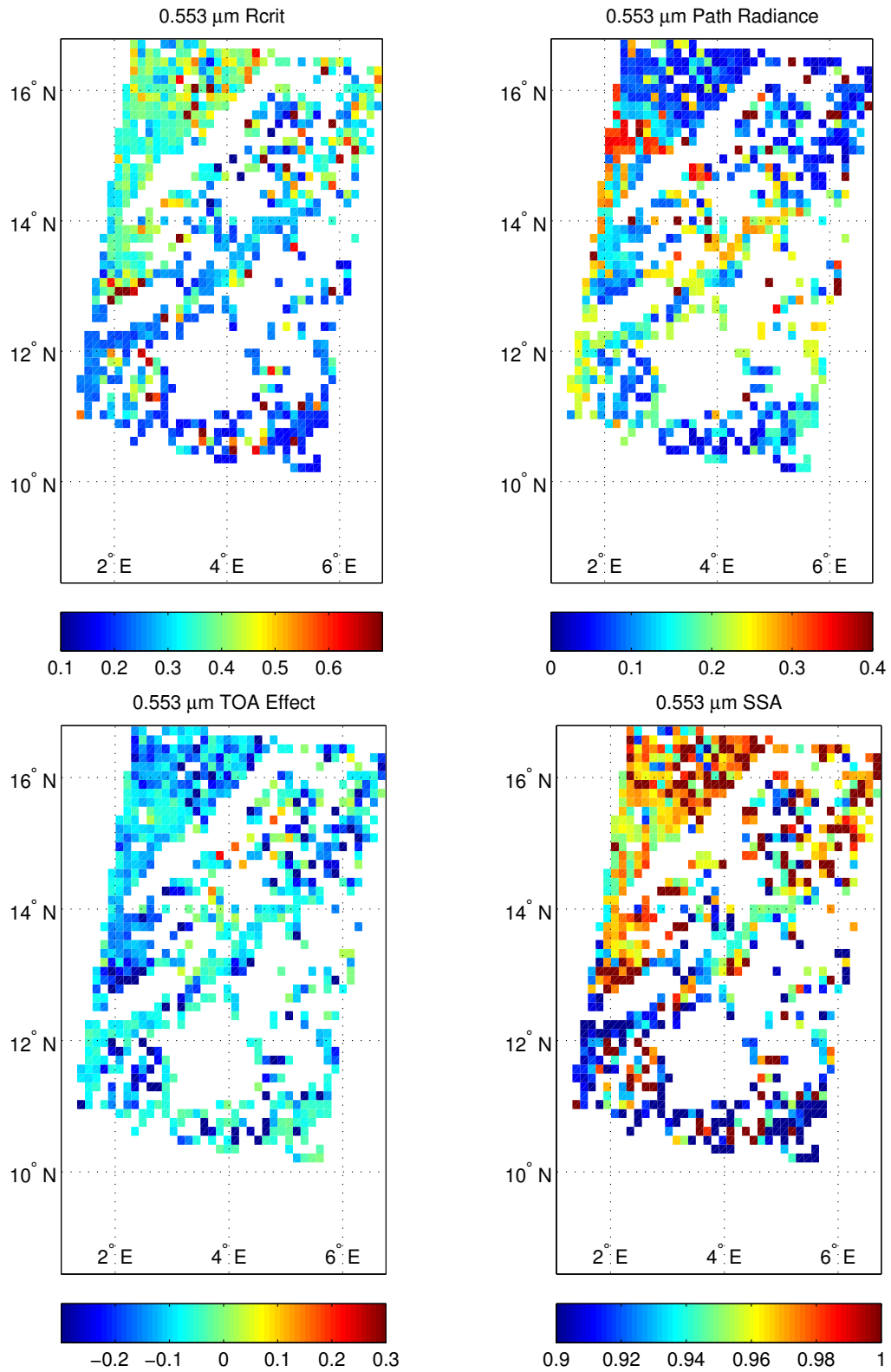


Figure C.35: Image retrievals of critical reflectance (upper left), path radiance (upper right), TOA radiative effect (lower left), and SSA (lower right) at 0.553  $\mu\text{m}$  for 18 November 2006 945 UTC (compared to -16 days) near Banizoumbou for the coarse aerosol model.

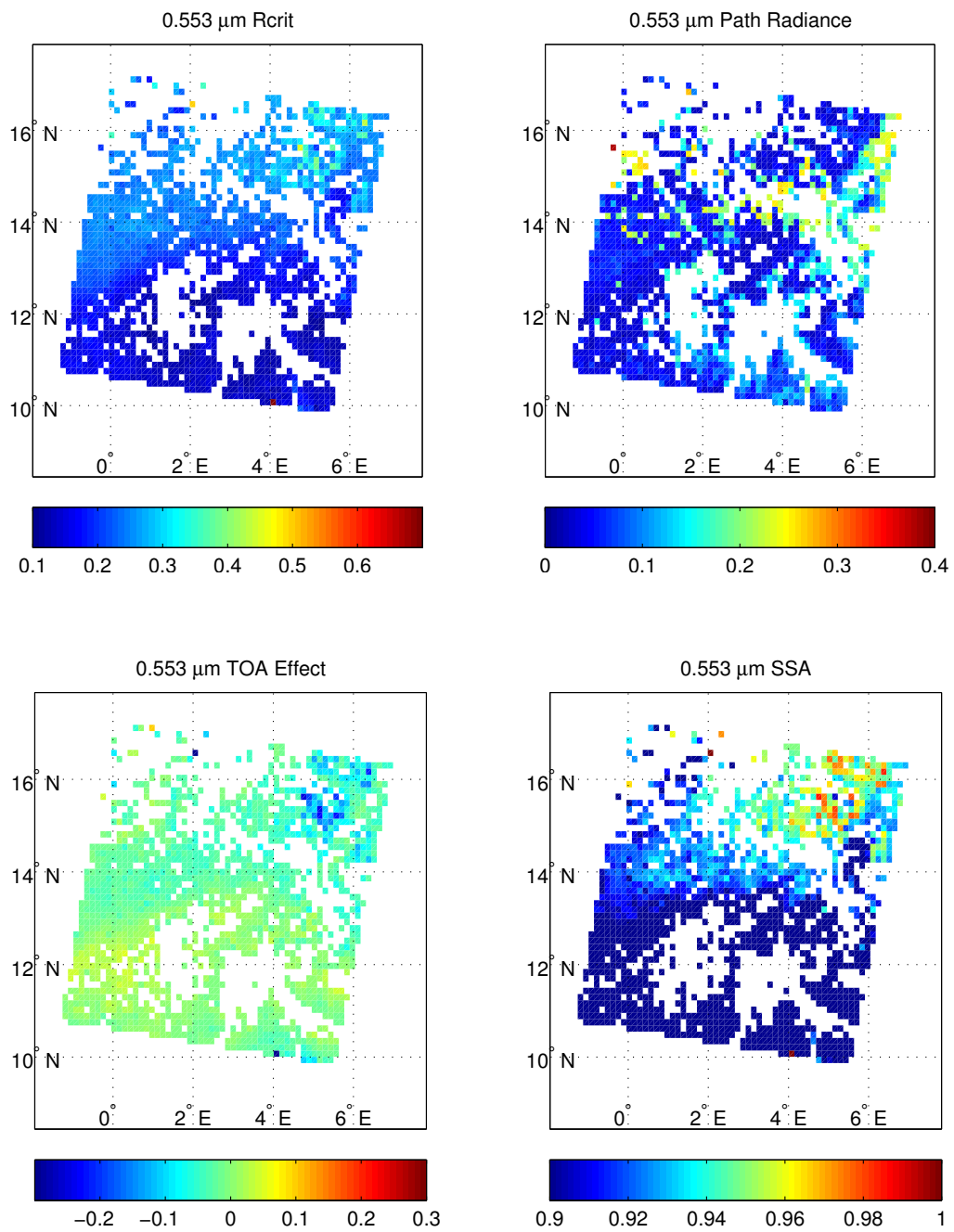


Figure C.36: Image retrievals of critical reflectance (upper left), path radiance (upper right), TOA radiative effect (lower left), and SSA (lower right) at 0.553  $\mu\text{m}$  for 7 December 2006 1015 UTC (compared to +16 days) near Banizoumbou for the bimodal spheroid aerosol model.

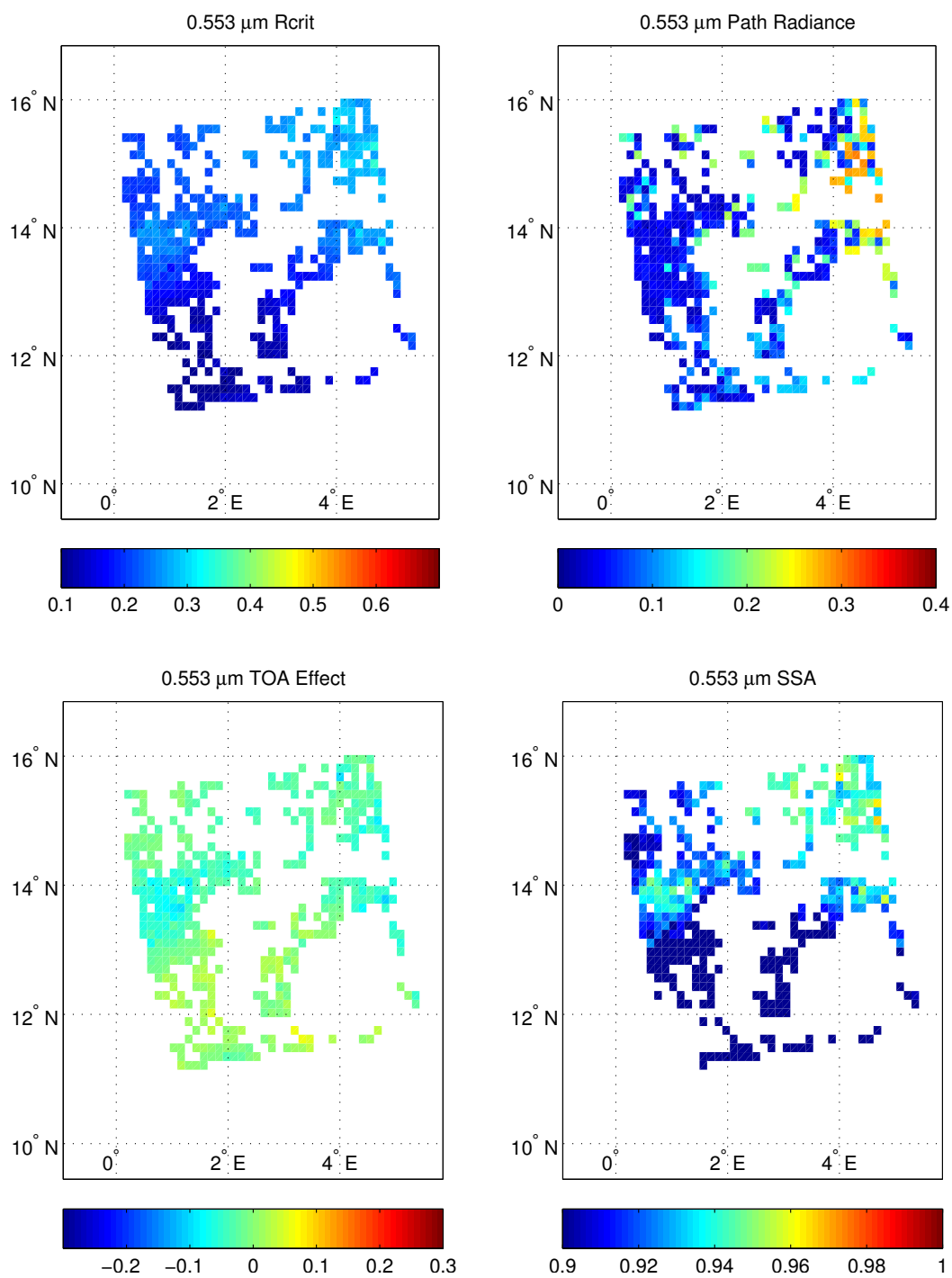


Figure C.37: Image retrievals of critical reflectance (upper left), path radiance (upper right), TOA radiative effect (lower left), and SSA (lower right) at 0.553  $\mu\text{m}$  for 7 December 2006 1320 UTC (compared to +16 days) near Banizoumbou for the bimodal spheroid aerosol model.

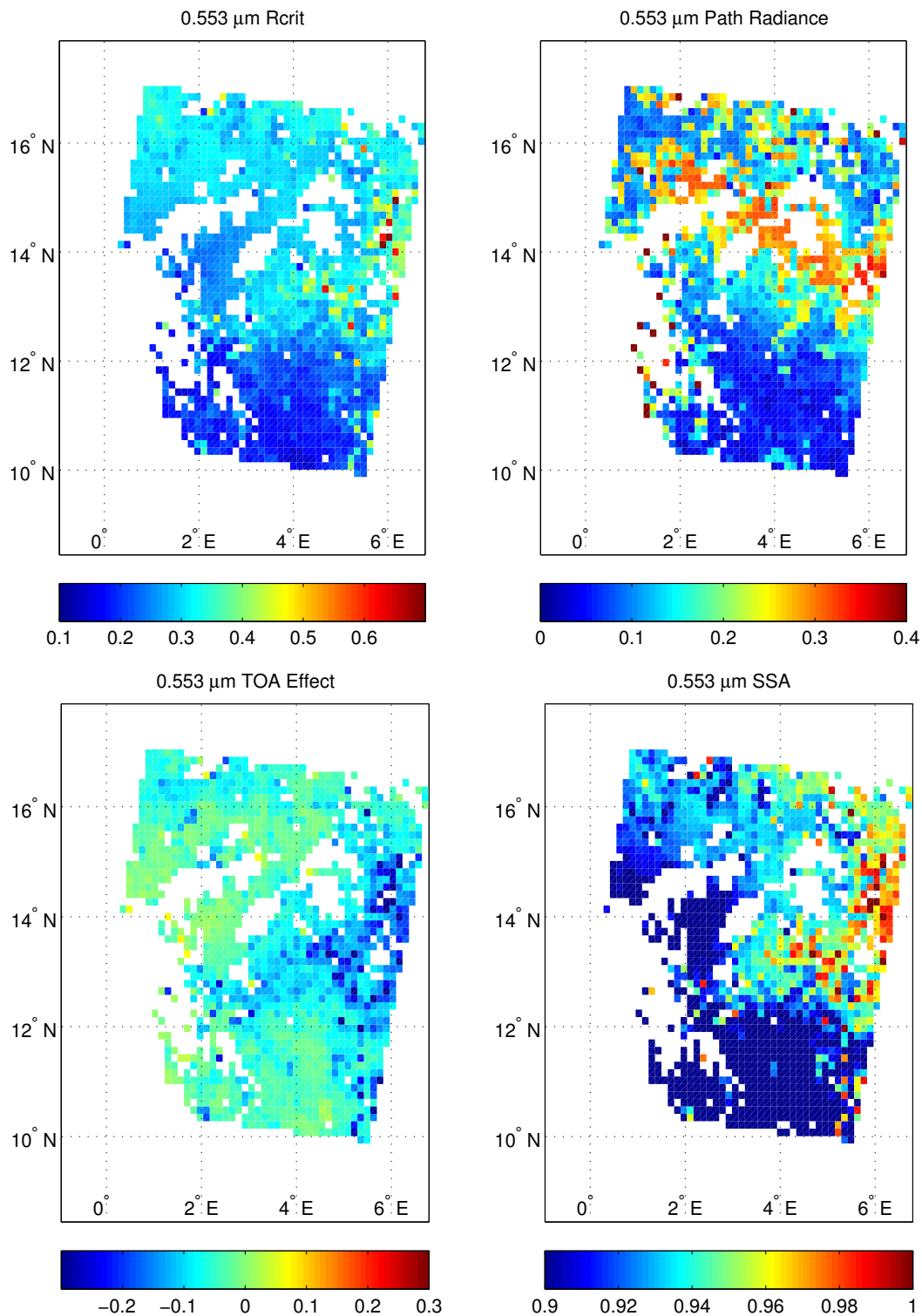


Figure C.38: Image retrievals of critical reflectance (upper left), path radiance (upper right), TOA radiative effect (lower left), and SSA (lower right) at 0.553 μm for 11 December 2006 950 UTC (compared to -16 days) near Banizoumbou for the bimodal spheroid aerosol model.

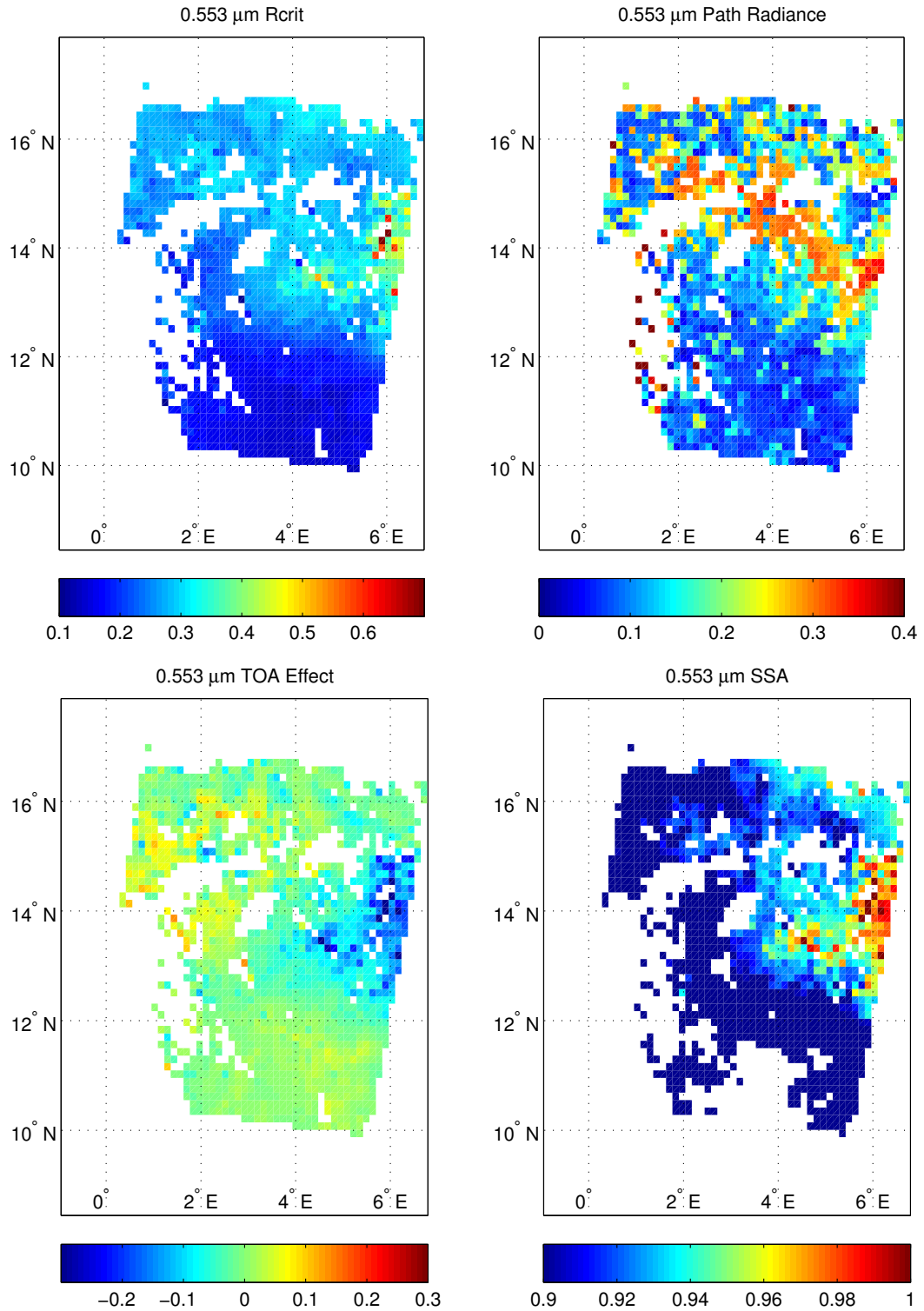


Figure C.39: Image retrievals of critical reflectance (upper left), path radiance (upper right), TOA radiative effect (lower left), and SSA (lower right) at 0.553  $\mu\text{m}$  for 11 December 2006 950 UTC (compared to +16 days) near Banizoumbou for the bimodal spheroid aerosol model.

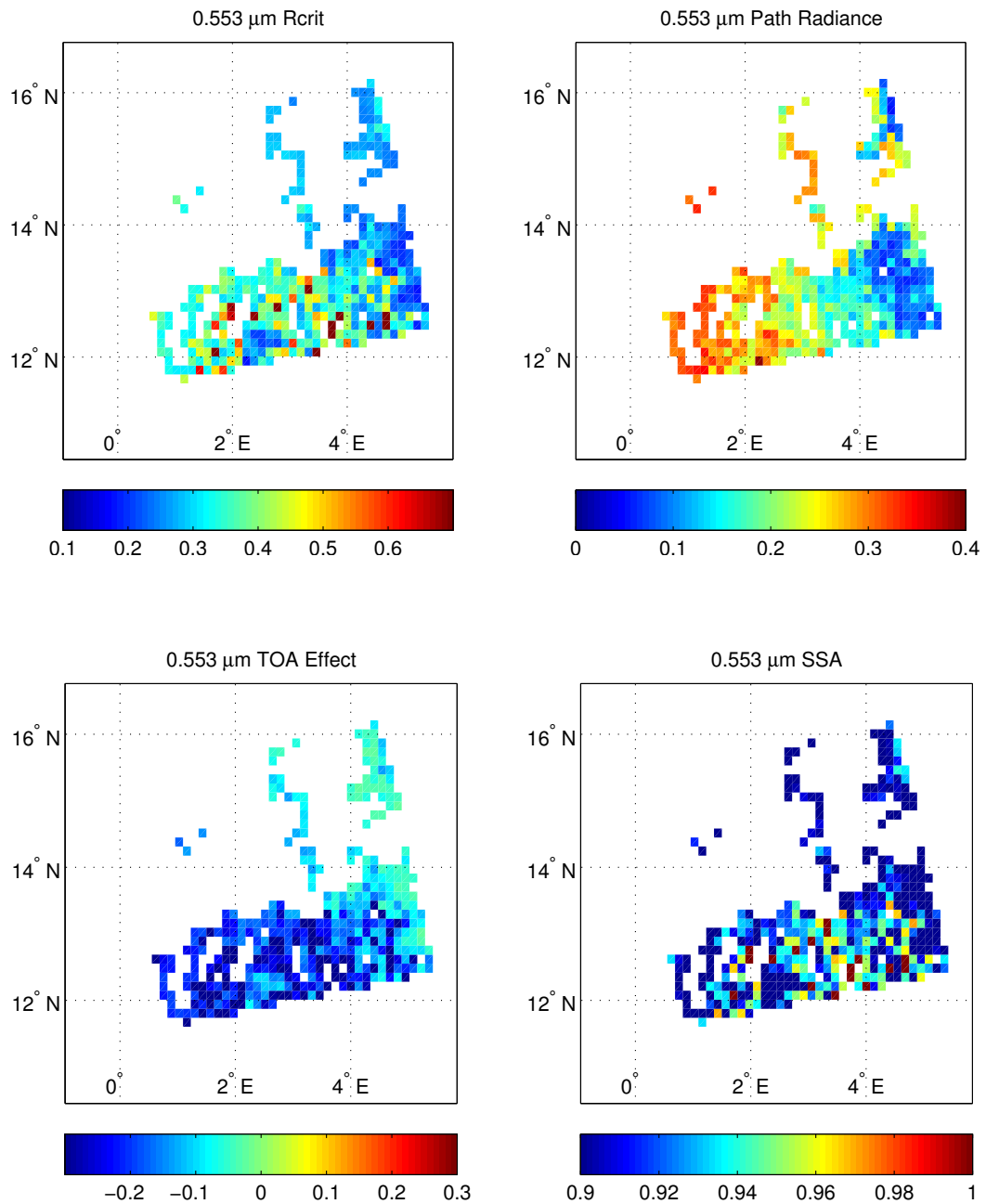


Figure C.40: Image retrievals of critical reflectance (upper left), path radiance (upper right), TOA radiative effect (lower left), and SSA (lower right) at 0.553 μm for 13 December 2006 1245 UTC (compared to -16 days) near Banizoumbou for the coarse aerosol model.

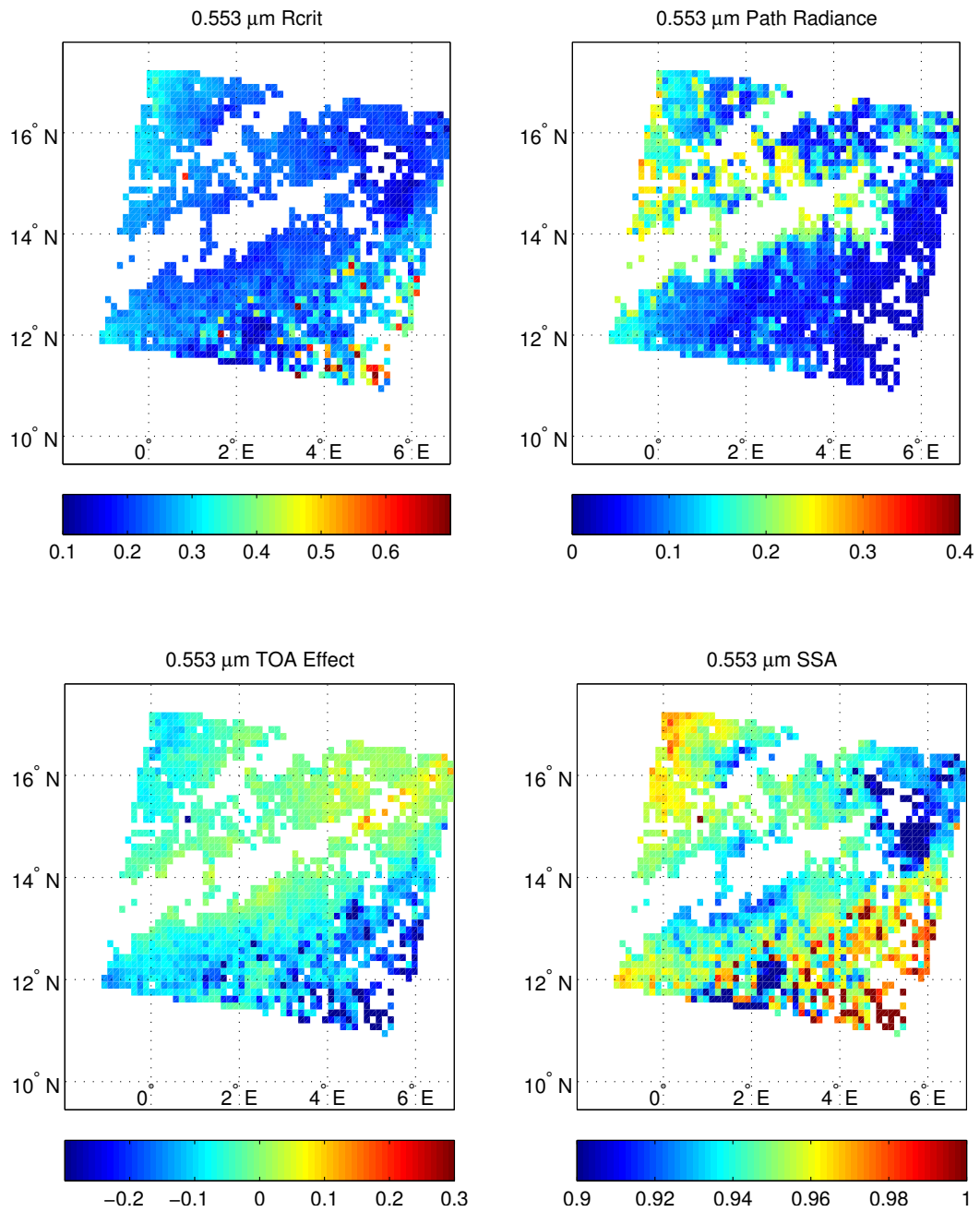


Figure C.41: Image retrievals of critical reflectance (upper left), path radiance (upper right), TOA radiative effect (lower left), and SSA (lower right) at 0.553  $\mu\text{m}$  for 14 December 2006 1020 UTC (compared to -16 days) near Banizoumbou for the coarse aerosol model.

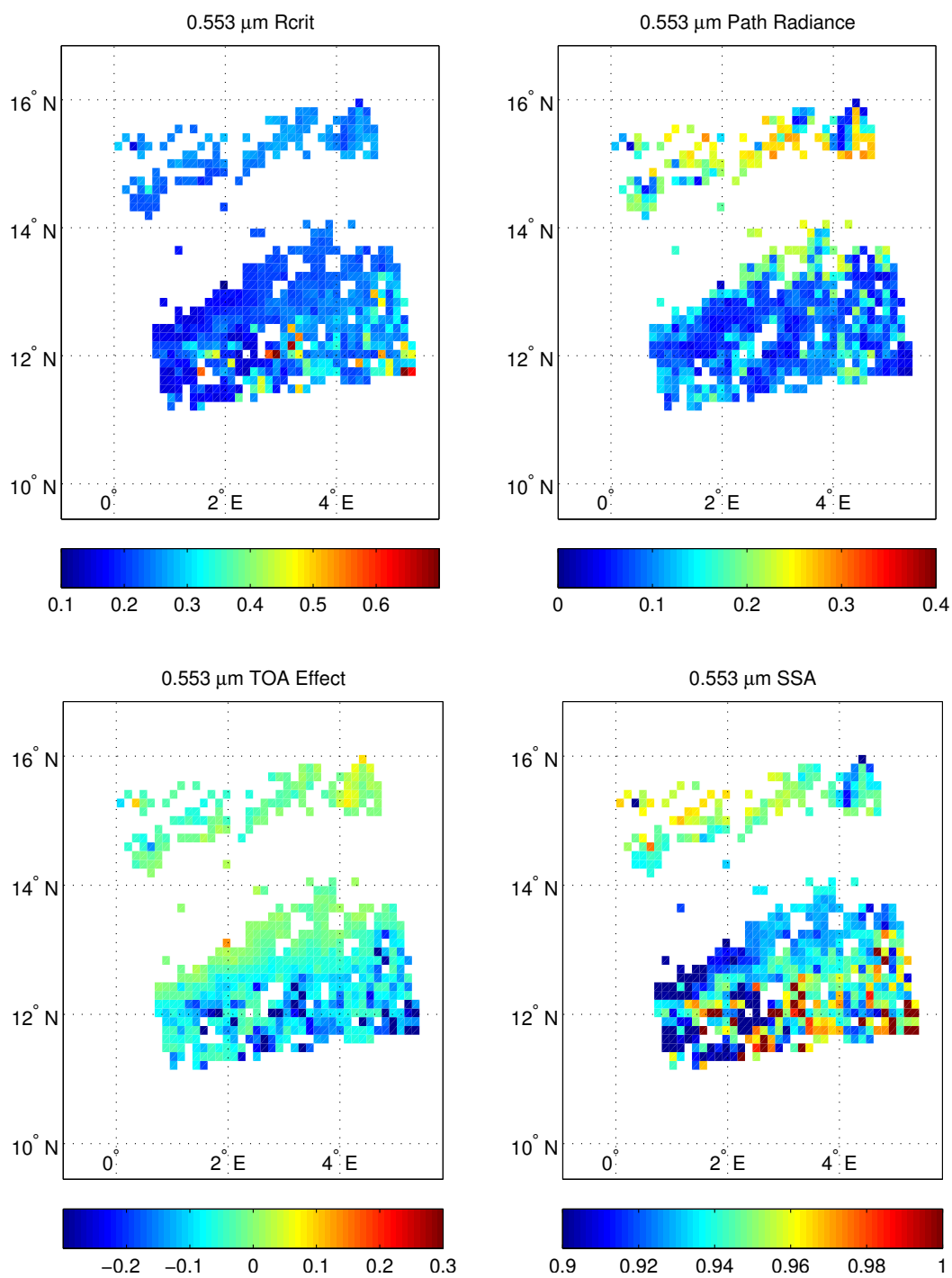


Figure C.42: Image retrievals of critical reflectance (upper left), path radiance (upper right), TOA radiative effect (lower left), and SSA (lower right) at 0.553 μm for 14 December 2006 1325 UTC (compared to -16 days) near Banizoumbou for the coarse aerosol model.

## **Appendix D Spectral results near AERONET sites**

The following pages contain the spectral path radiance and critical reflectance in the upper panels, and SSA results in the lower panels for the 27 cases at Tamanrasset, and 15 cases at Banizoumbou. Results are shown for 5 x 5 pixel averages (~75 x 75 km). All Tamanrasset cases are for the coarse aerosol model, and are shown with inversion estimates calculated from both methods described in Chapter 3. Results for Banizoumbou are shown for both the coarse and bimodal spheroid aerosol models, with uncertainty estimates calculated using Equation 3.1.

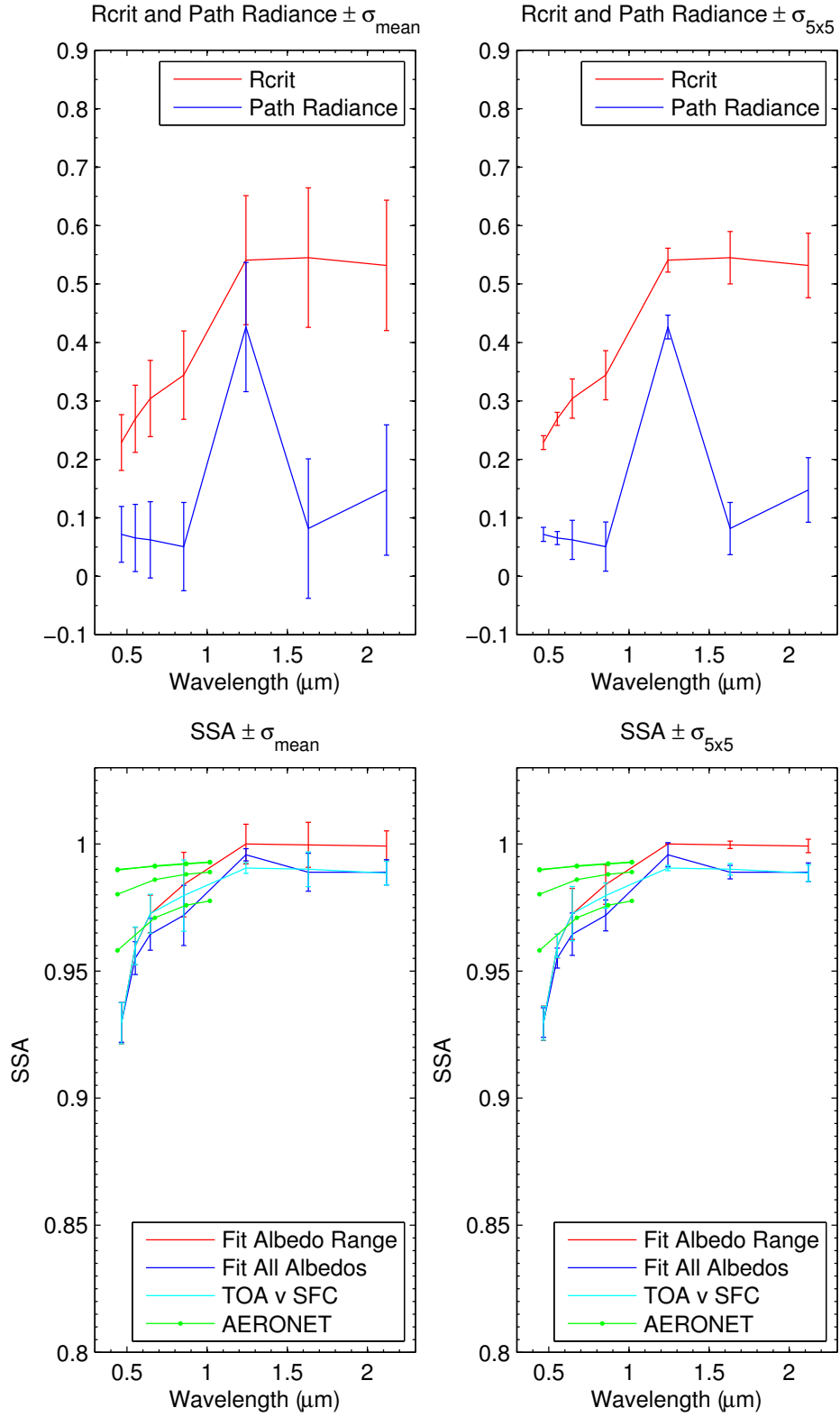


Figure D.1: Spectral plots of critical reflectance and path radiance (upper panels) and SSA (lower panels) with error bars using the two error estimation methods, for 14 December 2006 1045 UTC (compared to -16 days) at the Tamanrasset site. AERONET retrievals for the day are also shown.

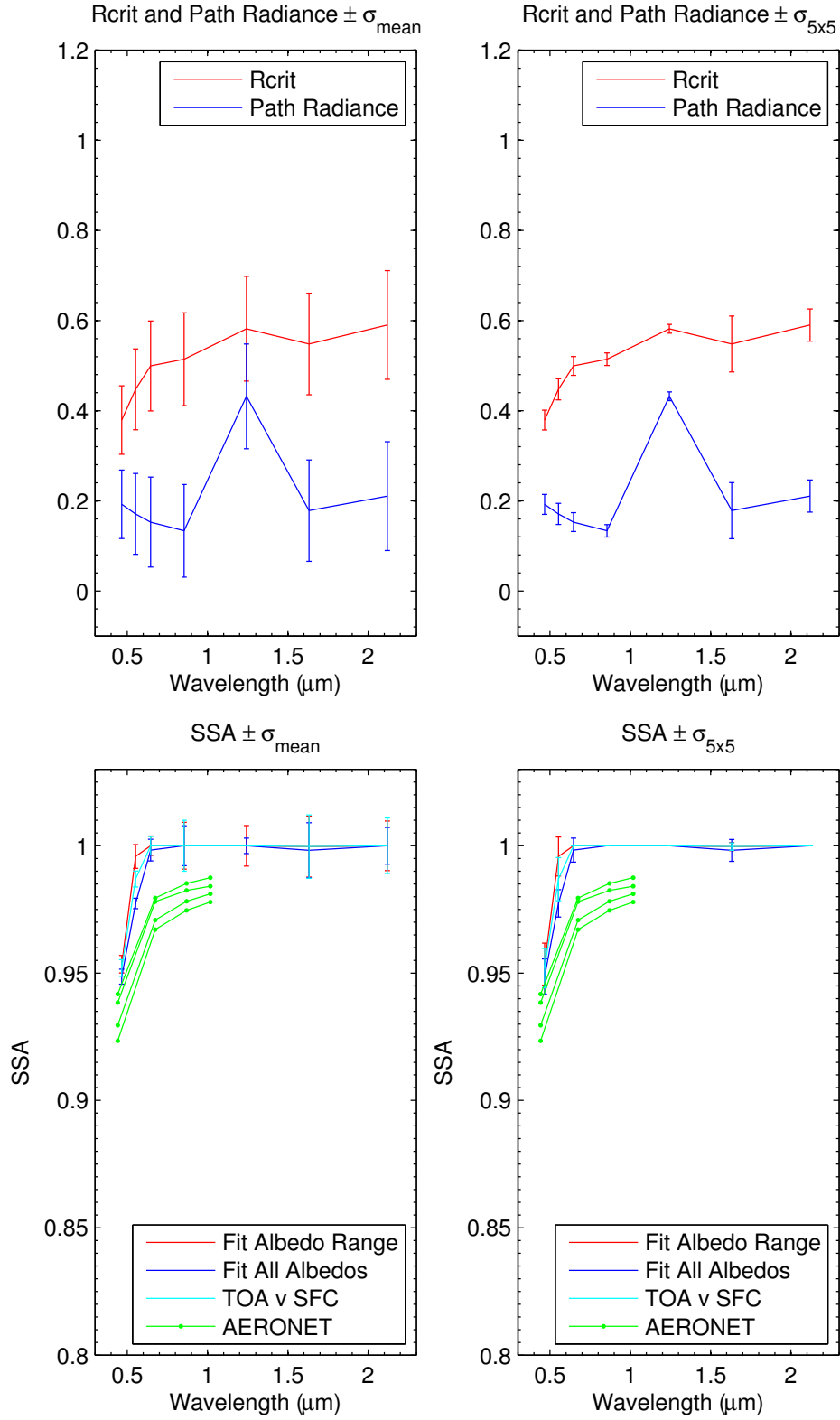


Figure D.2: Spectral plots of critical reflectance and path radiance (upper panels) and SSA (lower panels) with error bars using the two error estimation methods, for 22 February 2007 945 UTC (compared to -16 days) at the Tamanrasset site. AERONET retrievals for the day are also shown.

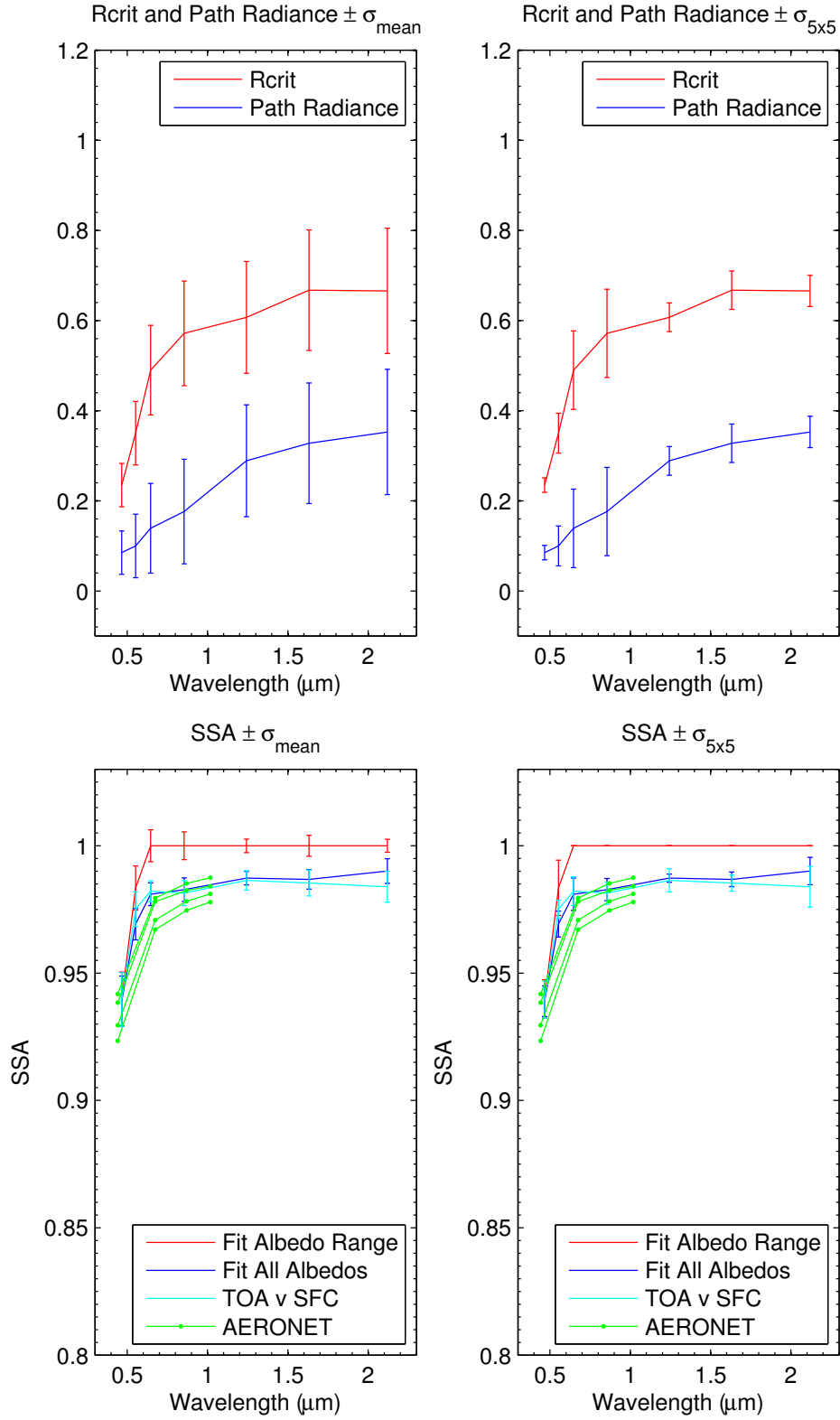


Figure D.3: Spectral plots of critical reflectance and path radiance (upper panels) and SSA (lower panels) with error bars using the two error estimation methods, for 22 February 2007 1250 UTC (compared to -16 days) at the Tamanrasset site. AERONET retrievals for the day are also shown.

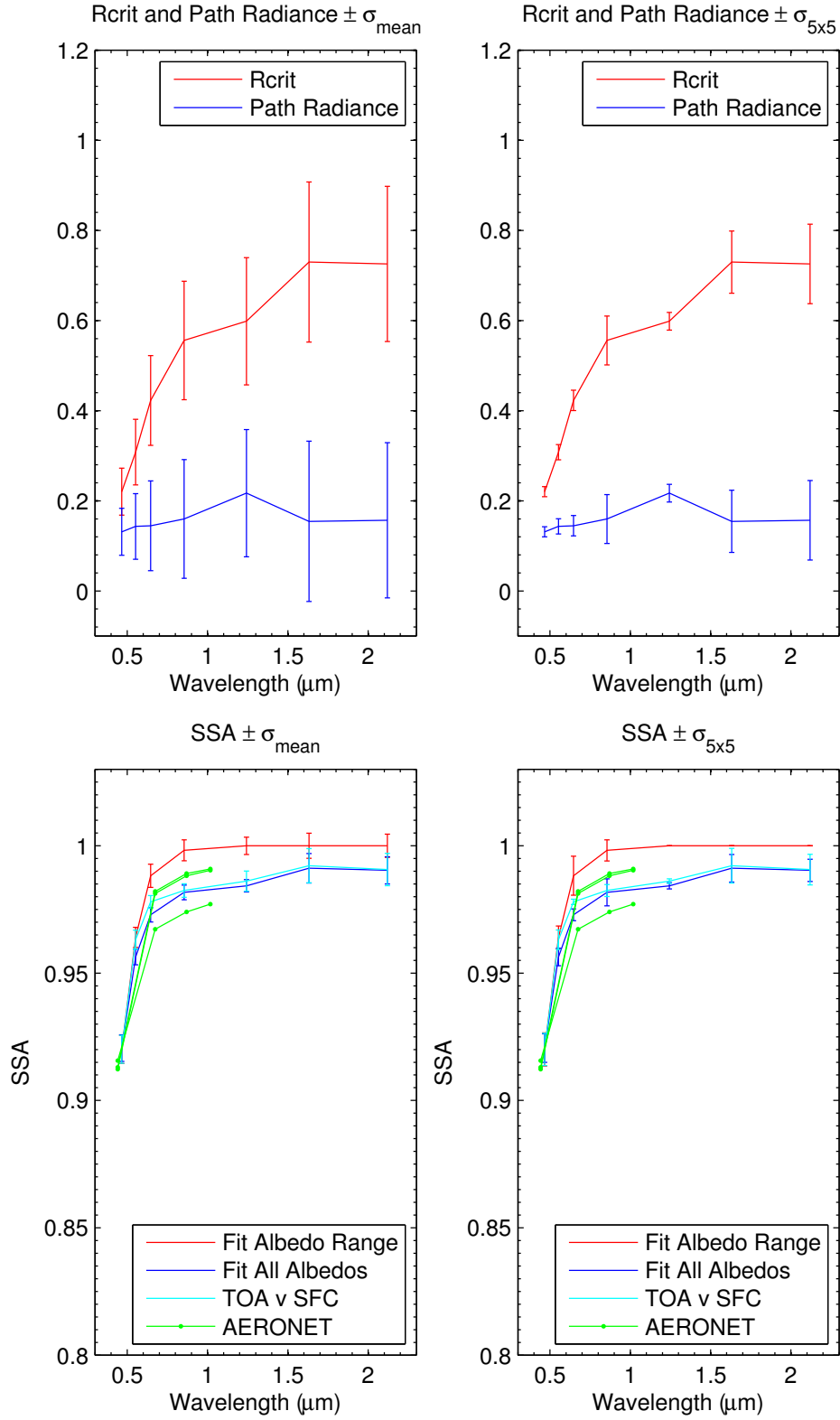


Figure D.4: Spectral plots of critical reflectance and path radiance (upper panels) and SSA (lower panels) with error bars using the two error estimation methods, for 9 March 2007 1040 UTC (compared to -16 days) at the Tamanrasset site. AERONET retrievals for the day are also shown.

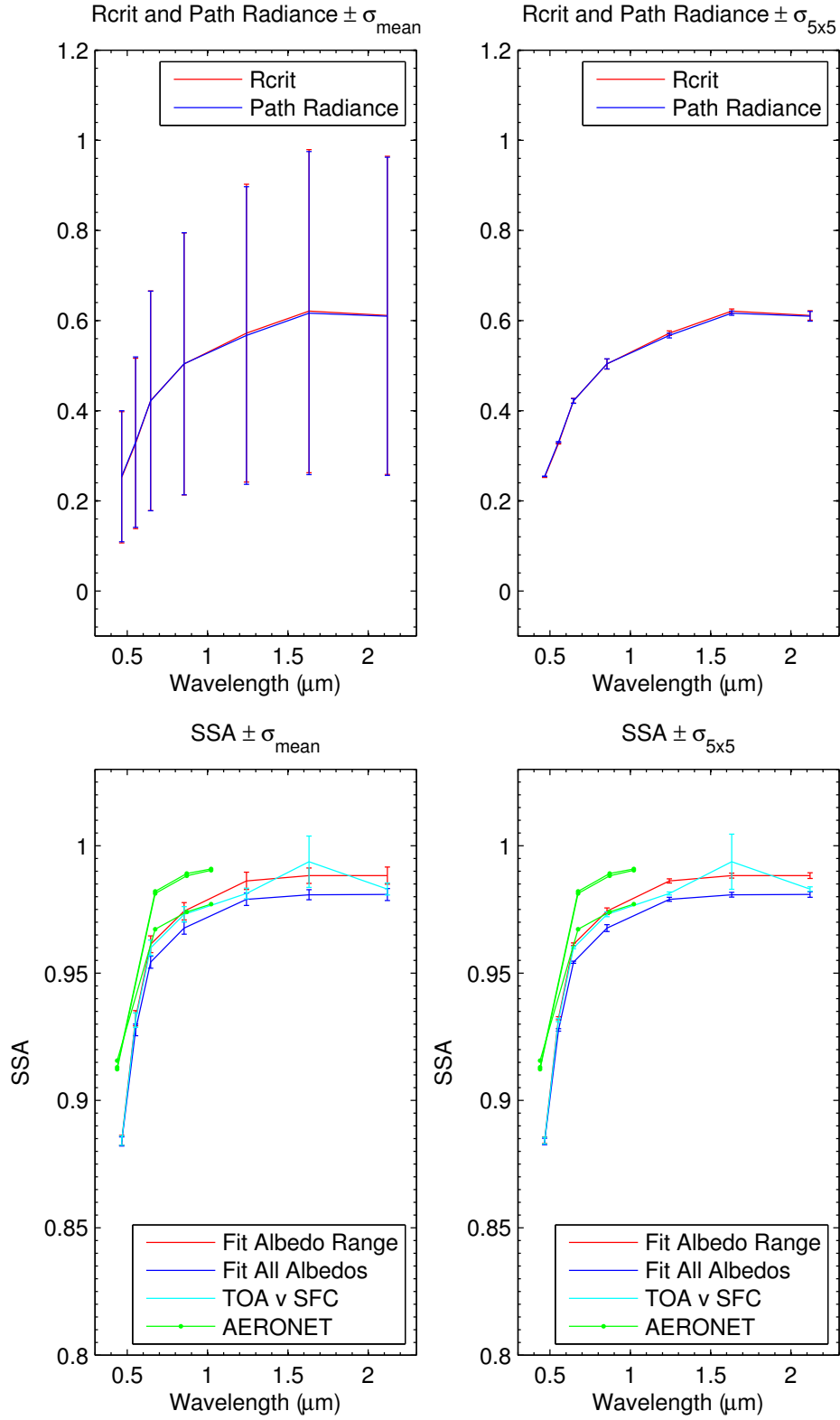


Figure D.5: Spectral plots of critical reflectance and path radiance (upper panels) and SSA (lower panels) with error bars using the two error estimation methods, for 9 March 2006 1210 UTC (compared to -16 days) at the Tamanrasset site. AERONET retrievals for the day are also shown.

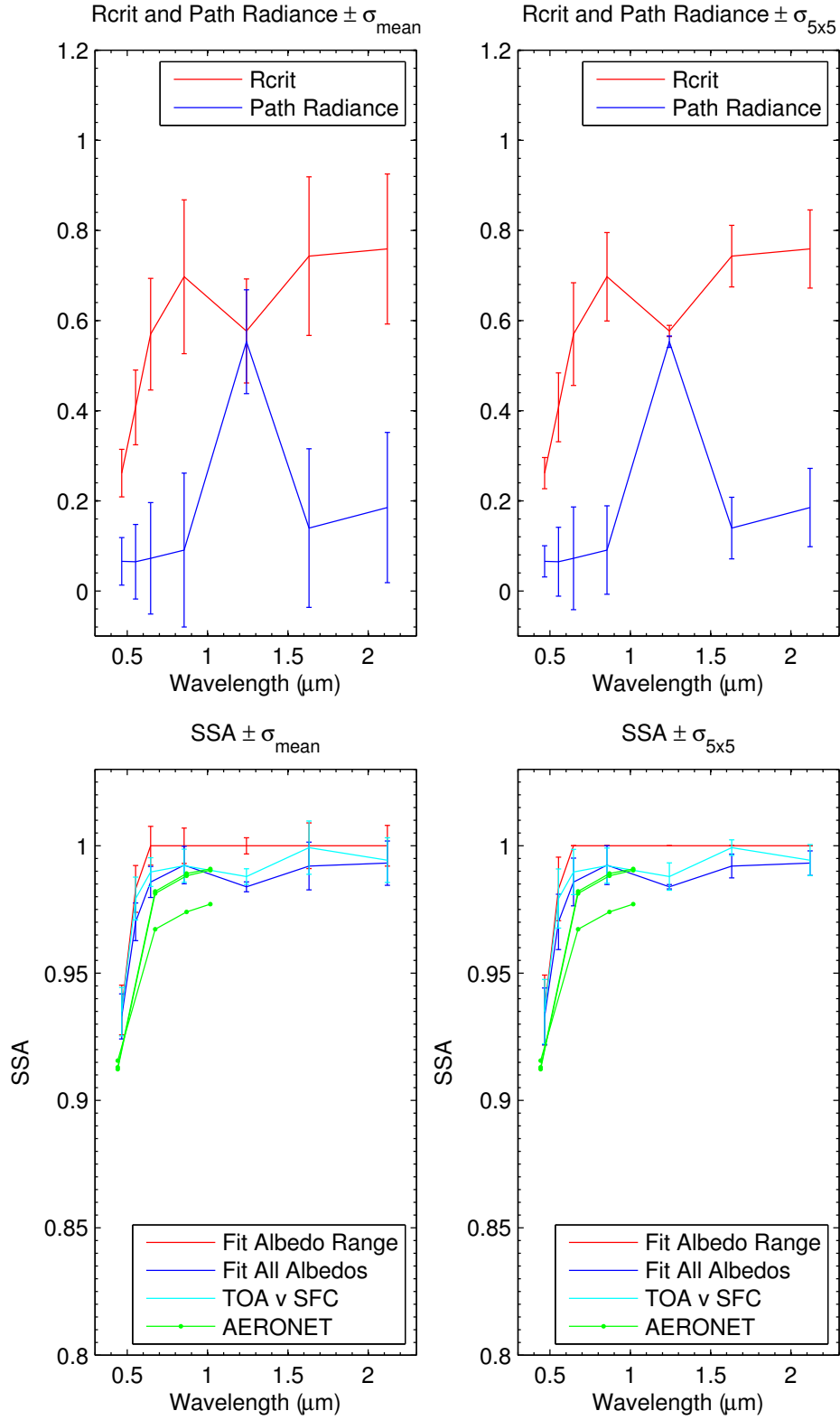


Figure D.6: Spectral plots of critical reflectance and path radiance (upper panels) and SSA (lower panels) with error bars using the two error estimation methods, for 9 March 2007 1040 UTC (compared to +16 days) at the Tamanrasset site. AERONET retrievals for the day are also shown.

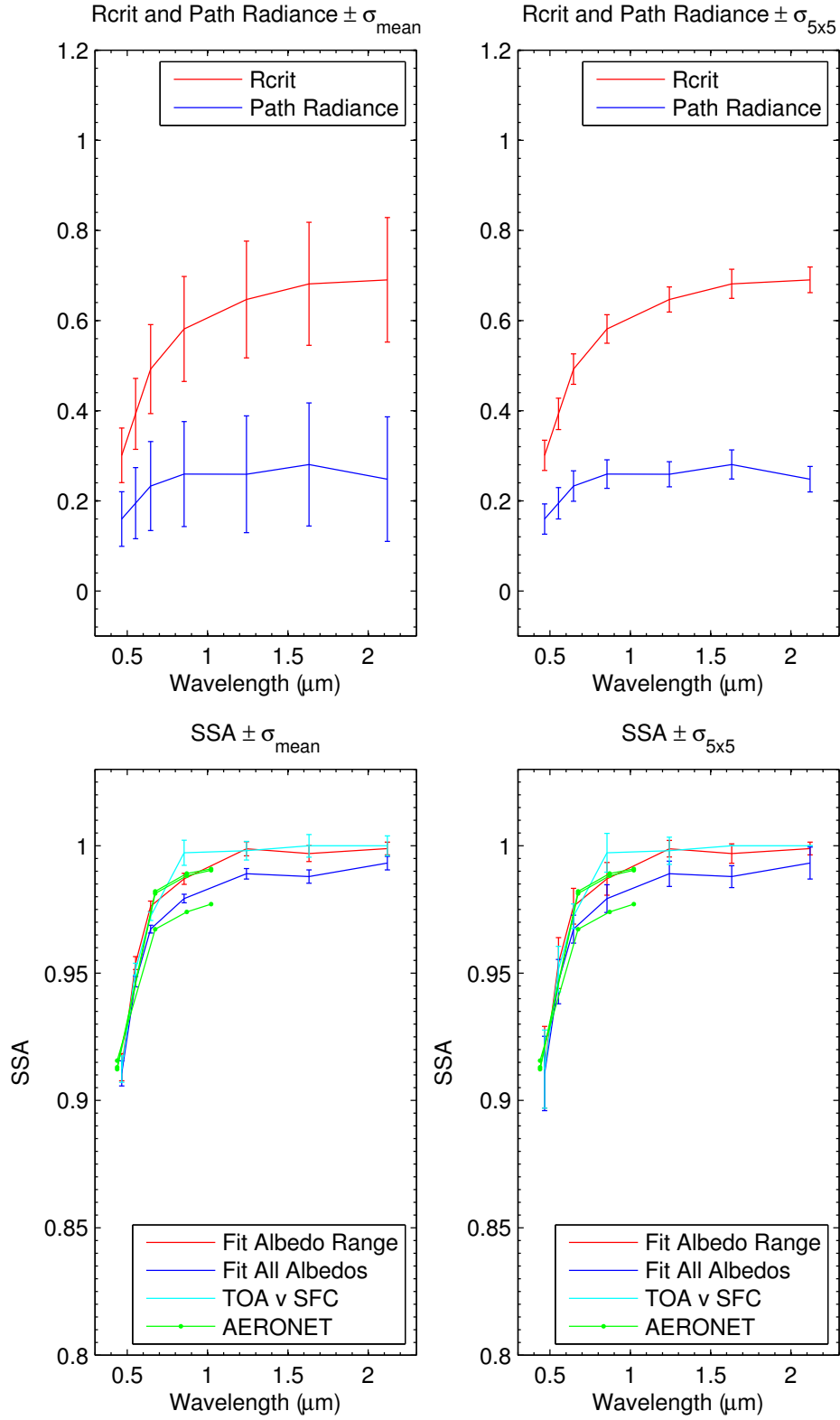


Figure D.7: Spectral plots of critical reflectance and path radiance (upper panels) and SSA (lower panels) with error bars using the two error estimation methods, for 9 March 2007 1210 UTC (compared to +16 days) at the Tamanrasset site. AERONET retrievals for the day are also shown.

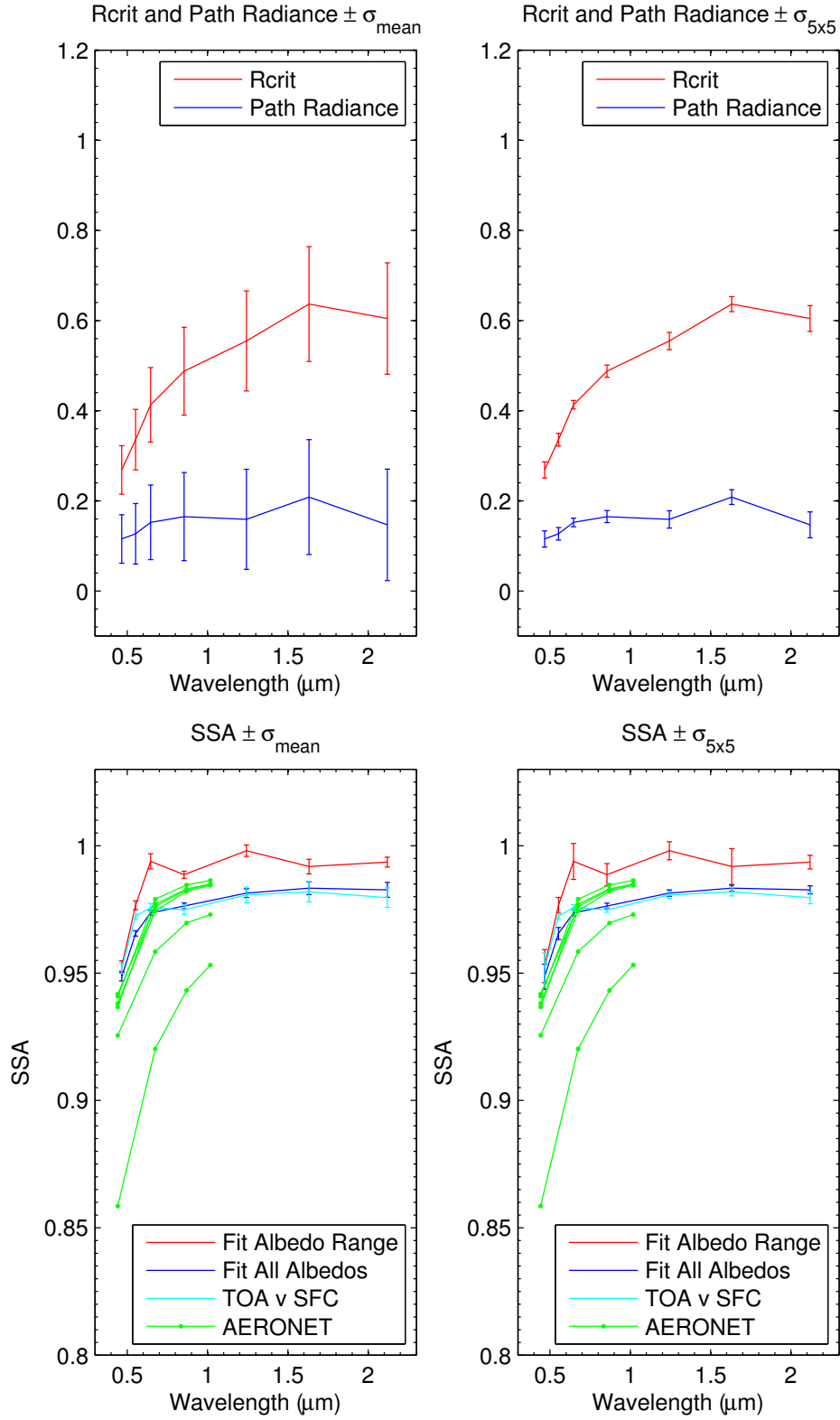


Figure D.8: Spectral plots of critical reflectance and path radiance (upper panels) and SSA (lower panels) with error bars using the two error estimation methods, for 19 March 2007 1245 UTC (compared to -16 days) at the Tamanrasset site. AERONET retrievals for the day are also shown.

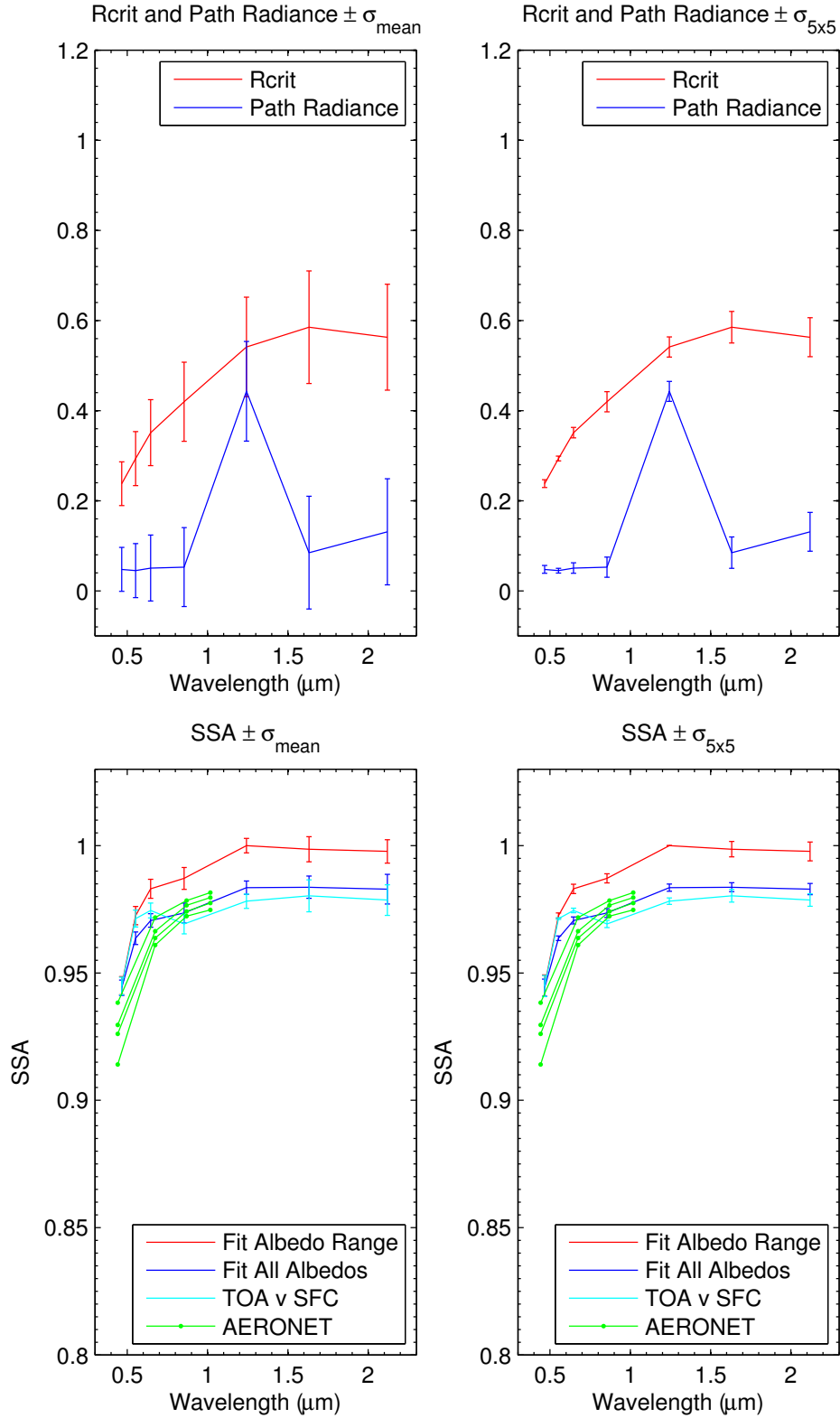


Figure D.9: Spectral plots of critical reflectance and path radiance (upper panels) and SSA (lower panels) with error bars using the two error estimation methods, for 20 March 2007 1020 UTC (compared to +16 days) at the Tamanrasset site. AERONET retrievals for the day are also shown.

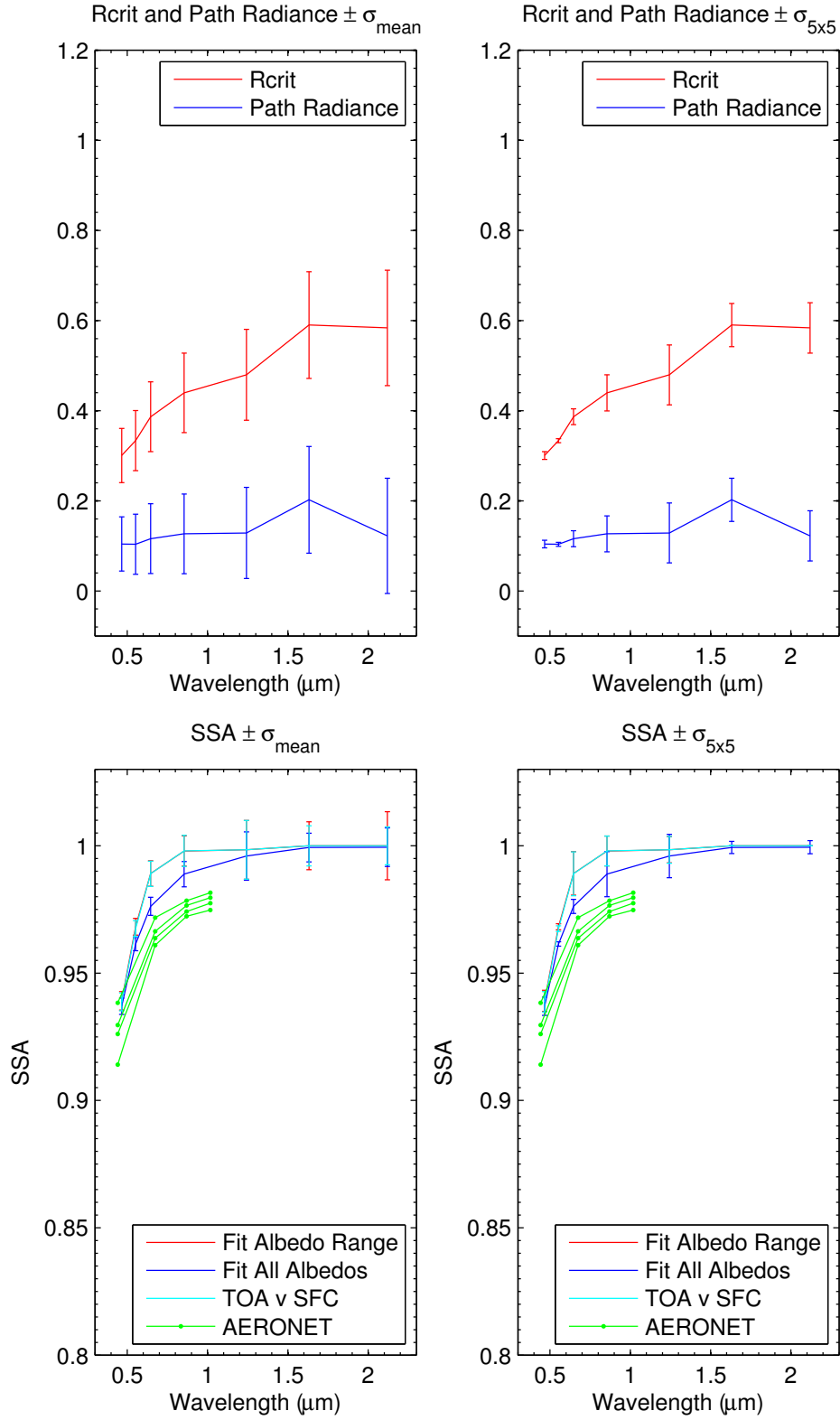


Figure D.10: Spectral plots of critical reflectance and path radiance (upper panels) and SSA (lower panels) with error bars using the two error estimation methods, for 20 March 2007 1330 UTC (compared to +16 days) at the Tamanrasset site. AERONET retrievals for the day are also shown.

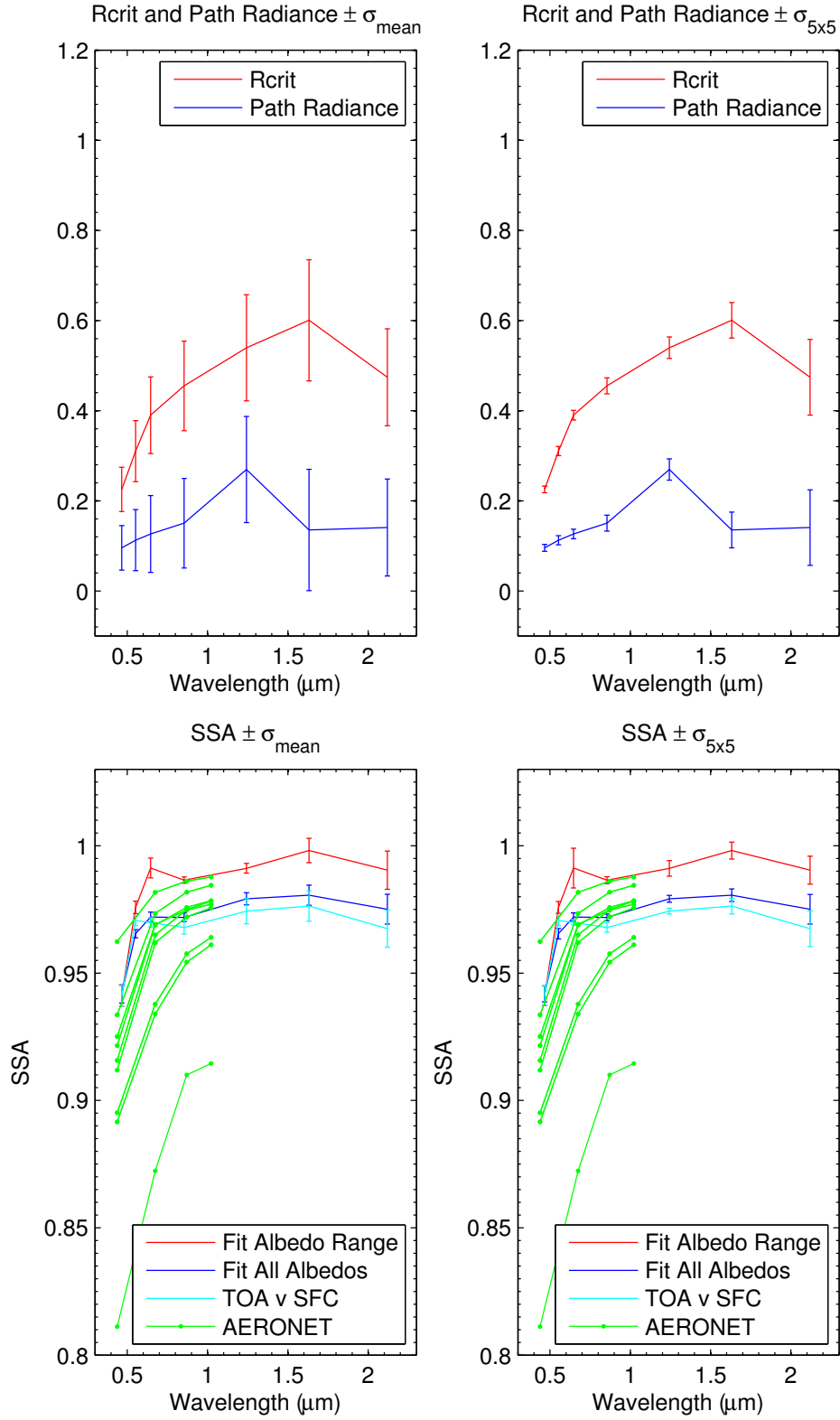


Figure D.11: Spectral plots of critical reflectance and path radiance (upper panels) and SSA (lower panels) with error bars using the two error estimation methods, for 14 May 2007 1025 UTC (compared to -16 days) at the Tamanrasset site. AERONET retrievals for the day are also shown.

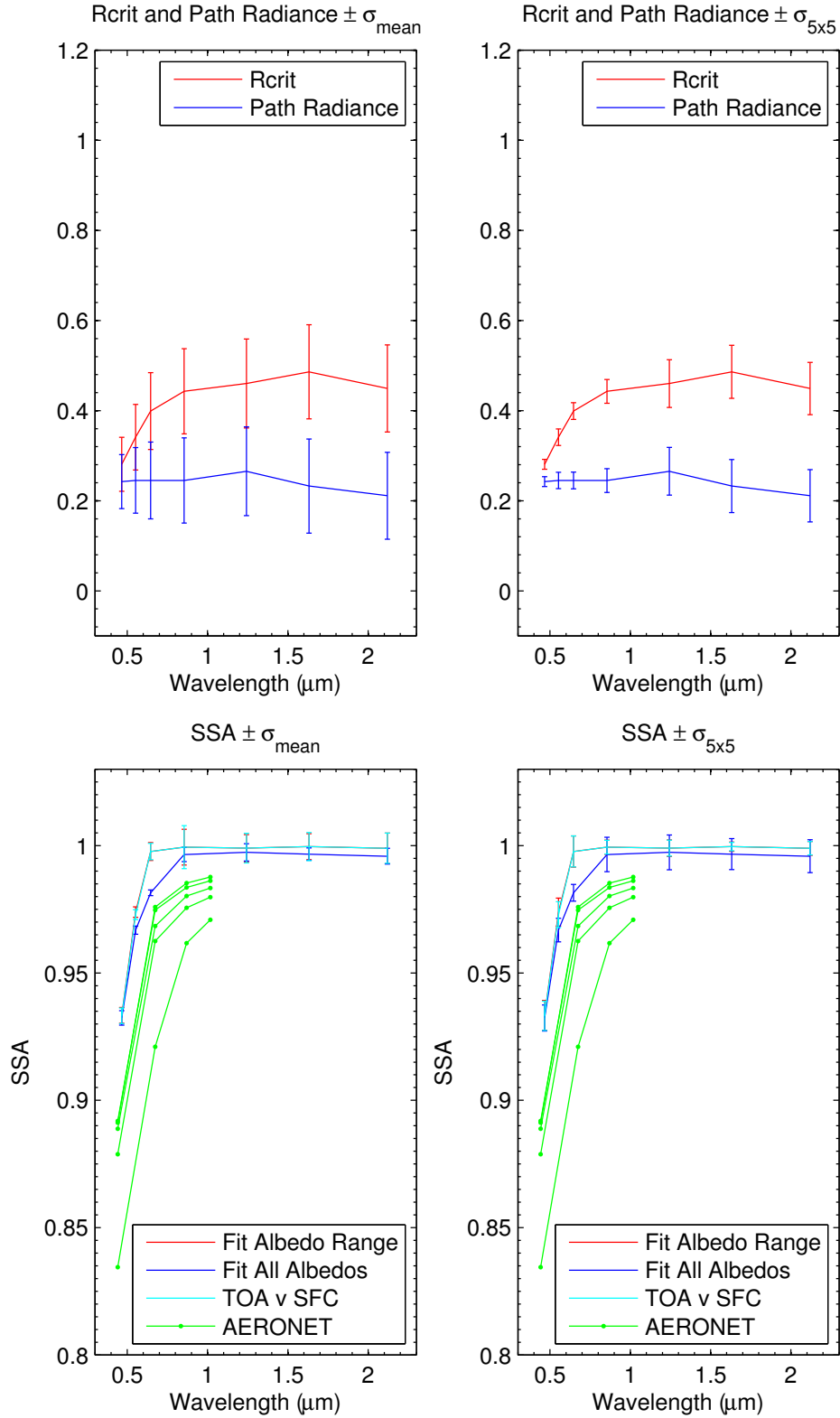


Figure D.12: Spectral plots of critical reflectance and path radiance (upper panels) and SSA (lower panels) with error bars using the two error estimation methods, for 23 July 2007 950 UTC (compared to -16 days) at the Tamanrasset site. AERONET retrievals for the day are also shown.

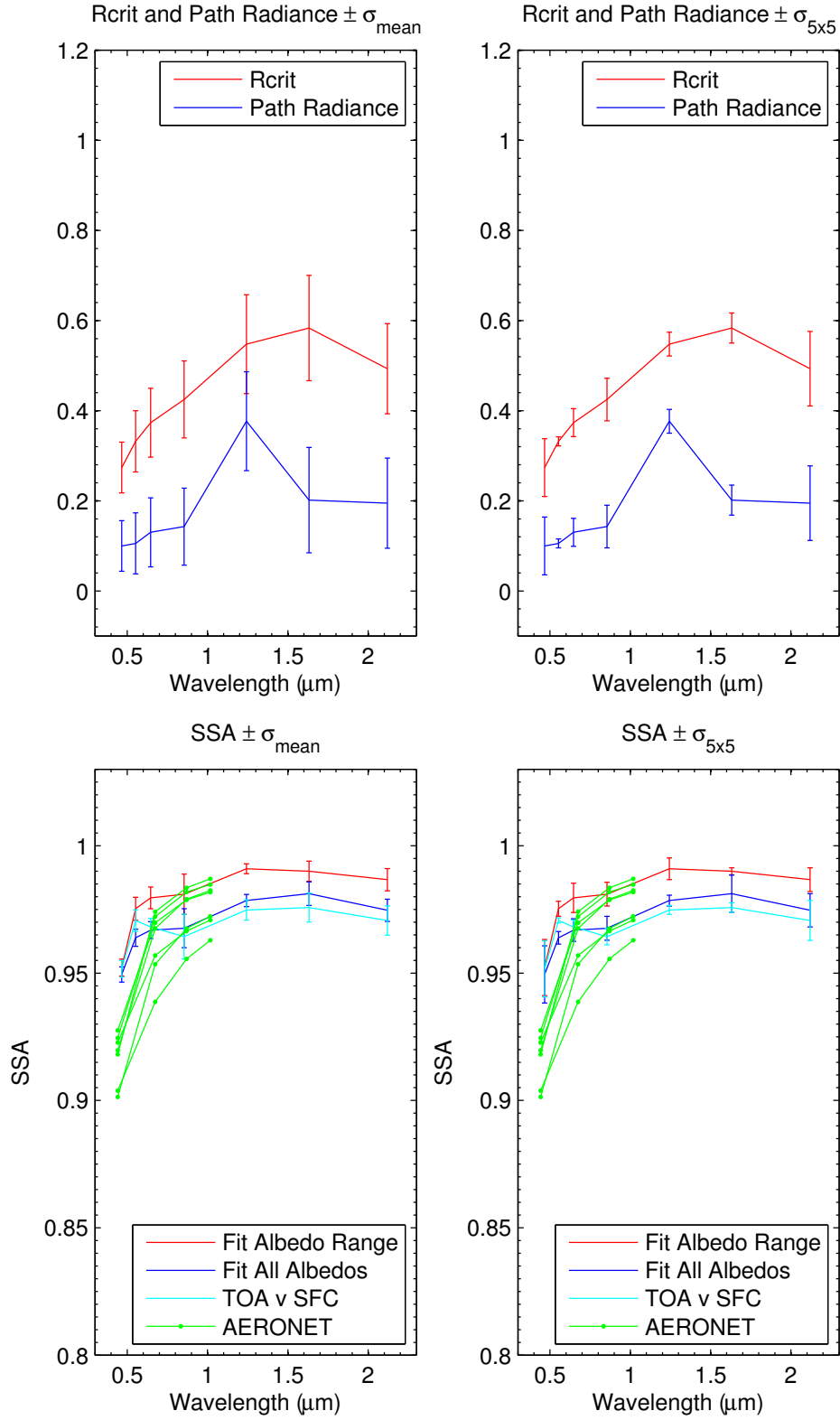


Figure D.13: Spectral plots of critical reflectance and path radiance (upper panels) and SSA (lower panels) with error bars using the two error estimation methods, for 4 August 2007 1015 UTC (compared to -16 days) at the Tamanrasset site. AERONET retrievals for the day are also shown.

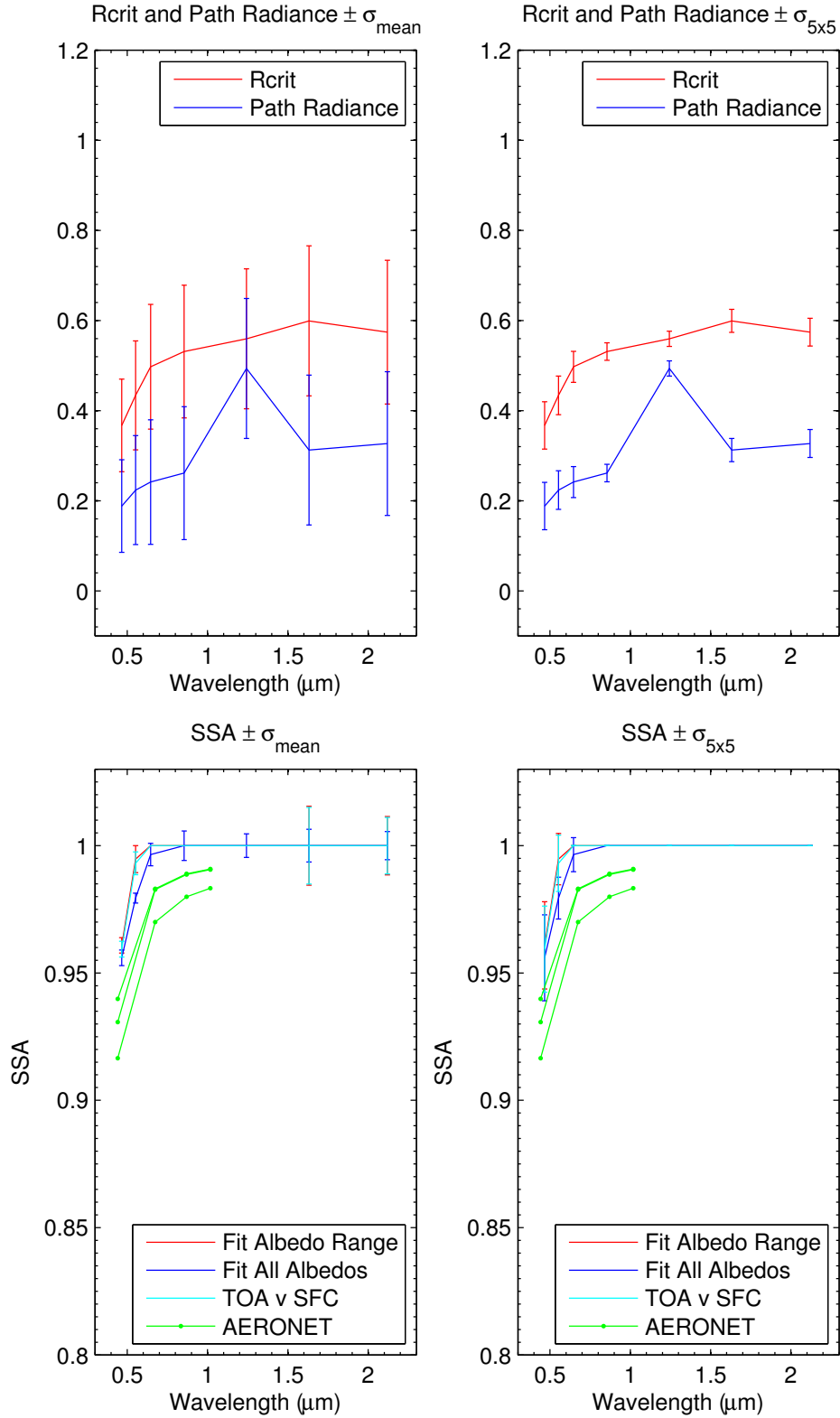


Figure D.14: Spectral plots of critical reflectance and path radiance (upper panels) and SSA (lower panels) with error bars using the two error estimation methods, for 6 January 2008 955 UTC (compared to -16 days) at the Tamanrasset site. AERONET retrievals for the day are also shown.

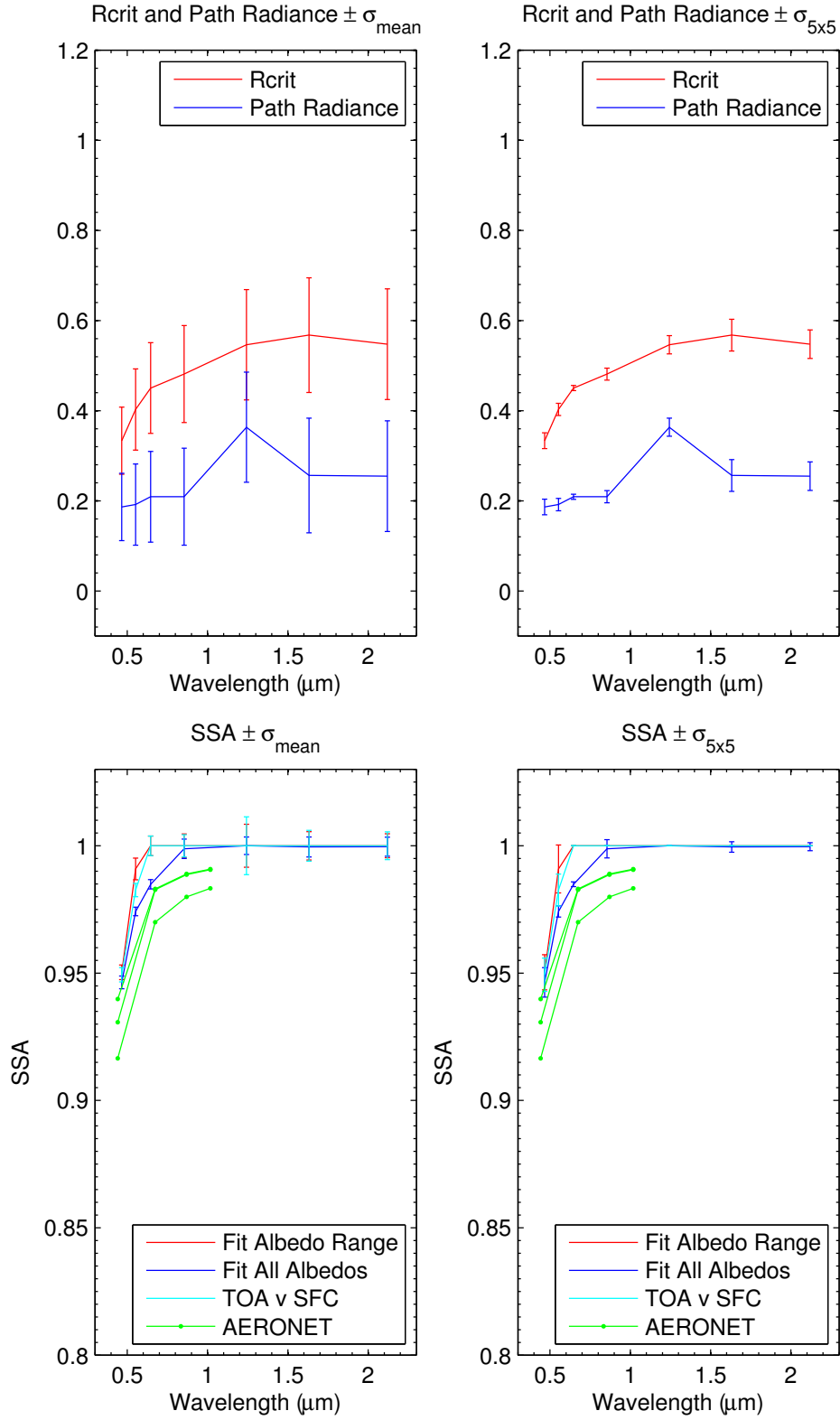


Figure D.15: Spectral plots of critical reflectance and path radiance (upper panels) and SSA (lower panels) with error bars using the two error estimation methods, for 6 January 2008 955 UTC (compared to +16 days) at the Tamanrasset site. AERONET retrievals for the day are also shown.

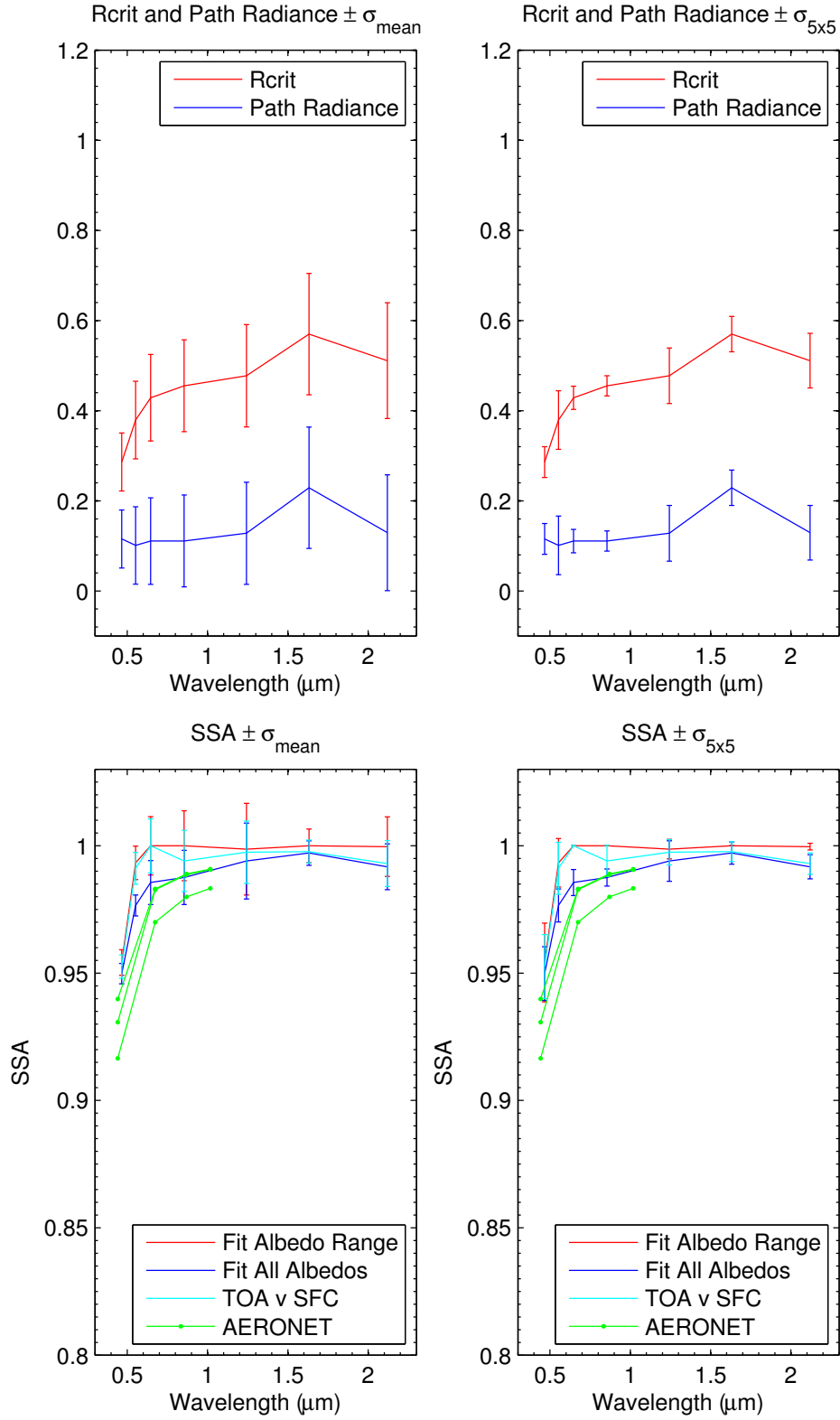


Figure D.16: Spectral plots of critical reflectance and path radiance (upper panels) and SSA (lower panels) with error bars using the two error estimation methods, for 6 January 2008 1305 UTC (compared to +16 days) at the Tamanrasset site. AERONET retrievals for the day are also shown.

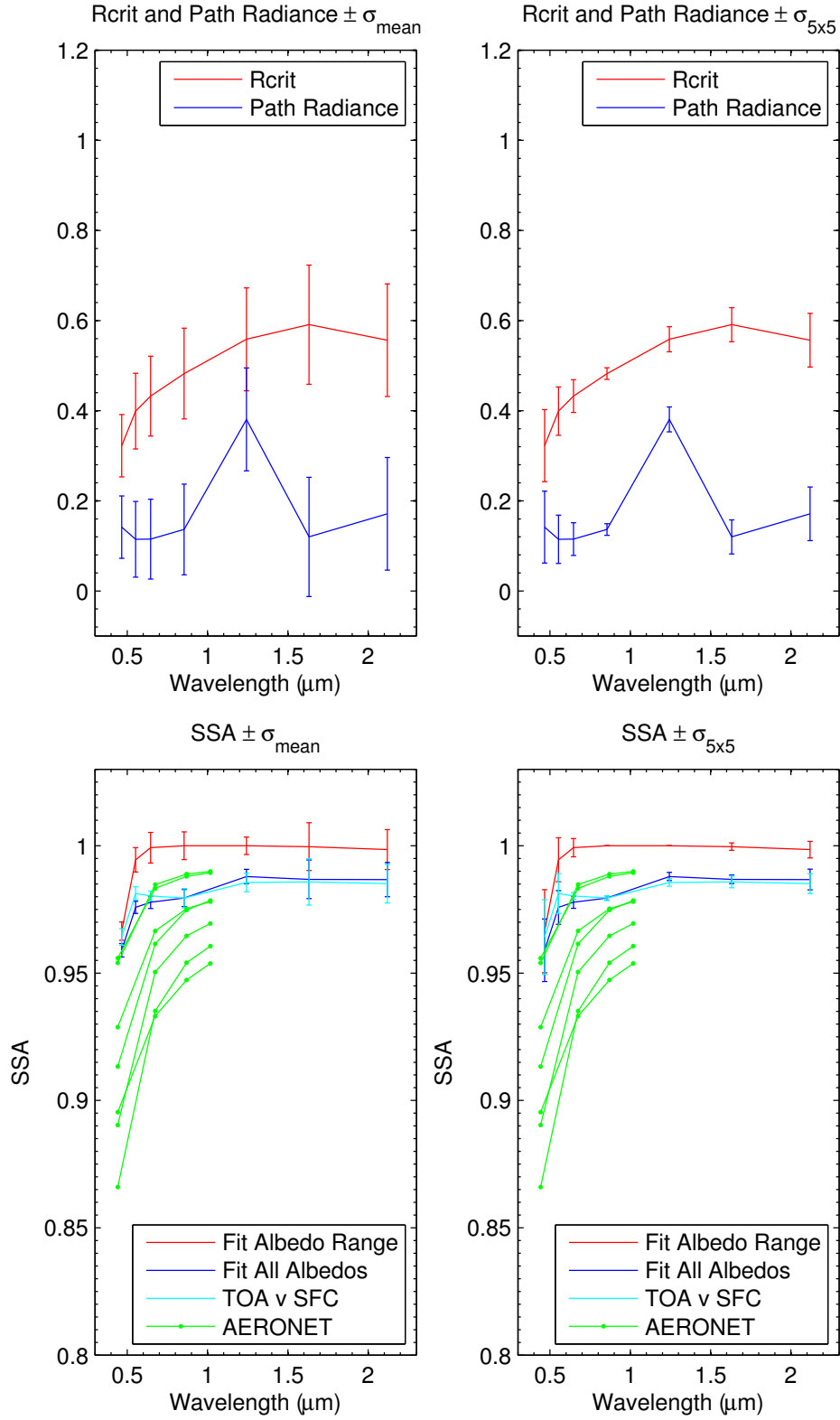


Figure D.17: Spectral plots of critical reflectance and path radiance (upper panels) and SSA (lower panels) with error bars using the two error estimation methods, for 28 February 2008 1015 UTC (compared to +16 days) at the Tamanrasset site. AERONET retrievals for the day are also shown.

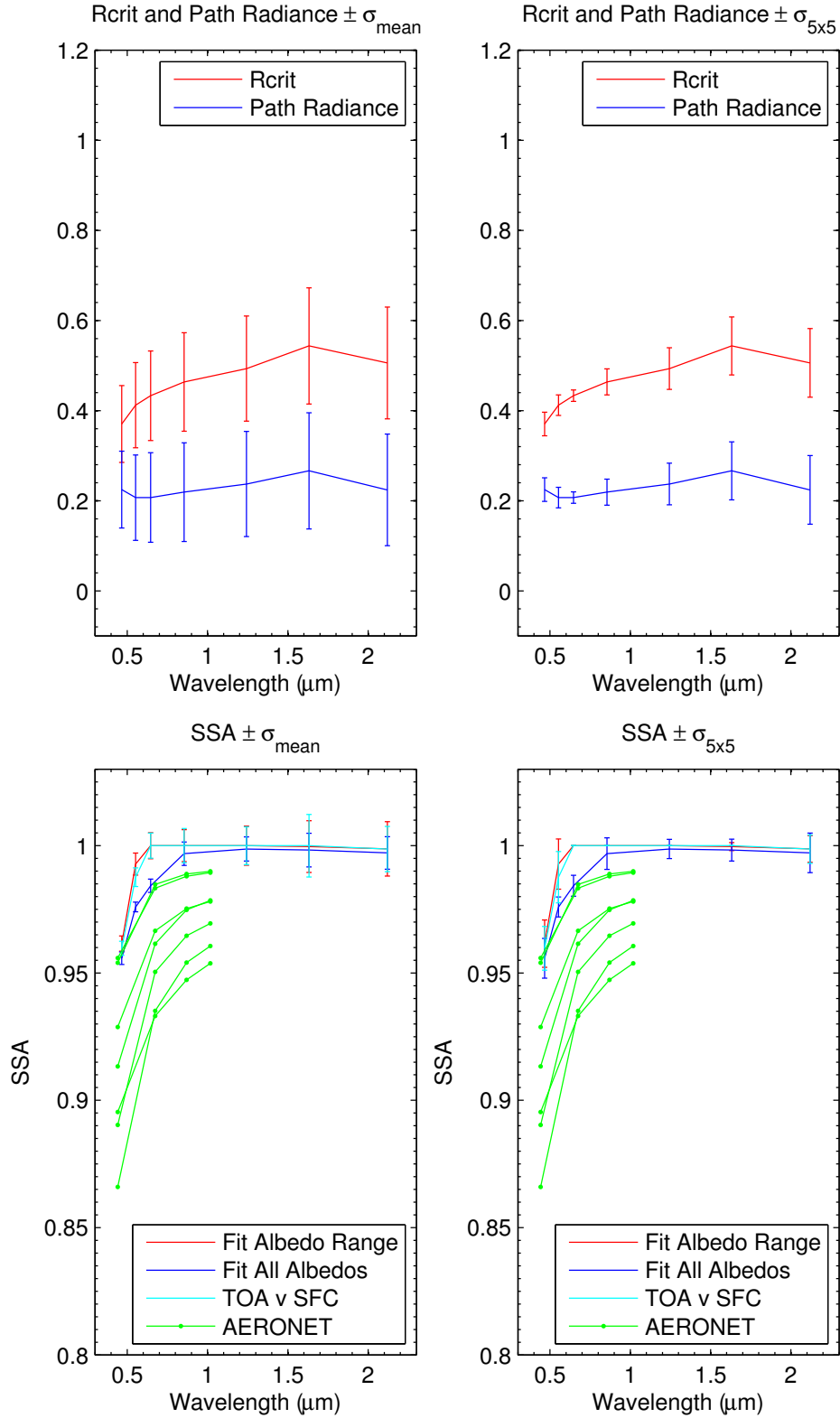


Figure D.18: Spectral plots of critical reflectance and path radiance (upper panels) and SSA (lower panels) with error bars using the two error estimation methods, for 28 February 2008 1320 UTC (compared to +16 days) at the Tamanrasset site. AERONET retrievals for the day are also shown.

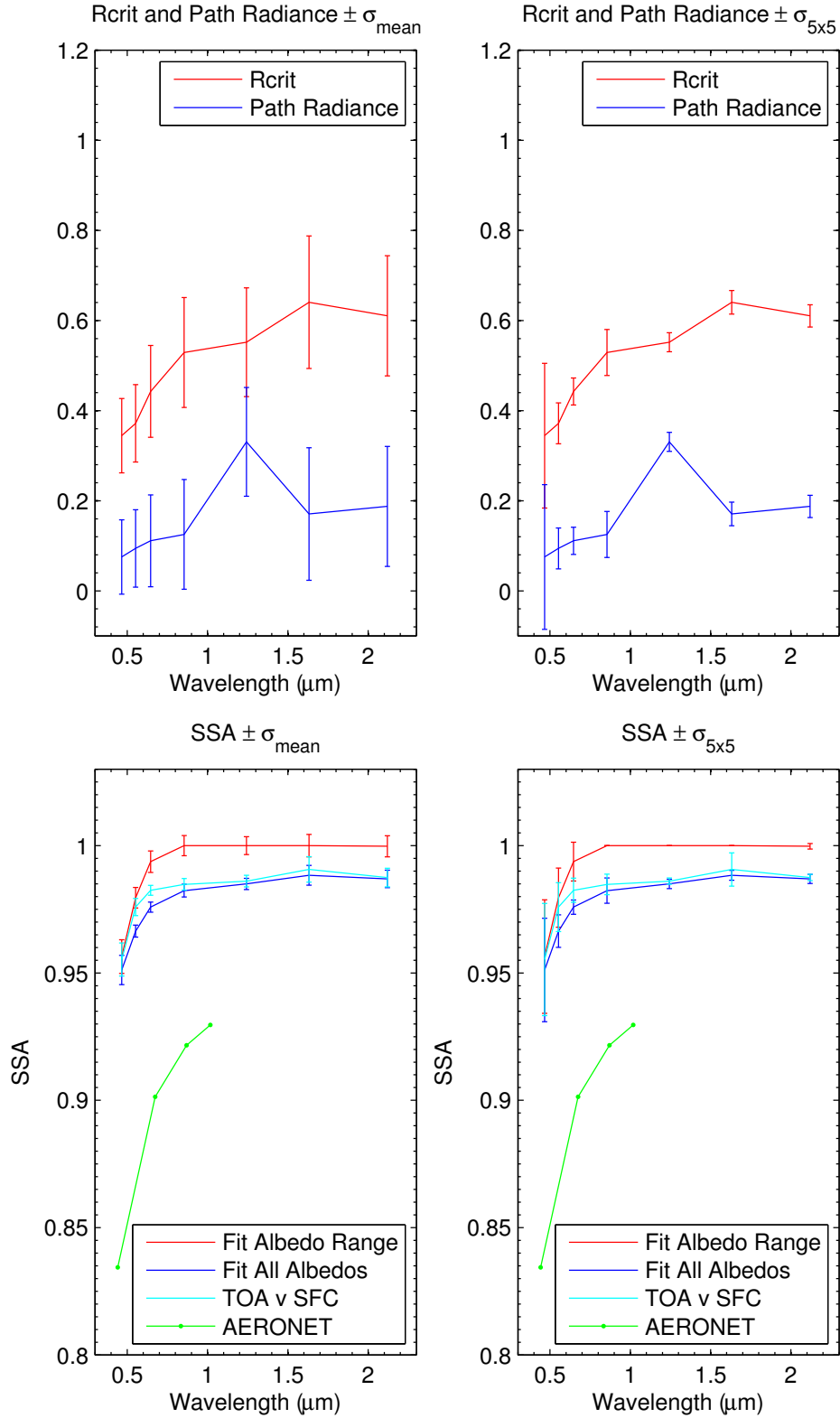


Figure D.19: Spectral plots of critical reflectance and path radiance (upper panels) and SSA (lower panels) with error bars using the two error estimation methods, for 3 April 2008 1045 UTC (compared to -16 days) at the Tamanrasset site. AERONET retrievals for the day are also shown.

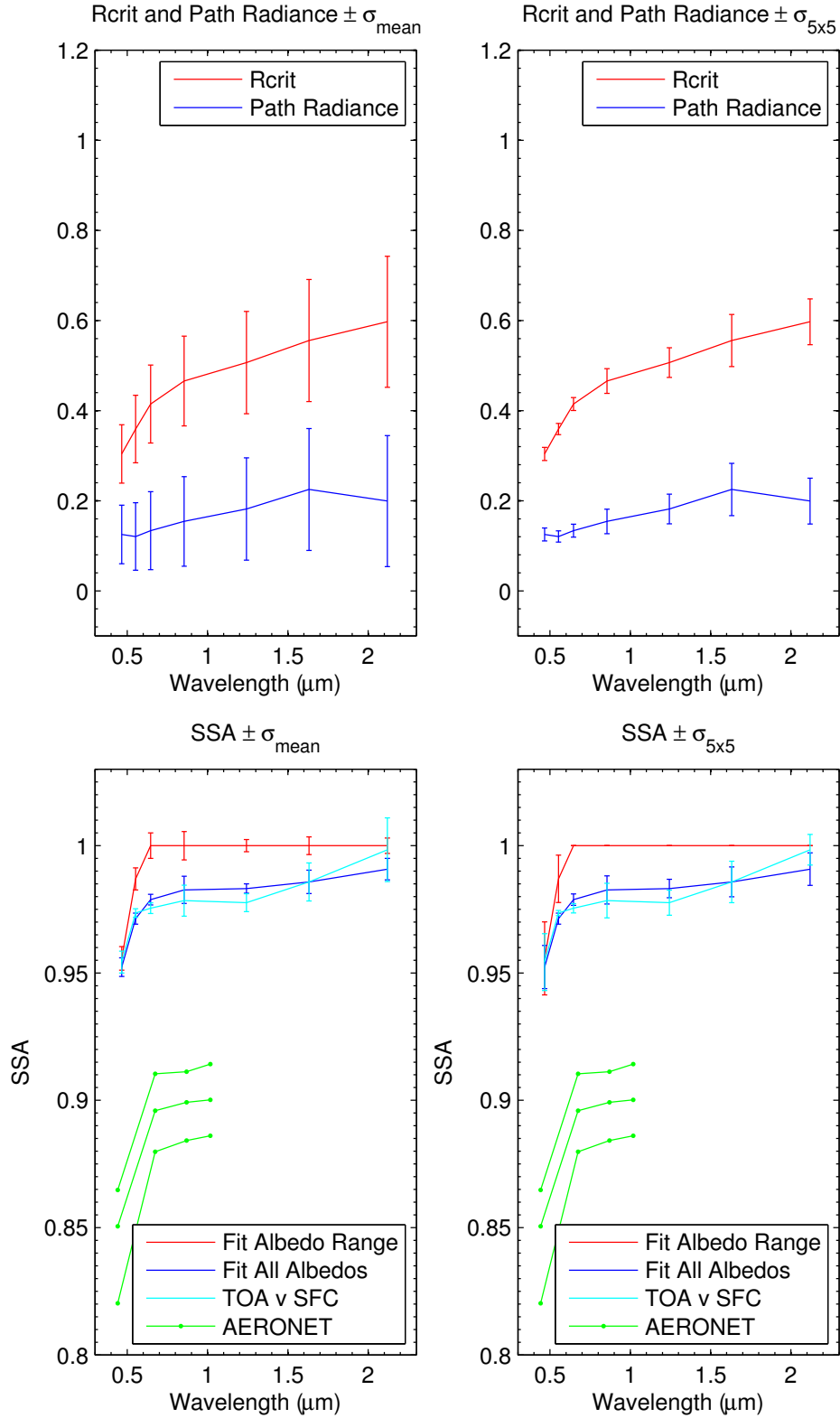


Figure D.20: Spectral plots of critical reflectance and path radiance (upper panels) and SSA (lower panels) with error bars using the two error estimation methods, for 14 April 2008 1025 UTC (compared to -16 days) at the Tamanrasset site. AERONET retrievals for the day are also shown.

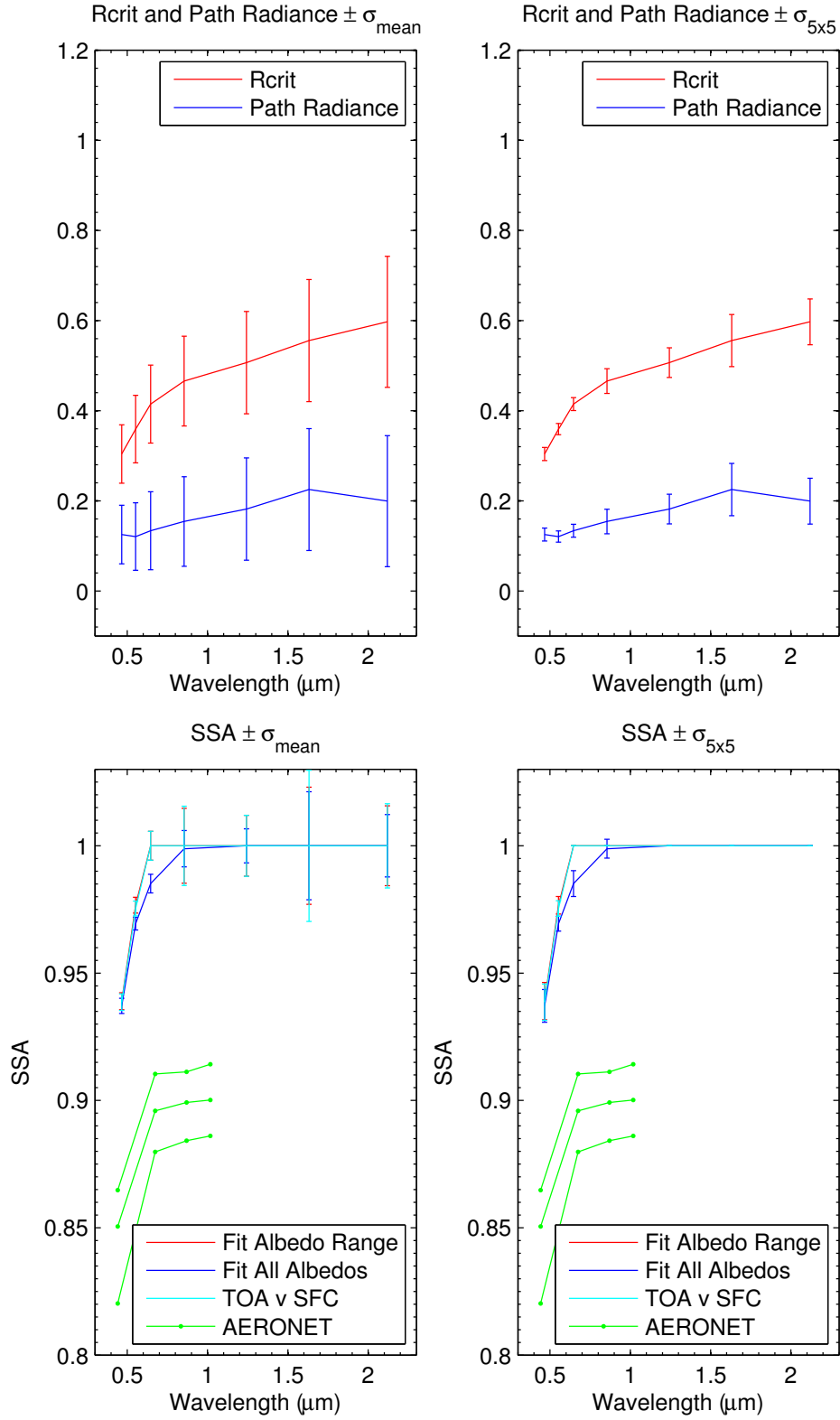


Figure D.21: Spectral plots of critical reflectance and path radiance (upper panels) and SSA (lower panels) with error bars using the two error estimation methods, for 14 April 2008 1335 UTC (compared to -16 days) at the Tamanrasset site. AERONET retrievals for the day are also shown.

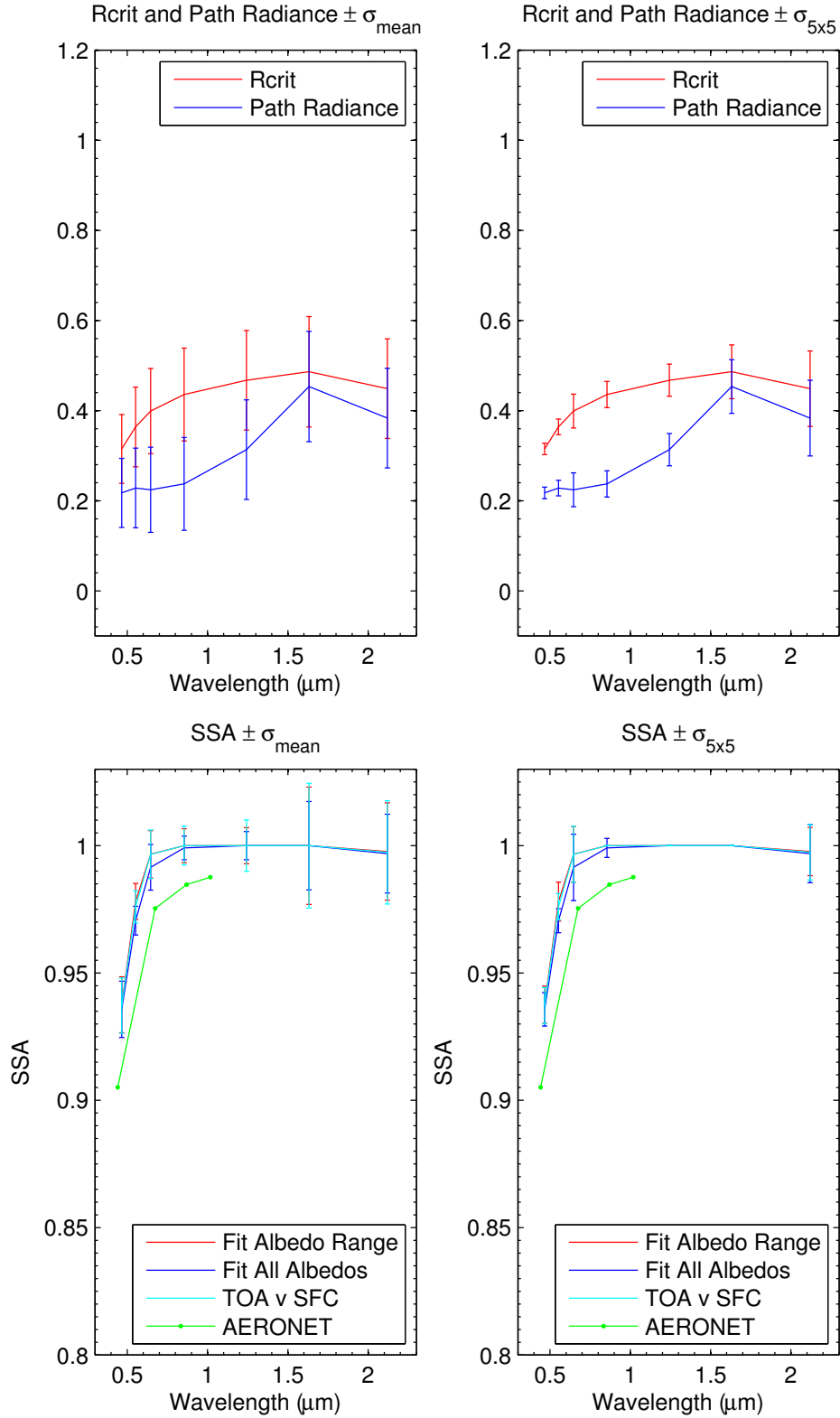


Figure D.22: Spectral plots of critical reflectance and path radiance (upper panels) and SSA (lower panels) with error bars using the two error estimation methods, for 27 July 2008 935 UTC (compared to +16 days) at the Tamanrasset site. AERONET retrievals for the day are also shown.

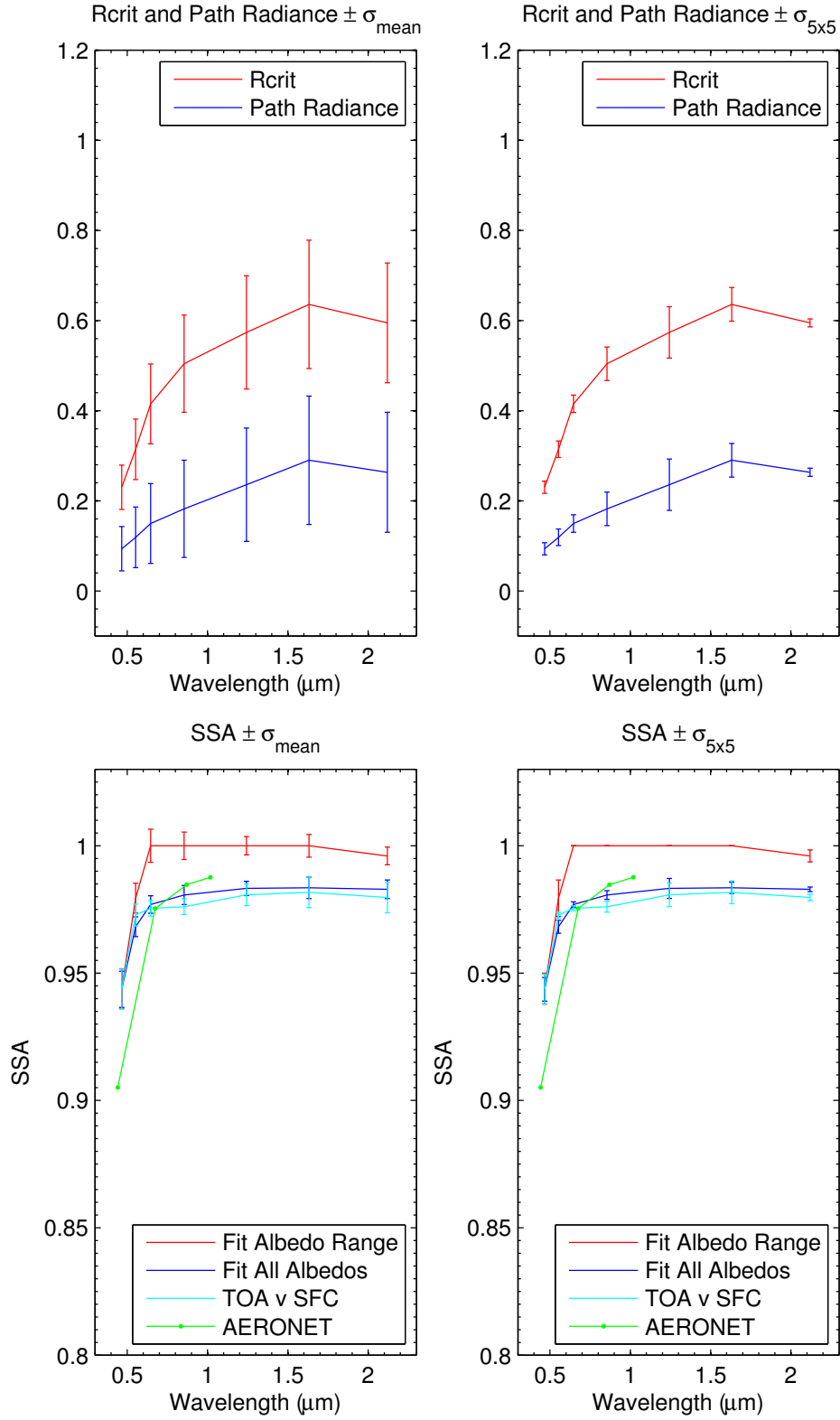


Figure D.23: Spectral plots of critical reflectance and path radiance (upper panels) and SSA (lower panels) with error bars using the two error estimation methods, for 27 July 2008 1245 UTC (compared to +16 days) at the Tamanrasset site. AERONET retrievals for the day are also shown.

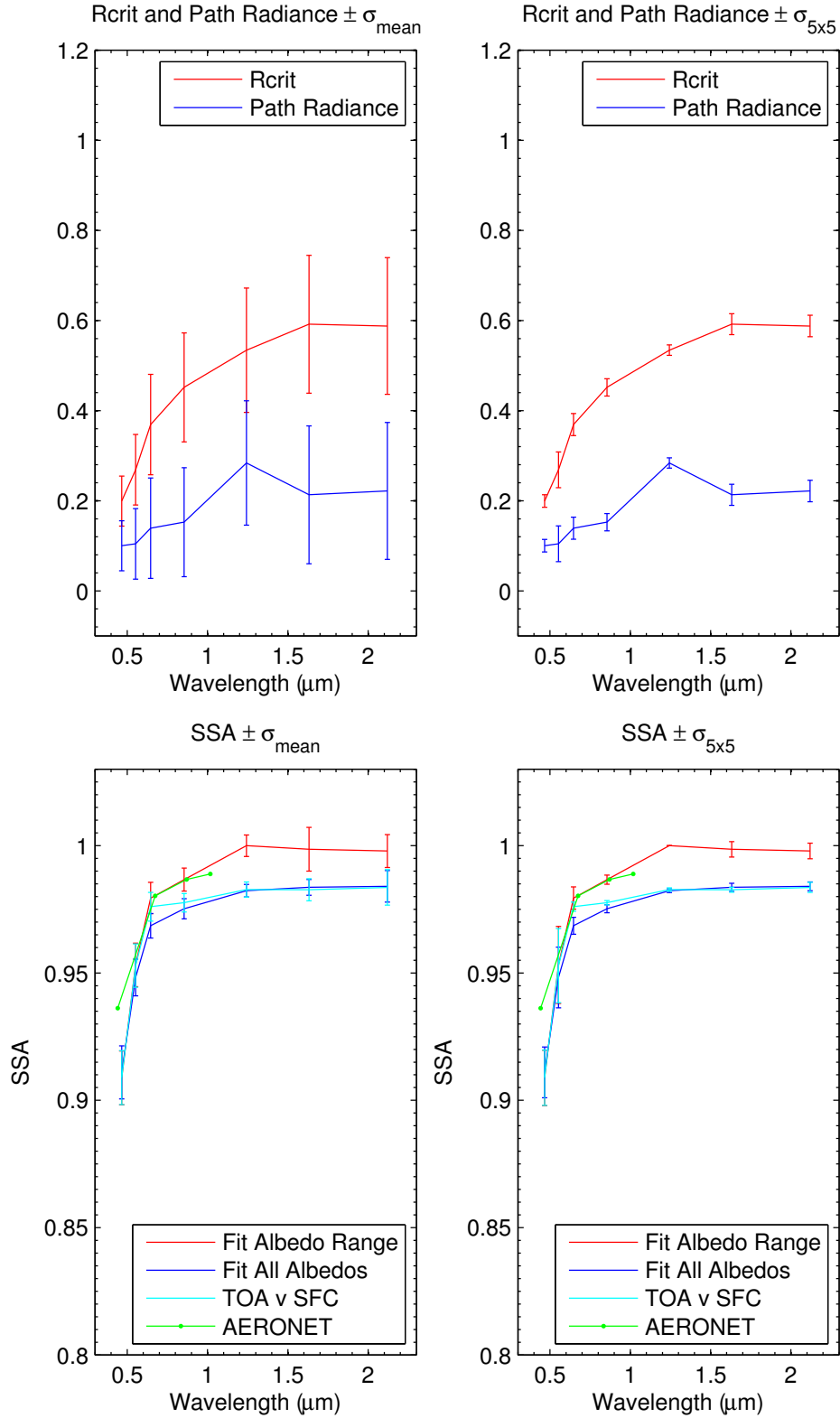


Figure D.24: Spectral plots of critical reflectance and path radiance (upper panels) and SSA (lower panels) with error bars using the two error estimation methods, for 3 September 2008 1040 UTC (compared to -16 days) at the Tamanrasset site. AERONET retrievals for the day are also shown.

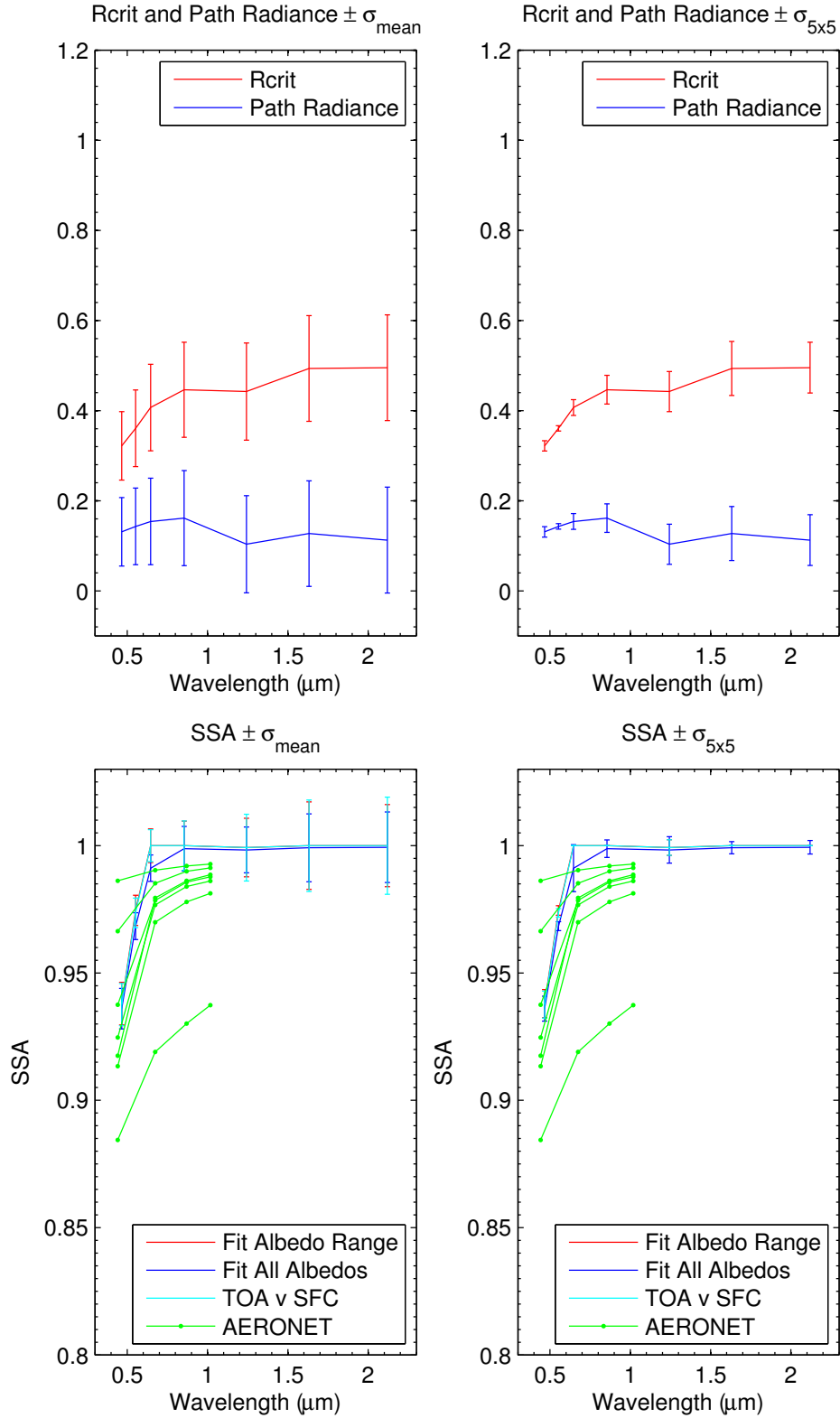


Figure D.25: Spectral plots of critical reflectance and path radiance (upper panels) and SSA (lower panels) with error bars using the two error estimation methods, for 29 September 2008 935 UTC (compared to +16 days) at the Tamanrasset site. AERONET retrievals for the day are also shown.

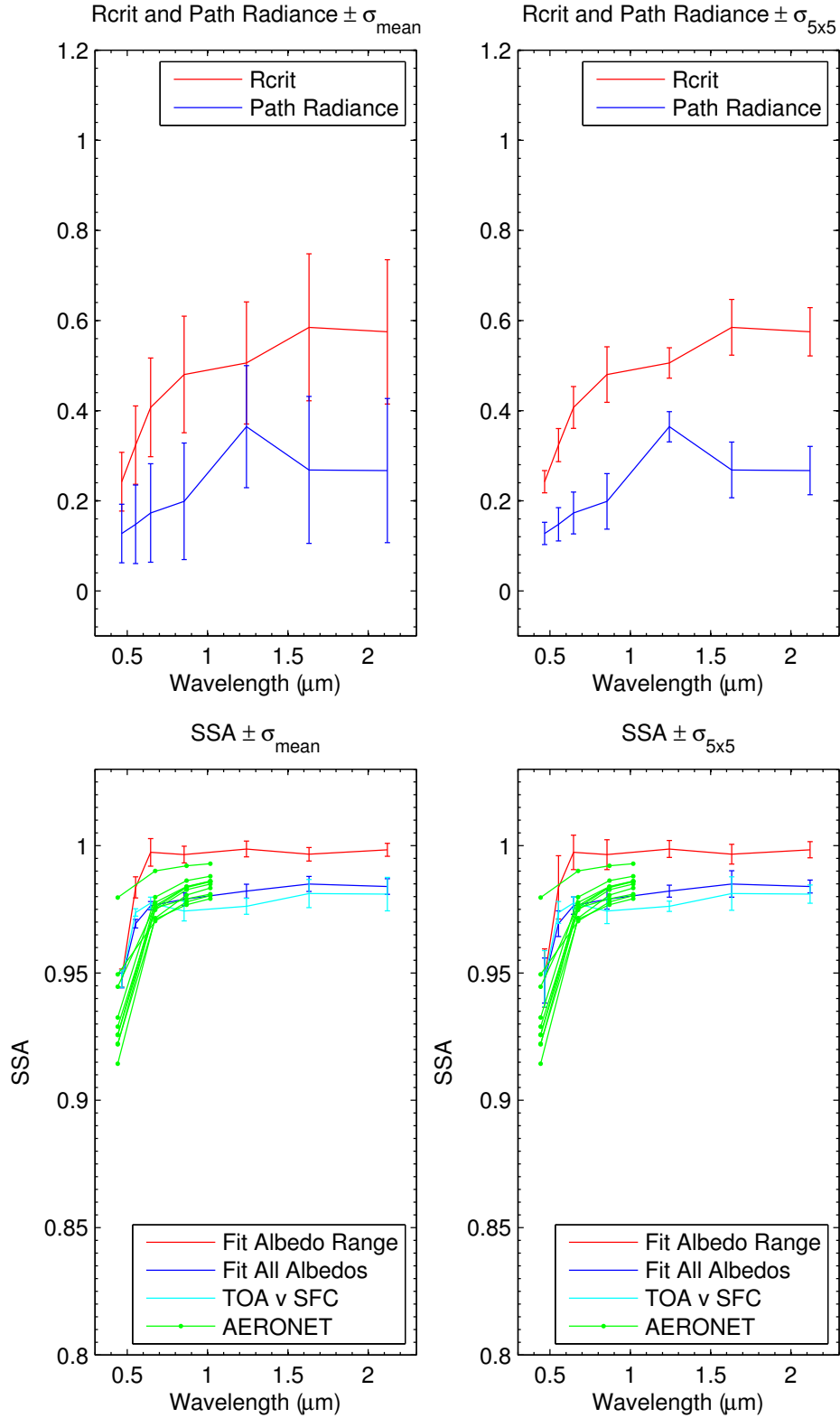


Figure D.26: Spectral plots of critical reflectance and path radiance (upper panels) and SSA (lower panels) with error bars using the two error estimation methods, for 30 September 2008 1020 UTC (compared to +16 days) at the Tamanrasset site. AERONET retrievals for the day are also shown.

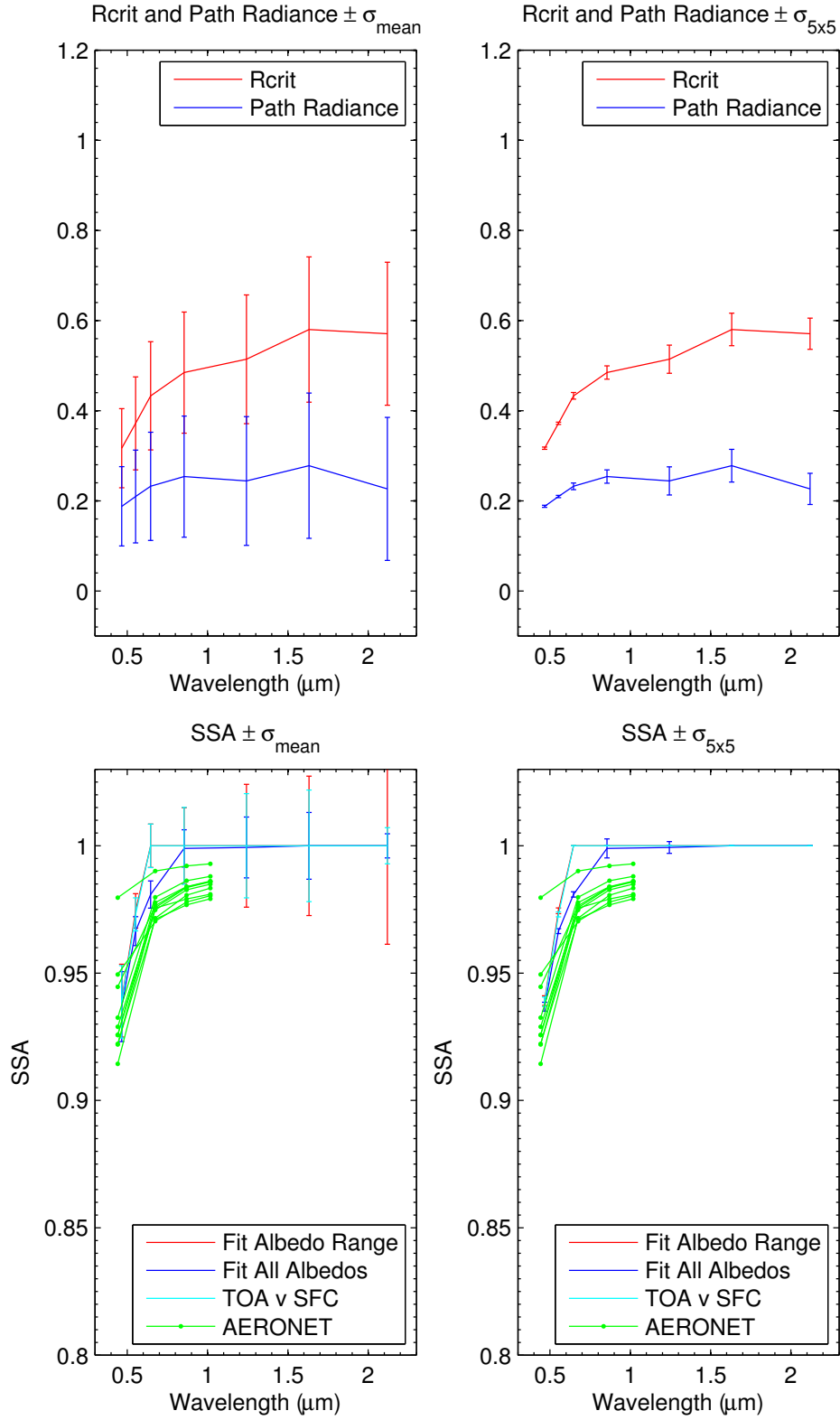


Figure D.27: Spectral plots of critical reflectance and path radiance (upper panels) and SSA (lower panels), with error bars using the two error estimation methods, for 30 September 2008 1330 UTC (compared to +16 days) at the Tamanrasset site. AERONET retrievals for the day are also shown.

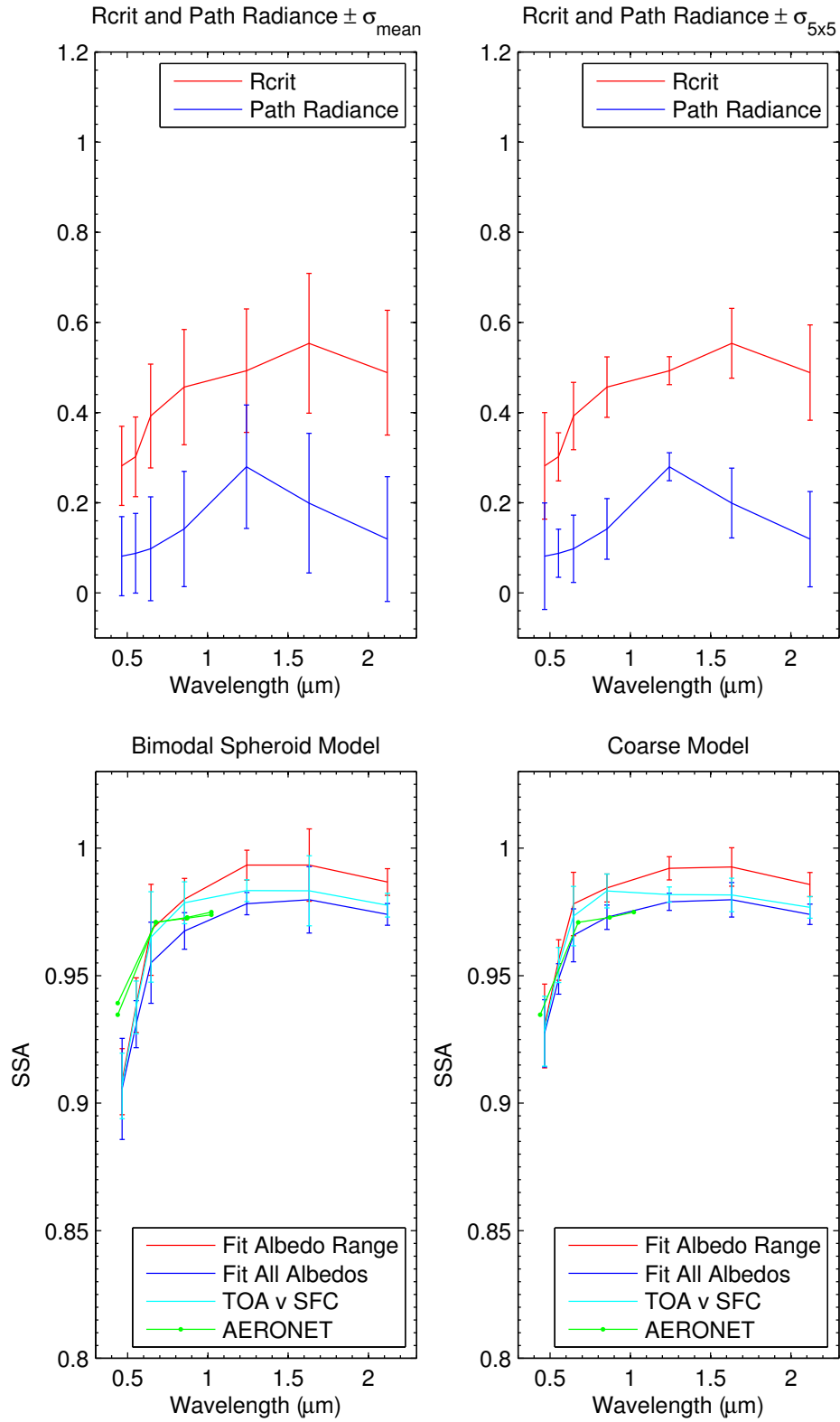


Figure D.28: Spectral plots of critical reflectance and path radiance (upper panels) and SSA retrieved for the bimodal spheroid model (lower left) and coarse model (lower right) for 13 March 2006 1045 UTC (compared to -16 days) at the Banizoumbou site. Error bars for the SSA are the  $\sigma_{\text{mean}}$  estimates. AERONET retrievals for the day are also shown.

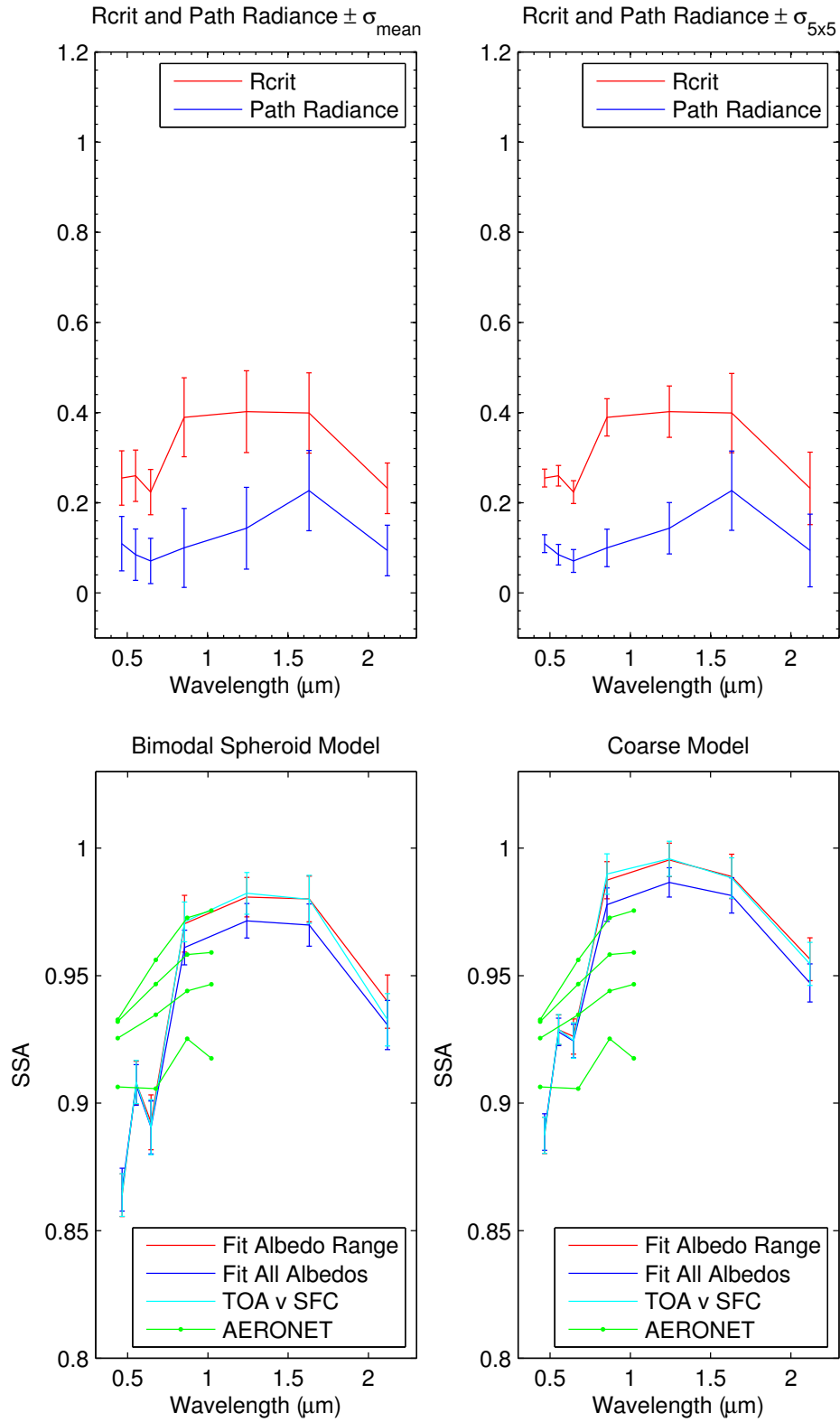


Figure D.29: Spectral plots of critical reflectance and path radiance (upper panels) and SSA retrieved for the bimodal spheroid model (lower left) and coarse model (lower right) for 16 October 2006 1345 UTC (compared to +16 days) at the Banizoumbou site. Error bars for the SSA are the  $\sigma_{\text{mean}}$  estimates. AERONET retrievals for the day are also shown.

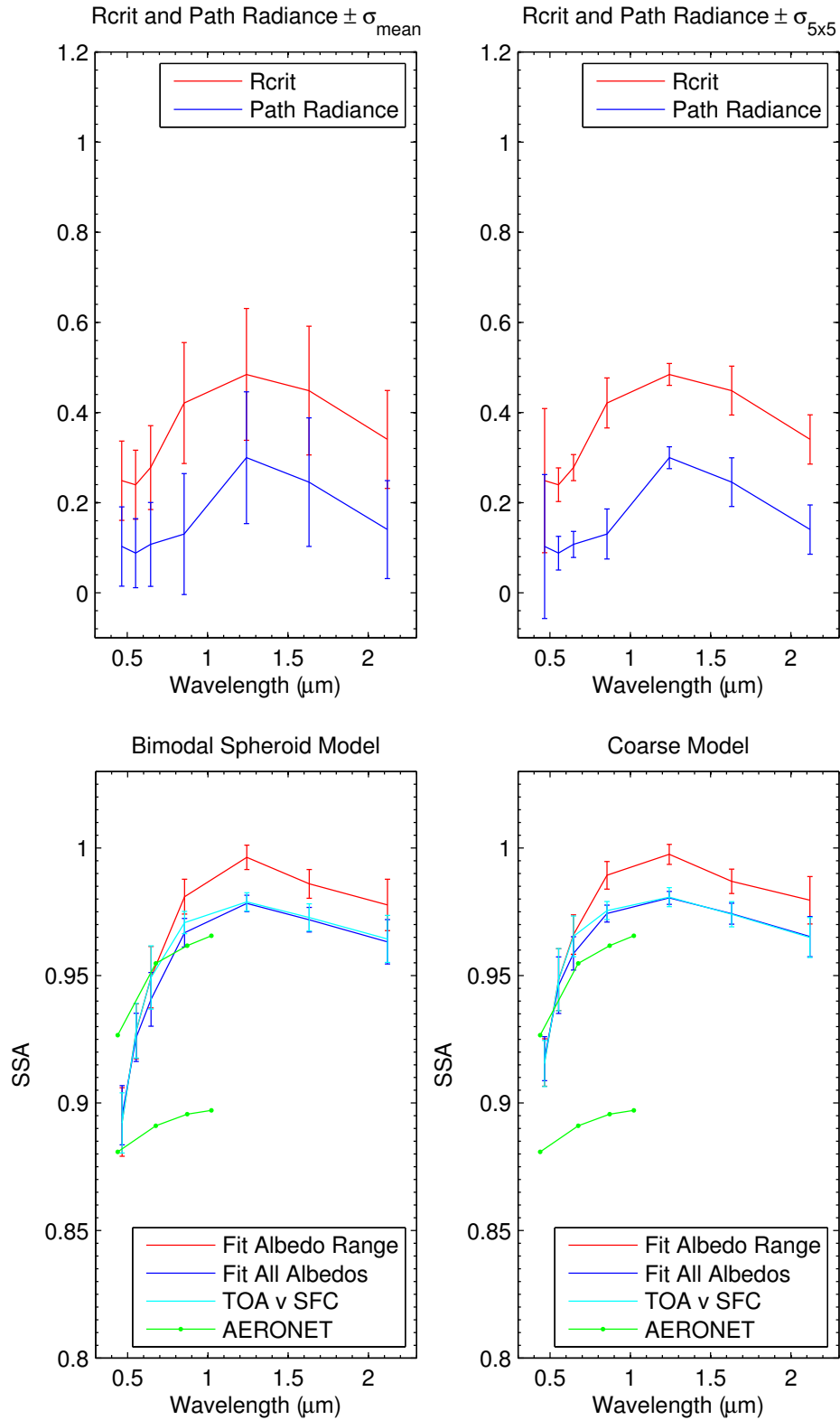


Figure D.30: Spectral plots of critical reflectance and path radiance (upper panels) and SSA retrieved for the bimodal spheroid model (lower left) and coarse model (lower right) for 10 November 2006 1035 UTC (compared to +16 days) at the Banizoumbou site. Error bars for the SSA are the  $\sigma_{\text{mean}}$  estimates. AERONET retrievals for the day are also shown.

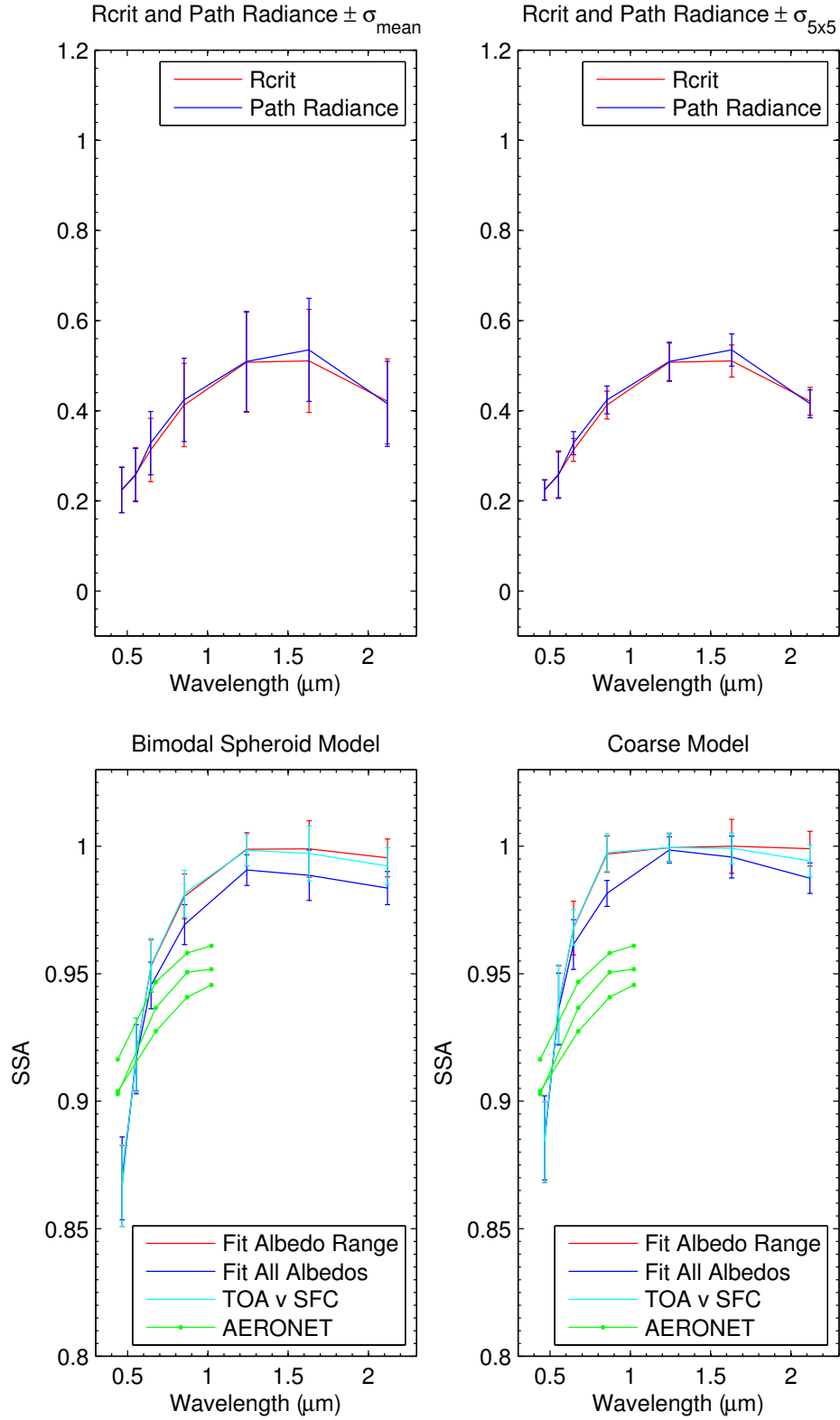


Figure D.31: Spectral plots of critical reflectance and path radiance (upper panels) and SSA retrieved for the bimodal spheroid model (lower left) and coarse model (lower right) for 16 November 2006 955 UTC (compared to -16 days) at the Banizoumbou site. Error bars for the SSA are the  $\sigma_{\text{mean}}$  estimates. AERONET retrievals for the day are also shown.

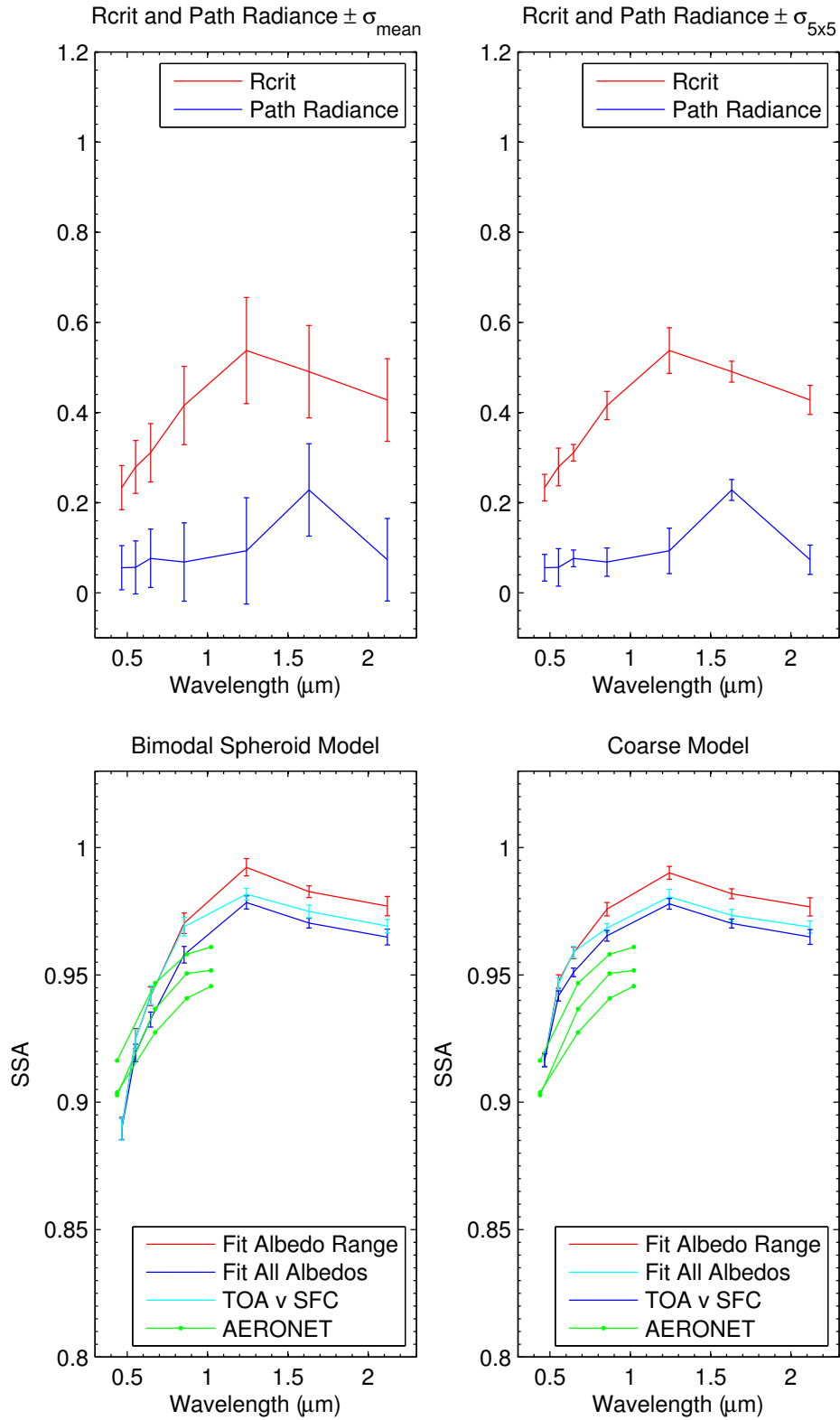


Figure D.32: Spectral plots of critical reflectance and path radiance (upper panels) and SSA retrieved for the bimodal spheroid model (lower left) and coarse model (lower right) for 16 November 2006 1300 UTC (compared to -16 days) at the Banizoumbou site. Error bars for the SSA are the  $\sigma_{\text{mean}}$  estimates. AERONET retrievals for the day are also shown.

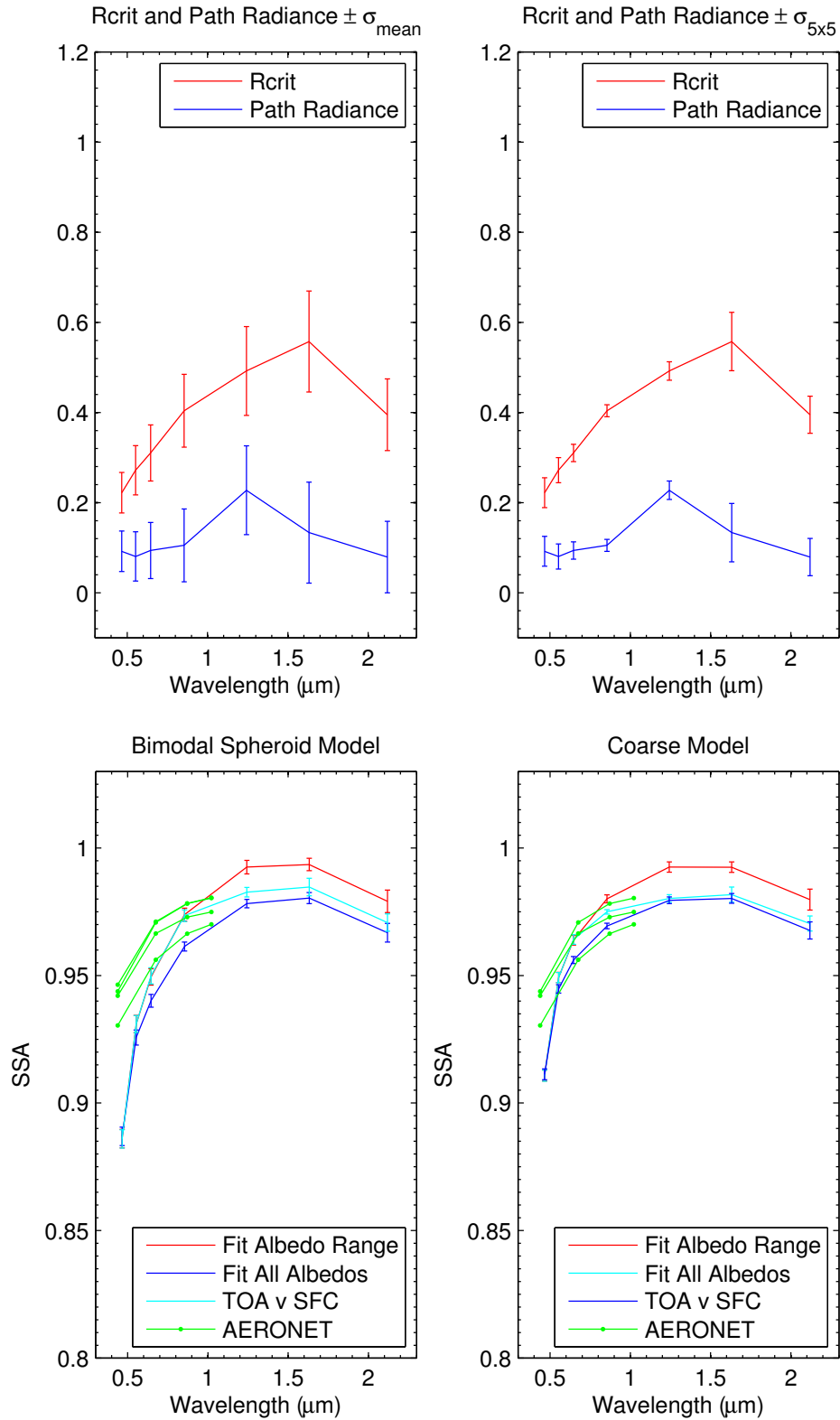


Figure D.33: Spectral plots of critical reflectance and path radiance (upper panels) and SSA retrieved for the bimodal spheroid model (lower left) and coarse model (lower right) for 17 November 2006 1040 UTC (compared to -16 days) at the Banizoumbou site. Error bars for the SSA are the  $\sigma_{\text{mean}}$  estimates. AERONET retrievals for the day are also shown.

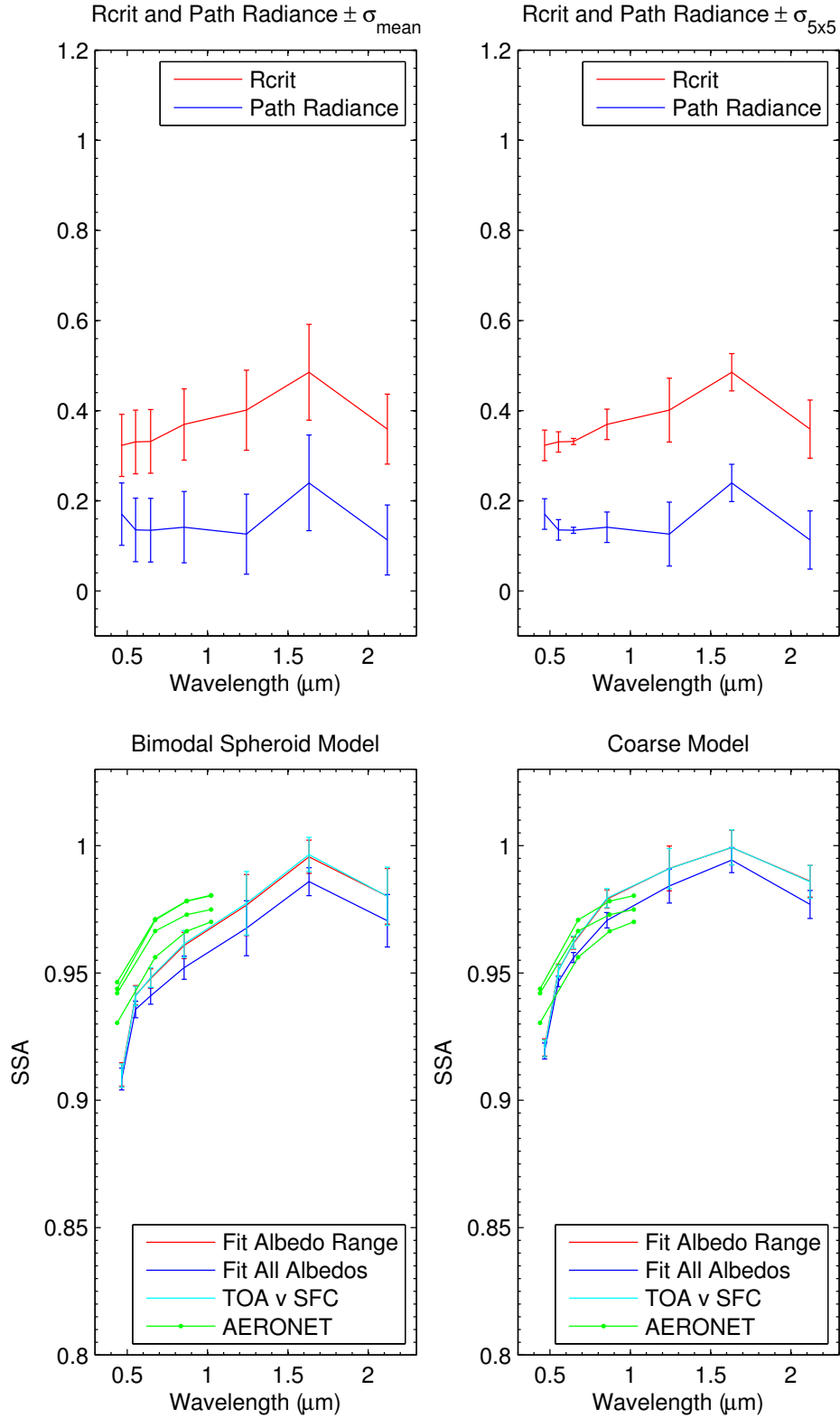


Figure D.34: Spectral plots of critical reflectance and path radiance (upper panels) and SSA retrieved for the bimodal spheroid model (lower left) and coarse model (lower right) for 17 November 2006 1345 UTC (compared to -16 days) at the Banizoumbou site. Error bars for the SSA are the  $\sigma_{\text{mean}}$  estimates. AERONET retrievals for the day are also shown.

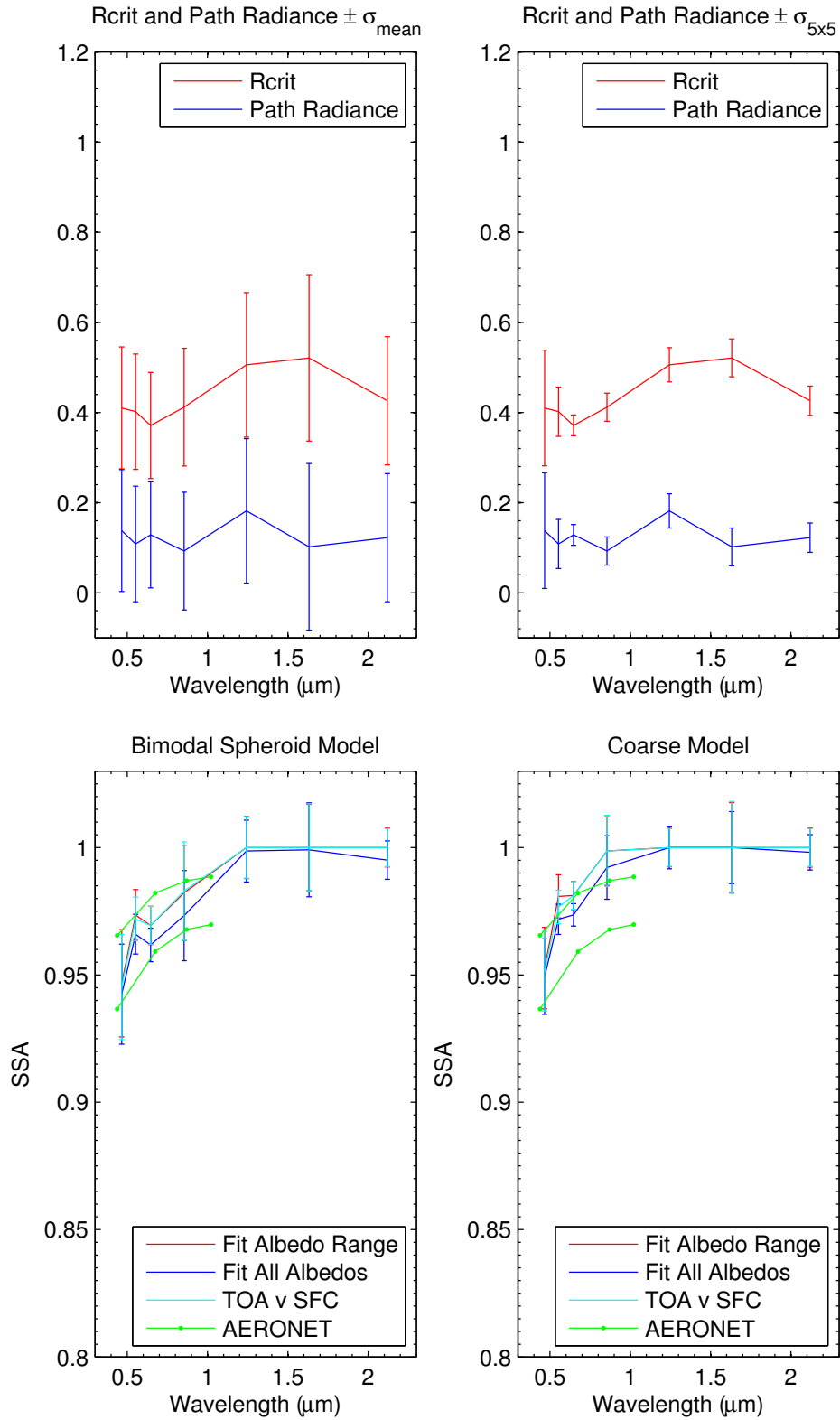


Figure D.35: Spectral plots of critical reflectance and path radiance (upper panels) and SSA retrieved for the bimodal spheroid model (lower left) and coarse model (lower right) for 18 November 2006 945 UTC (compared to -16 days) at the Banizoumbou site. Error bars for the SSA are the  $\sigma_{\text{mean}}$  estimates. AERONET retrievals for the day are also shown.

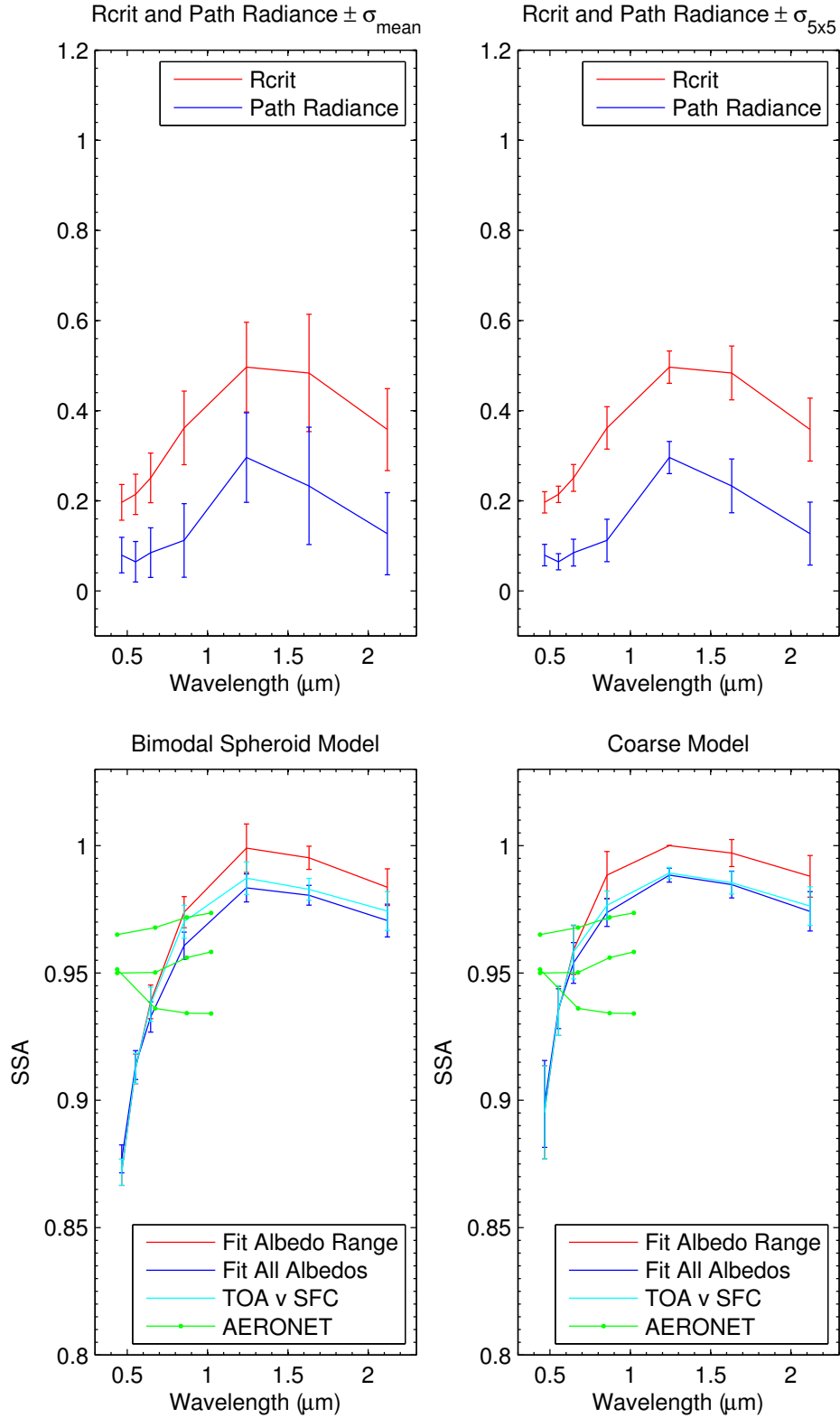


Figure D.36: Spectral plots of critical reflectance and path radiance (upper panels) and SSA retrieved for the bimodal spheroid model (lower left) and coarse model (lower right) for 7 December 2006 1015 UTC (compared to +16 days) at the Banizoumbou site. Error bars for the SSA are the  $\sigma_{\text{mean}}$  estimates. AERONET retrievals for the day are also shown.

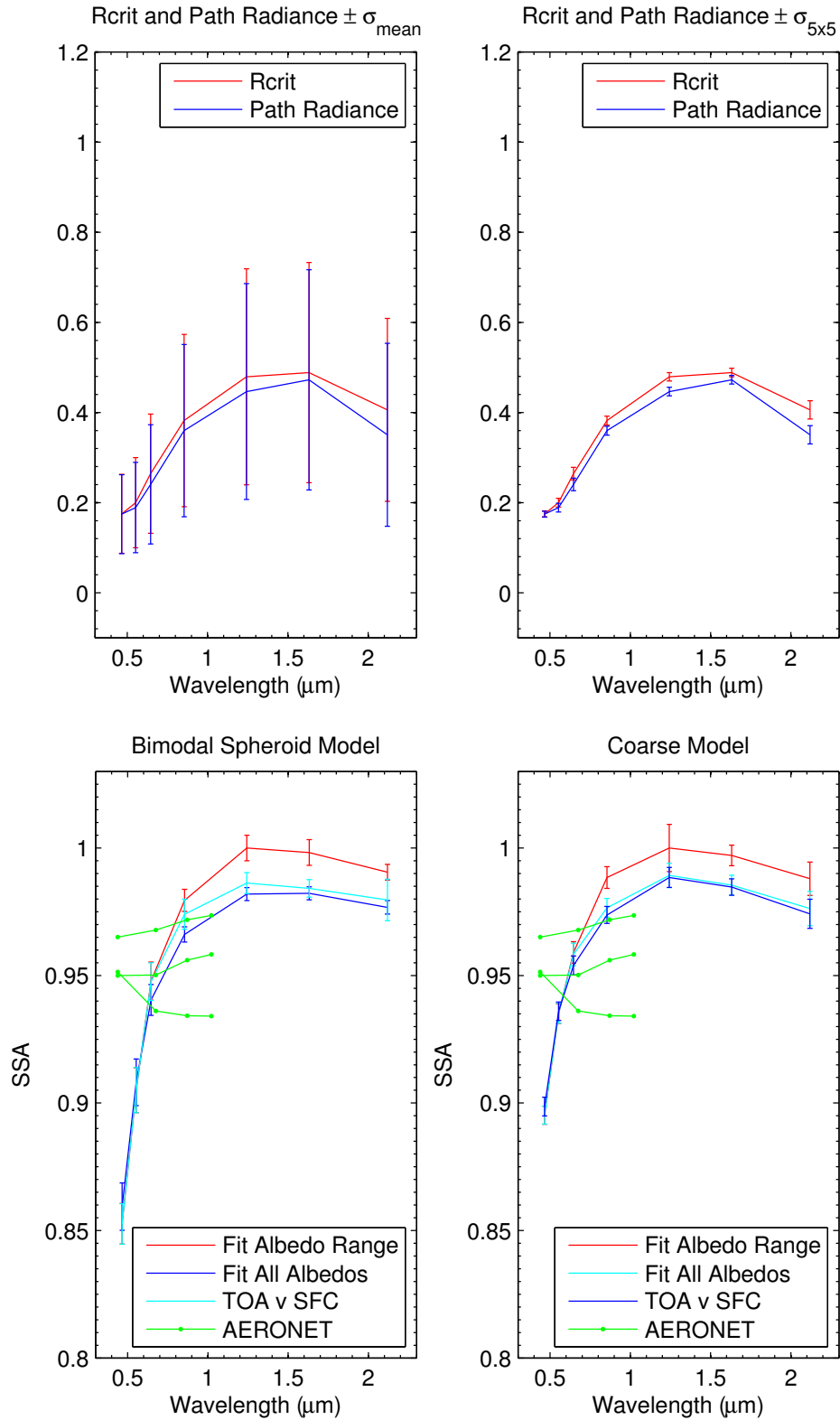


Figure D.37: Spectral plots of critical reflectance and path radiance (upper panels) and SSA retrieved for the bimodal spheroid model (lower left) and coarse model (lower right) for 7 December 2006 1320 UTC (compared to +16 days) at the Banizoumbou site. Error bars for the SSA are the  $\sigma_{\text{mean}}$  estimates. AERONET retrievals for the day are also shown.

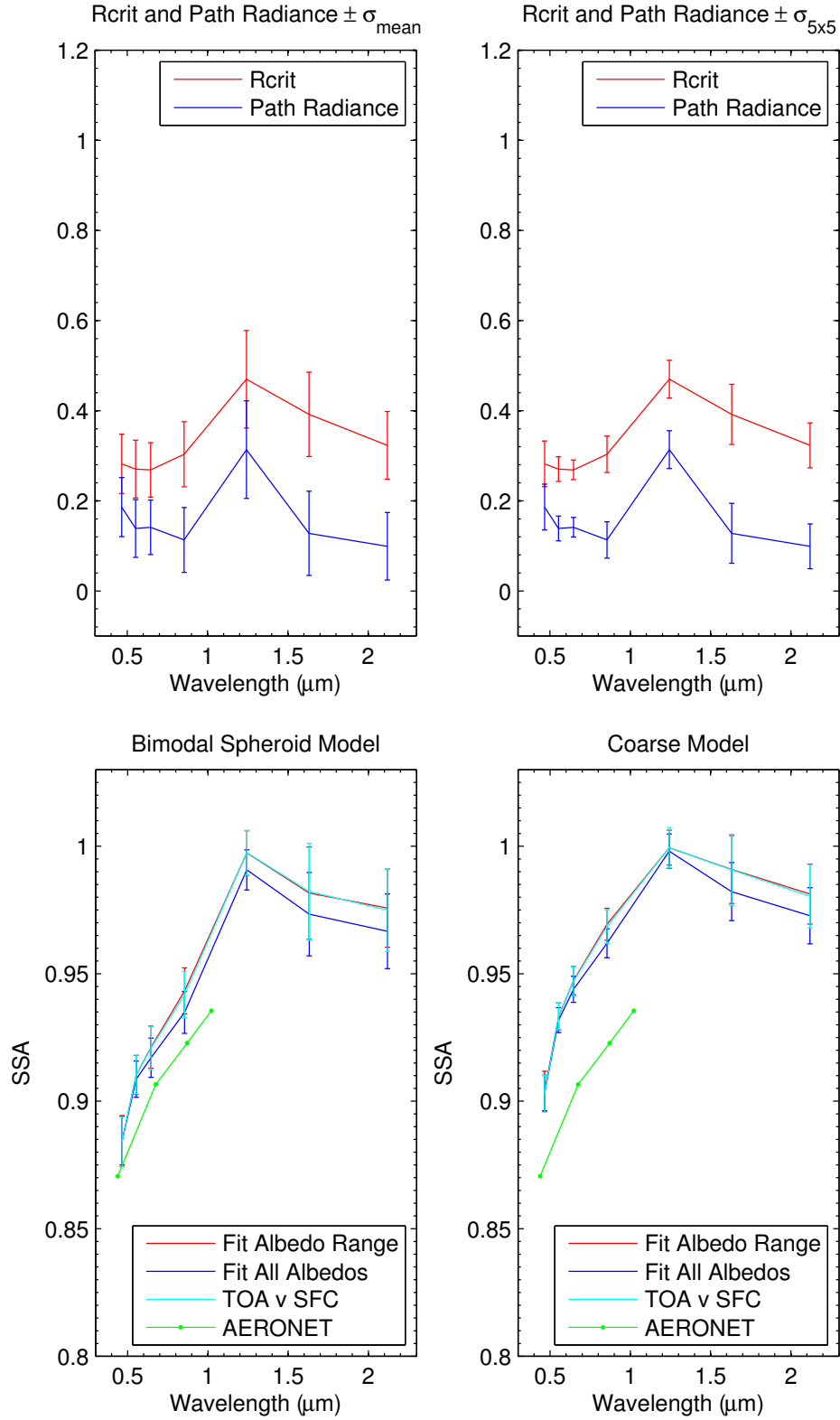


Figure D.38: Spectral plots of critical reflectance and path radiance (upper panels) and SSA retrieved for the bimodal spheroid model (lower left) and coarse model (lower right) for 11 December 2006 950 UTC (compared to -16 days) at the Banizoumbou site. Error bars for the SSA are the  $\sigma_{\text{mean}}$  estimates. AERONET retrievals for the day are also shown.

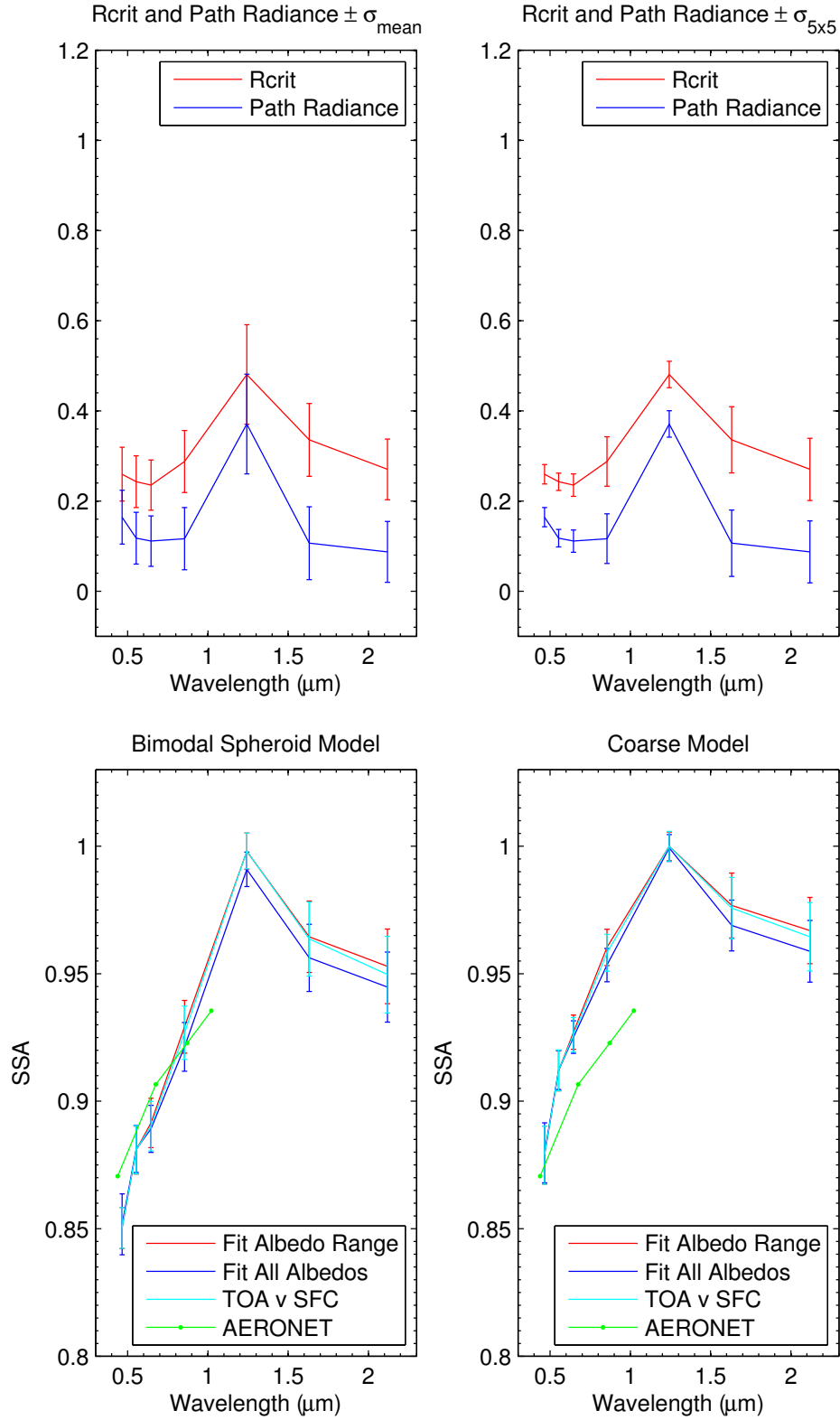


Figure D.39: Spectral plots of critical reflectance and path radiance (upper panels) and SSA retrieved for the bimodal spheroid model (lower left) and coarse model (lower right) for 11 December 2006 950 UTC (compared to +16 days) at the Banizoumbou site. Error bars for the SSA are the  $\sigma_{\text{mean}}$  estimates. AERONET retrievals for the day are also shown.

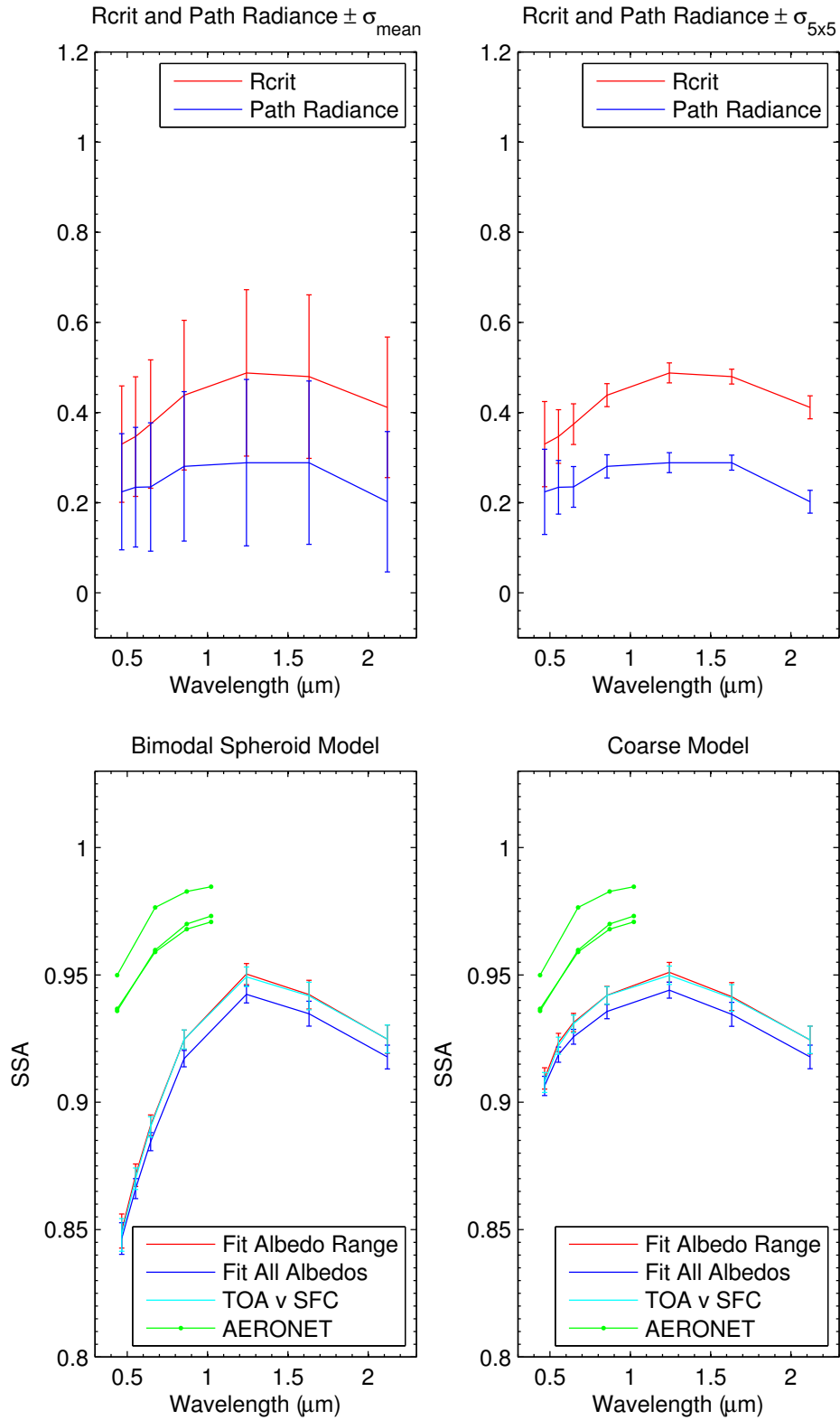


Figure D.40: Spectral plots of critical reflectance and path radiance (upper panels) and SSA retrieved for the bimodal spheroid model (lower left) and coarse model (lower right) for 13 December 2006 1245 UTC (compared to -16 days) at the Banizoumbou site. Error bars for the SSA are the  $\sigma_{\text{mean}}$  estimates. AERONET retrievals for the day are also shown.

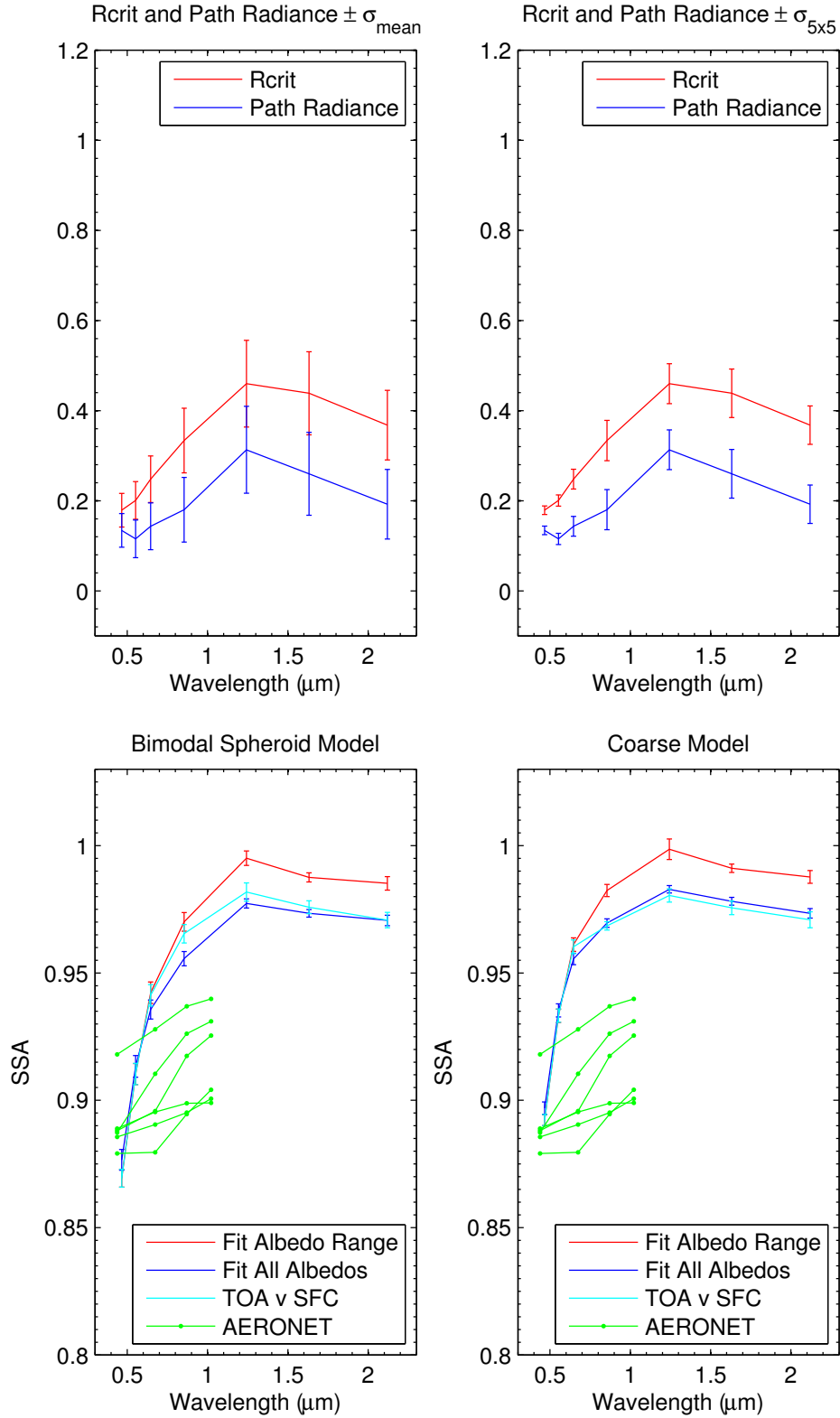


Figure D.41: Spectral plots of critical reflectance and path radiance (upper panels) and SSA retrieved for the bimodal spheroid model (lower left) and coarse model (lower right) for 14 December 2006 1020 UTC (compared to -16 days) at the Banizoumbou site. Error bars for the SSA are the  $\sigma_{\text{mean}}$  estimates. AERONET retrievals for the day are also shown.

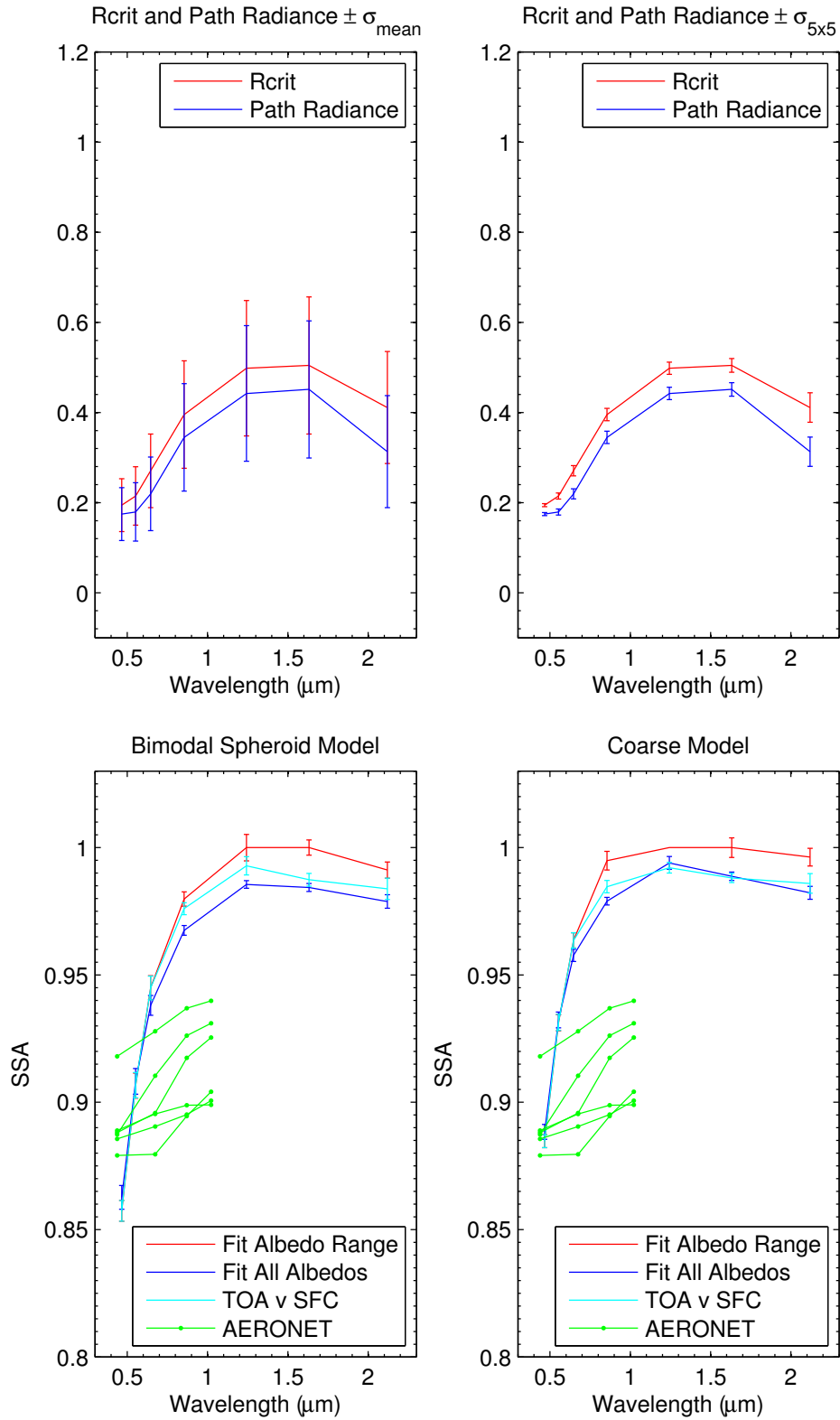


Figure D.42: Spectral plots of critical reflectance and path radiance (upper panels) and SSA retrieved for the bimodal spheroid model (lower left) and coarse model (lower right) for 14 December 2006 1325 UTC (compared to -16 days) at the Banizoumbou site. Error bars for the SSA are the  $\sigma_{\text{mean}}$  estimates. AERONET retrievals for the day are also shown.